

HIGH DIELECTRIC CONSTANT 0-3 CERAMIC-POLYMER COMPOSITES

Except where reference is made to the work of others, the work described in this dissertation is my own or was done in collaboration with my advisory committee. This dissertation does not include proprietary or classified information.

Xiaobing Shan

Certificate of Approval:

Dong-Joo Kim
Associate Professor
Materials Engineering

Zhongyang Cheng, Chair
Associate Professor
Materials Engineering

Jeffrey Fergus
Associate Professor
Materials Engineering

Maria Lujan Auad
Assistant Professor
Polymer and Fiber Engineering

George T. Flowers
Dean
Graduate School

HIGH DIELECTRIC CONSTANT 0-3 CERAMIC-POLYMER COMPOSITES

Xiaobing Shan

A Dissertation

Submitted to

the Graduate Faculty of

Auburn University

in Partial Fulfillment of the

Requirements for the

Degree of

Doctor of Philosophy

Auburn, Alabama

August 10, 2009

HIGH DIELECTRIC CONSTANT 0-3 CERAMIC-POLYMER COMPOSITES

Xiaobing Shan

Permission is granted to Auburn University to make copies of this dissertation at its discretion, upon the request of individuals or institutions and at their expense.
The author reserves all publication rights.

Signature of Author

Date of Graduation

VITA

Xiaobing Shan, son of Dexi Shan and Fengling Lu, was born on July 17, 1977, in the city of Nanjing, China. He entered Yancheng Institute of Technology in August 1996 and graduated in June 2000 with Bachelor degree in Materials Engineering. He joined the graduate program in Nanjing University of Technology in August 2000 and graduated with Master degree in Materials Science in June 2003. He then got involved with fundamental research in Shanghai Institute of Ceramics, Chinese Academy of Sciences (CAS) to work as a research assistant until July 2004. He joined the graduate program at Auburn University in August 2004 to pursue his Ph.D degree in Materials Engineering.

DISSERTATION ABSTRACT

HIGH DIELECTRIC CONSTANT 0-3 CERAMIC-POLYMER COMPOSITES

Xiaobing Shan

Doctor of Philosophy, August 10, 2009
(M.S., Nanjing University of Technology, 2003)
(B.S., Yancheng Institute of Technology, 2000)

327 Typed Pages

Directed by Zhongyang Cheng

0-3 ceramic-polymer composites using both nano-size and micro-size $\text{CaCu}_3\text{Ti}_4\text{O}_{12}$ ceramic particles were studied.

The micro-size ceramic particles were prepared from the $\text{CaCu}_3\text{Ti}_4\text{O}_{12}$ pellets by milling. The $\text{CaCu}_3\text{Ti}_4\text{O}_{12}$ ceramics were prepared using conventional solid-state reaction under different conditions, such as molding pressure, milling media and time, and calcination temperature and time. Based on the analysis of the dielectric spectrum, it was found that the dielectric responses of $\text{CaCu}_3\text{Ti}_4\text{O}_{12}$ ceramics are determined by three different processes. The effect of thickness of the ceramics on the dielectric properties was observed and studied. Although the dielectric response at low frequency increases with decreasing thickness, the dielectric behavior for the high frequency relaxation process is weakly dependent on thickness.

0-3 composites with different concentrations (0-50 vo% $\text{CaCu}_3\text{Ti}_4\text{O}_{12}$ ceramics) were prepared using solution casting. However, a clear polymer-rich layer was found in

as-cast film due to the poor wettability between ceramic and polymer matrix. The HP was used to modify the morphology of the composites. Different configurations were studied for the HP process. Composites with a dielectric constant of 510 at 1 kHz were obtained in 50vol% $\text{CaCu}_3\text{Ti}_4\text{O}_{12}$ composite with CC HP at room temperature. It was found that the relaxation time of the major relaxation process obtained in the composite changes with processing condition, such as annealing, HP and concentration. It indicates that the interfacial layers between ceramic particles and polymer matrix play an important role on the dielectric response of the composite. As for the HP samples, it was interestingly observed that as HP time changes, there is a critical HP time at which the composite exhibits a much higher dielectric constant. Based on the dielectric spectrum of the composites at different temperatures, it was concluded that the loss of the composites at low frequency is controlled by a relaxation process.

For the $\text{CaCu}_3\text{Ti}_4\text{O}_{12}/\text{P}(\text{VDF-TrFE})$ composite, the dielectric response is strongly dependent on temperature due to the fact that the dielectric constant of $\text{P}(\text{VDF-TrFE})$ is strongly dependent of temperature. However, as for the $\text{CaCu}_3\text{Ti}_4\text{O}_{12}/\text{P}(\text{VDF-CTFE})$ composites, the dielectric constant of the composite is almost independent of temperature and the composite has a small loss. For example, composites with a dielectric constant of 151 and loss of 0.14 at 1 kHz were obtained at room temperature. A clear difference between nano-size and micro-size $\text{CaCu}_3\text{Ti}_4\text{O}_{12}$ composite was observed. Moreover, It was also found that the difference of dielectric constant between nano-size and micro-size particles in $\text{P}(\text{VDF-CTFE})$ copolymer is much smaller than that in $\text{P}(\text{VDF-TrFE})$ copolymer.

ACKNOWLEDGEMENTS

I would like to give my gratitude to my advisor, Dr. Zhongyang Cheng, who has guided my thinking to reach my full potential through the completion of my research and dissertation in the past years. He has provided solid support and motivation in helping me reach my goals, both professionally and personally during my every bit of stay in Auburn.

I would like to express my sincere thanks to all my committee members, Dr. Maria Lujan Auad, Dr. Jeffrey Fergus and Dr. Dong-Joo Kim for their kind support and valuable suggestions in making my dream come true. Thanks to Mr. Roy Howard, Mr. L.C. Mathison and Mr. Levar Odum for providing continuous support for all these years.

I would like to gratefully acknowledge all my group members, Dr. Zhimin Li, Dr. Suiqiong Li, Lisa Orona, Yuhong Wang, Xin Yang, Liling Fu, Kewei Zhang, Levar Odum, Peixuan Wu, Lin Zhang, Zack Lamb, David Busby for all their supports and help to my research. Especially many thanks to Dr. Suiqiong Li, Levar Odum, Zack Lamb, Lin Zhang, Peixuan Wu, and Houmin Li for their kind generous help to my project. I appreciate the encouragement of all my friends and I would like to mention Dr. Nofrijon Sofyan, Dr. Li Chen and many more.

I am indebted to my family, especially my mother for her encouragement and support throughout my entire education. Without her support and encouragement, it is hard to imagine how much I can complete. Finally, I would like to acknowledge the financial support for this work from an Auburn University Competitive Research Grant and 3M Non-Tenured Faculty Grant. I also appreciated the support and research work at Pacific Northwest National Lab (PNNL).

Dedicated to my wonderful mother, who was not well educated, but gave me so much courage, strength and faith to complete my Doctor of Philosophy degree.

Style manual or journal used: Macromolecules

Computer software used: Microsoft Word, Excel, PowerPoint

TABLE OF CONTENTS

LIST OF FIGURES	xiv
LIST OF TABLES	xxxii

CHAPTER 1

INTRODUCTION AND RESEARCH OBJECTIVES	1
1.1 Theory of Dielectric Materials.....	2
1.1.1 Permittivity	2
1.1.2 Origins of Permittivity	3
1.1.3 Dielectric Relaxation	7
1.1.4 Cole and Cole plot	9
1.2 Classification of Dielectric Materials	10
1.2.1 Nonpolar Materials	10
1.2.2 Polar Materials.....	10
1.2.2.1 Ferroelectric Ceramic and Polymer.....	11
1.2.2.2 Ferroelectric Polymers	16
1.3 Energy Storage Density	17
1.4 Applications of Dielectric Materials.....	18
1.5 Calcium Copper Titanate $\text{CaCu}_3\text{Ti}_4\text{O}_{12}$	20
1.5.1 Crystallographic Structure of $\text{CaCu}_3\text{Ti}_4\text{O}_{12}$	21
1.5.2 Origin of Colossal Dielectric Response	23
1.6 Ceramic-Polymer Composites	27
1.6.1 General Concepts for Composites	27
1.6.2 Mixing Rule for Permittivity in Two-Phase Composites	29
1.7 Current Developments of Polymer-Matrix Composite.....	32
1.7.1 Ferroelectric Ceramic/Polymer Composite.....	32
1.7.2 Conductive Filler/Polymer Composites	34

1.8 Interface Effect in Composites.....	35
1.8.1 Interfacial Forces	38
1.8.2 Dielectric Properties.....	39
1.9 Objectives of This Research	44
References.....	45
CHAPTER 2	
MATERIALS PREPARATION AND CHARACTERIZATION METHODS.....	53
2.1 Ceramic Synthesis.....	53
2.2 Ceramic-Polymer 0-3 Composite Fabrication	56
2.2.1 Ceramic-Polymer 0-3 Composite Casting Procedure	56
2.2.2 Optimization of Ceramic-Polymer 0-3 Composite	58
2.2.2.1 Hot Pressing Process	58
2.2.2.2 Silane Coupling Process.....	60
2.2.2.3 Annealing Process	61
2.3 Materials Characterization Methods	61
2.3.1 Crystalline Structure Determination Using Wide Angle X-ray Diffraction	61
2.3.2 Microstructure Analysis Using SEM.....	61
2.3.3 Dielectric Analysis Using Impedance Analyzer.....	64
References.....	66
CHAPTER 3	
PROCESSING AND CHARACTERIZATION OF $\text{CaCu}_3\text{Ti}_4\text{O}_{12}$ CERAMIC.....	67
3.1 Introduction.....	67
3.2 Experimental.....	67
3.3 Results and Discussion	68
3.3.1 Solid State Synthesis.....	68
3.3.2 Effect of Processing On Dielectric Properties	71
3.3.2.1 Effect of Molding Pressure.....	71
3.3.2.2 Effect of Ball Milling Time and Sintering time	76
3.3.2.3 Effect of Calcination Temperature and Milling Solvent.....	82

3.3.2.4 Effect of Thickness on Dielectric Properties.....	89
3.3.2.4 Effect of CuO Doping on Dielectric Properties	98
3.3.2.5 Effect of the Annealing Time on Dielectric Properties	112
3.3.2.6 Impedance Analysis	115
3.4 Summary	118
References.....	119

CHAPTER 4

PROCESS INFLUENCE ON THE DIELECTRIC PROPERTIES OF

CaCu ₃ Ti ₄ O ₁₂ /P(VDF-TrFE) COMPOSITES	120
4.1 Introduction.....	120
4.2 Experimental	120
4.3 Results and Discussion	121
4.3.1 Dielectric Behavior and Annealing Effect.....	121
4.3.2 Hot Pressing Effect	129
4.3.3 Multiple-Layer Configuration.....	140
4.3.3.1 Dielectric Response using PC Hot Pressing.....	140
4.3.3.2 Dielectric Response using CC Hot Pressing	147
4.3.3.3 Uniformity of 0-3 Composite under CC Hot Pressing.....	162
4.3.3.4 Temperature Dependent of Dielectric Response.....	171
4.3.3.5 Impedance Analysis	191
4.3.4 P-E Hysteresis Loop	199
4.3.5 Polymer Matrix Effect on Dielectric Behavior.....	205
4.3.5.1 Dielectric Behavior.....	205
4.3.5.2 Hot Pressing Effect.....	210
4.3.5.3 Temperature Dependent of Dielectric Response.....	216
4.4 Summary	224
References.....	226

CHAPTER 5

STUDY OF DIELECTRIC BEHAVIOR ON THE $\text{CaCu}_3\text{Ti}_4\text{O}_{12}$ -BASED COMPOSITES

.....	227
5.1 Introduction.....	227
5.2 Experimental.....	228
5.3 Results and Discussion	228
5.3.1 Size Effect on Dielectric Behavior	228
5.3.1.1 Dielectric Behavior.....	229
5.3.1.2 Hot Pressing Effect.....	233
5.3.1.3 Hot Pressing Time on Dielectric Properties	239
5.3.1.4 Temperature Dependent of Dielectric Response.....	249
5.3.1.5 P-E Hysteresis Loop.....	253
5.3.1.6 Polymer Matrix Effect on Dielectric Behavior	262
5.3.2 Silane Coupling Effect on Dielectric Behavior	268
5.3.2.1 Theoretical Calculation for Silane Coupling Agent.....	268
5.3.3.1 Dielectric Behavior.....	271
5.3.3.3 Silane Concentration Effect on Dielectric Behavior	278
5.3.3.4 Temperature Dependent of Dielectric Response.....	282
5.3.3.5 Size Effect on Dielectric Behavior.....	285
5.4 Summary.....	290
References.....	291

CHAPTER 6

CONCLUSION AND FUTURE WORKS

6.1 Summary of Results and Conclusions	292
6.2 Future Works	293

LIST OF FIGURES

Figure 1-1 Schematics of (a) electron polarization, (b) ionic polarization, (c) orientational polarization, (d) space charge polarization.	5
Figure 1-2 The influence of the polarization: (a) real part of relative permittivity and (b) imaginary part of relative permittivity with frequency.....	6
Figure 1-3 Argand diagram for dielectric material with only one relaxation time based on Debye equation.	8
Figure 1-4 The schematic of ϵ'_r , ϵ''_r and $\tan \delta$ as functions of ω based on Debye equation.....	8
Figure 1-5 The Cole-Cole plot for dielectric material with a set of relaxation time based on Cole-cole equation.	10
Figure 1-6 P-E loop of ferroelectric.....	13
Figure 1-7 Effect of grain size on permittivity of BaTiO_3^4 . (Relative permittivity is represented by ϵ'_r , which is described in Section 1.1).....	13
Figure 1-8 Dielectric permittivity of PMN: (a) at various amplitudes, E_m (1-0.01, 2-0.5, 3-1, 4-1.5, 5-2 kV/cm), and (b) various frequencies, ω (1-1 kHz, 2-100 Hz, 3-20 Hz) of the ac field ³⁴ . (ϵ' is equivalent to ϵ'_r , which is described in Section 1.1).....	14
Figure 1-9 Relationship of electric displacement \vec{D} vs. electric field \vec{E} : (a) linear; (b) nonlinear with positive curvature; (c) nonlinear with negative curvature.	17
Figure 1-10 The classified categories of dielectric materials ⁵⁶ . (ϵ' is equivalent to ϵ'_r , which is described in Section 1.1).	19
Figure 1-11 The temperature dependence of dielectric constant and loss.....	20
Figure 1-12 The structure of $\text{CaCu}_3\text{Ti}_4\text{O}_{12}$ (Cu-blue, Oxygen-red, Ca-yellow) ⁶¹	22
Figure 1-13 The schematic of twin boundary in $\text{CaCu}_3\text{Ti}_4\text{O}_{12}$ ⁷²	24

Figure 1-14 (a) Temperature-dependent dielectric constants and (b) conductivities of single-crystalline $\text{CaCu}_3\text{Ti}_4\text{O}_{12}$ with sputter gold (solid lines) and silver-paint contacts (symbols) at various frequencies ⁷⁸ . The dashed and dashed-dotted lines in (b) show an estimate of the intrinsic bulk dc conductivity and the contribution of the insulating layer. (ϵ' is equivalent to ϵ'_r , which is described in Section 1.1).	25
Figure 1-15 (a) Frequency-dependent dielectric constants, (b) loss, and (c) conductivities of single crystalline $\text{CaCu}_3\text{Ti}_4\text{O}_{12}$ with silver-paint contacts at various temperatures ⁷⁸ . (ϵ' and ϵ'' are equivalent to ϵ'_r and ϵ''_r , respectively, which are described in Section 1.1)	26
Figure 1-16 Ten dimension patterns in diphasic composites ⁷⁹	28
Figure 1-17 Schematic of (a) parallel and (b) series connections.	29
Figure 1-18 Schematic of dielectric constant of two phases 1 and 2 vs. their volume fraction in the mixture: 1, parallel connection; 2, series connection; 3, real composite...	30
Figure 1-19 (a) percentage volume of interface as function of interface thickness d for particle sizes 10, 1 and 0.5 nm. (b) Schematic of particle A from micrometric to nanometric and then to sub-nanometric size. The interface increasingly dominates ¹⁰³	36
Figure 1-20 Interfacial regions as a function of filler particle size. The filler is shown in red, the interfacial region in dark blue and bulk polymer in pale blue. (a) Large particle produce low radius of curvature and relative less polymer in the interfacial regions. (b) The same volume of filler broken into small particles creates a high radius of curvature and more polymer in the interfacial region ¹⁰⁴	37
Figure 1-21 Schematic of electrical layers of extended interface ¹⁰³	39
Figure 1-22 The dielectric response vs. alumina volume fraction at 100 kHz and 25°C ¹¹² . (ϵ is equivalent to ϵ'_r , which is described in Section 1.1).	42
Figure 1-23 The correlation between the interfacial area and the dielectric enhancement in PI-alumina nanocomposite ¹¹² . (ϵ is equivalent to ϵ'_r , which is described in Section 1.1).	42
Figure 1-24 Comparison of the Vo-Shi model prediction with experimental results on PI-alumina nanocomposites and epoxy-(PMN-PT) composites, respectively. Also shown are the prediction by Maxwell-wagner rule for both systems ¹¹² . (ϵ is equivalent to ϵ'_r , which is described in Section 1.1. K is a constant that is dependent on the degree of particle clustering influencing the surface area and the thickness of the interface region between the nanoparticles.)	43
Figure 2-1 Image of 48000 Barnstead Thermolyne furnace.	54

Figure 2-2 Image of Al ₂ O ₃ crucible and sintered ceramic pellet	55
Figure 2-3 SEM image of milled CaCu ₃ Ti ₄ O ₁₂ powder.	56
Figure 2-4 Particle size distribution of milled CaCu ₃ Ti ₄ O ₁₂ powder.	57
Figure 2-5 Image of flexible CaCu ₃ Ti ₄ O ₁₂ - P(VDF-TrFE) 0-3 composite.....	57
Figure 2-6 Process flowchart for CaCu ₃ Ti ₄ O ₁₂ -P(VDF-TrFE) 0-3 composite fabrication.	58
Figure 2-7 The schematic of (a) PC hot pressing and (b) CC hot pressing.	59
Figure 2-8 The schematic of silane coupling agent reaction process with P(VDF-TrFE) and CaCu ₃ Ti ₄ O ₁₂	60
Figure 2-9 Image of Pelco SC-6 sputter coater.....	63
Figure 2-10 Measurement setup of Scanning Electron Microscopy (SEM).....	63
Figure 2-11 Image of mask with diameter of 1.7 millimeter.	65
Figure 2-12 Image of Agilent 4294A impedance analyzer.....	65
Figure 2-13 Setup of home-made probe for temperature dependence measurement.	66
Figure 3-1 XRD patterns on the CaCu ₃ Ti ₄ O ₁₂ : (a) calcination at 1075°C after 48, 72 and 96 hrs milling; (b) calcination at 900°C after 48, 72 and 96 hrs milling according to the procedure #1 and 2 in table 3-1.....	70
Figure 3-2 Dielectric response vs. frequency for CaCu ₃ Ti ₄ O ₁₂ samples with 24 hrs D.I water ball milling, calcinated at 1075 °C, and then sintered at 1075 °C for 1 hr, 24 hrs, 48 hrs and 72 hrs using (a) 2500 PSI, and (b) 3000 PSI pellet molding pressure.	73
Figure 3-3 SEM fractographs of CaCu ₃ Ti ₄ O ₁₂ after 24 hrs D.I water ball milling, calcinated at 1075 °C, sintered at 1075 °C for (a) 1 hrs, (b) 24 hrs, (c) 48 hrs (d) 72 hr using 2500 PSI pellet molding pressure.....	74
Figure 3-4 SEM fractographs of CaCu ₃ Ti ₄ O ₁₂ after 24 hrs D.I water ball milling, calcinated at 1075 °C, sintered at 1075 °C for (a) 1 hr, (b) 24 hrs, (c) 48 hrs (d) 72 hrs by 3000 PSI pellet molding pressure.	75
Figure 3-5 Dielectric response vs. frequency for samples: (a), (b) and (c) after 48, 72 and 96 hrs milling respectively, calcining at 1075 °C for 12 hrs, then sintering at 1075 °C for 24, 48, and 72 hrs according to procedure #1 in table 3-1.....	78

Figure 3-6 SEM fractographs of $\text{CaCu}_3\text{Ti}_4\text{O}_{12}$ for 48 hrs D.I water ball milling, calcining at 1075°C for 12 hrs, then sintering at 1075°C for (a) 24 hrs, (b) 48 hrs, (c) 72 hrs.....	79
Figure 3-7 SEM fractographs of $\text{CaCu}_3\text{Ti}_4\text{O}_{12}$ for 72 hrs D.I water ball milling, calcining at 1075°C for 12 hrs, then sintering at 1075°C for (a) 24 hrs, (b) 48 hrs, (c) 72 hrs.....	80
Figure 3-8 SEM fractographs of $\text{CaCu}_3\text{Ti}_4\text{O}_{12}$ for 96 hrs D.I water ball milling, calcining at 1075°C for 12 hrs, then sintering at 1075°C for (a) 24 hrs, (b) 48 hrs, (c) 72 hrs.....	81
Figure 3-9 Dielectric response vs. frequency for samples: (a), (b) and (c) after 48, 72 and 96 hrs milling respectively, then sintering for 24, 48, and 72 hrs according to procedure #2 in Table 3-1.....	84
Figure 3-10 SEM fractographs of $\text{CaCu}_3\text{Ti}_4\text{O}_{12}$ for 48 hrs D.I water ball milling, calcinated at 900°C , then sintering at 1075°C for (a) 24 hrs, (b) 48 hrs, (c) 72 hrs.	85
Figure 3-11 Dielectric response vs. frequency for samples: (a) after 72 hrs milling according to procedure #3 in Table 3-1; (b) after 72 hrs milling according to procedure #4 in Table 3-1.....	88
Figure 3-12 Dielectric response vs. frequency for samples with different sample thickness (1.60 mm, 0.78 mm, 0.60 mm and 0.36 mm, respectively) after 96 hrs milling and then 24 hrs sintering according to procedure #2 in Table 3-1.	91
Figure 3-13 Dielectric response vs. frequency for samples with different sample thickness (1.25 mm, 0.79 mm, 0.60 mm and 0.39 mm, respectively) after 96 hrs milling and then 48 hrs sintering according to procedure #2 in Table 3-1.	91
Figure 3-14 Dielectric response vs. frequency for samples with different sample thickness (1.13 mm, 0.81 mm, 0.60 mm and 0.38 mm, respectively) after 96 hrs milling and then 72 hrs sintering according to procedure #2 in Table 3-1.	92
Figure 3-15 Illustration of edge, middle, core areas in $\text{CaCu}_3\text{Ti}_4\text{O}_{12}$ ceramic pellet for SEM fractographs.	92
Figure 3-16 SEM fractographs of $\text{CaCu}_3\text{Ti}_4\text{O}_{12}$ after 96 hrs milling and then 24 hrs sintering according to procedure #2 in Table 3-1: (a) edge area, (b) middle area, (c) core area.	93
Figure 3-17 SEM fractographs of $\text{CaCu}_3\text{Ti}_4\text{O}_{12}$ after 96 hrs milling and then 48 hrs sintering according to procedure #2 in Table 3-1: (a) edge area, (b) middle area, (c) core area.	94
Figure 3-18 SEM fractographs of $\text{CaCu}_3\text{Ti}_4\text{O}_{12}$ after 96 hrs milling and then 72 hrs sintering according to procedure #2 in Table 3-1: (a) edge area, (b) middle area, (c) core area.	95

Figure 3-19 Cole-cole plot of the dielectric data of samples with different sample thickness (0.78 mm, 0.60 mm and 0.36 mm, respectively) after 96 hrs milling and then 24 hrs sintering according to procedure #2 in Table 3-1.	96
Figure 3-20 Cole-cole plot of the dielectric data of samples with different sample thickness (0.79 mm, 0.60 mm and 0.39 mm, respectively) after 96 hrs milling and then 48 hrs sintering according to procedure #2 in Table 3-1.	96
Figure 3-21 Cole-cole plot of the dielectric data of samples with different sample thickness (0.81 mm, 0.60 mm and 0.38 mm, respectively) after 96 hrs milling and then 72 hrs sintering according to procedure #2 in Table 3-1.	97
Figure 3-22 The relationship of $\Delta\epsilon$ ($\epsilon_{rs}-\epsilon_{r\infty}$) vs. sample thickness after 96 hrs milling and then 24, 48 and 72 hrs sintering according to procedure #2 in Table 3-1.....	97
Figure 3-23 Dielectric response vs. frequency of the $\text{CaCu}_3\text{Ti}_4\text{O}_{12}$ after 72 hrs D.I water ball milling according to procedure #1 in table 3-1 with (a) 5 % CuO doping; (b) 10 % CuO doping.....	99
Figure 3-24 SEM fractographs and EDS analysis results of $\text{CaCu}_3\text{Ti}_4\text{O}_{12}$ with 5% CuO dopant sintering for 24 hrs at site #1.....	100
Figure 3-25 SEM fractographs and EDS analysis results of $\text{CaCu}_3\text{Ti}_4\text{O}_{12}$ with 5% CuO dopant sintering for 24 hrs at site #2.....	101
Figure 3-26 SEM fractographs and EDS analysis results of $\text{CaCu}_3\text{Ti}_4\text{O}_{12}$ with 5% CuO dopant sintering for 48 hrs at site #1.....	102
Figure 3-27 SEM fractographs and EDS analysis results of $\text{CaCu}_3\text{Ti}_4\text{O}_{12}$ with 5% CuO dopant sintering for 48 hrs at site #2.....	103
Figure 3-28 SEM fractographs and EDS analysis results of $\text{CaCu}_3\text{Ti}_4\text{O}_{12}$ with 5% CuO dopant sintering for 72 hrs at site #1.....	104
Figure 3-29 SEM fractographs and EDS analysis results of $\text{CaCu}_3\text{Ti}_4\text{O}_{12}$ with 5% CuO dopant sintering for 72 hrs at site #2.....	105
Figure 3-30 SEM fractographs and EDS analysis results of $\text{CaCu}_3\text{Ti}_4\text{O}_{12}$ with 10% CuO dopant sintering for 24 hrs at site #1.....	106
Figure 3-31 SEM fractographs and EDS analysis results of $\text{CaCu}_3\text{Ti}_4\text{O}_{12}$ with 10% CuO dopant sintering for 24 hrs at site #2.....	107
Figure 3-32 SEM fractographs and EDS analysis results of $\text{CaCu}_3\text{Ti}_4\text{O}_{12}$ with 10% CuO dopant sintering for 48 hrs at site #1.....	108

Figure 3-33 SEM fractographs and EDS analysis results of $\text{CaCu}_3\text{Ti}_4\text{O}_{12}$ with 10% CuO dopant sintering for 48 hrs at site #2.....	109
Figure 3-34 SEM fractographs and EDS analysis results of $\text{CaCu}_3\text{Ti}_4\text{O}_{12}$ with 10% CuO dopant sintering for 72 hrs at site #1.....	110
Figure 3-35 SEM fractographs and EDS analysis results of $\text{CaCu}_3\text{Ti}_4\text{O}_{12}$ with 10% CuO dopant sintering for 72 hrs at site #2.....	111
Figure 3-36 Dielectric response vs. frequency for $\text{CaCu}_3\text{Ti}_4\text{O}_{12}$ samples with initial 48 hrs milling according to procedure #1 in table 3-1: (a) post annealing in vacuum for different time at 1000 °C; (b) post annealing in flowing argon for different time at 1000 °C; (c) post annealing in flowing argon at different temperature for 1 hr.....	113
Figure 3-37 SEM fractographs of $\text{CaCu}_3\text{Ti}_4\text{O}_{12}$ with post annealing in flowing argon at 1000 °C for 10 hrs with magnification of : (a)-1 X150, (a)-2 X450, (a)-3 X450; for 24 hr: (b)-1 X150, (b)-2 X450, (b)-3 X450.....	114
Figure 3-38 Impedance plot of $\text{CaCu}_3\text{Ti}_4\text{O}_{12}$ calcinating at 1075 °C and then sintering at 1075 °C for 24, 48 and 72 hrs after (a) 48 hrs D.I water ball milling; (b) 72 hrs D.I water ball milling; (c) 96 hrs D.I water ball milling.....	116
Figure 3-39 Impedance plot of $\text{CaCu}_3\text{Ti}_4\text{O}_{12}$ calcinating at 900 °C and then sintering at 1075 °C for 24, 48 and 72 hrs after (a) 48 hrs D.I water ball milling; (b) 72 hrs D.I water ball milling; (c) 96 hrs D.I water ball milling.....	117
Figure 4-1 Dielectric response vs. frequency of pure P(VDF-TrFE) film: (a) casting at 123	
Figure 4-2 Dielectric response vs. frequency of 1 layer $\text{CaCu}_3\text{Ti}_4\text{O}_{12}$ /P(VDF-TrFE) composite (10 vol% CCTO) without annealing, with annealing in comparison with P(VDF-TrFE).....	123
Figure 4-3 Dielectric response vs. frequency of 1 layer $\text{CaCu}_3\text{Ti}_4\text{O}_{12}$ /P(VDF-TrFE) composite (20 vol% CCTO) without annealing, with annealing in comparison with P(VDF-TrFE).....	124
Figure 4-4 Dielectric response vs. frequency of 1 layer $\text{CaCu}_3\text{Ti}_4\text{O}_{12}$ /P(VDF-TrFE) composite (30 vol% CCTO) without annealing, with annealing in comparison with P(VDF-TrFE).....	124
Figure 4-5 Dielectric response vs. frequency of 1 layer $\text{CaCu}_3\text{Ti}_4\text{O}_{12}$ /P(VDF-TrFE) composite (40 vol% $\text{CaCu}_3\text{Ti}_4\text{O}_{12}$) without annealing, with annealing in comparison with P(VDF-TrFE).....	125

Figure 4-6 Dielectric response vs. frequency of 1 layer $\text{CaCu}_3\text{Ti}_4\text{O}_{12}/\text{P}(\text{VDF-TrFE})$ composite (50 vol% $\text{CaCu}_3\text{Ti}_4\text{O}_{12}$) without annealing, with annealing in comparison with $\text{P}(\text{VDF-TrFE})$	125
Figure 4-7 Dependence of dielectric response (1 kHz) on the $\text{CaCu}_3\text{Ti}_4\text{O}_{12}$ concentration for 1 layer $\text{CaCu}_3\text{Ti}_4\text{O}_{12}/\text{P}(\text{VDF-TrFE})$ composite at room temperature without annealing and with annealing respectively.....	126
Figure 4-8 Cole-cole plot of the dielectric data of (a) 1 layer and (b) 1 annealed layer $\text{CaCu}_3\text{Ti}_4\text{O}_{12}/\text{P}(\text{VDF-TrFE})$ composite with 10 to 50 vol% $\text{CaCu}_3\text{Ti}_4\text{O}_{12}$ powder at RT.	127
Figure 4-9 The relationship of relaxation time and $\text{CaCu}_3\text{Ti}_4\text{O}_{12}$ volume concentration between 1 layer and 1 annealed layer $\text{CaCu}_3\text{Ti}_4\text{O}_{12}/\text{P}(\text{VDF-TrFE})$ composite samples with 10 to 50 vol% $\text{CaCu}_3\text{Ti}_4\text{O}_{12}$ powder.....	128
Figure 4-10 Dielectric response vs. frequency of 1 layer $\text{CaCu}_3\text{Ti}_4\text{O}_{12}/\text{P}(\text{VDF-TrFE})$ composite with 10 vol% $\text{CaCu}_3\text{Ti}_4\text{O}_{12}$ powder: (a) without annealing; (b) with annealing.	131
Figure 4-11 Dielectric response vs. frequency of 1 layer $\text{CaCu}_3\text{Ti}_4\text{O}_{12}/\text{P}(\text{VDF-TrFE})$ composite with 20 vol% $\text{CaCu}_3\text{Ti}_4\text{O}_{12}$ powder: (a) without annealing; (b) with annealing.	132
Figure 4-12 Dielectric response vs. frequency of 1 layer $\text{CaCu}_3\text{Ti}_4\text{O}_{12}/\text{P}(\text{VDF-TrFE})$ composite with 30 vol% $\text{CaCu}_3\text{Ti}_4\text{O}_{12}$ powder: (a) without annealing; (b) with annealing.	133
Figure 4-13 Dielectric response vs. frequency of 1 layer $\text{CaCu}_3\text{Ti}_4\text{O}_{12}/\text{P}(\text{VDF-TrFE})$ composite with 40 vol% $\text{CaCu}_3\text{Ti}_4\text{O}_{12}$ powder: (a) without annealing; (b) with annealing.	134
Figure 4-14 Dielectric response vs. frequency of 1 layer $\text{CaCu}_3\text{Ti}_4\text{O}_{12}/\text{P}(\text{VDF-TrFE})$ composite with 50 vol% $\text{CaCu}_3\text{Ti}_4\text{O}_{12}$ powder: (a) without annealing; (b) with annealing.	135
Figure 4-15 Dependence of dielectric constant (1 kHz) on the $\text{CaCu}_3\text{Ti}_4\text{O}_{12}$ concentration using 1 layers hot pressing (HP) at room temperature: (a) without annealing; (b) with annealing.....	136
Figure 4-16 Cole-cole plot of the dielectric data of 1 layer HP annealed $\text{CaCu}_3\text{Ti}_4\text{O}_{12}/\text{P}(\text{VDF-TrFE})$ composite with 10 to 50 vol% $\text{CaCu}_3\text{Ti}_4\text{O}_{12}$ powder.....	137
Figure 4-17 Comparison of the present model predictions with experimental data for 1 HP layer $\text{CaCu}_3\text{Ti}_4\text{O}_{12}/\text{P}(\text{VDF-TrFE})$ sample.	138

Figure 4-18 Comparison of the present model predictions with experimental data for 1 layer HP annealed $\text{CaCu}_3\text{Ti}_4\text{O}_{12}/\text{P}(\text{VDF-TrFE})$ sample.	138
Figure 4-19 Dielectric response vs. frequency of the $\text{CaCu}_3\text{Ti}_4\text{O}_{12}/\text{P}(\text{VDF-TrFE})$ composites with 10 vol% $\text{CaCu}_3\text{Ti}_4\text{O}_{12}$ powder: (a) without annealing; (b) with annealing.	141
Figure 4-20 Dielectric response vs. frequency of the $\text{CaCu}_3\text{Ti}_4\text{O}_{12}/\text{P}(\text{VDF-TrFE})$ composites with 20 vol% $\text{CaCu}_3\text{Ti}_4\text{O}_{12}$ powder: (a) without annealing; (b) with annealing.	142
Figure 4-21 Dielectric response vs. frequency of the $\text{CaCu}_3\text{Ti}_4\text{O}_{12}/\text{P}(\text{VDF-TrFE})$ composites with 30 vol% $\text{CaCu}_3\text{Ti}_4\text{O}_{12}$ powder: (a) without annealing; (b) with annealing.	143
Figure 4-22 Dielectric response vs. frequency of the $\text{CaCu}_3\text{Ti}_4\text{O}_{12}/\text{P}(\text{VDF-TrFE})$ composites with 40 vol% $\text{CaCu}_3\text{Ti}_4\text{O}_{12}$ powder: (a) without annealing; (b) with annealing.	144
Figure 4-23 Dielectric response vs. frequency of the $\text{CaCu}_3\text{Ti}_4\text{O}_{12}/\text{P}(\text{VDF-TrFE})$ composites with 50 vol% $\text{CaCu}_3\text{Ti}_4\text{O}_{12}$ powder: (a) without annealing; (b) with annealing.	145
Figure 4-24 SEM fractographs of $\text{CaCu}_3\text{Ti}_4\text{O}_{12}/\text{P}(\text{VDF-TrFE})$ composites with 50 vol% $\text{CaCu}_3\text{Ti}_4\text{O}_{12}$ powder using hot pressing for 10 seconds, (a) 1 layer without hot pressing, (b) 2 layer PC pressing, (c) 3 layer PC pressing, (d) 4 layer PC pressing, (e) 5 layer PC pressing, (f) 6 layer PC pressing respectively.....	146
Figure 4-25 Dielectric response vs. frequency of the $\text{CaCu}_3\text{Ti}_4\text{O}_{12}/\text{P}(\text{VDF-TrFE})$ composites with 10~50 vol% $\text{CaCu}_3\text{Ti}_4\text{O}_{12}$ powder: (a) 2 layer; (b) 4 layer; (c) 6 layer after 10s CC HP.	150
Figure 4-26 Dielectric response vs. frequency of the $\text{CaCu}_3\text{Ti}_4\text{O}_{12}/\text{P}(\text{VDF-TrFE})$ composites with 10~50 vol% $\text{CaCu}_3\text{Ti}_4\text{O}_{12}$ powder: (a) 2 layer; (b) 4 layer; (c) 6 layer after 20s CC HP.	151
Figure 4-27 Dielectric response vs. frequency of the $\text{CaCu}_3\text{Ti}_4\text{O}_{12}/\text{P}(\text{VDF-TrFE})$ composites with 10~50 vol% $\text{CaCu}_3\text{Ti}_4\text{O}_{12}$ powder: (a) 2 layer; (b) 4 layer; (c) 6 layer after 30s CC HP.	152
Figure 4-28 Dependence of dielectric response (1 kHz) on the $\text{CaCu}_3\text{Ti}_4\text{O}_{12}$ concentration using 2 layer CC hot pressing (HP) for 10, 20, and 30s at room temperature.....	154
Figure 4-29 Dependence of dielectric response (1 kHz) on the $\text{CaCu}_3\text{Ti}_4\text{O}_{12}$ concentration using 4 layer CC hot pressing (HP) for 10, 20, and 30s at room temperature.....	154

Figure 4-30 Dependence of dielectric response (1 kHz) on the $\text{CaCu}_3\text{Ti}_4\text{O}_{12}$ concentration using 4 layer CC hot pressing (HP) for 10, 20, and 30s at room temperature.....	155
Figure 4-31 Comparison of the present model predictions with experimental data for 2 layer 30s CC-HP $\text{CaCu}_3\text{Ti}_4\text{O}_{12}/\text{P}(\text{VDF}-\text{TrFE})$ sample.	156
Figure 4-32 Comparison of the present model predictions with experimental data for 4 layer 30s CC-HP $\text{CaCu}_3\text{Ti}_4\text{O}_{12}/\text{P}(\text{VDF}-\text{TrFE})$ sample.	156
Figure 4-33 Comparison of the present model predictions with experimental data for 6 layer 30s CC-HP $\text{CaCu}_3\text{Ti}_4\text{O}_{12}/\text{P}(\text{VDF}-\text{TrFE})$ sample.	157
Figure 4-34 Comparison of the present model predictions with highest experimental data for 10, 20, 30, 40 and 50 vol% $\text{CaCu}_3\text{Ti}_4\text{O}_{12}/\text{P}(\text{VDF}-\text{TrFE})$ sample in this work.....	157
Figure 4-35 SEM fractographs of $\text{CaCu}_3\text{Ti}_4\text{O}_{12}/\text{P}(\text{VDF}-\text{TrFE})$ composites with 50 vol% CCTO powder using 2 layer CC hot pressing for: (a) 10s; (b) 20s; and (c) 30s respectively.	159
Figure 4-36 SEM fractographs of $\text{CaCu}_3\text{Ti}_4\text{O}_{12}/\text{P}(\text{VDF}-\text{TrFE})$ composites with 50 vol% CCTO powder using 4 layer CC hot pressing for: (a) 10s; (b) 20s; and (c) 30s respectively.	160
Figure 4-37 SEM fractographs of $\text{CaCu}_3\text{Ti}_4\text{O}_{12}/\text{P}(\text{VDF}-\text{TrFE})$ composites with 50 vol% CCTO powder using 6 layer CC hot pressing for: (a) 10s; (b) 20s; and (c) 30s respectively.	161
Figure 4-38 Dielectric response vs. frequency of 4 layer $\text{CaCu}_3\text{Ti}_4\text{O}_{12}/\text{P}(\text{VDF}-\text{TrFE})$ composites with 40 vol% $\text{CaCu}_3\text{Ti}_4\text{O}_{12}$ powder using CC HP for 10s: (a) Reliability measurements; (b) Reliability results (Error bars indicate standard deviation).....	163
Figure 4-39 Dielectric response vs. frequency of 4 layer $\text{CaCu}_3\text{Ti}_4\text{O}_{12}/\text{P}(\text{VDF}-\text{TrFE})$ composites with 40 vol% $\text{CaCu}_3\text{Ti}_4\text{O}_{12}$ powder using CC HP for 20s: (a) Reliability measurements; (b) Reliability results (Error bars indicate standard deviation).....	164
Figure 4-40 Dielectric response vs. frequency of 4 layer $\text{CaCu}_3\text{Ti}_4\text{O}_{12}/\text{P}(\text{VDF}-\text{TrFE})$ composites with 40 vol% $\text{CaCu}_3\text{Ti}_4\text{O}_{12}$ powder using CC HP for 30s: (a) Reliability measurements; (b) Reliability results (Error bars indicate standard deviation).....	165
Figure 4-41 Dielectric response vs. frequency of 4 layer $\text{CaCu}_3\text{Ti}_4\text{O}_{12}/\text{P}(\text{VDF}-\text{TrFE})$ composites with 50 vol% $\text{CaCu}_3\text{Ti}_4\text{O}_{12}$ powder using CC HP for 10s: (a) Reliability measurements; (b) Reliability results (Error bars indicate standard deviation).....	166
Figure 4-42 Dielectric response vs. frequency of 4 layer $\text{CaCu}_3\text{Ti}_4\text{O}_{12}/\text{P}(\text{VDF}-\text{TrFE})$ composites with 50 vol% $\text{CaCu}_3\text{Ti}_4\text{O}_{12}$ powder using CC HP for 20s: (a) Reliability measurements; (b) Reliability results (Error bars indicate standard deviation).....	167

Figure 4-43 Dielectric response vs. frequency of 4 layer $\text{CaCu}_3\text{Ti}_4\text{O}_{12}/\text{P}(\text{VDF-TrFE})$ composites with 40 vol% $\text{CaCu}_3\text{Ti}_4\text{O}_{12}$ powder using CC HP for 30s: (a) Reliability measurements; (b) Reliability results (Error bars indicate standard deviation).....	168
Figure 4-44 Temperature dependence of the 2, 4, 6 layer $\text{CaCu}_3\text{Ti}_4\text{O}_{12}/\text{P}(\text{VDF-TrFE})$ composites with 50 vol% $\text{CaCu}_3\text{Ti}_4\text{O}_{12}$ powder for: (a) 10s CC HP, (b) 20s CC HP, and (c) 30s CC HP, repectivley.	175
Figure 4-45 Temperature dependence of the $\text{CaCu}_3\text{Ti}_4\text{O}_{12}/\text{P}(\text{VDF-TrFE})$ composites with 50 vol% $\text{CaCu}_3\text{Ti}_4\text{O}_{12}$ powder using: (a) 2 layer CC HP, (b) 4 layer CC HP, and (c) 6 layer CC HP for 10, 20, and 30s, respectively.....	176
Figure 4-46 Dielectric response vs. frequency: (a) ϵ'_r vs. frequency, (b) $\tan \delta$ vs. frequency, (c) ϵ''_r vs. frequency of 2 layer 10s CC HP $\text{CaCu}_3\text{Ti}_4\text{O}_{12}/\text{P}(\text{VDF-TrFE})$ composite with 50 vol% $\text{CaCu}_3\text{Ti}_4\text{O}_{12}$ powder.....	177
Figure 4-47 Dielectric response vs. frequency: (a) ϵ'_r vs. frequency, (b) $\tan \delta$ vs. frequency, (c) ϵ''_r vs. frequency of 2 layer 20s CC HP $\text{CaCu}_3\text{Ti}_4\text{O}_{12}/\text{P}(\text{VDF-TrFE})$ composite with 50 vol% $\text{CaCu}_3\text{Ti}_4\text{O}_{12}$ powder.....	178
Figure 4-48 Dielectric response vs. frequency: (a) ϵ'_r vs. frequency, (b) $\tan \delta$ vs. frequency, (c) ϵ''_r vs. frequency of 2 layer 30s CC HP $\text{CaCu}_3\text{Ti}_4\text{O}_{12}/\text{P}(\text{VDF-TrFE})$ composite with 50 vol% $\text{CaCu}_3\text{Ti}_4\text{O}_{12}$ powder.....	179
Figure 4-49 Dielectric response vs. frequency: (a) ϵ'_r vs. frequency, (b) $\tan \delta$ vs. frequency, (c) ϵ''_r vs. frequency of 4 layer 10s CC HP $\text{CaCu}_3\text{Ti}_4\text{O}_{12}/\text{P}(\text{VDF-TrFE})$ composite with 50 vol% $\text{CaCu}_3\text{Ti}_4\text{O}_{12}$ powder.....	180
Figure 4-50 Dielectric response vs. frequency: (a) ϵ'_r vs. frequency, (b) $\tan \delta$ vs. frequency, (c) ϵ''_r vs. frequency of 4 layer 20s CC HP $\text{CaCu}_3\text{Ti}_4\text{O}_{12}/\text{P}(\text{VDF-TrFE})$ composite with 50 vol% $\text{CaCu}_3\text{Ti}_4\text{O}_{12}$ powder.....	181
Figure 4-51 Dielectric response vs. frequency: (a) ϵ'_r vs. frequency, (b) $\tan \delta$ vs. frequency, (c) ϵ''_r vs. frequency of 4 layer 30s CC HP $\text{CaCu}_3\text{Ti}_4\text{O}_{12}/\text{P}(\text{VDF-TrFE})$ composite with 50 vol% $\text{CaCu}_3\text{Ti}_4\text{O}_{12}$ powder.....	182
Figure 4-52 Dielectric response vs. frequency: (a) ϵ'_r vs. frequency, (b) $\tan \delta$ vs. frequency, (c) ϵ''_r vs. frequency of 6 layer 10s CC HP $\text{CaCu}_3\text{Ti}_4\text{O}_{12}/\text{P}(\text{VDF-TrFE})$ composite with 50 vol% $\text{CaCu}_3\text{Ti}_4\text{O}_{12}$ powder.....	183
Figure 4-53 Dielectric response vs. frequency: (a) ϵ'_r vs. frequency, (b) $\tan \delta$ vs. frequency, (c) ϵ''_r vs. frequency of 6 layer 20s CC HP $\text{CaCu}_3\text{Ti}_4\text{O}_{12}/\text{P}(\text{VDF-TrFE})$ composite with 50 vol% $\text{CaCu}_3\text{Ti}_4\text{O}_{12}$ powder.....	184

Figure 4-54 Dielectric response vs. frequency: (a) ϵ'_r vs. frequency, (b) $\tan \delta$ vs. frequency, (c) ϵ''_r vs. frequency of 6 layer 30s CC HP $\text{CaCu}_3\text{Ti}_4\text{O}_{12}/\text{P}(\text{VDF-TrFE})$ composite with 50 vol% $\text{CaCu}_3\text{Ti}_4\text{O}_{12}$ powder.....	185
Figure 4-55 The relationship of $\text{Ln}(\epsilon''_r)$ vs. $\text{Ln}(f)$ of 6 layer 10s CC HP $\text{CaCu}_3\text{Ti}_4\text{O}_{12}/\text{P}(\text{VDF-TrFE})$ composite with 50 vol% $\text{CaCu}_3\text{Ti}_4\text{O}_{12}$ powder.....	186
Figure 4-56 The relationship of $\text{Ln}(\epsilon''_r)$ vs. $\text{Ln}(f)$ of 6 layer 20s CC HP $\text{CaCu}_3\text{Ti}_4\text{O}_{12}/\text{P}(\text{VDF-TrFE})$ composite with 50 vol% $\text{CaCu}_3\text{Ti}_4\text{O}_{12}$ powder.....	186
Figure 4-57 The relationship of $\text{Ln}(\epsilon''_r)$ vs. $\text{Ln}(f)$ of 6 layer 30s CC HP $\text{CaCu}_3\text{Ti}_4\text{O}_{12}/\text{P}(\text{VDF-TrFE})$ composite with 50 vol% $\text{CaCu}_3\text{Ti}_4\text{O}_{12}$ powder.....	187
Figure 4-58 The relationship of $\text{Ln}(\epsilon''_r)$ vs. temperature of 6 layer 10s CC HP $\text{CaCu}_3\text{Ti}_4\text{O}_{12}/\text{P}(\text{VDF-TrFE})$ composite with 50 vol% $\text{CaCu}_3\text{Ti}_4\text{O}_{12}$ powder.....	189
Figure 4-59 The relationship of $\text{Ln}(\epsilon''_r)$ vs. temperature of 6 layer 20s CC HP $\text{CaCu}_3\text{Ti}_4\text{O}_{12}/\text{P}(\text{VDF-TrFE})$ composite with 50 vol% $\text{CaCu}_3\text{Ti}_4\text{O}_{12}$ powder.....	189
Figure 4-60 The relationship of $\text{Ln}(\epsilon''_r)$ vs. temperature of 6 layer 30s CC HP $\text{CaCu}_3\text{Ti}_4\text{O}_{12}/\text{P}(\text{VDF-TrFE})$ composite with 50 vol% $\text{CaCu}_3\text{Ti}_4\text{O}_{12}$ powder.....	190
Figure 4-61 Cole-cole plot of the dielectric data of 2, 4 and 6 layer $\text{CaCu}_3\text{Ti}_4\text{O}_{12}/\text{P}(\text{VDF-TrFE})$ composite with 50 vol% $\text{CaCu}_3\text{Ti}_4\text{O}_{12}$ powder and HP for (a) 10s, (b) 20s and (c) 30s, respectively.....	193
Figure 4-62 Cole-cole plot of the dielectric data of (a) 2 layer, (b) 4 layer and (c) 6 layer $\text{CaCu}_3\text{Ti}_4\text{O}_{12}/\text{P}(\text{VDF-TrFE})$ composite with 50vol% $\text{CaCu}_3\text{Ti}_4\text{O}_{12}$ powder and HP for 10s, 20s and 30s, respectively.	194
Figure 4-63 Cole-cole plot of the dielectric data of 6 layer $\text{CaCu}_3\text{Ti}_4\text{O}_{12}/\text{P}(\text{VDF-TrFE})$ composite with 10 to 50vol% $\text{CaCu}_3\text{Ti}_4\text{O}_{12}$ powder and HP for (a) 10s, (b) 20s and (c) 30s, respectively.....	195
Figure 4-64 Polarization electric hysteresis loop for pure $\text{P}(\text{VDF-TrFE})$	200
Figure 4-65 Polarization electric hysteresis loop for 1 layer $\text{CaCu}_3\text{Ti}_4\text{O}_{12}/\text{P}(\text{VDF-TrFE})$ composites with 10 vol% $\text{CaCu}_3\text{Ti}_4\text{O}_{12}$ powder.	200
Figure 4-66 Polarization electric hysteresis loop for 1 layer $\text{CaCu}_3\text{Ti}_4\text{O}_{12}/\text{P}(\text{VDF-TrFE})$ composites with 20 vol% $\text{CaCu}_3\text{Ti}_4\text{O}_{12}$ powder.	201
Figure 4-67 Polarization electric hysteresis loop for 1 layer $\text{CaCu}_3\text{Ti}_4\text{O}_{12}/\text{P}(\text{VDF-TrFE})$ composites with 30 vol% $\text{CaCu}_3\text{Ti}_4\text{O}_{12}$ powder.	201

Figure 4-68 Polarization electric hysteresis loop for 1 layer $\text{CaCu}_3\text{Ti}_4\text{O}_{12}/\text{P}(\text{VDF-TrFE})$ composites with 40 vol% $\text{CaCu}_3\text{Ti}_4\text{O}_{12}$ powder.	202
Figure 4-69 Polarization electric hysteresis loop for 1 layer $\text{CaCu}_3\text{Ti}_4\text{O}_{12}/\text{P}(\text{VDF-TrFE})$ composites with 50 vol% $\text{CaCu}_3\text{Ti}_4\text{O}_{12}$ powder.	202
Figure 4-70 Polarization electric hysteresis loop for 2 layer $\text{CaCu}_3\text{Ti}_4\text{O}_{12}/\text{P}(\text{VDF-TrFE})$ composites with 50 vol% $\text{CaCu}_3\text{Ti}_4\text{O}_{12}$ powder using CC HP for 10s.	203
Figure 4-71 Polarization electric hysteresis loop for 4 layer $\text{CaCu}_3\text{Ti}_4\text{O}_{12}/\text{P}(\text{VDF-TrFE})$ composites with 50 vol% $\text{CaCu}_3\text{Ti}_4\text{O}_{12}$ powder using CC HP for 10s.	203
Figure 4-72 Polarization electric hysteresis loop for 6 layer $\text{CaCu}_3\text{Ti}_4\text{O}_{12}/\text{P}(\text{VDF-TrFE})$ composites with 50 vol% $\text{CaCu}_3\text{Ti}_4\text{O}_{12}$ powder using CC HP for 10s.	204
Figure 4-73 Dielectric response vs. frequency of 1 layer $\text{CaCu}_3\text{Ti}_4\text{O}_{12}/\text{VC88}$ composite (10 vol% μ -size $\text{CaCu}_3\text{Ti}_4\text{O}_{12}$) without annealing and with annealing.	206
Figure 4-74 Dielectric response vs. frequency of 1 layer $\text{CaCu}_3\text{Ti}_4\text{O}_{12}/\text{VC88}$ composite (20 vol% μ -size $\text{CaCu}_3\text{Ti}_4\text{O}_{12}$) without annealing and with annealing.	206
Figure 4-75 Dielectric response vs. frequency of 1 layer $\text{CaCu}_3\text{Ti}_4\text{O}_{12}/\text{VC88}$ composite (30 vol% μ -size $\text{CaCu}_3\text{Ti}_4\text{O}_{12}$) without annealing and with annealing.	207
Figure 4-76 Dielectric response vs. frequency of 1 layer $\text{CaCu}_3\text{Ti}_4\text{O}_{12}/\text{VC88}$ composite (40 vol% μ -size $\text{CaCu}_3\text{Ti}_4\text{O}_{12}$) without annealing and with annealing.	207
Figure 4-77 Dielectric response vs. frequency of 1 layer $\text{CaCu}_3\text{Ti}_4\text{O}_{12}/\text{VC88}$ composite (50 vol% μ -size $\text{CaCu}_3\text{Ti}_4\text{O}_{12}$) without annealing and with annealing.	208
Figure 4-78 Dependence of dielectric response on $\text{CaCu}_3\text{Ti}_4\text{O}_{12}$ concentration (μ -size $\text{CaCu}_3\text{Ti}_4\text{O}_{12}$) for 1 layer $\text{CaCu}_3\text{Ti}_4\text{O}_{12}/\text{VC88}$ composite at room temperature.	209
Figure 4-79 Dielectric response vs. frequency of multiple layers $\text{CaCu}_3\text{Ti}_4\text{O}_{12}/\text{VC88}$ composite (10 vol% μ -size $\text{CaCu}_3\text{Ti}_4\text{O}_{12}$) with CC HP for 10s and annealing at 125 °C.	211
Figure 4-80 Dielectric response vs. frequency of multiple layers $\text{CaCu}_3\text{Ti}_4\text{O}_{12}/\text{VC88}$ composite (20 vol% μ -size $\text{CaCu}_3\text{Ti}_4\text{O}_{12}$) with CC HP for 10s and annealing at 125 °C.	211
Figure 4-81 Dielectric response vs. frequency of multiple layers $\text{CaCu}_3\text{Ti}_4\text{O}_{12}/\text{VC88}$ composite (30 vol% μ -size $\text{CaCu}_3\text{Ti}_4\text{O}_{12}$) with CC HP for 10s and annealing at 125 °C.	212

Figure 4-82 Dielectric response vs. frequency of multiple layers $\text{CaCu}_3\text{Ti}_4\text{O}_{12}/\text{VC88}$ composite (40 vol% μ -size $\text{CaCu}_3\text{Ti}_4\text{O}_{12}$) with CC HP for 10s and annealing at 125 °C.	212
Figure 4-83 Dielectric response vs. frequency of multiple layers $\text{CaCu}_3\text{Ti}_4\text{O}_{12}/\text{VC88}$ composite (50 vol% μ -size $\text{CaCu}_3\text{Ti}_4\text{O}_{12}$) with CC HP for 10s and annealing at 125 °C.	213
Figure 4-84 Dependence of dielectric response on $\text{CaCu}_3\text{Ti}_4\text{O}_{12}$ concentration for $\text{CaCu}_3\text{Ti}_4\text{O}_{12}/\text{VC88}$ composite (μ -size $\text{CaCu}_3\text{Ti}_4\text{O}_{12}$) using 10s CC HP for 2, 4, and 6 layer respectively at room temperature.....	214
Figure 4-85 SEM fractographs of 1 layer annealed $\text{CaCu}_3\text{Ti}_4\text{O}_{12}/\text{VC88}$ composite (50 vol% μ -size $\text{CaCu}_3\text{Ti}_4\text{O}_{12}$).	214
Figure 4-86 SEM fractographs of $\text{CaCu}_3\text{Ti}_4\text{O}_{12}/\text{VC88}$ composites (50 vol% μ -size $\text{CaCu}_3\text{Ti}_4\text{O}_{12}$) using 10s CC HP for (a) 2 layer, (b) 4 layer and (c) 6 layers, respectively.	215
Figure 4-87 Temperature dependence of pure VC88.	217
Figure 4-88 Temperature dependence of $\text{CaCu}_3\text{Ti}_4\text{O}_{12}/\text{VC88}$ composite (10 vol% μ -size $\text{CaCu}_3\text{Ti}_4\text{O}_{12}$) with: (a) 2 layer, (b) 4 layer, and (c) 6 layer 10s CC HP.....	218
Figure 4-89 Temperature dependence of $\text{CaCu}_3\text{Ti}_4\text{O}_{12}/\text{VC88}$ composite (20 vol% μ -size $\text{CaCu}_3\text{Ti}_4\text{O}_{12}$) with: (a) 2 layer, (b) 4 layer, and (c) 6 layer 10s CC HP.....	219
Figure 4-90 Temperature dependence of $\text{CaCu}_3\text{Ti}_4\text{O}_{12}/\text{VC88}$ composite (30 vol% μ -size $\text{CaCu}_3\text{Ti}_4\text{O}_{12}$) with: (a) 2 layer, (b) 4 layer, and (c) 6 layer 10s CC HP.....	220
Figure 4-91 Temperature dependence of $\text{CaCu}_3\text{Ti}_4\text{O}_{12}/\text{VC88}$ composite (40 vol% μ -size $\text{CaCu}_3\text{Ti}_4\text{O}_{12}$) with: (a) 2 layer, (b) 4 layer, and (c) 6 layer 10s CC HP.....	221
Figure 4-92 Temperature dependence of $\text{CaCu}_3\text{Ti}_4\text{O}_{12}/\text{VC88}$ composite (50 vol% μ -size $\text{CaCu}_3\text{Ti}_4\text{O}_{12}$) with: (a) 2 layer, (b) 4 layer, and (c) 6 layer 10s CC HP.....	222
Figure 5-1 Dielectric response vs. frequency of 1 layer $\text{CaCu}_3\text{Ti}_4\text{O}_{12}/\text{P}(\text{VDF-TrFE})$ composite (10, 20, 30, 40, and 50 vol% nano-size $\text{CaCu}_3\text{Ti}_4\text{O}_{12}$) with annealing in comparison with $\text{P}(\text{VDF-TrFE})$: (a) Dielectric constant vs. frequency; (b) Dielectric loss vs. frequency.	230
Figure 5-2 Dependence of dielectric response on $\text{CaCu}_3\text{Ti}_4\text{O}_{12}$ concentration for 1 layer $\text{CaCu}_3\text{Ti}_4\text{O}_{12}/\text{P}(\text{VDF-TrFE})$ composite (nano-size / μ -size $\text{CaCu}_3\text{Ti}_4\text{O}_{12}$) at room temperature with annealing at 125 °C for 8 hr.	231

Figure 5-3 SEM fractographs of annealed $\text{CaCu}_3\text{Ti}_4\text{O}_{12}/\text{P}(\text{VDF}-\text{TrFE})$ composites with 50 vol%: (a) nano-size; (b) μ -size $\text{CaCu}_3\text{Ti}_4\text{O}_{12}$ ceramic powder.	232
Figure 5-4 Dielectric response vs. frequency of multiple layers $\text{CaCu}_3\text{Ti}_4\text{O}_{12}/\text{P}(\text{VDF}-\text{TrFE})$ composite (10 vol% nano-size $\text{CaCu}_3\text{Ti}_4\text{O}_{12}$) with CC HP for 10s and annealing at 125 °C.....	234
Figure 5-5 Dielectric response vs. frequency of multiple layers $\text{CaCu}_3\text{Ti}_4\text{O}_{12}/\text{P}(\text{VDF}-\text{TrFE})$ composite (20 vol% nano-size $\text{CaCu}_3\text{Ti}_4\text{O}_{12}$) with CC HP for 10s and annealing at 125 °C.....	234
Figure 5-6 Dielectric response vs. frequency of multiple layers $\text{CaCu}_3\text{Ti}_4\text{O}_{12}/\text{P}(\text{VDF}-\text{TrFE})$ composite (30 vol% nano-size $\text{CaCu}_3\text{Ti}_4\text{O}_{12}$) with CC HP for 10s and annealing at 125 °C.....	235
Figure 5-7 Dielectric response vs. frequency of multiple layers $\text{CaCu}_3\text{Ti}_4\text{O}_{12}/\text{P}(\text{VDF}-\text{TrFE})$ composite (40 vol% nano-size $\text{CaCu}_3\text{Ti}_4\text{O}_{12}$) with CC HP for 10s and annealing at 125 °C.....	235
Figure 5-8 Dielectric response vs. frequency of multiple layers $\text{CaCu}_3\text{Ti}_4\text{O}_{12}/\text{P}(\text{VDF}-\text{TrFE})$ composite (20 vol% nano-size $\text{CaCu}_3\text{Ti}_4\text{O}_{12}$) with CC HP for 10s and annealing at 125 °C.....	236
Figure 5-9 Dependence of dielectric response on $\text{CaCu}_3\text{Ti}_4\text{O}_{12}$ concentration (nano-size $\text{CaCu}_3\text{Ti}_4\text{O}_{12}$) using 10s CC HP for 2, 4, and 6 layers respectively at room temperature.	237
Figure 5-10 SEM fractographs of $\text{CaCu}_3\text{Ti}_4\text{O}_{12}/\text{P}(\text{VDF}-\text{TrFE})$ composites (50vol% nano-size $\text{CaCu}_3\text{Ti}_4\text{O}_{12}$) using 10s CC HP for (a) 2 layer, (b) 4 layer and (c) 6 layers, respectively.	238
Figure 5-11 Dielectric response vs. frequency of multiple layers $\text{CaCu}_3\text{Ti}_4\text{O}_{12}/\text{P}(\text{VDF}-\text{TrFE})$ composite (10 vol% nano-size $\text{CaCu}_3\text{Ti}_4\text{O}_{12}$) with CC HP for 30s and annealing at 125 °C.....	241
Figure 5-12 Dielectric response vs. frequency of multiple layers $\text{CaCu}_3\text{Ti}_4\text{O}_{12}/\text{P}(\text{VDF}-\text{TrFE})$ composite (20 vol% nano-size $\text{CaCu}_3\text{Ti}_4\text{O}_{12}$) with CC HP for 30s and annealing at 125 °C.....	241
Figure 5-13 Dielectric response vs. frequency of multiple layers $\text{CaCu}_3\text{Ti}_4\text{O}_{12}/\text{P}(\text{VDF}-\text{TrFE})$ composite (30 vol% nano-size $\text{CaCu}_3\text{Ti}_4\text{O}_{12}$) with CC HP for 30s and annealing at 125 °C.....	242
Figure 5-14 Dielectric response vs. frequency of multiple layers $\text{CaCu}_3\text{Ti}_4\text{O}_{12}/\text{P}(\text{VDF}-\text{TrFE})$ composite (40 vol% nano-size $\text{CaCu}_3\text{Ti}_4\text{O}_{12}$) with CC HP for 30s and annealing at 125 °C.....	242

Figure 5-15 Dielectric response vs. frequency of multiple layers $\text{CaCu}_3\text{Ti}_4\text{O}_{12}/\text{P}(\text{VDF}-\text{TrFE})$ composite (50 vol% nano-size $\text{CaCu}_3\text{Ti}_4\text{O}_{12}$) with CC HP for 30s and annealing at 125 °C.....	243
Figure 5-16 Dependence of dielectric response on $\text{CaCu}_3\text{Ti}_4\text{O}_{12}$ concentration (nano-size $\text{CaCu}_3\text{Ti}_4\text{O}_{12}$) using 30s CC HP for 2, 4, and 6 layers respectively at room temperature.	244
Figure 5-17 Comparison of the present model predictions with experimental data for 2 layer CC HP 30s annealed $\text{CaCu}_3\text{Ti}_4\text{O}_{12}/\text{P}(\text{VDF}-\text{TrFE})$ sample.	244
Figure 5-18 Comparison of the present model predictions with experimental data for 4 layer CC HP 30s annealed $\text{CaCu}_3\text{Ti}_4\text{O}_{12}/\text{P}(\text{VDF}-\text{TrFE})$ sample.	245
Figure 5-19 Comparison of the present model predictions with experimental data for 6 layer CC HP 30s annealed $\text{CaCu}_3\text{Ti}_4\text{O}_{12}/\text{P}(\text{VDF}-\text{TrFE})$ sample.	245
Figure 5-20 Dielectric response vs. frequency of multiple layers $\text{CaCu}_3\text{Ti}_4\text{O}_{12}/\text{P}(\text{VDF}-\text{TrFE})$ composite (50 vol% nano-size $\text{CaCu}_3\text{Ti}_4\text{O}_{12}$): (a) 2 layer CC HP, (b) 4 layer CC HP, (c) 6 layer CC HP for 10, 20, 30 and 40s.....	247
Figure 5-21 Dependence of dielectric response on $\text{CaCu}_3\text{Ti}_4\text{O}_{12}$ concentration (50 vol% nano-size $\text{CaCu}_3\text{Ti}_4\text{O}_{12}$) of 2, 4 and 6 layers CC HP for 10, 20, 30 and 40s at room temperature, respectively.	248
Figure 5-22 Temperature dependence of the 2 layers $\text{CaCu}_3\text{Ti}_4\text{O}_{12}/\text{P}(\text{VDF}-\text{TrFE})$ composite (50 vol% nano-size $\text{CaCu}_3\text{Ti}_4\text{O}_{12}$) for: (a) 10s, and (b) 30s CC HP.....	250
Figure 5-23 Temperature dependence of the 4 layers $\text{CaCu}_3\text{Ti}_4\text{O}_{12}/\text{P}(\text{VDF}-\text{TrFE})$ composite (50 vol% nano-size $\text{CaCu}_3\text{Ti}_4\text{O}_{12}$) for: (a) 10s, and (b) 30s CC HP.....	251
Figure 5-24 Temperature dependence of the 6 layers $\text{CaCu}_3\text{Ti}_4\text{O}_{12}/\text{P}(\text{VDF}-\text{TrFE})$ composite (50 vol% nano-size $\text{CaCu}_3\text{Ti}_4\text{O}_{12}$) for: (a) 10s, and (b) 30s CC HP.....	252
Figure 5-25 Polarization electric hysteresis loop for one layer $\text{CaCu}_3\text{Ti}_4\text{O}_{12}/\text{P}(\text{VDF}-\text{TrFE})$ composites with 10 vol% $\text{CaCu}_3\text{Ti}_4\text{O}_{12}$ powder.	254
Figure 5-26 Polarization electric hysteresis loop for one layer $\text{CaCu}_3\text{Ti}_4\text{O}_{12}/\text{P}(\text{VDF}-\text{TrFE})$ composites with 20 vol% $\text{CaCu}_3\text{Ti}_4\text{O}_{12}$ powder.	254
Figure 5-27 Polarization electric hysteresis loop for one layer $\text{CaCu}_3\text{Ti}_4\text{O}_{12}/\text{P}(\text{VDF}-\text{TrFE})$ composites with 30 vol% $\text{CaCu}_3\text{Ti}_4\text{O}_{12}$ powder.	255
Figure 5-28 Polarization electric hysteresis loop for one layer $\text{CaCu}_3\text{Ti}_4\text{O}_{12}/\text{P}(\text{VDF}-\text{TrFE})$ composites with 40 vol% $\text{CaCu}_3\text{Ti}_4\text{O}_{12}$ powder.	255

Figure 5-29 Polarization electric hysteresis loop for one layer $\text{CaCu}_3\text{Ti}_4\text{O}_{12}/\text{P}(\text{VDF-TrFE})$ composites with 50 vol% $\text{CaCu}_3\text{Ti}_4\text{O}_{12}$ powder.	256
Figure 5-30 Polarization electric hysteresis loop for two layer $\text{CaCu}_3\text{Ti}_4\text{O}_{12}/\text{P}(\text{VDF-TrFE})$ composites with 50 vol% $\text{CaCu}_3\text{Ti}_4\text{O}_{12}$ powder.	256
Figure 5-31 Polarization electric hysteresis loop for two layer $\text{CaCu}_3\text{Ti}_4\text{O}_{12}/\text{P}(\text{VDF-TrFE})$ composites with 50 vol% $\text{CaCu}_3\text{Ti}_4\text{O}_{12}$ powder.	257
Figure 5-32 Polarization electric hysteresis loop for two layer $\text{CaCu}_3\text{Ti}_4\text{O}_{12}/\text{P}(\text{VDF-TrFE})$ composites with 50 vol% $\text{CaCu}_3\text{Ti}_4\text{O}_{12}$ powder.	257
Figure 5-33 Polarization electric hysteresis loop for one layer $\text{CaCu}_3\text{Ti}_4\text{O}_{12}/\text{P}(\text{VDF-TrFE})$ composites with 10 vol% $\text{CaCu}_3\text{Ti}_4\text{O}_{12}$ powder at 95 °C.	258
Figure 5-34 Polarization electric hysteresis loop for one layer $\text{CaCu}_3\text{Ti}_4\text{O}_{12}/\text{P}(\text{VDF-TrFE})$ composites with 20 vol% $\text{CaCu}_3\text{Ti}_4\text{O}_{12}$ powder at 95 °C.	258
Figure 5-35 Polarization electric hysteresis loop for one layer $\text{CaCu}_3\text{Ti}_4\text{O}_{12}/\text{P}(\text{VDF-TrFE})$ composites with 30 vol% $\text{CaCu}_3\text{Ti}_4\text{O}_{12}$ powder at 95 °C.	259
Figure 5-36 Polarization electric hysteresis loop for one layer $\text{CaCu}_3\text{Ti}_4\text{O}_{12}/\text{P}(\text{VDF-TrFE})$ composites with 40 vol% $\text{CaCu}_3\text{Ti}_4\text{O}_{12}$ powder at 95 °C.	259
Figure 5-37 Polarization electric hysteresis loop for one layer $\text{CaCu}_3\text{Ti}_4\text{O}_{12}/\text{P}(\text{VDF-TrFE})$ composites with 50 vol% $\text{CaCu}_3\text{Ti}_4\text{O}_{12}$ powder at 95 °C.	260
Figure 5-38 Dielectric response vs. frequency of $\text{CaCu}_3\text{Ti}_4\text{O}_{12}/\text{P}(\text{VDF-TrFE})$ composite (10 vol% nano-size $\text{CaCu}_3\text{Ti}_4\text{O}_{12}$) : (a) as-casted 1 layer vs. as annealed 1 layer, (b) 2, 4, and 6 layers CC HP for 10s.....	263
Figure 5-39 SEM fractographs of 1 layer annealed $\text{CaCu}_3\text{Ti}_4\text{O}_{12}/\text{VC88}$ composite (50 vol% nano-size $\text{CaCu}_3\text{Ti}_4\text{O}_{12}$).....	264
Figure 5-40 SEM fractographs of $\text{CaCu}_3\text{Ti}_4\text{O}_{12}/\text{VC88}$ composites (50 vol% nano-size $\text{CaCu}_3\text{Ti}_4\text{O}_{12}$) using 10s CC HP for (a) 2 layer, (b) 4 layer and (c) 6 layers, respectively.	265
Figure 5-41 Temperature dependence of 1 layer $\text{CaCu}_3\text{Ti}_4\text{O}_{12}/\text{VC88}$ composite (50 vol% nano-size $\text{CaCu}_3\text{Ti}_4\text{O}_{12}$).....	266
Figure 5-42 Temperature dependence of 2 layer $\text{CaCu}_3\text{Ti}_4\text{O}_{12}/\text{VC88}$ composite for 10s CC HP (50 vol% nano-size $\text{CaCu}_3\text{Ti}_4\text{O}_{12}$).....	266
Figure 5-43 Temperature dependence of 4 layer $\text{CaCu}_3\text{Ti}_4\text{O}_{12}/\text{VC88}$ composite for 10s CC HP (50 vol% nano-size $\text{CaCu}_3\text{Ti}_4\text{O}_{12}$).....	267

Figure 5-44 Temperature dependence of 6 layer $\text{CaCu}_3\text{Ti}_4\text{O}_{12}/\text{VC88}$ composite for 10s CC HP (50 vol% nano-size $\text{CaCu}_3\text{Ti}_4\text{O}_{12}$).....	267
Figure 5-45 The molecule structure of the silane coupling agent ($\text{C}_8\text{H}_4\text{Cl}_3\text{F}_{13}\text{Si}$).	269
Figure 5-46 Dielectric response vs. frequency of 1 layer $\text{CaCu}_3\text{Ti}_4\text{O}_{12}/\text{P}(\text{VDF-TrFE})$ composite (10 vol% μ -size $\text{CaCu}_3\text{Ti}_4\text{O}_{12}$) with (a) 1, (b) 5, and (c) 10 wt% silane.	272
Figure 5-47 Dielectric response vs. frequency of 1 layer $\text{CaCu}_3\text{Ti}_4\text{O}_{12}/\text{P}(\text{VDF-TrFE})$ composite (20 vol% μ -size $\text{CaCu}_3\text{Ti}_4\text{O}_{12}$) with (a) 1, (b) 5, and (c) 10 wt% silane.	273
Figure 5-48 Dielectric response vs. frequency of 1 layer $\text{CaCu}_3\text{Ti}_4\text{O}_{12}/\text{P}(\text{VDF-TrFE})$ composite (30 vol% μ -size $\text{CaCu}_3\text{Ti}_4\text{O}_{12}$) with (a) 1, (b) 5, and (c) 10 wt% silane.	274
Figure 5-49 Dielectric response vs. frequency of 1 layer $\text{CaCu}_3\text{Ti}_4\text{O}_{12}/\text{P}(\text{VDF-TrFE})$ composite (40 vol% μ -size $\text{CaCu}_3\text{Ti}_4\text{O}_{12}$) with (a) 1, (b) 5, and (c) 10 wt% silane.	275
Figure 5-50 Dielectric response vs. frequency of 1 layer $\text{CaCu}_3\text{Ti}_4\text{O}_{12}/\text{P}(\text{VDF-TrFE})$ composite (50 vol% μ -size $\text{CaCu}_3\text{Ti}_4\text{O}_{12}$) with (a) 1, (b) 5, and (c) 10 wt% silane.	276
Figure 5-51 Dielectric response vs. frequency of 1 layer $\text{CaCu}_3\text{Ti}_4\text{O}_{12}/\text{P}(\text{VDF-TrFE})$ composite (50 vol% μ -size $\text{CaCu}_3\text{Ti}_4\text{O}_{12}$) with (a) 0.3, (b) 0.5 and (c) 0.75 wt% silane.	279
Figure 5-52 Dependence of dielectric response vs. silane coupling concentration in $\text{CaCu}_3\text{Ti}_4\text{O}_{12}/\text{P}(\text{VDF-TrFE})$ composite (μ -size $\text{CaCu}_3\text{Ti}_4\text{O}_{12}$): (a) 1 layer vs. 1 annealed layer, (b) multiple layers using 10s CC HP at room temperature.....	280
Figure 5-53 SEM fractographs of 1 layer $\text{CaCu}_3\text{Ti}_4\text{O}_{12}/\text{P}(\text{VDF-TrFE})$ composites (50vol% μ -size $\text{CaCu}_3\text{Ti}_4\text{O}_{12}$) with: (a) 0.3 wt%, (b) 0.5 wt%, (c) 0.75 wt%, (d) 1 wt%, (e) 5 wt% and (f) 10 wt% silane, respectively.....	281
Figure 5-54 Temperature dependence of one layer $\text{CaCu}_3\text{Ti}_4\text{O}_{12}/\text{P}(\text{VDF-TrFE})$ composite (50 vol% μ -size $\text{CaCu}_3\text{Ti}_4\text{O}_{12}$) with 0.75 wt% silane.	283
Figure 5-55 Temperature dependence of one layer $\text{CaCu}_3\text{Ti}_4\text{O}_{12}/\text{P}(\text{VDF-TrFE})$ composite (50 vol% μ -size $\text{CaCu}_3\text{Ti}_4\text{O}_{12}$) with 0.75 wt% silane.	283
Figure 5-56 Temperature dependence of one layer $\text{CaCu}_3\text{Ti}_4\text{O}_{12}/\text{P}(\text{VDF-TrFE})$ composite (50 vol% μ -size $\text{CaCu}_3\text{Ti}_4\text{O}_{12}$) with 1 wt% silane.	284
Figure 5-57 Dielectric response vs. frequency of 1 layer $\text{CaCu}_3\text{Ti}_4\text{O}_{12}/\text{P}(\text{VDF-TrFE})$ composite (50 vol% nano-size $\text{CaCu}_3\text{Ti}_4\text{O}_{12}$) with (a) 1, (b) 5 and (c) 10 wt% silane...	286

Figure 5-58 SEM fractographs of one layer $\text{CaCu}_3\text{Ti}_4\text{O}_{12}$ /P(VDF-TrFE) composites (50vol% nano-size $\text{CaCu}_3\text{Ti}_4\text{O}_{12}$) with: (a) 1, (b) 5 and (c) 10 wt% silane, respectively.	288
Figure 5-59 Temperature dependence of one layer $\text{CaCu}_3\text{Ti}_4\text{O}_{12}$ /P(VDF-TrFE) composite (50 vol% μ -size $\text{CaCu}_3\text{Ti}_4\text{O}_{12}$) with 1 wt% silane.	289

LIST OF TABLES

Table 1-1 Summary of dielectric data for <i>FE</i> ceramics and polymers.	15
Table 1-2 Mechanical and dielectric properties for <i>FE</i> ceramics	15
Table 1-3 Dielectric constant ϵ' , & dielectric strength \vec{E}_b of some current.....	18
Table 1-4 Dielectric and cell edge data for $\text{ACu}_3\text{Ti}_4\text{O}_{12}$ (at 25 °C) ⁵⁸	22
Table 1-5 Dielectric property of some commercial composite products ⁹³	33
Table 1-6 Dielectric properties of some current ceramic-polymer composites at RT.....	33
Table 2-1 The $\text{CaCu}_3\text{Ti}_4\text{O}_{12}$ processing conditions.	55
Table 2-2 Volumetric ratio table for $\text{CaCu}_3\text{Ti}_4\text{O}_{12}$ - P(VDF-TrFE) composite samples...	59
Table 2-3 Physical and chemical properties of silane coupling agent.	60
Table 3-1 The $\text{CaCu}_3\text{Ti}_4\text{O}_{12}$ processing conditions.	69
Table 3-2 Shrinking rate of the pellet.	86
Table 3-3 Density of the pellet: g/cm^3	86
Table 4-1 Summary of dielectric data for 1 layer $\text{CaCu}_3\text{Ti}_4\text{O}_{12}$ /P(VDF-TrFE) composite (μ -size $\text{CaCu}_3\text{Ti}_4\text{O}_{12}$) (1 kHz).....	126
Table 4-2 Summary of dielectric data for 1 layer $\text{CaCu}_3\text{Ti}_4\text{O}_{12}$ /P(VDF-TrFE) composite (μ -size $\text{CaCu}_3\text{Ti}_4\text{O}_{12}$) with hot pressing (1 kHz).	137
Table 4-3 Summary of fitted dielectric data for $\text{CaCu}_3\text{Ti}_4\text{O}_{12}$ in 1 layer $\text{CaCu}_3\text{Ti}_4\text{O}_{12}$ /P(VDF-TrFE) composite (μ -size $\text{CaCu}_3\text{Ti}_4\text{O}_{12}$) with hot pressing (1 kHz).	139
Table 4-4 Summary of dielectric data for multiple layer $\text{CaCu}_3\text{Ti}_4\text{O}_{12}$ /P(VDF-TrFE) composite (μ -size $\text{CaCu}_3\text{Ti}_4\text{O}_{12}$) with CC hot pressing for 10s (1 kHz).	153
Table 4-5 Summary of dielectric data for multiple layer $\text{CaCu}_3\text{Ti}_4\text{O}_{12}$ /P(VDF-TrFE) composite (μ -size $\text{CaCu}_3\text{Ti}_4\text{O}_{12}$) with CC hot pressing for 20s (1 kHz).	153

Table 4-6 Summary of dielectric data for multiple layer $\text{CaCu}_3\text{Ti}_4\text{O}_{12}/\text{P}(\text{VDF-TrFE})$ composite (μ -size $\text{CaCu}_3\text{Ti}_4\text{O}_{12}$) with CC hot pressing for 30s (1 kHz).	153
Table 4-7 Summary of fitted dielectric data for $\text{CaCu}_3\text{Ti}_4\text{O}_{12}$ multiple layer $\text{CaCu}_3\text{Ti}_4\text{O}_{12}/\text{P}(\text{VDF-TrFE})$ composite (μ -size $\text{CaCu}_3\text{Ti}_4\text{O}_{12}$) with CC hot pressing for 30s (1 kHz).....	158
Table 4-8 Summary of reliability measurements of 4 layer CC HP $\text{CaCu}_3\text{Ti}_4\text{O}_{12}/\text{P}(\text{VDF-TrFE})$ composite with 40 vol% μ -size $\text{CaCu}_3\text{Ti}_4\text{O}_{12}$ powder (1 kHz).....	169
Table 4-9 Summary of reliability measurements of 4 layer CC HP $\text{CaCu}_3\text{Ti}_4\text{O}_{12}/\text{P}(\text{VDF-TrFE})$ composite with 50 vol% μ -size $\text{CaCu}_3\text{Ti}_4\text{O}_{12}$ powder (1 kHz).....	170
Table 4-10 Summary of fitting results for 6 layer $\text{CaCu}_3\text{Ti}_4\text{O}_{12}/\text{P}(\text{VDF-TrFE})$ composite with 50 vol% μ -size $\text{CaCu}_3\text{Ti}_4\text{O}_{12}$ powder after 10s CC HP.....	187
Table 4-11 Summary of fitting results for 6 layer $\text{CaCu}_3\text{Ti}_4\text{O}_{12}/\text{P}(\text{VDF-TrFE})$ composite with 50 vol% μ -size $\text{CaCu}_3\text{Ti}_4\text{O}_{12}$ powder after 20s CC HP.....	188
Table 4-12 Summary of fitting results for 6 layer $\text{CaCu}_3\text{Ti}_4\text{O}_{12}/\text{P}(\text{VDF-TrFE})$ composite with 50 vol% μ -size $\text{CaCu}_3\text{Ti}_4\text{O}_{12}$ powder after 30s CC HP.....	188
Table 4-13 Summary of activation energy for 6 layer $\text{CaCu}_3\text{Ti}_4\text{O}_{12}/\text{P}(\text{VDF-TrFE})$ composite with 50 vol% μ -size $\text{CaCu}_3\text{Ti}_4\text{O}_{12}$ powder after 10s, 20s, and 30s CC HP... ..	190
Table 4-14 Fitting results for 1 layer annealed $\text{CaCu}_3\text{Ti}_4\text{O}_{12}/\text{P}(\text{VDF-TrFE})$ composite with 10 to 50 vol% μ -size $\text{CaCu}_3\text{Ti}_4\text{O}_{12}$ powder.	196
Table 4-15 Fitting results for 2, 4 and 6 layer annealed $\text{CaCu}_3\text{Ti}_4\text{O}_{12}/\text{P}(\text{VDF-TrFE})$ composite with 10 vol% μ -size $\text{CaCu}_3\text{Ti}_4\text{O}_{12}$ powder CC HP for 10, 20 and 30s.....	196
Table 4-16 Fitting results for 2, 4 and 6 layer annealed $\text{CaCu}_3\text{Ti}_4\text{O}_{12}/\text{P}(\text{VDF-TrFE})$ composite with 20 vol% μ -size $\text{CaCu}_3\text{Ti}_4\text{O}_{12}$ powder CC HP for 10, 20 and 30s.....	197
Table 4-17 Fitting results for 2, 4 and 6 layer annealed $\text{CaCu}_3\text{Ti}_4\text{O}_{12}/\text{P}(\text{VDF-TrFE})$ composite with 30 vol% μ -size $\text{CaCu}_3\text{Ti}_4\text{O}_{12}$ powder CC HP for 10, 20 and 30s.....	197
Table 4-18 Fitting results for 2, 4 and 6 layer annealed $\text{CaCu}_3\text{Ti}_4\text{O}_{12}/\text{P}(\text{VDF-TrFE})$ composite with 40 vol% μ -size $\text{CaCu}_3\text{Ti}_4\text{O}_{12}$ powder CC HP for 10, 20 and 30s.....	198
Table 4-19 Fitting results for 2, 4 and 6 layer annealed $\text{CaCu}_3\text{Ti}_4\text{O}_{12}/\text{P}(\text{VDF-TrFE})$ composite with 50 vol% μ -size $\text{CaCu}_3\text{Ti}_4\text{O}_{12}$ powder CC HP for 10, 20 and 30s.....	198
Table 4-20 Summary of dielectric data for 1 layer $\text{CaCu}_3\text{Ti}_4\text{O}_{12}/\text{VC88}$ composite (μ -size $\text{CaCu}_3\text{Ti}_4\text{O}_{12}$) (1 kHz).....	208

Table 4-21 Summary of dielectric data for multiple layers $\text{CaCu}_3\text{Ti}_4\text{O}_{12}/\text{VC88}$ composite in contrast to $\text{CaCu}_3\text{Ti}_4\text{O}_{12}/\text{P}(\text{VDF-TrFE})$ composite (μ -size $\text{CaCu}_3\text{Ti}_4\text{O}_{12}$) with CC hot pressing for 10s (1 kHz).....	213
Table 4-22 Summary of dielectric constant for multiple layers $\text{CaCu}_3\text{Ti}_4\text{O}_{12}/\text{VC88}$ composite (μ -size $\text{CaCu}_3\text{Ti}_4\text{O}_{12}$) with CC HP for 10s at different temperature (1 kHz).223	
Table 5-1 Summary of dielectric data for 1 layer $\text{CaCu}_3\text{Ti}_4\text{O}_{12}/\text{P}(\text{VDF-TrFE})$ composite (nano-size / μ -size $\text{CaCu}_3\text{Ti}_4\text{O}_{12}$) annealed at 125 °C (1 kHz).	231
Table 5-2 Summary of dielectric data for multiple layer $\text{CaCu}_3\text{Ti}_4\text{O}_{12}/\text{P}(\text{VDF-TrFE})$ composite (nano-size/ μ -size $\text{CaCu}_3\text{Ti}_4\text{O}_{12}$) with CC hot pressing for 10s (1 kHz).	236
Table 5-3 Summary of dielectric data for multiple layers $\text{CaCu}_3\text{Ti}_4\text{O}_{12}/\text{P}(\text{VDF-TrFE})$ composite (nano-size/ μ -size $\text{CaCu}_3\text{Ti}_4\text{O}_{12}$) with CC hot pressing for 30s (1 kHz).	243
Table 5-4 Summary of fitted dielectric data for $\text{CaCu}_3\text{Ti}_4\text{O}_{12}$ multiple layer $\text{CaCu}_3\text{Ti}_4\text{O}_{12}/\text{P}(\text{VDF-TrFE})$ composite (nano-size $\text{CaCu}_3\text{Ti}_4\text{O}_{12}$) with CC hot pressing for 30s (1 kHz).....	246
Table 5-5 Summary of dielectric data for multiple layers $\text{CaCu}_3\text{Ti}_4\text{O}_{12}/\text{P}(\text{VDF-TrFE})$ composite (50vol% nano-size $\text{CaCu}_3\text{Ti}_4\text{O}_{12}$) with CC hot pressing for 10, 20, 30 and 40s (1 kHz).	248
Table 5-6 Summary of P-E results for one layer 10 to 50 vol% $\text{CaCu}_3\text{Ti}_4\text{O}_{12}/\text{P}(\text{VDF-TrFE})$ composite at 95 °C.	261
Table 5-7 Summary of dielectric data for multiple layers $\text{CaCu}_3\text{Ti}_4\text{O}_{12}/\text{VC88}$ composite (nano-size / μ -size $\text{CaCu}_3\text{Ti}_4\text{O}_{12}$) annealed at 125 °C (1 kHz).	264
Table 5-8 Physical properties of silane coupling agent ($\text{C}_8\text{H}_4\text{Cl}_3\text{F}_{13}\text{Si}$) and ceramic ($\text{CaCu}_3\text{Ti}_4\text{O}_{12}$).	268
Table 5-9 Summary of dielectric data for 1 layer $\text{CaCu}_3\text{Ti}_4\text{O}_{12}/\text{P}(\text{VDF-TrFE})$ composite (μ -size $\text{CaCu}_3\text{Ti}_4\text{O}_{12}$) with 0, 1, 5 and 10 wt% silane with annealed at 125 °C (1 kHz).277	
Table 5-10 Summary of dielectric data for 1 layer $\text{CaCu}_3\text{Ti}_4\text{O}_{12}/\text{P}(\text{VDF-TrFE})$ composite (μ -size $\text{CaCu}_3\text{Ti}_4\text{O}_{12}$) with 0.3, 0.5, 0.75, 1, 5 and 10 wt% silane with annealed at 125°C (1 kHz).	280
Table 5-11 Summary of dielectric data for 1 layer $\text{CaCu}_3\text{Ti}_4\text{O}_{12}/\text{P}(\text{VDF-TrFE})$ composite (nano-size and μ -size $\text{CaCu}_3\text{Ti}_4\text{O}_{12}$) with 1, 5 and 10 wt% silane with annealed at 125 °C (1 kHz).	287

CHAPTER 1

INTRODUCTION AND RESEARCH OBJECTIVES

Dielectrics, which are materials responding to an external electric stimulation with a polarization, have been widely used in industries such as capacitors, insulation layer and energy storage devices.

From manufacture and device reliability point of view, dielectrics, which are flexible, easy to process, and can stand with high mechanical impact, are highly desirable. Conversely, from property point of view, dielectrics with high dielectric constant and high dielectric strength (or breakdown field E_b) are required for applications, such as high charge-storage density capacitor in *IC* due to the needs for miniaturizing devices¹⁻³.

The dielectrics can be inorganic materials, such as Ta_5O_2 , $BaTiO_3$ (BT), $PbTiO_3$ (PT), $Pb(Mg_{1/3}Nb_{2/3})O_3$ (PMN) etc, or organic materials such as polypropylene, polysulfone, polyester etc. Inorganic materials usually exhibit a high dielectric constant ($10^2 \sim 10^4$), but a low breakdown field and require a high processing temperature⁴⁻⁶. Conversely, organic materials can be processed at low temperature and exhibit high breakdown field (up to more than 500 *MV/m*), but very small dielectric constant (mostly less than 5)⁷⁻¹⁸. Therefore, a great deal of effort has gone into developing ceramic-polymer composites, such as $Pb(Mg_{1/3}Nb_{2/3})O_3$ -epoxy composite and $PbZrO_3$ -P(VDF-TrFE) composite, which are polymer matrix filled with high dielectric constant inorganic powders to create a new type of dielectric that is flexible and easy to process, and is of relative high dielectric constant and high breakdown strength¹⁹⁻²².

1.1 Theory of Dielectric Materials

1.1.1 Permittivity

Dielectrics respond to an electric field \vec{E} with polarization \vec{P} , which reflects the induced dipole moments \vec{p} . That is^{23,24}:

$$\vec{P} = \frac{\sum_{i=1}^N \vec{p}}{dv} \quad (1-1)$$

The permittivity ϵ is used to measure the polarization response of a material to the external electric field. Its definition in *DC* condition is shown as following^{4,25}:

$$\vec{D} = \epsilon_0 \vec{E} + \vec{P} \quad (1-2)$$

$$\vec{D} = \epsilon \vec{E} = \epsilon'_r \epsilon_0 \vec{E} \quad (1-3)$$

where \vec{D} is named as electric displacement, ϵ_0 is the permittivity in vacuum ($8.8541878176 \times 10^{-12} \text{ C}^2/\text{J}\cdot\text{m}$), ϵ is permittivity of the material between the plates, ϵ'_r is the relative permittivity (or dielectric constant) of a material.

Based on the equation (1-2) and (1-3), it can be transformed as:

$$\vec{P} = (\epsilon'_r - 1)\epsilon_0 \vec{E} = \chi \epsilon_0 \vec{E} \quad (1-4)$$

$$\chi = \epsilon'_r - 1 \quad (1-5)$$

where χ is the dielectric susceptibility of the material.

If a time-varying electric field is applied on a dielectric material, the relative permittivity changes with frequency and becomes complex:

$$\epsilon^*_r = \epsilon'_r - j\epsilon''_r \quad (1-6)$$

in which j is the imaginary unit, ϵ'_r and ϵ''_r are the real and imaginary part of relative permittivity respectively. The loss angle δ is defined as:

$$\tan \delta = \frac{\epsilon''_r}{\epsilon'_r} \quad (1-7)$$

where $\tan \delta$ is also named as loss factor.

The relationship between ϵ'_r and ϵ''_r can be described with the Kramers-Krong relations²⁵:

$$\varepsilon'_r(\omega) = \varepsilon_{r\infty} + \frac{2}{\pi} \int_0^\infty \frac{u\varepsilon''(u)}{u^2 - \omega^2} du \quad (1-8)$$

$$\varepsilon''_r(\omega) = \frac{2}{\pi} \int_0^\infty [\varepsilon'_r(u) - \varepsilon_{r\infty}] \frac{\omega}{u^2 - \omega^2} du \quad (1-9)$$

where $\varepsilon_{r\infty}$ is the permittivity at high frequency limit and ω is the angular frequency.

If let $\omega=0$, the above Equation (1-8) becomes:

$$\varepsilon'_r(0) = \varepsilon_{rs} = \varepsilon_{r\infty} + \frac{2}{\pi} \int_0^\infty \varepsilon''_r(u) \frac{du}{u}$$

$$\begin{aligned} \text{Therefore } \varepsilon_{rs} - \varepsilon_{r\infty} &= \frac{2}{\pi} \int_0^\infty \varepsilon''_r(u) \frac{du}{u} = \frac{2}{\pi} \int_0^\infty \varepsilon''_r(\omega) \frac{d\omega}{\omega} \\ &= \frac{2}{\pi} \int_0^\infty \varepsilon''_r(\omega) d(\ln \omega) \end{aligned}$$

$$\text{Or } \int_0^\infty \varepsilon''_r(\omega) d(\ln \omega) = \frac{\pi}{2} (\varepsilon_{rs} - \varepsilon_{r\infty}) \quad (1-10)$$

where ε_{rs} is also named as the static permittivity. Equation (1-10) implies that in order to obtain a higher $\varepsilon_{rs} - \varepsilon_{r\infty}$, then a higher ε''_r is required.

1.1.2 Origins of Permittivity

The polarization \vec{P} or the induced dipole moment in a dielectric material can originate from different mechanisms. In general, there are four mechanisms for a dielectric material (as illustrated in Figure 1-1)^{4, 25}.

- (1) **Electronic polarization:** The electric field causes the displacement of the outer electron cloud from the inner positive nucleus in Figure 1-1(a). The response time is about $10^{-14} \sim 10^{-16}$ s.
- (2) **Ionic polarization:** Ionic responds to an electric field with a change in the relative distance in between them in Figure 1-1(b) and the response time is varying from $10^{-12} \sim 10^{-13}$ s.
- (3) **Orientalional Polarization:** If there are dipoles in a material, the electric field generates a torque on each dipole, which causes dipoles aligned along the electric field direction. This is called orientational polarization, as shown in Figure 1-1(c).

The response time is strongly dependent on T and ranges over approximately $10^0 \sim 10^{-9} s$.

- (4) ***Space charge polarization***: When the space charge appears in the dielectric, the electric field generates a force on the charge carriers, which separates the positive and negative charges as shown in Figure 1-1(d). The response time which is strongly dependent on T is approximately $10^{-4} s$.

If the frequency $\ll 1/t$ (t : the response time) in a polarization, the corresponding polarization mechanism would result in a $\varepsilon''_r \approx 0$ and a ε'_r that is the static permittivity (as shown in Figure 1-2).

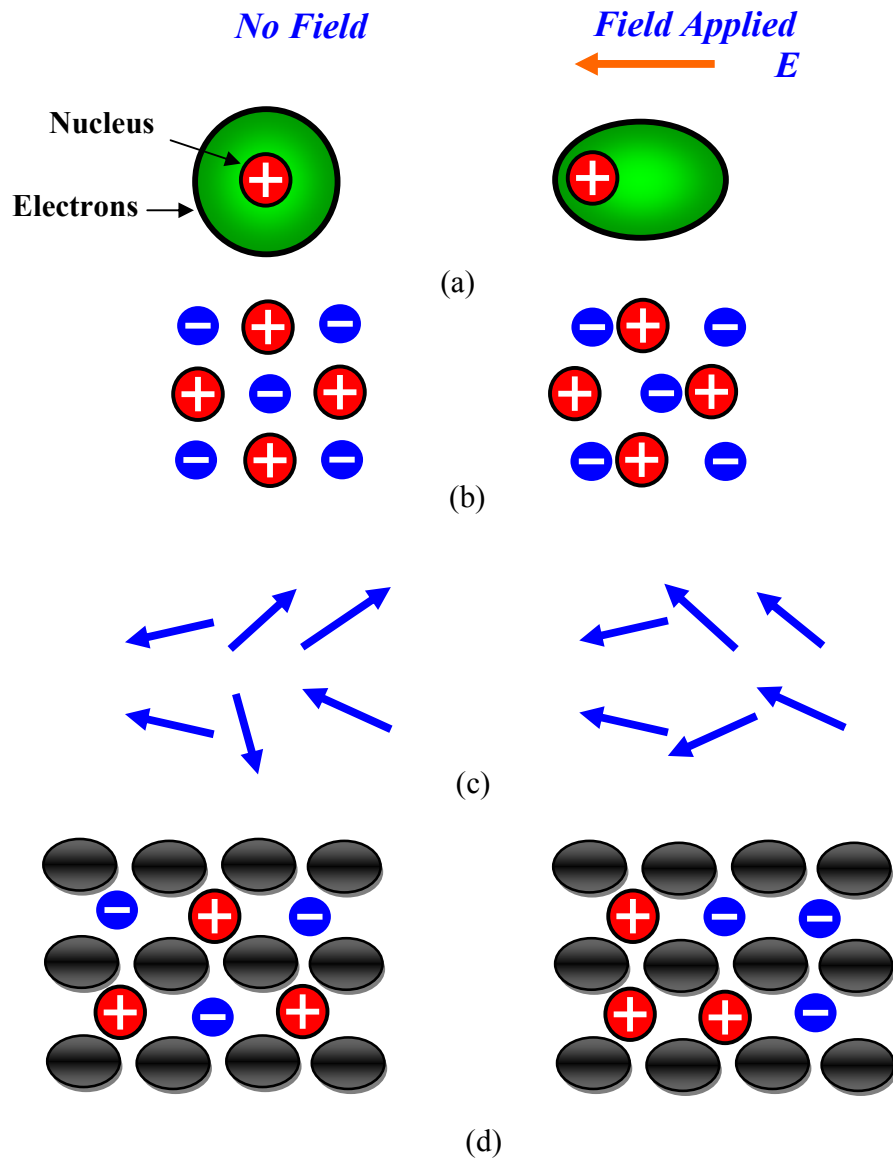


Figure 1-1 Schematics of (a) electron polarization, (b) ionic polarization, (c) orientational polarization, (d) space charge polarization.

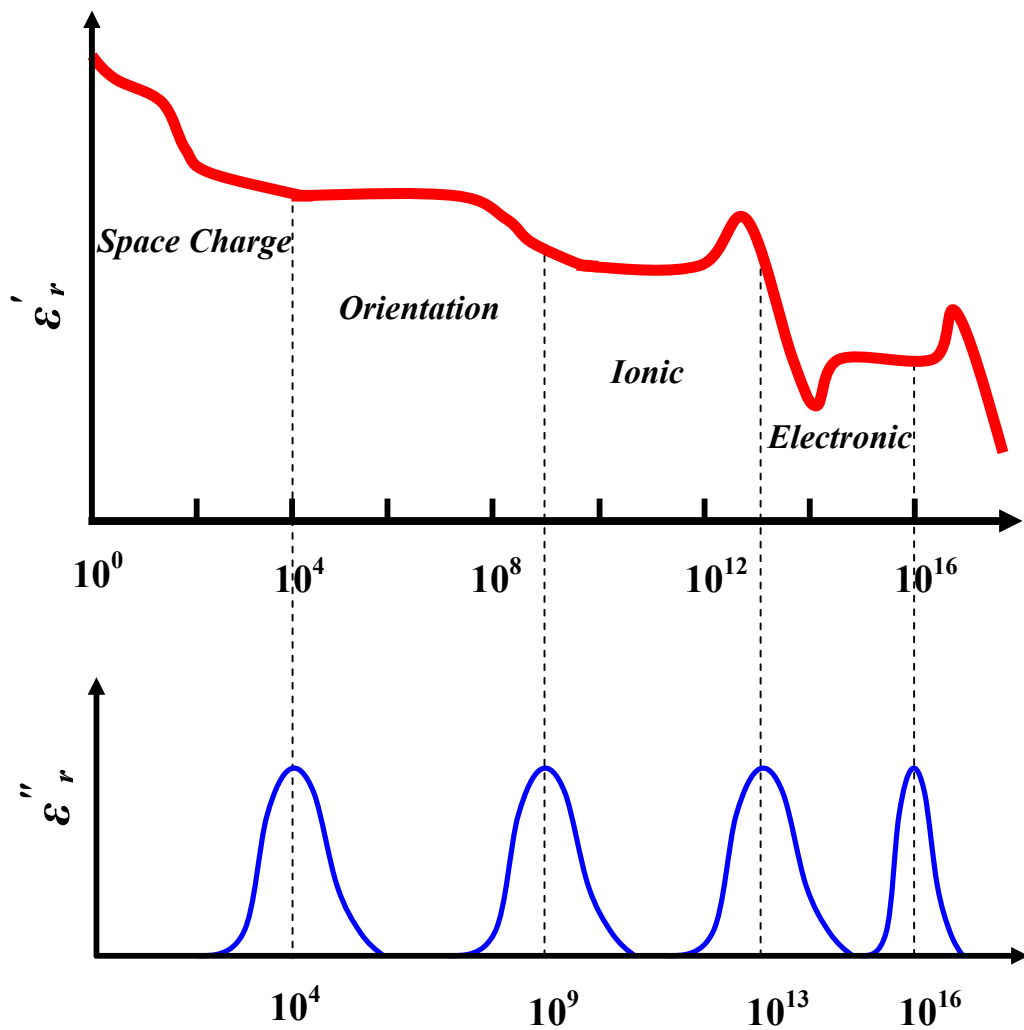


Figure 1-2 The influence of the polarization: (a) real part of relative permittivity and (b) imaginary part of relative permittivity with frequency.

1.1.3 Dielectric Relaxation

Dielectric relaxation refers to the relaxation response of a dielectric material to an external electric field, which exhibits a momentary delay in the dielectric response of a material. Dielectric theories for relaxation were developed and virtually have been applied in different systems.

Debye relaxation is the dielectric relaxation response of an ideal, non-interacting population of dipoles to an alternating external electric field. The Debye equation assumes that the conductivity of the material is zero, free orientation of non-interacting dipoles and all dipoles exhibit only one relaxation time. Thus, its dielectric permittivity can be written as²⁵:

$$\varepsilon_r^*(\omega) = \varepsilon_{r\infty} + \frac{\varepsilon_{rs} - \varepsilon_{r\infty}}{1 + j\omega\tau_0} \quad (1-11)$$

$$\text{Or } \varepsilon_r' = \varepsilon_{r\infty} + \frac{\varepsilon_{rs} - \varepsilon_{r\infty}}{1 + \omega^2\tau_0^2} \quad (1-12)$$

$$\varepsilon_r'' = \frac{(\varepsilon_{rs} - \varepsilon_{r\infty})\omega\tau_0}{1 + \omega^2\tau_0^2} \quad (1-13)$$

$$\tan \delta = \frac{\varepsilon_r''}{\varepsilon_r'} = \frac{(\varepsilon_{rs} - \varepsilon_{r\infty})\omega\tau_0}{\varepsilon_{rs} + \varepsilon_{r\infty} + \omega^2\tau_0^2} \quad (1-14)$$

where ε_{rs} is the static permittivity, $\varepsilon_{r\infty}$ is the permittivity at high frequency limit, τ_0 is the characteristic relaxation time and $\varepsilon_{rs} - \varepsilon_{r\infty}$ reflects the strength of the relaxation process.

By combing the Equation (1-12) and (1-13), the equation without $\omega\tau_0$ can be written as:

$$\left(\varepsilon_r' - \frac{\varepsilon_{rs} + \varepsilon_{r\infty}}{2}\right)^2 + \varepsilon_r''^2 = \left(\frac{\varepsilon_{rs} - \varepsilon_{r\infty}}{2}\right)^2 \quad (1-15)$$

The schematic of $\varepsilon_r' - \varepsilon_r''$ relation is shown in Figure 1-3 and 1-4. The maximum value of ε_r'' occurs at ω_0 when:

$$\omega_0\tau_0 = 1 \quad (1-16)$$

The $\tan \delta$ reaches its maximum at ω_δ :

$$\tan \delta \Big|_{\omega=\omega_\delta} = \frac{\varepsilon_{rs} - \varepsilon_{r\infty}}{2(\varepsilon_{rs}\varepsilon_{r\infty})^{1/2}} \quad (1-17)$$

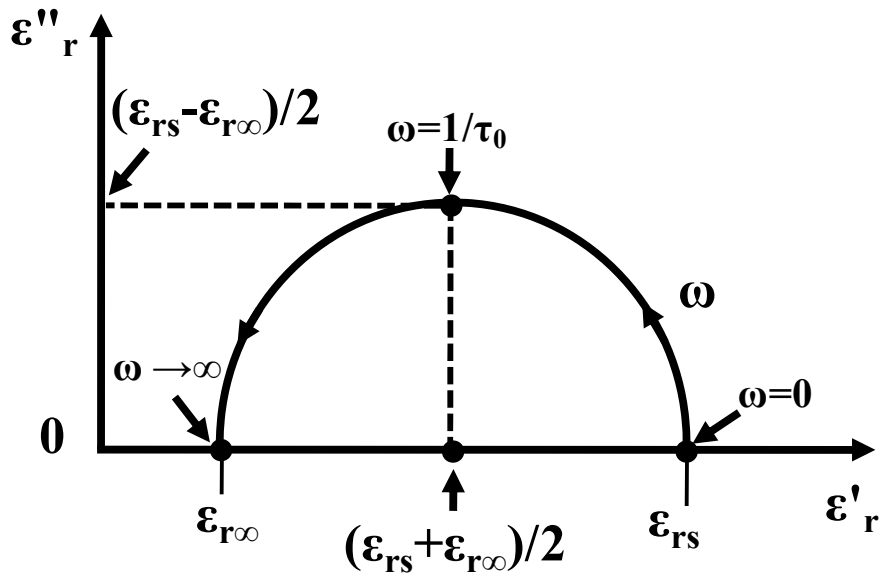


Figure 1-3 Argand diagram for dielectric material with only one relaxation time based on Debye equation.

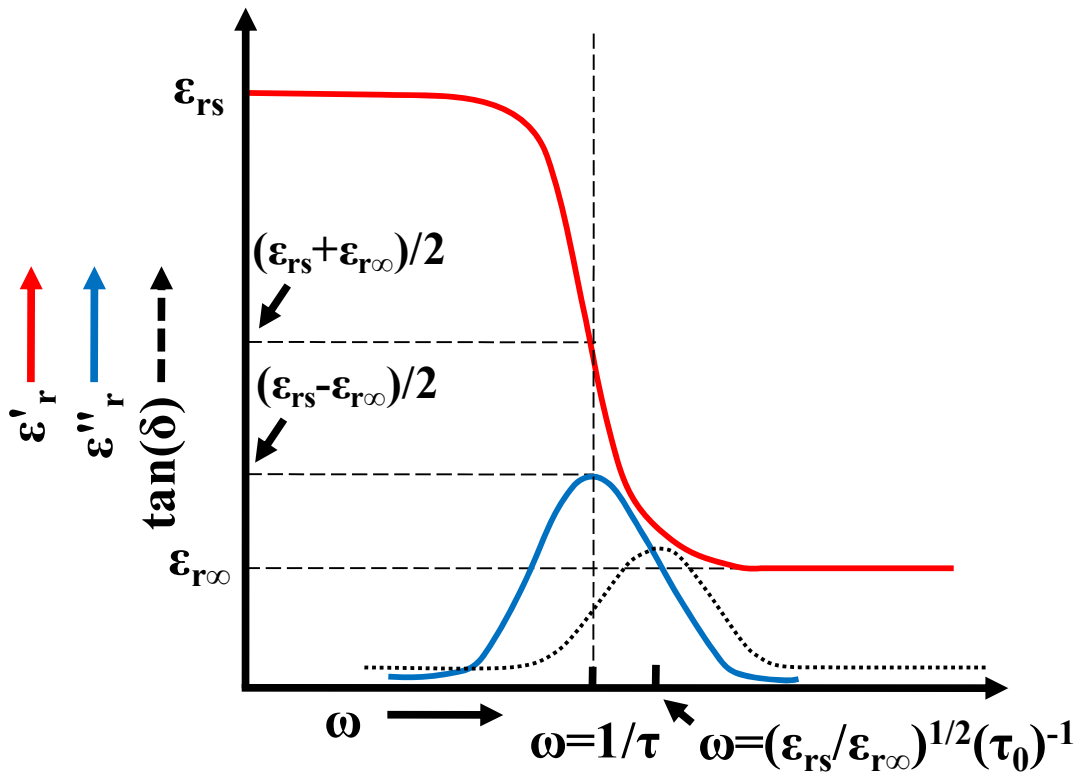


Figure 1-4 The schematic of ϵ'_r , ϵ''_r and $\tan \delta$ as functions of ω based on Debye equation.

1.1.4 Cole and Cole plot

Debye equation does not fit the experimental results for most dielectric materials that have a set of relaxation time. Therefore, there are many empirical relaxation equations that have been introduced to describe the relaxation phenomena. For example, Cole and Cole equation is shown as^{25, 26}:

$$\varepsilon_r^*(\omega) = \varepsilon_{r\infty} + \frac{\varepsilon_{rs} - \varepsilon_{r\infty}}{1 + (j\omega\tau_0)^{1-\alpha}} \quad (1-18)$$

where α varies $0 < \alpha < 1$, and the maximum loss occurs at $\omega\tau_0 = 1$. Some experimental results agree well with Cole-Cole equation with $\alpha > 0$. After eliminating $\omega\tau_0$ from the equation

(1-18), it is an equation of a circle with center at $[\frac{\varepsilon_{rs} - \varepsilon_{r\infty}}{2}, -\frac{(\varepsilon_{rs} - \varepsilon_{r\infty})}{2} \tan \frac{\alpha\pi}{2}]$ and

radius of $[\frac{\varepsilon_{rs} - \varepsilon_{r\infty}}{2} \sec \frac{\alpha\pi}{2}]$ as shown in Figure 1-5. This is written as following:

$$[\varepsilon_r' - \frac{(\varepsilon_{rs} + \varepsilon_{r\infty})}{2}]^2 + [\varepsilon_r'' + \frac{(\varepsilon_{rs} - \varepsilon_{r\infty})}{2} \tan \frac{\alpha\pi}{2}]^2 = [\frac{\varepsilon_{rs} - \varepsilon_{r\infty}}{2} \sec \frac{\alpha\pi}{2}]^2 \quad (1-19)$$

The Davidson-Cole and Havriliak-Negami equations are given by²⁵:

$$\varepsilon_r^* - \varepsilon_{r\infty} = \frac{\varepsilon_{rs} - \varepsilon_{r\infty}}{(1 + j\omega\tau_0)^\beta} \quad (1-20)$$

$$\varepsilon_r^* - \varepsilon_{r\infty} = \frac{\varepsilon_{rs} - \varepsilon_{r\infty}}{[1 + (j\omega\tau_0)^{1-\alpha}]^\beta} \quad (1-21)$$

where $0 < \alpha < 1$ and $0 < \beta < 1$. If choosing the proper parameters α and β , the modification of the Cole-Cole equation can better fit experimental results. It has been found that several materials obey the Davidson-Cole equation, such as glycerol triacetate and pyralene. However, in other conditions, the Havriliak-Negami equation results a much better fit to most experimental results.

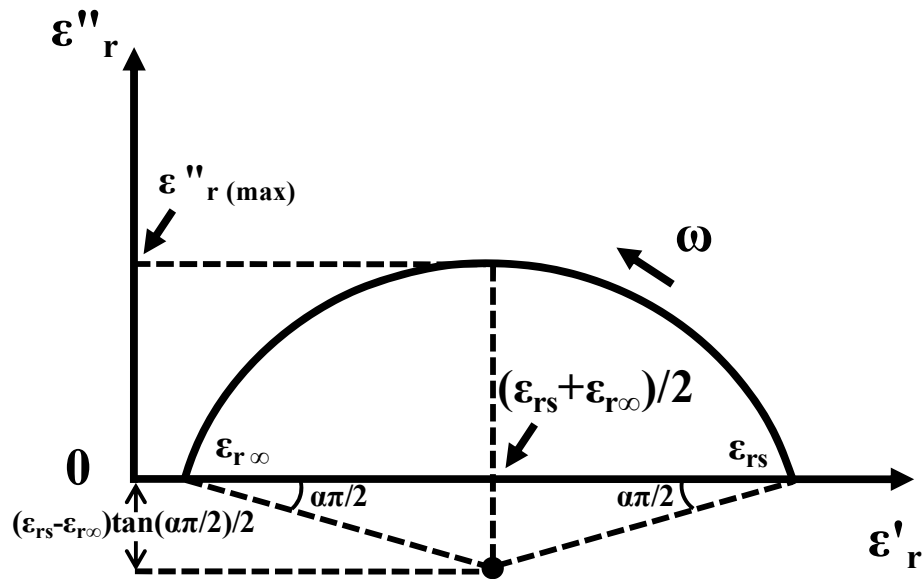


Figure 1-5 The Cole-Cole plot for dielectric material with a set of relaxation time based on Cole-cole equation.

1.2 Classification of Dielectric Materials

Dielectric materials can be classified into two major categories: nonpolar materials and polar materials²⁵.

1.2.1 Nonpolar Materials

A nonpolar material is defined as a material obtaining no permanent dipole moments. Their dielectric constants are relatively small, such as silicon ≈ 3.7 , diamonds $\approx 5.5\sim 10$, parfin $\approx 1.9\sim 2.5$, and carbon tetrachloride ≈ 2.0 .

1.2.2 Polar Materials

A polar material is defined as a material possessing a permanent dipole moment which is associated with molecule or unit cell. Among those materials, if crystals have spontaneous polarization, then it is called Pyroelectric crystals. The ferroelectric crystals are categorized into Pyroelectric crystals, but they also have reversible polarization^{4, 27}. There is a critical temperature, called the Curie temperature, which marks the dramatic change from the ordered to the disordered in phase. At this temperature, the dielectric constant can reach values three to four orders of magnitude higher than that in the

disordered phase. Among polar materials, the ferroelectrics, due to their dielectric constants as high as 5,000~18,000, have attracted a lot of attention and will be discussed later in detail.

1.2.2.1 Ferroelectric Ceramic and Polymer

A ferroelectric crystal exhibits a reversible spontaneous electric polarization and a hysteresis loop. As the electric field E increases, the polarization will reach its saturation value. Ferroelectric (FE) behaves uniquely and is characterized by a P_s which can be switched by an electric field E . Saturated polarization P_s is the state when the increase of electric field cannot lead to an increase on the polarization, such that an increase of electric field produces no significant change in energy density. Coercive field E_c is the applied electric field required to reduce the polarization to zero. After the removal of the applied field, polarization is not zero but a finite value called as the remnant polarization P_r ^{25, 28-30}. The basic feature of a FE is shown in Figure 1-6.

FE goes through a phase transition from a FE phase to a PE phase (paraelectrics) at a temperature T_c (Curie temperature) at which its dielectric constant reaches its maximum value^{4, 25, 27} as shown in Figure 1-7. When above curie temperature T_c , the dielectric constant of ferroelectric materials obey closely the Curie-Weiss relation^{4, 25}:

$$\varepsilon'_r = \frac{C}{T - T_c} \quad (1-22)$$

where C is the Curie constant.

FE can be inorganic materials such as BaTiO₃ (BT), PbTiO₃ (PT), or organic materials such as P(VDF-TrFE), nylon³⁰. Although FE exhibited high dielectric constant, the dielectric constant is strongly dependent on temperature. There are a lot of research works to broaden the permittivity versus temperature. By substituting Ti with other cations such as Sr etc, T_c can be reduced. At the same time, by using La³⁺, Nb⁵⁺ doping in BaTiO₃, it can inhibit grain growth and then has the effect of enhancing the permittivity below T_c . For example, with 1.5 wt% Nb oxide doping, it can result in a dielectric constant of 5000~18,000 below T_c (~130 °C)³¹. Besides BaTiO₃, Lead magnesium niobate (PMN) is another important ferroelectric material. For pure PMN, the dielectric

constant is about 16,000³²⁻³⁴ and the relaxation phenomena between permittivity and temperature is shown in Figure 1-8³⁴.

As shown in Table 1-2, *FE* ceramics have high dielectric constant, but they exhibit low dielectric strength, tend to be brittle and generally need high processing temperature. Despite the low dielectric constant in *FE* polymers, *FE* polymers display high dielectric strength, relative flexibility and require low processing temperature in contrast with *FE* ceramics.

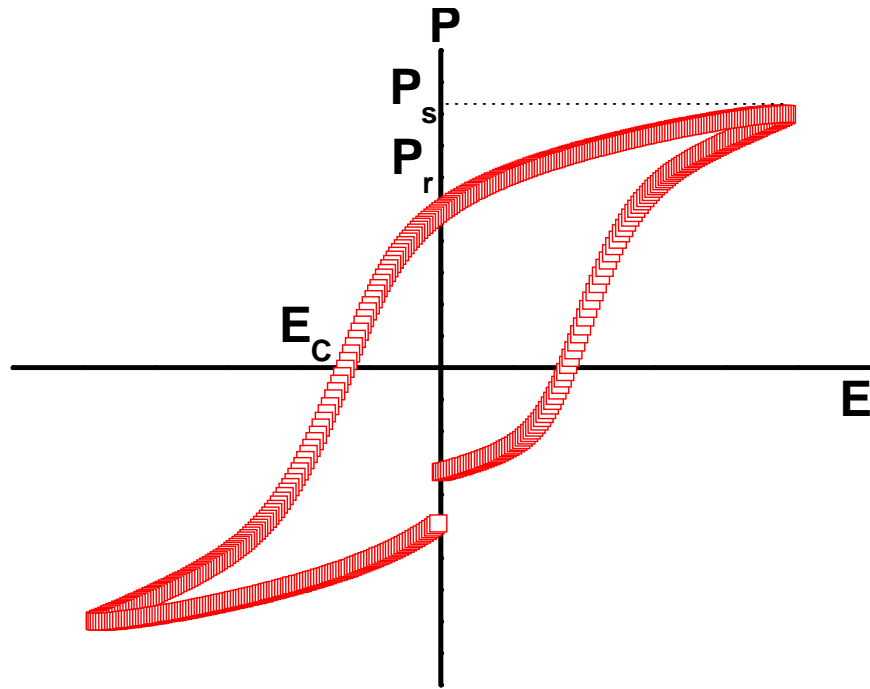


Figure 1-6 P-E loop of ferroelectric.

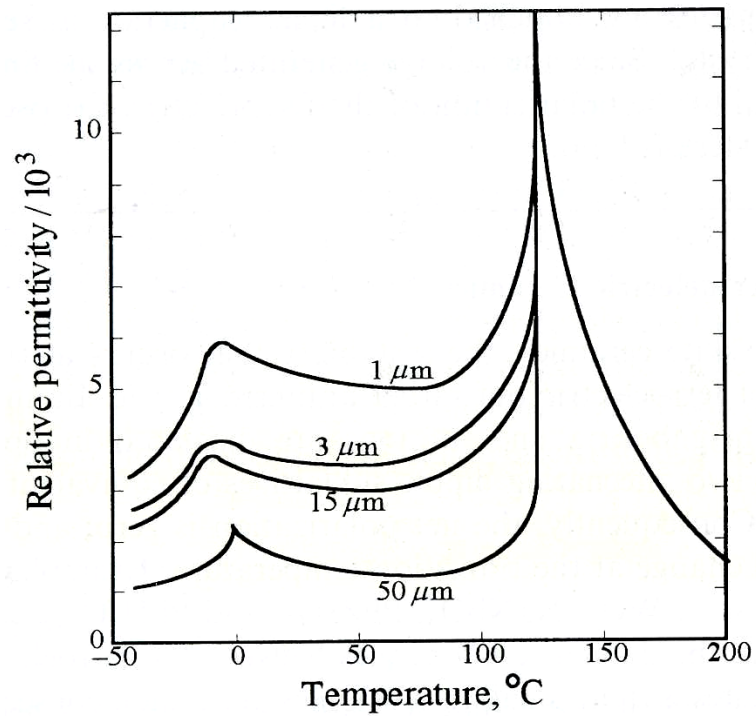


Figure 1-7 Effect of grain size on permittivity of BaTiO_3 . (Relative permittivity is represented by ϵ' , which is described in Section 1.1).

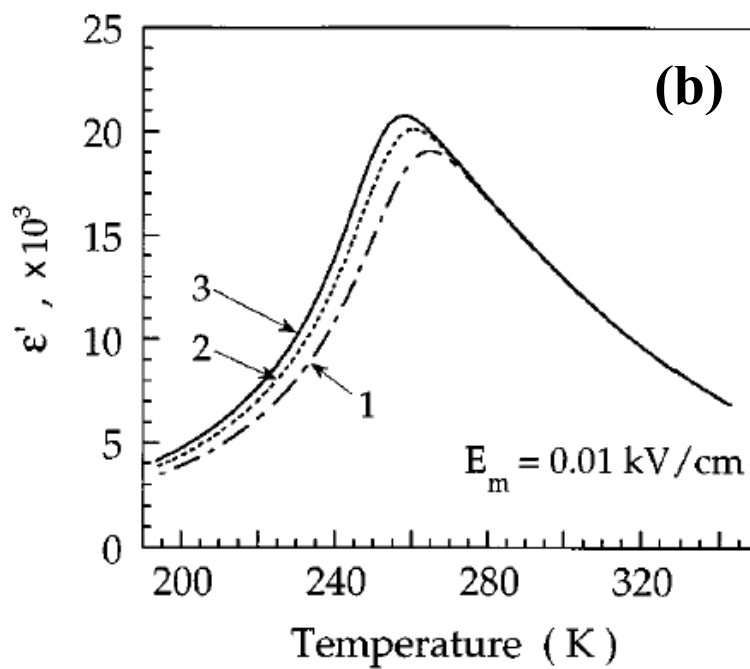
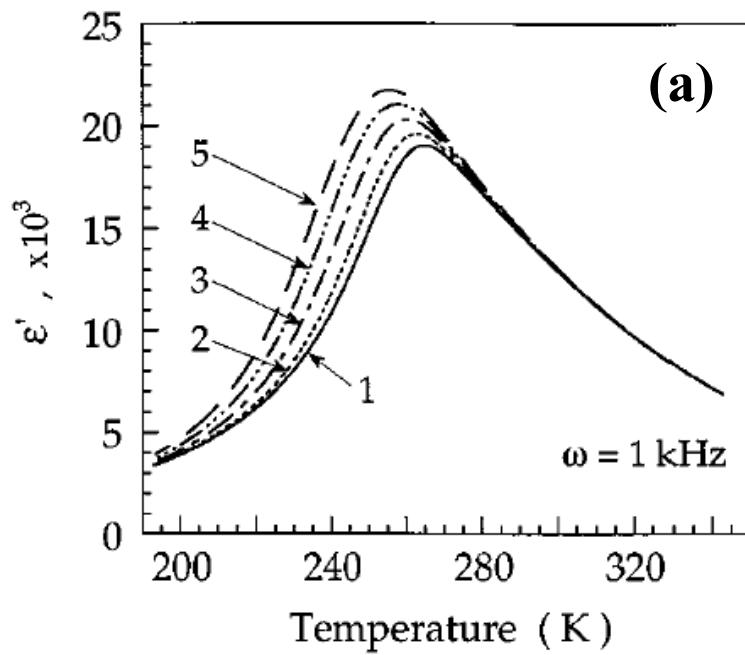


Figure 1-8 Dielectric permittivity of PMN: (a) at various amplitudes, E_m (1-0.01, 2-0.5, 3-1, 4-1.5, 5-2 kV/cm), and (b) various frequencies, ω (1-1 kHz, 2-100 Hz, 3-20 Hz) of the ac field³⁴. (ϵ' is equivalent to ϵ'' , which is described in Section 1.1).

Table 1-1 Summary of dielectric data for *FE* ceramics and polymers.

Materials	T_c , °C	ϵ'_r at T_c	P_s , C/m ²	Ref.
Rochelle salt	24	5,000	0.25 (RT)	⁴
BaTiO ₃	120	1,600	0.26 (RT)	⁴
KNbO ₃	434	4,200	0.26 (RT)	⁴
P(VDF-TrFE)	65	70	0.10 (RT)	^{12, 30}

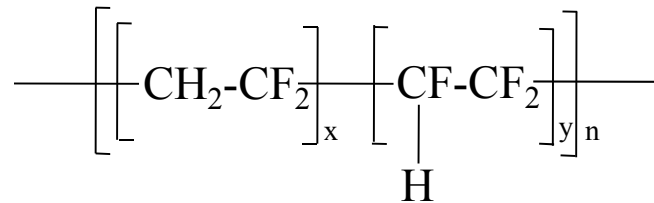
Table 1-2 Mechanical and dielectric properties for *FE* ceramics and polymers at RT and T_c .

	Density (g/cc)	Y (GPa)	$\epsilon'_{r(max)}/\text{loss}$ (1 kHz)	T_c , °C	Ref.
BT (<i>BaTiO</i> ₃)	>5.55	67	1,450/0.008	120	³⁵
PMN (<i>Pb(Mg</i> _{1/3} <i>Nb</i> _{2/3} <i>)O</i> ₃)	>6.1	61	5,500/0.05	-15	³⁶
PZT (<i>Pb(Zr</i> _{0.52} <i>Ti</i> _{0.48} <i>)O</i> ₃)	>7.55	63	1,340/0.004	300	^{37, 38}
PNN (<i>Pb(Ni</i> _{1/3} <i>Nb</i> _{2/3} <i>)O</i> ₃)	>7.8	55	5,500/0.023	150	³⁶
PVDF	1.76	2.0	5.6/0.05	80	³⁹
P(VDF-TrFE) 50/50mol%	1.8	2.3	15/0.075	70	^{12, 40}

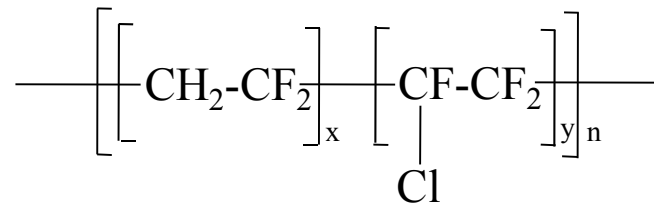
1.2.2.2 Ferroelectric Polymers

Poly(vinylidene fluoride) (PVDF) exhibits the high dielectric constant (≈ 11), as well as better piezoelectricity and ferroelectricity⁴¹⁻⁴³. PVDF was the first polymer that exhibits both significant piezoelectric and ferroelectric properties. The high electronegative fluorine atom with a van der Waals radius of 1.5 Å, is slightly larger than that of hydrogen about 1.2 Å, so the monomer unit has a net dipole moment of about 7.06×10^{-30} Cm^{25,30}. The monomer unit is -CH₂-CF₂-.

Among electroactive polymers, poly(vinylidene fluoride-trifluoroethylene) P(VDF-TrFE) copolymer has been widely studied^{7, 44-46}. With increasing film thickness and for longer annealing times, the dielectric constant for P(VDF-TrFE) was found to reach 10 after it was deposited on different substrates, such as Si and SiO₂⁴⁷. After irradiation with 4×10^5 Gy at 120 °C, it was found that a dielectric constant of 28 at 1 kHz was reached in P(VDF-TrFE) 50/50 copolymer⁷. Moreover, its dielectric properties are dependent on composition: the higher -VDF, then the higher piezoelectric coefficients. Therefore, P(VDF-TrFE) 55/45 copolymer exhibits higher dielectric constant, but low piezoelectric coefficients. The chemical structure of P(VDF-TrFE) is shown as following:



Recently, it was found that a new copolymer P(VDF-CTFE) can withstand high electric field^{8, 48}, as well as exhibiting a high dielectric constant (≈ 10). The chemical structure of P(VDF-CTFE) is shown as following:



1.3 Energy Storage Density

The energy stored in a dielectric material under an electric field \vec{E} can be expressed by the shadow area in Figure 1-9 in which different relationships between \vec{E} and \vec{D} are presented^{8, 49}:

$$W_E = \int \vec{E} \cdot d\vec{D} \quad (1-23)$$

where W_E is energy storage density defined as the energy stored in a unit volume (J/m^3).

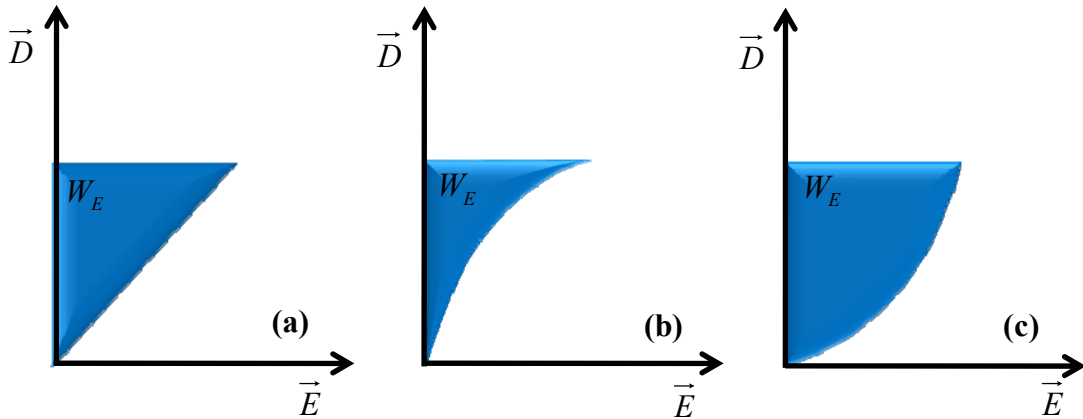


Figure 1-9 Relationship of electric displacement \vec{D} vs. electric field \vec{E} : (a) linear; (b) nonlinear with positive curvature; (c) nonlinear with negative curvature.

Based on Figure 1-9 and Equation (1-23), it can be concluded that a higher \vec{D} and a higher \vec{E} are very important to achieve a higher energy density. Additionally, the curvature of \vec{D} vs. \vec{E} is also very critical to the W_E .

For linear dielectrics, the W_E can be simplified as⁸:

$$W_E = \frac{1}{2} \epsilon'_r \epsilon_0 \vec{E}^2 \quad (1-24)$$

According to Equation (1-24), a higher dielectric strength, which would allow a high electric field to be applied and a higher permittivity, are highly desirable for the dielectrics used in energy storage devices. The dielectric constant and strength of some inorganic and organic materials are given in Table 1-3. As shown in Table 1-3, inorganic materials usually exhibit high dielectric constants, however, their dielectric strengths \vec{E}_b are very low. On the other hand, organic materials have very high dielectric strengths \vec{E}_b ,

but low dielectric constants. Due to inorganic materials' low \vec{E}_b , inorganic materials usually have small energy densities, whereas organic materials have higher energy densities due to their high dielectric strengths which have been shown in Table 1-3. Therefore, there is a great need to develop a new hybrid ceramic-polymer composite which exhibits high dielectric constant, as well as high dielectric strength.

Table 1-3 Dielectric constant ϵ'_r & dielectric strength \vec{E}_b of some current dielectric materials.

	Materials	ϵ'_r	\vec{E}_b (MV/m)	W_E at $\frac{1}{2}\vec{E}_b$ (kJ/m ³)	Ref.
Inorganic	Air	1.007	3	0.01	⁵⁰
	Tantalum oxide	11	4	0.20	⁶
	Quartz, fused	3.85	20	1.70	⁵¹
	Reconstitute mica	7.8	64	17.67	^{52, 53}
	High-Voltage ceramic	500~6000	2	27	^{54, 55}
Organic	Epoxy	4	16	1.10	³⁶
	Polyester	3.4	28	2.90	³⁶
	Polysulfone	3.2	100	35	³⁶
	Polypropylene	2.3	140	49	³⁶
	Kapton (Polyimide)	3.6	339	312	³⁶

1.4 Applications of Dielectric Materials

Dielectric materials have many applications, such as capacitors and electronic package. For dielectric materials used in capacitors, they have two primary functions: (a) energy storage, (b) capacitive coupling in electrical circuit. For electronic package purpose, dielectric materials are used to enclose and protect an electronic device in order to reduce the overall noise between operating supplies such as power and ground. Based on the application, the dielectrics used in capacitors have been categorized into three classes by the Electronic Industries Association (EIA)^{4, 25}:

Class I: Dielectric materials with a relatively low permittivity (15~500) and a dielectric loss ≤ 0.003 over a working temperature range from -55 °C to +85 °C.

Class II: Dielectric materials based on ferroelectrics with high permittivity (500~20,000).

Class III: Dielectric materials based on conductive phase with very high capacitances and very low breakdown field.

Those materials are presented in Figure 1-10 with their ϵ'_r and $\tan \delta$. Dielectric materials for temperature compensating capacitor ($|\Delta\epsilon| \leq 5\%$) are mainly based on barium titanate with titanium dioxide and calcium titanate in order to increase the dielectric constant or to get desired temperature curve. Those materials are presented in lower-left corner of Figure 1-10⁵⁶.

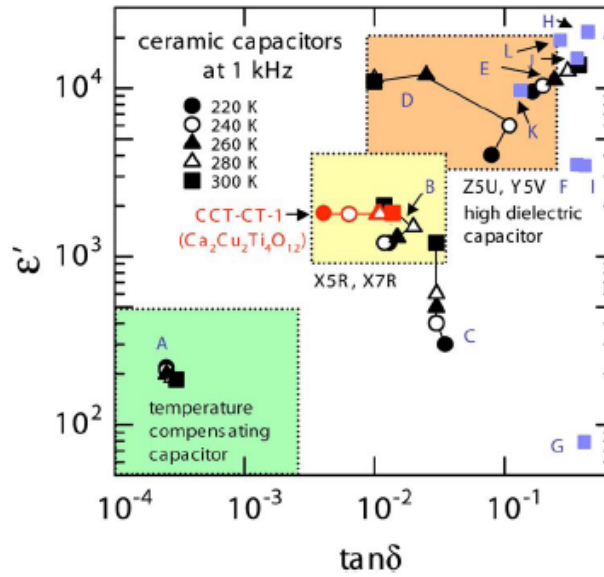


Figure 1-10 The classified categories of dielectric materials⁵⁶. (ϵ' is equivalent to ϵ'_r , which is described in Section 1.1).

High dielectric constant capacitor category can be mainly classified into X5R, X7R, Z5U and Y5U based on temperature coefficient of capacitance (TCC) by the Electronic Industries Association (EIA) standards. Those materials are presented in high-right corner of Figure 1-10²⁵.

- I. For X5R, $|\Delta\epsilon'_r| \leq 15\%$ from $-55\text{ }^\circ\text{C}$ to $+85\text{ }^\circ\text{C}$.
For X7R, $|\Delta\epsilon'_r| \leq 15\%$ from $-55\text{ }^\circ\text{C}$ to $+125\text{ }^\circ\text{C}$.
- II. For Z5U, $-55\% \leq \Delta\epsilon'_r \leq 22\%$ from $+10\text{ }^\circ\text{C}$ to $+85\text{ }^\circ\text{C}$.
- III. For Y5V, $-82\% \leq \Delta\epsilon'_r \leq 22\%$ from $-30\text{ }^\circ\text{C}$ to $+85\text{ }^\circ\text{C}$.

1.5 Calcium Copper Titanate $\text{CaCu}_3\text{Ti}_4\text{O}_{12}$

Recently, a new material $\text{CaCu}_3\text{Ti}_4\text{O}_{12}$ with perovskite-related structure and very different dielectric properties has been reported by M.A.Subramanian^{57, 58}. In order to grow $\text{CaCu}_3\text{Ti}_4\text{O}_{12}$ phase, both conventional powder-sintering techniques and mechanical alloying have been used^{57, 59-61}. By calcining at 900-1,000 °C, a high dielectric constant of 12,000 was reported, and it is found that by decreasing the calcination temperature to around 800 °C, the dielectric constant has been improved to 10^5 and remains almost constant at temperature between 100 and 600 K (Figure 1-11). In Figure 1-11, the dielectric response is around 100 fold drop around 100 k. However, no detectable crystallographic structure change has been probed⁶¹. A dielectric constant for $\text{CaCu}_3\text{Ti}_4\text{O}_{12}$ as high as 20,000 for ceramics and 300,000 for single crystals at 1 kHz and room temperature has been reported^{59, 61}.

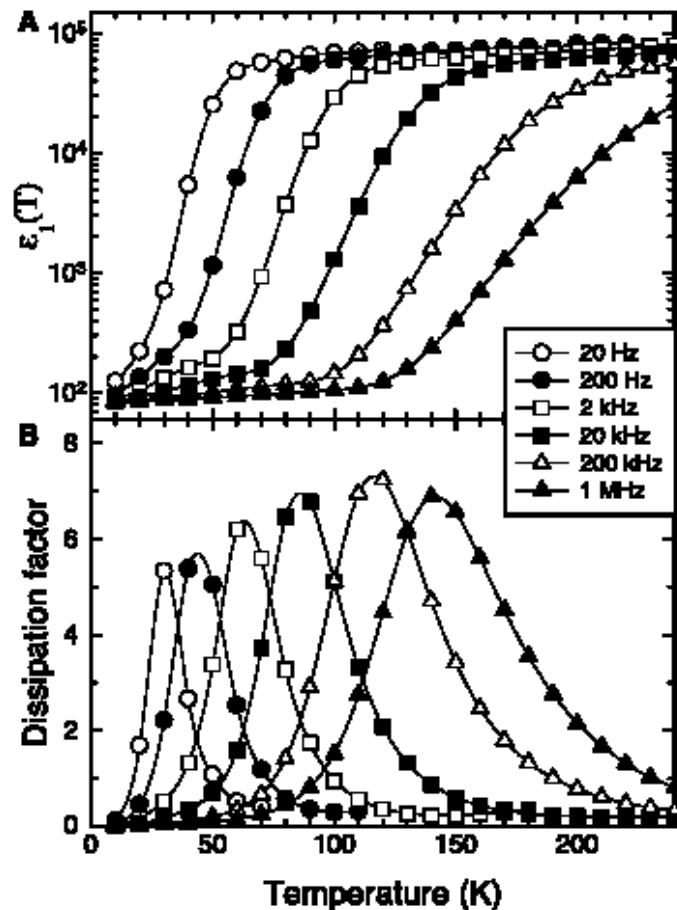


Figure 1-11 The temperature dependence of dielectric constant and loss in $\text{CaCu}_3\text{Ti}_4\text{O}_{12}$ ⁶¹. (ϵ_1 is equivalent to ϵ'_r , which is described in Section 1.1).

1.5.1 Crystallographic Structure of $\text{CaCu}_3\text{Ti}_4\text{O}_{12}$

The $\text{ACu}_3\text{Ti}_4\text{O}_{12}$ (A=trivalent rare earth or Bi) family of compound was found in 1967 and accurate structure was determined in 1979. The dielectric constant and loss of $\text{ACu}_3\text{Ti}_4\text{O}_{12}$ family are shown in Table 1-4.

Neutron powder diffraction of $\text{CaCu}_3\text{Ti}_4\text{O}_{12}$ indicates a cubic-perovskite structure with $\text{Im}\bar{3}$ group symmetry and cubic lattice parameter $a=7.391 \text{ \AA}$ ⁶¹. Figure 1-12 shows the structure of $\text{CaCu}_3\text{Ti}_4\text{O}_{12}$. In comparison with ferroelectrics, the high dielectric constant originates from the rattling of Ti^{4+} within the TiO_6 octahedron. Moreover, the $\text{CaCu}_3\text{Ti}_4\text{O}_{12}$ exhibits more constraint than ferroelectrics. The TiO_6 octahedra tilt and form a square planar arrangement around Cu^{2+} . Based on structure calculations, it is found that the Ti-O bonds are under tension and increase the polarization of the TiO_6 octahedra⁵⁷.

Due to fact that $\text{CaCu}_3\text{Ti}_4\text{O}_{12}$ is weak scatter, there are only five predicted modes around 444, 453, 510, 576 and 761 cm^{-1} in raman scattering. Among those modes, 444, 453 and 510 cm^{-1} are related to TiO_6 rotationlike modes, 576 cm^{-1} is due to Ti-O-Ti anti-streching and 761 cm^{-1} is assigned to TiO_6 octahedra^{62, 63}. Moreover, based on raman spectra and XRD diffraction, there is no evidence found to prove any structure phase transformation up to 46 GPa⁶⁴. However, Fagan *et al.* reported that when pressure is > 3.0 GPa, the stable structure is rhombohedra (R3) instead of cubic ($\text{Im}\bar{3}$)⁶⁵. Besides high pressure influence, the gain size effects on the dielectric constant of the $\text{CaCu}_3\text{Ti}_4\text{O}_{12}$ have been studied⁶⁶. It was observed that the dielectric constant became four times higher varying 2,000 to 8,000 as the grain size increased from 1.3 μm to 4.1 μm .

Table 1-4 Dielectric and cell edge data for $ACu_3Ti_4O_{12}$ (at 25 °C)⁵⁸.

Compound	Relative dielectric constant (ϵ'_r)	Loss tangent ($tg\delta$)	a (Å at 25 °C)
$CaCu_3Ti_4O_{12}$	10286	0.067	7.391
$CdCu_3Ti_4O_{12}$	409	0.093	7.384
$La_{2/3}Cu_3Ti_4O_{12}$	418	0.060	7.427
$Sm_{2/3}Cu_3Ti_4O_{12}$	1665	0.048	7.400
$Dy_{2/3}Cu_3Ti_4O_{12}$	1633	0.040	7.386
$YCu_3Ti_3FeO_{12}$	33	0.308	7.383
$Bi_{2/3}Cu_3Ti_4O_{12}$	1871	0.065	7.413
$BiCu_3Ti_3FeO_{12}$	692	0.082	7.445
$LaCu_3Ti_3FeO_{12}$	44	0.339	7.454
$NdCu_3Ti_3FeO_{12}$	52	0.325	7.426

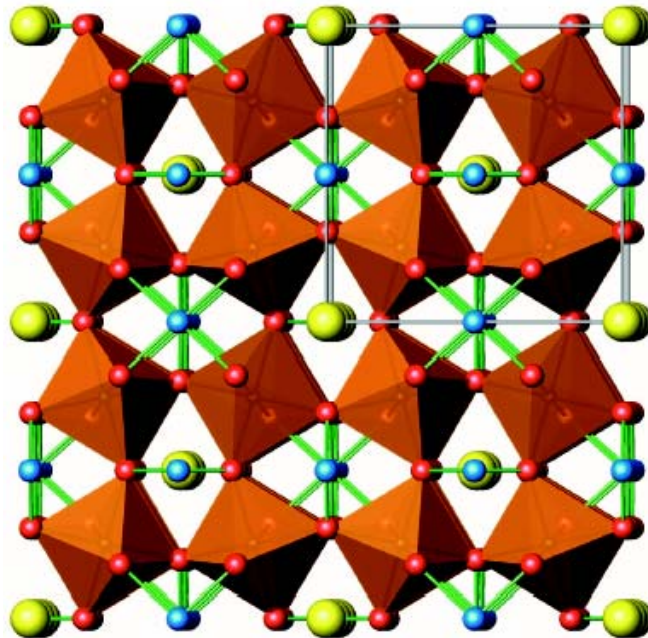


Figure 1-12 The structure of $CaCu_3Ti_4O_{12}$ (Cu-blue, Oxygen-red, Ca-yellow)⁶¹.

1.5.2 Origin of Colossal Dielectric Response

A few explanations on the colossal dielectric response of $\text{CaCu}_3\text{Ti}_4\text{O}_{12}$ have been proposed. After having studied by x-ray, optical-, and neutron-diffraction techniques, impedance spectroscopy, and theoretical electronic structure calculations, it is unlikely that the large dielectric response is related with intrinsic properties^{58, 59, 61, 67-72}. Intrinsic means $\text{CaCu}_3\text{Ti}_4\text{O}_{12}$ is a perfectly stoichiometric, defect free single-domain crystal. Based on experimental results, different explanations have been proposed:

1. Subramanian *et al.* thought the high dielectric constant originates from the creation of internal barrier layer capacitances (IBLC)^{57, 58}, presumably at twin boundaries (Figure 1-13) which has been detected by Wu *et al.* in high-resolution TEM⁷². In boundary layer dielectrics, an effective circuit of parallel capacitors formed from microcrystalline grains is thought to give rise to high dielectric response.

2. Wu *et al.* pointed out for polycrystalline samples, the main defects lie at grain boundary, while for a single crystal, they will be the dislocations and planar defects. Since the disorder-induced lattice discontinuity or displacement will result in IBLC and change the dielectric response of the material, this cation disorder could have significant implications on the origin of the colossal dielectric responses.

3. Lunkenheimer *et al.* suggested it might be due to Maxwell-Wagner-type contribution of depletion layers at the interface between sample and contacts⁷¹.

4. Cohen *et al.* thought the high dielectric constant originates from the inhomogeneity of local dielectric boundaries where twin, Ca ordering, and antiphase boundaries exist⁶⁹.

5. Adams *et al.* suggested due to the limited reoxidation in the furnace, there is the formation of semiconducting grains and insulating grain boundaries⁵⁹. Sinclair *et al.* also thought the semiconductivity of grain is because of the oxygen loss at high temperature⁶⁷.

6. Besides those explanations, other theories such as the electrode/sample effects, doping effect etc, have been proposed⁷³⁻⁷⁷. Broadband dielectric spectroscopy studies up to 1.3 GHz by Krohns *et al.* have been carried out⁷⁸. Temperature dependent results based on two different types of contacts (silver-paint and sputtered gold) exhibited significant difference which proved the surface-related origin of the high permittivity value in Figure 1-14. At the same time in broadband frequency studies, besides the Maxwell-Wagner

relaxation, a second relaxation mode showed up as $T > 180$ K for 5 Hz in Figure 1-15. Krohns *et al.* further confirmed that the second relaxation should be caused by a second surface layer. Thus based on experimental results, Krohns *et al.* suggested that two relaxations existed: one is related with the internal barrier layer capacitor (IBLC) and the other with surface barrier layer capacitor (SBLC).

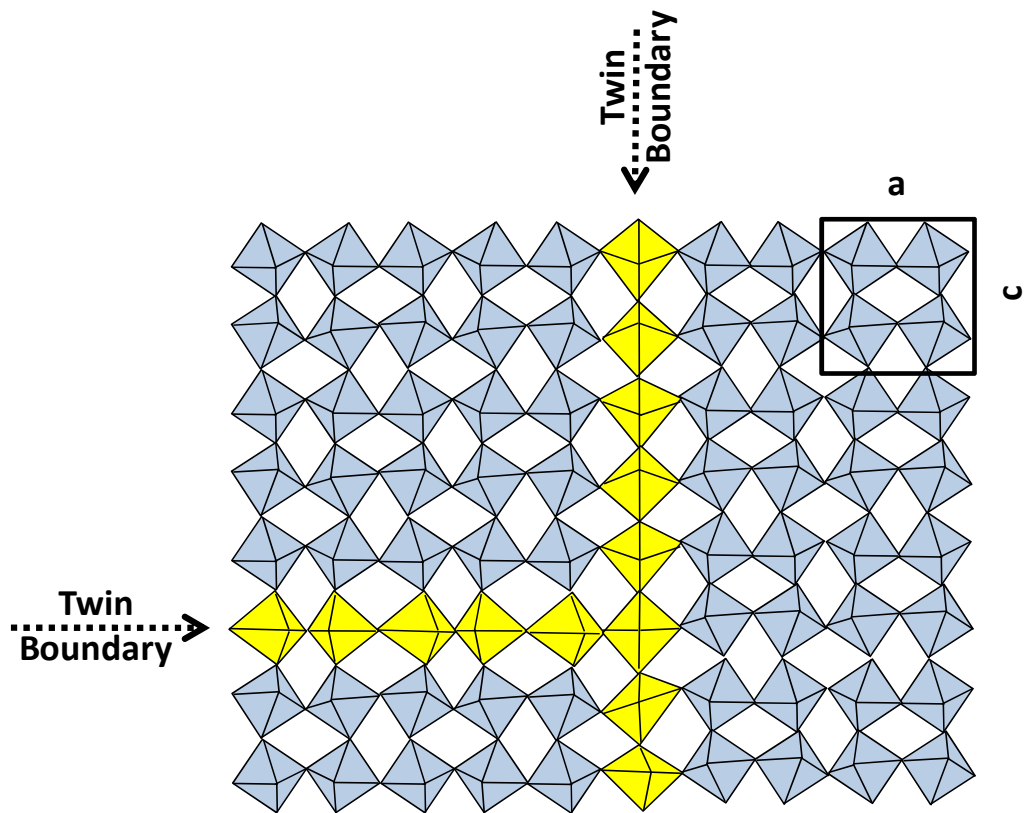


Figure 1-13 The schematic of twin boundary in $\text{CaCu}_3\text{Ti}_4\text{O}_{12}$ ⁷².

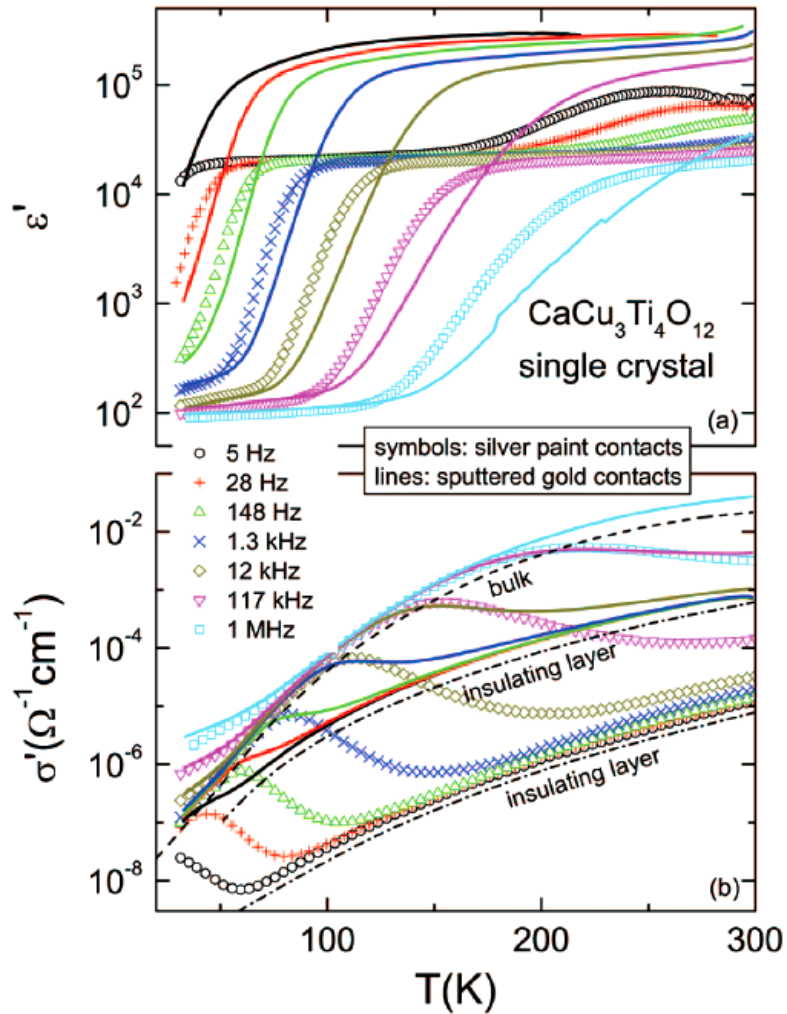


Figure 1-14 (a) Temperature-dependent dielectric constants and (b) conductivities of single-crystalline $\text{CaCu}_3\text{Ti}_4\text{O}_{12}$ with sputter gold (solid lines) and silver-paint contacts (symbols) at various frequencies⁷⁸. The dashed and dashed-dotted lines in (b) show an estimate of the intrinsic bulk dc conductivity and the contribution of the insulating layer. (ϵ' is equivalent to ϵ'' , which is described in Section 1.1).

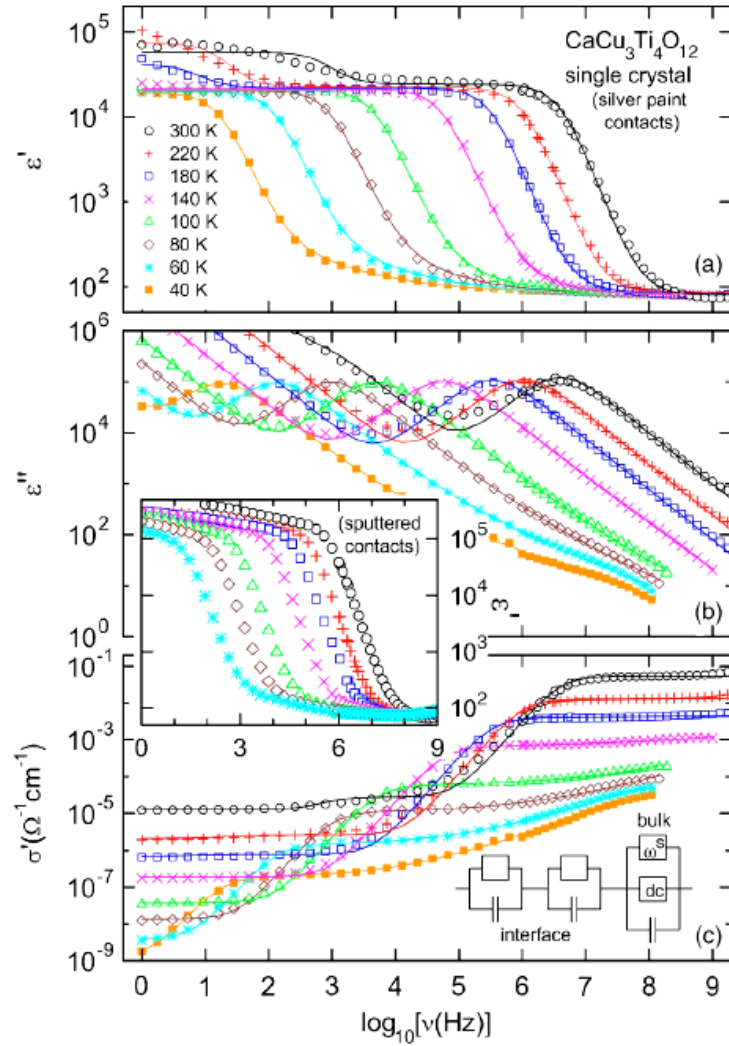


Figure 1-15 (a) Frequency-dependent dielectric constants, (b) loss, and (c) conductivities of single crystalline $\text{CaCu}_3\text{Ti}_4\text{O}_{12}$ with silver-paint contacts at various temperatures⁷⁸. (ϵ' and ϵ'' are equivalent to ϵ'_r and ϵ''_r , respectively, which are described in Section 1.1).

1.6 Ceramic-Polymer Composites

Both advantages and disadvantages of ceramic and polymer have been well discussed in previous sections. In order to combine superior properties of both polymer and ceramics which result in far better performance than those constituent materials, ceramic-polymer composites have been studied as dielectric materials in order to fabricate a flexible hybrid material with better dielectric properties, such as high dielectric constant ϵ' , and high dielectric strength \vec{E}_b .

1.6.1 General Concepts for Composites

The physical properties of composites can be the sum, combination, and product of properties of its constituents based on the properties or connectivity. For example, the total mass is simply the sum of their individual ones. The connectivity was first classified by Newnham *et al*⁷⁹. Based on their connectivity and morphology of each phase, the dimension is defined as 0-0, 1-0, 2-0, 3-0, 1-1, 2-1, 3-1, 2-2, 3-2, and 3-3 for a 2-phase composite as shown in Figure 1-16, where 0/1/2/3 represent the number of dimensions for each component in the composite^{30, 79}. For example, for 0-3 composite it is defined as 0-dimension particle (usually the ceramic particle) and is embedded inside 3-dimensions polymer matrix as shown in Figure 1-16 (blue color: polymer matrix, white color: ceramic particle).

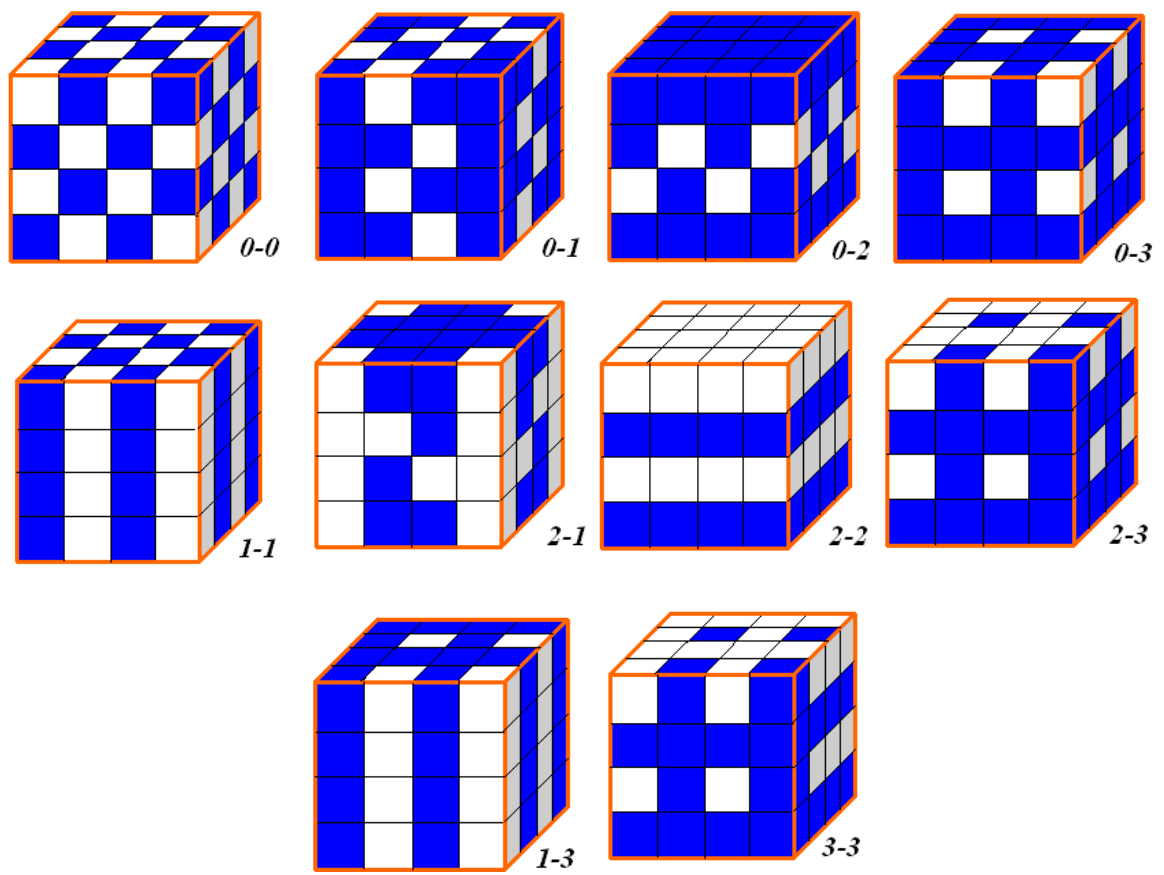


Figure 1-16 Ten dimension patterns in diphasic composites⁷⁹.

1.6.2 Mixing Rule for Permittivity in Two-Phase Composites

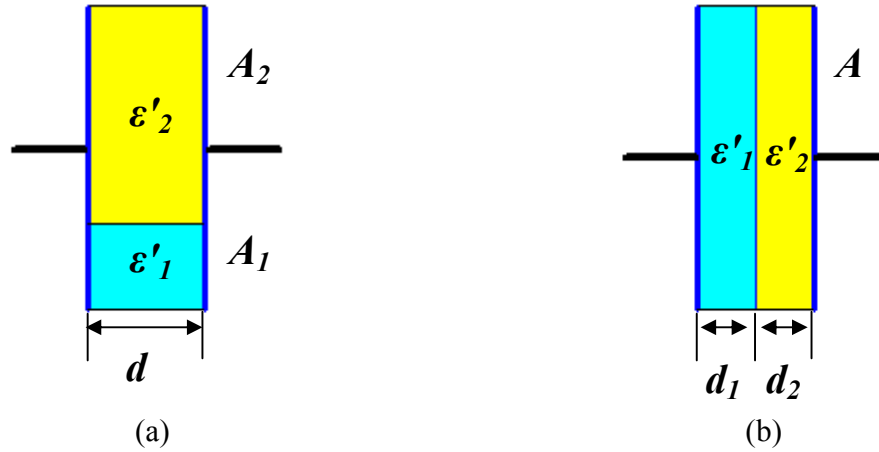


Figure 1-17 Schematic of (a) parallel and (b) series connections.

It is known that the dielectric property of the composite is a function of many factors: 1) size and shape of ceramic particles; 2) dielectric constants of ceramic particles and polymer respectively; 3) morphology distribution of ceramic in the polymer matrix; 4) volume fraction of ceramic in the composite; 5) the appearance of interfacial layer between ceramic and polymer.

For a 2-phase composite, the parallel and series connectivity as shown in Figure 1-17 are two simple cases. The effective dielectric constant ϵ' is³⁰:

$$\epsilon'^n = v_1 \epsilon_1'^n + v_2 \epsilon_2'^n \quad (1-25)$$

where: v_1 and v_2 are the volume fraction of the ceramic particles and polymer matrix respectively ($v_1 = \frac{A_1}{A}$ and $v_2 = \frac{A_2}{A}$ in parallel case; $v_1 = \frac{d_1}{d_1 + d_2}$ and $v_2 = \frac{d_2}{d_1 + d_2}$ in series case), ϵ'_1 and ϵ'_2 are the dielectric constant of the ceramic particles and polymer matrix respectively, and n is +1 and -1 for parallel and series connection, respectively.

In most cases, ceramic-polymer 2-phase composites are statistical mixtures of its components, so the effective dielectric constant of the composite should lie between the values determined by Equation (1-25) for $n=-1$ and $n=1$ as is illustrated in the shadow area in Figure 1-18.

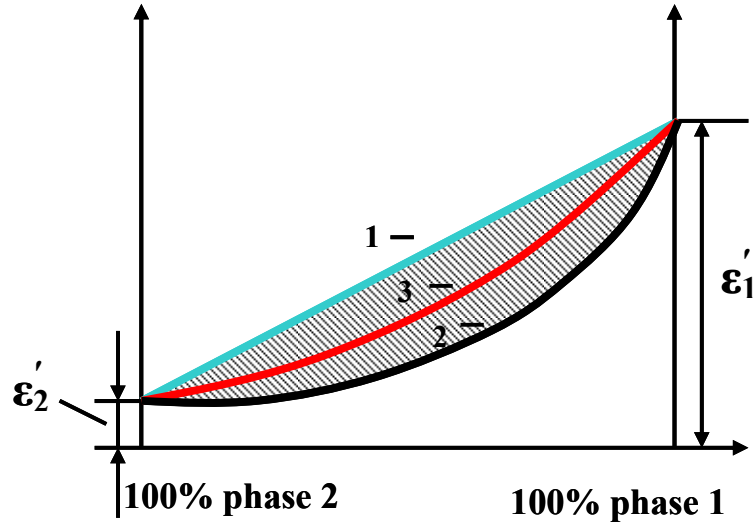


Figure 1-18 Schematic of dielectric constant of two phases 1 and 2 vs. their volume fraction in the mixture: 1, parallel connection; 2, series connection; 3, real composite.

Ceramic-polymer 0-3 composites are widely used due to the fact that it is flexible and easy to fabricate. Different models have been introduced to simulate the effective dielectric constant of these composites.

For a random ceramic-polymer 0-3 composite, Lichtenecker's logarithmic law of mixing is shown as following³⁰:

$$\log \varepsilon' = v_1 \log \varepsilon'_1 + v_2 \log \varepsilon'_2 \quad (1-26)$$

Lichtenecker's equation is modified as:

$$\log \varepsilon' = \log \varepsilon'_2 + (1 - k)v_1 \log\left(\frac{\varepsilon'_1}{\varepsilon'_2}\right) \quad (1-27)$$

where k is a fitting constant for composite material. The value for k is around 0.3 for most well dispersed ceramic-polymer composites.

Das-Gupta *et al.* also suggested⁸⁰:

$$\varepsilon' = \varepsilon'_2 \frac{2(1 - v_1)\varepsilon'_2 + (1 + 2v_1)\varepsilon'_1}{(2 + v_1)\varepsilon'_2 + (1 - v_1)\varepsilon'_1} \quad (1-28)$$

If ceramic particles are sphere in shape, then the Maxwell-Wagner mixing rule is used^{81, 82}:

$$\varepsilon' = \varepsilon'_2 \frac{2\varepsilon'_2 + \varepsilon'_1 + 2v_1(\varepsilon'_1 - \varepsilon'_2)}{2\varepsilon'_2 + \varepsilon'_1 - v_1(\varepsilon'_1 - \varepsilon'_2)} \quad (1-29)$$

Maxwell-Wagner mixing rule is effective for infinite dilution of the dispersed phase that the spherical ceramic particles are separated by distances greater than their characteristic size.

If ellipsoidal ceramic particles are randomly distributed into an a polymer matrix, the effective dielectric constant ε' is⁸³:

$$\varepsilon' = \frac{v_1 \varepsilon'_1 \beta + (1 - v_1) \varepsilon'_2}{v_1 \beta + 1 - v_1} \quad (1-30)$$

where β is the field factor ($\beta = \frac{1}{1 + L \cdot (\varepsilon'_1 / \varepsilon'_2 - 1)}$) and L is defined as the “equivalent” depolarization coefficient of the particles in the direction of the applied field ($0 < L < 1$).

Regarding ellipsoid ceramic particles in polymer matrix, another estimation equation is given by Yamada *et al.*:

$$\varepsilon' = \varepsilon'_2 \left[1 + \frac{nv_1(\varepsilon'_1 - \varepsilon'_2)}{n\varepsilon'_2 + (\varepsilon'_1 - \varepsilon'_2)(1 - v_1)} \right] \quad (1-31)$$

where n is a constant related to geometry of ceramic particles.

Based on the percolation theory, the Bruggeman model was developed^{30, 84}:

$$v_1 \left(\frac{\varepsilon'_1 - \varepsilon'}{\varepsilon'_1 + 2\varepsilon'} \right) + (1 - v_1) \left(\frac{\varepsilon'_2 - \varepsilon'}{\varepsilon'_2 + 2\varepsilon'} \right) = 0 \quad (1-32)$$

1.7 Current Developments of Polymer-Matrix Composite

1.7.1 Ferroelectric Ceramic/Polymer Composite

Composites based on ferroelectric fillers, such as BaTiO₃ (BT), PbZrO₃ (PZT), Ba_{0.65}Sr_{0.35}TiO₃ (BST) and Pb(Mg_{1/3} Nb_{2/3})O₃ (PMN), have been studied and the dielectric properties in some commercial products are shown in Table 1-5. Most of the research has focused on polymer matrices, such as PMMA, Epoxy, and recently more on PVDF-based polymers due to their high dielectric constant.

Composites with PMMA and BT have been fabricated without any considerable gradient in ceramic powder concentration⁸⁵⁻⁸⁷. A linear relationship between BT volume fraction and the effective dielectric constant was observed in PMMA and BT composite and as there are 60 vol.% BT, the dielectric constant is about 40³⁰. If replacing PMMA with Epoxy, a dielectric constant of 44 with 40 vol.% BT was reported by Kuo *et al*⁸⁸, while the dielectric constant of composite with 40 vol.% PMN in Epoxy is 24.

As mentioned above, in order to improve the dielectric constant, composite with P(VDF-TrFE) and PMN-PT (PMN and PT based solid solution) was prepared and a dielectric constant of 200 at 1 kHz was reached²². By combining P(VDF-TrFE) and BST with irradiation, a dielectric constant as high as 150 at 1 kHz (RT) and 200 at 1 kHz (curie temperature) was achieved⁸⁹. Beside a two components composite, a three phase composite with carbon fiber (CF), BT and PVDF has been successfully fabricated with dielectric constant of 100 with 15 vol. % CF⁹⁰. Moreover, another important ferroelectrics is PZT, which has been widely studied by using different polymer matrices, such as PU, PVDF etc. When there are 30 vol.% PZT, the dielectric constant of 24 has been reported in 0-3 composite with PU as matrix, while in PVDF matrix, a dielectric constant of 40 was achieved^{91,92}. The summary for ceramic-polymer composite is shown in Table 1-6.

Table 1-5 Dielectric property of some commercial composite products⁹³.

Company name	Product name	Product thickness (μm)	ϵ'_r (max)	Capacitance density (nF/in^2)
Motorola Labs and Vantico AG	CFP (Ceramic-filled BaTiO ₃ photodielectric liquid)	12	20-22	10
3M	C-Ply (BaTiO ₃ in epoxy matrix)	4~25	14~18	5~30
Sanmina	BC 2000 and EmCap (BaTiO ₃ in epoxy matrix)	50~100	4-36	0.5~2.1
DuPont	Ferroelectric materials in glass powder	—	—	100-180

Table 1-6 Dielectric properties of some current ceramic-polymer composites at RT.

Ceramic-polymer Composite		$\epsilon'_r / \epsilon''_{loss}$ (1 kHz)	Ref.
Ceramic	Polymer		
BT	PMMA	40/0.012~0.016	30
BT	Epoxy resin	44/0.2	88
BT	Polystyrene	100/0.5	94
CF+BT	PVDF	100/0.06	90
PMN	Epoxy resin	24/0.05	88
PMN-PT	Irradiated P(VDF-TrFE)	200/0.25	22
PZT	PU	24/0.8	92
PZT	PVDF	40/0.08	91
PZT	PVDF+PANI	100/0.04	95
PZT	PVC+graphite	360/0.34	96
BST	P(VDF-TrFE)	200/0.03	89

1.7.2 Conductive Filler/Polymer Composites

Conductive filler/polymer composites are another approach towards high dielectric constant materials, which belong to conductor-insulator composite based on percolation theory⁹⁷⁻¹⁰¹. The percolative equation is given as following:

$$\varepsilon' = \varepsilon'_m \left(\frac{f_c - f}{f_c} \right)^{-q} \quad (1-33)$$

where ε' is the effective dielectric constant, ε'_m is the dielectric constant of the matrix, f_c is the percolation threshold, q is the critical exponent (~ 1 for three-dimensional composites). Ultra high dielectric constant can be expected with conductive filler/polymer composites when the concentration of the conductive filler is approaching the percolation threshold due to the fact that the percolative approach requires much lower volume concentration of the filler compared to traditional approach of high dielectric constant particle in a polymer matrix. Therefore, this material option provides advantageous characteristics over the conventional ceramic/polymer composites, especially ultra high dielectric constant with balanced mechanical performance. A polymer matrix composite based on metal powders such as Ni, Cu, Al etc has been fabricated with a high dielectric constant, and better flexibility. Dang *et al.* has proposed a new composite based on LTNO (Li and Ti doped NiO) and PVDF in which the dielectric constant can be optimized to 400 at room temperature at 1 kHz with 30 vol.% LTNO⁹⁷. By doping with multiwalled carbon nanotube (MWNT), it is reported a dielectric constant of about 900 at RT has been achieved in PVDF monopolymer as the MWNT volume fraction increasing to 0.08⁹⁸. Furthermore, the interfacial effect on the percolative behavior was studied and it was found that the percolation threshold varied from 7 vol% to 10 vol% as the filler size increased from 3.5 μm to 5 μm ¹⁰¹. Up to now, more efforts were focused on developing a material which could fulfill the ultimate goal between high dielectric constant and low dielectric loss.

1.8 Interface Effect in Composites

In the previous modeling studied on ceramic-polymer 0-3 composites, the effective dielectric constant was only dependent on the dielectric constant of the ceramic particles and polymer matrix. However, accurately predicting the effective dielectric constant has proven to be difficult. More recently, many researchers working on dielectric behavior have been focusing on the interface effect at the atomic or molecular level of materials¹⁰²⁻¹⁰⁴.

By considering the interface between two uniform materials phases, there are interactions between those atoms and its surroundings via a combination of both short or long-rang forces. Although the forces change over atomic distances and fluctuate because of thermal activity, there will be mean properties characteristic of the bulk phase. As approaching the interface or the boundary, those forces will become increasingly modified. The effective thickness may be less than 1 nm if there are only short-range forces, or 10 nm if the interface is electrically charged. It is well known that interfaces have played an important role in controlling electron and ion transportation in composite systems¹⁰³. In a composite system, as the phase *A* which is a finite-size particle is surrounded by a phase *B*, then the interface between *A* and *B* phases will exhibit significant dominance as the particle size decreases. It is clear that the interface volume exceeds 50 vol% of the particle volume when the particle diameter is less than 5 nm as shown in Figure 1-20. The interfacial layer even constitutes at low filler concentration and shows different properties from the bulks as shown in Figure 1-21. The interfacial properties may begin to vary when the bulk phase disappears. For example, with atomic doping of a semiconductor crystal, even though the dopant has small influence on structure, it can cause a remarkable change of the electrical properties of the “composites”. Especially, the influence of interfaces with nanometric size particles is highly significant.

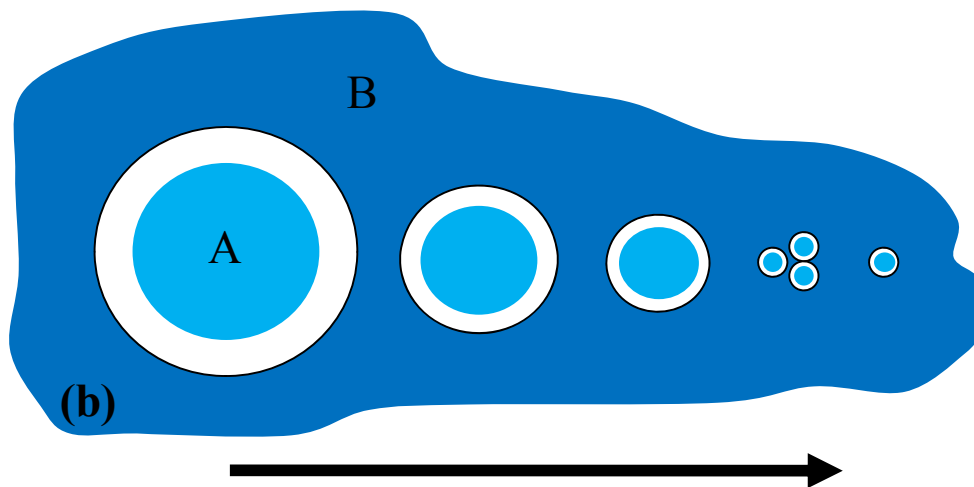
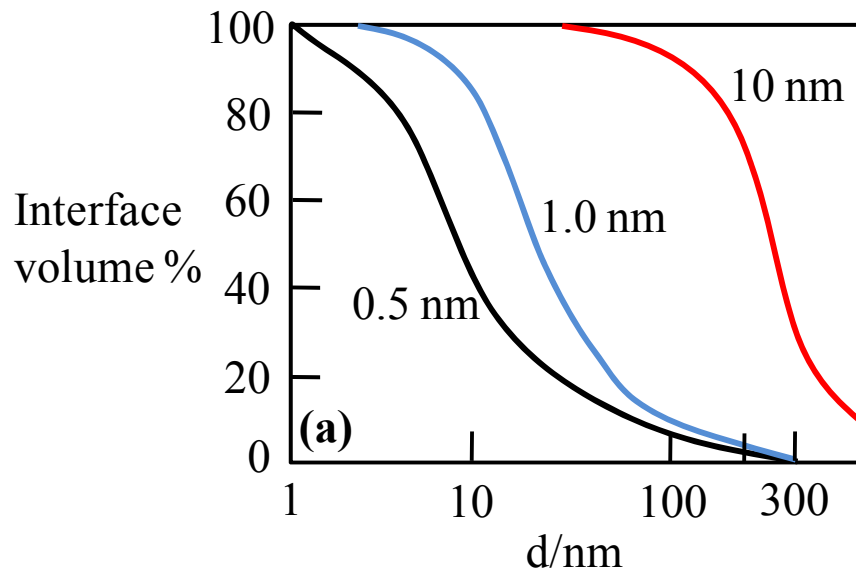


Figure 1-19 (a) percentage volume of interface as function of interface thickness d for particle sizes 10, 1 and 0.5 nm. (b) Schematic of particle A from micrometric to nanometric and then to sub-nanometric size. The interface increasingly dominates¹⁰³.

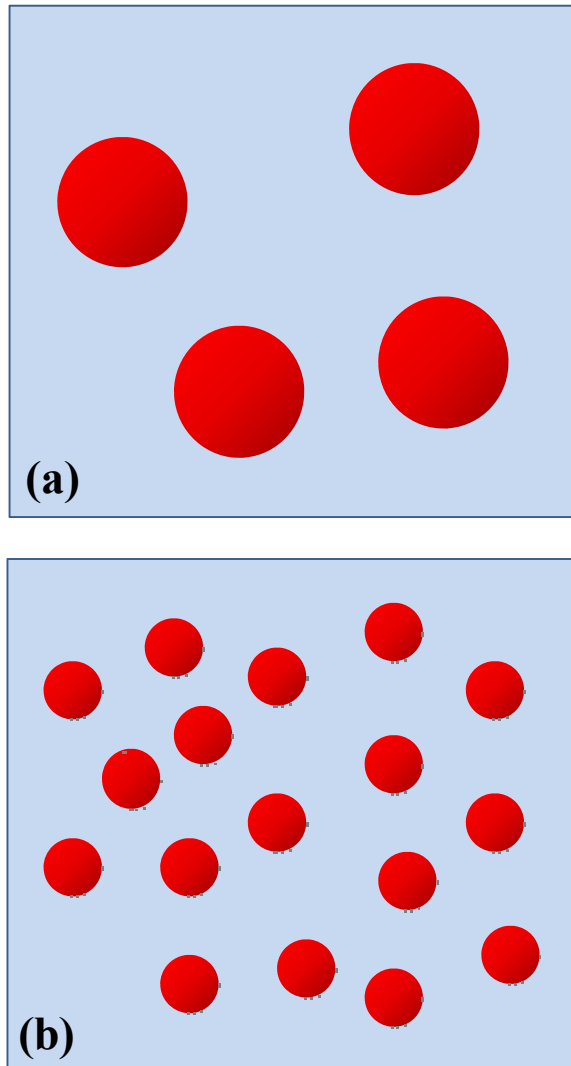


Figure 1-20 Interfacial regions as a function of filler particle size. The filler is shown in red, the interfacial region in dark blue and bulk polymer in pale blue. (a) Large particle produce low radius of curvature and relative less polymer in the interfacial regions. (b) The same volume of filler broken into small particles creates a high radius of curvature and more polymer in the interfacial region¹⁰⁴.

1.8.1 Interfacial Forces

As the atoms are close to each other, there are repulsive short-range forces, which originate from quantum mechanical overlap interactions between the electron clouds of the atoms, and are responsible for covalent bonding, charge-transfer reactions and steric interactions. Besides the short-range forces, the others are electrostatic forces. Those forces usually involve negative electrons and positive nuclei of the system and then lead to dipole moments. All the dipole-related polarization forces are confined in moderate range, which exhibit attractive in nature known as Waals forces.

The term quasi-planar interface has been applied to describe the interfaces in many composite situations as shown in Figure 1-22, where in general three layers can be distinguished. On the left side of the interface, there is a double layer in *A* related with surface states and arising from immobile charged impurities, trapped carriers and mobile electrons and holes in *A* phase. In particular, the corresponding strength and extent of the *A* layer will only depend on the value of conductivity. Next to the double layer, is the Stern or Helmholtz double layer, which is about 1 nm and may exhibit high charge density. The Helmholtz double layer consists of dipoles in left side and the outer Helmholtz plane (OHP) in right side, as shown in Figure 1-22. Extending beyond the OHP into phase *B* is the so-called Gouy-Chapman layer. Due to the fact that this is region of mobile charge, it will have a significant role in influencing the dispersion of the *A* particles in the *B* matrix and secondly in determining the dielectric and conductive properties of the resulting composite¹⁰³.

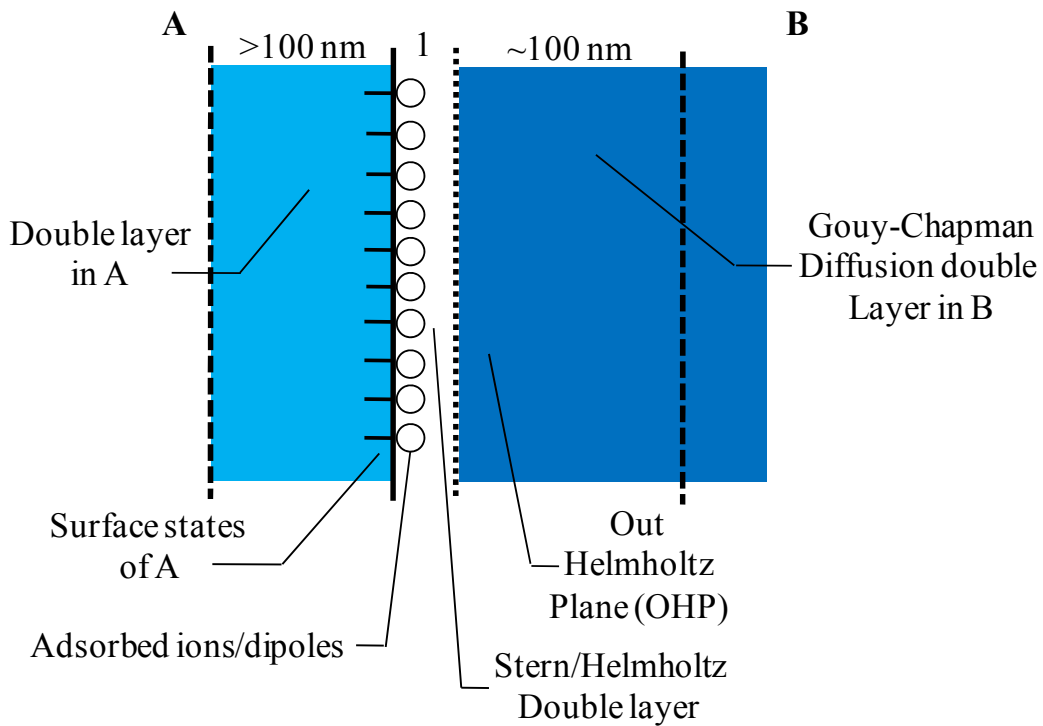


Figure 1-21 Schematic of electrical layers of extended interface¹⁰³.

1.8.2 Dielectric Properties

It is well known that the dielectric properties will be increasingly dominated by their interfacial interactions with their environment, whose outcome is frequently a degree of polarization and charge separation. Based on the influence of interfaces to dielectrics, they can have both passive and active roles, although the distinction is not so clear.

Passive Interfaces

Since last century, the determination of satisfactory models for the effective macroscopic dielectric function, ϵ' , of the composite materials has received extensive attention¹⁰⁵. In the beginning, the Maxwell-Wagner model, in which spherical non-interacting particles, A with permittivity ϵ'_A are dispersed in matrix B , of permittivity ϵ'_B , has been applied^{81, 82}. Many methods are related to the analysis by Maxwell-Garnett¹⁰⁶. It is noted that the effective macroscopic dielectric function, ϵ' , is not solely determined by

the volume fraction and permittivity of the A and B phases but also by the shape of the A particles, their orientation and their interaction, which have been well discussed⁸³.

As mentioned before, none of these models take into account the existence of finite interface between *A* and *B* phases. The experimental results of Bowler on particles with coatings marked a transition towards employing more realistic interfaces. Bowler indicated that the thickness and uniformity of the coating can have a significant effect on the frequency-dependence of effective macroscopic dielectric function, ϵ'_A ¹⁰⁷. Furthermore, the work of Xue on loss-free two-component composites further demonstrates that the important role played by interfaces on dielectric properties¹⁰⁸. In some special situation, the interface has become inevitably a large part of the device volume in the development of nanometric devices. For instance, in order to reduce the transistor size, it requires a reduction of gate area and SiO₂ gate thickness to maintain its capacitance. However, it is found that a lesser thickness will cause interfaces deficient in oxygen and less insulating to dominate the gate properties, so a fully insulating gate of SiO₂ requires a minimal thickness of 0.4 nm. In order to solve the problem, alternative dielectrics with higher permittivity and better interfaces are being pursued¹⁰⁹.

Active Interfaces

In the above discussion, so far interfaces are considered as passive dielectrics, but they can often take on an active role. O'Konski has confirmed the effect of interfacial conduction on the overall dielectric properties of a random suspension of spherical particles in a dielectric medium¹¹⁰. At low frequencies or high conductivity, charge carriers can be efficiently transferred by the applied field around the particle interface, which induce polarization at opposite ends of the particle and creates a large dipole. Therefore, the effective dielectric constant of the system ϵ' , can then exceed ϵ'_A . Reversely, the polarization is reduced at high frequency due to their less transferring efficiency around interface. The permittivity ϵ' is then determined by ϵ'_A , ϵ'_B and their corresponding volume concentration of particles.

Moreover, this model has been developed further by Chew and Sen¹¹¹. This modified model emphasized the importance of the counter-ion component of the diffuse double layer on the *A* particle. Besides the polarization charge in the double layer, it

indicated that a neutral cloud of charge developed outside it and then it is followed by a charge transferring into and across *B* phase by diffusion. The consequence of this modified model shows that at low frequencies, an out of phase dipole moment forms due to an out of phase and large diffusion cloud. Therefore, it substantially weakens the dipole moment as the frequency increases and then leads to a broader frequency response of the permittivity than the Debye response and similar to the empirical Cole-Cole function frequency employed.

Murugaraj *et al* have reported the results about dielectric enhance in polymer-nanoparticle composites through interphase polarization¹¹². As shown Figure 1-23, it was found in this study that the dielectric constant increased monotonically with increasing polyimide (PI)-alumina volume concentration well above the predicted value by Maxwell's rule below the percolation threshold. More studies have proved that the measured $\epsilon_{composite}$ values were found to exceed the corresponding nanoparticle such as $\epsilon_{polymer} < \epsilon_{particle} < \epsilon_{composite}$, which is in contrast to the conventional composite where $\epsilon_{polymer} < \epsilon_{composite} < \epsilon_{particle}$. The observed dielectric enhancement ($\epsilon_{composite} - \epsilon_{Maxwell}$) exhibited a correlation with the total surface area of the nanoparticle as shown in 1-24 and 1-25, which supported that the enhanced dielectric behavior originated from interfacial interaction and then demonstrated the critical role of the interfacial regions within the nanocomposites in enhancing their dielectric characteristics.

Quantitative studies on the interfacial layer using model nanocomposites have been carried out^{104, 113, 114}. Work such as mixing nanosized silica into polystyrene matrix indicated that suppressing T_g occurred. Based on this finding, quantitative mimicking of T_g shifting pursued¹⁰⁴. This is the first time that this behavior has been quantitatively studied in a controlled nanocomposite system, and quantitative correlation between thin-film thickness and effective interparticle spacing was established. Experimental results showed that a measurable change in T_g can occur at effective interfacial spacing, which is about 500 nm. These results were larger than the expected theoretical value¹¹⁵, but correlate with other studies that exhibited large change in T_g at nanoparticle loading as low as 1 vol%¹¹⁶. In addition, using modeling, it would be possible to alter interfacial interaction energy between the silica and polymer using surface modification. Therefore, the results provided a framework for understanding and designing new nanocomposite

materials and also could lend insight on the glass-transition phenomenon for polymer in confined geometries.

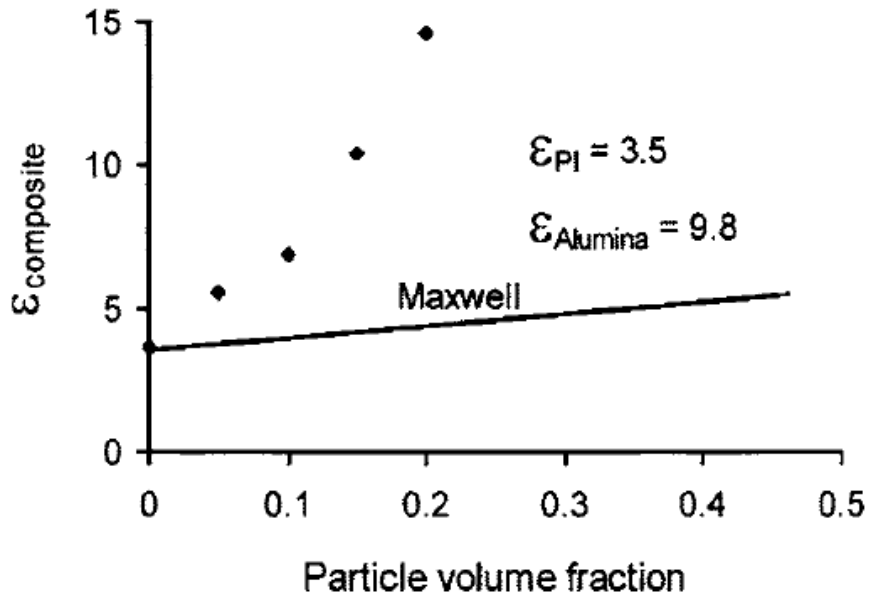


Figure 1-22 The dielectric response vs. alumina volume fraction at 100 kHz and 25°C¹¹². (ϵ is equivalent to ϵ' , which is described in Section 1.1).

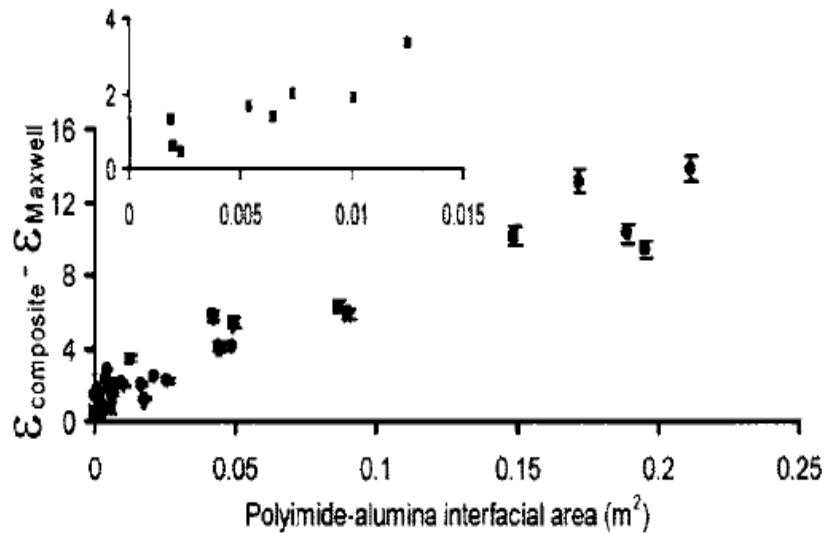


Figure 1-23 The correlation between the interfacial area and the dielectric enhancement in PI-alumina nanocomposite¹¹². (ϵ is equivalent to ϵ' , which is described in Section 1.1).

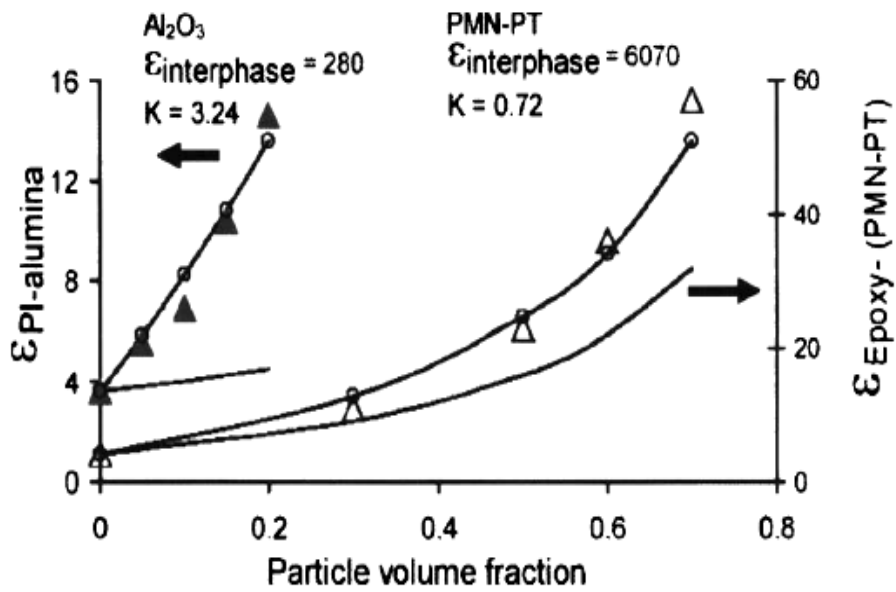


Figure 1-24 Comparison of the Vo-Shi model prediction with experimental results on PI-alumina nanocomposites and epoxy-(PMN-PT) composites, respectively. Also shown are the prediction by Maxwell-wagner rule for both systems¹¹². (ϵ is equivalent to ϵ' , which is described in Section 1.1. K is a constant that is dependent on the degree of particle clustering influencing the surface area and the thickness of the interface region between the nanoparticles.).

1.9 Objectives of This Research

In this work, ceramic-polymer 0-3 composites based on $\text{CaCu}_3\text{Ti}_4\text{O}_{12}$ ceramic particles as filler are studied. Two different polymer matrices will be employed as matrices in this work: 1). P(VDF-TrFE) 55/45 mol% copolymer which exhibits a high dielectric constant and a weak piezoelectric effect, 2). P(VDF-CTFE) 88/12 mol% (VC88) which exhibits high a dielectric constant and no piezoelectric effect with weak temperature dependence. The goal for this work is to develop 0-3 composite with high dielectric constant. In order to achieve the goal, the following objectives are designed:

1. Preparation of $\text{CaCu}_3\text{Ti}_4\text{O}_{12}$ ceramic with high dielectric constant and low dielectric loss;
2. Investigation of the polarization mechanism in $\text{CaCu}_3\text{Ti}_4\text{O}_{12}$ ceramic;
3. Fabrication of micro-size $\text{CaCu}_3\text{Ti}_4\text{O}_{12}$ -based composite with different processes, such as as-casing, annealing, hot pressing and hot pressing time;
4. Determination of the origin of the loss observed in the composite at low frequency;
5. Fabrication of nano-size $\text{CaCu}_3\text{Ti}_4\text{O}_{12}$ -based composite with different processes, such as as-casing, annealing, hot pressing and hot pressing time;
6. Property characterization and microstructure study on $\text{CaCu}_3\text{Ti}_4\text{O}_{12}$ -based composite.

References

1. Rao, Y.; Ogitani, S.; Kohl, P.; Wong, C. P. *J. Appl. Poly. Sci* **2002**, 83, 1084-1090.
2. Rao, Y.; Wong, C. P. *J. Appl. Poly. Sci* **2004**, 92, 2228-2231.
3. Zhang, Q. M.; Li, H.; Poh, M.; Xia, F.; Cheng, Z.-Y.; Xu, H.; Huang, C. *Nature* **2002**, 419, (19), 284-287.
4. Barsoum, M. W., *Fundamentals of Ceramics*. Institute of Physics Publishing: Bristol and Philadelphia, 1997.
5. Taylor, G. W., *Ferroelectricity and Related Phenomena*. Gordon and Breach Science Publishers: New York-London-Paris-Chiba-Ken, 1984; Vol. 3.
6. Cava, R. F.; Peck, W. F. J.; Krajewski, J. J. *Nature* **1995**, 377, (6546), 215-217.
7. Zhang, Q. M.; Bharti, V.; Zhao, X. *Science* **1998**, 280, (26), 2101-2104.
8. Baojin Chu; Xin Zhou; Kailiang Ren; Bret Neese; Minren Lin; Qing Wang; F.Bauer; Q.M.Zhang. *Science* **2006**, 313, (21), 334-336
9. Xia, F.; Cheng, Z.-Y.; Xu, H. S.; Li, H. F.; Zhang, Q. M.; Kavarnos, G. J.; Ting, R. Y.; Abdul-Sedat, G.; Belfield, K. D. *Adv. Mater* **2002**, 14, (21), 1574-1577
10. Simpson, J. O.; Clair, A. K. S. *Thin Solid Films* **1997**, 480, 308-309.
11. Matsuura, T.; Hasuda, Y.; Nishi, S.; Yamada, N. *Macromolecules* **1991**, 24, (18), 5001-5005.
12. Bharti, V.; H.S.Xu; G.Shanthi; Q.M.Zhang. *J. Appl. Phys* **2000**, 87, (1), 452-461.
13. http://www.westlakeplastics.com/pdf/film_pvdf.pdf.
14. http://www.solvayadvancedpolymers.com/static/wma/pdf/8/0/4/6./Primospire_P R250.pdf.
15. <http://www.solvayadvancedpolymers.com/static/wma/pdf/3/7/1/6/P3500NTLCD .pdf>.

16. <http://www.goodfellow.com/csp/active/static/A/Polyvinylidene fluoride.HTML>.
17. <http://www.bayplastics.co.uk/data%20sheets/axxis/prod-axxis-datasheet-Axpet sheet.htm>.
18. http://www2.dupont.com/Kapton/en_US/assets/downloads/pdf/E_H-78305.pdf.
19. Newnham, R. E. *Ann. Rev. Mat. Sci* **1986**, 16, 47-68.
20. Dias, C. J.; Das-Gupta, D. K., *Ferroelectric Polymer and Ceramic-Polymer Composites*. Trans Tech Publications Ltd., Switzerland: 1994; p 217.
21. Gregorio, R.; Jr., M. C.; Bernardino, F. E. *J. Mater. Sci.* **1996**, 31, 2925-2930
22. Bai, Y.; Cheng, Z.-Y.; Bharti, V.; Xu, H. S.; Zhang, Q. M. *Appl. Phys. Lett* **2000**, 76, 3804-3806.
23. VonHippel, A. R., *Dielectric Materials and Applications*. Cambridge: Technology Press of MIT: Boston, 1954.
24. VonHippel, A. R., *Dielectrics and Waves*. Wiley: New York, 1954.
25. Kao, K. C., *Dielectric Phenomena in Solids*. Elsevier Academic Press: San Diego, CA, 2004.
26. Xie, H. K.; Kao, K. C. *IEEE Trans Electr Insul* **1985**, EI-20, 293-294.
27. Newnham, R. E., *Properties of Materials*. Oxford University Press: New York, 2005.
28. Kittel, C., *Introduction to Solid State Physics*. Wiley: New York, 1988.
29. Mitsui, T., *An introduction to the Physics of Ferroelectrics*. Gordon and Breach Science Publishers: New York-London-Paris, 1976.
30. Nalwa, H. S., *Ferroelectric Polymers: chemistry, physics, and applications*. Marcel Dekker, Inc.: New York. Basel. Hong Kong, 1995.

31. Munpakdee, A.; Tontragoon, J.; Siriwitayakron, K.; Tunkasiri, T. *J of Mater Sci Lett* **2003**, 22, 1307-1310.
32. Koyuncu, M.; Pilgrim, S. M. *J. Am. Ceram. Soc* **1999**, 82, (11), 3075-3079.
33. Swartz, S. L.; Shrout, T. R.; Schulze, W. A.; Cross, L. E. *J. Am. Ceram. Soc* **1984**, 67, (5), 311-315.
34. Glazounov, A. E.; Tagantsev, A. K.; Bell, A. J. *Phys.Rev.B* **1996**, 53, 11281-11284.
35. <http://www.memsnets.org/material/bariumtitanatebatio3bulk>.
36. <http://www.matweb.com/search/SearchSubcat.asp>.
37. <http://www.memsnets.org/material/leadzirconatetitanatepzt>.
38. Zhu, B. P.; Wu, D. W.; Zhou, Q. F.; Shi, J.; Shung, K. K. *Appl. Phys. Lett* **2008**, 93, 012905-3.
39. Goosey, M., *Plastics for electronics*. Springer: 1999.
40. <http://www.memsnets.org/material/pvdftrfecopolymerofvinylidene fluoride/trifluoroethylene film/>.
41. He, X.; Yao, K. *Appl. Phys. Lett* **2006**, 89, 112909.
42. Ang, C.; Yu, Z.; L.E.Cross. *Appl. Phys. Lett* **2003**, 83, (9), 1821-1823.
43. Xu, T.-B.; Cheng, Z.-Y.; Zhang, Q. M. *Appl. Phys. Lett* **2002**, 80, 1082.
44. Omote, K.; Ohigashi, H.; Koga, K. *J.Appl. Phys* **1997**, 81, (6).
45. Cheng, Z. Y.; Bharti, V.; Xu, H. S.; Wang, S.; Zhang, Q. M. *J.Appl. Phys* **1999**, 86, (4), 2208-2214.
46. Cheng, Z.-Y.; Zhang, Q. M. *J.Appl. Phys* **2002**, 92, (11), 67496755.

47. Li, Y. X.; Yan, I.; Shrestha, R. P.; Yang, D.; Irene, E. A. *J Vac Sci Tech A* **2007**, *25*, (2), 275-280.
48. Li, Z. M.; Wang, Y.; Cheng, Z.-Y. *Appl. Phys. Lett* **2006**, *88*, (6), 062904-1-3.
49. Arbatti, M. Development of High-Dielectric-Constant Polymer-Ceramic Composites Based on Calcium Copper Titanate. Auburn University, Alabama, 2004.
50. http://library.thinkquest.org/10784/dielectric_strength.html.
51. <http://www.goodfellow.com/csp/active/gfMaterialInfo.csp?MATID=SI61&material=1>.
52. www.csgnetwork.com/dieconstantstable.html.
53. www.tpub.com/content/neets/14193/css/14193_138.htm.
54. www.my.execpc.com/~endlr/dielectric_const_.html.
55. Branwood, A.; Hurd, J. D.; Tredgold, R. H. *Br.J.Appl.Phys.* **1962**, *13*, 528.
56. Kobayashi, W.; Terasaki, I. *Appl. Phys. Lett* **2005**, *87*, 032902.
57. Subramanian, M. A.; Li, D.; Duan, N.; B. A. Reisner; Sleight, A. W. *J Solid State Chem* **2000**, *151*, 323-325.
58. Subramanian, M. A.; A.W.Sleight. *Solid State Sciences* **2002**, *4*, 347-351.
59. Adams, T. B.; Sinclair, D. C.; R.West, A. *Adv.Mater.* **2002**, *14*, (18), 1321-1323.
60. Almeida, A. F. L.; Oliveira, R. S. d.; Go'es, J. C.; Sasaki, J. M.; A.G. Souza Filho; Filho, J. M.; Sombra, A. S. B. *Mat.Sci.Eng B* **2002**, *96*, 275-283.
61. Homes, C. C.; Vogt, T.; Shapiro, S. M.; Wakimoto, S.; Ramirez, A. P. *Science* **2001**, *293*, (27), 673-676.

62. Almeida, A. F. L.; P.B.A.Fechine; Góes, J. C.; Valente, M. A.; Miranda, M. A. R.; A.S.B.Sombra. *Mat.Sci.Eng B* **2004**, 111, 113-123.
63. Kretly, L. C.; Almeida, A. F. L.; R.S de Oliveira; J.M Sasaki; Sombra, A. S. B. *Microwave and Optical Tech Lett* **2003**, 39, 145-150.
64. Valim, D.; Filho, A. G. S.; Freire, P. T. C.; Fagan, S. B.; Ayala, A. P.; Filho, J. M.; Almeida, A. F. L.; Fechine, P. B. A.; Sombra, A. S. B.; Olsen, J. S.; Gerward, L. *Phys.Rev.B* **2004**, 70, 132103.
65. Fagan, S. B.; Filho, A. G. S.; Ayala, A. P.; Filho, J. M. *Phys.Rev.B* **2005**, 72, 014106.
66. Brize, V.; Gruener, G.; Wolfman, J.; Fatyeyeva, K.; Tabellout, M.; Gervais, M.; Gervais, F. *Mat.Sci.Eng B* **2006**, 129, 135-138.
67. Sinclair, D. C.; Adams, T. B.; Morrison, F. D.; West, A. R. *Appl. Phys.Lett* **2002**, 80, 2153-2155.
68. Fang, T.-T.; Shiau, H.-K. *J. Am. Ceram. Soc* **2004**, 87, (11), 2072-2079.
69. Cohen, M. H.; Neaton, J. B.; Lixin He; Vanderbilt, D. *J.Appl.Phys* **2003**, 94, 3299-3306.
70. Lunkenheimer, P.; Bobnar, V.; Pronin, A. V.; Ritus, A. I.; Volkov, A. A.; Loidl, A. *Phys.Rev.B* **2002**, 66, 052105.
71. Lunkenheimer, P.; Fichtl, R.; Ebbinghaus, S. G.; Loidl, A. *Phys.Rev.B* **2004**, 70, 172102.
72. Wu, L.; Y. Zhu; S. Park; S. Shapiro; Shirane, G. *Phys.Rev.B* **2005**, 71, 014118.
73. Zhang, L. *Appl. Phys. Lett* **2005**, 87, 022907-3.
74. Yang, J.; Shen, M.; Fang, L. *Mat. Lett* **2005**, 59, 3990-3993.

75. Fang, T.-T.; Mei, L.-T.; Ho, H.-F. *Acta.Mater* **2006**, 54, (10), 2867-2875.
76. Patterson, E. A.; Kwon, S.; Huang, C.-C.; Cann, D. P. *Appl. Phys.Lett* **2005**, 87, 182911.
77. Capsoni, D.; Bini, M.; V.Massarotti; G.Chiodelli; M.C.Mozzatic; Azzoni, C. B. *J Solid State Chem* **2004**, 177, 4494-4500.
78. Krohns, S.; Lunkenheimer, P.; Ebbinghaus, S. G.; Loidl, A. *J.Appl. Phys* **2008**, 103, 084107-9.
79. Newnham, R. E.; Skinner, D. P.; Cross, L. E. *Mat.Res.Bull* **1978**, 13, 525-536.
80. Das-Gupta, D. K.; K, D. *Thin Solid Films* **1988**, 158, (1), 93-105.
81. Maxwell, J. C., *Electricity and Magnetism*. Clarendon Press, Oxford: 1892; p 452.
82. Wagner, K. W., *Die Isolierstoffe der Elektrotechnik*. Springer, Berlin: 1924; Vol. 1 (H.Schering, ed.).
83. Gao, L.; Gu, J. Z. *J. Phys. D: Appl. Phys.* **2002**, 35, 267-271.
84. Hung, T. V.; Frank, G. S. *Microelectronics Journal* **2002**, 33, 409-415.
85. Mazur, K. In *Dielectric and electret properties of PMMA/BaTiO₃ Composite* Z.N.WSP in Katowice, Phys.Sec, Polish, 1968; Polish, 1968.
86. Mazur, K. The mechanism of build-up of homocharge in the electrets of PMMA/BaTiO₃ Composite. Silesian University, Katowice, Poland, 1968.
87. Mazur, K.; Handerek, J.; Piech, T. *Acta.Phys* **1970**, A, 37-31.
88. Kuo, D.-H.; Chang, C.-C.; Su, T.-Y.; Wang, W.-K.; Lin, B.-Y. *Mat.Chem.Phys* **2004**, 85, 201-206.
89. Adikary, S. U.; Chan, H. L. W.; Choy, C. L.; Sundar, B.; Wilson, I. H. *Composites Science and Technology* **2002**, 62, 2161-2167.

90. Dang, Z.-M.; Fan, L.-Z.; Chen, Y.; Fan, C.-W. *Chem.Phys.Lett* **2003**, 369, 95-100.
91. Hilczler, B.; Kulek, J.; Markiewicz, E.; Kosec, M.; Malic, B. *J of Non-crystalline solids* **2002**, 305, 167-173.
92. Lam, K. S.; Wong, Y. W.; Tai, L. S.; Poon, Y. M.; Shin, F. G. *J.Appl. Phys* **2004**, 96, (7), 3896-3899.
93. Jillek, W.; Yung, W. K. C. *Int J Adv Manuf Technol* **2005**, 25, (3-4), 350-360.
94. Dang, Z.-M.; Zheng, Y.; Xu, H.-P. *J Appl Polymer Sci* **2008**, 110, (6), 3473-3479.
95. Xu, R.; Chen, W.; Zhou, J.; Li, Y.; Sun, H. *J Wuhan Univ of Tech (Mater.Sci.Ed)* **2006**, 21, (1), 84-87.
96. Liu, X.-F.; Xiong, C.-X.; Sun, H.-J.; Dong, L.-J.; Li, R.; Liu, Y. *Mat.Sci.Eng B* **2006**, 127, 261-266.
97. Dang, Z.-M.; Wang, L.; Wang, H. *Appl. Phys. Lett* **2005**, 86, 172905-3.
98. Dang, Z.-M.; Wang, L.; Yin, Y.; Zhang, Q.; Lei, Q.-Q. *Adv. Mater* **2007**, 19, (6), 852-857.
99. Wang, L.; Dang, Z.-M. *Appl. Phys. Lett* **2005**, 87, 042903--3.
100. Yao, S.; Dang, Z.-M.; Xu, H.; Jiang, M.; Bai, J. *Appl. Phys. Lett* **2008**, 92, 082902-3.
101. Deepa, K. S.; Nisha, S. K.; P.Parameswaran; Sebastian, M. T.; James, J. *Appl. Phys. Lett* **2009**, 94, 142902-3.
102. Todd, M. G.; Shi, F. G. *J.Appl. Phys* **2003**, 94, (7), 4551-4557.
103. Lewis, T. J. *J. Phys. D: Appl. Phys.* **2005**, 38, 202-212.
104. Schadler, L. *Nature Mater* **2007**, 6, 257-258.

105. Tuncer, E.; Serdyuk, Y. V.; Gubanski, S. M. *IEEE Trans. Dielectrics Electr. Insulation* **2002**, 9, 809-828.
106. Maxwell-Garnett, J. C. *Phil.Trans.R.Soc. A* **1904**, 203, 385-420.
107. Bowler, N. *J. Phys. D: Appl. Phys.* **2004**, 37, 326-333.
108. Xue, Q. *Physica B* **2004**, 344, 129-132.
109. Alers, G. B.; Werder, D. J.; Chabal, Y.; Lu, H. C.; Gusev, E. P.; Garfunkel, E.; T.Gustafsson; Urdahl, R. S. *Appl. Phys. Lett* **1998**, 73, (11), 1517-1519.
110. O'Konski, C. T. *J.Phys.Chem* **1960**, 64, 605-619.
111. Chew, W. C.; Sen, P. N. *J.Chem.Phys* **1982**, 77, 4683-4693.
112. Murugaraj, P.; Mainwaring, D.; Mora-Huertas, N. *J.Appl. Phys* **2005**, 98, 054304-6.
113. Anne, M. M. *Nature Mater* **2005**, 4, 651-652.
114. Rittigstein, P.; Rodney, D. P.; Linda, J. B.; John, M. T. *Nature Mater* **2007**, 6, 278-282.
115. Desai, T.; Keblinski, P.; Kumar, S. K. *J.Chem.Phys* **2005**, 122, 134910.
116. Ash, B. J.; Siegel, R. W.; Schadler, L. S. *J. Polym. Sci. B* **2004**, 42, 4371-4383.

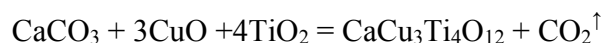
CHAPTER 2

MATERIALS PREPARATION AND CHARACTERIZATION METHODS

In this chapter, several experimental preparation and characterization methods will be addressed. Materials preparation methods, such as $\text{CaCu}_3\text{Ti}_4\text{O}_{12}$ ceramic synthesis and ceramic-polymer 0-3 composite fabrication, are presented in this work. At the same time, several materials characterization methods, such as X-ray diffraction (XRD), Scanning Electron Microscopy (SEM), Impedance analyzer, Polarization Measurement, are explained in detail.

2.1 Ceramic Synthesis

Polycrystalline samples of $\text{CaCu}_3\text{Ti}_4\text{O}_{12}$ were prepared by solid-state reaction. High purity metal oxide powders of calcium carbonate (CaCO_3 , 99.5 %, Alfa Aesar), copper oxide (CuO , 99.7 %, Alfa Aesar) and titanium dioxide (TiO_2 , 99.8 %, Alfa Aesar) were used to prepare the ceramics. The raw materials were weighted according to the stoichiometric ratio based on the following reaction^{1,2}:



The mixture of raw materials was grinded in a polyethylene bottle with zirconia grinding pellets. The weight ratio among the raw material, zirconia grinding pellet and mixing liquid media was 1: 2: 3, respectively. The mixing liquid media used in the experiments was either deionized (D.I) water or ethanol. After ball milling, the powder was sieved by using an 80 mesh copper sieve and then dried at 100 °C in an oven for 8 hours. The dry powder was calcined at 1075 °C or 900 °C in Al_2O_3 crucible for different times using a 48000 Barnstead Thermolyne furnace, as shown in Figure 2-1. The calcination results in a dark gray colored solid, which was ground to pass an 200 mesh

copper sieve to get fine powder. The final powder mixed with a binder was uniaxially pressed into pellets that have a diameter of 13 mm, a thickness of about 1.5 mm, and were sintered at 1075 °C for different times. The final ceramic pellet is shown in Figure 2-2. Those ceramic processing conditions are shown in Table 2-1.



Figure 2-1 Image of 48000 Barnstead Thermolyne furnace.

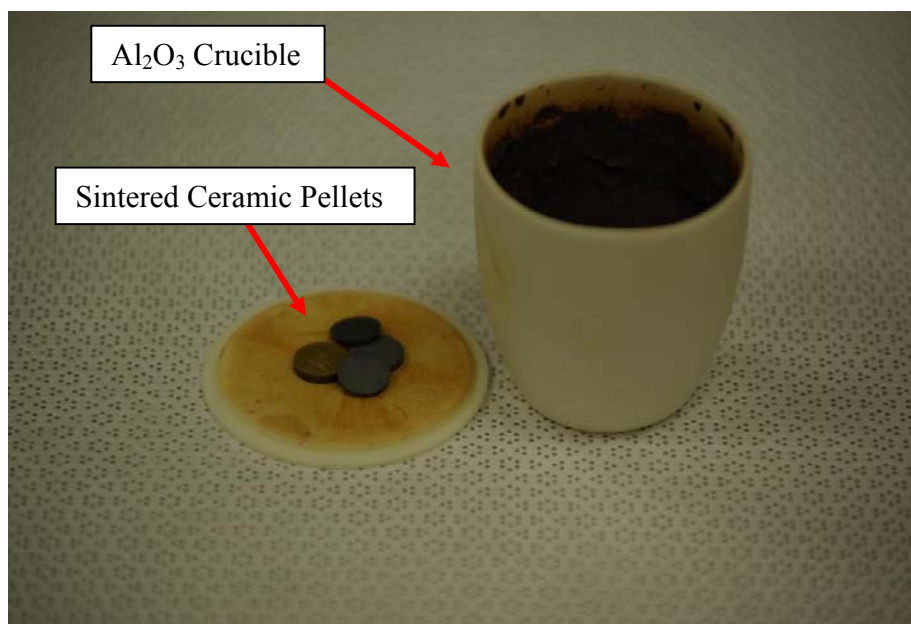


Figure 2-2 Image of Al_2O_3 crucible and sintered ceramic pellet.

Table 2-1 The $\text{CaCu}_3\text{Ti}_4\text{O}_{12}$ processing conditions.

Procedure No.	1 st powder milling	Calcination	2 nd powder milling	Sintering
1	D.I water ball mill ^[1]	1075 °C/12 hr	N/A	1075 °C ^[2]
2	D.I water ball mill ^[1]	900 °C/12 hr	N/A	1075 °C ^[2]
3	Ethanol ball mill ^[1]	900 °C/12 hr	N/A	1075 °C ^[2]
4	Ethanol ball mill ^[1]	900 °C/12 hr	Ethanol ball mill	1075 °C ^[2]

^[1] Ball mill for 48,72 and 96 hrs respectively.

^[2] Sintering for 24, 48 and 72 hrs respectively.

2.2 Ceramic-Polymer 0-3 Composite Fabrication

2.2.1 Ceramic-Polymer 0-3 Composite Casting Procedure

The $\text{CaCu}_3\text{Ti}_4\text{O}_{12}$ -P(VDF-TrFE) 0-3 composite was prepared by traditional casting method and hot pressing technique. P(VDF-TrFE) 55/45 mol% copolymer was dissolved in dimethyl formamide (DMF) under magnetic stirring for 5 hours. The image of milled $\text{CaCu}_3\text{Ti}_4\text{O}_{12}$ powder is shown in Figure 2-3 and its particle size distribution of milled $\text{CaCu}_3\text{Ti}_4\text{O}_{12}$ powder is given in Figure 2-4, with $D_{50} \approx 10.5 \mu\text{m}$ (weight percentage) from microtrac S3500 particle size analysis system. After the $\text{CaCu}_3\text{Ti}_4\text{O}_{12}$ powder had been added into the solution, it was stirred for 8 hours and then sonicated for about 20 minutes. The final $\text{CaCu}_3\text{Ti}_4\text{O}_{12}$ - P(VDF-TrFE) solution was casted on a glass plate at 70 °C for 8 hours. The final film was released from glass plate by immersing it into D.I water. The final product is a flexible film, as shown in Figure 2-5. In order to improve the wettability, hot pressing technique was used. The overall process flowchart for $\text{CaCu}_3\text{Ti}_4\text{O}_{12}$ - P(VDF-TrFE) 0-3 composite fabrication is shown in Figure 2-6.

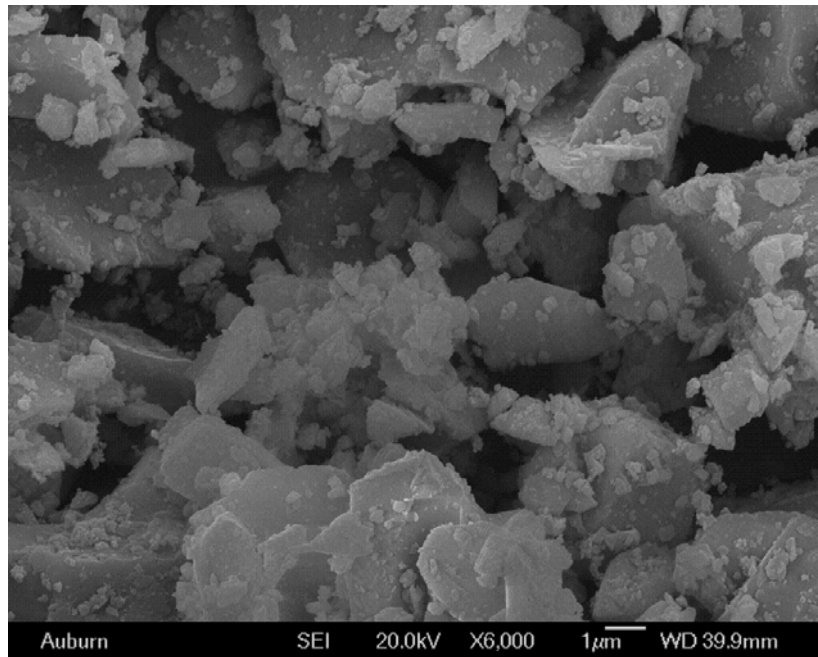


Figure 2-3 SEM image of milled $\text{CaCu}_3\text{Ti}_4\text{O}_{12}$ powder.

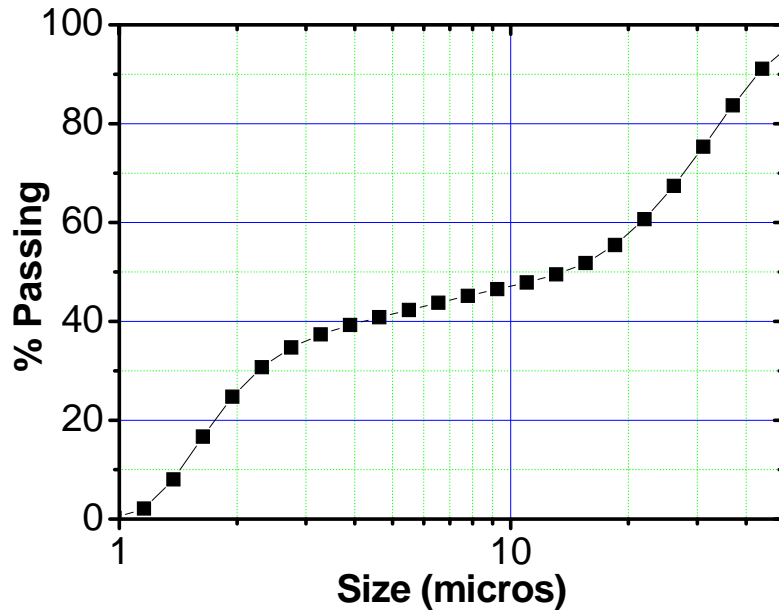


Figure 2-4 Particle size distribution of milled $\text{CaCu}_3\text{Ti}_4\text{O}_{12}$ powder.

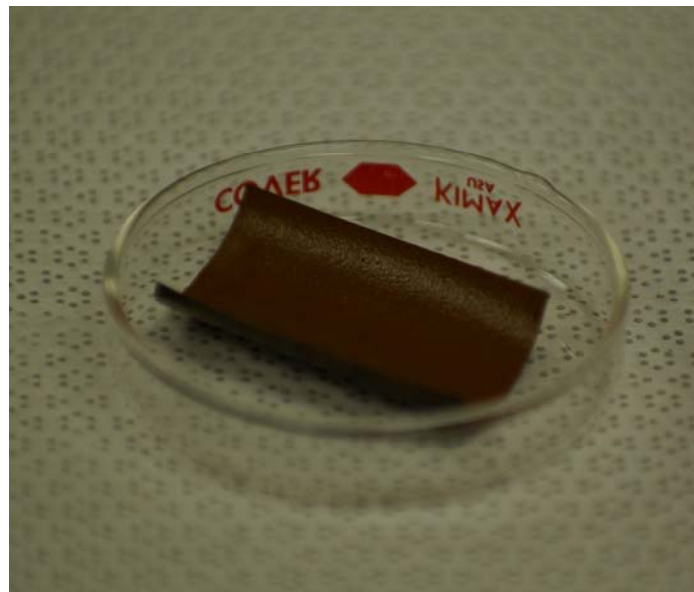


Figure 2-5 Image of flexible $\text{CaCu}_3\text{Ti}_4\text{O}_{12}$ - P(VDF-TrFE) 0-3 composite.

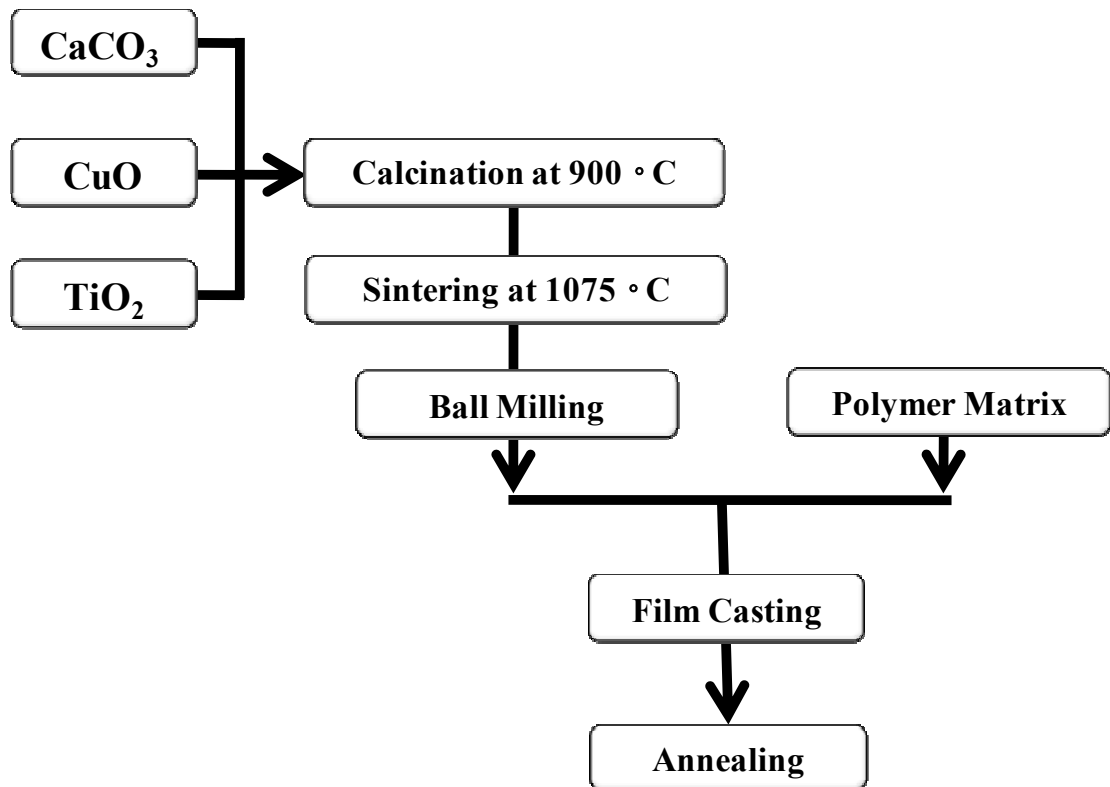


Figure 2-6 Process flowchart for $\text{CaCu}_3\text{Ti}_4\text{O}_{12}$ -P(VDF-TrFE) 0-3 composite fabrication.

2.2.2 Optimization of Ceramic-Polymer 0-3 Composite

The $\text{CaCu}_3\text{Ti}_4\text{O}_{12}$ - P(VDF-TrFE) composites with different $\text{CaCu}_3\text{Ti}_4\text{O}_{12}$ volume concentrations (10, 20, 30, 40, 50 vol%) were prepared. A volumetric ratio table for $\text{CaCu}_3\text{Ti}_4\text{O}_{12}$ - P(VDF-TrFE) samples over a 10 cm × 15 cm solution casting glass plate is given in Table 2-2. As shown in Table 2-2, a fixed amount of solvent (25 ml) was used in all the experiments.

2.2.2.1 Hot Pressing Process

In order to achieve further improvement in the uniformity of ceramic polymer 0-3 composite, the composite samples were pressed with high force (7.5 tons) and high temperature (200 °C). In this work, it was found the solution cast film consisted of two layers: polymer rich layer and ceramic rich layer³. Then, two different hot pressing patterns were studied, as shown in Figure 2-7: 1.) PC hot pressing: Polymer rich layer in

one film stacking with the ceramic rich layer in another film; 2.) CC hot pressing: Ceramic rich layer in one film stacking with the ceramic rich layer in another film.

Table 2-2 Volumetric ratio table for $\text{CaCu}_3\text{Ti}_4\text{O}_{12}$ - P(VDF-TrFE) composite samples.

Polymer ceramic volumetric ratios	55/45 P(VDF-TrFE) (g)	$\text{CaCu}_3\text{Ti}_4\text{O}_{12}$ (g)	Dimethyl formamide (ml)
100/0	3.2	0	10
90/10	6.09	1.98	25
80/20	4.66	3.41	25
70/30	3.55	4.45	25
60/40	2.74	5.35	25
55/50	2.04	5.97	25
40/60	1.49	6.54	25

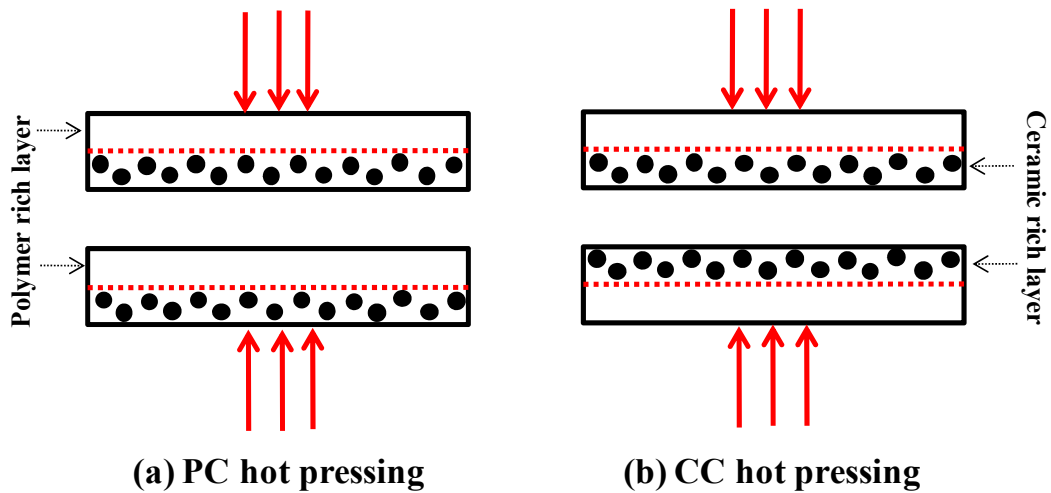


Figure 2-7 The schematic of (a) PC hot pressing and (b) CC hot pressing.

2.2.2.2 Silane Coupling Process

Besides the optimization method using hot pressing technology, the effect by using silane coupling agent was studied. In this work, $\text{CaCu}_3\text{Ti}_4\text{O}_{12}$ -P(VDF-TrFE) composites modified with 0.3, 0.5, 0.75, 1, 5, 10 wt% silane were prepared. The silane coupling agent is manufactured by Alfa Aesar (A Johnson Matthey Company) and its physical and chemical properties are listed in Table 2-3. It is believed that the bridge-linked action of silane coupling agent can improve the uniformity and then optimize the dielectric response of the composite. The schematic of silane coupling agent reaction process is shown in Figure 2-8.

Table 2-3 Physical and chemical properties of silane coupling agent.

Physical and chemical data	
Product name	1 H, 1H, 2H, 2H-Perfluorooctyltrichlorosilane
Synonyms	Trichloro- 1 H, 1H, 2H, 2H-Perfluorooctylsilane
CAS#	78560-45-9
% Weight	97
Flash Point	54°C
Boiling Point	84-85°C
Melting Point	No data
Solubility in water	Reacts
Density (g/ml)	1.638
Molecular Formula	$\text{C}_8\text{H}_4\text{Cl}_3\text{F}_{13}\text{Si}$
Molecular Weight (g/mol)	481.55

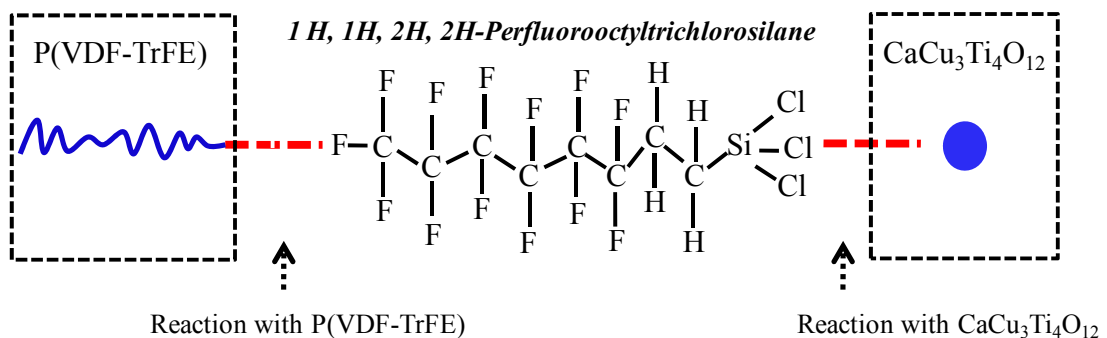


Figure 2-8 The schematic of silane coupling agent reaction process with P(VDF-TrFE) and $\text{CaCu}_3\text{Ti}_4\text{O}_{12}$.

2.2.2.3 Annealing Process

The removal of DMF solvent and the improvement in crystallinity of P(VDF-TrFE) played an important role on the overall electric properties of the $\text{CaCu}_3\text{Ti}_4\text{O}_{12}$ -P(VDF-TrFE) composites. Therefore, an additional process was carried out to study the dielectric response of the composite. As-casted composite films were securely sandwiched between two glass plates in an oven and the annealing process was kept at 125 °C for 8 hours.

2.3 Materials Characterization Methods

2.3.1 Crystalline Structure Determination Using Wide Angle X-ray Diffraction

X-ray diffraction (XRD) method has been widely used to characterize different materials such as ceramics and polymers. XRD can provide unique information about materials, such as phases, crystallinity, orientation, etc. The samples were placed on a home-made holder and then were inserted into a Rigaku DMAX-B vertical diffractometer. The X-ray diffraction was scanned at 40 kV and 30 mA with Ni-filtered, $\text{CuK}\alpha$ radiation (wavelength $\approx 1.54 \text{ \AA}$) and the intensity of diffracted X-ray was measured between 15 to 90 ° for $\text{CaCu}_3\text{Ti}_4\text{O}_{12}$ powder, or $\text{CaCu}_3\text{Ti}_4\text{O}_{12}$ -P(VDF-TrFE) composite, respectively. A scanning speed of 5 °/min and a sampling interval of 0.05 ° were used in this work. The obtained diffraction pattern was compared with standard JCPDF data library to confirm the presence of the phase in the materials by matching their unique peaks. The d -spacing can be calculated by Bragg's law as following⁴:

$$n\lambda = 2d \sin \theta \quad (2-1)$$

Where n is the layer index number, λ is the wavelength of X-rays, d is the spacing between the planes in the atomic lattice, θ is angle between the incident ray and the scattering planes.

2.3.2 Microstructure Analysis Using SEM

Scanning Electron Microscopy (SEM) is a type of electron microscope that images the sample surface with high-energy beam of electrons. By interacting with the atoms, those electrons can produce signals that contain information such as the surface morphology and composition distribution. The types of signals produced by the SEM

include: secondary electrons, back scattered electrons, characteristic X-ray, cathodoluminescence, and transmitted electrons. Among those signals, secondary electron imaging can produce very high-resolution images of sample surface, which is as high as 1 to 5 nm in size.

Samples obtained from the synthesis or fabrication process were stuck on conductive tape and then gold coating using a Pelco SC-6 sputter coater, as shown in Figure 2-9. JEOL JSM 7000F FE-SEM was operated at 20 kV to take the secondary electron images at high magnifications, and compositional analysis was completed using the Oxford Instruments Electron Dispersive X-ray Spectroscopy (EDS) system, as shown in Figure 2-10.

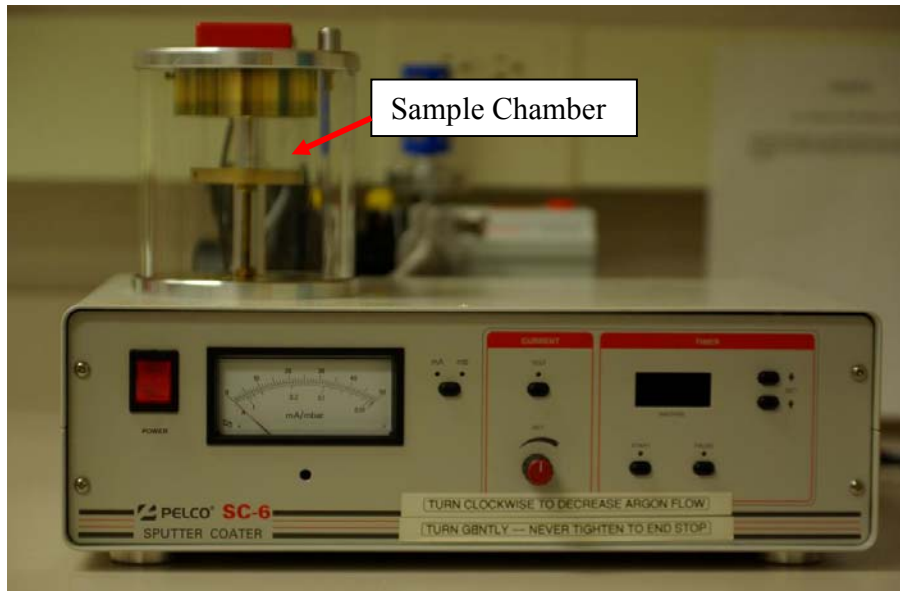


Figure 2-9 Image of Pelco SC-6 sputter coater.

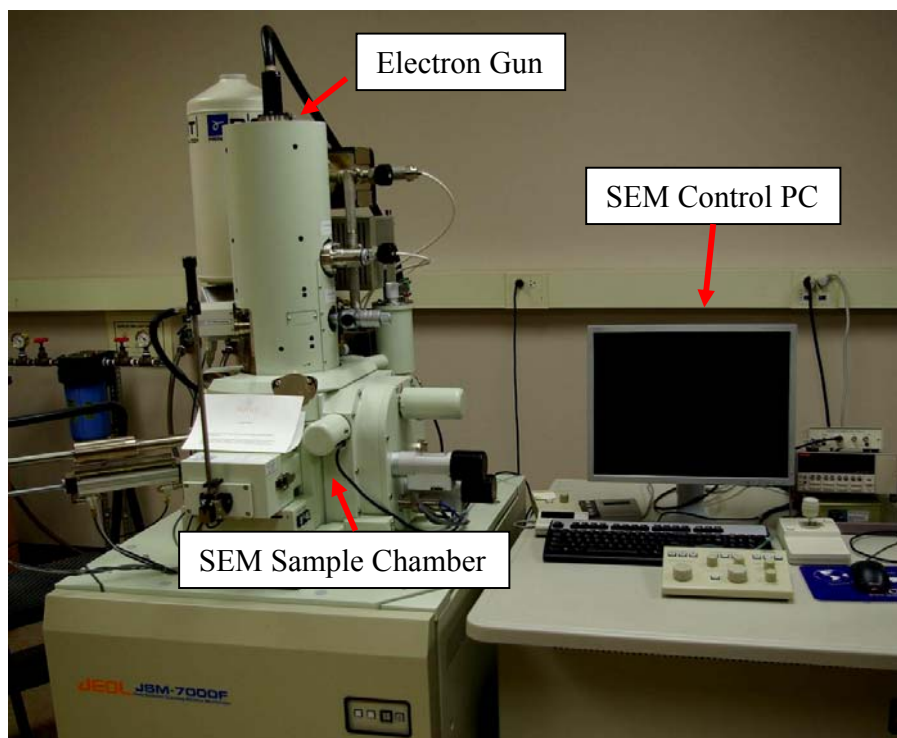


Figure 2-10 Measurement setup of Scanning Electron Microscopy (SEM).

2.3.3 Dielectric Analysis Using Impedance Analyzer

In order to characterize the electric properties of the material, there must be a conductive layer used as an electrode on the top. It can be done by either brushing pastes or sputtering metallic materials, such as gold and silver, on the surface of the sample. As for the ceramic pellets, they were polished with 1000 and 2000 grade 3M polishing paper separately in order to obtain a smooth surface prior to the sputtering process. Those ceramic samples were then sputtered with gold on top and bottom surfaces using a Pelco SC-6 sputter coater, as shown in Figure 2-9. However, special masks with diameter of 1.7 and 3.2 mm were designed for a composite purpose, as shown in Figure 2-11. A gold layer about 40 nm thickness was deposited. In the work, Agilent 4294A impedance analyzer (100 Hz to 1,000 kHz) was employed to characterize the dielectric property of the samples and the measured frequency range was 100 to 1,000 kHz, as shown in Figure 2-12. This experiment was calibrated each time to eliminate any background noise. In order to characterize the temperature dependence of the dielectric response, samples were held with a home-made measurement probe, as shown in Figure 2-13, and were then heated using a Fisher Isotemp 800 Series Programmable oven. When two parallel metal plates of area A are separated by a distance d with dielectric materials in between and then attached to the electric circuit, the capacitance can be expressed as^{2, 5-7}:

$$C = \frac{\epsilon'_r \epsilon_0 A}{d} \quad (2-2)$$

where: C is capacitance, ϵ'_r is the relative permittivity, ϵ_0 is the permittivity in vacuum, A is area of electrodes of the capacitor, d is distance between two conductive plates.



Figure 2-11 Image of mask with diameter of 1.7 millimeter.



Figure 2-12 Image of Agilent 4294A impedance analyzer.

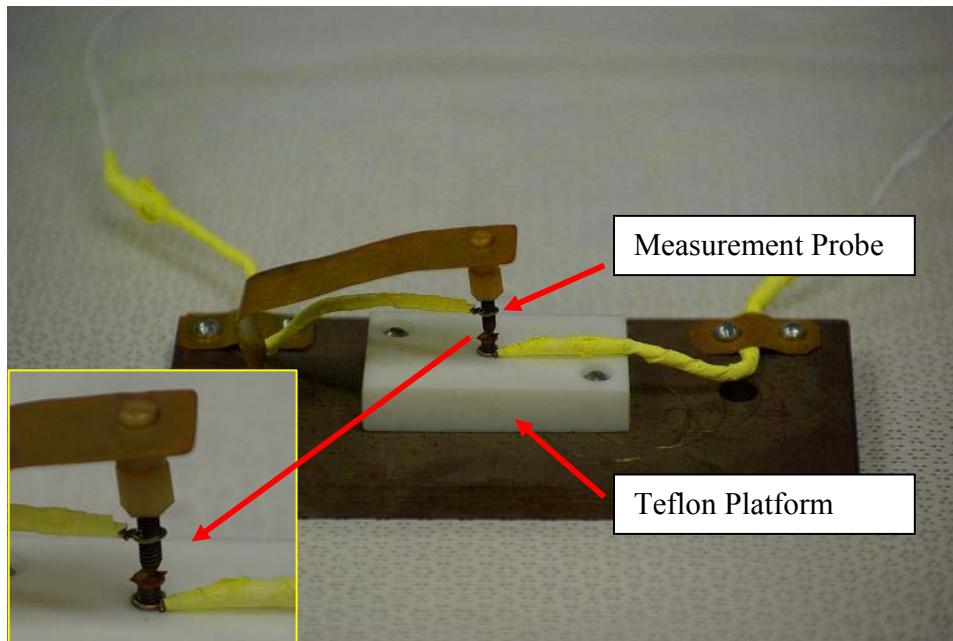


Figure 2-13 Setup of home-made probe for temperature dependence measurement.

References

1. Homes, C. C.; Vogt, T.; Shapiro, S. M.; Wakimoto, S.; Ramirez, A. P. *Science* **2001**, 293, (27), 673-676.
2. Arbatti, M. Development of High-Dielectric-Constant Polymer-Ceramic Composites Based on Calcium Copper Titanate. Auburn University, Alabama, 2004.
3. Arbatti, M.; Shan, X. B.; Cheng, Z.-Y. *Adv. Mater* **2007**, 19, 1369-1372.
4. Cullity, B. D.; Stock, S. R., *Elements of X-Ray Diffraction*. Prentice Hall: New Jersey, 2001.
5. Barsoum, M. W., *Fundamentals of Ceramics*. Institute of Physics Publishing: Bristol and Philadelphia, 1997.
6. Kao, K. C., *Dielectric Phenomena in Solids*. Elsevier Academic Press: San Diego, CA, 2004.
7. Rao, Y.; Ogitani, S.; Kohl, P.; Wong, C. P. *J. Appl. Poly. Sci* **2002**, 83, 1084-1090.

CHAPTER 3

PROCESSING AND CHARACTERIZATION OF $\text{CaCu}_3\text{Ti}_4\text{O}_{12}$ CERAMIC

3.1 Introduction

In this chapter, the research on the processing and characterization of $\text{CaCu}_3\text{Ti}_4\text{O}_{12}$ has been carried out and it is well known that the dielectric properties and microstructure of $\text{CaCu}_3\text{Ti}_4\text{O}_{12}$ varied with different processing conditions, such as calcination temperature, sintering time and post-annealing atmosphere, etc.

During the processing study on the $\text{CaCu}_3\text{Ti}_4\text{O}_{12}$ ceramic, it was observed that with suitable tuned processing parameters, better dielectric performance in $\text{CaCu}_3\text{Ti}_4\text{O}_{12}$ can be obtained, and this high performance $\text{CaCu}_3\text{Ti}_4\text{O}_{12}$ could directly benefit the following work in high dielectric constant $\text{CaCu}_3\text{Ti}_4\text{O}_{12}$ -composites study, which is going to be addressed in Chapter 4 and 5. Therefore in this work, the final goal is to pursue a rectified experimental route in order to produce high performance ceramic. In this chapter, we study the dielectric response of the $\text{CaCu}_3\text{Ti}_4\text{O}_{12}$ ceramic under different processing conditions, such as sintering temperature, sintering time and annealing condition, etc.

3.2 Experimental

High purity metal oxide powders of calcium carbonate (CaCO_3 , 99.5 %, Alfa Aesar), copper oxide (CuO , 99.7 %, Alfa Aesar) and titanium dioxide (TiO_2 , 99.8 %, Alfa Aesar) were used to prepare the polycrystalline samples of $\text{CaCu}_3\text{Ti}_4\text{O}_{12}$ by solid-state synthesis as described in Chapter 2¹.

Crystalline structure determination: X-ray diffraction (XRD) method has been utilized to characterize the phases of $\text{CaCu}_3\text{Ti}_4\text{O}_{12}$ ceramic and the measurement angle ranges from 20 to 75 °.

Dielectric properties: Those samples were polished and gold was coated on the surface of the pellets as electrodes. Agilent 4294A impedance analyzer was employed to characterize the dielectric property of the samples. The measured frequency range was from 100 Hz to 1 MHz and measured temperature ranged from 25 to 125 °C.

Microstructure analysis: The grain size and uniformity of the ceramic were determined by a scanning electron microscope with EDS (SEM JSM-7000F, JEOL). Compositional analysis was completed using the Oxford Instruments Electron Dispersive X-ray Spectroscopy (EDS) system.

3.3 Results and Discussion

3.3.1 Solid State Synthesis

The material $\text{CaCu}_3\text{Ti}_4\text{O}_{12}$ was first prepared using solid state synthesis. The ceramic processing conditions are described in Table 3-1. The phases involved in the formation of the $\text{CaCu}_3\text{Ti}_4\text{O}_{12}$ were examined using XRD. XRD patterns of calcined $\text{CaCu}_3\text{Ti}_4\text{O}_{12}$ obtained from the solid state reaction are shown in Figure 3-1.

Figure 3-1 shows XRD peaks from oxide mixtures which were calcined at different temperatures (1075 °C and 900 °C) for a period of 12 hours after 48, 72 and 96 hours ball milling process. After confirmation by the XRD of the references (JCPDS), XRD patterns of ceramics show the presence of $\text{CaCu}_3\text{Ti}_4\text{O}_{12}$ as a single phase and the lattice parameters are close to 7.393(4) Å, which is in agreement with the literature^{2,3} and reference card (75-2188) obtained from the Joint Committee on Powder Diffraction Standards (JCPDS)⁴. Those results suggest that almost all the raw materials have completely reacted and formed the expected main phases. However, it was found that there were two unexpected weak peaks at $2\theta \approx 33$ and 58 degrees for calcining at 1075 °C, and three weak peaks at $2\theta \approx 27$, 33 and 54 degrees for calcining at 900 °C. Moreover, all the samples calcining at 900 °C behaved with relatively high intensity compared to those at 1075 °C. It indicated that in comparison with calcining at 1075 °C, calcining at 900 °C is prone to result in higher percentage of main $\text{CaCu}_3\text{Ti}_4\text{O}_{12}$ phases, however due to its low calcination temperature, it also introduces more second phase as shown in Figure 3-1.

Table 3-1 The $\text{CaCu}_3\text{Ti}_4\text{O}_{12}$ processing conditions.

Procedure No.	1 st powder milling	Calcination	2 nd powder milling	Sintering
1	D.I water ball mill ^[1]	1075 °C/12hrs	N/A	1075 °C ^[2]
2	D.I water ball mill ^[1]	900 °C/12hrs	N/A	1075 °C ^[2]
3	Ethanol ball mill ^[1]	900 °C/12hrs	N/A	1075 °C ^[2]
4	Ethanol ball mill ^[1]	900 °C/12hrs	Ethanol ball mill	1075 °C ^[2]

^[1] Ball mill for 24, 48, 72 and 96 hrs respectively.

^[2] Sintering for 24, 48 and 72 hrs respectively.

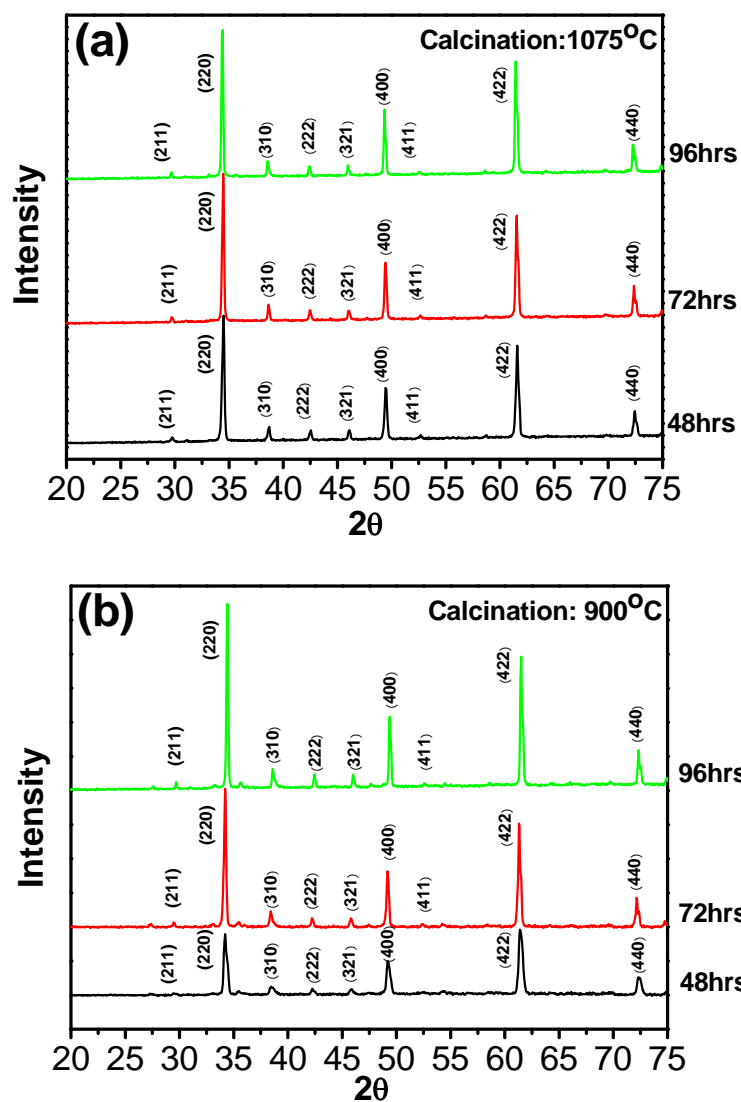


Figure 3-1 XRD patterns on the $\text{CaCu}_3\text{Ti}_4\text{O}_{12}$: (a) calcination at 1075°C after 48, 72 and 96 hrs milling; (b) calcination at 900°C after 48, 72 and 96 hrs milling according to the procedure #1 and 2 in table 3-1.

3.3.2 Effect of Processing On Dielectric Properties

The $\text{CaCu}_3\text{Ti}_4\text{O}_{12}$ exhibited an extraordinarily high dielectric constant, and current experiments have detected no presence of superstructure or crystal structure change. Based on those studies, it appears that the mechanism for the high permittivity is not intrinsic, so the processing may play an important role on the dielectric properties of $\text{CaCu}_3\text{Ti}_4\text{O}_{12}$. In the following study, the effect of processing on $\text{CaCu}_3\text{Ti}_4\text{O}_{12}$ is carried out. Several experimental routes were designed, such as different pellet molding pressures (2500 PSI and 3000 PSI), different ceramic milling time (48 hours, 72 hours and 96 hours), different sintering temperatures (24 hours, 48 hours and 72 hours), and different annealing atmospheres (vacuum and argon gas).

3.3.2.1 Effect of Molding Pressure

In this part, the effect of pellet molding pressure on the dielectric properties was studied under the same processing conditions, such as milling time, calcining and sintering temperature. The milling time for those ceramic samples were fixed at 24 hours and the calcining temperature and sintering temperature were set at 1075 °C, respectively. Their dielectric spectrums using different molding pressures are shown in Figure 3-2, and their corresponding SEM images of those fractured samples are listed in Figure 3-3 and 3-4.

In the ceramic processing, it is well known that in the preparation stage, the quality of molded ceramic pellet was critical for the final dielectric performance enhancement. Especially, with high molding pressure, it was prone to generate cracks inside the ceramic during the calcination process, which would then prevent the grain size growth and hinder final dielectric property improvement. Based on the results in Figure 3-2, those dielectric spectrums obtained in samples using two molding pressures behave very similarly. The dielectric constant varied from 17,000 to 23,000, and corresponding dielectric loss was stabilized below 0.25 at 1 kHz, as sintering time varied from 24 to 72 hours. It was also found that it tends to result in high loss at high frequency using 2500 PSI. Their SEM images in Figure 3-3 and 3-4 showed that they tend to give small morphology difference. The average grain size using 2500 PSI is: 6.8 μm , 7.5 μm , 11.1 μm and 16.5 μm for 1 hour, 24 hours, 48 hours and 72 hours sintering, while for 3000

PSI, 6.8 μm , 12.3 μm , 13.8 μm and 14.3 μm for 1 hour, 24 hours, 48 hours and 72 hours sintering, respectively. Based on experimental results, it indicated that ceramic sample using 2500 PSI exhibited lagged grain size growth. Especially for sintering 24 hours, the SEM image indicated that it was in the early calcination stage with average grain size of 7.5 μm for 2500 PSI, while the grain was about 12.3 μm with 3000 PSI molding pressure. Moreover, it was found that those samples under 3000 PSI exhibited more porosity, and this porosity phenomenon may be associated with its lower loss at high frequency. Later on, more studies on porosity will be carried out. This suggested that molding pressure could be used as an optimization method in following studies, and longer sintering time such as 24 to 72 hours was necessary in order to enhance the dielectric response.

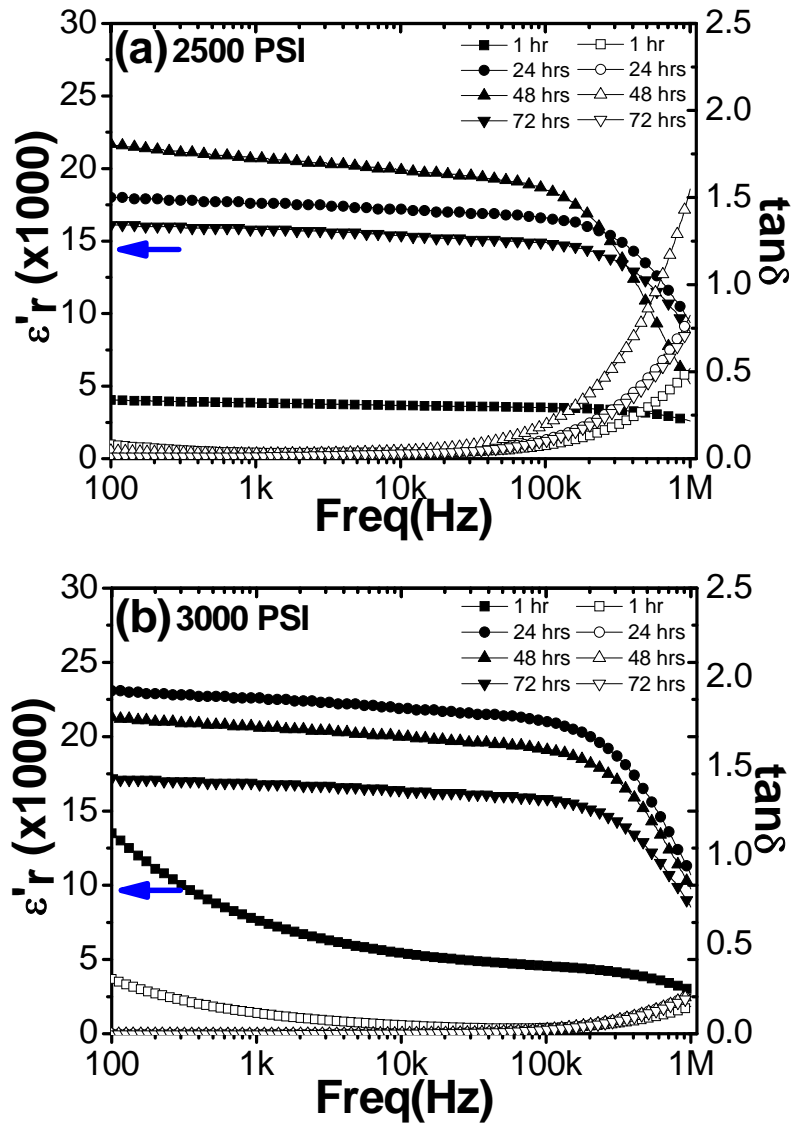


Figure 3-2 Dielectric response vs. frequency for $\text{CaCu}_3\text{Ti}_4\text{O}_{12}$ samples with 24 hrs D.I water ball milling, calcinated at 1075 °C, and then sintered at 1075 °C for 1 hr, 24 hrs, 48 hrs and 72 hrs using (a) 2500 PSI, and (b) 3000 PSI pellet molding pressure.

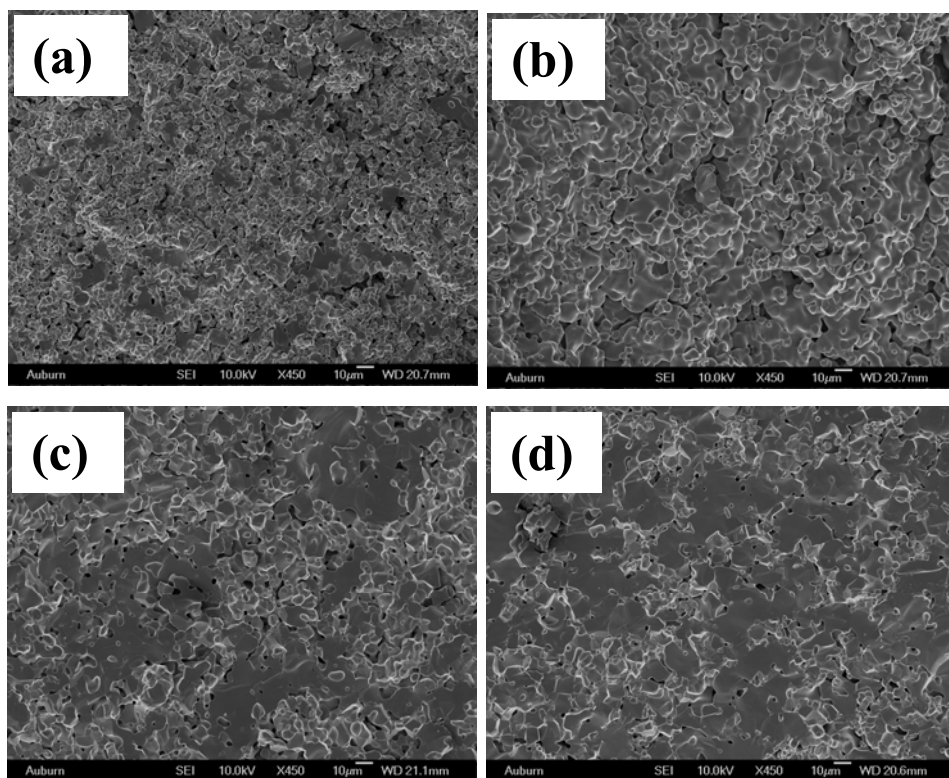


Figure 3-3 SEM fractographs of $\text{CaCu}_3\text{Ti}_4\text{O}_{12}$ after 24 hrs D.I water ball milling, calcinated at $1075\text{ }^\circ\text{C}$, sintered at $1075\text{ }^\circ\text{C}$ for (a) 1 hrs, (b) 24 hrs, (c) 48 hrs (d) 72 hr using 2500 PSI pellet molding pressure.

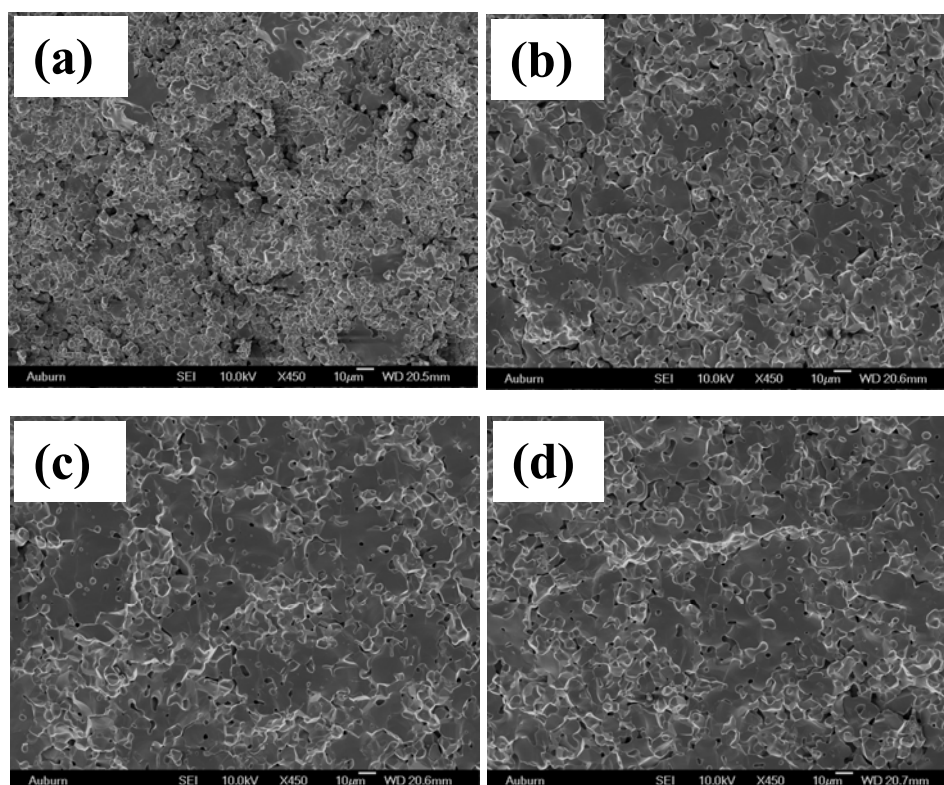


Figure 3-4 SEM fractographs of $\text{CaCu}_3\text{Ti}_4\text{O}_{12}$ after 24 hrs D.I water ball milling, calcinated at 1075 °C, sintered at 1075 °C for (a) 1 hr, (b) 24 hrs, (c) 48 hrs (d) 72 hrs by 3000 PSI pellet molding pressure.

3.3.2.2 Effect of Ball Milling Time and Sintering time

To further investigate the effect of processing on the dielectric properties of $\text{CaCu}_3\text{Ti}_4\text{O}_{12}$ ceramics, ceramic samples were prepared after 48, 72 and 96 hours ball milling and then sintering for 24, 48, and 72 hours respectively, according the procedure #1 in Table 3-1. The effects of milling time and sintering time have been studied. Their dielectric spectrums and SEM images are shown in Figure 3-5, 3-6, 3-7 and 3-8, respectively.

After the initial milling of raw powder for 48, 72, and 96 hours and then following calcination at $1075\text{ }^\circ\text{C}$, the average grain sizes were 2.242 ± 0.3 , 2.266 ± 0.4 and $2.372\pm 0.4\text{ }\mu\text{m}$, respectively. However, it was found that their dielectric response and the corresponding microstructure changed dramatically after sintering processing. As seen in Figure 3-5 (a), the dielectric constant at 1 kHz was about 24,000 to 42,000 for 48 hours milling, however, the dielectric constant increased abruptly from 70,000 to 85,000 at 1 kHz as for 96 hours milling in Figure 3-5 (c). This difference among different milling times was closely related with particle size reduction and the substantial reduction of the amount in the minor phases via longer milling time. Among those results, a relative better processing condition was observed with 96 hours milling and 72 hours sintering, at which a dielectric constant of 82,300 and loss of 0.12 were achieved. Since it is possible that longer milling time creates a more defect-laden particle which enhances the conductivity properties of the grain, this increase in the conductivity of the grain's core region could act to increase the permittivity of the materials⁵. After considering the results in Figure 3-5, longer milling time, such as 96 hours and sintering time such as 72 hours was prone to give better dielectric properties, and thus it can best illustrate the milling effect and sintering effect, respectively. SEM observations in Figure 3-6 indicated that the typical particle size was about 10 to $50\mu\text{m}$ for 48 hours milling. The grain size for 48 hours milling indicated an increasing trend as sintering time varying from 24 to 48 hours. However, there were substantial differences in the microstructure of the longer milling time, such as 72 and 96 hours, as seen in Figure 3-7 and 3-8. Especially for 96 hours milling, due to the way the material fractured it was difficult to distinguish the grain size, so no precise grain size was given, but it can be clearly seen that there was substantial grain growth, which would collaborate the fact of dielectric enhancements with extended

milling time. The improvement of the high frequency dielectric constant usually involves a variation of enhancement factors, such as no oxygen deficiency in the vicinity of grain boundaries, etc. They are closely related with the size of the $\text{CaCu}_3\text{Ti}_4\text{O}_{12}$ grain divided by the grain boundary thickness^{5, 6}. In short, the processing parameters, such as milling time and sintering time, were closely associated with the presence of large semiconducting grains which are seen in Figure 3-8, and could directly influence the final dielectric properties.

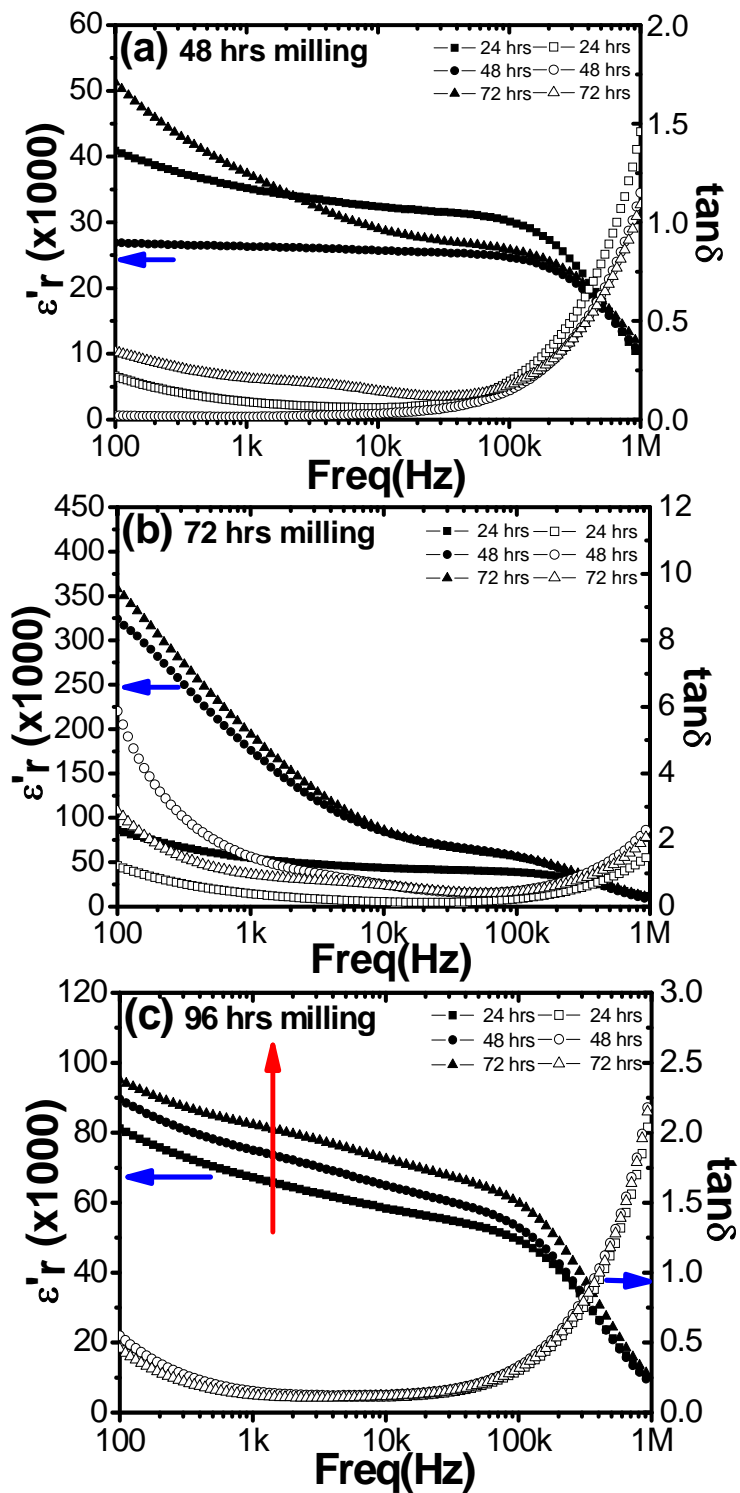


Figure 3-5 Dielectric response vs. frequency for samples: (a), (b) and (c) after 48, 72 and 96 hrs milling respectively, calcining at 1075 °C for 12 hrs, then sintering at 1075 °C for 24, 48, and 72 hrs according to procedure #1 in table 3-1.

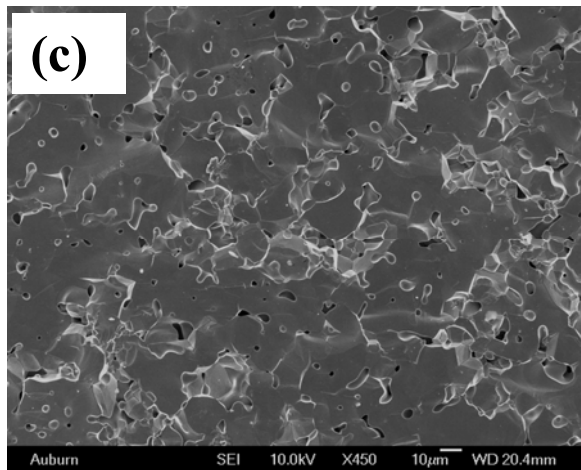
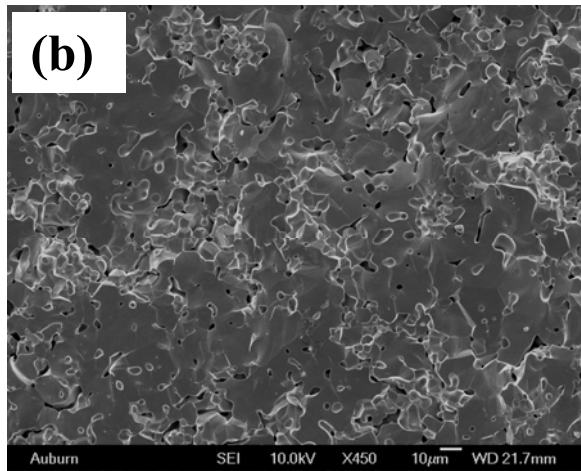
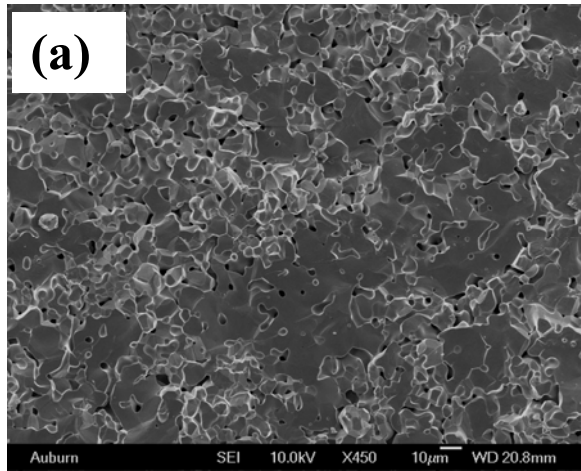


Figure 3-6 SEM fractographs of $\text{CaCu}_3\text{Ti}_4\text{O}_{12}$ for 48 hrs D.I water ball milling, calcining at 1075°C for 12 hrs, then sintering at 1075°C for (a) 24 hrs, (b) 48 hrs, (c) 72 hrs.

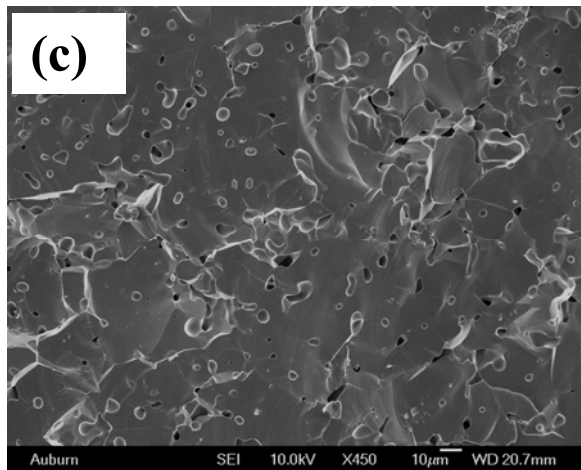
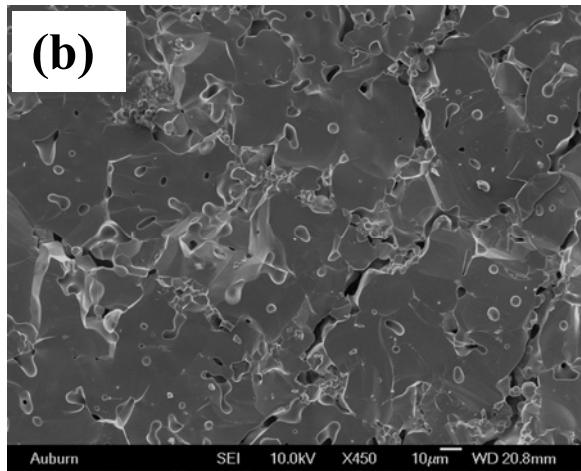
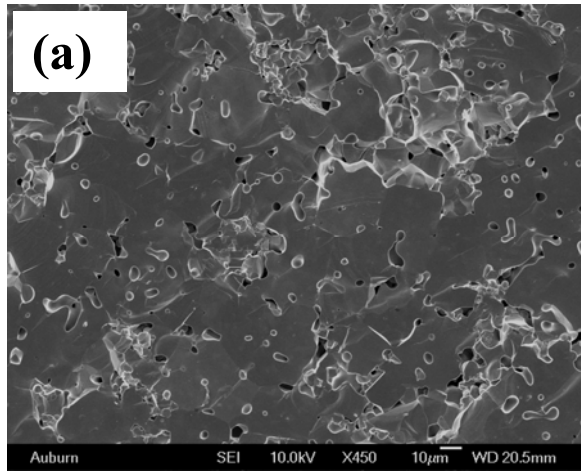


Figure 3-7 SEM fractographs of $\text{CaCu}_3\text{Ti}_4\text{O}_{12}$ for 72 hrs D.I water ball milling, calcining at 1075°C for 12 hrs, then sintering at 1075°C for (a) 24 hrs, (b) 48 hrs, (c) 72 hrs.

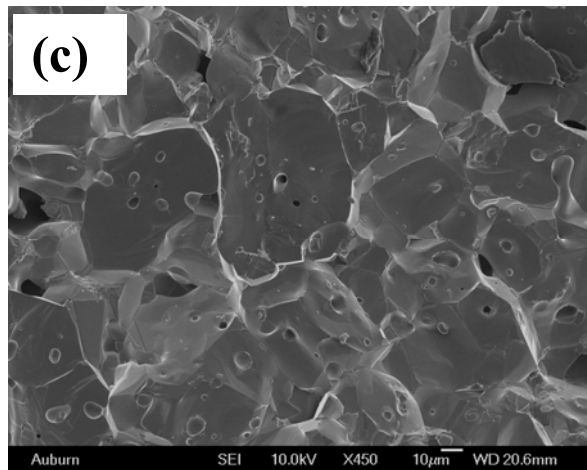
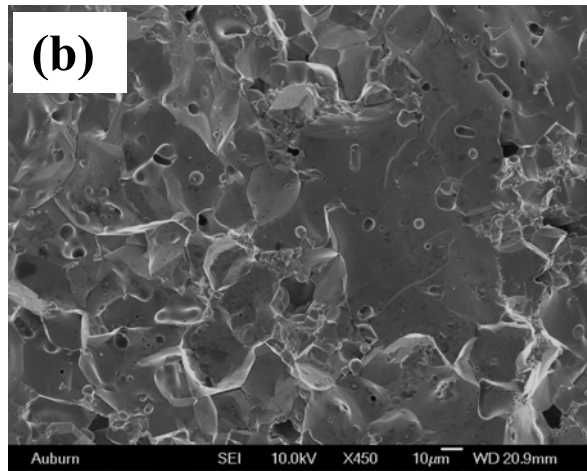
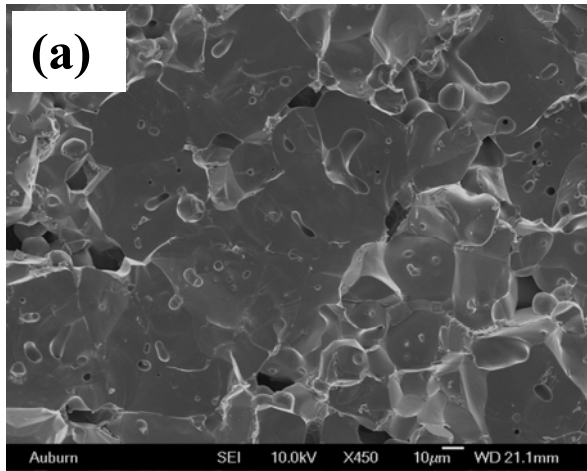


Figure 3-8 SEM fractographs of $\text{CaCu}_3\text{Ti}_4\text{O}_{12}$ for 96 hrs D.I water ball milling, calcining at 1075 °C for 12 hrs, then sintering at 1075 °C for (a) 24 hrs, (b) 48 hrs, (c) 72 hrs.

3.3.2.3 Effect of Calcination Temperature and Milling Solvent

Besides the milling effect and sintering effect to the $\text{CaCu}_3\text{Ti}_4\text{O}_{12}$, the calcination temperature of the material is crucial. Since the calcination temperature might change the densification and grain growth process, elaborate calcination characterization of the material is important to the dielectric enhancement.

The results in Figure 3-9 exhibit dielectric spectrum measured from $\text{CaCu}_3\text{Ti}_4\text{O}_{12}$ calcining at 900 °C. After the initial raw powder milling for 48, 72, and 96 hours and following calcination at 900°C, corresponding average grain sizes were 5.23 ± 1.1 , 5.45 ± 1.2 and 5.89 ± 1.3 μm respectively, which was relatively larger than the results calcining at 1075 °C. In comparison with those sintered samples under two different calcination processes, it was interesting to note that both shared similar trend that all the experimental results after 48 and 72 hours milling exhibited unsatisfactory dielectric response. Only when the milling time exceeds 96 hours which may reach its critical grain size that their dielectric response can be enhanced. Especially, it was found that the dielectric constant increased from 83,000 and 160,000, and dielectric loss remained as small as 0.15 at 1 kHz, as shown in Figure 3-5 and 3-9. With both calcination temperatures, it was clear that the dielectric response was not satisfactory, due to either the dielectric constant being relatively low, or the dielectric loss was high if milling time is bellow 72 hours, as shown in Figure 3-5 and Figure 3-9. The dielectric enhancement is obviously correlated with differences in ceramic microstructure and especially, with the average grain size. According to IBLC model, the enhancement of the dielectric constant was related to the ratio between grain and grain boundary thickness, and the dielectric constant of ceramic can be expressed as⁷:

$$\epsilon_{eff} = \epsilon_{gb} \frac{d_g + d_{gb}}{d_{gb}} \quad (3-1)$$

Where ϵ_{eff} is the effective dielectric constant of a given material, ϵ_{gb} is the dielectric constant of intrinsic bulk, d_g and d_{gb} are the thickness of the grains and grain boundary layers. Corresponding SEM images are shown in Figure 3-10. It can be clearly observed that the structure tends to be more homogeneous and substantial grain growth occurred with dimensions above 60 μm for $\text{CaCu}_3\text{Ti}_4\text{O}_{12}$ calcining at 900 °C, in comparison to 10 to 50 μm at 1075 °C in Figure 3-6. Based on the SEM images shown in Figure 3-10 and

dielectric results in Figure 3-9, the highest of dielectric constant at 1 kHz was up to 160,000 and accordingly, larger grain size was obtained in the same sample. In order to better understand what is occurring during sintering, the shrinkage rate and density change were been measured (see Table 3-2 and 3-3). The shrinkage rate of calcining at 900 °C was almost double that at 1075 °C, which strongly proved the better densification and grain growth. All the results together with the results in Tables 3-2 and 3-3 support the argument that lower calcination temperature such as at 900 °C is beneficial for density improvement and grain size growth, which then contributed the increasing of dielectric constant with extended milling time and sintering time.

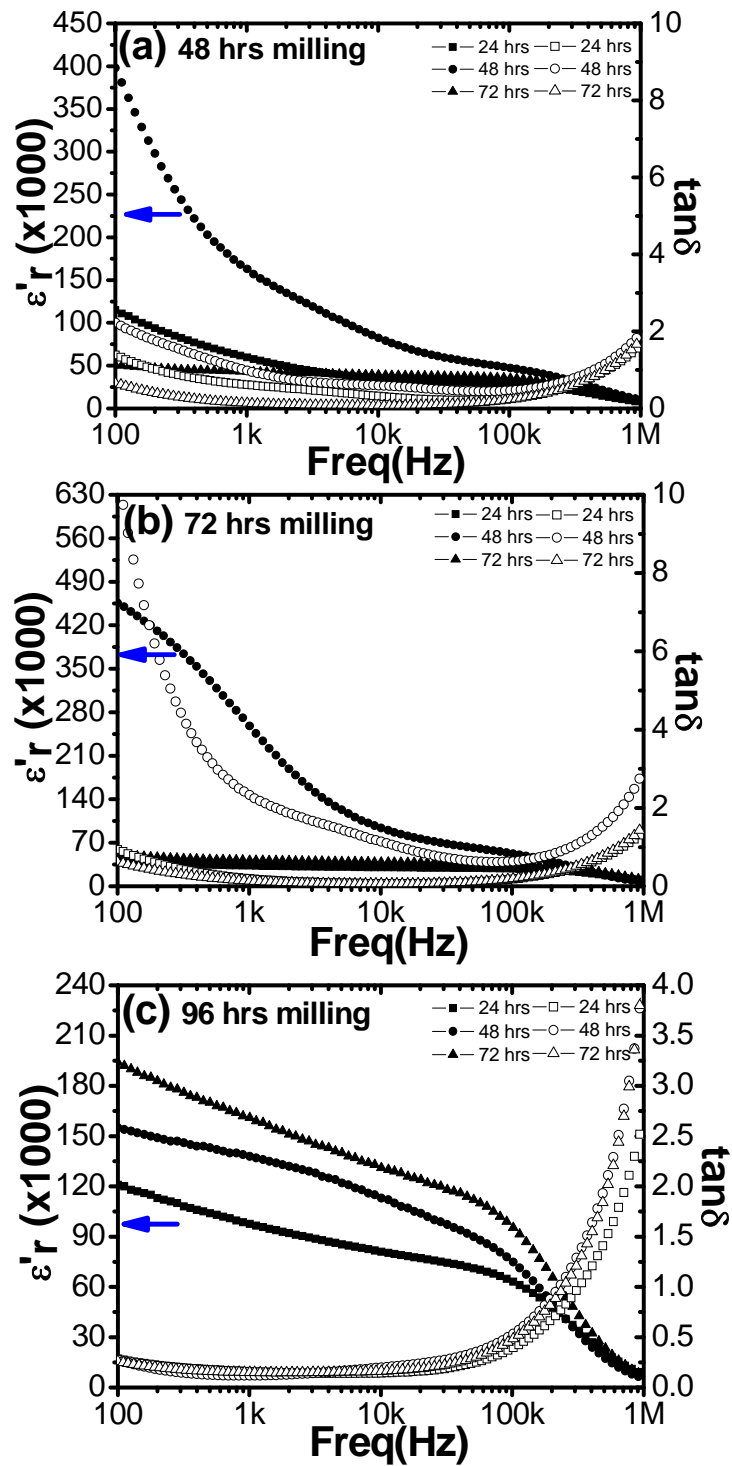


Figure 3-9 Dielectric response vs. frequency for samples: (a), (b) and (c) after 48, 72 and 96 hrs milling respectively, then sintering for 24, 48, and 72 hrs according to procedure #2 in Table 3-1.

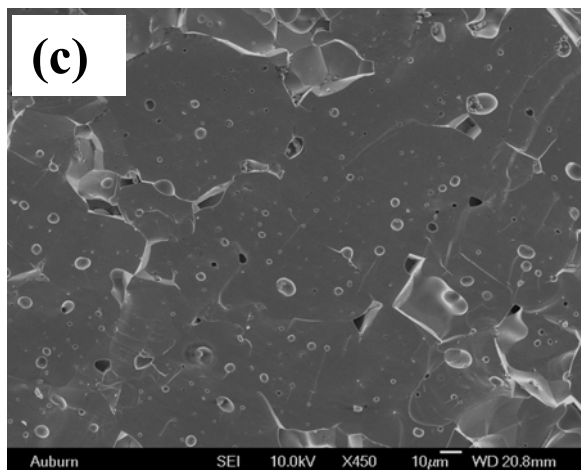
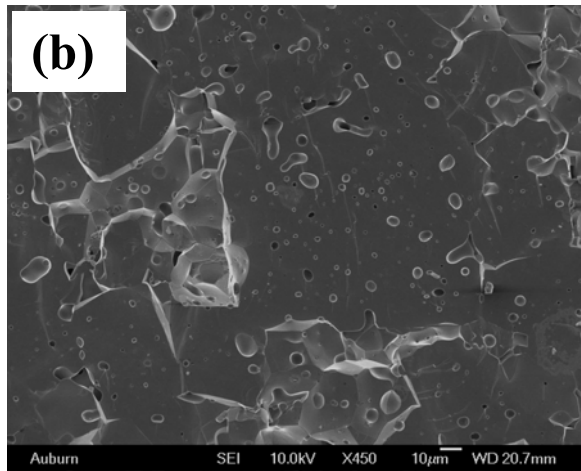
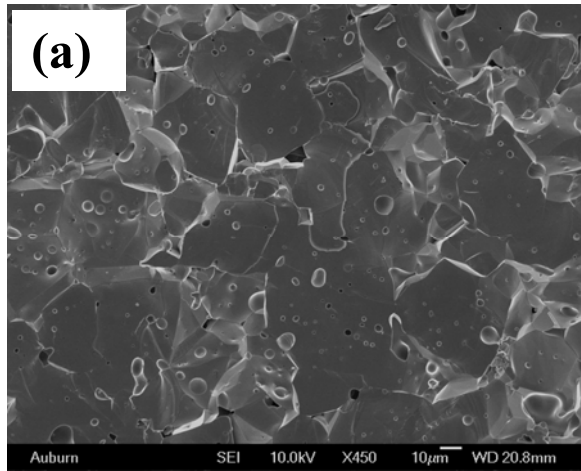


Figure 3-10 SEM fractographs of $\text{CaCu}_3\text{Ti}_4\text{O}_{12}$ for 48 hrs D.I water ball milling, calcinated at 900°C , then sintering at 1075°C for (a) 24 hrs, (b) 48 hrs, (c) 72 hrs.

Table 3-2 Shrinking rate of the pellet.

		[1]	[2]
Ball mill 48 hrs	Sintering 24 hrs	7.6%	14.1%
	Sintering 48 hrs	8.4%	14.2%
	Sintering 72 hrs	7.5%	14.2%
Ball mill 72 hrs	Sintering 24 hrs	9.1%	14.8%
	Sintering 48 hrs	9.5%	13.5%
	Sintering 72 hrs	9.5%	14.4%
Ball mill 96 hrs	Sintering 24 hrs	7.5%	15.1%
	Sintering 48 hrs	8.1%	14.0%
	Sintering 72 hrs	8.0%	14.0%

[1] Method one: Calcinations at 1075 °C for 12 hrs, then sintering at 1075 °C.

[2] Method two: Calcinations at 900 °C for 12 hrs, then sintering at 1075 °C.

* Sample diameter shrinking rate.

Table 3-3 Density of the pellet: g/cm³.

		[1]	[2]
Ball mill 48 hrs	Sintering 24 hrs	4.4	4.7
	Sintering 48 hrs	4.5	4.7
	Sintering 72 hrs	4.4	4.7
Ball mill 72 hrs	Sintering 24 hrs	4.6	4.8
	Sintering 48 hrs	4.7	4.8
	Sintering 72 hrs	4.5	4.9
Ball mill 96 hrs	Sintering 24 hrs	4.6	4.7
	Sintering 48 hrs	4.6	4.8
	Sintering 72 hrs	4.6	4.8

[1] Method one: Calcinations at 1075 °C for 12 hrs, then sintering at 1075 °C.

[2] Method two: Calcinations at 900 °C for 12 hrs, then sintering at 1075 °C.

Figure 3-11 (a) and (b) show the dielectric spectrums of the $\text{CaCu}_3\text{Ti}_4\text{O}_{12}$ with 72 hours ethanol milling, whose experimental route was based on the procedure #3 and #4 in Table 3-1. Compared with the D.I water milling results, due to the fact that ethanol can lower the surface energy of powder and thereby efficiently avoid agglomeration between particles, a better milling effect was achieved, and dielectric results were shown in Figure 3-11 (a). In addition, the dielectric properties were further enhanced by introducing a 2nd ethanol ball milling. For instance, with the same processing in Figure 3-11 (a) followed by a 2nd 24 hours ethanol ball milling after calcinations, the dielectric constant has been improved to 190,000, while loss remained as small as 0.152 at 1 kHz, as shown in Figure 3-11 (b) which was even better than the results with 96 hours D.I water milling as shown in Figure 3-9 (c). Those results have experimentally elucidated the fact that besides the influence of the thermal treatment, milling solvent also played important role in the dielectric response. Upon verification, the technique could prove useful in enhancing the dielectric properties of $\text{CaCu}_3\text{Ti}_4\text{O}_{12}$.

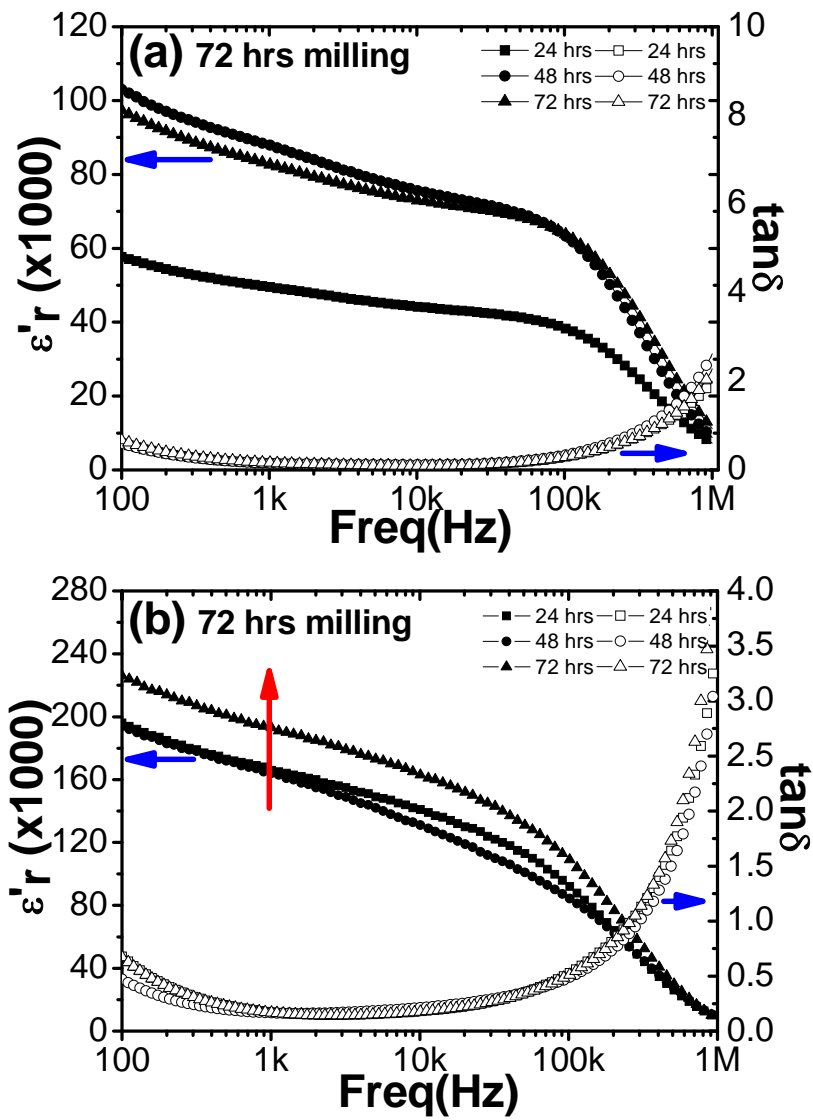


Figure 3-11 Dielectric response vs. frequency for samples: (a) after 72 hrs milling according to procedure #3 in Table 3-1; (b) after 72 hrs milling according to procedure #4 in Table 3-1.

3.3.2.4 Effect of Thickness on Dielectric Properties

Based on those SEM fractographs which were shown in Figure 3-6 to 3-8 and Figure 3-10, it was clear that there were pores on those ceramic samples. By extending the sintering time, those pores generally tended to diminish, while their dielectric properties also showed indication of enhancement. Therefore, those pores were obviously related to their corresponding dielectric properties. In order to better understand the role of those pores on dielectric properties, further experiments on the effect of thickness have been carried out. Ceramic samples after 96 hours milling according to procedure #2 in Table 3-1 were chosen in this study and their corresponding results were already shown in Figure 3-9 (c). For each sample, it was polished on both surfaces (top and bottom) to three different sample thicknesses, such as 0.79 mm, 0.60 mm and 0.38 mm, and their individual experimental results are shown in Figure 3-12 to 3-14. Due to the limitation of polishing techniques, thickness errors were allowed and corresponding $SD(Er\pm)$ were 0.015, 0 and 0.015 mm.

In Figures 3-12 to 3-14, it was curious to find that the corresponding dielectric constant was increasing with decreasing sample thickness. More specially, for example, for 24 hours sintering, it increased from 41,100 to 56,100, for 48 hours sintering, it increased from 186,000 to 289,000 and for 72 hours sintering, it changed from 199,000 to 238,000. Compared with the results in Figure 3-9 (c), those results were significantly improved, except the sample with 24 hours sintering. This difference originated from the fact that the dielectric property was not only influenced by sintering time, but also associated with their thickness. As the sintering time was short, such as 24 hours in this study, grain growth was between its initial stage and intermediate stage, which were characterized with neck growth and enclosing pore channels at grain edges. Thus, especially at the edge area in those sintered samples, their dielectric properties were easily prone to fluctuate. SEM fractographs of those samples before polishing processing are shown in Figures 3-16 to 3-18. For each sintered sample, three different locations, such as edge, middle and core areas were studied as shown in Figure 3-15. In Figures 3-16 to 3-18, they presented a slight increase on the pores' surface density as moving from edge to core area, for example, 51 to 60 pores for 24 hours sintering, 57 to 75 pores for 48 hours sintering and 55 to 100 pores for 72 hours sintering. Each individual pore

resembled one individual dipole in dielectrics, which can bound equal charge in magnitude but opposite in polarity. Therefore, it was found that with diminishing thickness, the increasing pore surface density lead to increasing quantities of dipole moments, which was associated with dielectric constant increase. SEM fractographs have collaborated with results in Figure 3-12 to 3-14. With further studies with Cole-Cole equations, analyzed results were shown in Figure 3-18 to 3-20. The empirical Cole-Cole relation is shown as following:

$$\varepsilon^* - \varepsilon_{r\infty} = \varepsilon'_r - \varepsilon_{r\infty} - j\varepsilon''_r = \frac{\varepsilon_{rs} - \varepsilon_{r\infty}}{1 + (j\omega\tau_0)^{1-\alpha}} \quad (3-2)$$

Based on the results in Figure 3-19 to 3-21, the relaxation time τ_0 for 24, 48 and 72 hours sintering increased from 0.215 μs to 0.318 μs , 0.937 μs to 1.707 μs and 0.959 μs to 1.667 μs , respectively. Figure 3-22 shows the relationship of $\Delta\varepsilon$ ($\varepsilon_s - \varepsilon_\infty$) vs. sample thickness and it was found that the $\Delta\varepsilon$ was increasing with decreasing thickness. As there are more dipoles inside, it corresponds to longer relaxation time, which has been well confirmed with Cole-Cole equations. All the experimental results have indicated that those pores in those ceramic samples played an important role in the dielectric properties.

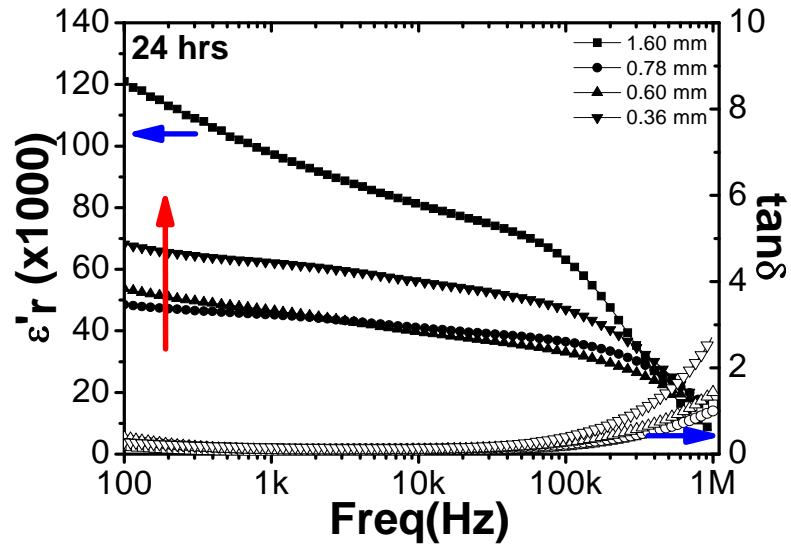


Figure 3-12 Dielectric response vs. frequency for samples with different sample thickness (1.60 mm, 0.78 mm, 0.60 mm and 0.36 mm, respectively) after 96 hrs milling and then 24 hrs sintering according to procedure #2 in Table 3-1.

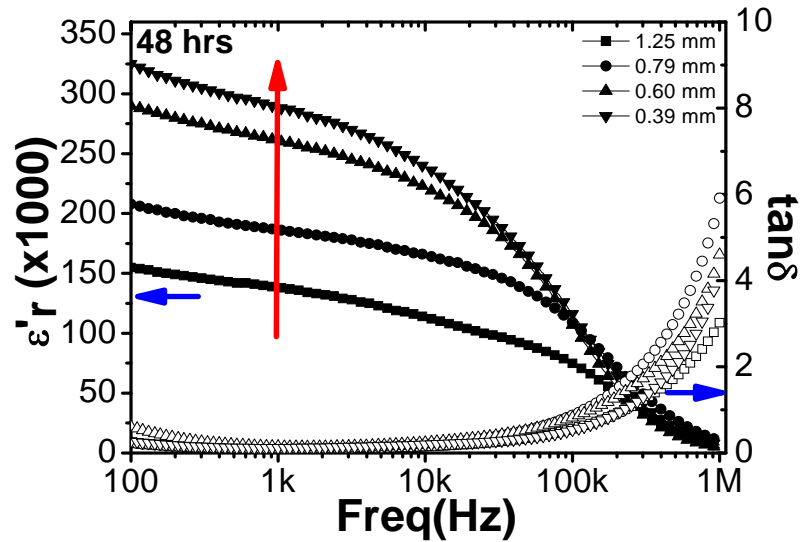


Figure 3-13 Dielectric response vs. frequency for samples with different sample thickness (1.25 mm, 0.79 mm, 0.60 mm and 0.39 mm, respectively) after 96 hrs milling and then 48 hrs sintering according to procedure #2 in Table 3-1.

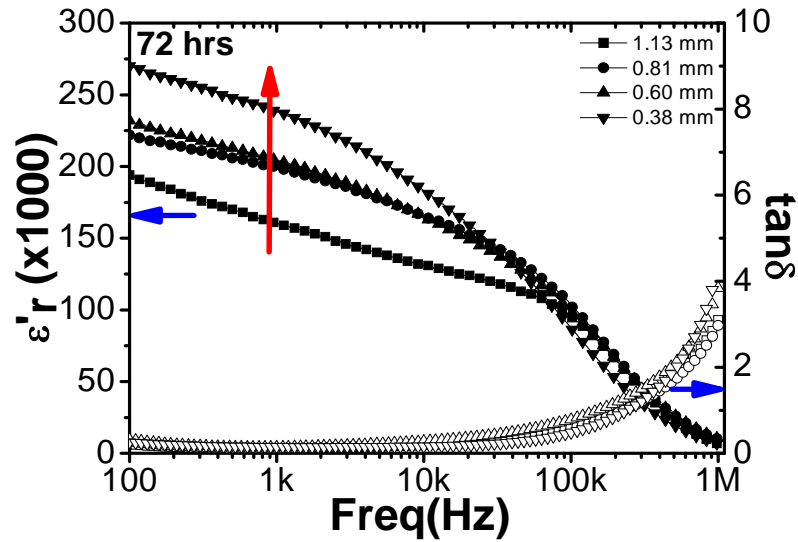


Figure 3-14 Dielectric response vs. frequency for samples with different sample thickness (1.13 mm, 0.81 mm, 0.60 mm and 0.38 mm, respectively) after 96 hrs milling and then 72 hrs sintering according to procedure #2 in Table 3-1.

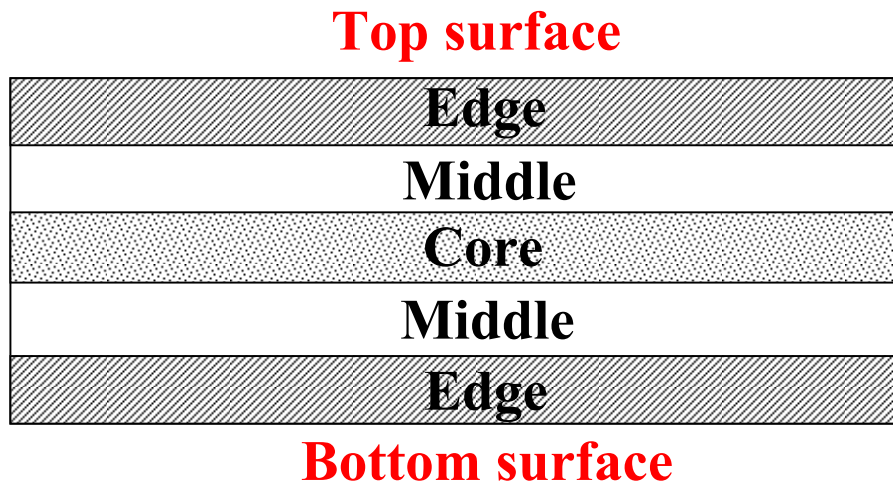


Figure 3-15 Illustration of edge, middle, core areas in $\text{CaCu}_3\text{Ti}_4\text{O}_{12}$ ceramic pellet for SEM fractographs.

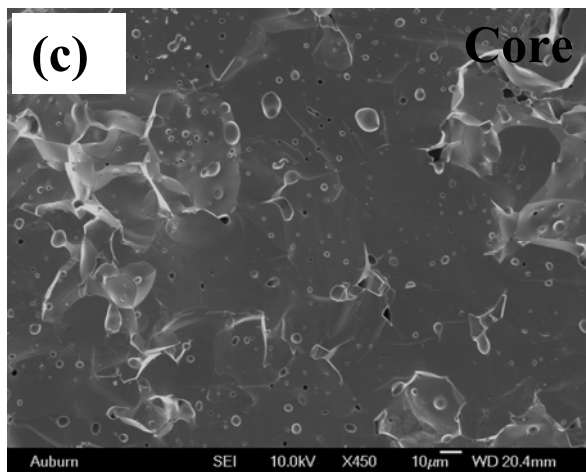
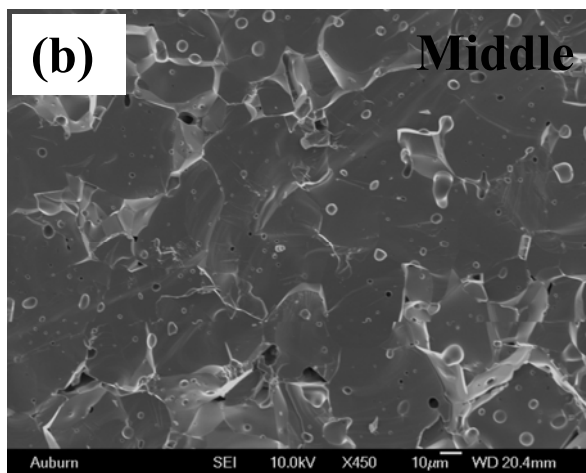
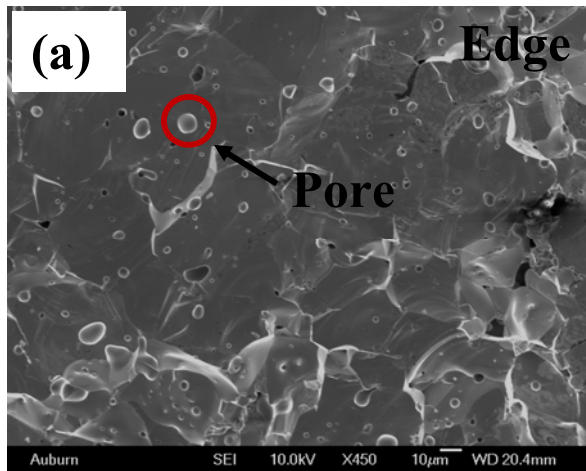


Figure 3-16 SEM fractographs of $\text{CaCu}_3\text{Ti}_4\text{O}_{12}$ after 96 hrs milling and then 24 hrs sintering according to procedure #2 in Table 3-1: (a) edge area, (b) middle area, (c) core area.

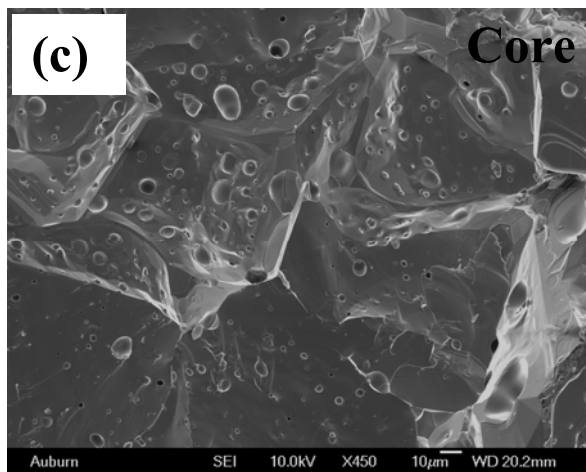
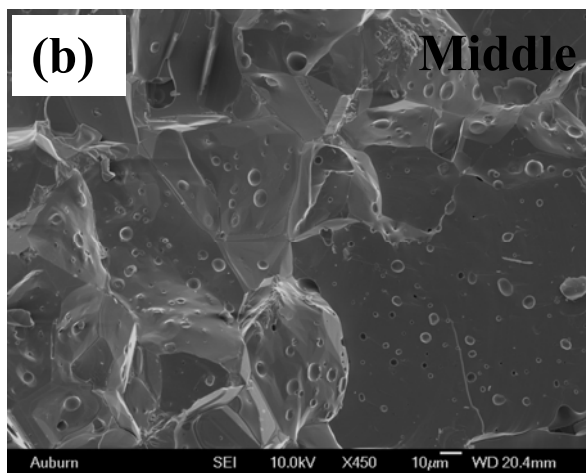
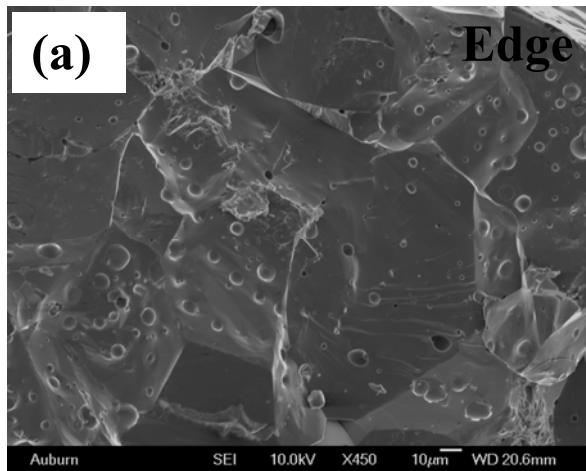


Figure 3-17 SEM fractographs of $\text{CaCu}_3\text{Ti}_4\text{O}_{12}$ after 96 hrs milling and then 48 hrs sintering according to procedure #2 in Table 3-1: (a) edge area, (b) middle area, (c) core area.

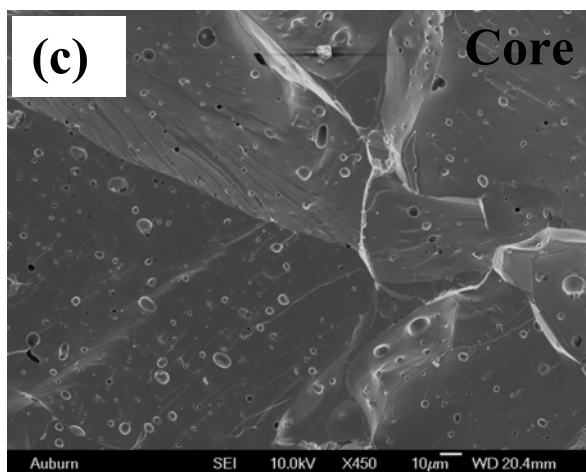
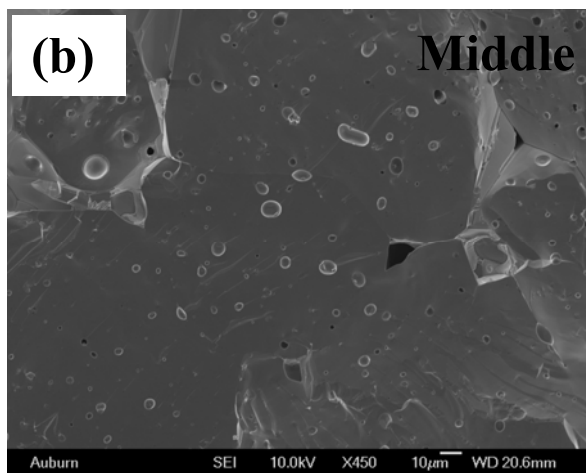
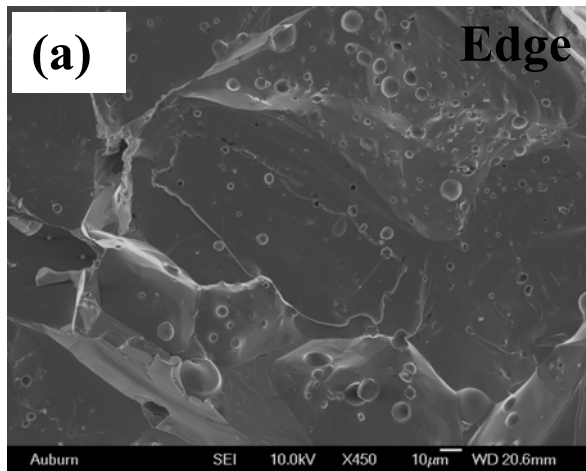


Figure 3-18 SEM fractographs of $\text{CaCu}_3\text{Ti}_4\text{O}_{12}$ after 96 hrs milling and then 72 hrs sintering according to procedure #2 in Table 3-1: (a) edge area, (b) middle area, (c) core area.

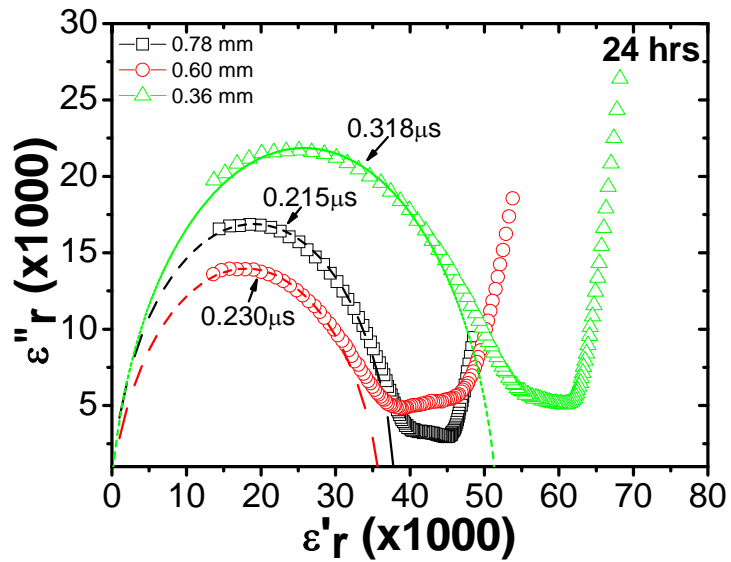


Figure 3-19 Cole-cole plot of the dielectric data of samples with different sample thickness (0.78 mm, 0.60 mm and 0.36 mm, respectively) after 96 hrs milling and then 24 hrs sintering according to procedure #2 in Table 3-1.

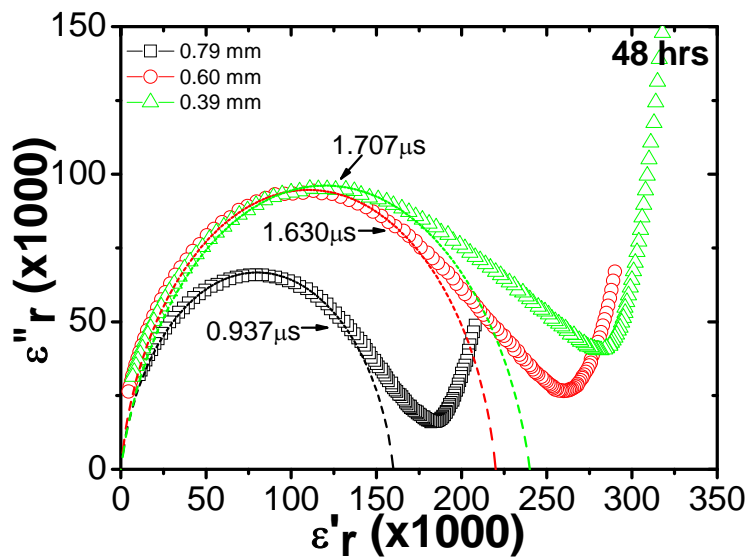


Figure 3-20 Cole-cole plot of the dielectric data of samples with different sample thickness (0.79 mm, 0.60 mm and 0.39 mm, respectively) after 96 hrs milling and then 48 hrs sintering according to procedure #2 in Table 3-1.

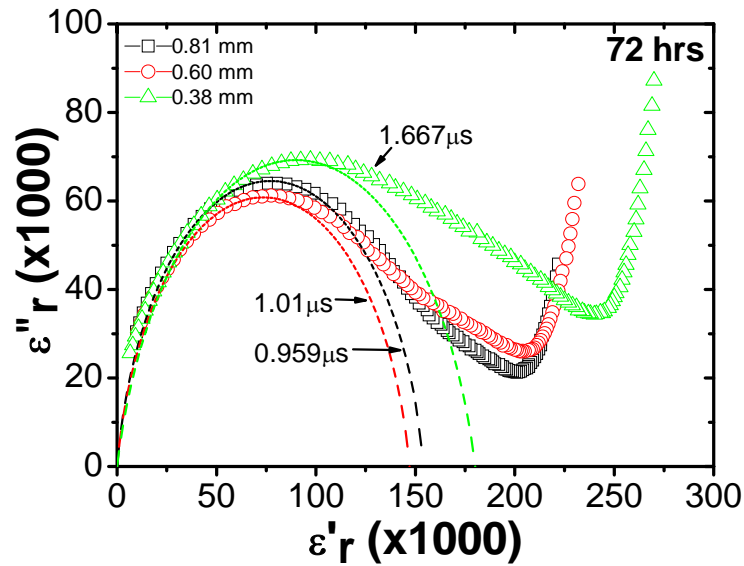


Figure 3-21 Cole-cole plot of the dielectric data of samples with different sample thickness (0.81 mm, 0.60 mm and 0.38 mm, respectively) after 96 hrs milling and then 72 hrs sintering according to procedure #2 in Table 3-1.

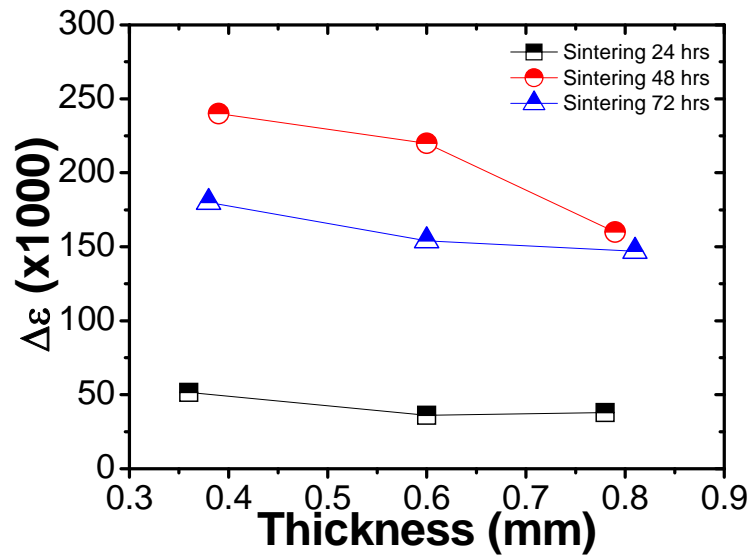


Figure 3-22 The relationship of $\Delta\epsilon$ ($\epsilon_{rs} - \epsilon_{rco}$) vs. sample thickness after 96 hrs milling and then 24, 48 and 72 hrs sintering according to procedure #2 in Table 3-1.

3.3.2.4 Effect of CuO Doping on Dielectric Properties

In order to study the dielectric behavior in $\text{CaCu}_3\text{Ti}_4\text{O}_{12}$, the effect of CuO doping was quantitatively evaluated in this study. $\text{CaCu}_3\text{Ti}_4\text{O}_{12}$ with 5% and 10% CuO doping were prepared according to procedure #1 after 72 hours D.I water milling in Table 3-1.

Many efforts have been devoted recently to understand the role of CuO on the enhancement of dielectric constant. It was generally thought when large abnormal grains are developed, the dielectric constant become improved⁸. For polycrystalline sample, the main defects are at grain boundary, however in single crystal, they are the dislocation and the planar defects, which could be caused by cation disorder⁹. It has been reported that those defects would form internal barrier layer capacitor (IBLC) and they would lead to unusual dielectric properties. In recent work, the discontinuous grain growth has been found in the place where there is the Cu-deficiency. The important role of CuO has been reported^{2, 10}. Those Cu ions are segregated at grain boundary and a second phase of CuO located at the triple-point site⁸. Experimental results show the formation of oxygen deficiency that happen in the grain is sufficient to establish conductivity within the grains⁶. With the CuO dopant, it enhances the oxygen deficiency and then improves the conductivity. It means that it is the high conductivity resulting in the high dielectric constant. Figure 3-23 shows the frequency spectra of dielectric constant and dielectric loss obtained on a representative sample as-sintered. It was found that the maximum dielectric constant was 15,900 at 1 kHz after 48 hours sintering with 5% CuO doping, while it increased to 28,200 at 1 kHz after 72 hours sintering with 10% CuO doping. At the same time, the dielectric loss remained as low as 0.06 to 0.13 at 1 kHz. It indicated that increasing of CuO doping altered the conductivity at the grain boundary and attributed the formation of IBLC under extended sintering time such as 72 hours, which would explain the improvement. This process is associated with the formation of a liquid CuO-TiO₂ phase during the sintering process, where the densification of the ceramic can be improved by liquid phase¹¹. In order to understand it, the EDS were carried out at two different sites: one was at grain and the other was at grain boundary. Figures 3-24 to 3-35 show the SEM and EDS results with 5% and 10% CuO doping after sintering for 24, 48 and 72 hours. Based on the EDS experiments, a strong Cu signal was detected along the grain boundaries, which reveals the segregations of Cu ions to the grain boundaries.

Especially for the 10% CuO, the signal of CuO increased from 50 to 69 wt%, which was correspondent to the enhancement of dielectric response. Combined with all the results, it was believed that CuO doping played an important role in attributing to the formation of the barrier layer capacitors.

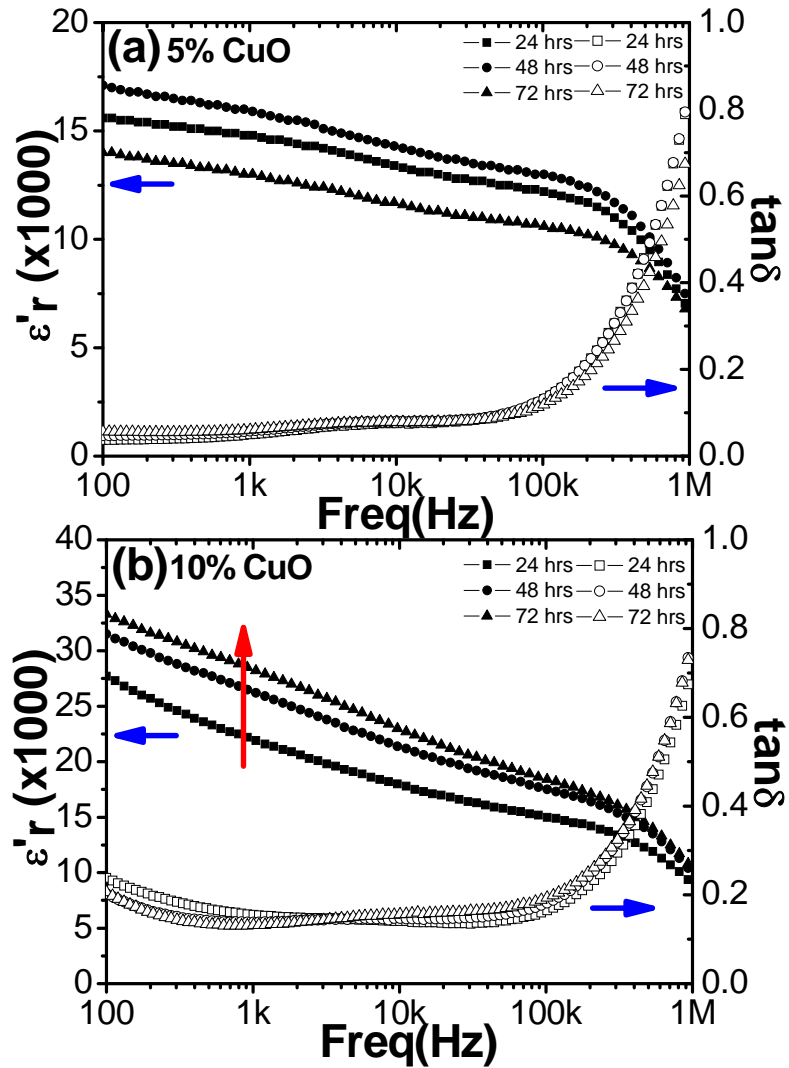
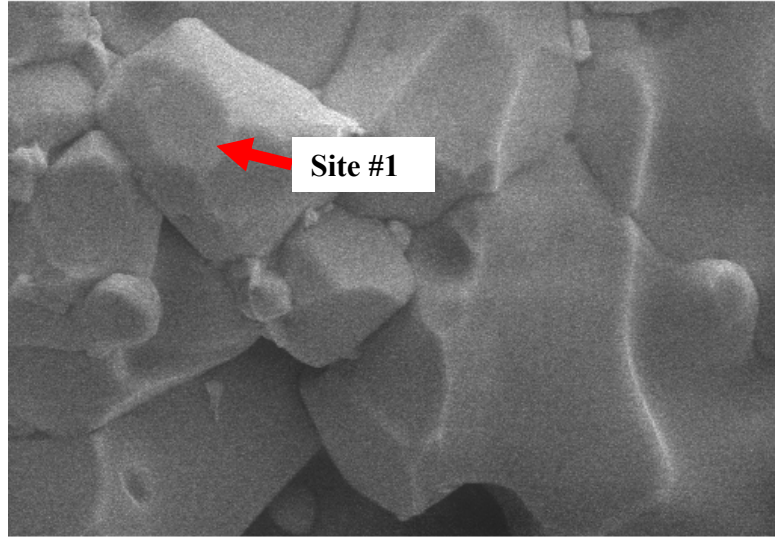
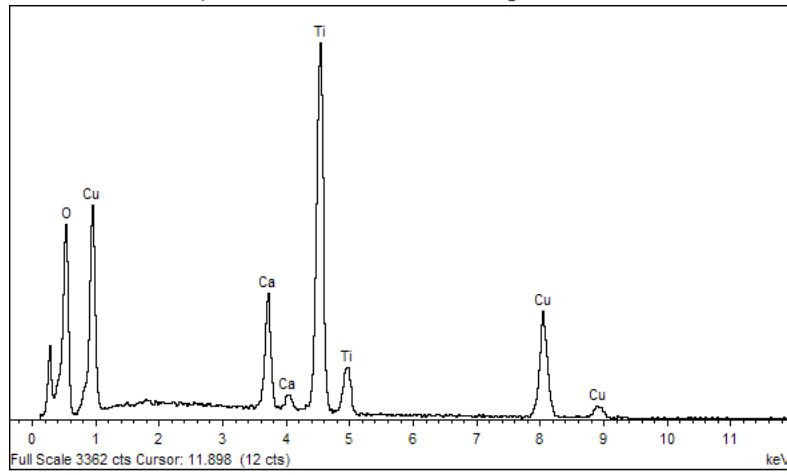


Figure 3-23 Dielectric response vs. frequency of the $\text{CaCu}_3\text{Ti}_4\text{O}_{12}$ after 72 hrs D.I water ball milling according to procedure #1 in table 3-1 with (a) 5 % CuO doping; (b) 10 % CuO doping

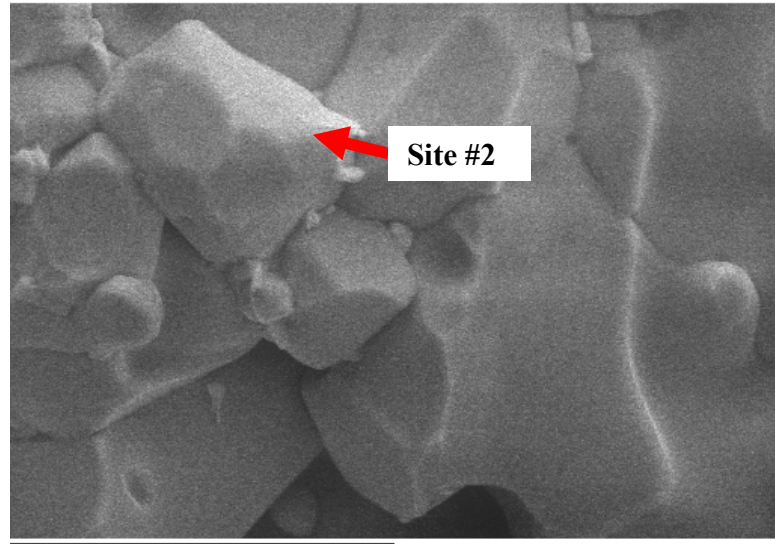


30µm Electron Image 1

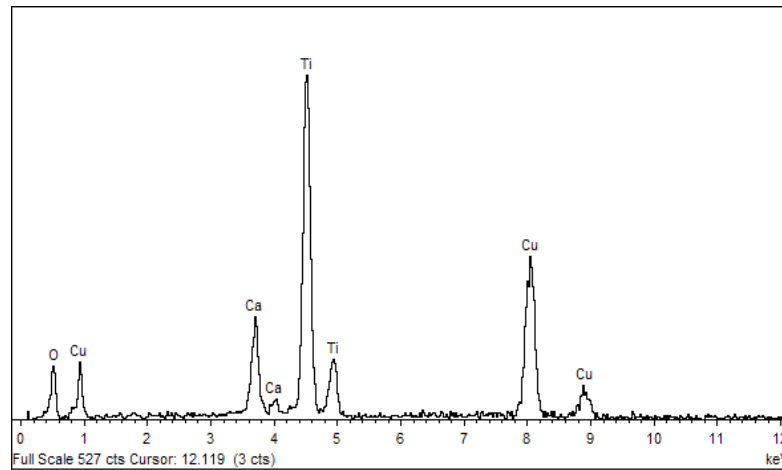


Element	App Conc.	Intensity Corr.	Weight%	Weight% Sigma	Atomic%
O K	19.86	0.4900	41.89	0.73	70.35
Ca K	6.02	1.1127	5.59	0.15	3.75
Ti K	23.15	0.8922	26.82	0.41	15.04
Cu K	21.21	0.8530	25.70	0.50	10.87
Totals			100.00		

Figure 3-24 SEM fractographs and EDS analysis results of $\text{CaCu}_3\text{Ti}_4\text{O}_{12}$ with 5% CuO dopant sintering for 24 hrs at site #1.

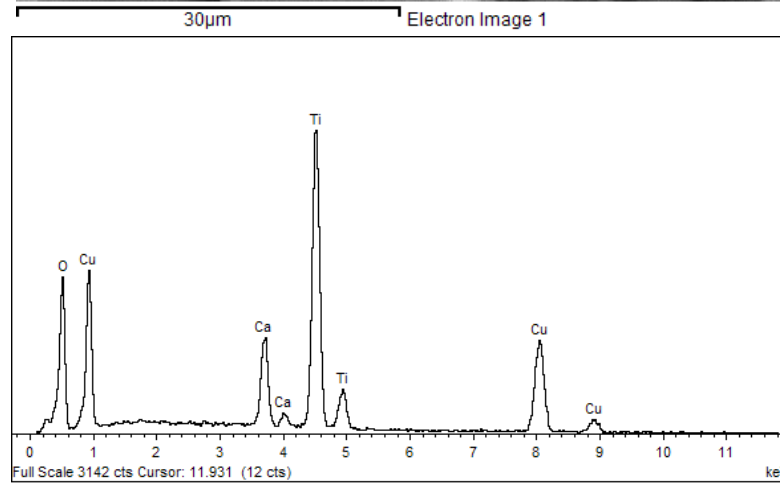
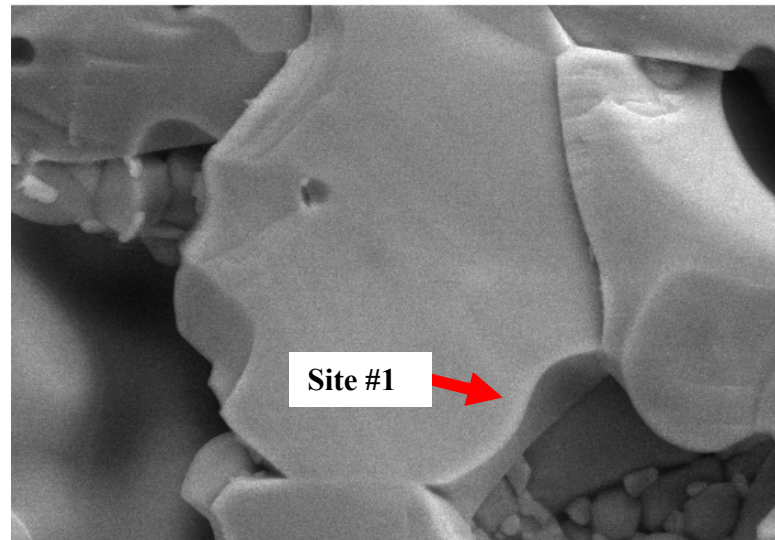


30µm Electron Image 1



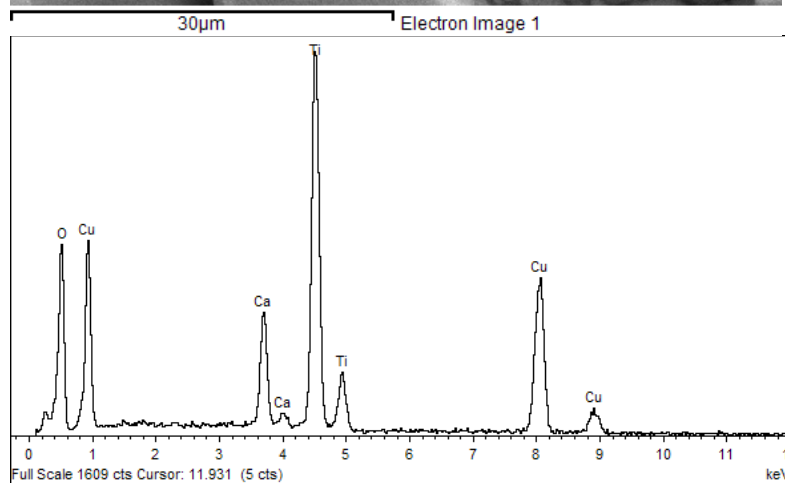
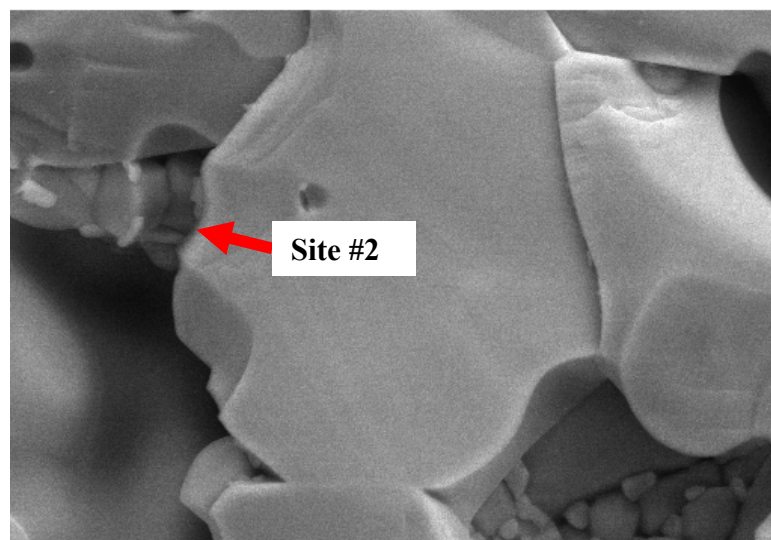
Element	App Conc.	Intensity Corr.	Weight%	Weight% Sigma	Atomic%
O K	2.22	0.4425	16.09	1.84	39.75
Ca K	1.85	1.1428	5.20	0.38	5.13
Ti K	8.86	0.9402	30.30	1.07	25.00
Cu K	13.75	0.9125	48.41	1.51	30.12
Totals			100.00		

Figure 3-25 SEM fractographs and EDS analysis results of $\text{CaCu}_3\text{Ti}_4\text{O}_{12}$ with 5% CuO dopant sintering for 24 hrs at site #2.



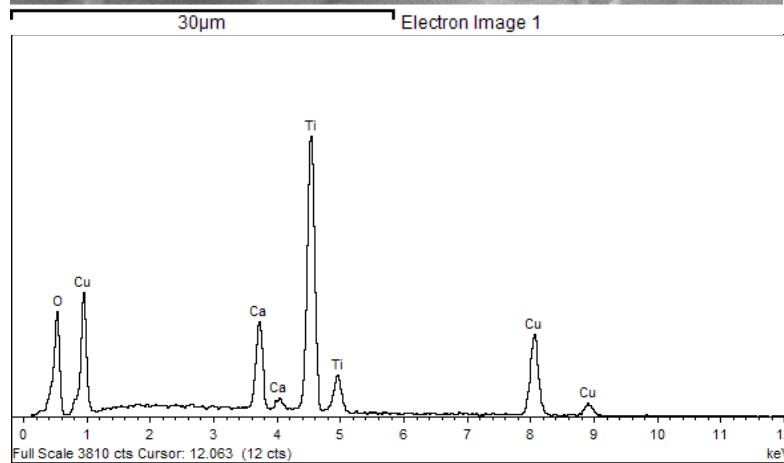
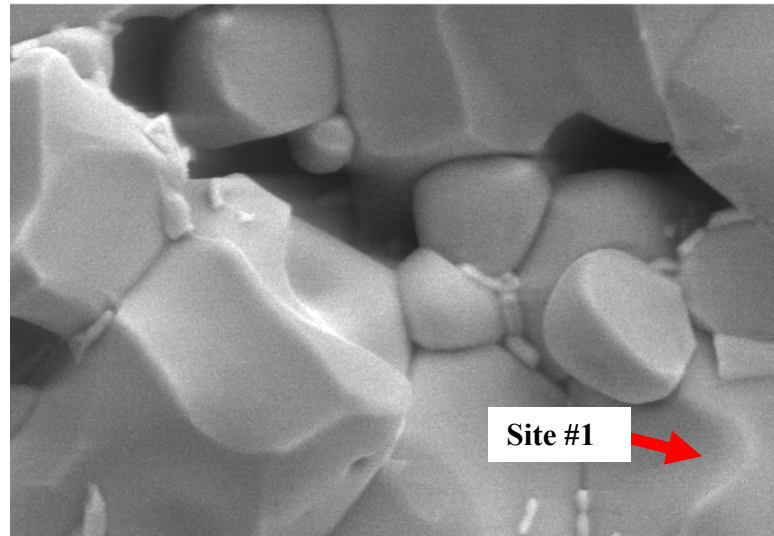
Element	App Conc.	Intensity Corrn.	Weight%	Weight% Sigma	Atomic%
O K	15.27	0.4936	39.34	0.81	68.32
Ca K	4.69	1.1140	5.36	0.16	3.72
Ti K	18.70	0.8978	26.51	0.45	15.38
Cu K	19.44	0.8597	28.79	0.57	12.59
Totals			100.00		

Figure 3-26 SEM fractographs and EDS analysis results of $\text{CaCu}_3\text{Ti}_4\text{O}_{12}$ with 5% CuO dopant sintering for 48 hrs at site #1.



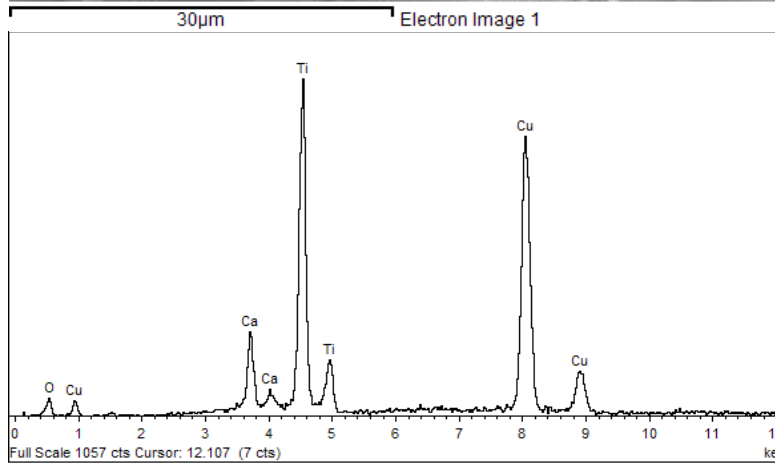
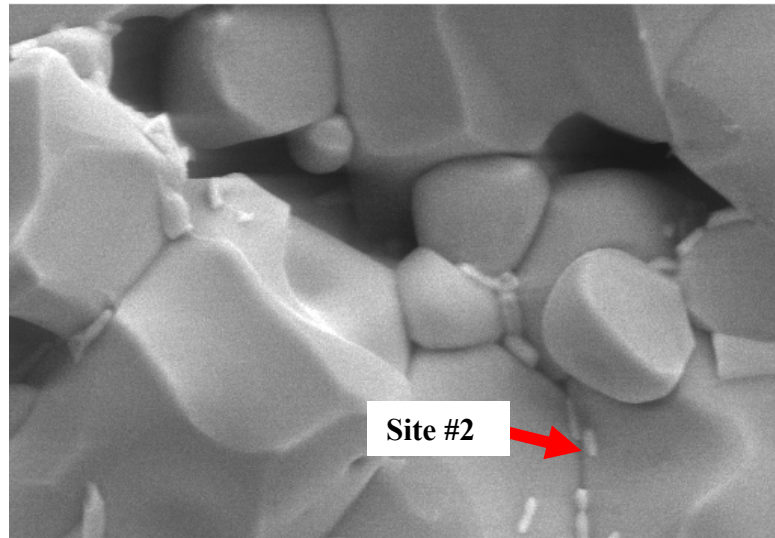
Element	App Conc.	Intensity Corr.	Weight%	Weight% Sigma	Atomic%
O K	9.51	0.5116	34.55	0.99	64.19
Ca K	2.93	1.1143	4.89	0.18	3.63
Ti K	12.29	0.9083	25.16	0.51	15.61
Cu K	16.62	0.8730	35.40	0.74	16.56
Totals			100.00		

Figure 3-27 SEM fractographs and EDS analysis results of $\text{CaCu}_3\text{Ti}_4\text{O}_{12}$ with 5% CuO dopant sintering for 48 hrs at site #2.



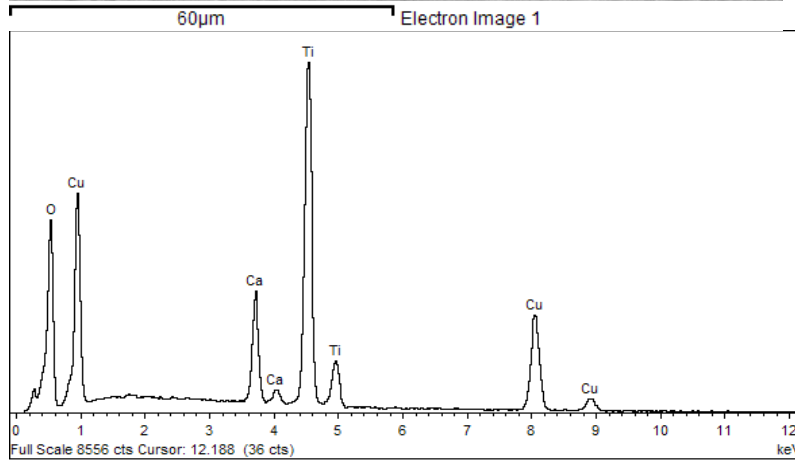
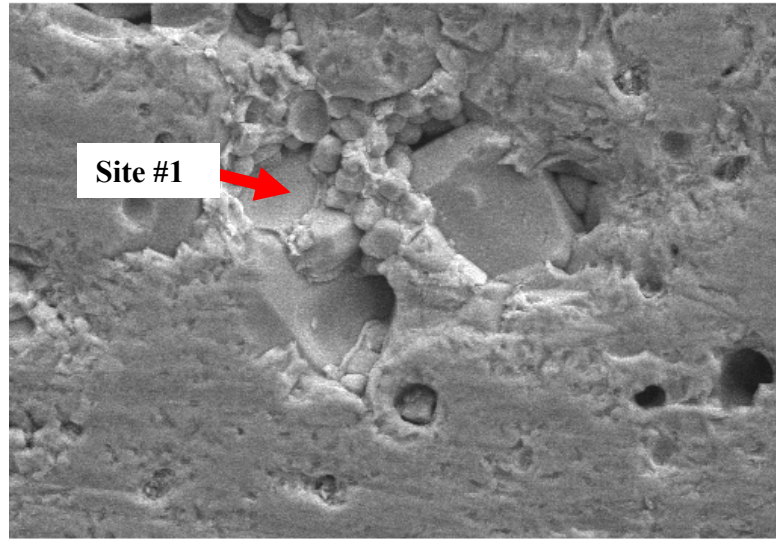
Element	App Conc.	Intensity Corn.	Weight%	Weight% Sigma	Atomic%
O K	12.47	0.4496	34.04	0.85	63.06
Ca K	5.63	1.1258	6.13	0.17	4.53
Ti K	21.79	0.9039	29.58	0.48	18.30
Cu K	21.38	0.8677	30.24	0.57	14.11
Totals			100.00		

Figure 3-28 SEM fractographs and EDS analysis results of $\text{CaCu}_3\text{Ti}_4\text{O}_{12}$ with 5% CuO dopant sintering for 72 hrs at site #1.



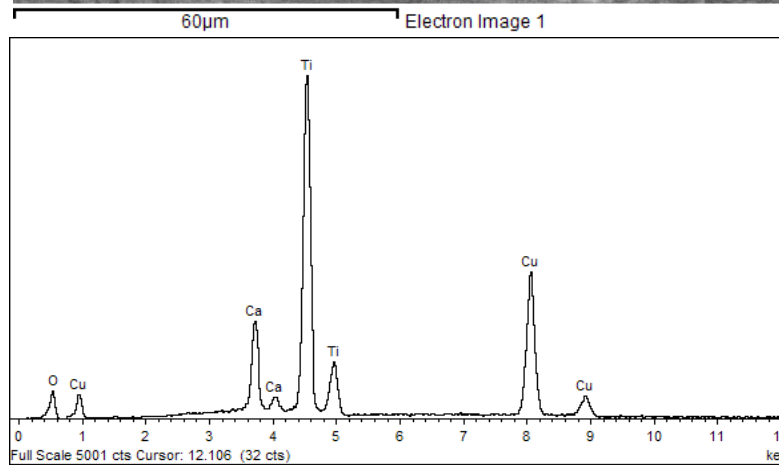
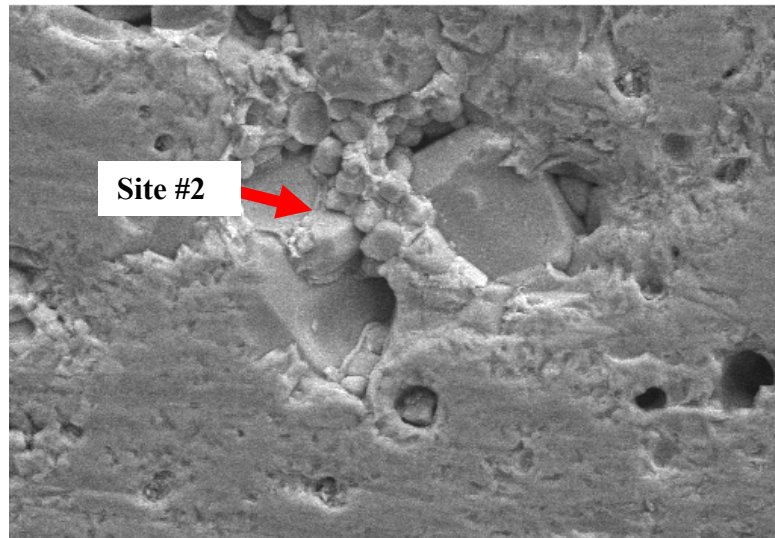
Element	App Conc.	Intensity Corm.	Weight%	Weight% Sigma	Atomic%
O K	0.59	0.5159	3.74	0.61	12.27
Ca K	1.35	1.1397	3.87	0.21	5.07
Ti K	6.94	0.9693	23.32	0.52	25.57
Cu K	20.25	0.9550	69.07	0.72	57.09
Totals			100.00		

Figure 3-29 SEM fractographs and EDS analysis results of $\text{CaCu}_3\text{Ti}_4\text{O}_{12}$ with 5% CuO dopant sintering for 72 hrs at site #2.



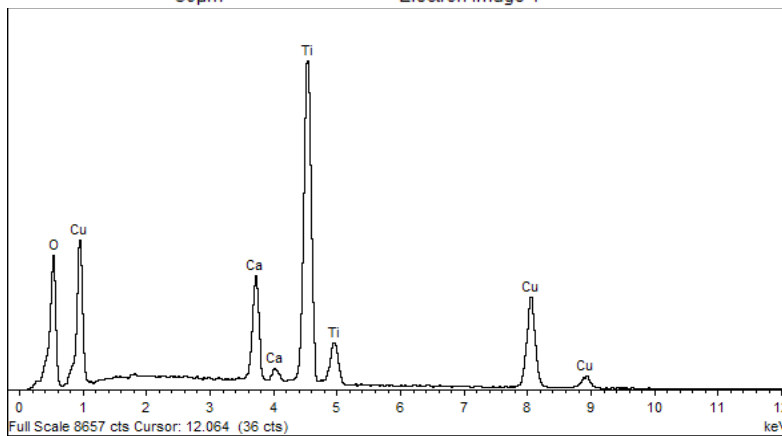
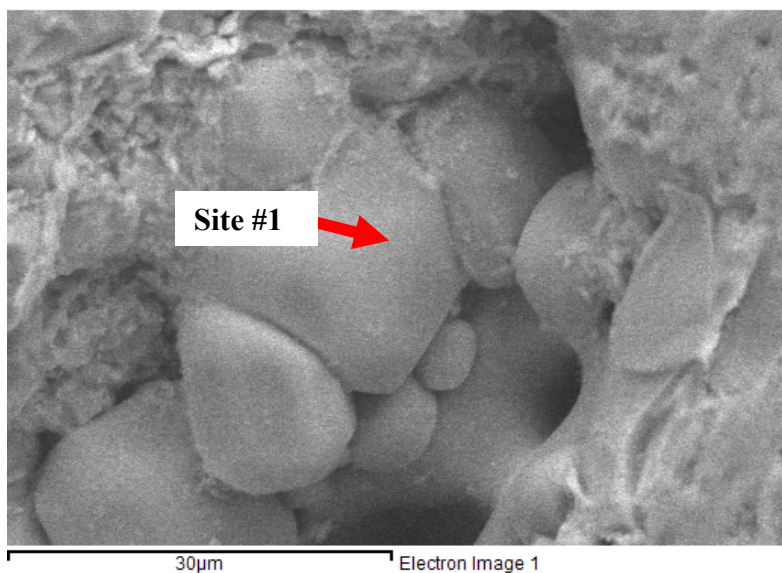
Element	App Conc.	Intensity Corr.	Weight%	Weight% Sigma	Atomic%
O K	25.24	0.4929	41.91	0.46	70.39
Ca K	7.53	1.1122	5.54	0.09	3.72
Ti K	29.04	0.8924	26.63	0.25	14.94
Cu K	27.03	0.8532	25.92	0.31	10.96
Totals			100.00		

Figure 3-30 SEM fractographs and EDS analysis results of $\text{CaCu}_3\text{Ti}_4\text{O}_{12}$ with 10% CuO dopant sintering for 24 hrs at site #1.



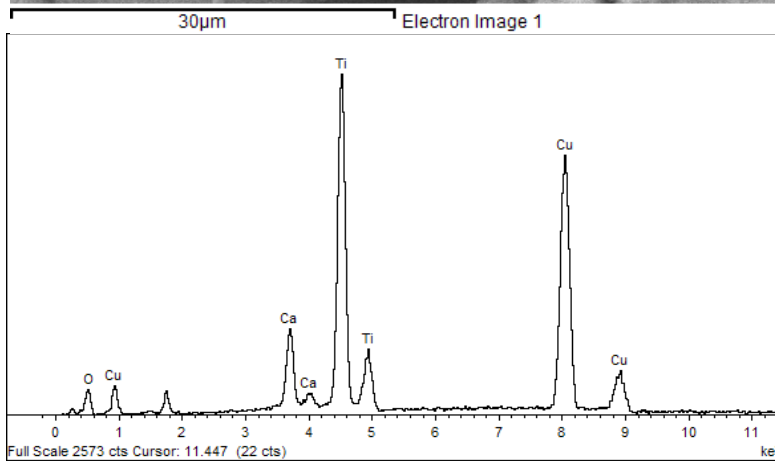
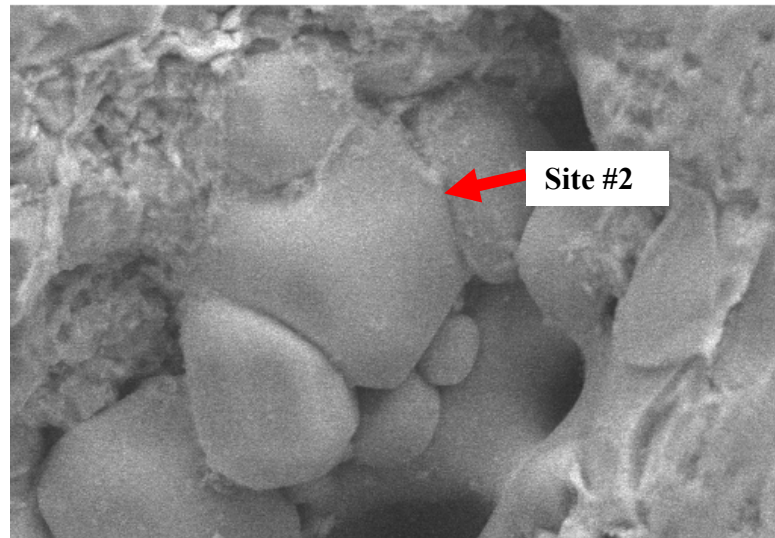
Element	App Conc.	Intensity Corn.	Weight%	Weight% Sigma	Atomic%
O K	2.05	0.4026	9.84	0.55	27.16
Ca K	3.66	1.1572	6.11	0.14	6.73
Ti K	16.71	0.9479	33.99	0.37	31.33
Cu K	23.96	0.9231	50.06	0.47	34.78
Totals			100.00		

Figure 3-31 SEM fractographs and EDS analysis results of $\text{CaCu}_3\text{Ti}_4\text{O}_{12}$ with 10% CuO dopant sintering for 24 hrs at site #2.



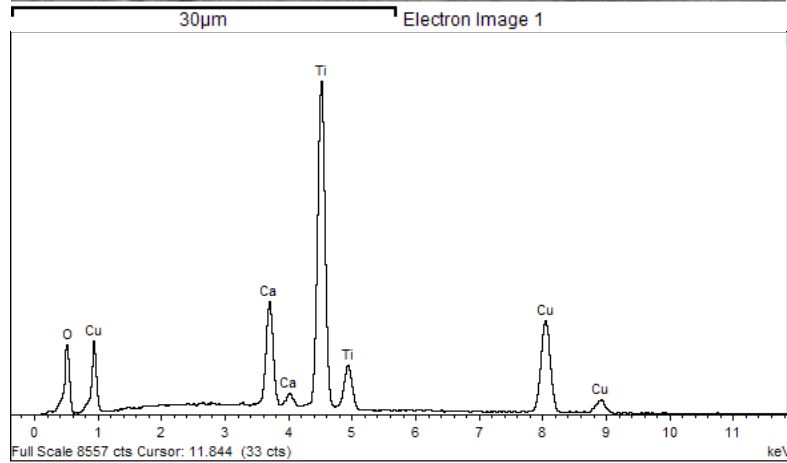
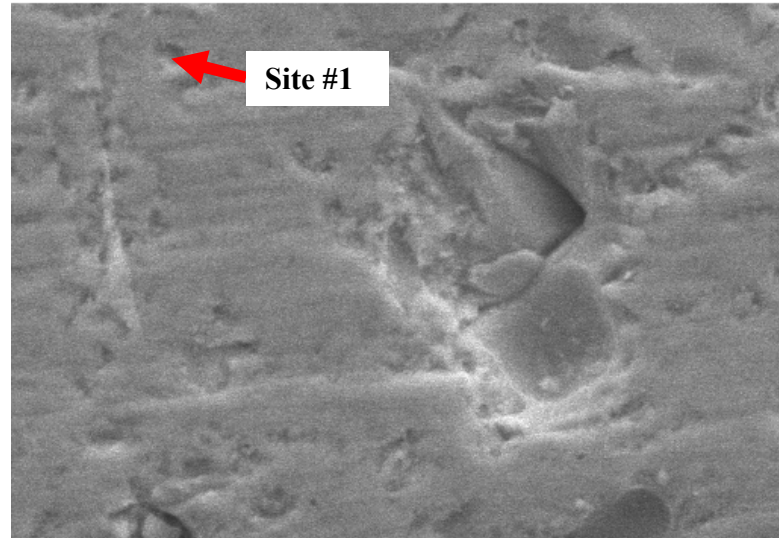
Element	App Conc.	Intensity Corr.	Weight%	Weight% Sigma	Atomic%
O K	17.75	0.4584	36.45	0.50	65.42
Ca K	7.11	1.1225	5.97	0.10	4.27
Ti K	27.70	0.9003	28.98	0.28	17.38
Cu K	26.20	0.8630	28.60	0.34	12.93
Totals			100.00		

Figure 3-32 SEM fractographs and EDS analysis results of $\text{CaCu}_3\text{Ti}_4\text{O}_{12}$ with 10% CuO dopant sintering for 48 hrs at site #1.



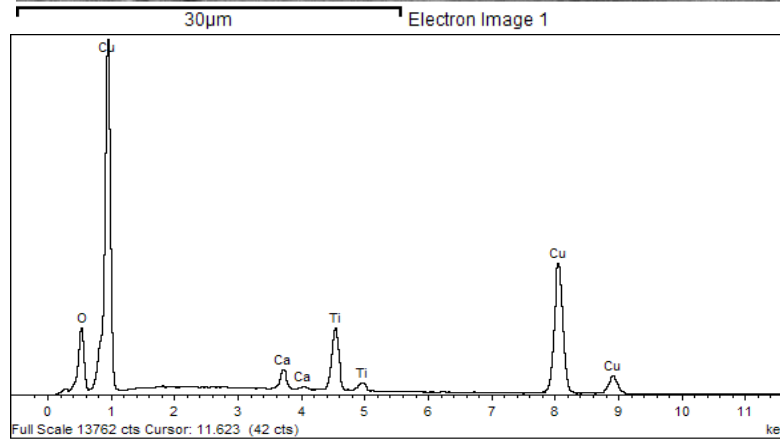
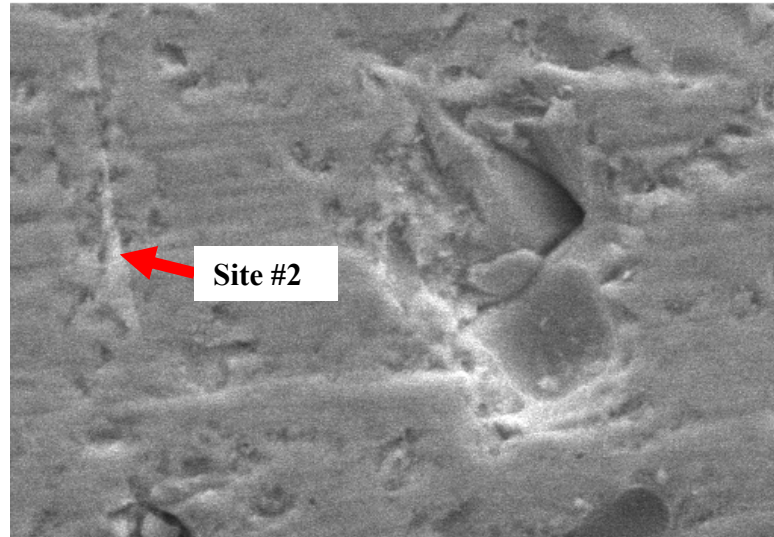
Element	App Conc.	Intensity Corr.	Weight%	Weight% Sigma	Atomic%
O K	1.01	0.4980	5.72	0.49	17.81
Ca K	1.62	1.1413	3.99	0.13	4.97
Ti K	8.61	0.9650	25.03	0.36	26.04
Cu K	22.03	0.9476	65.26	0.51	51.19
Totals			100.00		

Figure 3-33 SEM fractographs and EDS analysis results of $\text{CaCu}_3\text{Ti}_4\text{O}_{12}$ with 10% CuO dopant sintering for 48 hrs at site #2.



Element	App Conc.	Intensity Corn.	Weight%	Weight% Sigma	Atomic%
O K	9.29	0.4042	25.84	0.55	53.50
Ca K	7.07	1.1422	6.96	0.12	5.75
Ti K	27.34	0.9151	33.57	0.33	23.22
Cu K	26.39	0.8819	33.63	0.38	17.53
Totals			100.00		

Figure 3-34 SEM fractographs and EDS analysis results of $\text{CaCu}_3\text{Ti}_4\text{O}_{12}$ with 10% CuO dopant sintering for 72 hrs at site #1.



Element	App Conc.	Intensity Corr.	Weight%	Weight% Sigma	Atomic%
O K	14.65	0.8022	18.56	0.38	46.21
Ca K	2.34	1.0952	2.17	0.07	2.16
Ti K	8.84	0.9506	9.45	0.14	7.86
Cu K	64.09	0.9335	69.82	0.37	43.77
Totals			100.00		

Figure 3-35 SEM fractographs and EDS analysis results of $\text{CaCu}_3\text{Ti}_4\text{O}_{12}$ with 10% CuO dopant sintering for 72 hrs at site #2.

3.3.2.5 Effect of the Annealing Time on Dielectric Properties

Ceramic samples prepared according to procedure #1 in Table 3-1 with sintering 24 hours were treated with post-annealing such as vacuum or argon. Figure 3-36 (a), (b) and (c) show their dielectric spectrum of the $\text{CaCu}_3\text{Ti}_4\text{O}_{12}$ subjected to post-annealing. As annealed in vacuum or argon at 1000 °C, an increase in dielectric constant at 1 kHz from 1,210 to 62,900 in vacuum for 1 to 5 hours and 425,000 to 4,010,000 in argon for 1 to 24 hours were observed as shown in Figure 3-36 (a) and (b). XRD results confirmed that there were no phase changes, and SEM images reveal no differences with its as-sintered ceramics, except a heavy oxidation layer on the sample surfaces in Figure 3-37. Wang and Zhang¹² have reported that the dielectric peak can be eliminated by annealing in oxidizing (O_2) atmosphere and created by annealing in reducing (N_2) atmosphere. This demonstrated that the colossal dielectric constant was closely related with oxygen vacancies which enabled the grains of the $\text{CaCu}_3\text{Ti}_4\text{O}_{12}$ ceramic to be more conductive. The increase in conductivity of the grains would lead to enhanced dielectric constant⁵. Later on, in the following annealing study, it exhibits the similar trend that the dielectric constant at 1 kHz increased with annealing time, which may be associated with oxygen vacancy accumulation. Moreover, it was interesting to observe that with longer annealing time, for example in argon as shown in Figure 3-36 (b), the dielectric constant at 1 kHz initially kept increasing to 4,010,000 and then slowly decreased to 425,000 while annealing up to 24 hours. Similarly, the trend was also observed as the annealing temperature varied from 800 to 1100 °C, and the optimized temperature was found at 1020 °C, as shown in Figure 3-36 (c). Upon annealing, the grain boundaries reoxidized faster than the bulk of the grain, which enhanced the conductivity of the bulk of the grains. Thus, based on the results, it was believed that the dielectric response subjected to post-annealing was related to a dynamic oxidation/reduction process.

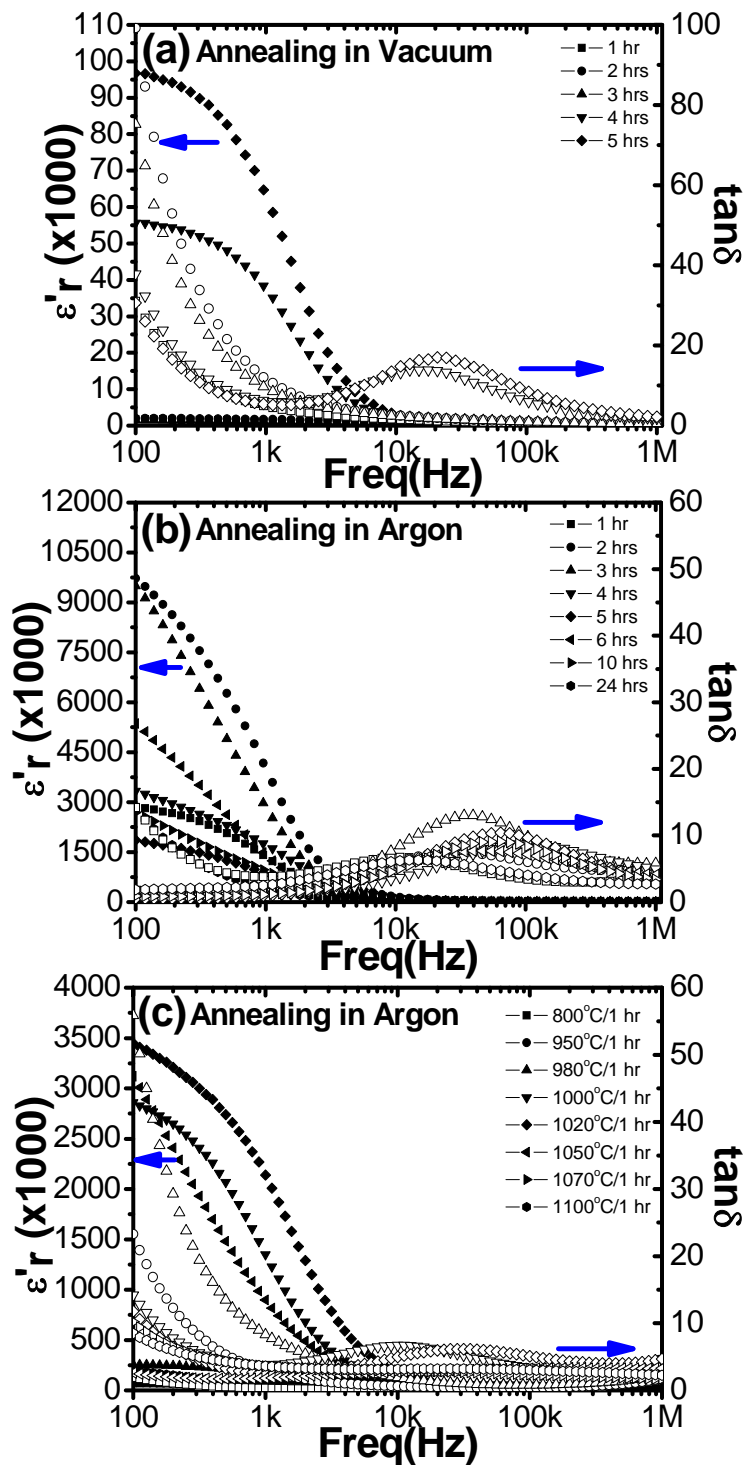


Figure 3-36 Dielectric response vs. frequency for $\text{CaCu}_3\text{Ti}_4\text{O}_{12}$ samples with initial 48 hrs milling according to procedure #1 in table 3-1: (a) post annealing in vacuum for different time at 1000 °C; (b) post annealing in flowing argon for different time at 1000 °C; (c) post annealing in flowing argon at different temperature for 1 hr.

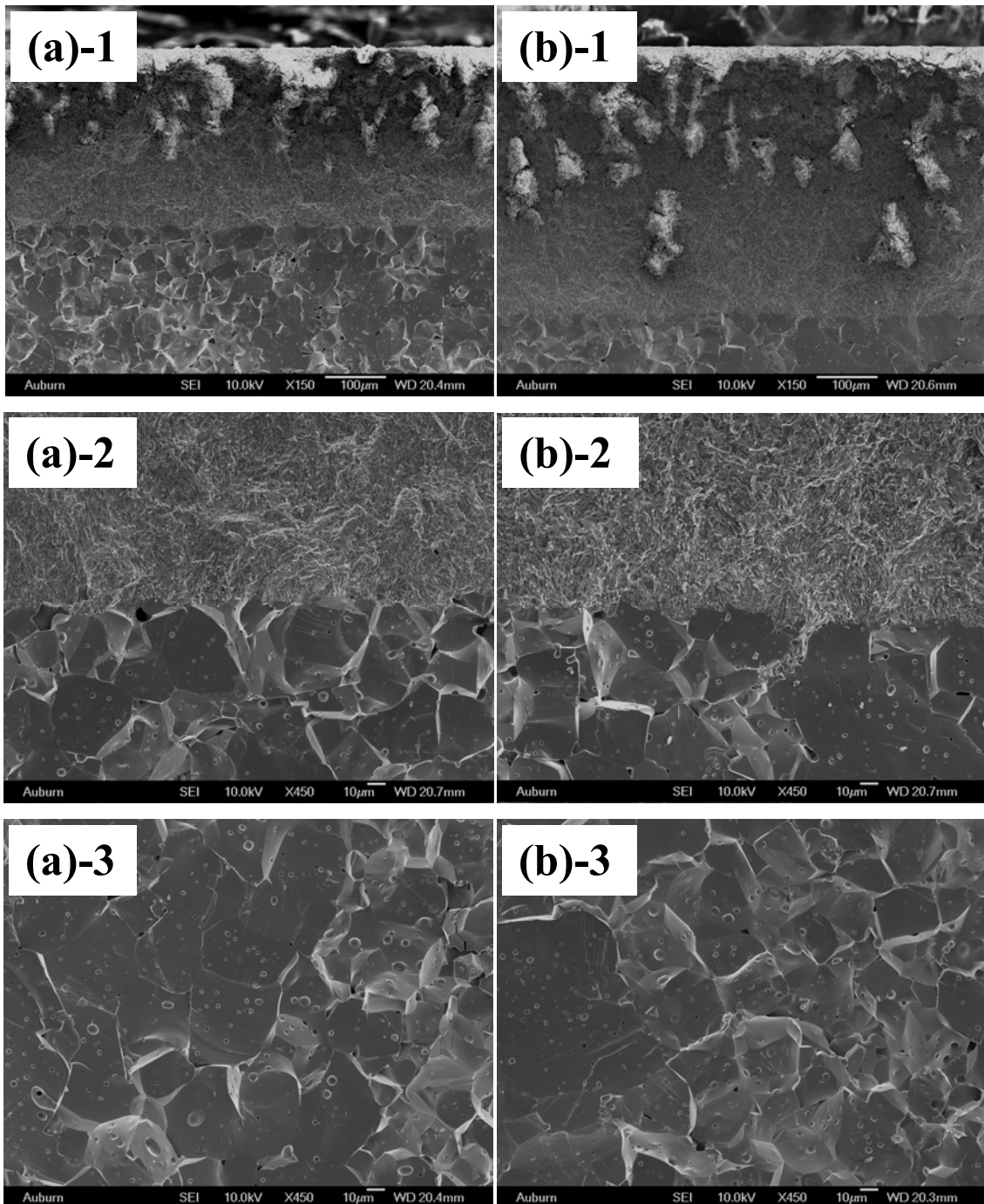


Figure 3-37 SEM fractographs of $\text{CaCu}_3\text{Ti}_4\text{O}_{12}$ with post annealing in flowing argon at 1000°C for 10 hrs with magnification of : (a)-1 X150, (a)-2 X450, (a)-3 X450; for 24 hrs: (b)-1 X150, (b)-2 X450, (b)-3 X450.

3.3.2.6 Impedance Analysis

Corresponding to the results in Figure 3-5 and 3-9, the complex permittivity plots ϵ'_r vs. ϵ''_r are shown in Figure 3-38 and 3-39. Debye equation was applied for dynamic polarization, which only behaved one relaxation time. For the polycrystalline $\text{CaCu}_3\text{Ti}_4\text{O}_{12}$ ceramic, it required for multiple relaxation times, so Debye equations cannot be treated as an effective tool, and it can be fitted by Cole-Cole equations (Equation 3-2) to understand its mechanisms.

In the those figures, there are two obvious half circles, which demonstrate there are two mechanisms dominating the high permittivity in $\text{CaCu}_3\text{Ti}_4\text{O}_{12}$. As known, the first circle in high frequency is due to the grain relaxation, and the second half circle is due to the grain boundary relaxation. The fitting data in Figure 3-38 and 3-39 fit well with the first half circle into the semicircular arc with the center underneath the abscissa. With the increasing ball milling time, such as 48 to 96 hours, and calcining at 1075 °C, the α decreased slowly from 0.055 to 0.028, while the relaxation time τ varied from 0.18 to 0.45 μs . As for calcining at 900 °C, the α changed from 0.02 to 0.01, and the relaxation time τ increased from 0.3 to 0.7 μs . It is interesting to note that the relaxation time increased with milling time and decreased with calcining temperature. The relaxation time tends to become longer, indicating it needs more time for dipole orientation. With increasing milling time and decreased calcining temperature, the energy barrier between the grain and grain boundary becomes smaller, which leads to more grain growth than usual. Comparing the results milling for 48, 72 hours, the complex permittivity plots ϵ'_r vs. ϵ''_r for milling 96 hours become more complicated. It is found that besides the obvious two half circles, there is one more small circle between the two half circles, which demonstrates there exists the third mechanism (III), other than the grain relaxation (I) and grain boundary relaxation (II)¹³.

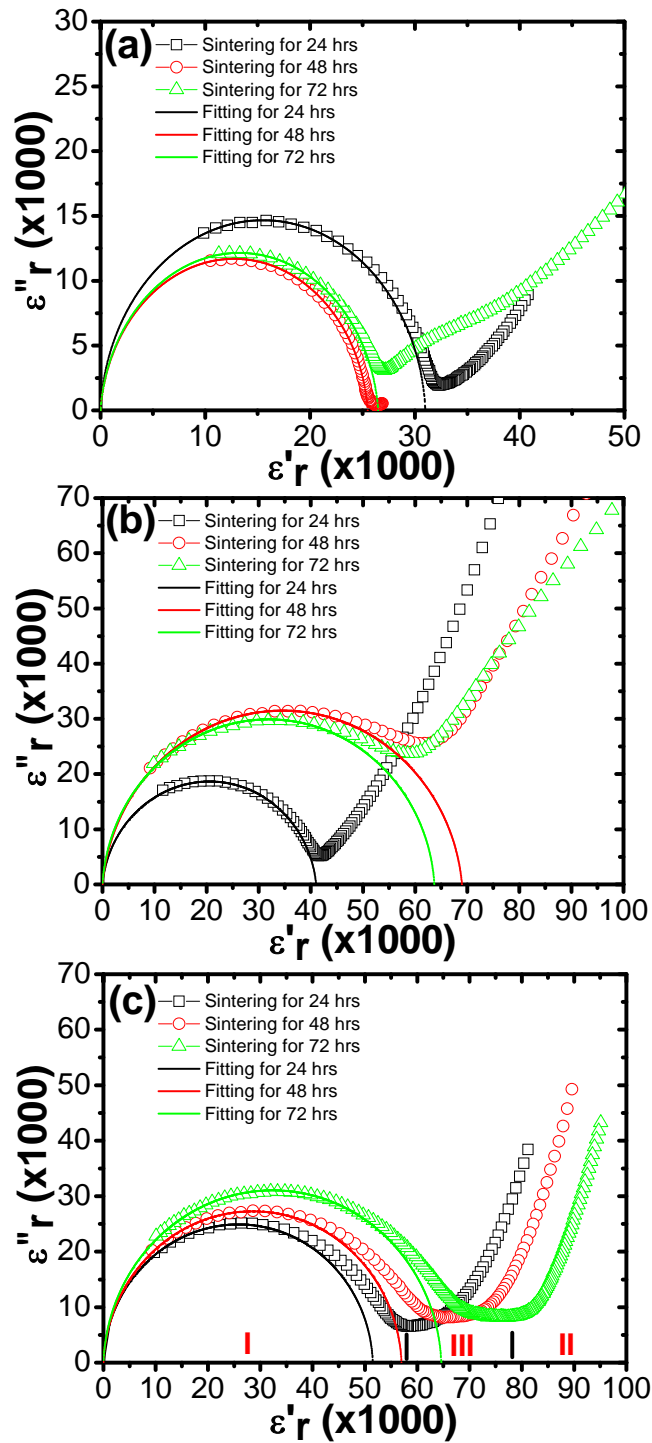


Figure 3-38 Impedance plot of $\text{CaCu}_3\text{Ti}_4\text{O}_{12}$ calcinating at 1075°C and then sintering at 1075°C for 24, 48 and 72 hrs after (a) 48 hrs D.I water ball milling; (b) 72 hrs D.I water ball milling; (c) 96 hrs D.I water ball milling.

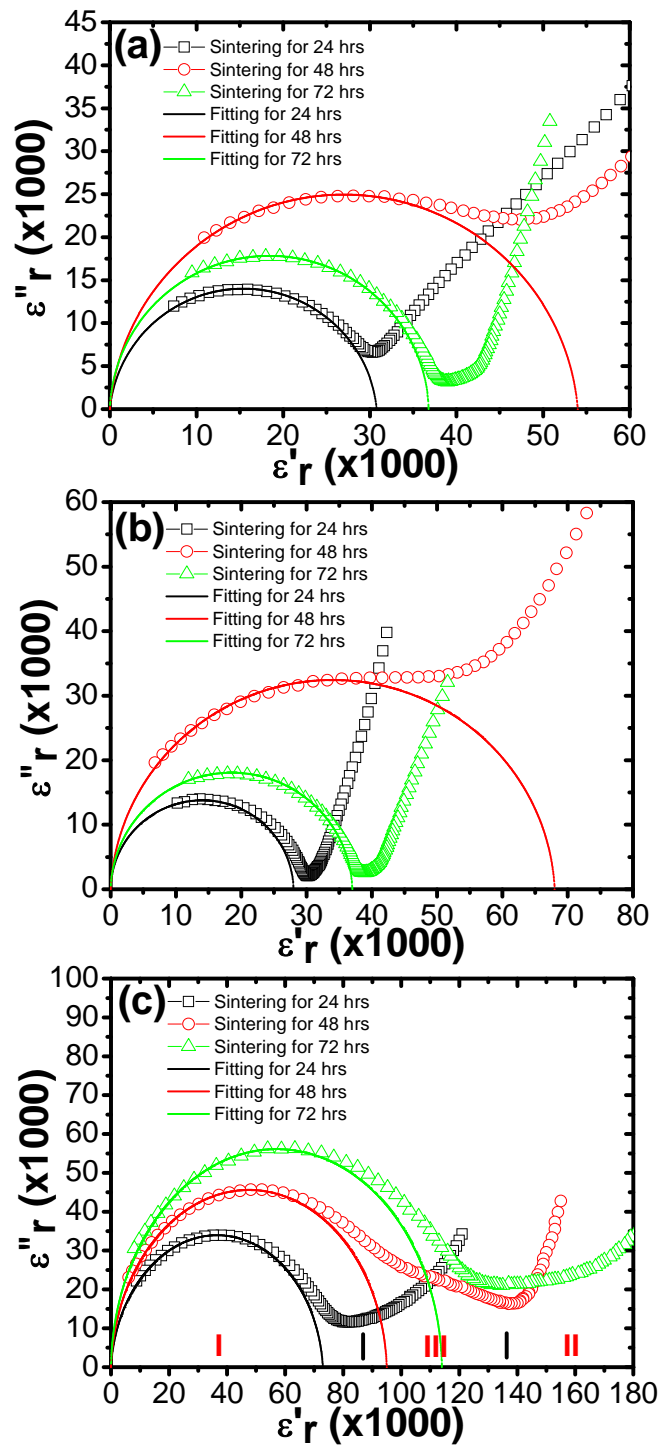


Figure 3-39 Impedance plot of $\text{CaCu}_3\text{Ti}_4\text{O}_{12}$ calcinating at 900°C and then sintering at 1075°C for 24, 48 and 72 hrs after (a) 48 hrs D.I water ball milling; (b) 72 hrs D.I water ball milling; (c) 96 hrs D.I water ball milling.

3.4 Summary

The influence of process parameters such as molding pressure, milling condition, milling media, calcination temperature and sintering time on the dielectric properties of the $\text{CaCu}_3\text{Ti}_4\text{O}_{12}$ ceramic was studied. Ceramic samples with a dielectric constant of 160,000 and loss of 0.15 at 1 kHz were obtained after calcination at 900 °C and sintering at 1075 °C for 72 hours, which is then adopted for the 0-3 composite study described in Chapter 4 and 5. The structure and morphology of the ceramics were studied using XRD and SEM. Their dielectric responses were studied over a frequency range from 100 to 1 MHz. It was found that the dielectric response of the ceramic is determined by three different processes. The pores structure observed in ceramic may be responsible for the observed high dielectric constant. When the ceramic disks were polished down to different thicknesses, it was found that although the dielectric response at low frequency is strongly dependent on the thickness, the high frequency relaxation process is weakly dependent on the thickness, and this thickness dependence cannot be explained using surface relaxation model. It was interesting to note that the relaxation time was increasing with decreasing thickness, which may be associated with the fact that the more dipoles, the longer relaxation time.

References

- (1) Arbatti, M. Development of High-Dielectric-Constant Polymer-Ceramic Composites Based on Calcium Copper Titanate. Auburn University, Alabama, 2004.
- (2) Subramanian, M. A.; Li, D.; Duan, N.; B. A. Reisner; Sleight, A. W. *J Solid State Chem* **2000**, 151, 323-325.
- (3) Almeida, A. F. L.; Fechine, P. B. A.; Graca, M. P. F.; Valente, M. A.; Sombra, A. S. B. *J Mater Sci: Mater Electron* **2008**, 8, 9675.
- (4) Joint committee on Powder Diffraction Standard (JCPDS). In International Centre for Diffraction Data, (JCPDS File 75-2188): 1979.
- (5) Raevskia, I. P.; Prosandeev, S. A.; Bogatin, A. S.; Malitskaya, M. A.; Jastrabik, L. *J.Appl. Phys* **2003**, 93, (7), 4130-4136.
- (6) Cohen, M. H.; Neaton, J. B.; Lixin He; Vanderbilt, D. *J.Appl.Phys* **2003**, 94, 3299-3306.
- (7) Liu, J.; Duan, C.-G.; Yin, W.-G.; Mei, W. N.; Smith, R. W.; Hardy, J. R. *Phys.Rev.B* **2004**, 70, 144106.
- (8) Fang, T.-T.; Shiau, H.-K. *J. Am. Ceram. Soc* **2004**, 87, (11), 2072-2079.
- (9) Wu, L.; Y. Zhu; S. Park; S. Shapiro; Shirane, G. *Phys.Rev.B* **2005**, 71, 014118.
- (10) Capsoni, D.; Bini, M.; V.Massarotti; G.Chiodelli; M.C.Mozzatic; Azzoni, C. B. *J Solid State Chem* **2004**, 177, 4494-4500.
- (11) Marchin, L.; Guillemet-Fritsch, S.; Durand, B.; Levchenko, A. A.; Navrotsky, A.; Lebey, T. *J. Am. Ceram. Soc* **2008**, 91, 485 - 489.
- (12) Wang, C. C.; Zhang, L. W. *Phys.Rev.B* **2006**, 74, 024106.
- (13) Cheng, Z. Y.; Bharti, V.; Xu, H. S.; Wang, S.; Zhang, Q. M. *J.Appl. Phys* **1999**, 86, (4), 2208-2214.

CHAPTER 4

PROCESS INFLUENCE ON THE DIELECTRIC PROPERTIES OF $\text{CaCu}_3\text{Ti}_4\text{O}_{12}/\text{P}(\text{VDF-TrFE})$ COMPOSITES

4.1 Introduction

In this chapter, a 0-3 composite based on $\text{CaCu}_3\text{Ti}_4\text{O}_{12}$ ceramic was studied^{1, 2}. Processing influence on the dielectric properties in the $\text{CaCu}_3\text{Ti}_4\text{O}_{12} / \text{P}(\text{VDF-TrFE})$ composites was studied. To improve the uniformity of the composite, the processing effects, such as hot pressing pattern, number of pressing layers, and hot pressing time, were investigated. The dielectric constant exhibited a complicated law with $\text{CaCu}_3\text{Ti}_4\text{O}_{12}$ powder concentration, number of layers and time. Based on SEM images, the experimental results can be better understood with different effective dielectric constant fitting models. Moreover, The effect of polymer matrix is compared between two different polymer matrices systems: $\text{P}(\text{VDF-TrFE})$ and $\text{P}(\text{VDF-CTFE})$ 88/12 (VC88). Due to its relative high dielectric constant and less temperature dependence in $\text{CaCu}_3\text{Ti}_4\text{O}_{12}/\text{VC88}$ composite, this composite is very suitable for future smart material application.

4.2 Experimental

According to the procedure in Chapter 3, $\text{CaCu}_3\text{Ti}_4\text{O}_{12}$ ceramic with high dielectric constant was successfully fabricated after 96 hours milling, calcining at 900 °C and then sintering at 1075 °C for 72 hours. These ceramics exhibited a high dielectric constant ($\approx 160,000$) with weak temperature dependence below 1 MHz. The ceramic pellets were milled to particles with $D_{50} \approx 10.5 \mu\text{m}$ (particle size percentage). Due to $\text{P}(\text{VDF-TrFE})$ exhibiting high dielectric strength and relative high dielectric constant (≈ 14 at RT), it was selected as the polymer matrix in this work.

The $\text{CaCu}_3\text{Ti}_4\text{O}_{12}$ -P(VDF-TrFE) 0-3 composite was prepared by solution casting method at 70 °C/8 hours. In order to achieve high uniformity in 0-3 composite, hot pressing technique and annealing processing were adopted. The composite samples were hot pressed at a force of 7.5 tons and temperature of 200 °C. The final as-casted film consisted of two layers: polymer rich layer and ceramic rich layer. Then two different hot pressing patterns were studied³: 1) PC hot pressing: Polymer rich layer in one film stacking with the ceramic rich layer in another film; 2) CC hot pressing: Ceramic rich layer in one film stacking with the ceramic rich layer in another film. In order to study the polymer matrix effect, P(VDF-CTFE) 88/12 mol% (VC88) copolymer was selected as alternative polymer matrix in comparison to its counterpart P(VDF-TrFE) 55/45 mol%.

Dielectric properties: Gold was coated on the surface of the pellets as electrodes using a Pelco SC-6 sputter coater. Agilent 4294A impedance analyzer was employed to characterize the dielectric property of the samples. The measured frequency range was from 100 Hz to 1 MHz.

Microstructure analysis: The grain size and uniformity of the ceramic were determined by scanning electron microscope with EDS (SEM JSM-7000F, JEOL).

4.3 Results and Discussion

4.3.1 Dielectric Behavior and Annealing Effect

The annealing effect study was performed on $\text{CaCu}_3\text{Ti}_4\text{O}_{12}$ /P(VDF-TrFE) composites after they were casted at 70 °C for 8 hours. The annealing temperature was fixed at 125 °C and the $\text{CaCu}_3\text{Ti}_4\text{O}_{12}$ volume concentration in 0-3 composites varied from 10 to 50. The dielectric results from the pure P(VDF-TrFE) film are shown in Figure 4-1. As comparing with those one layer pure polymer films and as-casted composite samples, their annealing results are shown in Figure 4-2 to 4-6.

Figure 4-1 plots the dielectric responses versus the frequency after casting and annealing respectively. It is well known that the thermal annealing processing will result in a high crystallinity, which corresponds to higher dielectric response^{4, 5, 6}. Figures 4-2 to 4-6 plot the data between non-annealing samples and annealing samples with different $\text{CaCu}_3\text{Ti}_4\text{O}_{12}$ concentrations, 10, 20, 30, 40, and 50 vol% respectively to present this general trend for the annealing effect. As we can observe from Figure 4-2 to 4-6, almost all the annealing samples possessed relative high dielectric constant in comparison with

un-annealed samples. More specifically: 18 to 25 for 10 vol% $\text{CaCu}_3\text{Ti}_4\text{O}_{12}$ composite, 23 to 34 for 20 vol% $\text{CaCu}_3\text{Ti}_4\text{O}_{12}$ composite, 32 to 43 for 30 vol% $\text{CaCu}_3\text{Ti}_4\text{O}_{12}$ composite, 65 to 105 for 40 vol% $\text{CaCu}_3\text{Ti}_4\text{O}_{12}$ composite, and 67 to 69 for 50 vol% $\text{CaCu}_3\text{Ti}_4\text{O}_{12}$ composite. Those results are shown in Table 4-1 and Figure 4-7. Based on the results in Figure 4-7, the dielectric constant of non-annealing increased from 18 to 67. While it is interesting to find that the dielectric constant of annealing sample exhibited similar trend at low $\text{CaCu}_3\text{Ti}_4\text{O}_{12}$ concentration, it reached a maximum value of 105 at 40 vol% and was followed by a decrease to 69 at 50 vol%. By assuming that the annealing process does not change the morphology of the composite, this behavior may stem from the fact that annealing can improve the crystallinity of the polymer and also the overall density of the composite by evaporating the remaining solvent. However, another possible explanation for the increase in dielectric constant may stem from the knowledge that the annealing process enhances the interlinking between ceramic and polymer matrix and caused the crystallinity improvement, which also consequently enhanced the interfacial layer effect.

The major relaxation process of the composites was analyzed and it was found that the dielectric results in Figure 4-1 to 4-7 can be fitted well using the Cole-Cole equation:

$$\varepsilon^* = \varepsilon_{r\infty} + \frac{\varepsilon_{rs} - \varepsilon_{r\infty}}{1 + (j\omega\tau_0)^{1-\alpha}} \quad (4-1)$$

Where ε_{rs} is the static permittivity at low frequency limit, $\varepsilon_{r\infty}$ is the permittivity at high frequency limit, τ_0 is the characteristic relaxation time, α varies from $0 < \alpha < 1$. The detail fitting results are shown in Figure 4-8. From the view of relaxation time, annealed samples tend to have longer relaxation time than their counterparts without annealing. As the concentration varied from 10 to 50 vol%, the relaxation time τ started from $0.159\mu\text{s}$ and then reached to a maximum value of $0.230\mu\text{s}$ at 40 vol% in non-annealed samples. Correspondingly, in the annealed sample, the maximum value changed to $0.373\mu\text{s}$ at 40 vol% as shown in Figure 4-9. As it is known that for one layer composite, the structure was not so uniform, which generally presented separating layers between ceramic and polymer. Thus, it indicated that for a heterogeneous structure with series layers separation, better dielectric response occurs while longer relaxation time dominates.

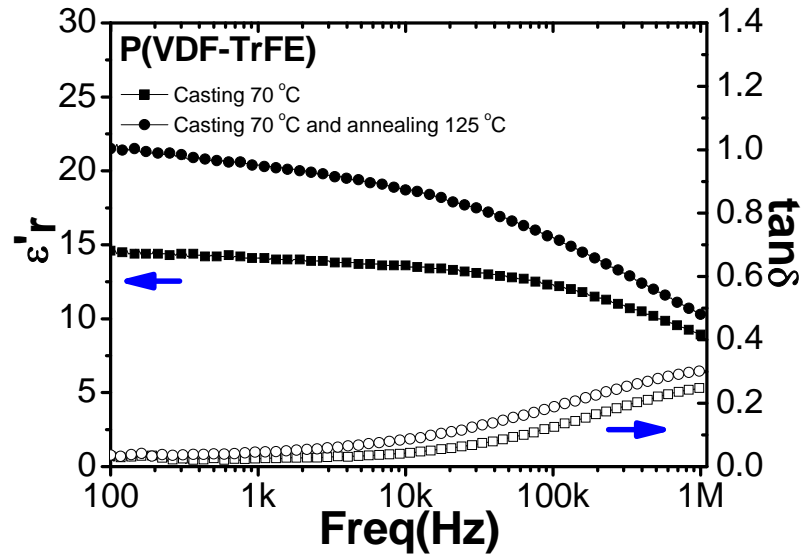


Figure 4-1 Dielectric response vs. frequency of pure P(VDF-TrFE) film: (a) casting at 70 °C/8 hrs; (b) casting at 70 °C/8 hrs and annealing at 125 °C/8 hrs.

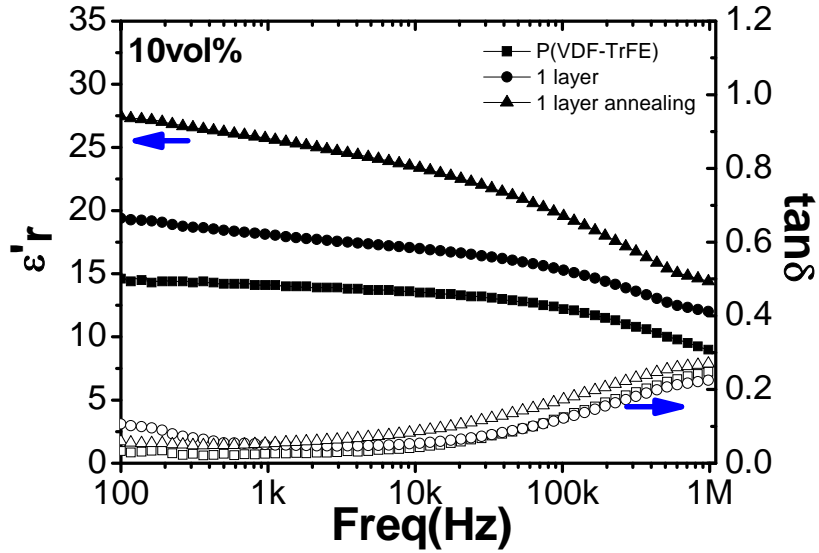


Figure 4-2 Dielectric response vs. frequency of 1 layer $\text{CaCu}_3\text{Ti}_4\text{O}_{12}$ /P(VDF-TrFE) composite (10 vol% CCTO) without annealing, with annealing in comparison with P(VDF-TrFE).

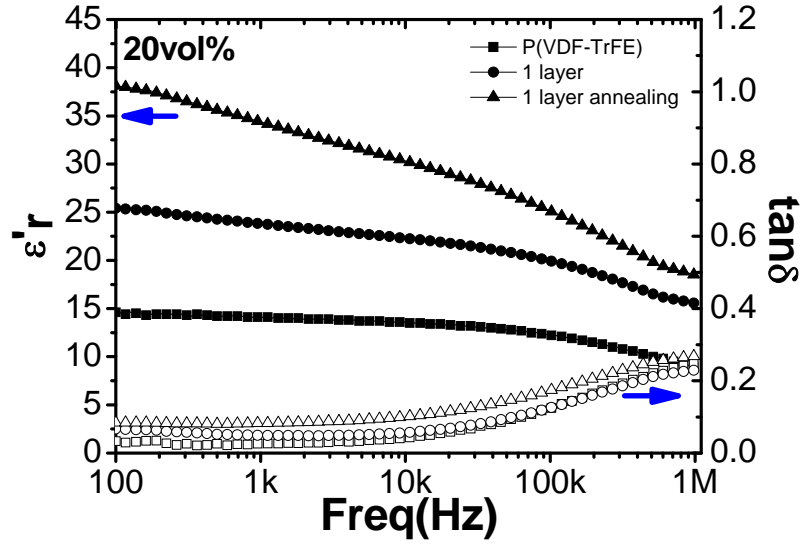


Figure 4-3 Dielectric response vs. frequency of 1 layer $\text{CaCu}_3\text{Ti}_4\text{O}_{12}/\text{P}(\text{VDF-TrFE})$ composite (20 vol% CCTO) without annealing, with annealing in comparison with P(VDF-TrFE).

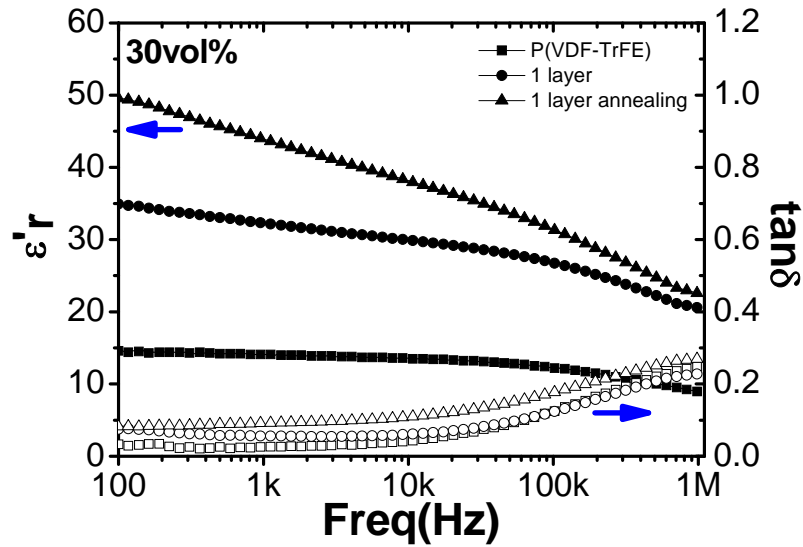


Figure 4-4 Dielectric response vs. frequency of 1 layer $\text{CaCu}_3\text{Ti}_4\text{O}_{12}/\text{P}(\text{VDF-TrFE})$ composite (30 vol% CCTO) without annealing, with annealing in comparison with P(VDF-TrFE).

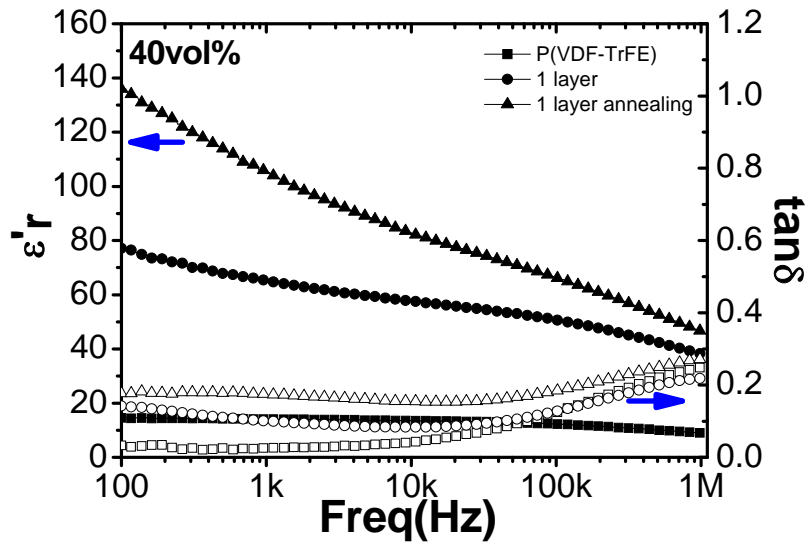


Figure 4-5 Dielectric response vs. frequency of 1 layer CaCu₃Ti₄O₁₂/P(VDF-TrFE) composite (40 vol% CaCu₃Ti₄O₁₂) without annealing, with annealing in comparison with P(VDF-TrFE).

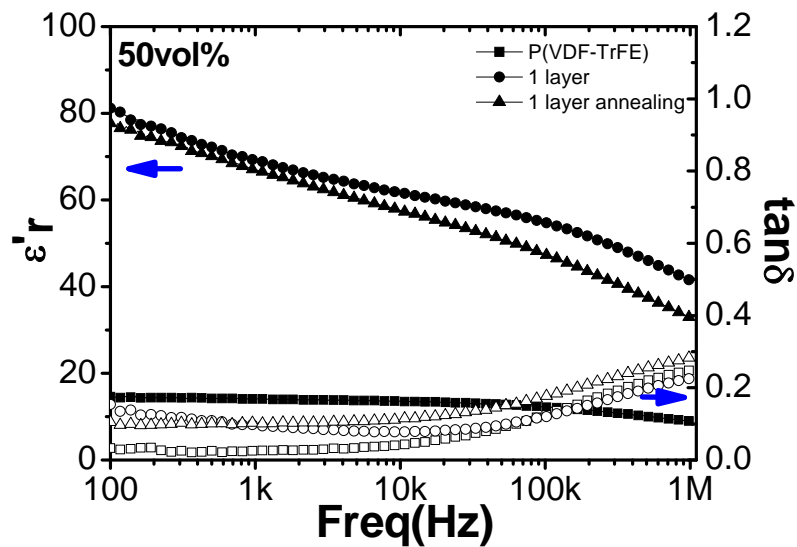


Figure 4-6 Dielectric response vs. frequency of 1 layer CaCu₃Ti₄O₁₂/P(VDF-TrFE) composite (50 vol% CaCu₃Ti₄O₁₂) without annealing, with annealing in comparison with P(VDF-TrFE).

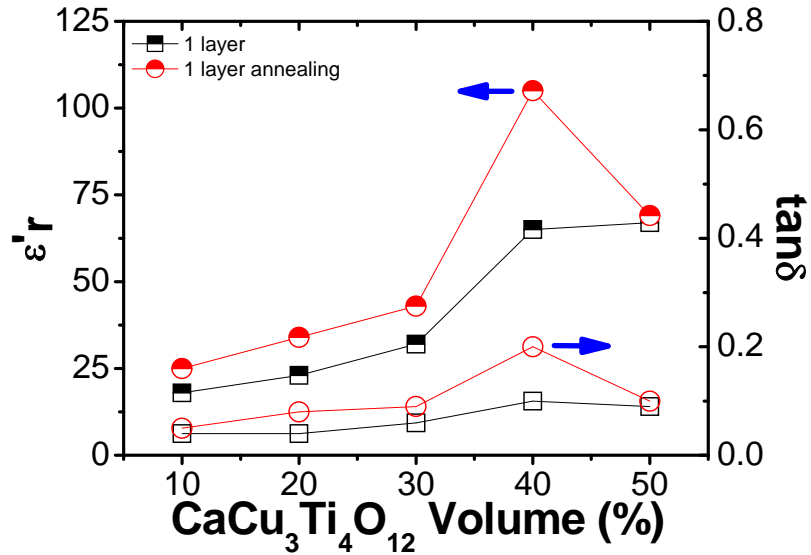


Figure 4-7 Dependence of dielectric response (1 kHz) on the $\text{CaCu}_3\text{Ti}_4\text{O}_{12}$ concentration for 1 layer $\text{CaCu}_3\text{Ti}_4\text{O}_{12}/\text{P}(\text{VDF-TrFE})$ composite at room temperature without annealing and with annealing respectively.

Table 4-1 Summary of dielectric data for 1 layer $\text{CaCu}_3\text{Ti}_4\text{O}_{12}/\text{P}(\text{VDF-TrFE})$ composite (μ -size $\text{CaCu}_3\text{Ti}_4\text{O}_{12}$) (1 kHz).

	$\text{CaCu}_3\text{Ti}_4\text{O}_{12}$ Concentration (vol%)				
	10 vol%	20 vol%	30 vol%	40 vol%	50 vol%
1 layer ^[1]	18/0.04	23/0.04	32/0.06	65/0.1	67/0.09
1 layer annealing ^[2]	25/0.05	34/0.08	43/0.09	105/0.2	69/0.1

^[1]: Casting at 70 °C/8 hrs.

^[2]: Casting at 70 °C/8 hrs and annealing at 125 °C/8 hrs.

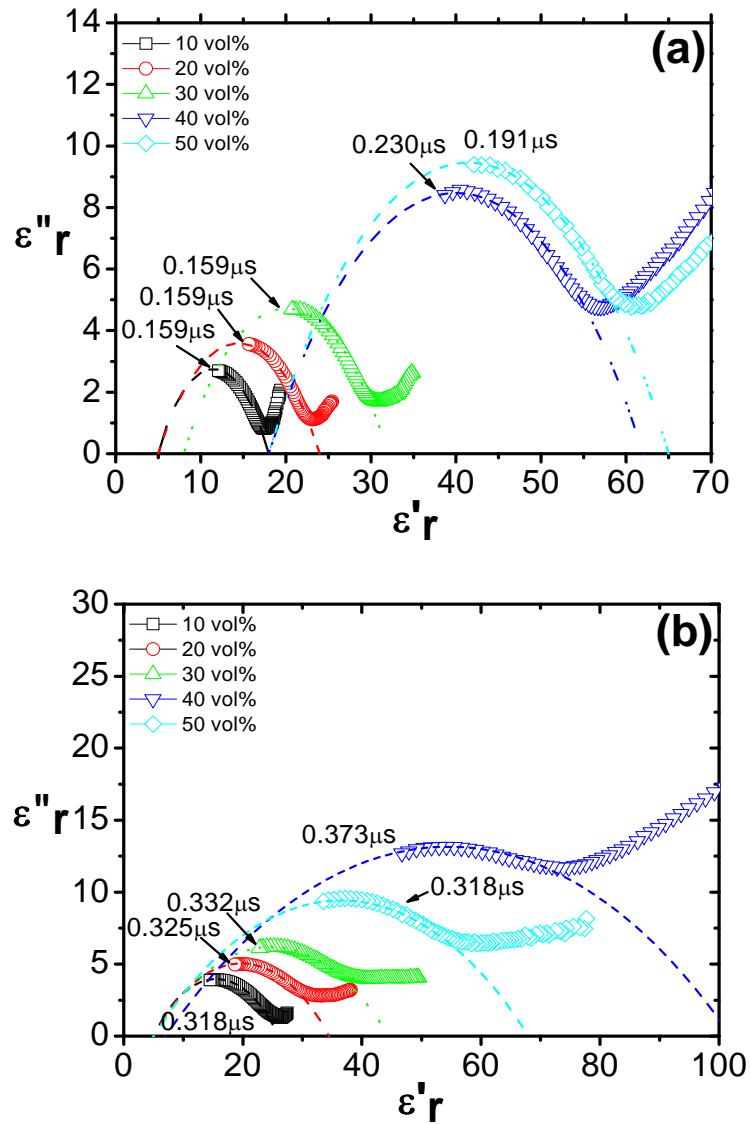


Figure 4-8 Cole-cole plot of the dielectric data of (a) 1 layer and (b) 1 annealed layer $\text{CaCu}_3\text{Ti}_4\text{O}_{12}/\text{P}(\text{VDF-TrFE})$ composite with 10 to 50 vol% $\text{CaCu}_3\text{Ti}_4\text{O}_{12}$ powder at RT.

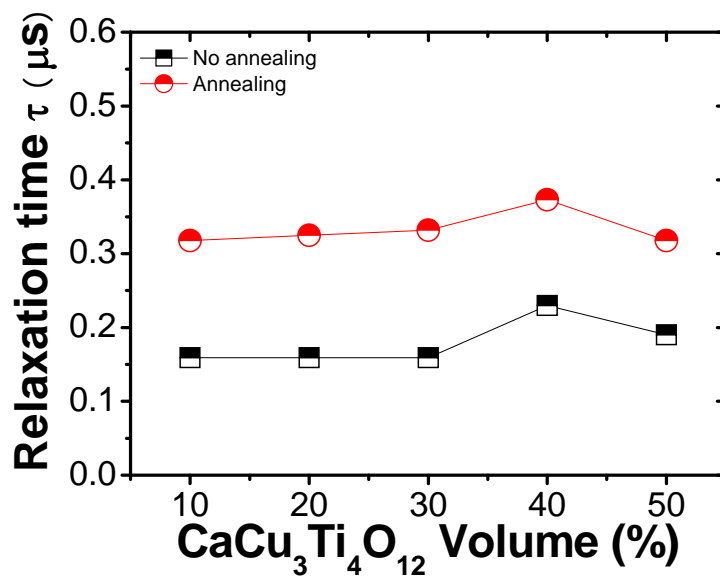


Figure 4-9 The relationship of relaxation time and $\text{CaCu}_3\text{Ti}_4\text{O}_{12}$ volume concentration between 1 layer and 1 annealed layer $\text{CaCu}_3\text{Ti}_4\text{O}_{12}$ /P(VDF-TrFE) composite samples with 10 to 50 vol% $\text{CaCu}_3\text{Ti}_4\text{O}_{12}$ powder.

4.3.2 Hot Pressing Effect

The hot pressing processing (HP) was carried out with 7.5 tons force and a temperature at 200 °C for different times, such as 10s in this study. Figure 4-10 to 4-15 show the dielectric results with hot pressing (HP), and the $\text{CaCu}_3\text{Ti}_4\text{O}_{12}$ volume concentration in 0-3 composites varies from 10 to 60. Table 4-2 summarizes all results regarding annealing and HP processing.

The dielectric properties of the composites were significantly influenced by HP process, as illustrated in Figure 4-10 to 4-15. It was found that no matter whether composites were annealed or not, the dielectric results generally exhibited an increasing trend after HP. When the $\text{CaCu}_3\text{Ti}_4\text{O}_{12}$ volume concentration varied from 10 to 50, the dielectric constant revealed similar tendencies as those in the non-treatment sample; however, it exhibited even higher dielectric constant and experienced a maximum value of 78 at 40 vol%. While for the samples treated with annealing, the dielectric results were even promising with HP. A dielectric constant of 148 and dielectric loss of 0.2 at 1 kHz were achieved. That is, HP results in a higher dielectric constant, as summarized in Table 4-2. Moreover, it was also interestingly noted that they tended to exhibit small dielectric loss at low frequency range with HP as for 10, 20 and 30 vol% composite. As stated before, the increasing of dielectric constant with annealing process is due to the crystallinity improvement, however this did not optimize their microstructure and the as-casted composite still consisted of polymer-rich layer and ceramic-rich layer. With HP processing, it enables the diffusion of ceramic particle into polymer and leads to more uniform structure. Thus, an improved dielectric response originated from a more homogenous structure between ceramic particle and polymer matrix.

Their dielectric responses were further analyzed with Cole-Cole equation, as shown in Figure 4-16. Based on the results in Figure 4-18, the relaxation time τ first decreased from 0.332 μs to 0.283 μs , and then increased to 0.310 μs . It is evident that the relaxation time τ experienced a minimum value of 0.283 μs at 40 vol%, which corresponds to the maximum dielectric constant in Figure 4-16. HP process is prone to alter the morphology of composite, which tries to minimize the series polymer and ceramic separation and can result in a more homogenous structure. In this case, different

from those none-HP-treated results, as shown in Figure 4-8 to 4-9, improved dielectric response occurs while there is fast relaxation time in HP process.

Figure 4-17 to 4-18 present a comparison between the model prediction and experimental data for the effective dielectric constant of $\text{CaCu}_3\text{Ti}_4\text{O}_{12}/\text{P}(\text{VDF-TrFE})$ composite after HP processing. Also shown are the predictions based on: logarithmic mixing (LM) law, modified logarithmic mixing (MLM) law, Maxwell-Wagner (MW) model, Yamada (YA) model, series model and Bruggeman (BM) model. Based on the previous experimental results in Figures 4-1, the values of $\varepsilon'_{r-\text{polymerc}}$ were predetermined as 20 and 14 respectively prior to the fitting, depending on whether the composite annealed or not. The summary of fitted dielectric data from prediction models is shown in Table 4-3. Based on the fitting results in Figure 4-17, 4-18 and Table 4-3, it was found that the LM, MLM, YA and BM models achieved better matches to experimental data than MW and series models from 0 to 50 vol%, even though MW model exhibited very good fitting results in low volume concentration range. This is believed to be related with the limitation of the model equation itself, because they are only good for composite with small effective dielectric constants; for example, 59 at 50 vol% for MW model and 39 at 50 vol% for series model. These fitted experimental results in Table 4-3 also proven the annealing effect since all annealed results are larger than these without annealing.

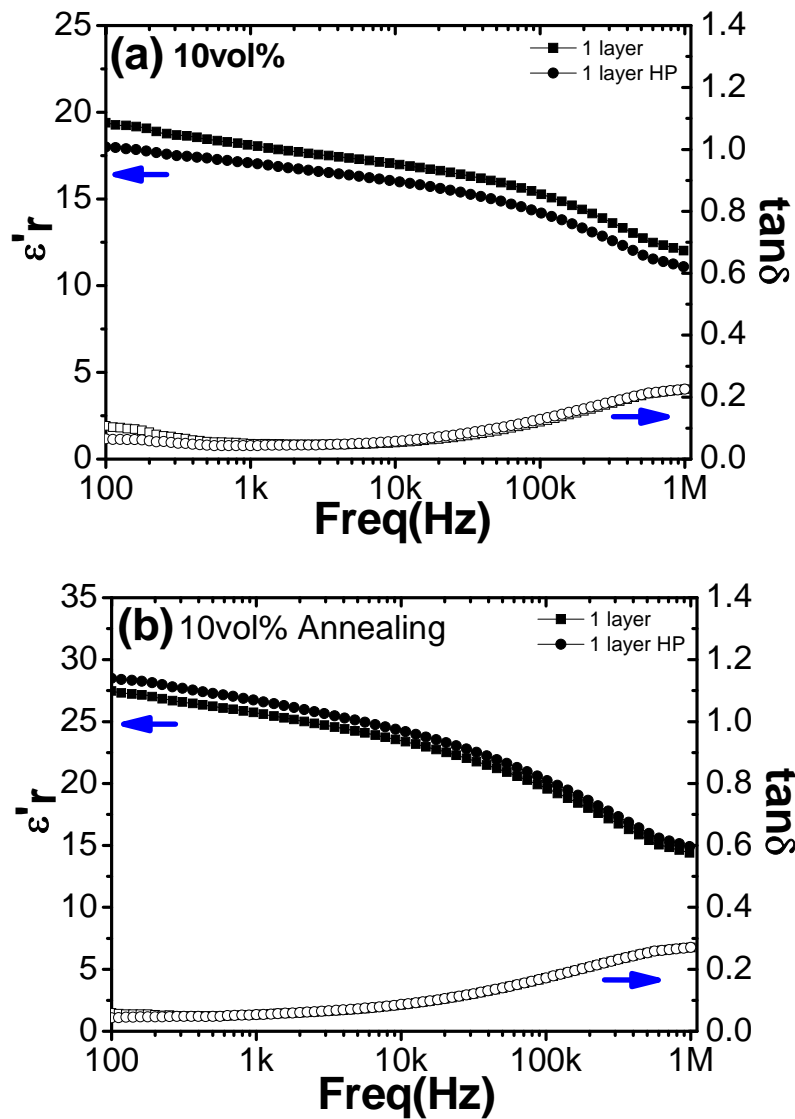


Figure 4-10 Dielectric response vs. frequency of 1 layer $\text{CaCu}_3\text{Ti}_4\text{O}_{12}/\text{P}(\text{VDF-TrFE})$ composite with 10 vol% $\text{CaCu}_3\text{Ti}_4\text{O}_{12}$ powder: (a) without annealing; (b) with annealing.

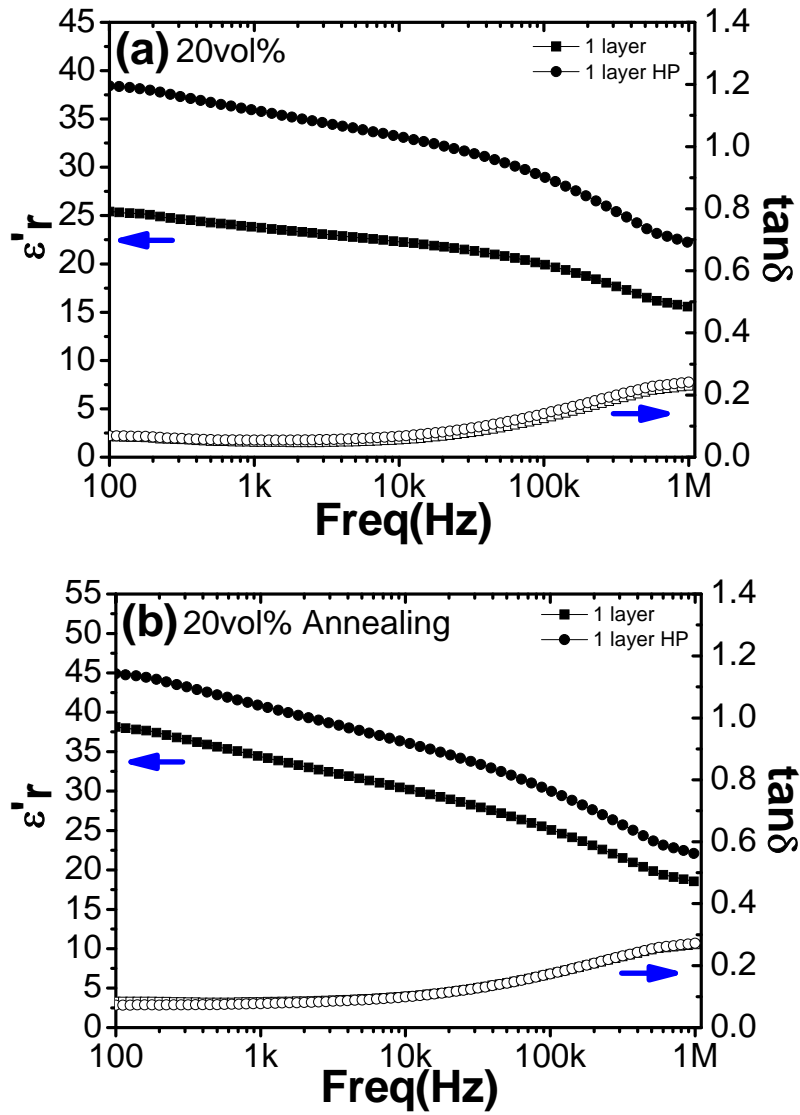


Figure 4-11 Dielectric response vs. frequency of 1 layer $\text{CaCu}_3\text{Ti}_4\text{O}_{12}/\text{P}(\text{VDF-TrFE})$ composite with 20 vol% $\text{CaCu}_3\text{Ti}_4\text{O}_{12}$ powder: (a) without annealing; (b) with annealing.

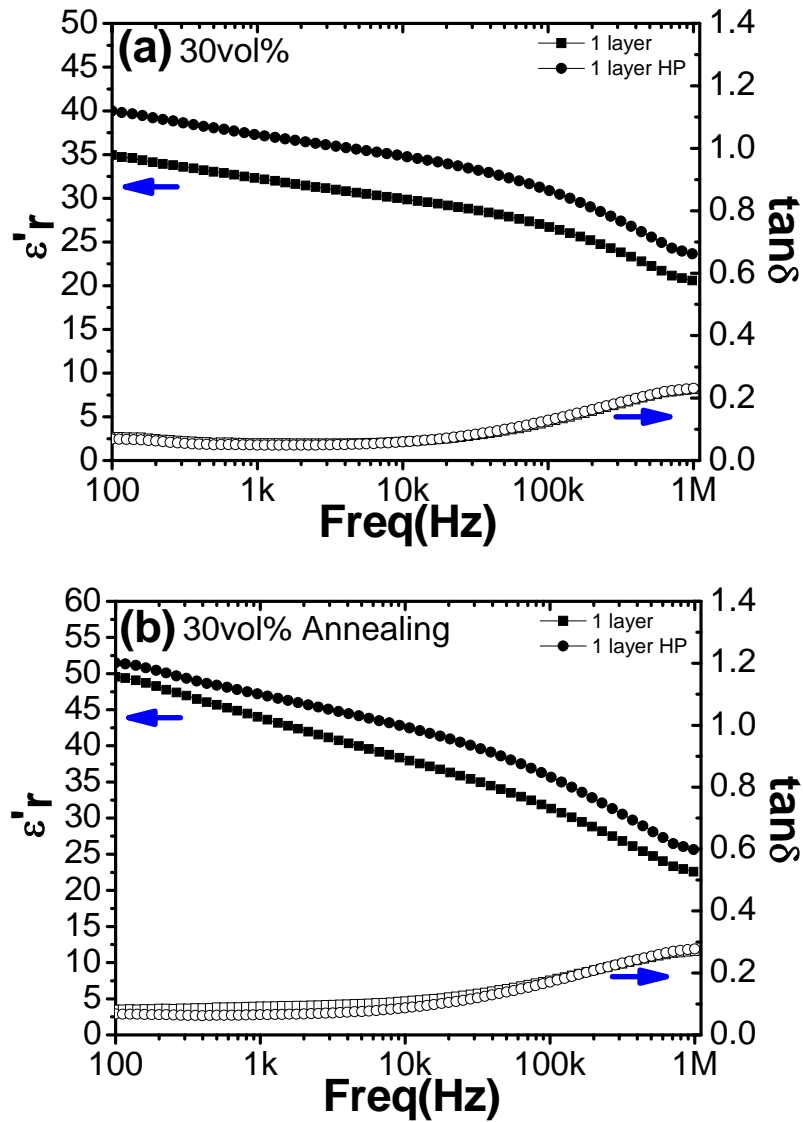


Figure 4-12 Dielectric response vs. frequency of 1 layer $\text{CaCu}_3\text{Ti}_4\text{O}_{12}/\text{P}(\text{VDF-TrFE})$ composite with 30 vol% $\text{CaCu}_3\text{Ti}_4\text{O}_{12}$ powder: (a) without annealing; (b) with annealing.

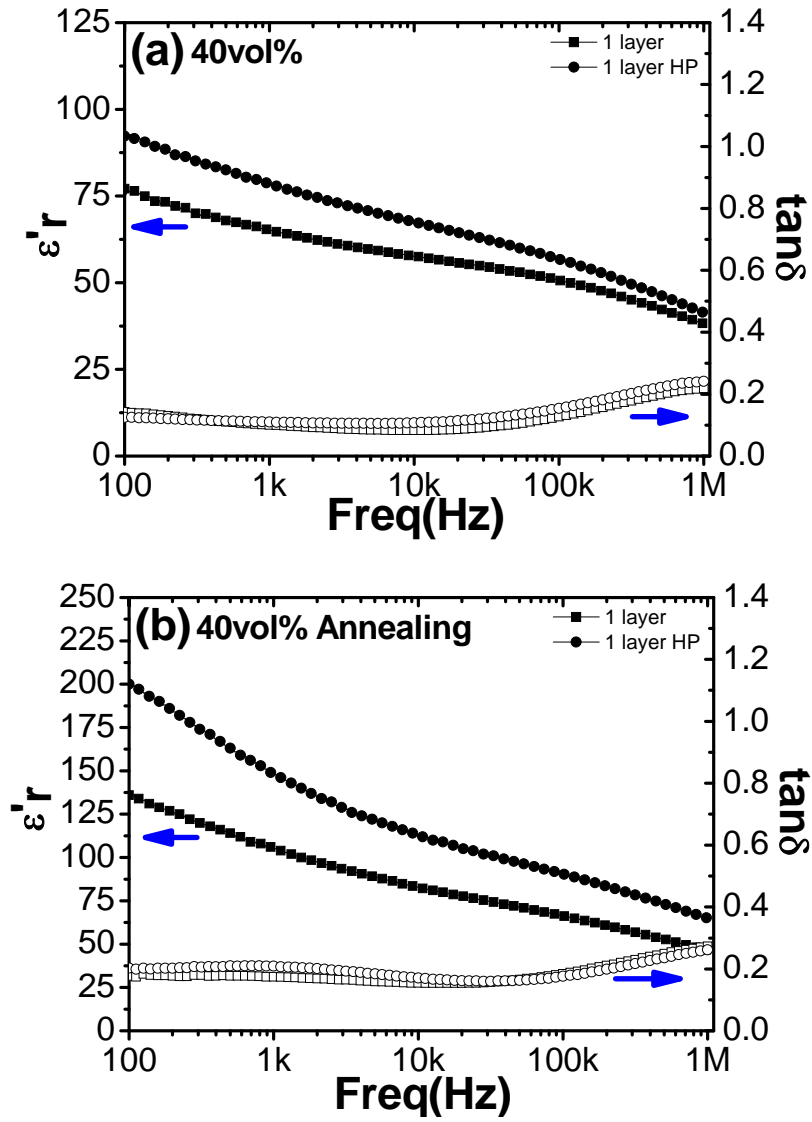


Figure 4-13 Dielectric response vs. frequency of 1 layer $\text{CaCu}_3\text{Ti}_4\text{O}_{12}/\text{P}(\text{VDF}-\text{TrFE})$ composite with 40 vol% $\text{CaCu}_3\text{Ti}_4\text{O}_{12}$ powder: (a) without annealing; (b) with annealing.

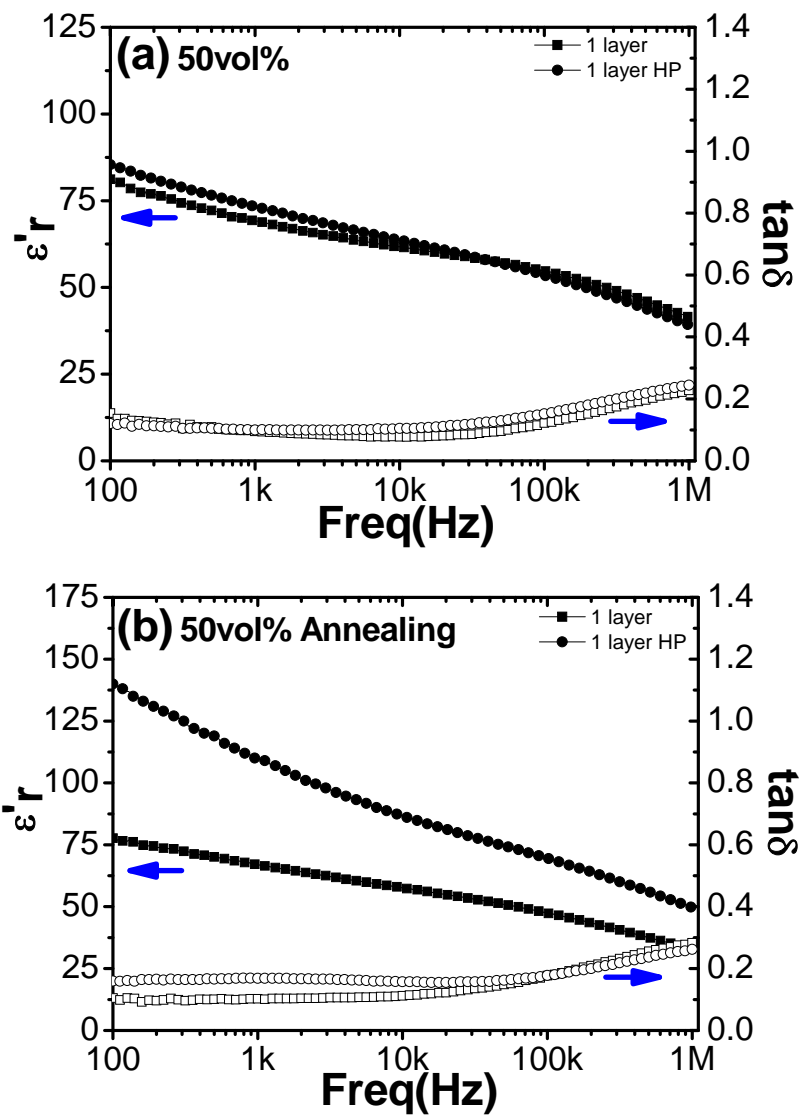


Figure 4-14 Dielectric response vs. frequency of 1 layer $\text{CaCu}_3\text{Ti}_4\text{O}_{12}/\text{P}(\text{VDF-TrFE})$ composite with 50 vol% $\text{CaCu}_3\text{Ti}_4\text{O}_{12}$ powder: (a) without annealing; (b) with annealing.

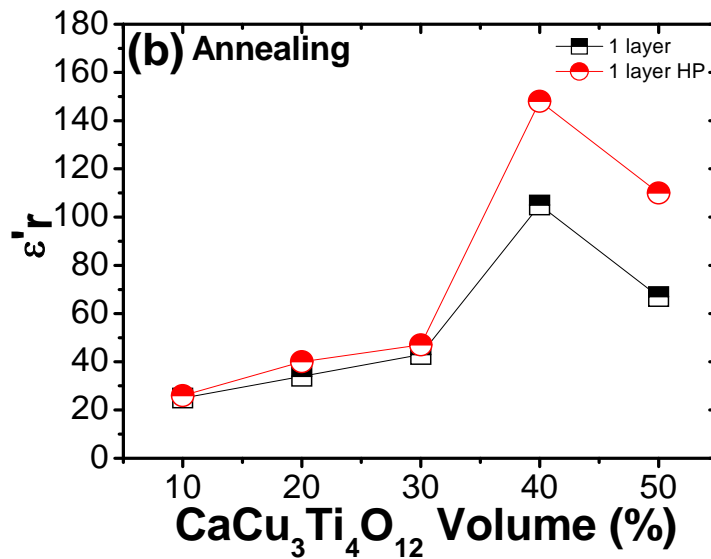
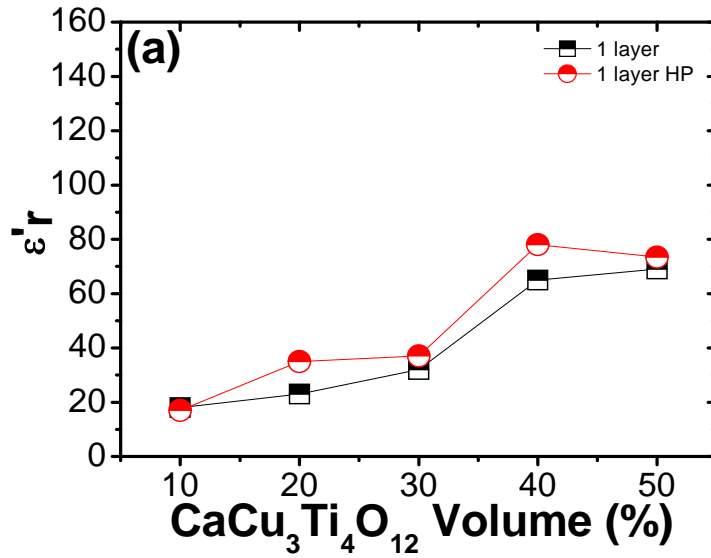


Figure 4-15 Dependence of dielectric constant (1 kHz) on the CaCu₃Ti₄O₁₂ concentration using 1 layers hot pressing (HP) at room temperature: (a) without annealing; (b) with annealing.

Table 4-2 Summary of dielectric data for 1 layer $\text{CaCu}_3\text{Ti}_4\text{O}_{12}$ /P(VDF-TrFE) composite (μ -size $\text{CaCu}_3\text{Ti}_4\text{O}_{12}$) with hot pressing (1 kHz).

	$\text{CaCu}_3\text{Ti}_4\text{O}_{12}$ Concentration (vol%)				
	10 vol%	20 vol%	30 vol%	40 vol%	50 vol%
As casted 1 layer ^[1]	18/0.04	23/0.04	32/0.06	65/0.1	67/0.1
Annealed 1 layer ^[2]	25/0.05	34/0.08	43/0.09	105/0.2	69/0.1
1 layer HP ^[3]	17/0.04	35/0.05	37/0.05	78/0.1	73/0.1
Annealed 1 layer HP ^[4]	26/0.05	40/0.07	47/0.07	148/0.2	110/0.2

[1]: Casting at 70 °C/8 hrs.

[2]: Casting at 70 °C/8 hrs and annealing at 125 °C/8 hrs.

[3]: Casting at 70 °C/8 hrs and hot pressing at 200 °C.

[4]: Casting at 70 °C/8 hrs, hot pressing at 200 °C and then annealing at 125 °C/8 hrs.

HP: Hot pressing.

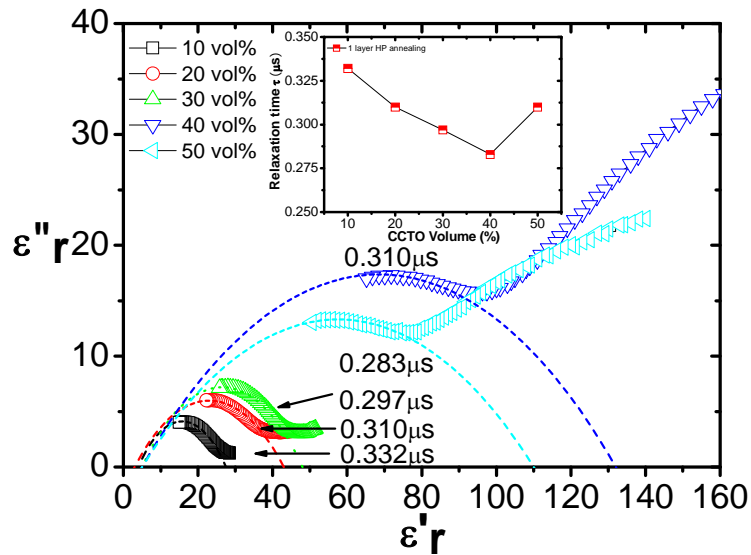


Figure 4-16 Cole-cole plot of the dielectric data of 1 layer HP annealed $\text{CaCu}_3\text{Ti}_4\text{O}_{12}$ /P(VDF-TrFE) composite with 10 to 50 vol% $\text{CaCu}_3\text{Ti}_4\text{O}_{12}$ powder.

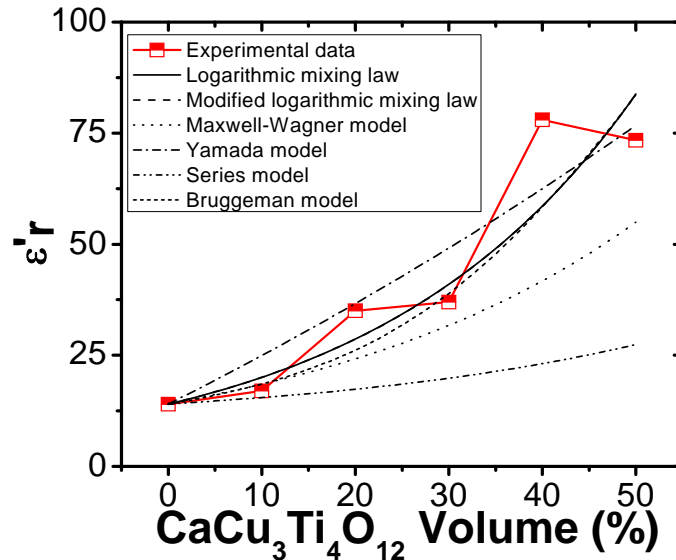


Figure 4-17 Comparison of the present model predictions with experimental data for 1 HP layer $\text{CaCu}_3\text{Ti}_4\text{O}_{12}/\text{P}(\text{VDF}-\text{TrFE})$ sample.

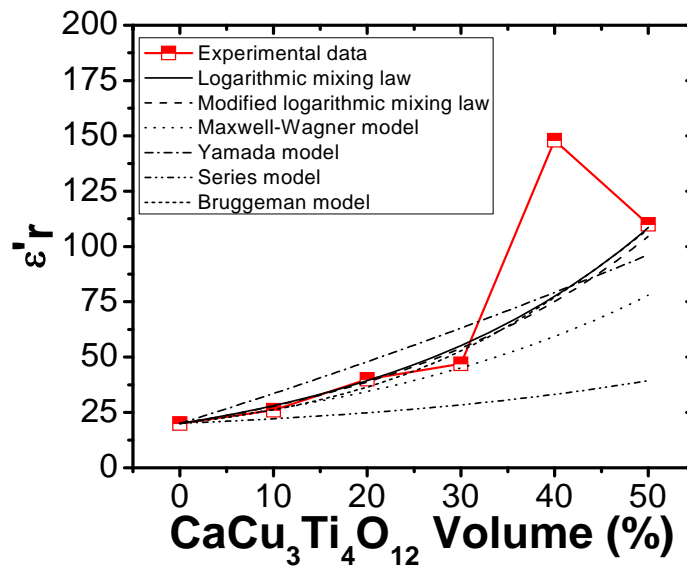


Figure 4-18 Comparison of the present model predictions with experimental data for 1 layer HP annealed $\text{CaCu}_3\text{Ti}_4\text{O}_{12}/\text{P}(\text{VDF}-\text{TrFE})$ sample.

Table 4-3 Summary of fitted dielectric data for $\text{CaCu}_3\text{Ti}_4\text{O}_{12}$ in 1 layer $\text{CaCu}_3\text{Ti}_4\text{O}_{12}/\text{P}(\text{VDF}-\text{TrFE})$ composite (μ -size $\text{CaCu}_3\text{Ti}_4\text{O}_{12}$) with hot pressing (1 kHz).

	1 layer HP ^[1]	Annealed 1 layer HP ^[2]
Logarithmic mixing law	502	580
Modified logarithmic mixing law	17,980	18,000
Maxwell-Wagner model	∞	∞
Yamada model	167	200
Series model	∞	∞
Bruggeman model	240	300

^[1]: Casting at 70 °C/8 hrs and hot pressing at 200 °C.

^[2]: Casting at 70 °C/8 hrs, hot pressing at 200 °C and then annealing at 125 °C/8 hrs.

HP: Hot pressing.

Modified logarithmic mixing law: $k=0.5$.

Yamada model: $N=25$.

4.3.3 Multiple-Layer Configuration

4.3.3.1 Dielectric Response using PC Hot Pressing

In order to further study its processing influence on the dielectric response, multilayer $\text{CaCu}_3\text{Ti}_4\text{O}_{12}/\text{P}(\text{VDF-TrFE})$ as-cast composites were used for hot pressing. Dielectric responses of these samples before and after annealing are shown in Figure 4-19 to 4-23. Those multilayer composite samples were hot pressed using PC hot pressing method, as described in Chapter 2, and multilayer composites varied from two layers to six layers.

Figure 4-19 to 4-23 show the dielectric response of multilayer composite using PC hot pressing for 10s. The maximum dielectric constant increased from 34 to 179 at 1 kHz at RT for none-annealing samples, and 34 to 234 at 1 kHz at RT for annealing samples, as the $\text{CaCu}_3\text{Ti}_4\text{O}_{12}$ concentration increased. However, for each concentration, the maximum dielectric constant was obtained on the HP samples with different number of layers. For example, the maximum value for 10 vol% samples appeared in two layers HP, as well as four layers in 20 vol%, five layers in 30 vol%, three layers in 40 vol% and three layers in 50 vol% samples. In order to understand the changes in dielectric constant, the microstructure of the multiple layers composite was examined using SEM. These results for 50 vol% samples are shown in Figure 4-24. Compared to other multiple layers composite by PC hot pressing, only three layers display good ceramic distribution into polymer matrix, which tend to minimize the thin apparent interfacial layer between $\text{CaCu}_3\text{Ti}_4\text{O}_{12}$ and $\text{P}(\text{VDF-TrFE})$, and corresponding dielectric constant can reach as high as 147 at 1 kHz. As seen in Figure 4-24, the dispersions of ceramic to polymer in the two layer, four layer, five layer and six layer composites are poor, and they exhibit more pores and apparent polymer aggregation which influences its dielectric performance. Confirmed by their dielectric results in Figures 4-19 to 4-23 and the morphologies in Figure 4-24, it is believed that the abrupt increase in the dielectric constant using PC hot pressing may originate from the improvement of the uniform structure.

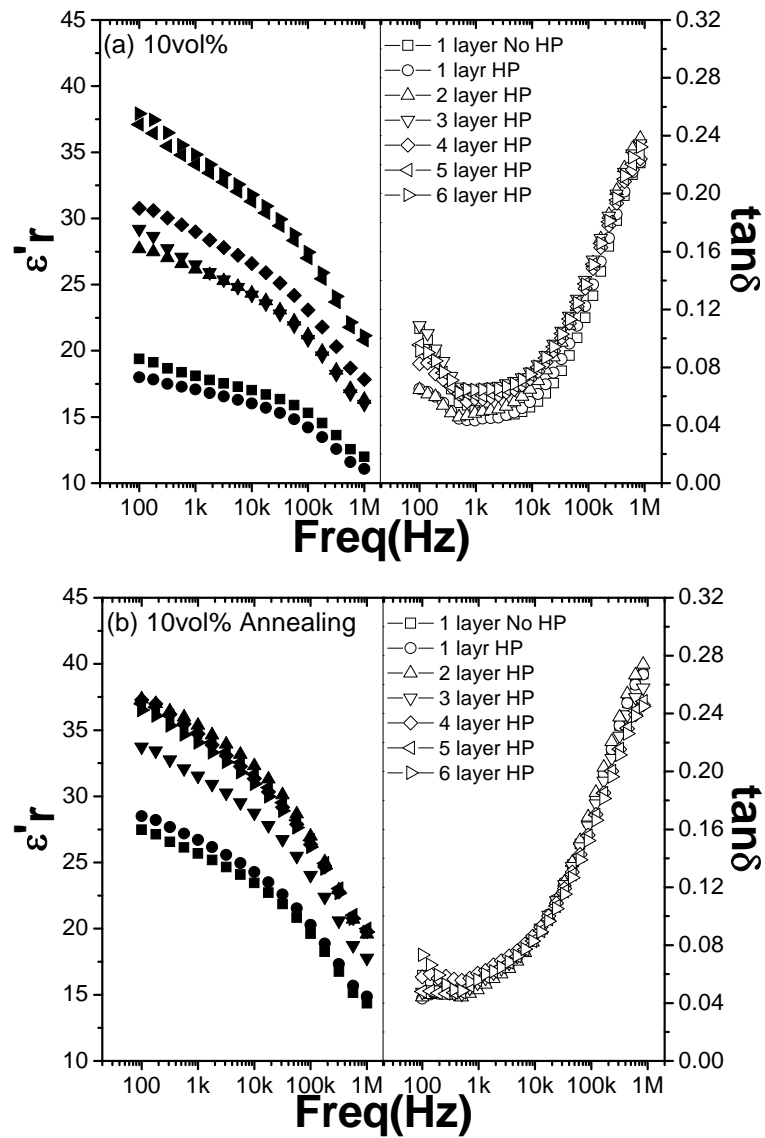


Figure 4-19 Dielectric response vs. frequency of the $\text{CaCu}_3\text{Ti}_4\text{O}_{12}/\text{P}(\text{VDF-TrFE})$ composites with 10 vol% $\text{CaCu}_3\text{Ti}_4\text{O}_{12}$ powder: (a) without annealing; (b) with annealing.

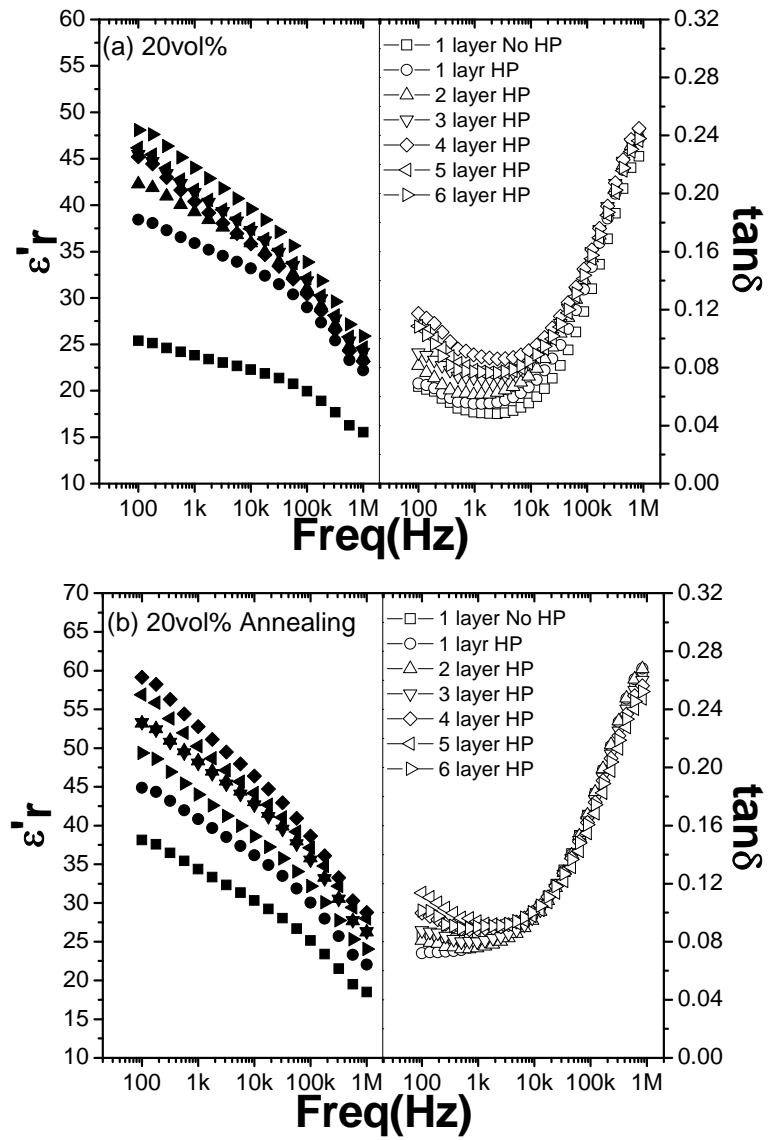


Figure 4-20 Dielectric response vs. frequency of the CaCu₃Ti₄O₁₂/P(VDF-TrFE) composites with 20 vol% CaCu₃Ti₄O₁₂ powder: (a) without annealing; (b) with annealing.

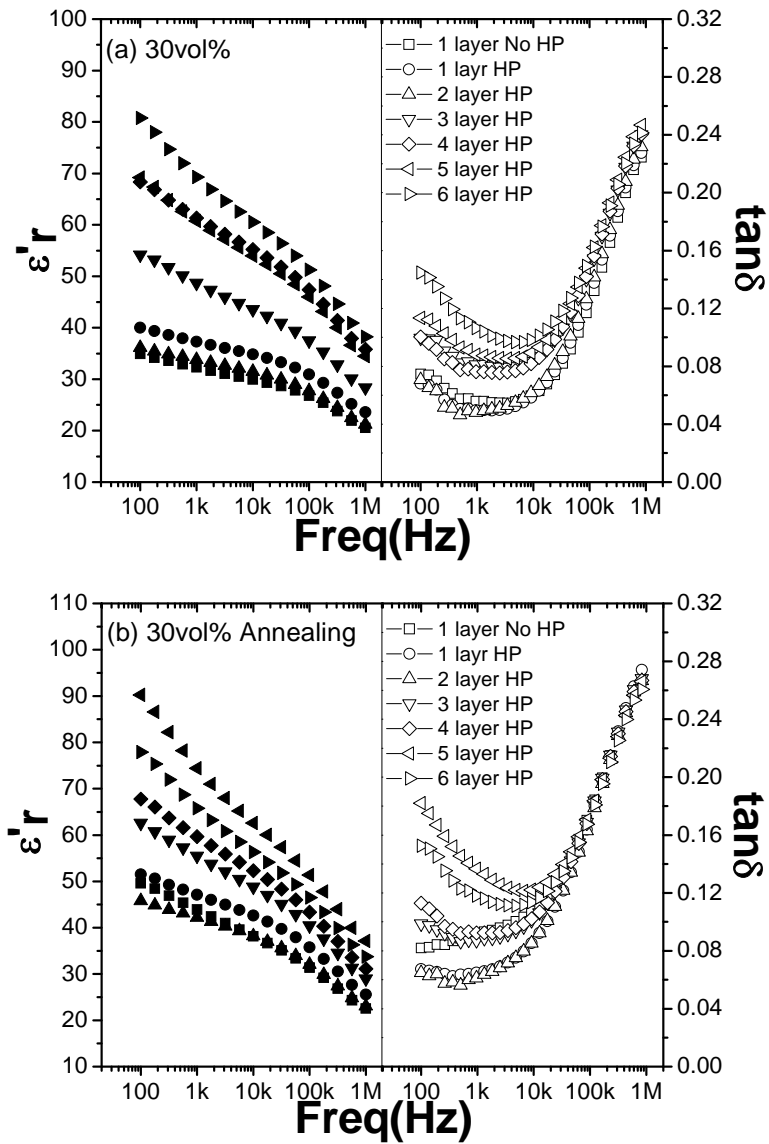


Figure 4-21 Dielectric response vs. frequency of the $\text{CaCu}_3\text{Ti}_4\text{O}_{12}/\text{P}(\text{VDF-TrFE})$ composites with 30 vol% $\text{CaCu}_3\text{Ti}_4\text{O}_{12}$ powder: (a) without annealing; (b) with annealing.

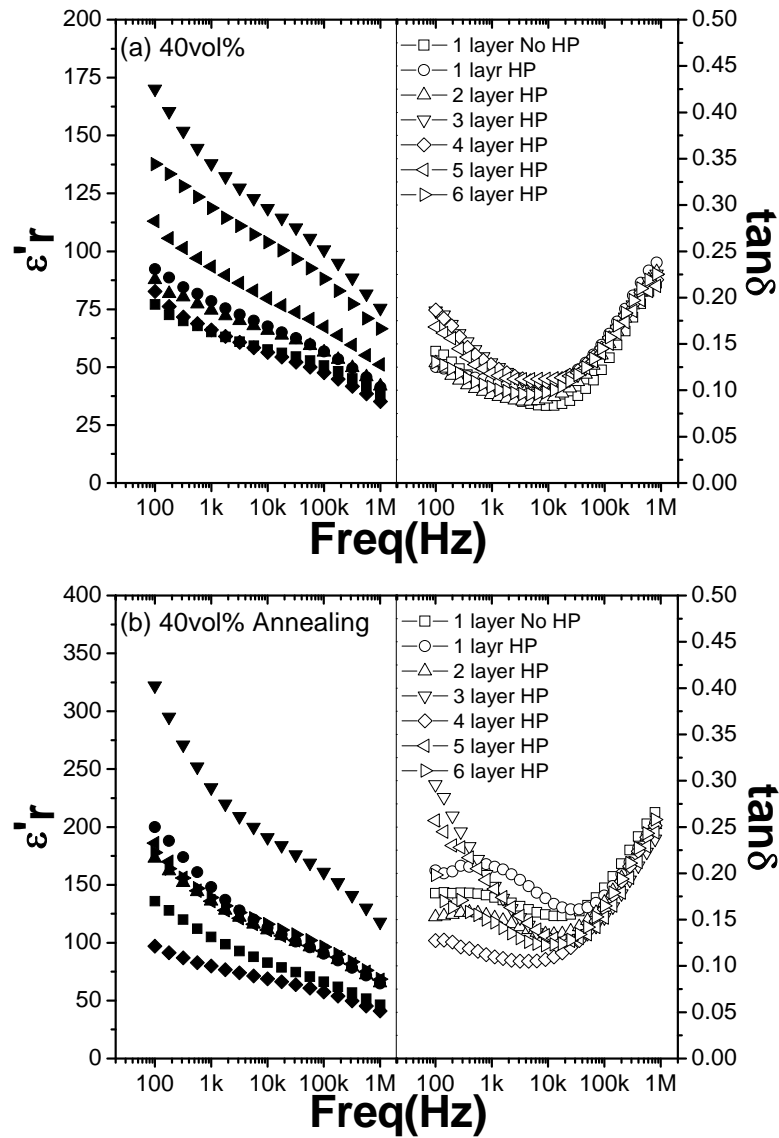


Figure 4-22 Dielectric response vs. frequency of the CaCu₃Ti₄O₁₂/P(VDF-TrFE) composites with 40 vol% CaCu₃Ti₄O₁₂ powder: (a) without annealing; (b) with annealing.

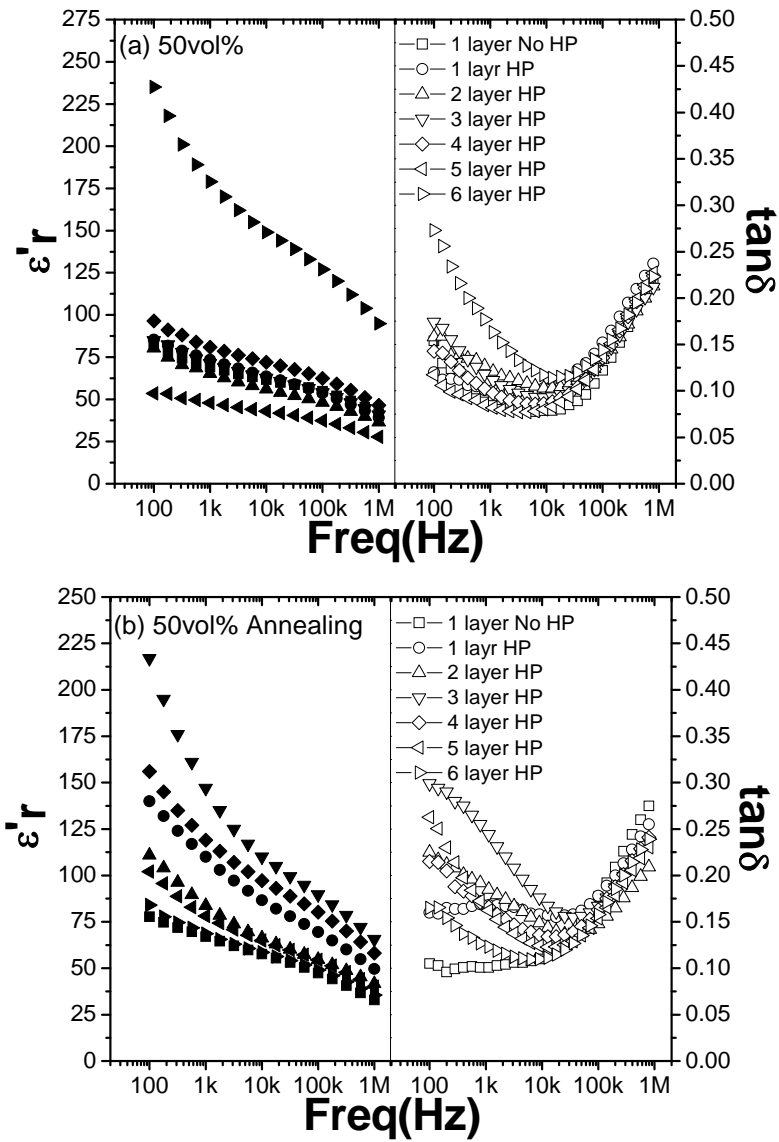


Figure 4-23 Dielectric response vs. frequency of the CaCu₃Ti₄O₁₂/P(VDF-TrFE) composites with 50 vol% CaCu₃Ti₄O₁₂ powder: (a) without annealing; (b) with annealing.

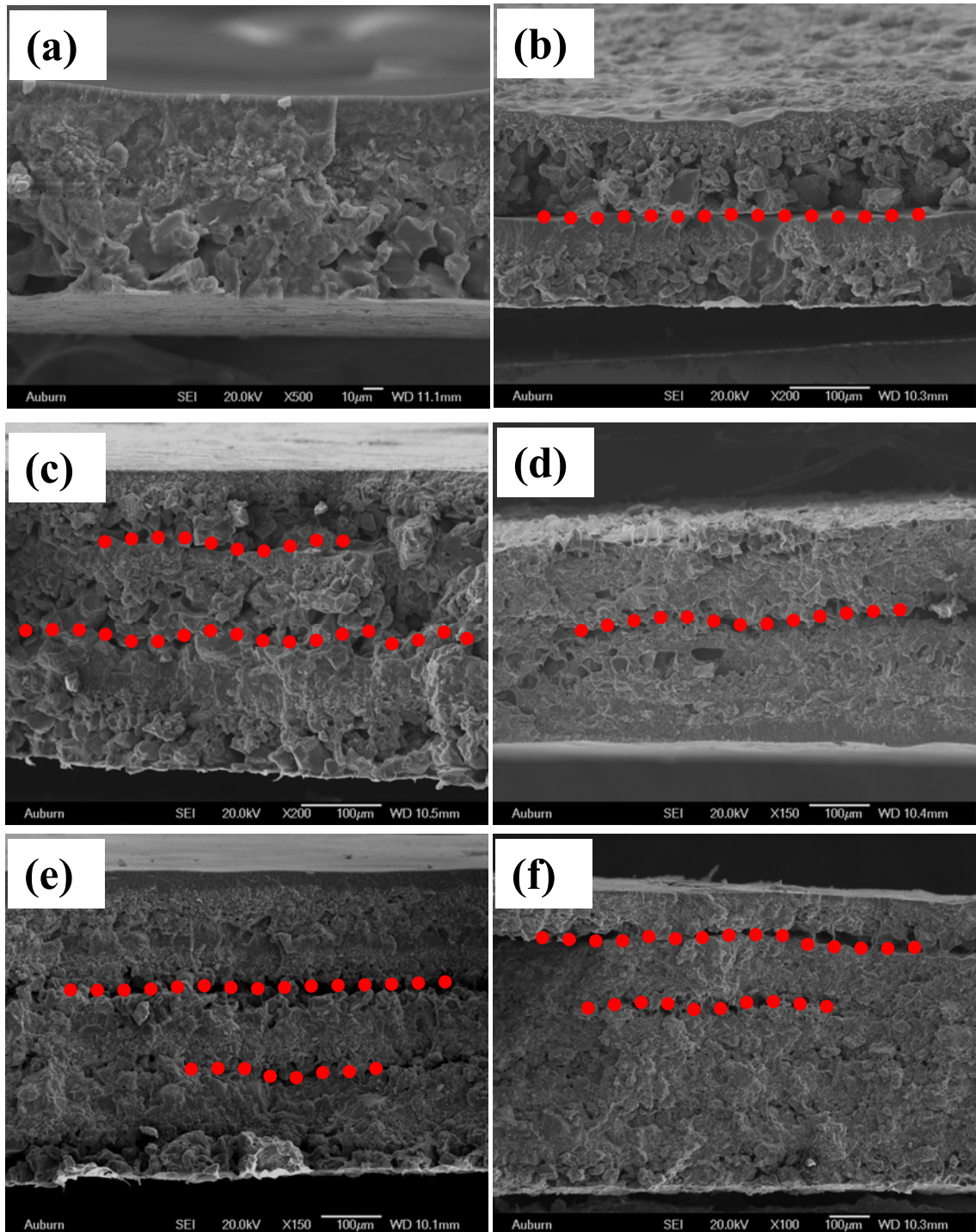


Figure 4-24 SEM fractographs of $\text{CaCu}_3\text{Ti}_4\text{O}_{12}/\text{P}(\text{VDF}-\text{TrFE})$ composites with 50 vol% $\text{CaCu}_3\text{Ti}_4\text{O}_{12}$ powder using hot pressing for 10 seconds, (a) 1 layer without hot pressing, (b) 2 layer PC pressing, (c) 3 layer PC pressing, (d) 4 layer PC pressing, (e) 5 layer PC pressing, (f) 6 layer PC pressing respectively.

4.3.3.2 Dielectric Response using CC Hot Pressing

Multilayer $\text{CaCu}_3\text{Ti}_4\text{O}_{12}/\text{P}(\text{VDF-TrFE})$ composites, such as two, four, and six layer, were prepared using CC hot pressing as described in Chapter 2. Figure 4-25 shows the dielectric responses of $\text{CaCu}_3\text{Ti}_4\text{O}_{12}/\text{P}(\text{VDF-TrFE})$ composite with CC hot pressing for 10s. Table 4-4 summarizes their corresponding dielectric constant at 1 kHz.

Clearly, the dielectric constant is higher, for example, as the concentration increased from 10 to 50 vol%: the dielectric response steadily increased from 28 to 333 and then decreased to 165 at 1 kHz, as shown in Figure 4-25 (a) and Table 4-4. However, as for more layers such as four and six layer, the dielectric constant exhibited less tendency of increasing. This phenomenon can be associated with their thickness: relative fast diffusions between ceramic particle and polymer matrix usually take place at samples with relative small thickness. Thus, in order to achieve enhancement in four and six layers composites, extended hot pressing time is necessary. Figure 4-26 to 4-27 plot the results of the composites after CC hot pressing for 20s and 30s, respectively. Tables 4-5 to 4-6 summarize their corresponding dielectric constants and loss at 1 kHz. As the hot pressing time changed to 20s, both two layer and four layer composites displayed the similar trend that they experienced maximum value. However, for six layer composites, there was no maximum peak, and they steadily increased to 328 at 50 vol% $\text{CaCu}_3\text{Ti}_4\text{O}_{12}$. Those experimental results have confirmed the conclusion that a relatively longer hot pressing time is necessary for multiple layer composites in order to achieve optimization. As increasing to 30s, a dielectric constant of 510 and dielectric loss of 0.25 were realized at 50 vol% $\text{CaCu}_3\text{Ti}_4\text{O}_{12}$ powder.

Besides the effect of multiple layers versus $\text{CaCu}_3\text{Ti}_4\text{O}_{12}$ volume concentration, the influence of hot pressing time on the dielectric response has been observed. The dependence of dielectric constant on $\text{CaCu}_3\text{Ti}_4\text{O}_{12}$ concentration under two, four and six layer CC hot pressing for different time is carefully studied in Figure 4-28 to 4-30.

The plot in Figure 4-28 elucidated that when the $\text{CaCu}_3\text{Ti}_4\text{O}_{12}$ concentration ranged from 10 to 60 vol%, the dielectric constant presented an increasing relationship with ceramic volume concentration, except at 40 vol%, where a dielectric constant of 368 was achieved. Furthermore, it was interestingly found that as pressing time increased from 20 to 30 seconds, a dielectric peak shifting from 40 vol% to a higher $\text{CaCu}_3\text{Ti}_4\text{O}_{12}$

concentration (50 vol%) appeared in the spectrum with two layer CC hot pressing. This peak stabilized at 50 vol%, as can be found in Figure 4-29 and 4-30. It indicated that hot pressing is a dynamic process which can alter the relative concentration gradient between ceramic and polymer. Especially for six layers CC pressing for 10 to 30s, an abrupt increase in dielectric constant at 1 kHz from 239 to 510 appeared. It is believed that this is rooted in the insulation-conduction transition.

Figure 4-31 to 4-33 elucidate the comparison between model prediction and experimental data for the effective constant of $\text{CaCu}_3\text{Ti}_4\text{O}_{12}/\text{P}(\text{VDF-TrFE})$ composite. The same models, such as logarithmic mixing (LM) law, modified logarithmic mixing (MLM) law, Maxwell-Wagner (MW) model, Yamada (YA) model, series model and Bruggeman (BM) model, were used for CC hot pressing model prediction. Similarly to the previous model fitting, the values of $\varepsilon'_{r-\text{polymerc}}$ were predetermined as 20 and 14. The values of $\varepsilon'_{r-\text{ceramic}}$ have been calculated and listed in Table 4-7. According to Figure 4-31 to 4-33, LM, MLM, and BM showed better fitting results in two layer composite samples, as well as in four layer and six layer samples. Furthermore, a maximum dielectric constant in each concentration, varying from 10 to 50 vol%, had been selected and was plotted in comparison with model fitting, as shown in Figure 4-34. Clearly, ML, MLM and BM models fitted very well at from 10 to 50 vol%, and especially, it was found that the BM model resulted in best match to experimental data. At the same time, it was known that the BM model was related to percolation, thus the fitting results indicated that high dielectric constant may originate from the percolation. In the overall fitting process, it was also noted that the MW and series models can only give close fitting results up to 40 vol%. Based on fitted experimental results in Table 4-7, the fitted dielectric constant generally presented an increasing trend with number of HP layers, and inversely, they have corroborated the important role of HP on the dielectric constant improvement.

Figure 4-35 to 4-37 show the SEM images of 50 vol% CC hot pressed $\text{CaCu}_3\text{Ti}_4\text{O}_{12}/\text{P}(\text{VDF-TrFE})$ composites. Compared with microstructures of PC HP samples, as shown in Figure 4-24, a more homogenous composite, without obvious polymer and ceramic segregation, and correspondingly, a higher dielectric constant were observed in CC HP. For instance with 10 second hot pressing, compared with 50 vol%, six layer PC hot pressed composite, the cross-section in 50 vol% six layer CC hot pressed

composite shows no signs of obvious segregation, and its dielectric constant increased from 147 to 182 in Figure 4-23 (b), and 4-25 (c). This is strongly corroborated by their SEM images as shown in Figure 4-24 (f) and 4-37 (a). In short, corroborated with the microstructure studies, their corresponding dielectric responses were relatively enhanced with CC hot pressing process, and this enhancement processing was even more experimentally controllable than its counterpart using PC hot pressing. However, based on the results, it was also found that the maximum dielectric constant was observed in samples with different number of layers, such as two layers in 10 vol% composite and six layers in 50 vol% composite with HP 10s, respectively. Moreover, the order of the number of layers corresponding to the maximum dielectric constant was changing as the HP time increasing from 10s to 30s, except for 50 vol%, where the maximum value was stabilized at six layers.

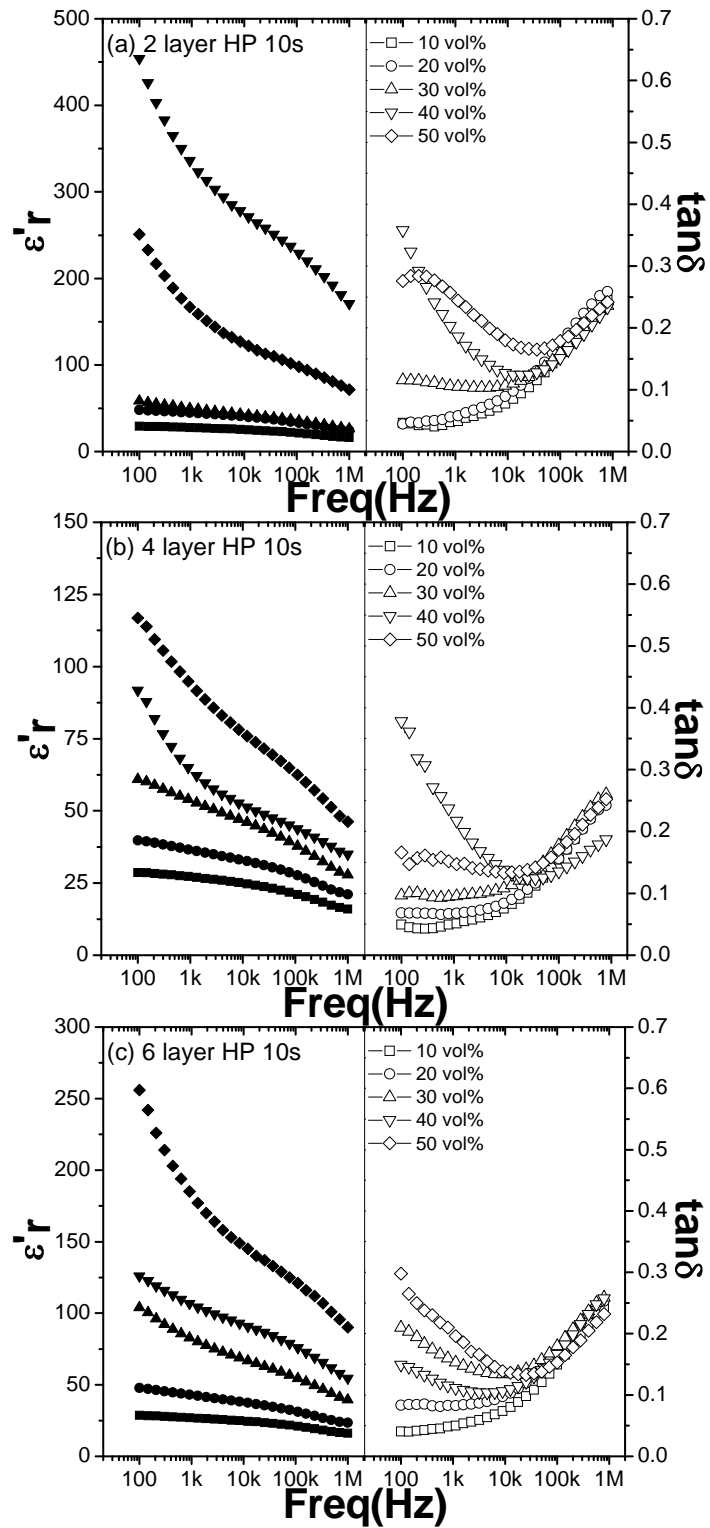


Figure 4-25 Dielectric response vs. frequency of the $\text{CaCu}_3\text{Ti}_4\text{O}_{12}/\text{P}(\text{VDF}-\text{TrFE})$ composites with 10~50 vol% $\text{CaCu}_3\text{Ti}_4\text{O}_{12}$ powder: (a) 2 layer; (b) 4 layer; (c) 6 layer after 10s CC HP.

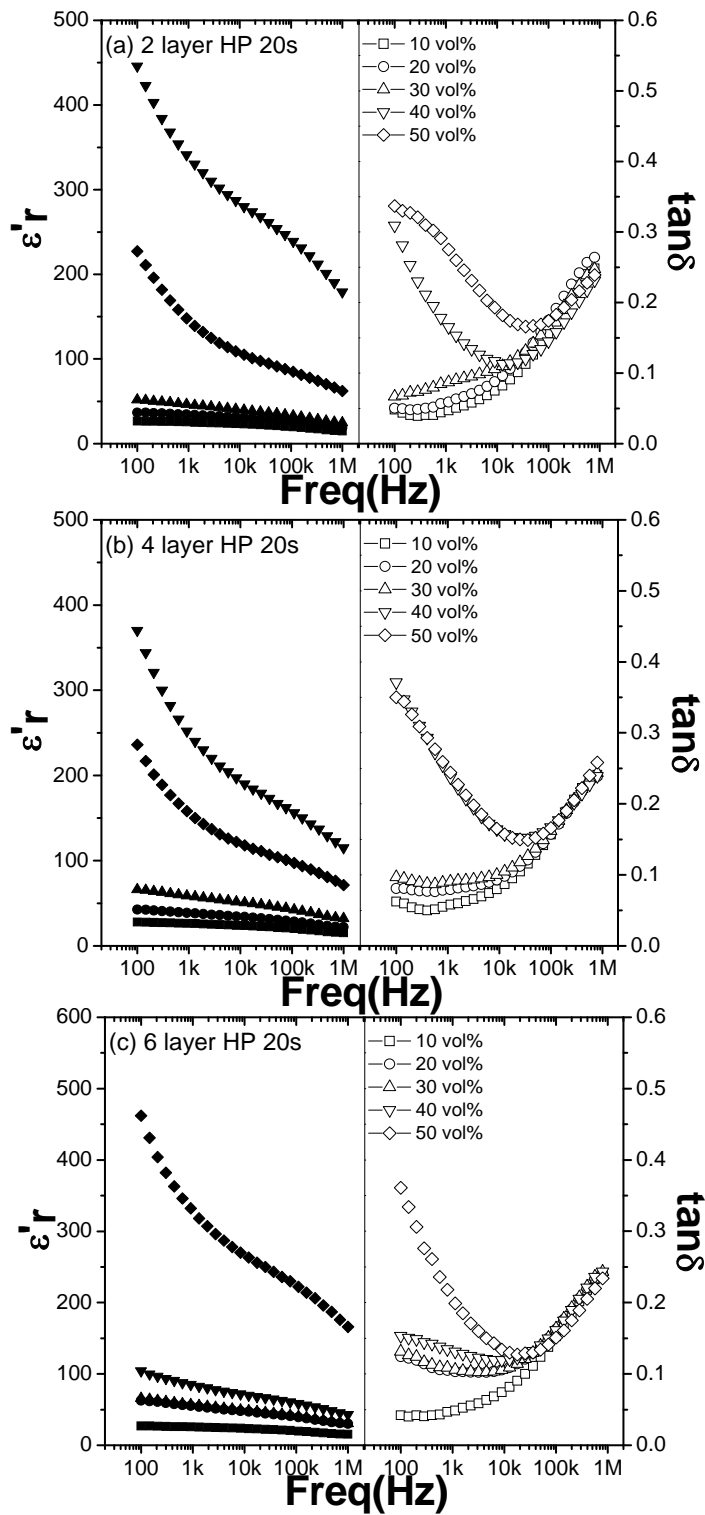


Figure 4-26 Dielectric response vs. frequency of the $\text{CaCu}_3\text{Ti}_4\text{O}_{12}/\text{P}(\text{VDF-TrFE})$ composites with 10~50 vol% $\text{CaCu}_3\text{Ti}_4\text{O}_{12}$ powder: (a) 2 layer; (b) 4 layer; (c) 6 layer after 20s CC HP.

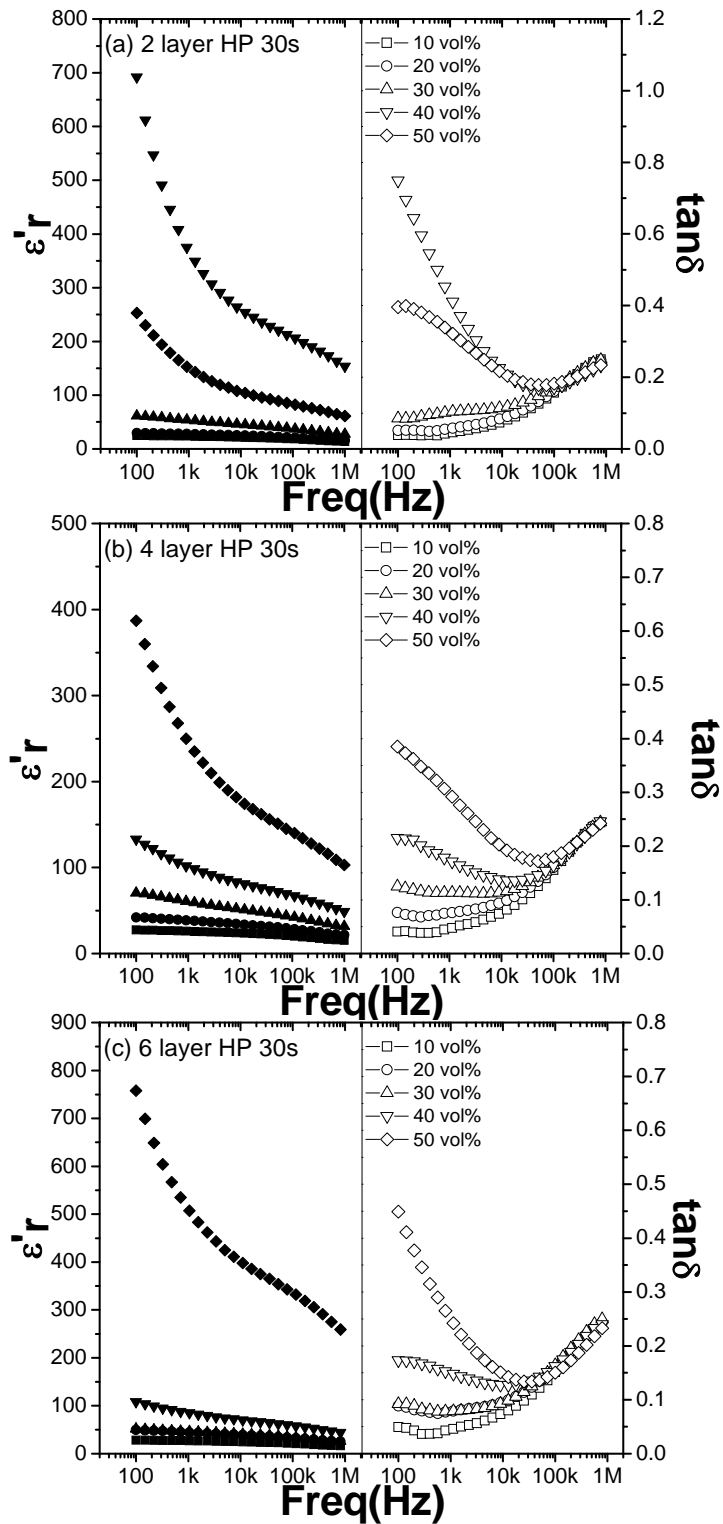


Figure 4-27 Dielectric response vs. frequency of the $\text{CaCu}_3\text{Ti}_4\text{O}_{12}/\text{P}(\text{VDF-TrFE})$ composites with 10~50 vol% $\text{CaCu}_3\text{Ti}_4\text{O}_{12}$ powder: (a) 2 layer; (b) 4 layer; (c) 6 layer after 30s CC HP.

Table 4-4 Summary of dielectric data for multiple layer $\text{CaCu}_3\text{Ti}_4\text{O}_{12}/\text{P}(\text{VDF}-\text{TrFE})$ composite (μ -size $\text{CaCu}_3\text{Ti}_4\text{O}_{12}$) with CC hot pressing for 10s (1 kHz).

	$\text{CaCu}_3\text{Ti}_4\text{O}_{12}$ Concentration (vol%)				
	10 vol%	20 vol%	30 vol%	40 vol%	50 vol%
2 layer	28/0.05	45/0.06	50/0.10	333/0.19	165/0.25
4 layer	27/0.05	37/0.07	54/0.10	64/0.22	94/0.15
6 layer	27/0.05	43/0.08	82/0.15	106/0.11	182/0.20

Table 4-5 Summary of dielectric data for multiple layer $\text{CaCu}_3\text{Ti}_4\text{O}_{12}/\text{P}(\text{VDF}-\text{TrFE})$ composite (μ -size $\text{CaCu}_3\text{Ti}_4\text{O}_{12}$) with CC hot pressing for 20s (1 kHz).

	$\text{CaCu}_3\text{Ti}_4\text{O}_{12}$ Concentration (vol%)				
	10 vol%	20 vol%	30 vol%	40 vol%	50 vol%
2 layer	25/0.05	35/0.06	46/0.09	338/0.17	146/0.28
4 layer	26/0.06	39/0.08	59/0.09	249/0.24	156/0.25
6 layer	26/0.05	55/0.10	57/0.11	84/0.13	328/0.20

Table 4-6 Summary of dielectric data for multiple layer $\text{CaCu}_3\text{Ti}_4\text{O}_{12}/\text{P}(\text{VDF}-\text{TrFE})$ composite (μ -size $\text{CaCu}_3\text{Ti}_4\text{O}_{12}$) with CC hot pressing for 30s (1 kHz).

	$\text{CaCu}_3\text{Ti}_4\text{O}_{12}$ Concentration (vol%)				
	10 vol%	20 vol%	30 vol%	40 vol%	50 vol%
2 layer	24/0.05	28/0.06	54/0.10	368/0.43	150/0.33
4 layer	26/0.05	39/0.08	61/0.11	101/0.17	246/0.30
6 layer	27/0.05	44/0.08	46/0.08	85/0.15	510/0.25

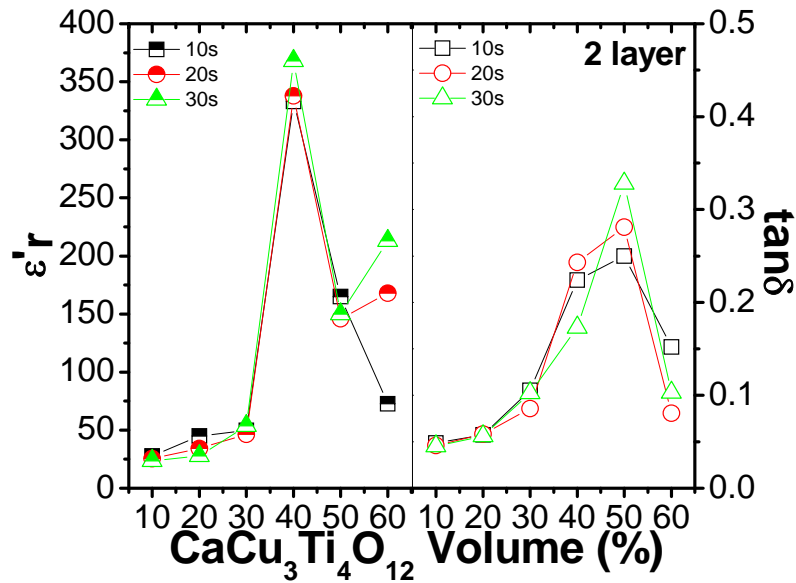


Figure 4-28 Dependence of dielectric response (1 kHz) on the $\text{CaCu}_3\text{Ti}_4\text{O}_{12}$ concentration using 2 layer CC hot pressing (HP) for 10, 20, and 30s at room temperature.

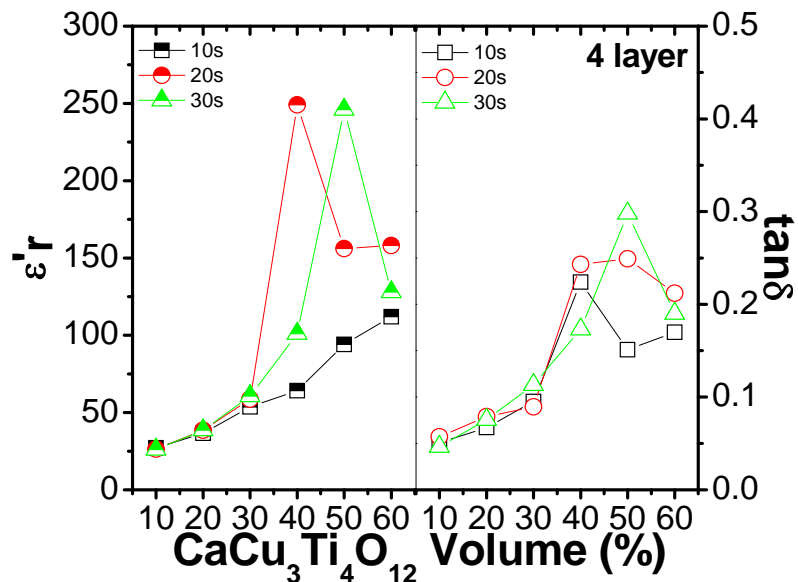


Figure 4-29 Dependence of dielectric response (1 kHz) on the $\text{CaCu}_3\text{Ti}_4\text{O}_{12}$ concentration using 4 layer CC hot pressing (HP) for 10, 20, and 30s at room temperature.

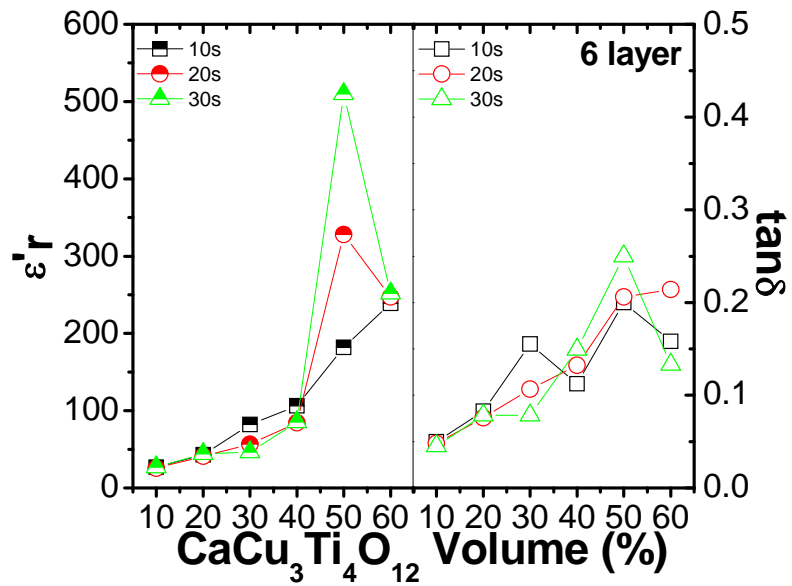


Figure 4-30 Dependence of dielectric response (1 kHz) on the $\text{CaCu}_3\text{Ti}_4\text{O}_{12}$ concentration using 4 layer CC hot pressing (HP) for 10, 20, and 30s at room temperature.

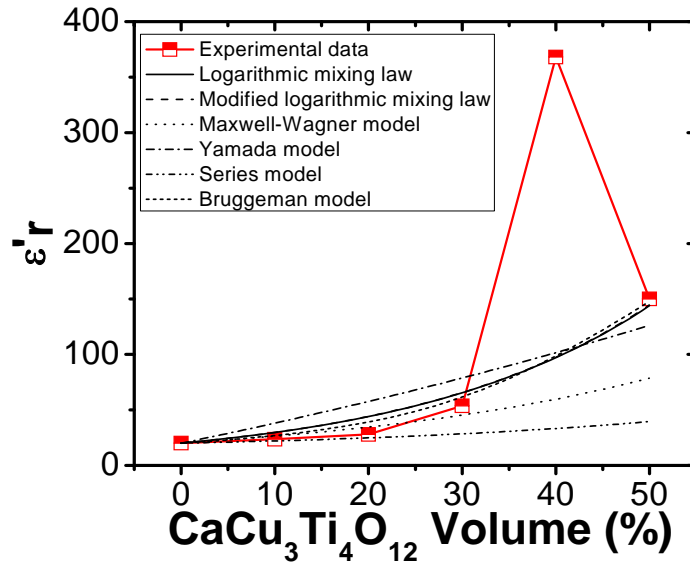


Figure 4-31 Comparison of the present model predictions with experimental data for 2 layer 30s CC-HP CaCu₃Ti₄O₁₂/P(VDF-TrFE) sample.

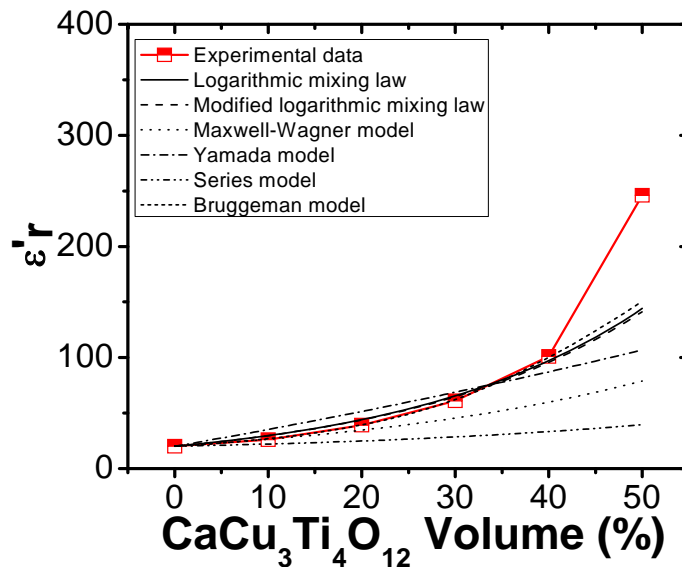


Figure 4-32 Comparison of the present model predictions with experimental data for 4 layer 30s CC-HP CaCu₃Ti₄O₁₂/P(VDF-TrFE) sample.

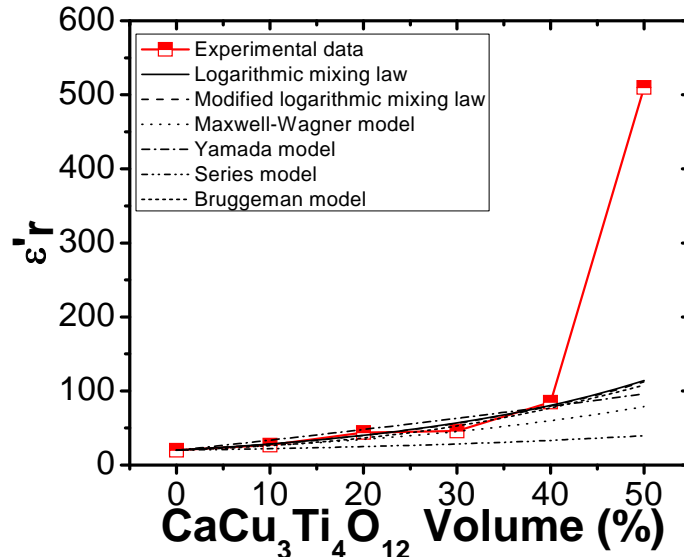


Figure 4-33 Comparison of the present model predictions with experimental data for 6 layer 30s CC-HP $\text{CaCu}_3\text{Ti}_4\text{O}_{12}/\text{P}(\text{VDF-TrFE})$ sample.

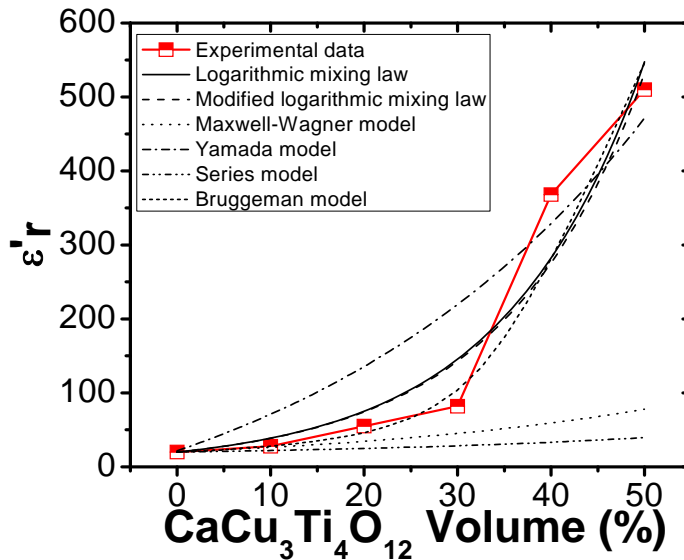


Figure 4-34 Comparison of the present model predictions with highest experimental data for 10, 20, 30, 40 and 50 vol% $\text{CaCu}_3\text{Ti}_4\text{O}_{12}/\text{P}(\text{VDF-TrFE})$ sample in this work.

Table 4-7 Summary of fitted dielectric data for $\text{CaCu}_3\text{Ti}_4\text{O}_{12}$ multiple layer $\text{CaCu}_3\text{Ti}_4\text{O}_{12}/\text{P}(\text{VDF}-\text{TrFE})$ composite (μ -size $\text{CaCu}_3\text{Ti}_4\text{O}_{12}$) with CC hot pressing for 30s (1 kHz).

	2 layer	4 layer	6 layer	Highest results
Logarithmic mixing law	1,040	1,040	650	15,000
Modified logarithmic mixing law	55,000	50,000	20,000	10,000,000
Maxwell-Wagner model	∞	∞	∞	∞
Yamada model	290	230	200	9550
Series model	∞	∞	∞	∞
Bruggeman model	450	460	300	2,020

Modified logarithmic mixing law: $k=0.5$.

Yamada model: $N=25$.

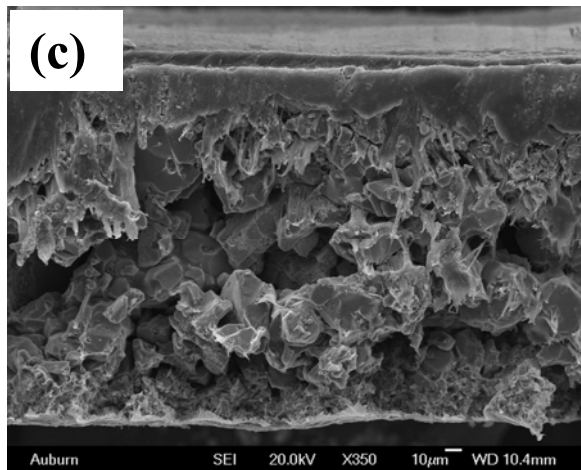
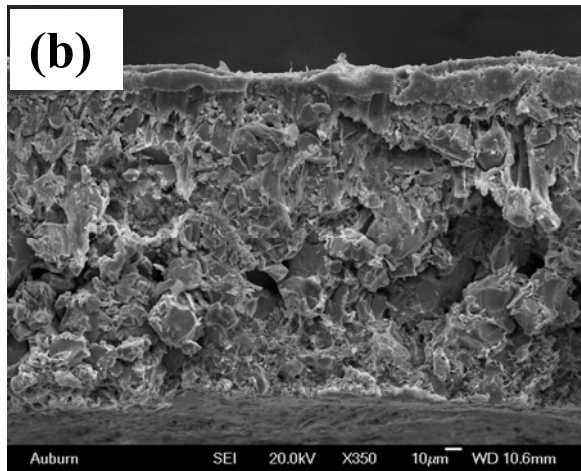
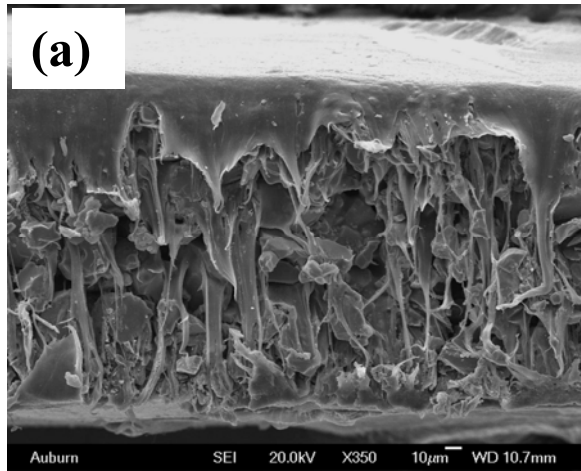


Figure 4-35 SEM fractographs of $\text{CaCu}_3\text{Ti}_4\text{O}_{12}/\text{P}(\text{VDF}-\text{TrFE})$ composites with 50 vol% CCTO powder using 2 layer CC hot pressing for: (a) 10s; (b) 20s; and (c) 30s respectively.

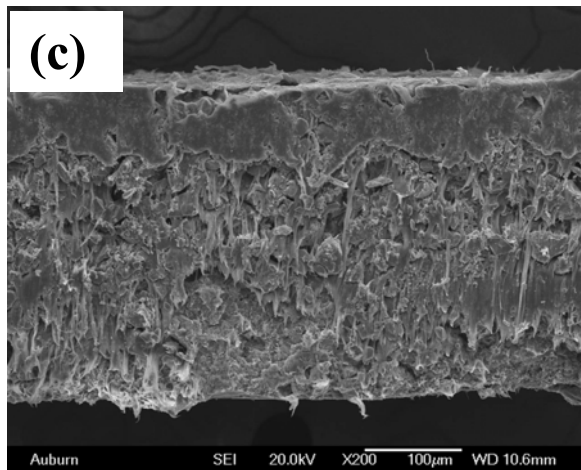
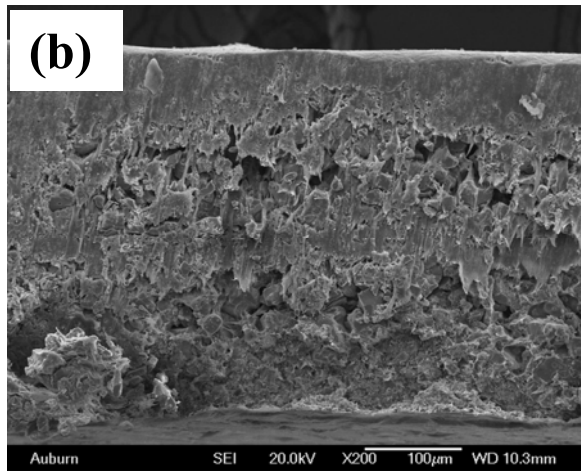
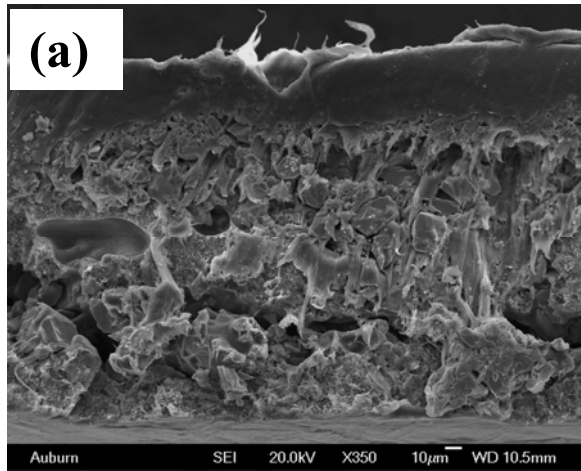


Figure 4-36 SEM fractographs of $\text{CaCu}_3\text{Ti}_4\text{O}_{12}/\text{P}(\text{VDF}-\text{TrFE})$ composites with 50 vol% CCTO powder using 4 layer CC hot pressing for: (a) 10s; (b) 20s; and (c) 30s respectively.

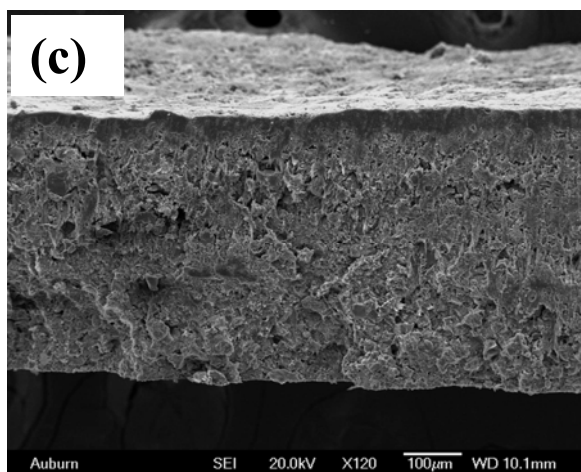
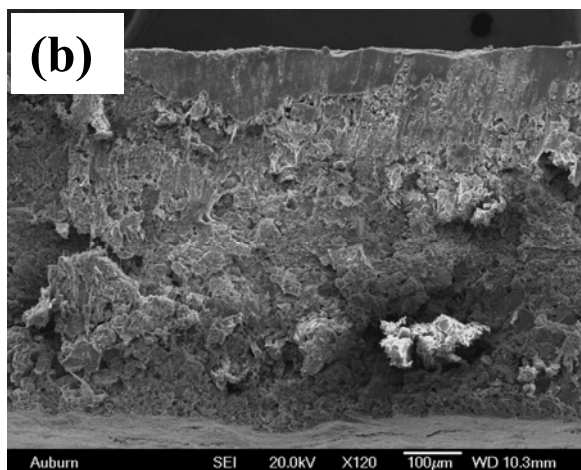
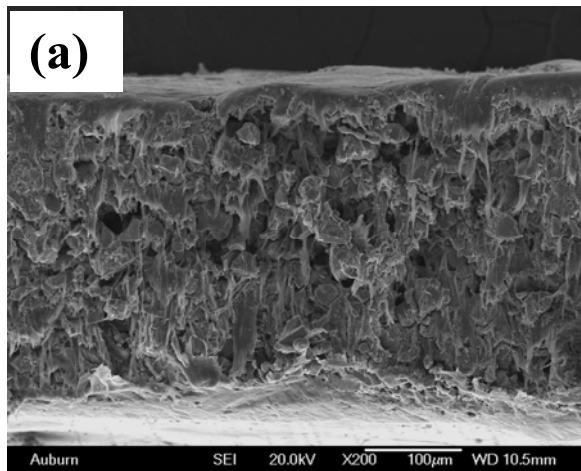


Figure 4-37 SEM fractographs of $\text{CaCu}_3\text{Ti}_4\text{O}_{12}/\text{P}(\text{VDF}-\text{TrFE})$ composites with 50 vol% CCTO powder using 6 layer CC hot pressing for: (a) 10s; (b) 20s; and (c) 30s respectively.

4.3.3.3 Uniformity of 0-3 Composite under CC Hot Pressing

In the previous experiments, the studies between PC hot pressing and CC hot pressing technologies were carried out, and it is found that CC hot pressing is more prone to achieve a homogenous structure with less porosity, which results in high dielectric constant. In this work, the repeatability on the dielectric constant was studied. For each sample with the same composition and processing conditions, three individual samples were prepared and corresponding measurements were carried out. Their corresponding experimental results are shown in Figure 4-38 to 4-43 and Table 4-8 to 4-9. 40 vol% and 50 vol% composites after four layer CC hot pressing for 10, 20, and 30s were chosen in this study.

In Figure 4-38 to 4-40, the variation of dielectric constant was observed to change with hot pressing time. Except hot pressing for 10s, extended hot pressing exhibited considerably small standard deviation. For example, 40 vol% after hot pressing for 10s, the SD was: ± 17 at 100 Hz, ± 24 at 1 kHz, ± 26 at 10 kHz, ± 24 at 100 kHz and ± 21 at 1 MHz, respectively, However for 20s HP, it changed to: ± 39 at 100 Hz, 14 at 1 kHz, 5.1 at 10 kHz, 3.5 kHz at 100 kHz and 2.3 Hz at 1 MHz respectively; and for 30s HP, ± 14 at 100 Hz, ± 8.1 at 1 kHz, ± 7.5 at 10 kHz, 5.6 at 100 kHz, and ± 5.9 at 1 MHz, respectively. Moreover, the reliability results on 50 vol% composites exhibited similar trends, as illustrated in Figure 4-41 to 4-43. There is no large apparent variation as the hot pressing increased to 30s. As stated earlier, the interface between ceramic and polymer layers was presented in a uniform fashion. Based on the experimental results, we can draw a conclusion that longer HP time tends to result in a more uniform sample and small $SD(Er\pm)$.

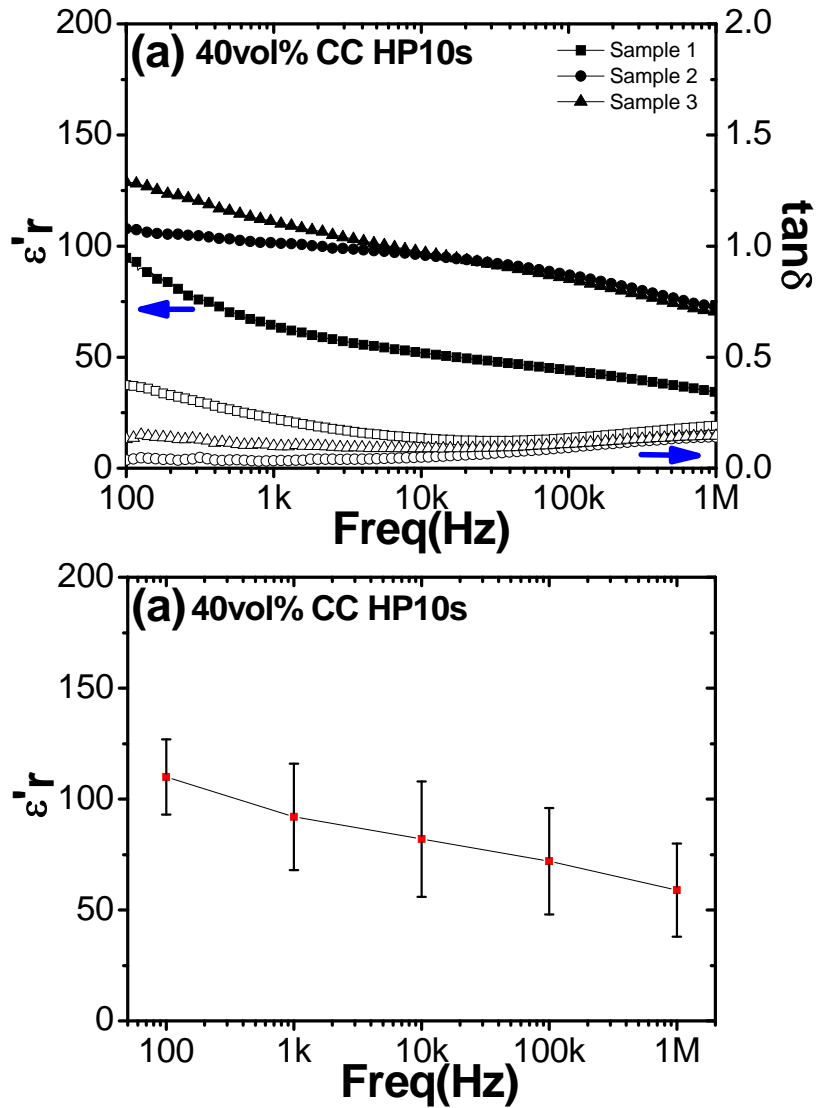


Figure 4-38 Dielectric response vs. frequency of 4 layer $\text{CaCu}_3\text{Ti}_4\text{O}_{12}/\text{P}(\text{VDF-TrFE})$ composites with 40 vol% $\text{CaCu}_3\text{Ti}_4\text{O}_{12}$ powder using CC HP for 10s: (a) Reliability measurements; (b) Reliability results (Error bars indicate standard deviation).

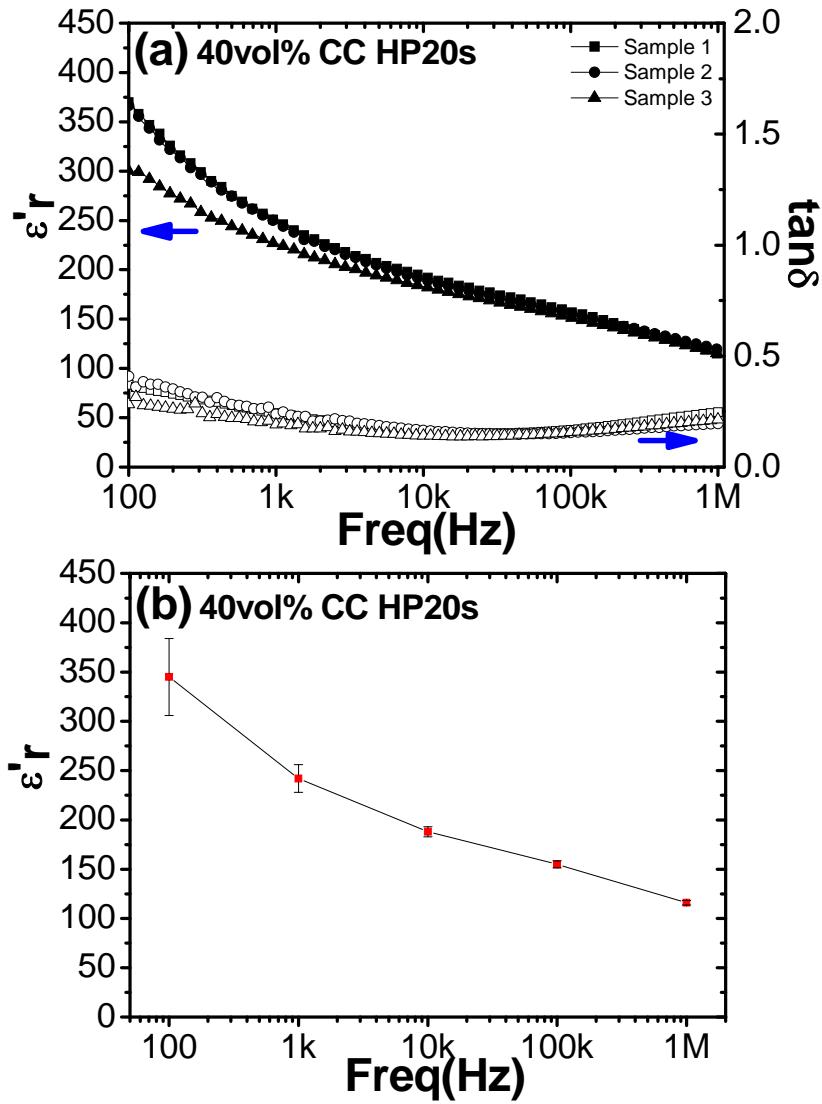


Figure 4-39 Dielectric response vs. frequency of 4 layer $\text{CaCu}_3\text{Ti}_4\text{O}_{12}/\text{P}(\text{VDF}-\text{TrFE})$ composites with 40 vol% $\text{CaCu}_3\text{Ti}_4\text{O}_{12}$ powder using CC HP for 20s: (a) Reliability measurements; (b) Reliability results (Error bars indicate standard deviation).

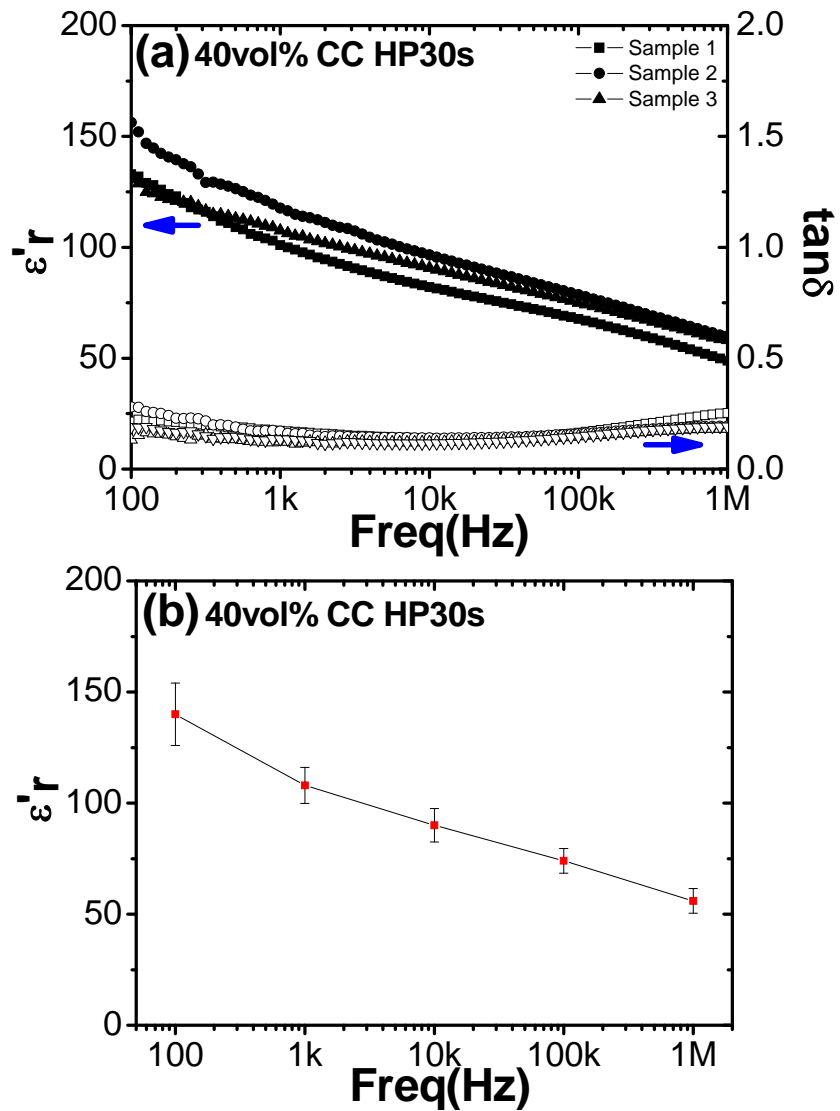


Figure 4-40 Dielectric response vs. frequency of 4 layer $\text{CaCu}_3\text{Ti}_4\text{O}_{12}/\text{P}(\text{VDF}-\text{TrFE})$ composites with 40 vol% $\text{CaCu}_3\text{Ti}_4\text{O}_{12}$ powder using CC HP for 30s: (a) Reliability measurements; (b) Reliability results (Error bars indicate standard deviation).

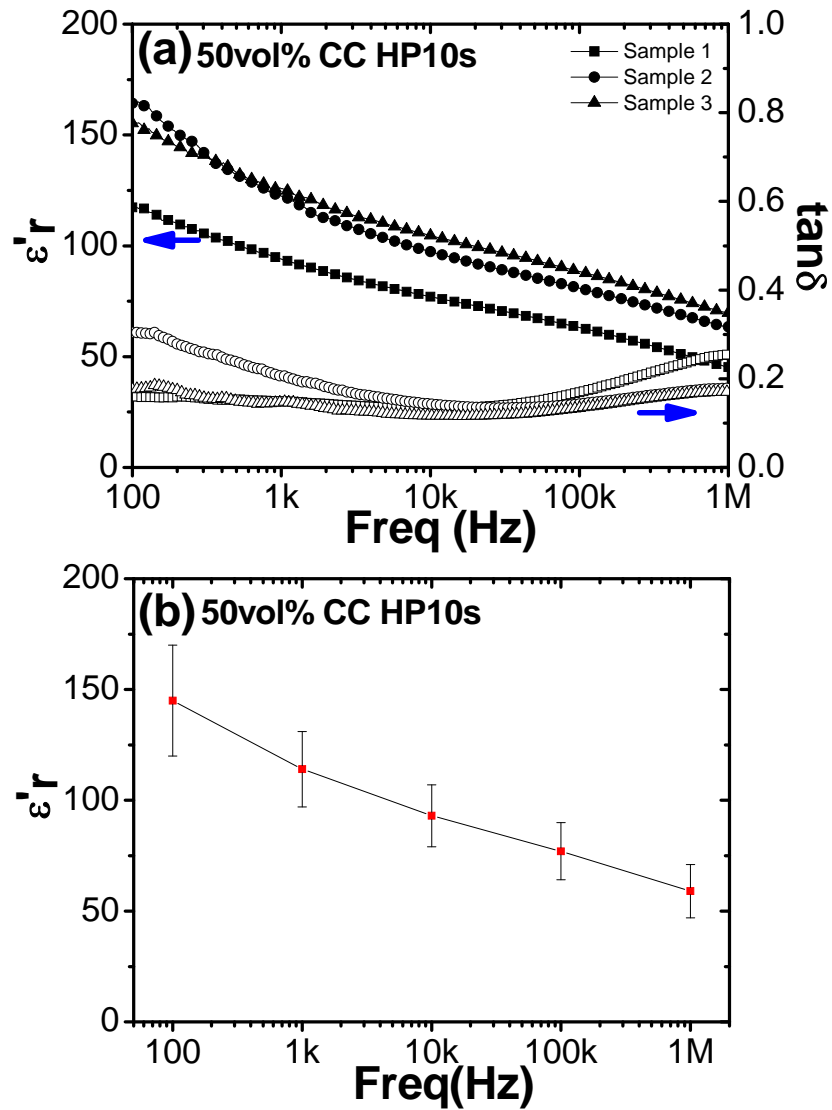


Figure 4-41 Dielectric response vs. frequency of 4 layer $\text{CaCu}_3\text{Ti}_4\text{O}_{12}/\text{P}(\text{VDF}-\text{TrFE})$ composites with 50 vol% $\text{CaCu}_3\text{Ti}_4\text{O}_{12}$ powder using CC HP for 10s: (a) Reliability measurements; (b) Reliability results (Error bars indicate standard deviation).

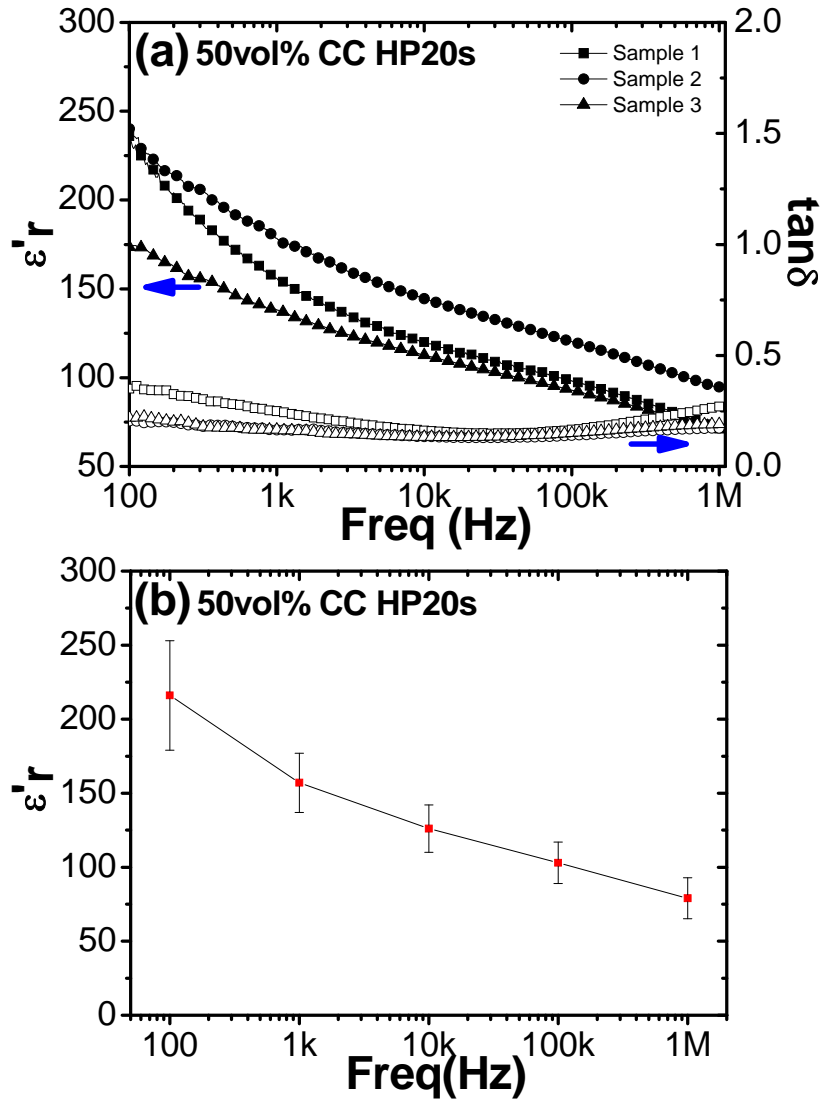


Figure 4-42 Dielectric response vs. frequency of 4 layer $\text{CaCu}_3\text{Ti}_4\text{O}_{12}/\text{P}(\text{VDF-TrFE})$ composites with 50 vol% $\text{CaCu}_3\text{Ti}_4\text{O}_{12}$ powder using CC HP for 20s: (a) Reliability measurements; (b) Reliability results (Error bars indicate standard deviation).

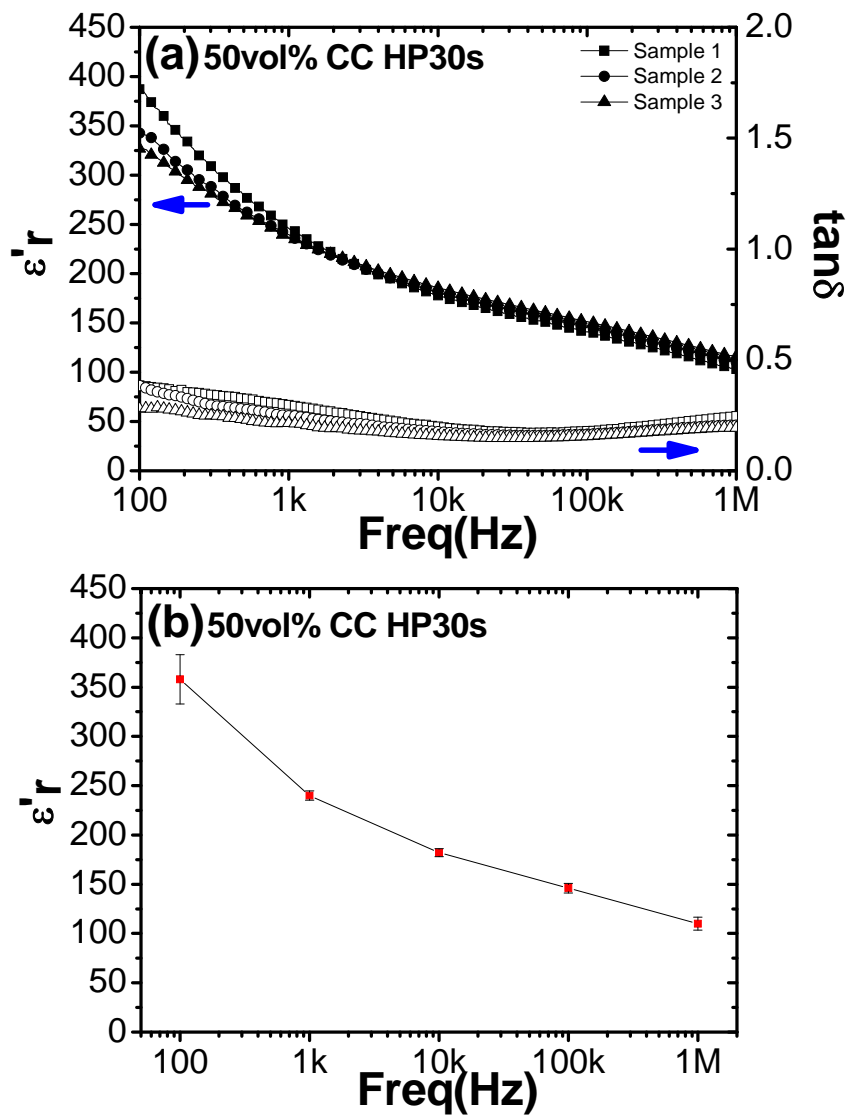


Figure 4-43 Dielectric response vs. frequency of 4 layer $\text{CaCu}_3\text{Ti}_4\text{O}_{12}/\text{P}(\text{VDF-TrFE})$ composites with 50 vol% $\text{CaCu}_3\text{Ti}_4\text{O}_{12}$ powder using CC HP for 30s: (a) Reliability measurements; (b) Reliability results (Error bars indicate standard deviation).

Table 4-8 Summary of reliability measurements of 4 layer CC HP CaCu₃Ti₄O₁₂/P(VDF-TrFE) composite with 40 vol% μ -size CaCu₃Ti₄O₁₂ powder (1 kHz).

	Sample	Dielectric property (ϵ'_r /Tan δ)				
		100	1k	10k	100k	1M
HP 10s	#1	95/0.37	64/0.22	52/0.13	44/0.13	34/0.19
	#2	107/0.03	101/0.03	96/0.05	87/0.09	73/0.14
	#3	128/0.13	110/0.1	97/0.09	85/0.11	70/0.14
	AVE	110/0.18	92/0.12	82/0.09	72/0.11	59/0.16
	SD \pm	17/0.17	24/0.10	26/0.04	24/0.02	21/0.02
	ϵ'_r	110(1 \pm 0.15)	92(1 \pm 0.26)	82(1 \pm 0.31)	72(1 \pm 0.33)	59(1 \pm 0.35)
	Tan δ	0.18(1 \pm 0.94)	0.12(1 \pm 0.83)	0.09(1 \pm 0.44)	0.11(1 \pm 0.18)	0.16(1 \pm 0.13)
HP 20s	#1	370/0.37	249/0.24	193/0.16	158/0.16	115/0.25
	#2	366/0.40	250/0.24	190/0.16	155/0.15	119/0.19
	#3	300/0.28	226/0.19	183/0.14	151/0.15	115/0.21
	AVE	345/0.35	242/0.22	188/0.15	155/0.15	116/0.22
	SD \pm	39/0.06	14/0.03	5/0.01	3/0.005	2/0.03
	ϵ'_r	345(1 \pm 0.11)	242(1 \pm 0.05)	188(1 \pm 0.03)	155(1 \pm 0.02)	116(1 \pm 0.18)
	Tan δ	0.35(1 \pm 0.17)	0.22(1 \pm 0.14)	0.15(1 \pm 0.07)	0.15(1 \pm 0.03)	0.22(1 \pm 0.14)
HP 30s	#1	133/0.21	101/0.17	82/0.13	68/0.16	49/0.25
	#2	156/0.27	117/0.17	97/0.13	79/0.16	60/0.19
	#3	130/0.13	107/0.12	91/0.12	75/0.15	58/0.18
	AVE	140/0.20	108/0.15	90/0.13	74/0.16	56/0.20
	SD \pm	14/0.07	8/0.03	7/0.005	6/0.006	6/0.04
	ϵ'_r	140(1 \pm 0.10)	108(1 \pm 0.07)	90(1 \pm 0.08)	74(1 \pm 0.08)	56(1 \pm 0.11)
	Tan δ	0.20(1 \pm 0.35)	0.15(1 \pm 0.20)	0.13(1 \pm 0.04)	0.16(1 \pm 0.04)	0.20(1 \pm 0.2)

Table 4-9 Summary of reliability measurements of 4 layer CC HP CaCu₃Ti₄O₁₂/P(VDF-TrFE) composite with 50 vol% μ -size CaCu₃Ti₄O₁₂ powder (1 kHz).

	Sample	$\epsilon'_r/\text{Tan}\delta$				
		100	1k	10k	100k	1M
HP 10s	#1	117/0.16	94/0.15	77/0.13	63/0.17	45/0.25
	#2	164/0.30	122/0.20	97/0.14	81/0.14	63/0.18
	#3	155/0.18	125/0.15	105/0.12	88/0.13	69/0.17
	AVE	145/0.21	114/0.17	93/0.13	77/0.15	59/0.20
	SD \pm	25/0.075	17/0.03	14/0.01	13/0.02	12/0.04
	ϵ'_r	145(1 \pm 0.17)	114(1 \pm 0.15)	93(1 \pm 0.15)	77(1 \pm 0.17)	59(1 \pm 0.20)
	Tan δ	0.21(1 \pm 0.36)	0.17(1 \pm 0.18)	0.13(1 \pm 0.08)	0.15(1 \pm 0.13)	0.20(1 \pm 0.2)
HP 20s	#1	236/0.35	156/0.25	120/0.16	98/0.17	71/0.21
	#2	240/0.20	178/0.17	144/0.14	120/0.14	95/0.17
	#3	174/0.22	138/0.17	113/0.13	93/0.15	71/0.19
	AVE	216/0.26	157/0.20	126/0.14	103/0.15	79/0.21
	SD \pm	37/0.08	20/0.05	16/0.015	14/0.015	14/0.02
	ϵ'_r	216(1 \pm 0.17)	157(1 \pm 0.13)	126(1 \pm 0.13)	103(1 \pm 0.14)	79(1 \pm 0.18)
	Tan δ	0.26(1 \pm 0.31)	0.20(1 \pm 0.25)	0.14(1 \pm 0.11)	0.15(1 \pm 0.10)	0.21(1 \pm 0.10)
HP 30s	#1	381/0.39	246/0.29	178/0.20	141/0.18	103/0.25
	#2	342/0.38	239/0.25	181/0.18	145/0.17	110/0.21
	#3	347/0.28	237/0.22	186/0.16	151/0.16	116/0.19
	AVE	358/0.35	240/0.26	182/0.18	146/0.17	110/0.21
	SD \pm	25/0.06	5/0.04	4/0.02	5/0.01	7/0.03
	ϵ'_r	358(1 \pm 0.07)	240(1 \pm 0.02)	182(1 \pm 0.02)	146(1 \pm 0.03)	110(1 \pm 0.06)
	Tan δ	0.35(1 \pm 0.17)	0.26(1 \pm 0.15)	0.18(1 \pm 0.11)	0.17(1 \pm 0.06)	0.21(1 \pm 0.14)

4.3.3.4 Temperature Dependent of Dielectric Response

Figure 4-44 shows the temperature dependence of the dielectric constant and the loss factor for $\text{CaCu}_3\text{Ti}_4\text{O}_{12}/\text{P}(\text{VDF-TrFE})$ composites with 50 vol% $\text{CaCu}_3\text{Ti}_4\text{O}_{12}$ concentration, where two, four and six CC layer samples were hot pressed for 10, 20 and 30s, respectively.

It was seen that the temperature dependence of the dielectric constant is strongly affected by hot pressing, increasing from 10 to 30s, and multiple layers, increasing from two to six. Additionally, they all experienced a maximum value and then leveled off, as clearly illustrated in Figure 4-45, which suggests a relaxation process. For example, for those multiple layers hot pressing for 10s, their corresponding maximum values were: 491, 381 and 514 for two, four and six layer, respectively. However, for HP 20s, those values were: 417, 467 and 859 for two, four and six layers respectively; and for HP 30s, the peak values increased to: 402, 648 and 1,240 for two, four and six layer respectively. The results obtained in the Figure 4-44 to 4-45 reflect the structure and dielectric behavior of $\text{CaCu}_3\text{Ti}_4\text{O}_{12}/\text{P}(\text{VDF-TrFE})$ composite were closely correlated with each other. As mentioned before, when the time is below its critical time such as 10s, those interfaces between ceramic and polymer layers still dominated, so the structure is relatively hard to control using CC HP. This explanation could be one possible reason why the dielectric constant is relatively small in comparison to extended time such as 20 and 30s. There is no indication of any phase transition: the $\text{CaCu}_3\text{Ti}_4\text{O}_{12}$ structure remains cubic and centric down to 35 K^{7,8}, and the $\text{CaCu}_3\text{Ti}_4\text{O}_{12}$ is in marked contrast to known ferroelectrics, which exhibit a dipole moment in the absence of an electric field. Therefore, the apparent relaxation process, as shown in Figure 4-45 is closely related with the polymer matrix $\text{P}(\text{VDF-TrFE})$ which exhibited relaxation process⁹. More study on the temperature dependence of the dielectric constant will be studied.

Moreover, it is known that complex permittivity is a complex function of both the frequency and the temperature, apart from the dependence of other parameters, such as pressure, etc. Based on those temperature dependent experiments, as shown in Figure 4-44 to 4-45, the dielectric response vs. frequency, such as ϵ'_r vs. frequency, $\tan \delta$ vs. frequency and ϵ''_r vs. frequency in $\text{CaCu}_3\text{Ti}_4\text{O}_{12}/\text{P}(\text{VDF-TrFE})$ composite with 50 vol% $\text{CaCu}_3\text{Ti}_4\text{O}_{12}$ powder is listed in Figure 4-46 to 4-54. Those six layer composite samples

were hot pressed for 10, 20 and 30s, respectively, and the temperature range chosen in this study was between 25 to 85 °C, which was just before its observed curie temperature about 90 °C. As mentioned before, the temperature dependence results indicated that it may be related with a relaxation-like phenomenon, however there posed a question: did the high dielectric loss observed in the composite truly originate from relaxation, or in fact was it associated with conductivity? More temperature dependence studies were carried out in order to understand this process. Results in Figure 4-46 to 4-54 indicated that no matter CC HP time in two, four and six layer composite, all the dielectric constant increased with temperature from 25 to 85 °C, while the dielectric loss tended to give the similar tendency from 25 to 75 °C and showed some variations at 80 and 85 °C for most of the samples. All the ε''_r results increased with temperature, which shared identical trend with the dielectric constant. Those behaviors in ε'_r and ε''_r are very similar to the typical relaxation phenomena, which shift to high frequency with increasing temperature. Moreover, those ε''_r of six layer composites are further analyzed using Cole-Cole equation at low frequency (100 to 250 Hz), and long relaxation time ($\omega\tau_0 \gg 1$) as following:

$$\varepsilon''_r(\omega) = (\varepsilon_{r_s} - \varepsilon_{r_\infty}) \frac{(\omega\tau_0)^{1-\alpha} \cos \frac{\pi}{2} \alpha}{1 + 2(\omega\tau_0)^{1-\alpha} \sin \frac{\pi}{2} \alpha + (\omega\tau_0)^{2(1-\alpha)}} \quad (4-2)$$

Because $\omega\tau_0 \gg 1$, thus Equation (4-2) becomes:

$$\varepsilon''_r(\omega) \approx (\varepsilon_{r_s} - \varepsilon_{r_\infty}) \frac{(\omega\tau_0)^{1-\alpha} \cos \frac{\pi}{2} \alpha}{(\omega\tau_0)^{2(1-\alpha)}} = (\varepsilon_{r_s} - \varepsilon_{r_\infty}) \frac{\cos \frac{\pi}{2} \alpha}{(\omega\tau_0)^{1-\alpha}} \quad (4-3)$$

Then by taking the nature logarithm of both sides of the Equation (4-3), we can get:

$$\begin{aligned} \ln[\varepsilon''_r(\omega)] &= \ln[(\varepsilon_{r_s} - \varepsilon_{r_\infty}) \cos \frac{\pi}{2} \alpha] - (1-\alpha) \ln(\omega\tau_0) \\ &= \ln[(\varepsilon_{r_s} - \varepsilon_{r_\infty}) \cos \frac{\pi}{2} \alpha] - (1-\alpha) \ln(\tau_0) - (1-\alpha) \ln(\omega) \end{aligned} \quad (4-4)$$

Equation (4-4) is equivalent to:

$$\ln[\varepsilon''_r(f)] = \ln[(\varepsilon_{r_s} - \varepsilon_{r_\infty}) \cos \frac{\pi}{2} \alpha] - (1-\alpha) \ln(\tau_0) - (1-\alpha) \ln(2\pi) - (1-\alpha) \ln(f) \quad (4-5)$$

Then Equation (4-5) is simplified as:

$$\ln[\varepsilon''_r(f)] = A - K \ln(f) \quad (4-6)$$

where A is $\ln[(\varepsilon_{r_s} - \varepsilon_{r_\infty}) \cos \frac{\pi}{2} \alpha] - (1 - \alpha) \ln(\tau_0) - (1 - \alpha) \ln(2\pi)$, and K is $(1 - \alpha)$. The relationships between $\ln(\varepsilon''_r)$ and $\ln(f)$ for six layer $\text{CaCu}_3\text{Ti}_4\text{O}_{12}/\text{P}(\text{VDF-TrFE})$ composite have been plotted in Figure 4-55 to 4-57. Incorporated with 10, 20 and 30s CC HP, temperatures varying from 25 to 85 °C were selected in the study. The fitting results are shown in Table 4-10 to 4-12. As found in Figure 4-55 to 4-57, they presented a linear trend between $\ln(\varepsilon''_r)$ and $\ln(f)$, whose slope was slightly increasing from 0.292 to 0.389 for 10s CC HP, 0.408 to 0.443 for 20s CC HP and 0.438 to 0.512 for 30s CC HP, as temperature increased from 25 to 85 °C.

If this behavior is related with conductivity, those ε''_r of six layers composites are written as below:

$$\varepsilon''_r(\omega) = \frac{\sigma}{\varepsilon_0 \omega} \quad (4-7)$$

Then by taking the nature logarithm of both sides of the Equation (4-7), we can get:

$$\ln[\varepsilon''_r(f)] = A' - \ln(f) \quad (4-8)$$

where A' is $\ln \sigma - \ln(\varepsilon_0) - \ln(2\pi)$. Based on the equation (4-8), the slope should equal to 1 for conductivity. However, comparing with the results in Figure 4-55 to 4-57, the real slope is much smaller than 1. All the results demonstrate that the high dielectric loss originates from relaxation process.

The relaxation time τ can be expressed by Arrhenius equation:

$$\tau = \tau_0 \exp\left(-\frac{E_a}{K_B T}\right) \quad (4-9)$$

Combined with Equation (4-4):

$$\ln[\varepsilon''_r(f)] = A'' + K'' \frac{1}{T} \quad (4-10)$$

Where A'' is $\ln[(\varepsilon_{r_s} - \varepsilon_{r_\infty}) \cos \frac{\pi}{2} \alpha] - (1 - \alpha) \ln(2\pi f) - (1 - \alpha) \tau_0$, K'' is $(1 - \alpha) \frac{E_a}{K_B}$, E_a is the activation energy for the process, K_B is the Boltzmann constant and T is the temperature in K. The values of α are selected from the Table 4-10 to 4-12, such as 0.31 for 10s, 0.43

for 20s and 0.47 for 30s. Figure 4-58 to 4-60 shows the plots for 6 layer composite. The summary of the results is listed in Table 4-13. The measurement result clearly shows that the temperature dependent process consisted of two temperature regions, which corresponded to two mechanisms. At low temperatures (25 to 45 °C), the calculated activation energy E_a increased from 0.06 to 0.21 eV at 100 Hz, while at high temperatures, the activation energy ranged from 0.29 to 0.38 eV at 100 Hz. Unlike the linear behavior of σ vs. $1/T$, experimental results further confirmed that this temperature dependent process originated from the relaxation process.

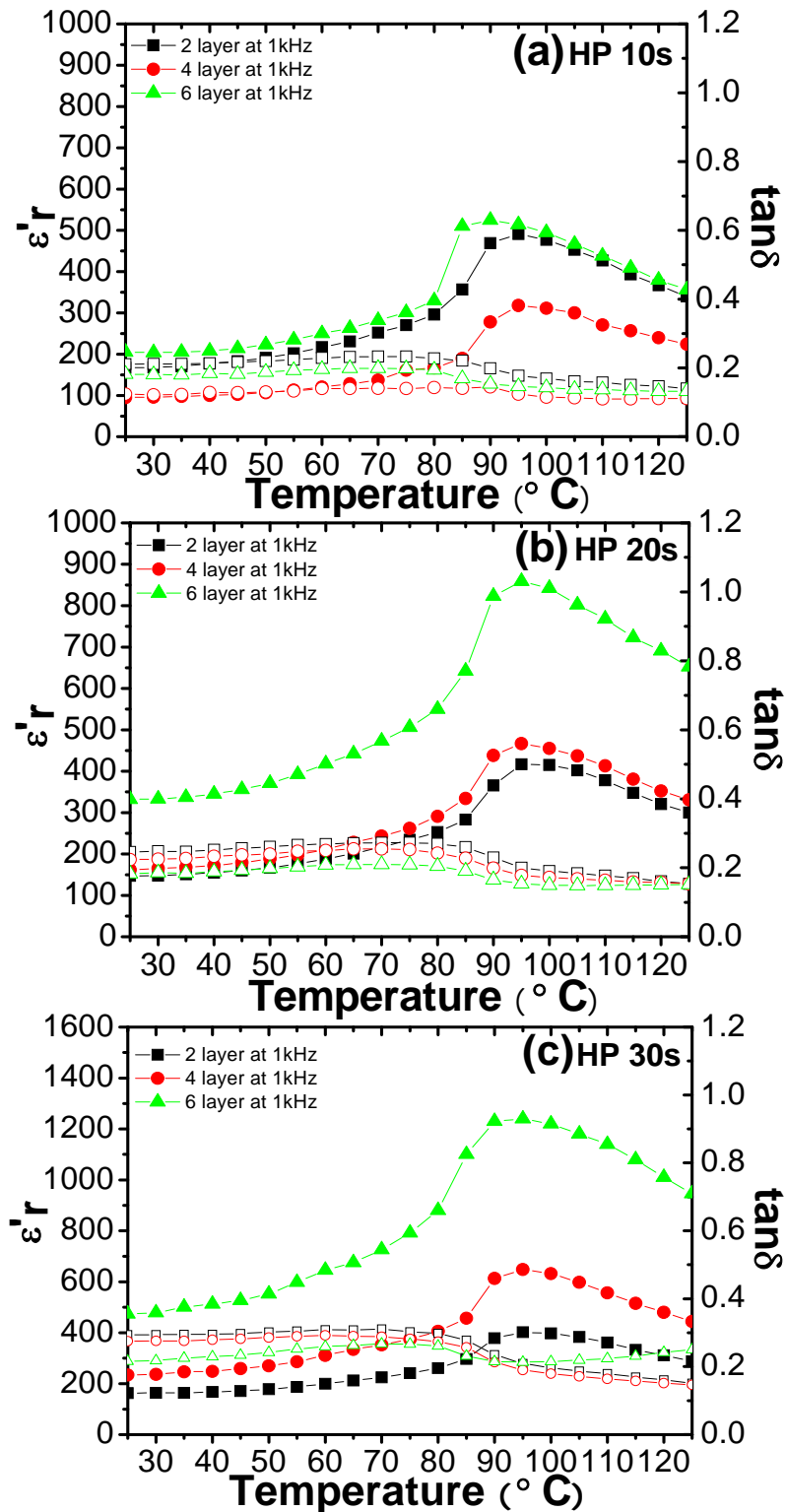


Figure 4-44 Temperature dependence of the 2, 4, 6 layer $\text{CaCu}_3\text{Ti}_4\text{O}_{12}/\text{P}(\text{VDF}-\text{TrFE})$ composites with 50 vol% $\text{CaCu}_3\text{Ti}_4\text{O}_{12}$ powder for: (a) 10s CC HP, (b) 20s CC HP, and (c) 30s CC HP, respectively.

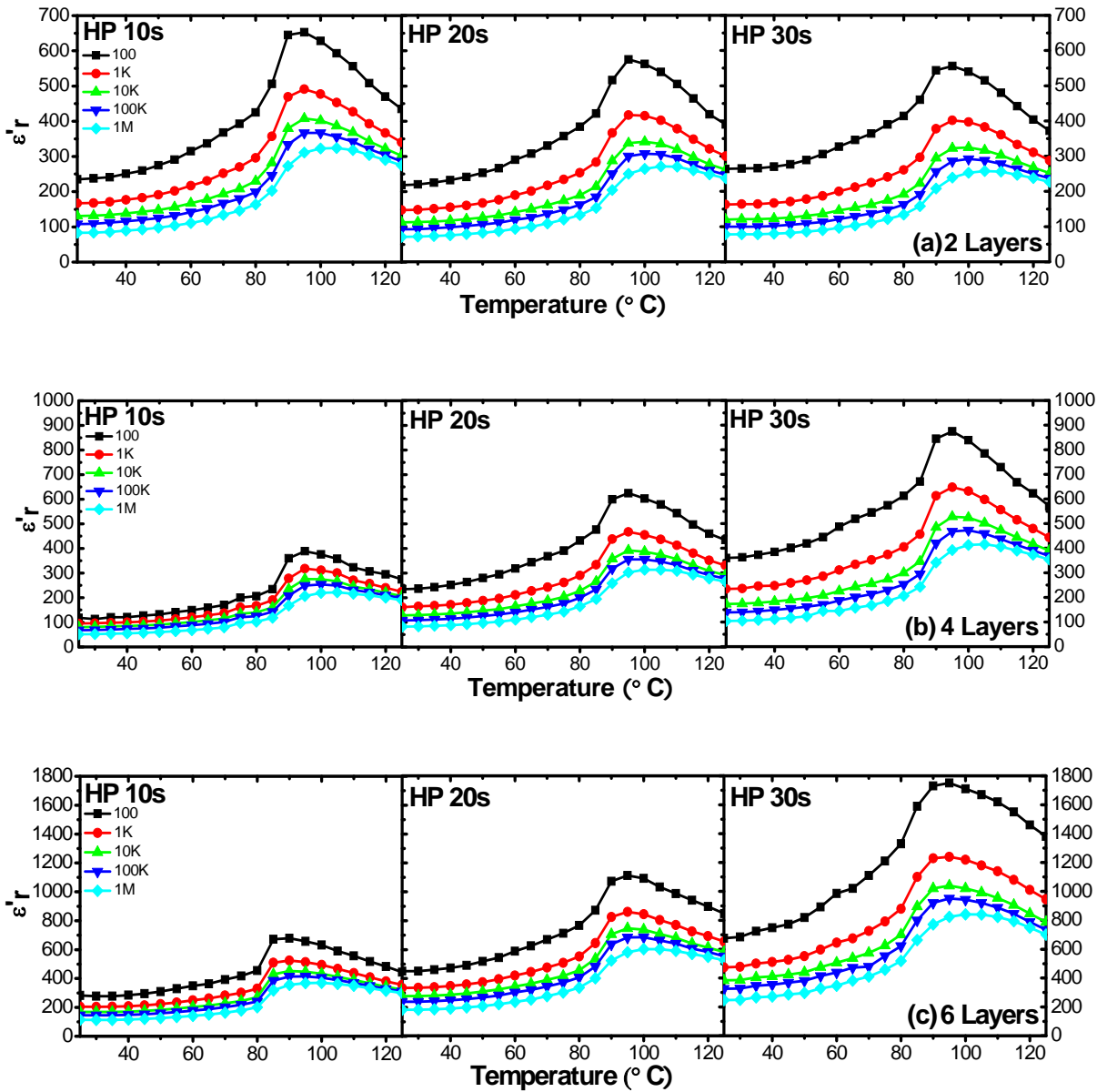


Figure 4-45 Temperature dependence of the $\text{CaCu}_3\text{Ti}_4\text{O}_{12}/\text{P}(\text{VDF-TrFE})$ composites with 50 vol% $\text{CaCu}_3\text{Ti}_4\text{O}_{12}$ powder using: (a) 2 layer CC HP, (b) 4 layer CC HP, and (c) 6 layer CC HP for 10, 20, and 30s, respectively.

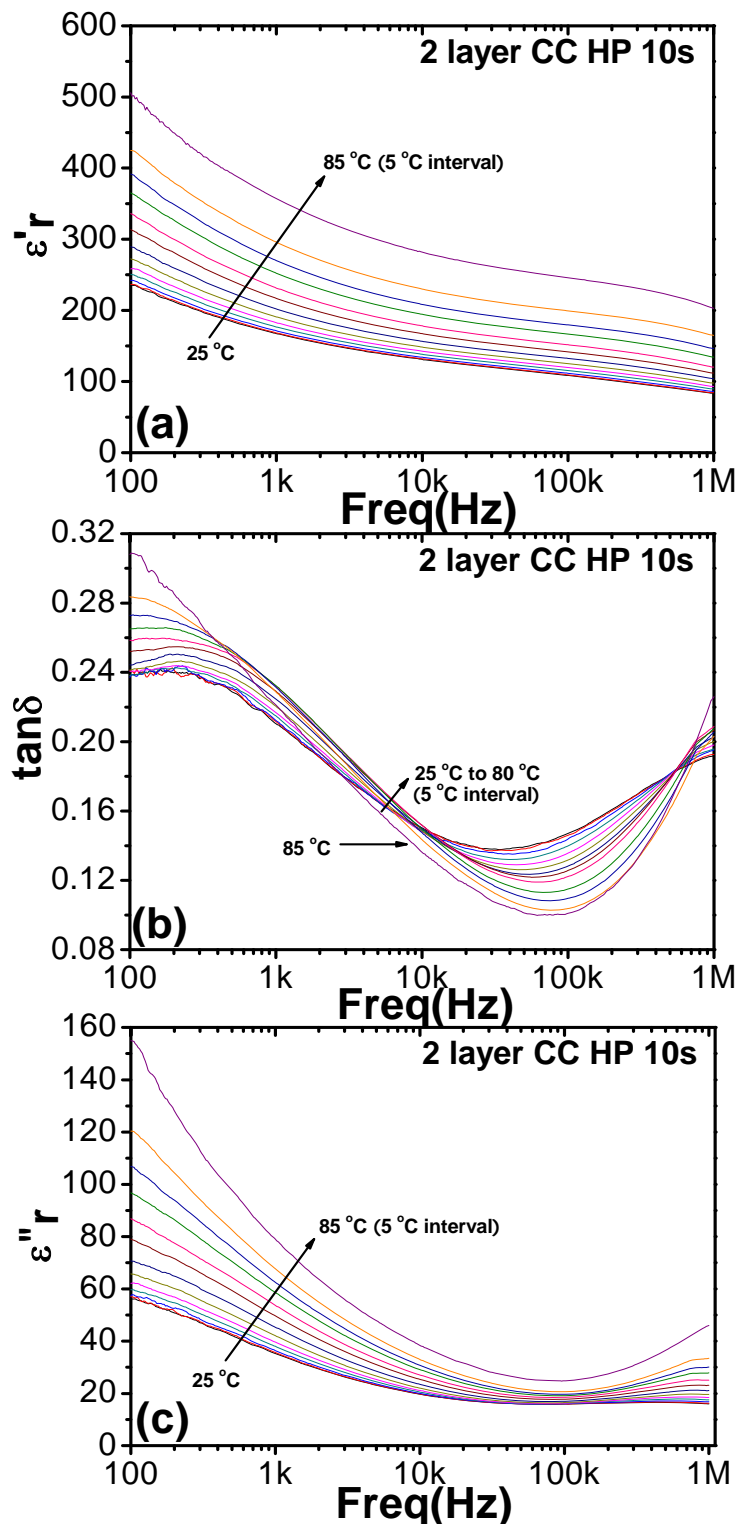


Figure 4-46 Dielectric response vs. frequency: (a) ϵ'_r vs. frequency, (b) $\tan \delta$ vs. frequency, (c) ϵ''_r vs. frequency of 2 layer 10s CC HP $\text{CaCu}_3\text{Ti}_4\text{O}_{12}/\text{P}(\text{VDF-TrFE})$ composite with 50 vol% $\text{CaCu}_3\text{Ti}_4\text{O}_{12}$ powder.

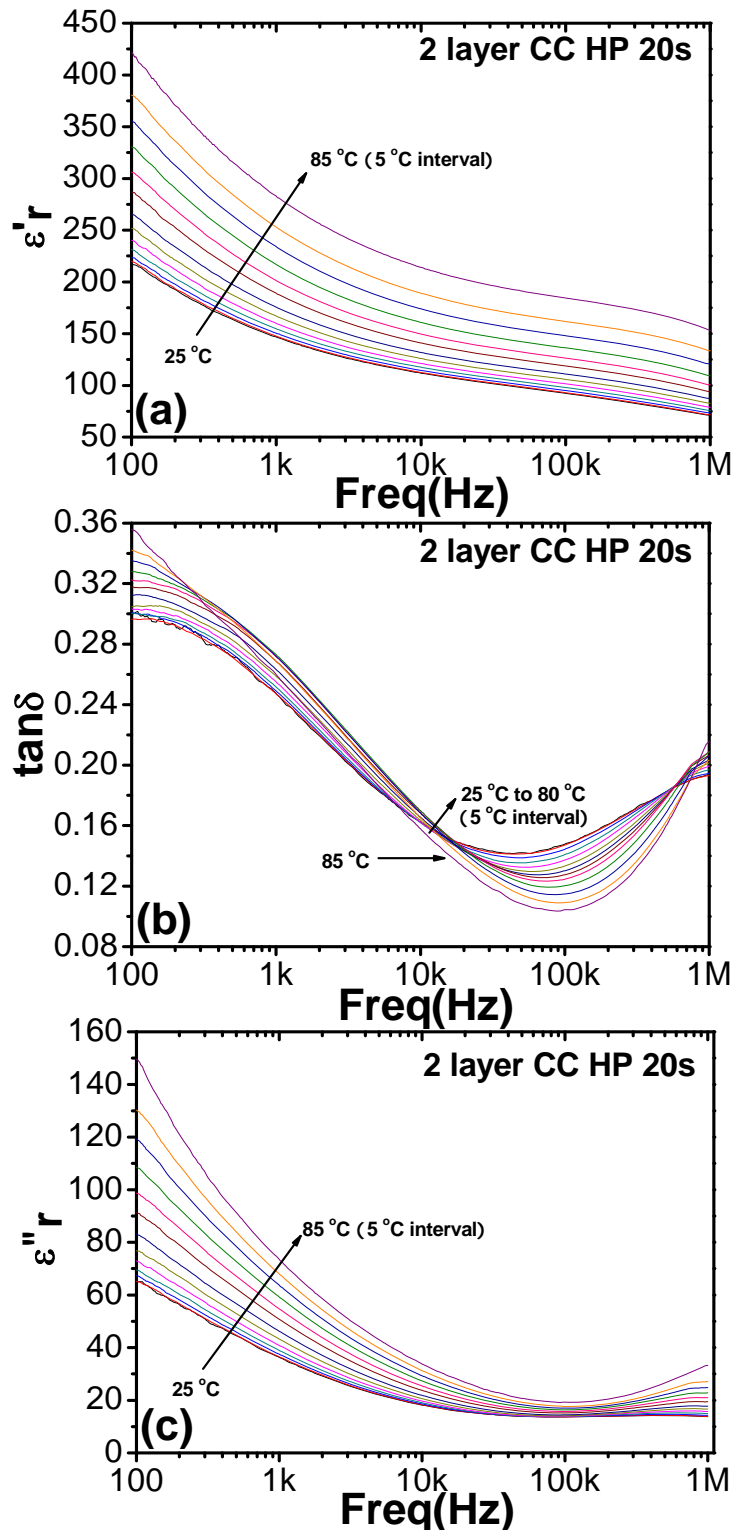


Figure 4-47 Dielectric response vs. frequency: (a) ϵ'_r vs. frequency, (b) $\tan \delta$ vs. frequency, (c) ϵ''_r vs. frequency of 2 layer 20s CC HP $\text{CaCu}_3\text{Ti}_4\text{O}_{12}/\text{P}(\text{VDF-TrFE})$ composite with 50 vol% $\text{CaCu}_3\text{Ti}_4\text{O}_{12}$ powder.

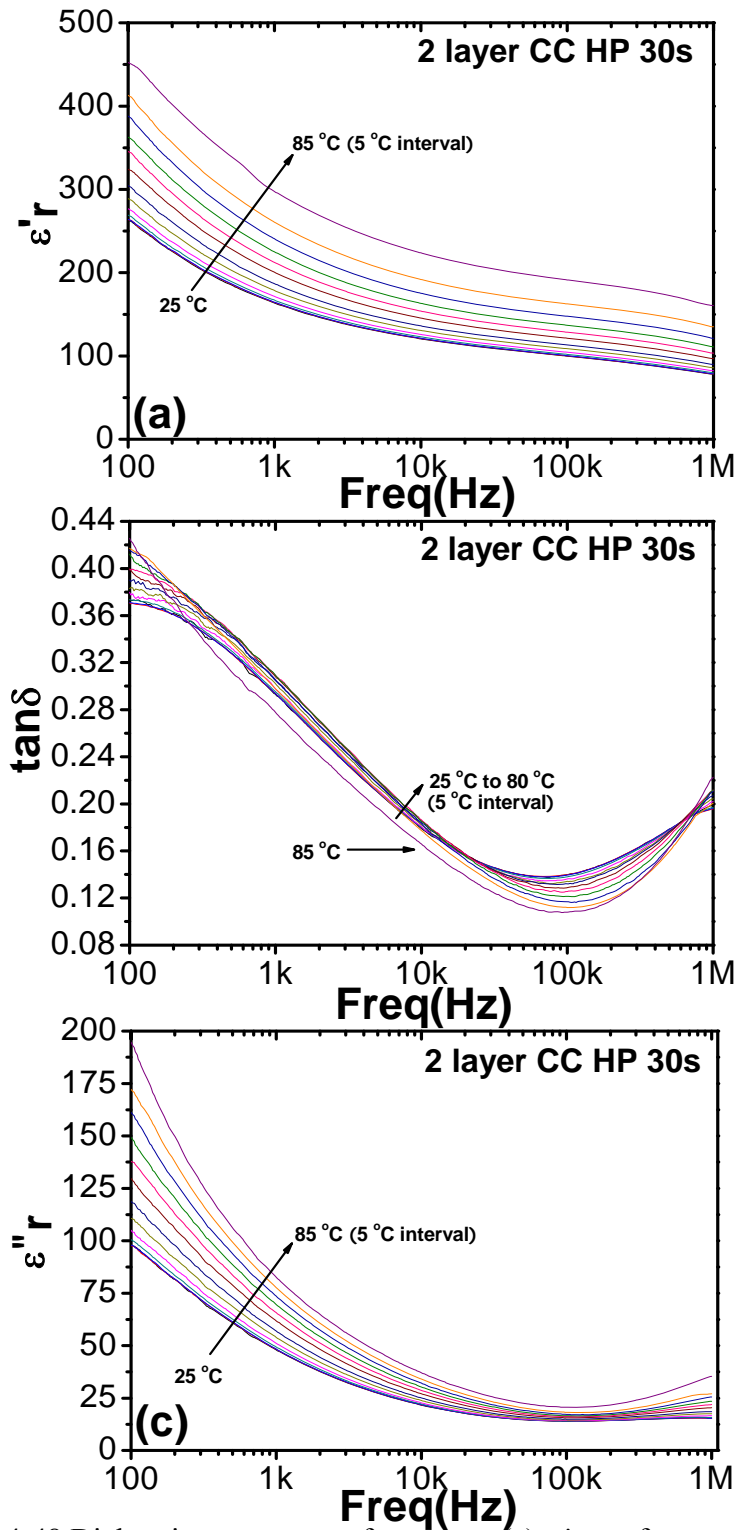


Figure 4-48 Dielectric response vs. frequency: (a) ϵ'_r vs. frequency, (b) $\tan \delta$ vs. frequency, (c) ϵ''_r vs. frequency of 2 layer 30s CC HP $\text{CaCu}_3\text{Ti}_4\text{O}_{12}/\text{P}(\text{VDF-TrFE})$ composite with 50 vol% $\text{CaCu}_3\text{Ti}_4\text{O}_{12}$ powder.

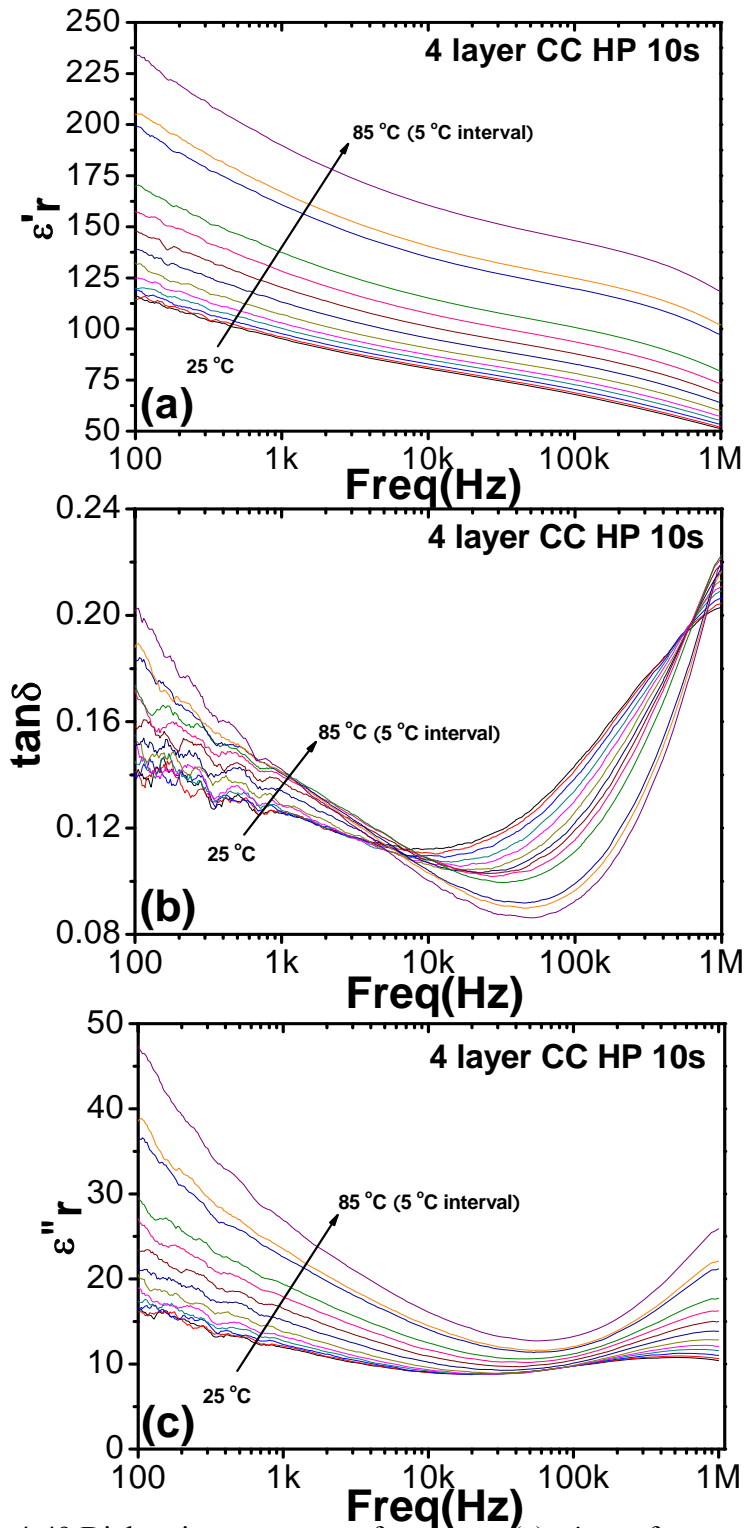


Figure 4-49 Dielectric response vs. frequency: (a) ϵ'_r vs. frequency, (b) $\tan \delta$ vs. frequency, (c) ϵ''_r vs. frequency of 4 layer 10s CC HP $\text{CaCu}_3\text{Ti}_4\text{O}_{12}/\text{P}(\text{VDF-TrFE})$ composite with 50 vol% $\text{CaCu}_3\text{Ti}_4\text{O}_{12}$ powder.

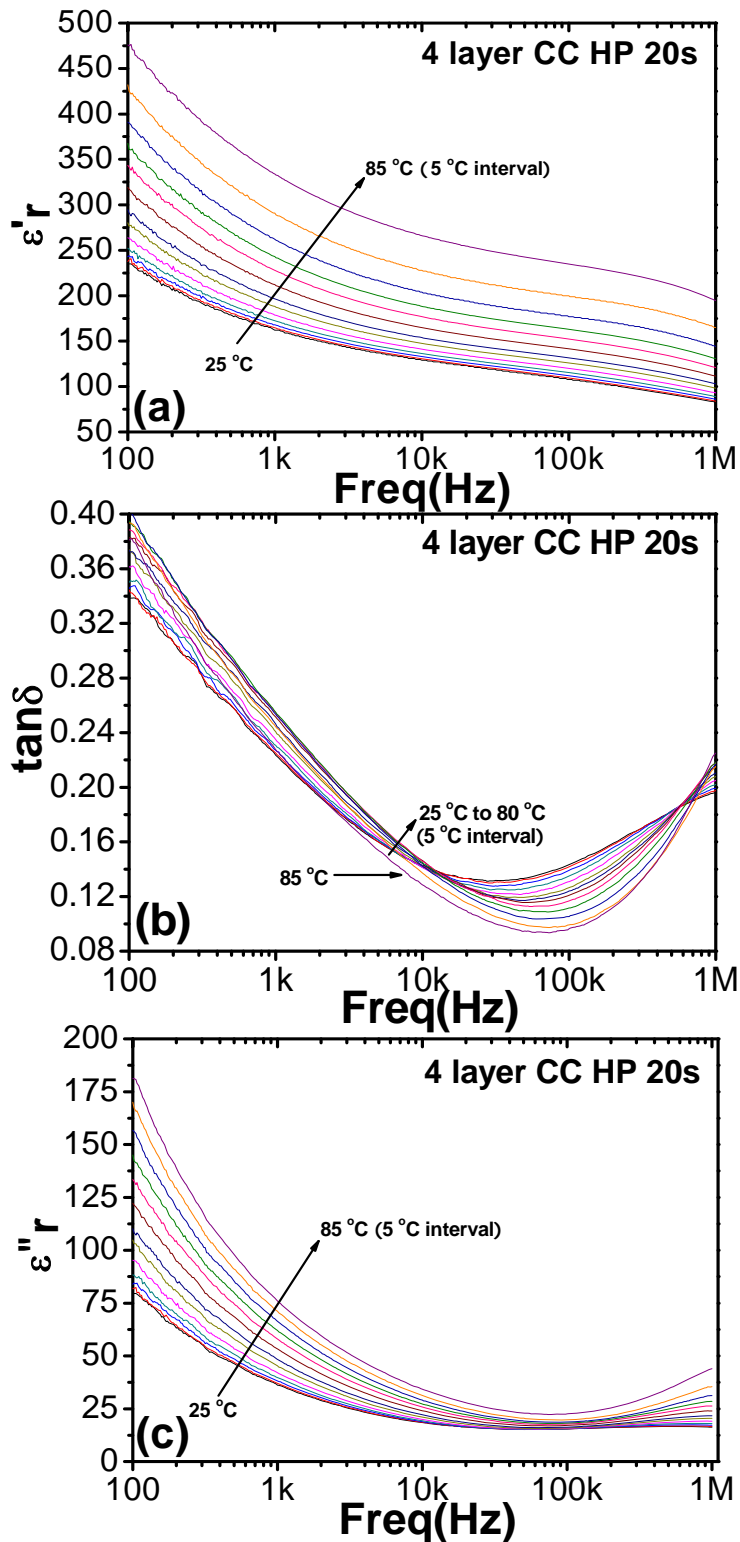


Figure 4-50 Dielectric response vs. frequency: (a) ϵ'_r vs. frequency, (b) $\tan \delta$ vs. frequency, (c) ϵ''_r vs. frequency of 4 layer 20s CC HP $\text{CaCu}_3\text{Ti}_4\text{O}_{12}/\text{P}(\text{VDF-TrFE})$ composite with 50 vol% $\text{CaCu}_3\text{Ti}_4\text{O}_{12}$ powder.

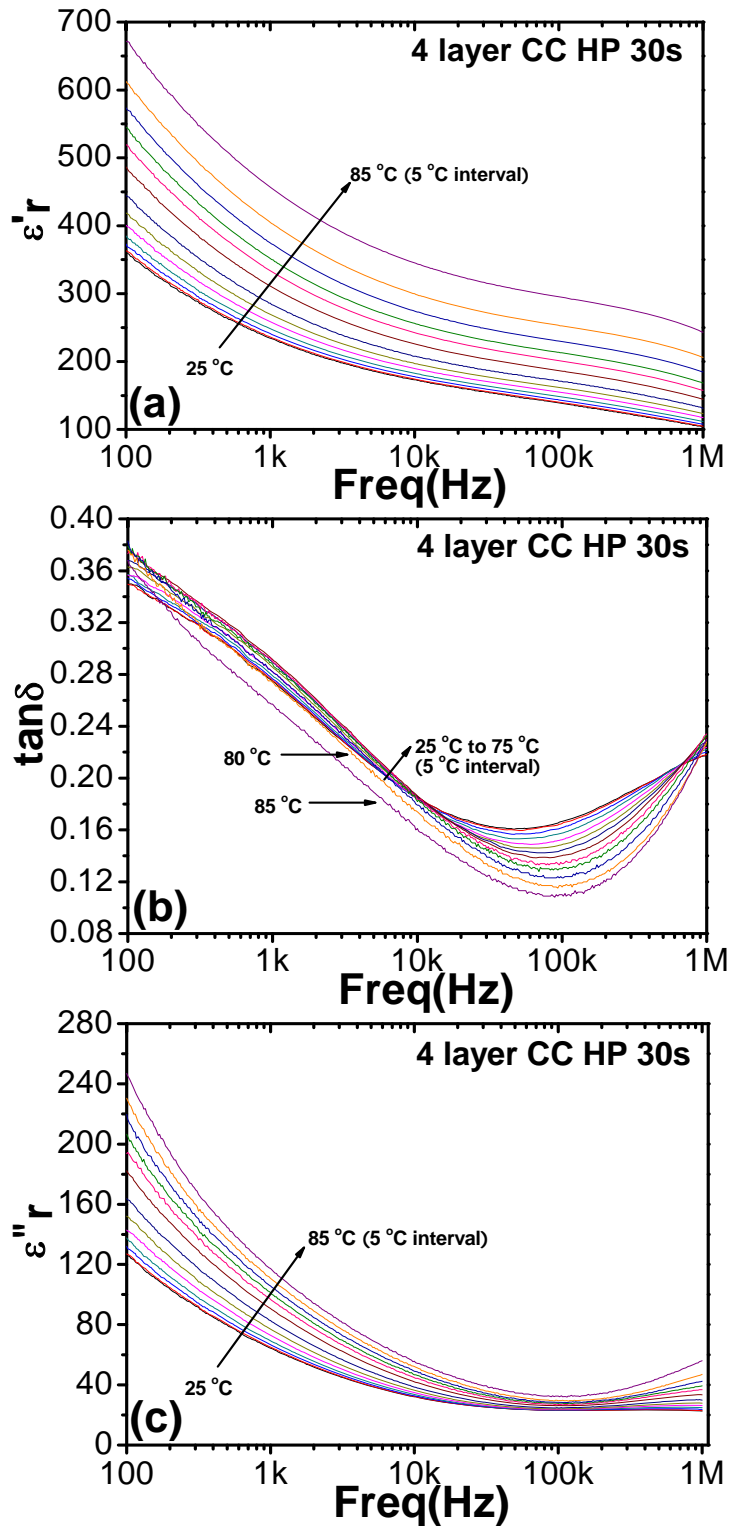


Figure 4-51 Dielectric response vs. frequency: (a) ϵ'_r vs. frequency, (b) $\tan \delta$ vs. frequency, (c) ϵ''_r vs. frequency of 4 layer 30s CC HP $\text{CaCu}_3\text{Ti}_4\text{O}_{12}/\text{P}(\text{VDF-TrFE})$ composite with 50 vol% $\text{CaCu}_3\text{Ti}_4\text{O}_{12}$ powder.

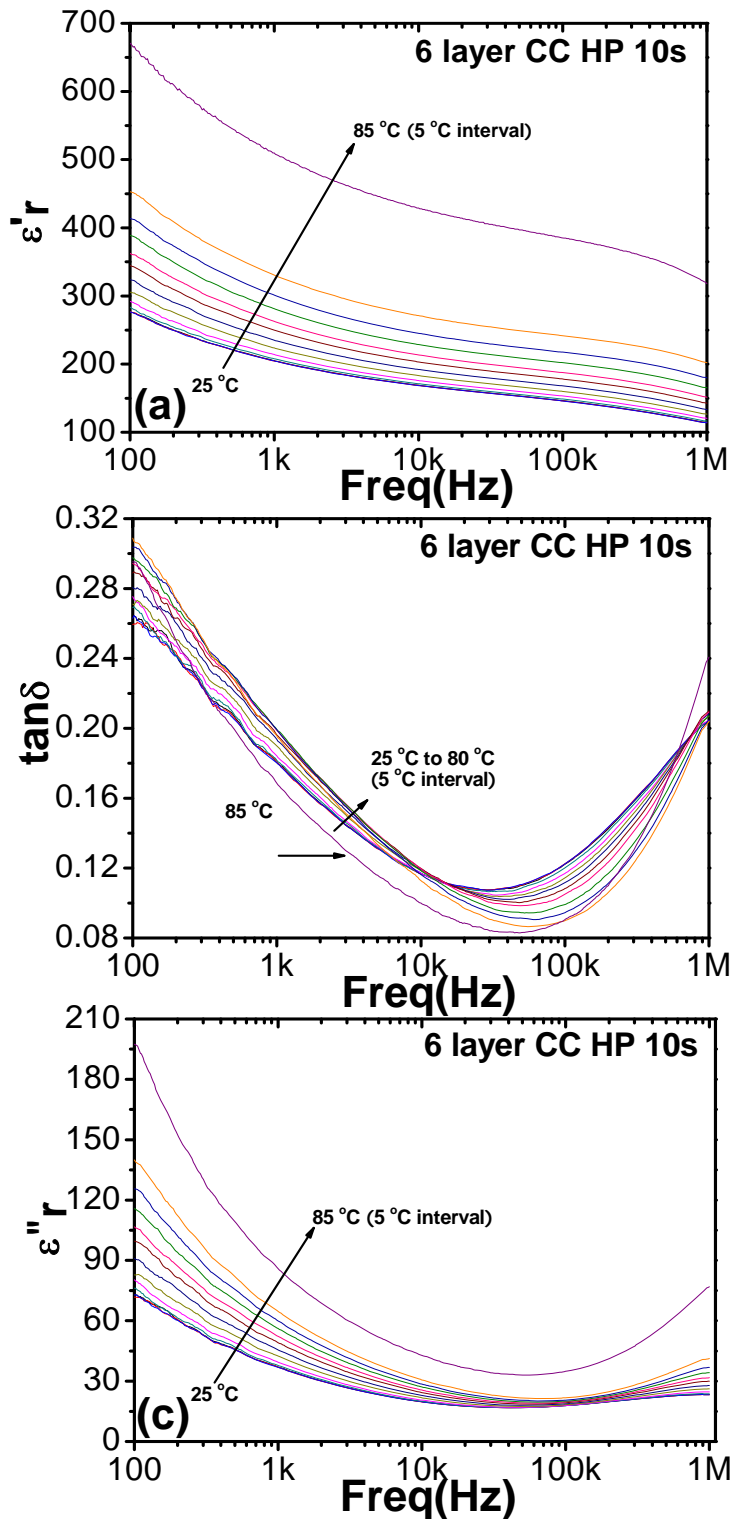


Figure 4-52 Dielectric response vs. frequency: (a) ϵ' , vs. frequency, (b) $\tan \delta$ vs. frequency, (c) ϵ'' , vs. frequency of 6 layer 10s CC HP $\text{CaCu}_3\text{Ti}_4\text{O}_{12}/\text{P}(\text{VDF-TrFE})$ composite with 50 vol% $\text{CaCu}_3\text{Ti}_4\text{O}_{12}$ powder.

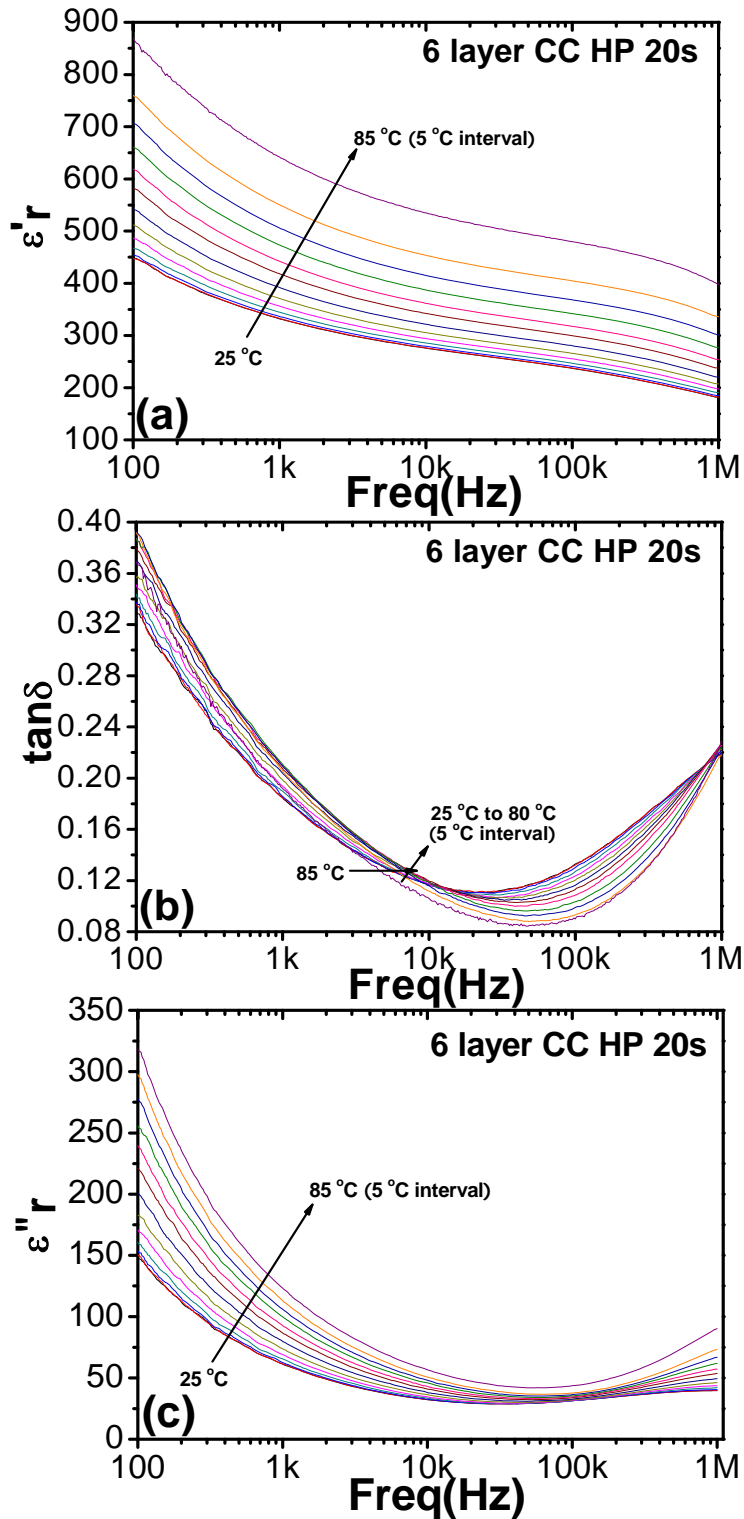


Figure 4-53 Dielectric response vs. frequency: (a) ϵ'_r vs. frequency, (b) $\tan \delta$ vs. frequency, (c) ϵ''_r vs. frequency of 6 layer 20s CC HP $\text{CaCu}_3\text{Ti}_4\text{O}_{12}/\text{P}(\text{VDF-TrFE})$ composite with 50 vol% $\text{CaCu}_3\text{Ti}_4\text{O}_{12}$ powder.

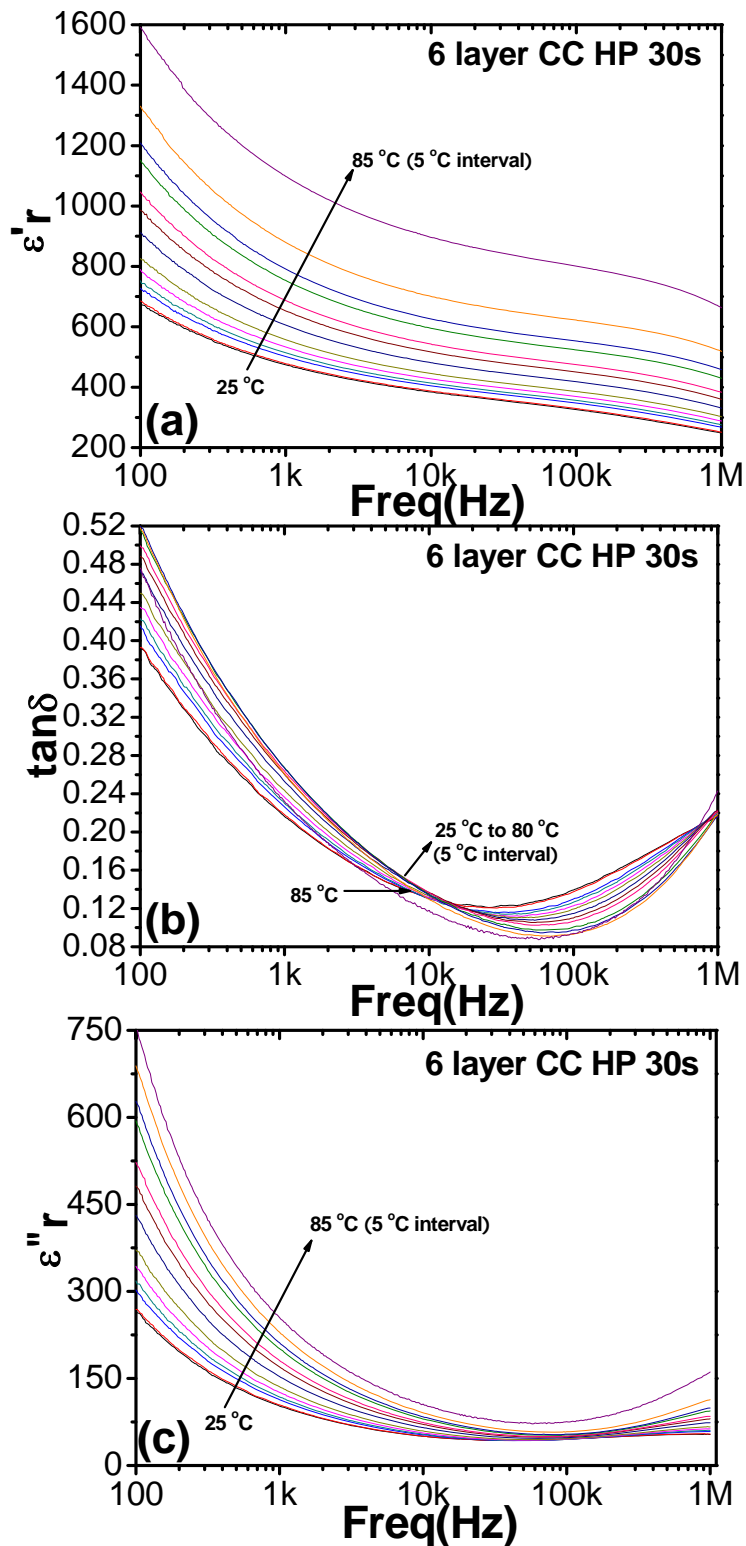


Figure 4-54 Dielectric response vs. frequency: (a) ϵ'_r vs. frequency, (b) $\tan \delta$ vs. frequency, (c) ϵ''_r vs. frequency of 6 layer 30s CC HP $\text{CaCu}_3\text{Ti}_4\text{O}_{12}/\text{P}(\text{VDF-TrFE})$ composite with 50 vol% $\text{CaCu}_3\text{Ti}_4\text{O}_{12}$ powder.

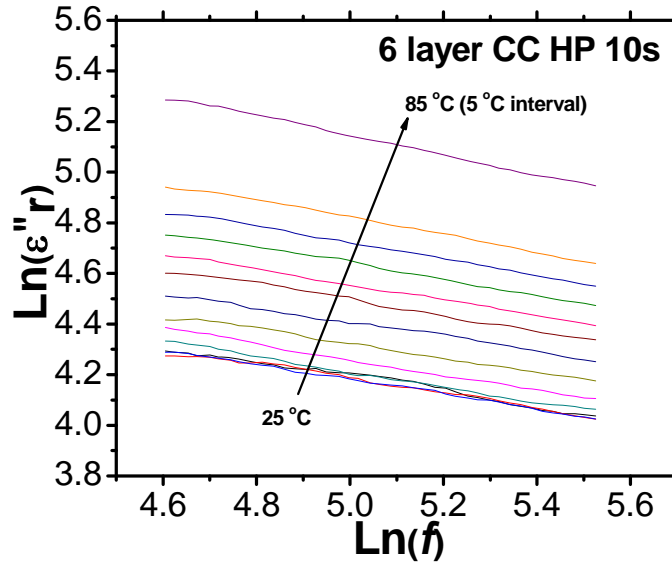


Figure 4-55 The relationship of $Ln(\epsilon''_r)$ vs. $Ln(f)$ of 6 layer 10s CC HP $\text{CaCu}_3\text{Ti}_4\text{O}_{12}/\text{P}(\text{VDF-TrFE})$ composite with 50 vol% $\text{CaCu}_3\text{Ti}_4\text{O}_{12}$ powder.

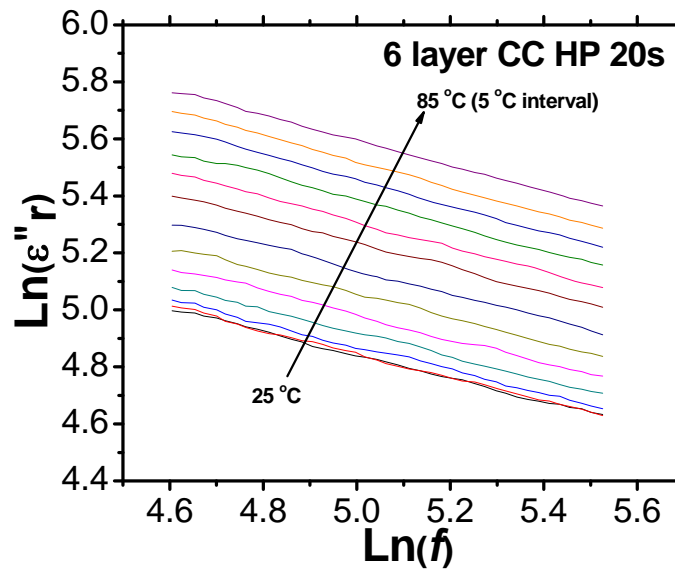


Figure 4-56 The relationship of $Ln(\epsilon''_r)$ vs. $Ln(f)$ of 6 layer 20s CC HP $\text{CaCu}_3\text{Ti}_4\text{O}_{12}/\text{P}(\text{VDF-TrFE})$ composite with 50 vol% $\text{CaCu}_3\text{Ti}_4\text{O}_{12}$ powder.

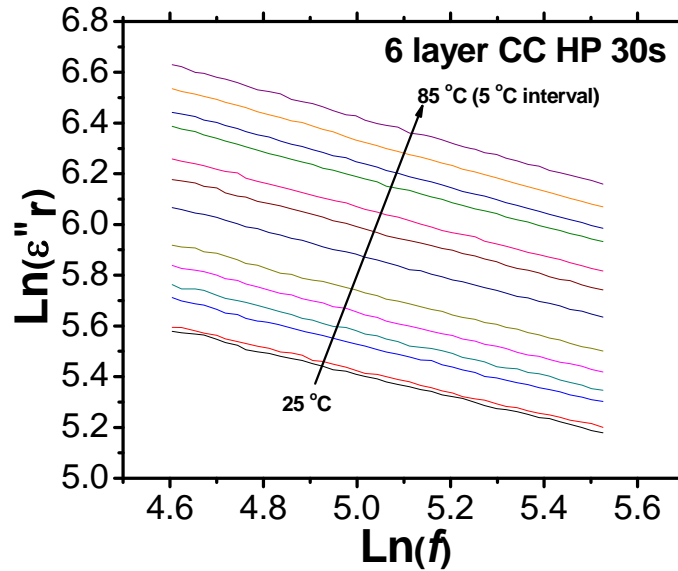


Figure 4-57 The relationship of $\text{Ln}(\varepsilon''_r)$ vs. $\text{Ln}(f)$ of 6 layer 30s CC HP $\text{CaCu}_3\text{Ti}_4\text{O}_{12}/\text{P}(\text{VDF-TrFE})$ composite with 50 vol% $\text{CaCu}_3\text{Ti}_4\text{O}_{12}$ powder.

Table 4-10 Summary of fitting results for 6 layer $\text{CaCu}_3\text{Ti}_4\text{O}_{12}/\text{P}(\text{VDF-TrFE})$ composite with 50 vol% μ -size $\text{CaCu}_3\text{Ti}_4\text{O}_{12}$ powder after 10s CC HP.

	A	K	α	SD\pm	P
25 °C	5.656	0.292	0.708	0.01108	<0.0001
30 °C	5.611	0.285	0.715	0.00831	<0.0001
35 °C	5.645	0.293	0.707	0.00405	<0.0001
40 °C	5.729	0.303	0.697	0.00515	<0.0001
45 °C	5.804	0.308	0.692	0.00482	<0.0001
50 °C	5.740	0.283	0.717	0.00555	<0.0001
55 °C	5.813	0.281	0.719	0.00572	<0.0001
60 °C	6.048	0.310	0.690	0.00628	<0.0001
65 °C	6.080	0.304	0.696	0.00343	<0.0001
70 °C	6.222	0.316	0.684	0.00507	<0.0001
75 °C	6.331	0.322	0.678	0.00417	<0.0001
80 °C	6.518	0.339	0.661	0.00525	<0.0001
85 °C	7.092	0.389	0.611	0.00447	<0.0001
AVE	6.022	0.310	0.690	0.00564	<0.0001

Table 4-11 Summary of fitting results for 6 layer $\text{CaCu}_3\text{Ti}_4\text{O}_{12}/\text{P}(\text{VDF}-\text{TrFE})$ composite with 50 vol% μ -size $\text{CaCu}_3\text{Ti}_4\text{O}_{12}$ powder after 20s CC HP.

	A	K	α	SD\pm	P
25 °C	6.883	0.408	0.592	0.00446	<0.0001
30 °C	6.914	0.413	0.587	0.00475	<0.0001
35 °C	6.928	0.411	0.589	0.00480	<0.0001
40 °C	6.984	0.413	0.587	0.00406	<0.0001
45 °C	7.094	0.422	0.578	0.00565	<0.0001
50 °C	7.141	0.417	0.583	0.00448	<0.0001
55 °C	7.261	0.424	0.576	0.00500	<0.0001
60 °C	7.395	0.431	0.569	0.00392	<0.0001
65 °C	7.517	0.441	0.559	0.00385	<0.0001
70 °C	7.591	0.441	0.559	0.00582	<0.0001
75 °C	7.725	0.453	0.547	0.00342	<0.0001
80 °C	7.799	0.455	0.545	0.00321	<0.0001
85 °C	7.811	0.443	0.557	0.00290	<0.0001
AVE	7.311	0.429	0.571	0.00433	<0.0001

Table 4-12 Summary of fitting results for 6 layer $\text{CaCu}_3\text{Ti}_4\text{O}_{12}/\text{P}(\text{VDF}-\text{TrFE})$ composite with 50 vol% μ -size $\text{CaCu}_3\text{Ti}_4\text{O}_{12}$ powder after 30s CC HP.

	A	K	α	SD\pm	P
25 °C	7.604	0.438	0.562	0.00357	<0.0001
30 °C	7.614	0.437	0.563	0.00339	<0.0001
35 °C	7.753	0.437	0.563	0.00340	<0.0001
40 °C	7.848	0.453	0.547	0.00442	<0.0001
45 °C	7.959	0.460	0.540	0.00377	<0.0001
50 °C	8.032	0.458	0.542	0.00356	<0.0001
55 °C	8.241	0.472	0.528	0.00251	<0.0001
60 °C	8.385	0.478	0.522	0.00304	<0.0001
65 °C	8.499	0.486	0.514	0.00271	<0.0001
70 °C	8.664	0.495	0.505	0.00230	<0.0001
75 °C	8.762	0.503	0.497	0.00185	<0.0001
80 °C	8.898	0.512	0.488	0.00245	<0.0001
85 °C	8.985	0.512	0.488	0.00334	<0.0001
AVE	8.249	0.472	0.527	0.00310	<0.0001

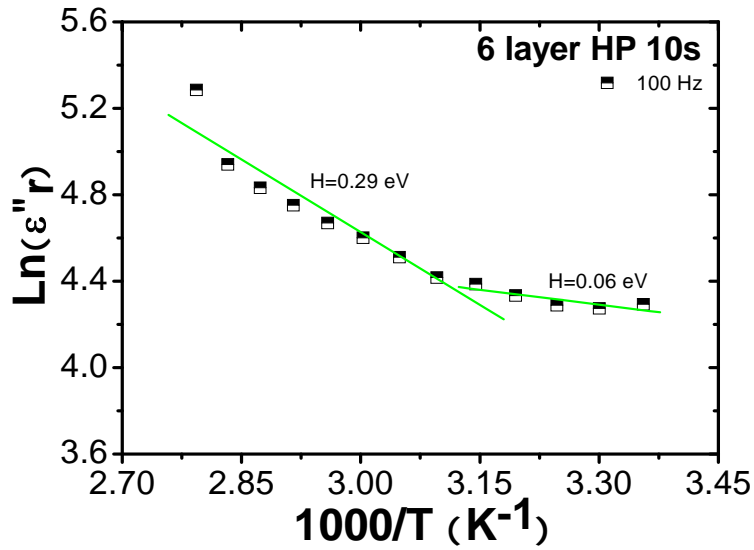


Figure 4-58 The relationship of $Ln(\epsilon''_r)$ vs. temperature of 6 layer 10s CC HP $CaCu_3Ti_4O_{12}/P(VDF-TrFE)$ composite with 50 vol% $CaCu_3Ti_4O_{12}$ powder.

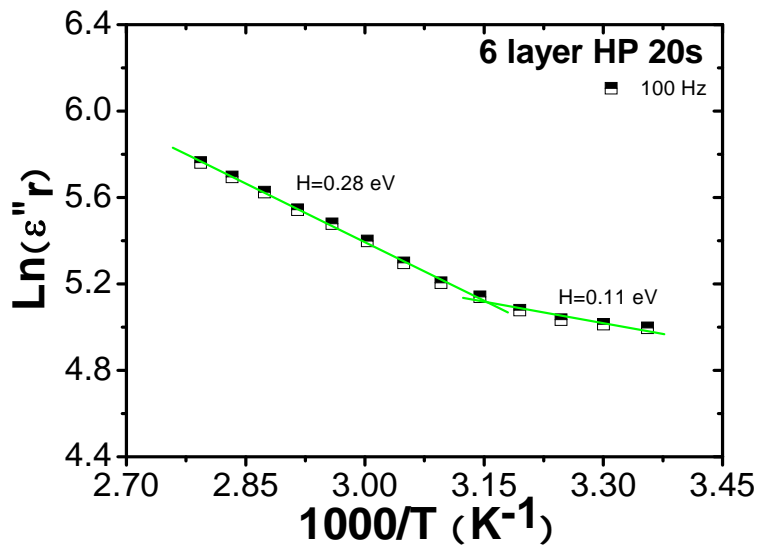


Figure 4-59 The relationship of $Ln(\epsilon''_r)$ vs. temperature of 6 layer 20s CC HP $CaCu_3Ti_4O_{12}/P(VDF-TrFE)$ composite with 50 vol% $CaCu_3Ti_4O_{12}$ powder.

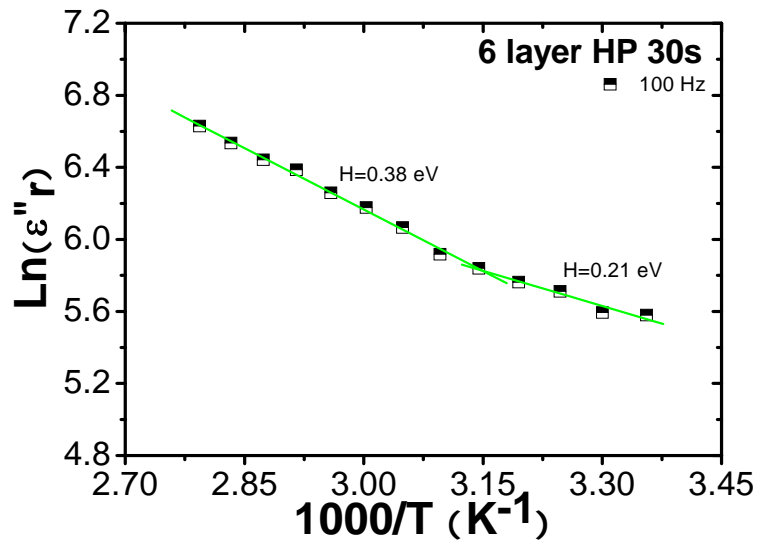


Figure 4-60 The relationship of $\text{Ln}(\epsilon''_r)$ vs. temperature of 6 layer 30s CC HP $\text{CaCu}_3\text{Ti}_4\text{O}_{12}/\text{P}(\text{VDF}-\text{TrFE})$ composite with 50 vol% $\text{CaCu}_3\text{Ti}_4\text{O}_{12}$ powder.

Table 4-13 Summary of activation energy for 6 layer $\text{CaCu}_3\text{Ti}_4\text{O}_{12}/\text{P}(\text{VDF}-\text{TrFE})$ composite with 50 vol% μ -size $\text{CaCu}_3\text{Ti}_4\text{O}_{12}$ powder after 10s, 20s, and 30s CC HP.

	Activation energy (eV)		
	6 layer HP 10s	6 layer HP 20s	6 layer HP 30s
25 ~45 °C (at 100 Hz)	0.06	0.11	0.21
45 ~85 °C (at 100 Hz)	0.29	0.28	0.38

4.3.3.5 Impedance Analysis

The relationship between the dielectric constant and loss of the CC hot pressed composite samples has been already discussed under different processings, such as hot pressing pattern and hot pressing time. Correspondingly, their complex permittivity plots ϵ'_r vs. ϵ''_r are shown in Figure 4-61 and 4-63. It is interesting to note besides the main relaxation process, a low frequency relaxation process is observed with up-right tail. This low-frequency process can be due to a heterogeneous relaxation process from the interface between the polymer matrix and $\text{CaCu}_3\text{Ti}_4\text{O}_{12}$ particle. The major relaxation process of the composites has been analyzed, and it was found that ϵ'_r vs. ϵ''_r plot can be well fitted using the Cole-Cole equation (4-1). The detail fitting summary is listed in Table 4-14 to 4-19.

Figure 4-61 shows the permittivity results of $\text{CaCu}_3\text{Ti}_4\text{O}_{12}/\text{P}(\text{VDF-TrFE})$ composites with 50 vol% $\text{CaCu}_3\text{Ti}_4\text{O}_{12}$ powder, which were hot pressed for two, four and six layers, respectively, with constant time such as 10, 20s and 30s. As the hot pressing time was set at 10s, the relaxation time τ decreased from 0.310 to 0.205 μs with increasing layers. When increasing from 20s and 30s, it exhibited a similar trend that relaxation time τ decreased from 0.325 to 0.159 μs and from 0.650 to 0.159 μs , respectively. Figure 4-62 illustrated the results of CC HP two, four and six layer $\text{CaCu}_3\text{Ti}_4\text{O}_{12}/\text{P}(\text{VDF-TrFE})$ composites with 50 vol% $\text{CaCu}_3\text{Ti}_4\text{O}_{12}$ powder, which were hot pressed for different time such as 10s, 20s and 30s, respectively. Corresponding to 10, 20 and 30s hot pressing, the relaxation time τ for two layer was 0.310, 0.325 and 0.650 μs respectively, and for four layer, it became 0.252, 0.179 and 0.504 μs . In both two and four layer hot pressing, they behaved in an increasing trend. However, it was found that the relaxation time τ for six layer was slightly decreasing from 0.20 to 0.16 μs . As it is known that less relaxation time τ means less polarization time, it could result in relative high dielectric constant at high frequency. Those fitting results indicated that multiple layers can uniformly distribute charge along the interface between ceramic and polymer layers and thus sample tends to give less polarization time. At the same time, it was found that only for six layers, hot pressing time can take effect. In Table 4-14 to 4-19, by considering the results in multiple layer HP samples at low $\text{CaCu}_3\text{Ti}_4\text{O}_{12}$ volume concentration such as 10 to 30 vol%, it was noted that one layer annealed samples

exhibited longer relaxation time τ , which varied from 0.2 to 0.3 μ s. At higher $\text{CaCu}_3\text{Ti}_4\text{O}_{12}$ volume concentration such as 40 and 50 vol%, less relaxation time τ can only take place with longer hot pressing time and extended multiple layers, which is very obviously for 50 vol%. In Figure 4-63, the relationship of the relaxation time vs. concentration for six layer HP 10s, 20s and 30s represented the similar trend that they have experienced a maximum value. This phenomenon is believed to be associated with a critical point which can reach structure optimization between ceramic and polymer matrix. All the results demonstrate that from the view of polarization time, hot pressing layer and its hot pressing time can arrange the charge distribution and then lead to fast response time and high dielectric constant at higher frequency.

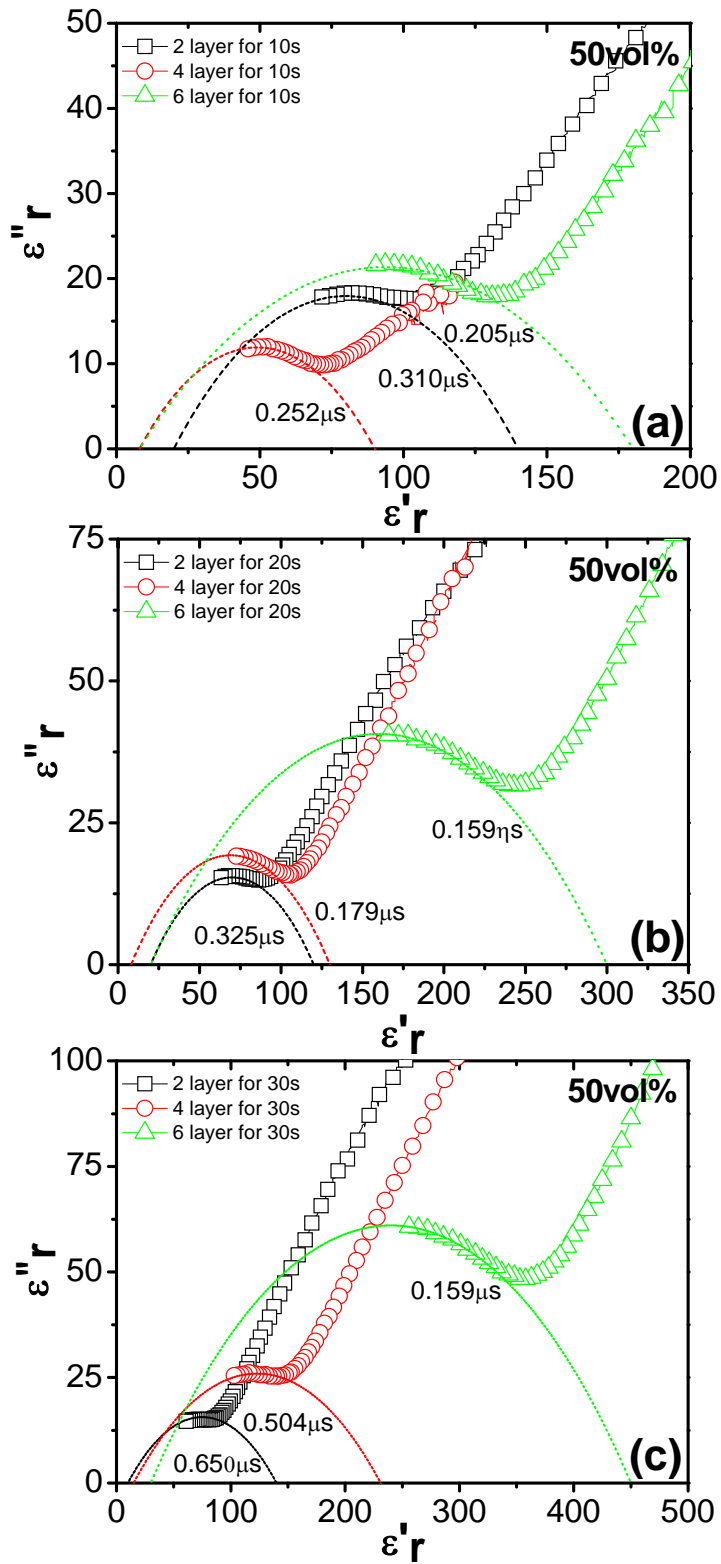


Figure 4-61 Cole-cole plot of the dielectric data of 2, 4 and 6 layer $\text{CaCu}_3\text{Ti}_4\text{O}_{12}/\text{P}(\text{VDF-TrFE})$ composite with 50 vol% $\text{CaCu}_3\text{Ti}_4\text{O}_{12}$ powder and HP for (a) 10s, (b) 20s and (c) 30s, respectively.

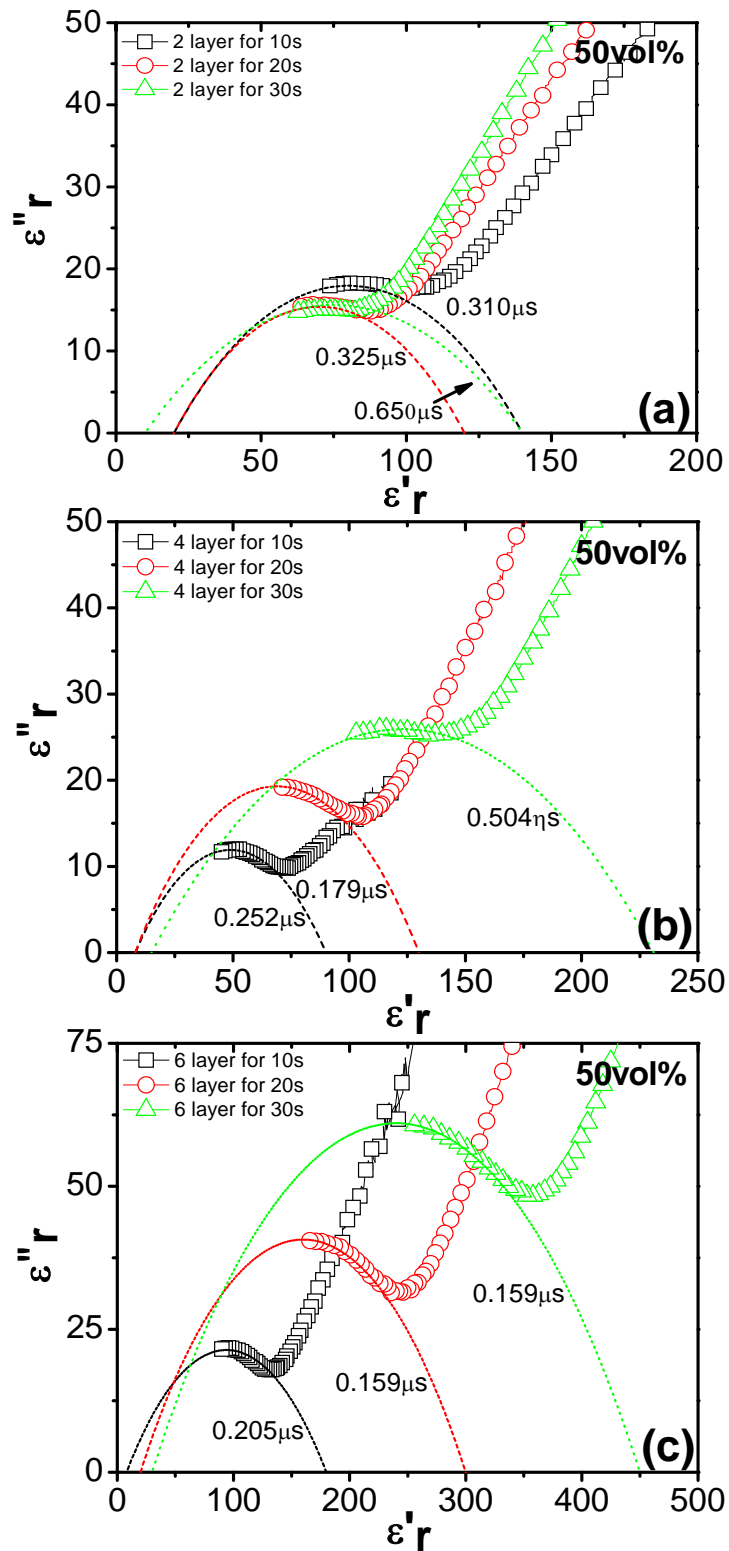


Figure 4-62 Cole-cole plot of the dielectric data of (a) 2 layer, (b) 4 layer and (c) 6 layer $\text{CaCu}_3\text{Ti}_4\text{O}_{12}/\text{P}(\text{VDF}-\text{TrFE})$ composite with 50vol% $\text{CaCu}_3\text{Ti}_4\text{O}_{12}$ powder and HP for 10s, 20s and 30s, respectively.

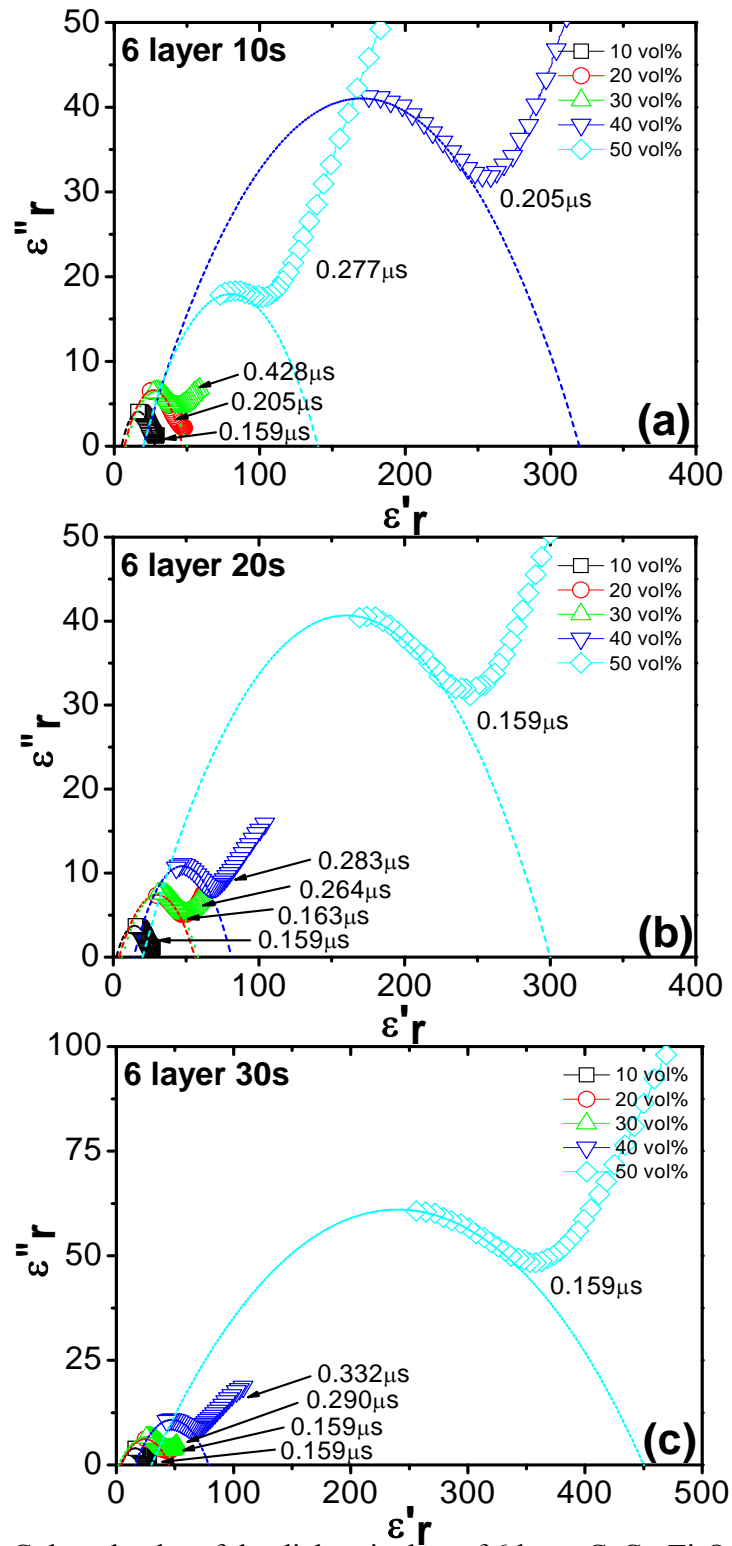


Figure 4-63 Cole-cole plot of the dielectric data of 6 layer $\text{CaCu}_3\text{Ti}_4\text{O}_{12}/\text{P}(\text{VDF}-\text{TrFE})$ composite with 10 to 50vol% $\text{CaCu}_3\text{Ti}_4\text{O}_{12}$ powder and HP for (a) 10s, (b) 20s and (c) 30s, respectively.

Table 4-14 Fitting results for 1 layer annealed $\text{CaCu}_3\text{Ti}_4\text{O}_{12}/\text{P}(\text{VDF}-\text{TrFE})$ composite with 10 to 50 vol% μ -size $\text{CaCu}_3\text{Ti}_4\text{O}_{12}$ powder.

	ϵ_{rs}	$\epsilon_{r\infty}$	$\Delta\epsilon (\epsilon_{rs}-\epsilon_{r\infty})$	α	$f(\text{Hz})$	$\tau (\mu\text{s})$
1 layer 10 vol%	26	5	31	0.54	501000	0.318
1 layer 20 vol%	35	5	30	0.58	490000	0.325
1 layer 30 vol%	45	5	40	0.61	479000	0.332
1 layer 40 vol%	102	7	95	0.65	427000	0.373
1 layer 50 vol%	68	5	63	0.63	501000	0.318

Table 4-15 Fitting results for 2, 4 and 6 layer annealed $\text{CaCu}_3\text{Ti}_4\text{O}_{12}/\text{P}(\text{VDF}-\text{TrFE})$ composite with 10 vol% μ -size $\text{CaCu}_3\text{Ti}_4\text{O}_{12}$ powder CC HP for 10, 20 and 30s.

	ϵ_{rs}	$\epsilon_{r\infty}$	$\Delta\epsilon (\epsilon_{rs}-\epsilon_{r\infty})$	α	$f(\text{Hz})$	$\tau (\mu\text{s})$
2 layer HP 10s	28	5	23	0.57	832000	0.193
2 layer HP 20s	26	4	22	0.57	977000	0.163
2 layer HP 30s	24	4	20	0.59	977000	0.163
4 layer HP 10s	28	4	24	0.59	1000000	0.159
4 layer HP 20s	27	4	23	0.59	1000000	0.159
4 layer HP 30s	27	4	23	0.58	1000000	0.159
6 layer HP 10s	27	4	23	0.57	1000000	0.159
6 layer HP 20s	27	2	25	0.63	1000000	0.159
6 layer HP 30s	28	4	26	0.59	1000000	0.159

Table 4-16 Fitting results for 2, 4 and 6 layer annealed $\text{CaCu}_3\text{Ti}_4\text{O}_{12}/\text{P}(\text{VDF-TrFE})$ composite with 20 vol% μ -size $\text{CaCu}_3\text{Ti}_4\text{O}_{12}$ powder CC HP for 10, 20 and 30s.

	ϵ_{rs}	$\epsilon_{r\infty}$	$\Delta\epsilon (\epsilon_{rs}-\epsilon_{r\infty})$	α	$f(\text{Hz})$	$\tau (\mu\text{s})$
2 layer HP 10s	47	7	40	0.59	447000	0.356
2 layer HP 20s	37	1	36	0.65	912000	0.175
2 layer HP 30s	29	1	28	0.64	1000000	0.159
4 layer HP 10s	38	3	35	0.63	1000000	0.159
4 layer HP 20s	39	5	34	0.62	933000	0.171
4 layer HP 30s	40	2	38	0.65	1000000	0.159
6 layer HP 10s	44	5	39	0.62	776000	0.205
6 layer HP 20s	56	4	52	0.65	977000	0.163
6 layer HP 30s	45	4	41	0.63	1000000	0.159

Table 4-17 Fitting results for 2, 4 and 6 layer annealed $\text{CaCu}_3\text{Ti}_4\text{O}_{12}/\text{P}(\text{VDF-TrFE})$ composite with 30 vol% μ -size $\text{CaCu}_3\text{Ti}_4\text{O}_{12}$ powder CC HP for 10, 20 and 30s.

	ϵ_{rs}	$\epsilon_{r\infty}$	$\Delta\epsilon (\epsilon_{rs}-\epsilon_{r\infty})$	α	$f(\text{Hz})$	$\tau (\mu\text{s})$
2 layer HP 10s	50	8	42	0.62	513000	0.310
2 layer HP 20s	47	5	42	0.63	575000	0.277
2 layer HP 30s	54	6	48	0.64	575000	0.277
4 layer HP 10s	54	8	46	0.60	427000	0.373
4 layer HP 20s	60	6	54	0.632	724000	0.220
4 layer HP 30s	61	6	55	0.639	741000	0.215
6 layer HP 10s	80	12	68	0.613	372000	0.428
6 layer HP 20s	58	6	52	0.636	603000	0.264
6 layer HP 30s	49	2	47	0.65	537000	0.290

Table 4-18 Fitting results for 2, 4 and 6 layer annealed $\text{CaCu}_3\text{Ti}_4\text{O}_{12}/\text{P}(\text{VDF-TrFE})$ composite with 40 vol% μ -size $\text{CaCu}_3\text{Ti}_4\text{O}_{12}$ powder CC HP for 10, 20 and 30s.

	ϵ_{rs}	$\epsilon_{r\infty}$	$\Delta\epsilon (\epsilon_{rs}-\epsilon_{r\infty})$	α	$f(\text{Hz})$	$\tau (\mu\text{s})$
2 layer HP 10s	320	20	300	0.66	1000000	0.159
2 layer HP 20s	320	20	300	0.64	>1000000	0.159
2 layer HP 30s	320	20	300	0.69	513000	0.310
4 layer HP 10s	60	8	52	0.68	1000000	0.159
4 layer HP 20s	230	8	222	0.675	832000	0.191
4 layer HP 30s	102	1	101	0.69	794000	0.201
6 layer HP 10s	108	13	95	0.619	575000	0.277
6 layer HP 20s	81	14	67	0.602	562000	0.283
6 layer HP 30s	79	16	63	0.58	479000	0.332

Table 4-19 Fitting results for 2, 4 and 6 layer annealed $\text{CaCu}_3\text{Ti}_4\text{O}_{12}/\text{P}(\text{VDF-TrFE})$ composite with 50 vol% μ -size $\text{CaCu}_3\text{Ti}_4\text{O}_{12}$ powder CC HP for 10, 20 and 30s.

	ϵ_{rs}	$\epsilon_{r\infty}$	$\Delta\epsilon (\epsilon_{rs}-\epsilon_{r\infty})$	α	$f(\text{Hz})$	$\tau (\mu\text{s})$
2 layer HP 10s	140	20	120	0.63	513000	0.310
2 layer HP 20s	120	20	100	0.62	490000	0.325
2 layer HP 30s	140	10	130	0.70	245000	0.650
4 layer HP 10s	90	8	82	0.64	631000	0.252
4 layer HP 20s	130	8	122	0.61	891000	0.179
4 layer HP 30s	231	15	216	0.70	316000	0.504
6 layer HP 10s	180	8	172	0.69	776000	0.205
6 layer HP 20s	300	20	280	0.64	1000000	0.159
6 layer HP 30s	450	30	420	0.64	1000000	0.159

4.3.4 P-E Hysteresis Loop

For dielectric materials, the polarization electric (P-E) hysteresis loop is a very useful material property since the loop is related to its energy storage ability. The polarization electric hysteresis loop can be expressed in terms of three parameters: coercive field (E_c), remnant polarization (P_r), and the saturated polarization (P_s) under external electric field. The P-E hysteresis loops of pure P(VDF-TrFE) copolymer are given in Figure 4-64 for reference. The decrease of polarization level and coercive field in the irradiated copolymer may be due to the introduction of defects into the polymer chains using high-energy radiation. The P-E loops of one layer $\text{CaCu}_3\text{Ti}_4\text{O}_{12}$ /P(VDF-TrFE) composite with 10 to 50 vol% $\text{CaCu}_3\text{Ti}_4\text{O}_{12}$ are shown in Figure 4-65 to 4-69, and those results for multiple layers, such as two, four and six layers after CC HP 10s, are shown in Figure 4-70 to 4-72.

In Figure 4-65 to 4-69, the $\text{CaCu}_3\text{Ti}_4\text{O}_{12}$ concentration played an important role on the break-down electric field for $\text{CaCu}_3\text{Ti}_4\text{O}_{12}$ /P(VDF-TrFE) composite. With the increasing of ceramic concentration from 10 to 50 vol%, the break-down electric field generally decreased from 47 MV/m to 1.1 MV/m. Besides the $\text{CaCu}_3\text{Ti}_4\text{O}_{12}$ concentration, it is clear that the remnant polarization (P_r) has been significantly influenced by the multiple layers, such as two to six layer. The remnant polarization (P_r) value of 0.04 C/m^2 decreased to 0.02 C/m^2 and the break-down electric field increased from 1.1 to 5.5 MV/m, as illustrated in Figure 4-69 and 4-70. In the four and six layer composites, as shown in Figure 4-71 and 4-72, the remnant polarization (P_r) exhibited the similar value of 0.04 C/cm^2 , while the break-down field decreased from 0.9 to 0.7 MV/m. Therefore, the significant effect of HP multiple layers on remnant polarization and break-down field was observed. A possible reason for this behavior may come from the polymer matrix, which contributes to the relaxor-ferroelectric behavior. Another possible reason, with high volume percentage of ceramic powder such as 50 vol%, the diminishing of the interface between polymer and ceramic can uniformly disperse the electric charge and avoid their accumulation on the interface to improve the break-down field. Thus, it is believed to be responsible for the decreasing of the remnant polarization (P_r) and improving of maximum electric field. Based on the polarization electric hysteresis, they have corroborated the statement that hot pressing layer plays an important role on the

dielectric response, which is consistent with the previous results such as annealing effect and hot pressing effect.

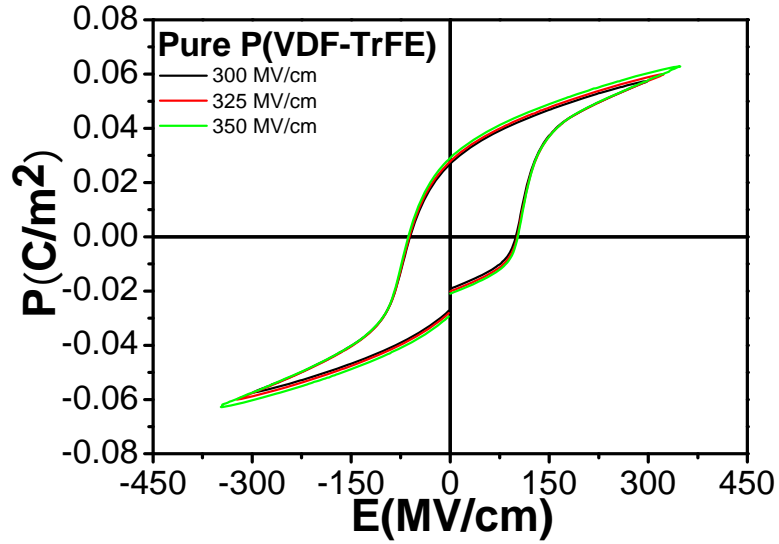


Figure 4-64 Polarization electric hysteresis loop for pure P(VDF-TrFE).

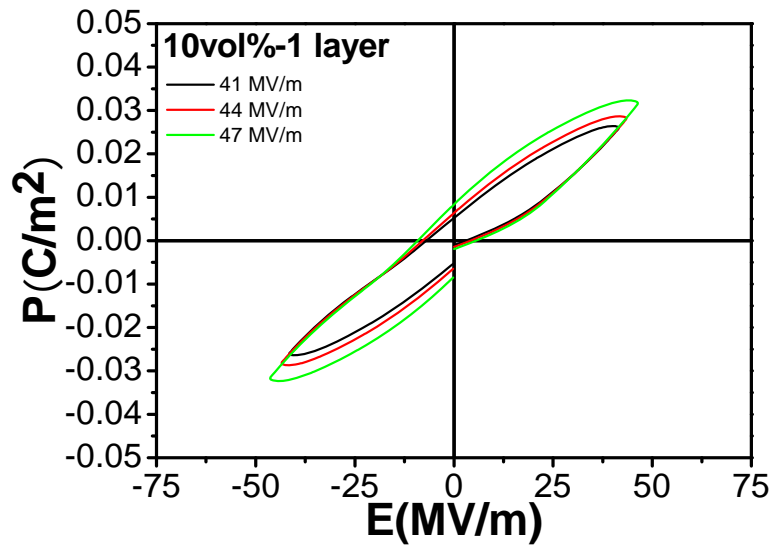


Figure 4-65 Polarization electric hysteresis loop for 1 layer $CaCu_3Ti_4O_{12}/P(VDF-TrFE)$ composites with 10 vol% $CaCu_3Ti_4O_{12}$ powder.

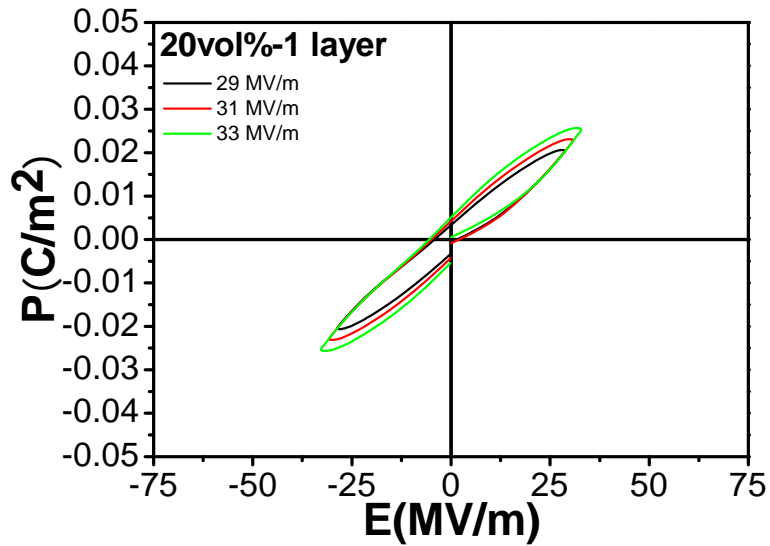


Figure 4-66 Polarization electric hysteresis loop for 1 layer $\text{CaCu}_3\text{Ti}_4\text{O}_{12}/\text{P}(\text{VDF}-\text{TrFE})$ composites with 20 vol% $\text{CaCu}_3\text{Ti}_4\text{O}_{12}$ powder.

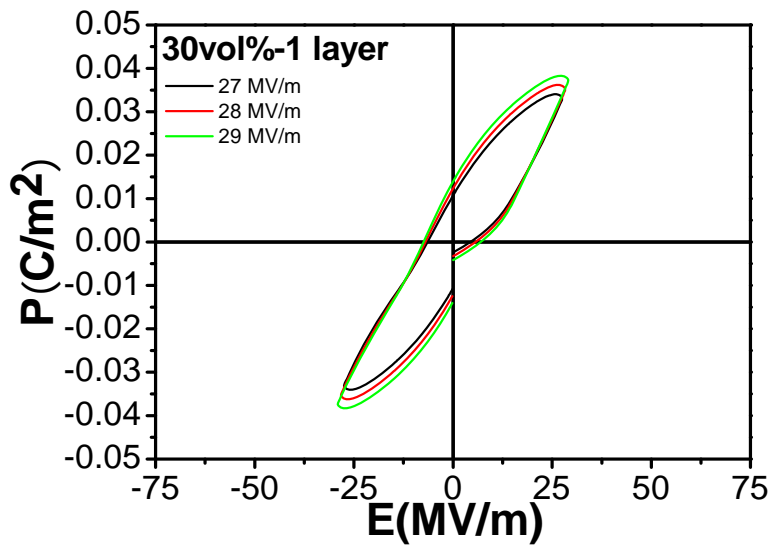


Figure 4-67 Polarization electric hysteresis loop for 1 layer $\text{CaCu}_3\text{Ti}_4\text{O}_{12}/\text{P}(\text{VDF}-\text{TrFE})$ composites with 30 vol% $\text{CaCu}_3\text{Ti}_4\text{O}_{12}$ powder.

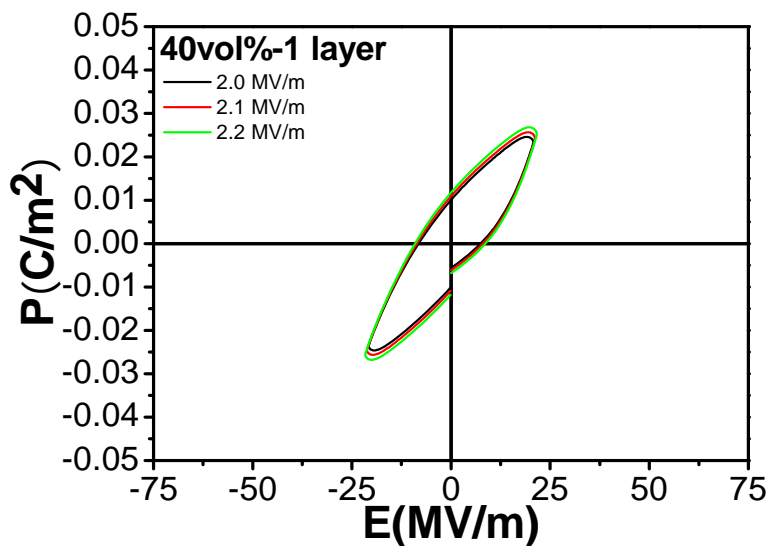


Figure 4-68 Polarization electric hysteresis loop for 1 layer $CaCu_3Ti_4O_{12}/P(VDF-TrFE)$ composites with 40 vol% $CaCu_3Ti_4O_{12}$ powder.

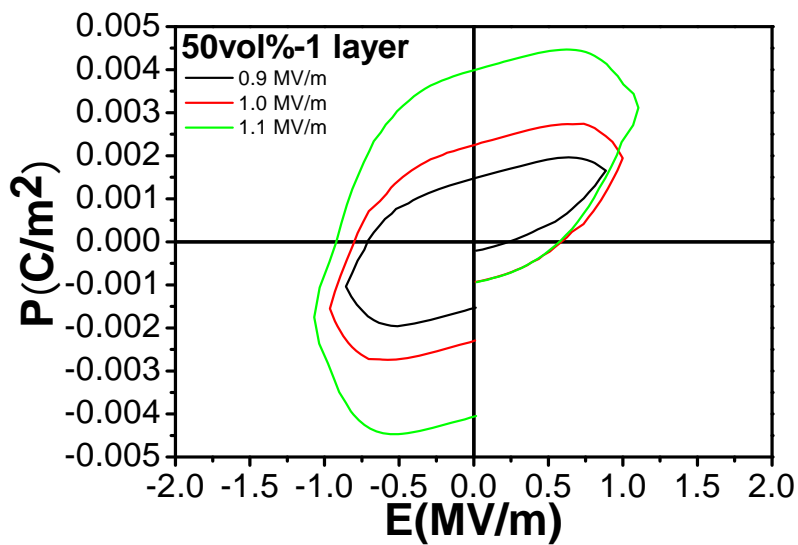


Figure 4-69 Polarization electric hysteresis loop for 1 layer $CaCu_3Ti_4O_{12}/P(VDF-TrFE)$ composites with 50 vol% $CaCu_3Ti_4O_{12}$ powder.

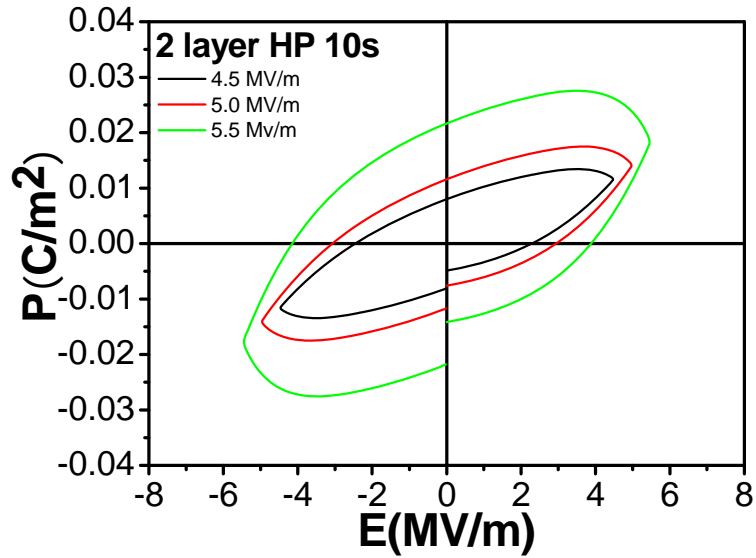


Figure 4-70 Polarization electric hysteresis loop for 2 layer $\text{CaCu}_3\text{Ti}_4\text{O}_{12}/\text{P}(\text{VDF}-\text{TrFE})$ composites with 50 vol% $\text{CaCu}_3\text{Ti}_4\text{O}_{12}$ powder using CC HP for 10s.

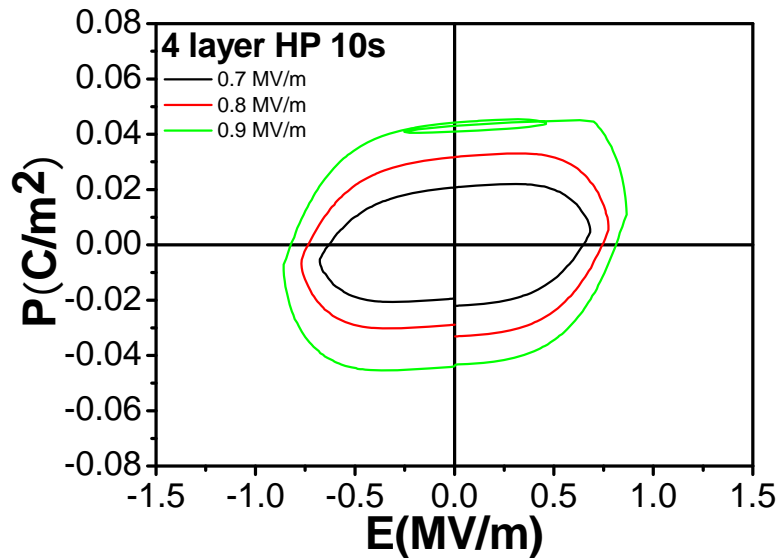


Figure 4-71 Polarization electric hysteresis loop for 4 layer $\text{CaCu}_3\text{Ti}_4\text{O}_{12}/\text{P}(\text{VDF}-\text{TrFE})$ composites with 50 vol% $\text{CaCu}_3\text{Ti}_4\text{O}_{12}$ powder using CC HP for 10s.

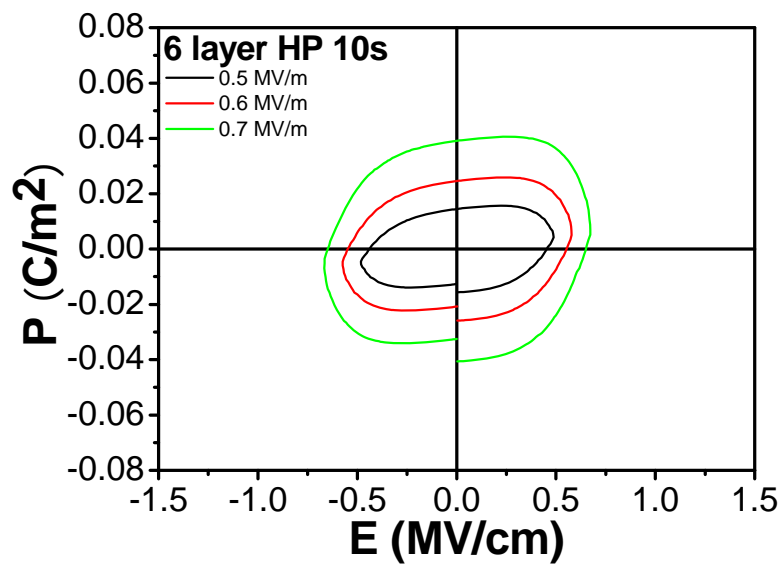


Figure 4-72 Polarization electric hysteresis loop for 6 layer $\text{CaCu}_3\text{Ti}_4\text{O}_{12}/\text{P}(\text{VDF-TrFE})$ composites with 50 vol% $\text{CaCu}_3\text{Ti}_4\text{O}_{12}$ powder using CC HP for 10s

4.3.5 Polymer Matrix Effect on Dielectric Behavior

The dielectric properties of $\text{CaCu}_3\text{Ti}_4\text{O}_{12}/\text{P}(\text{VDF-TrFE})$ composite have already been discussed previously. It is known that its dielectric properties vary with different processing, such as annealing, hot pressing, etc. However, none of the experiments involved the study of the influence of polymer matrix. In this work, polymer matrix, such as $\text{P}(\text{VDF-CTFE})$ 88/12 mol% (VC88), was introduced and its influence of polymer matrix will be witnessed.

4.3.5.1 Dielectric Behavior

As mentioned above, the dielectric properties of $\text{CaCu}_3\text{Ti}_4\text{O}_{12}/\text{VC88}$ composite will be studied in this work. The annealing effect on $\text{CaCu}_3\text{Ti}_4\text{O}_{12}/\text{VC88}$ composite was carried out with casting at $70\text{ }^\circ\text{C}/8$ hours and then annealing at $125\text{ }^\circ\text{C}/8$ hours. The volume concentration of $\text{CaCu}_3\text{Ti}_4\text{O}_{12}$ varies from 10 to 50. The dielectric results of one layer as-casted composite samples are shown in Figure 4-73 to 4-77. The summary of dielectric constant at 1 kHz is shown in Table 4-20.

Based on the results in Figure 4-73 to 4-77, it presented an increasing trend from 19 to 45 at 1 kHz for one layer as-casted sample. However, it was found that as for the as-annealed samples, there was a maximum peak of 35 at 30 vol%, which resemble the dielectric properties of one layer as-annealed $\text{CaCu}_3\text{Ti}_4\text{O}_{12}/\text{P}(\text{VDF-TrFE})$ sample, and is associated with crystallinity improvement. With careful observation, it was found that the overall dielectric property of an as-casted sample was generally better than as-annealed ones, as shown in Figure 4-78. It indicated that annealed treatment could only have limited effect on the $\text{CaCu}_3\text{Ti}_4\text{O}_{12}/\text{VC88}$ composite.

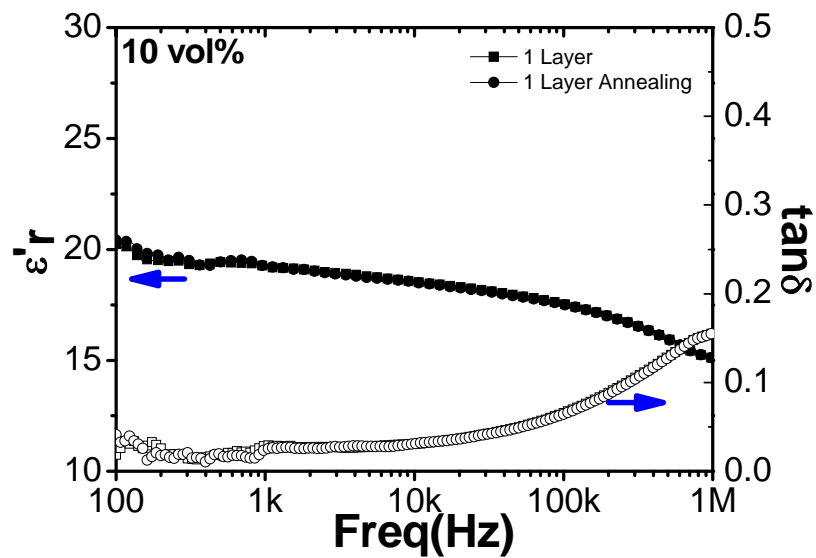


Figure 4-73 Dielectric response vs. frequency of 1 layer $\text{CaCu}_3\text{Ti}_4\text{O}_{12}/\text{VC88}$ composite (10 vol% μ -size $\text{CaCu}_3\text{Ti}_4\text{O}_{12}$) without annealing and with annealing.

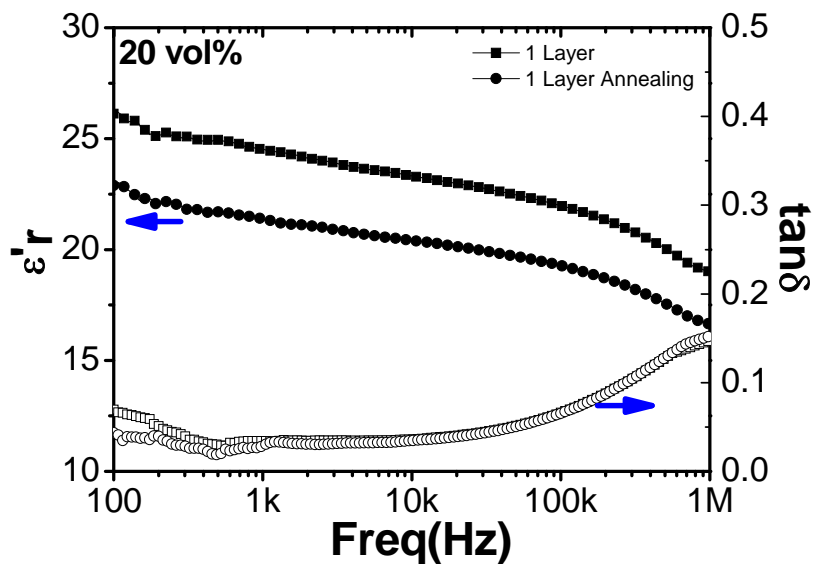


Figure 4-74 Dielectric response vs. frequency of 1 layer $\text{CaCu}_3\text{Ti}_4\text{O}_{12}/\text{VC88}$ composite (20 vol% μ -size $\text{CaCu}_3\text{Ti}_4\text{O}_{12}$) without annealing and with annealing.

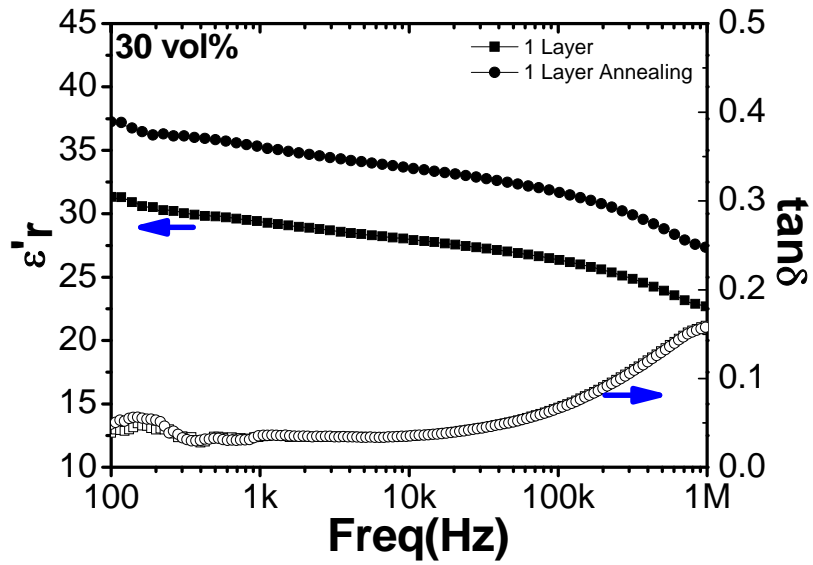


Figure 4-75 Dielectric response vs. frequency of 1 layer $\text{CaCu}_3\text{Ti}_4\text{O}_{12}/\text{VC88}$ composite (30 vol% μ -size $\text{CaCu}_3\text{Ti}_4\text{O}_{12}$) without annealing and with annealing.

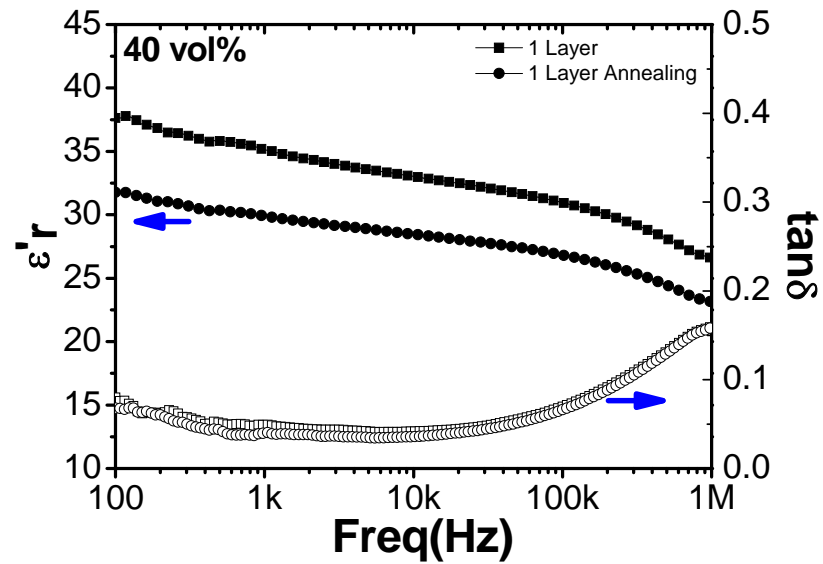


Figure 4-76 Dielectric response vs. frequency of 1 layer $\text{CaCu}_3\text{Ti}_4\text{O}_{12}/\text{VC88}$ composite (40 vol% μ -size $\text{CaCu}_3\text{Ti}_4\text{O}_{12}$) without annealing and with annealing.

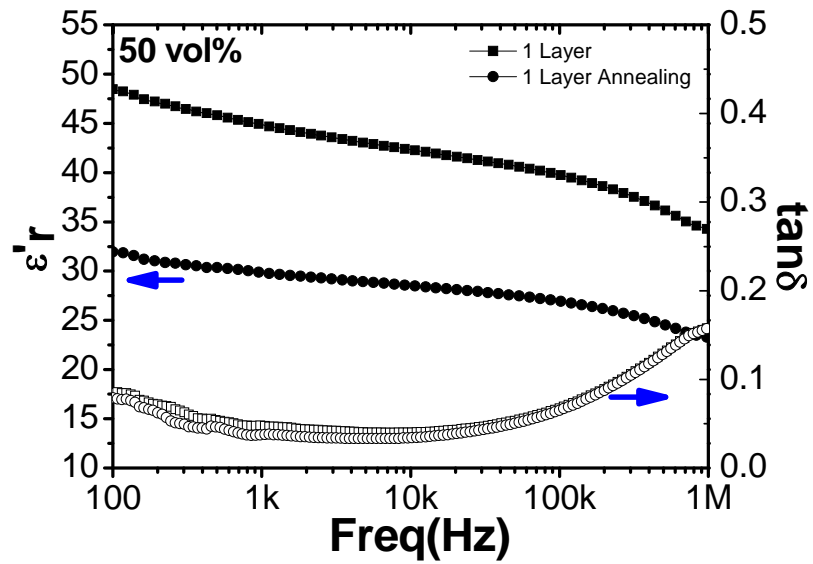


Figure 4-77 Dielectric response vs. frequency of 1 layer $\text{CaCu}_3\text{Ti}_4\text{O}_{12}/\text{VC88}$ composite (50 vol% μ -size $\text{CaCu}_3\text{Ti}_4\text{O}_{12}$) without annealing and with annealing.

Table 4-20 Summary of dielectric data for 1 layer $\text{CaCu}_3\text{Ti}_4\text{O}_{12}/\text{VC88}$ composite (μ -size $\text{CaCu}_3\text{Ti}_4\text{O}_{12}$) (1 kHz).

	$\text{CaCu}_3\text{Ti}_4\text{O}_{12}$ Concentration (vol%)				
	10 vol%	20 vol%	30 vol%	40 vol%	50 vol%
1 layer ^[1]	19/0.03	25/0.03	29/0.03	35/0.05	45/0.05
1 layer ^[2]	19/0.02	21/0.03	35/0.04	30/0.04	30/0.04

^[1]: Casting at 70°C/8 hrs.

^[2]: Casting at 70°C/8 hrs and annealing at 125 °C/8 hrs.

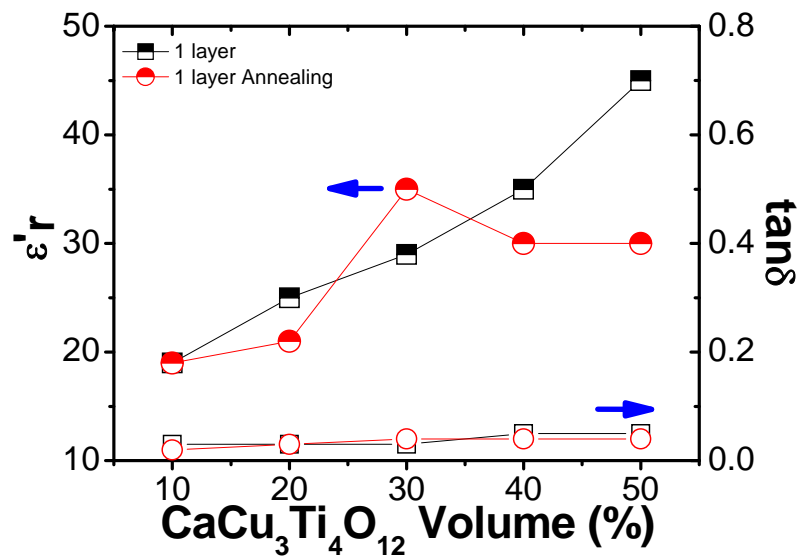


Figure 4-78 Dependence of dielectric response on $\text{CaCu}_3\text{Ti}_4\text{O}_{12}$ concentration (μ -size $\text{CaCu}_3\text{Ti}_4\text{O}_{12}$) for 1 layer $\text{CaCu}_3\text{Ti}_4\text{O}_{12}/\text{VC88}$ composite at room temperature.

4.3.5.2 Hot Pressing Effect

Figure 4-79 to 4-83 illustrate the dielectric response of $\text{CaCu}_3\text{Ti}_4\text{O}_{12}/\text{VC88}$ composite with CC HP. Since it is well discussed in Chapter 4 that CC HP process is more promising than PC HP, more studies about CC HP will be discussed in this work. $\text{CaCu}_3\text{Ti}_4\text{O}_{12}/\text{VC88}$ composite samples were hot pressed for two, four and six layers, and Table 4-21 lists their corresponding summary at 1 kHz.

Based on the those results in Figure 4-79 to 4-83, it shared the same trend in polymer matrix VC88 as well as in P(VDF-TrFE), when the volume concentration of $\text{CaCu}_3\text{Ti}_4\text{O}_{12}$ was as low as 10 and 20. Their differences in dielectric constant within different HP layers are very small. The reason is very straightforward: the polymer matrix with a relatively large proportion already has enough capability to accommodate the ceramic particle, and it can neutralize the influence of multiple layer to the microstructure, which is closely associated with the dielectric response. At the same time, it is observed that when the volume concentration of $\text{CaCu}_3\text{Ti}_4\text{O}_{12}$ exceeded 20, we find that the influence of multiple layers dominated, since there existed large portions of ceramic particle. For all the concentration from 30 to 50 vol%, maximum value happened with four layers CC HP. With CC HP, the best value is 151 for four layers CC HP, while the dielectric loss remained at 0.14, as shown in Figure 4-84. The dielectric results are very close with the results in $\text{CaCu}_3\text{Ti}_4\text{O}_{12}/\text{P}(\text{VDF-TrFE})$ composite, as seen in Table 4-2.

Figure 4-85 shows the SEM image of one layer $\text{CaCu}_3\text{Ti}_4\text{O}_{12}/\text{VC88}$ composite. According to the SEM image, its microstructure was very similar with the one in $\text{CaCu}_3\text{Ti}_4\text{O}_{12}/\text{P}(\text{VDF-TrFE})$ composites. It consisted of one ceramic layer and one thin polymer layers. However, with the CC HP, this obvious interface between ceramic and polymer layer disappeared when they were hot pressed for 10s with two, four and six layers, as seen in Figure 4-85. In comparison with Figure 4-85 and 4-86, it has corroborated their corresponding dielectric results.

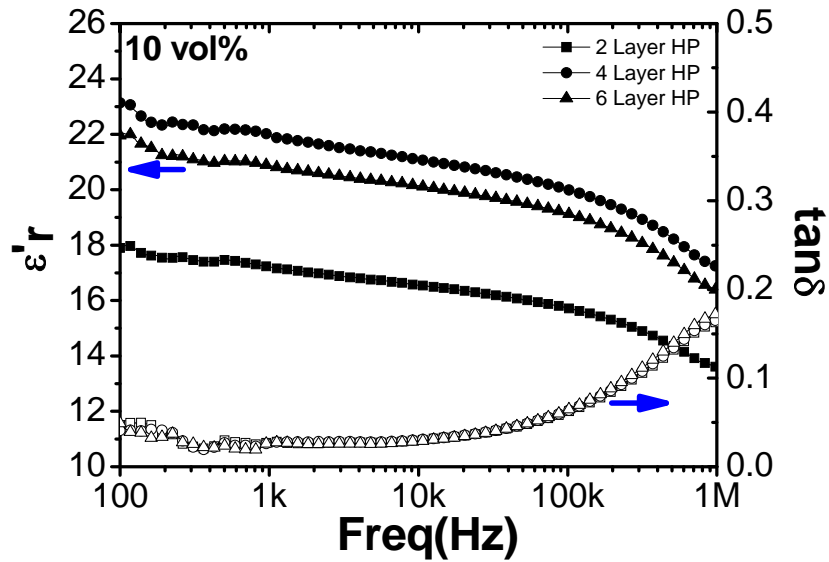


Figure 4-79 Dielectric response vs. frequency of multiple layers $\text{CaCu}_3\text{Ti}_4\text{O}_{12}$ /VC88 composite (10 vol% μ -size $\text{CaCu}_3\text{Ti}_4\text{O}_{12}$) with CC HP for 10s and annealing at 125 °C.

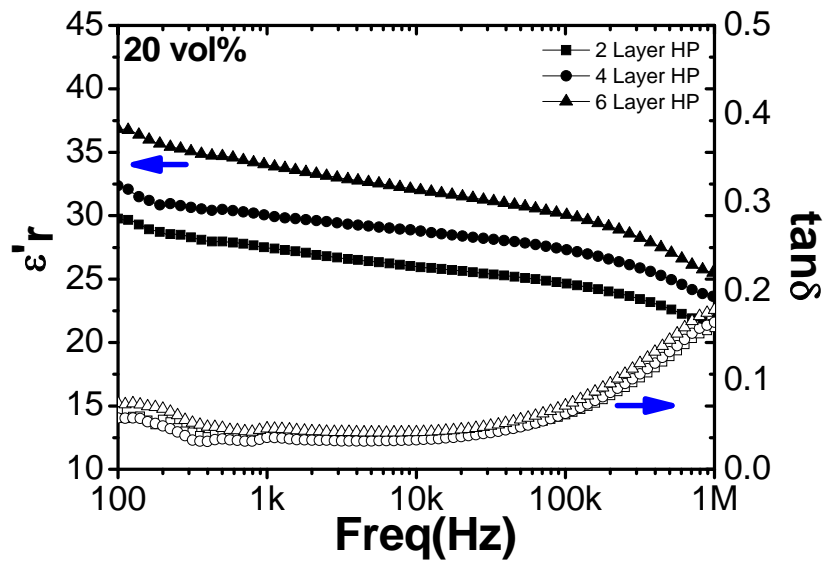


Figure 4-80 Dielectric response vs. frequency of multiple layers $\text{CaCu}_3\text{Ti}_4\text{O}_{12}$ /VC88 composite (20 vol% μ -size $\text{CaCu}_3\text{Ti}_4\text{O}_{12}$) with CC HP for 10s and annealing at 125 °C.

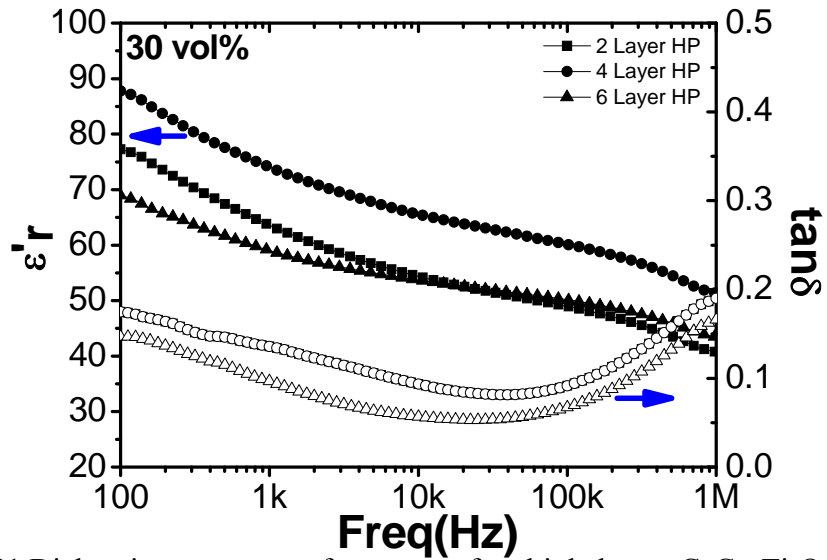


Figure 4-81 Dielectric response vs. frequency of multiple layers $\text{CaCu}_3\text{Ti}_4\text{O}_{12}/\text{VC88}$ composite (30 vol% μ -size $\text{CaCu}_3\text{Ti}_4\text{O}_{12}$) with CC HP for 10s and annealing at 125 °C.

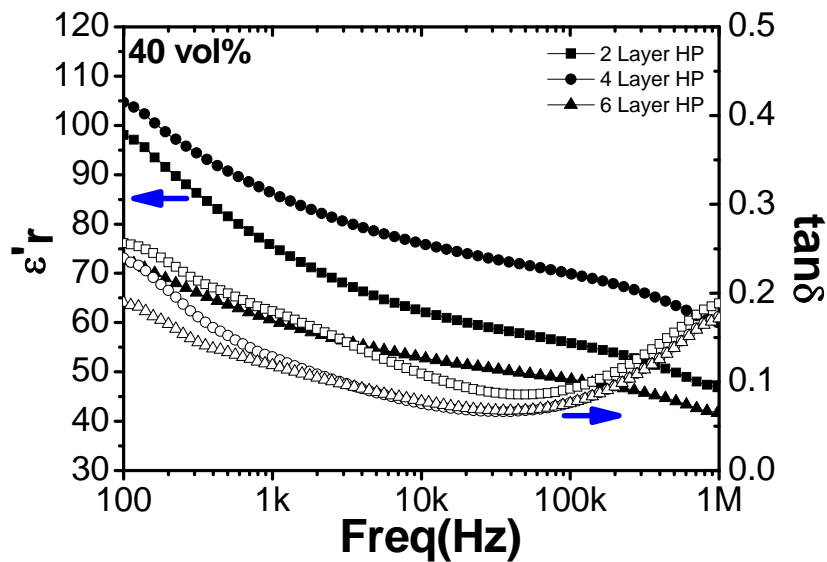


Figure 4-82 Dielectric response vs. frequency of multiple layers $\text{CaCu}_3\text{Ti}_4\text{O}_{12}/\text{VC88}$ composite (40 vol% μ -size $\text{CaCu}_3\text{Ti}_4\text{O}_{12}$) with CC HP for 10s and annealing at 125 °C.

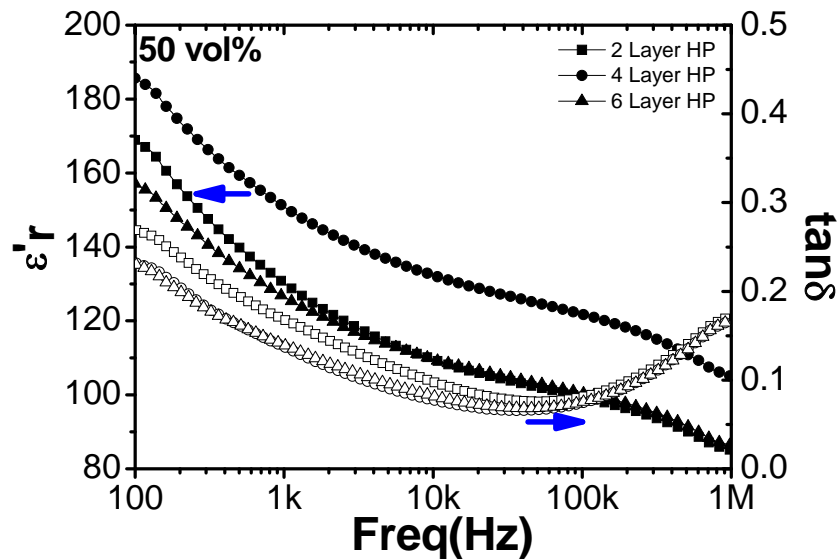


Figure 4-83 Dielectric response vs. frequency of multiple layers $\text{CaCu}_3\text{Ti}_4\text{O}_{12}/\text{VC88}$ composite (50 vol% μ -size $\text{CaCu}_3\text{Ti}_4\text{O}_{12}$) with CC HP for 10s and annealing at 125 °C.

Table 4-21 Summary of dielectric data for multiple layers $\text{CaCu}_3\text{Ti}_4\text{O}_{12}/\text{VC88}$ composite in contrast to $\text{CaCu}_3\text{Ti}_4\text{O}_{12}/\text{P}(\text{VDF}-\text{TrFE})$ composite (μ -size $\text{CaCu}_3\text{Ti}_4\text{O}_{12}$) with CC hot pressing for 10s (1 kHz).

	$\text{CaCu}_3\text{Ti}_4\text{O}_{12}$ Concentration (vol%)				
	10 vol%	20 vol%	30 vol%	40 vol%	50 vol%
2 layer ^[1]	17/0.03	28/0.04	64/0.14	76/0.18	130/0.17
4 layer ^[1]	22/0.03	30/0.04	74/0.14	86/0.13	151/0.14
6 layer ^[1]	21/0.03	34/0.05	59/0.10	61/0.12	126/0.14
2 layer ^[2]	28/0.05	45/0.06	50/0.1	333/0.19	165/0.25
4 layer ^[2]	27/0.05	37/0.07	54/0.10	64/0.22	94/0.15
6 layer ^[2]	27/0.05	43/0.08	82/0.15	106/0.11	182/0.20

^[1]: $\text{CaCu}_3\text{Ti}_4\text{O}_{12}/\text{VC88}$ composite (μ -size $\text{CaCu}_3\text{Ti}_4\text{O}_{12}$).

^[2]: $\text{CaCu}_3\text{Ti}_4\text{O}_{12}/\text{P}(\text{VDF}-\text{TrFE})$ composite (μ -size $\text{CaCu}_3\text{Ti}_4\text{O}_{12}$).

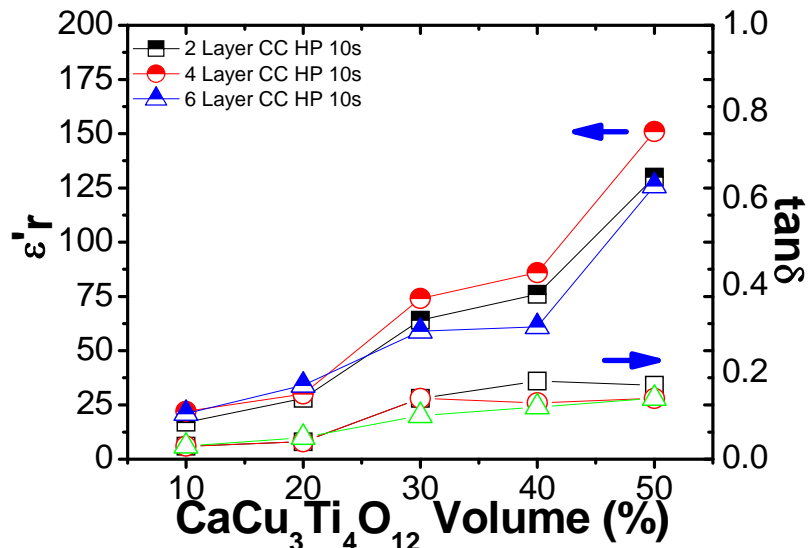


Figure 4-84 Dependence of dielectric response on $\text{CaCu}_3\text{Ti}_4\text{O}_{12}$ concentration for $\text{CaCu}_3\text{Ti}_4\text{O}_{12}/\text{VC88}$ composite (μ -size $\text{CaCu}_3\text{Ti}_4\text{O}_{12}$) using 10s CC HP for 2, 4, and 6 layer respectively at room temperature.

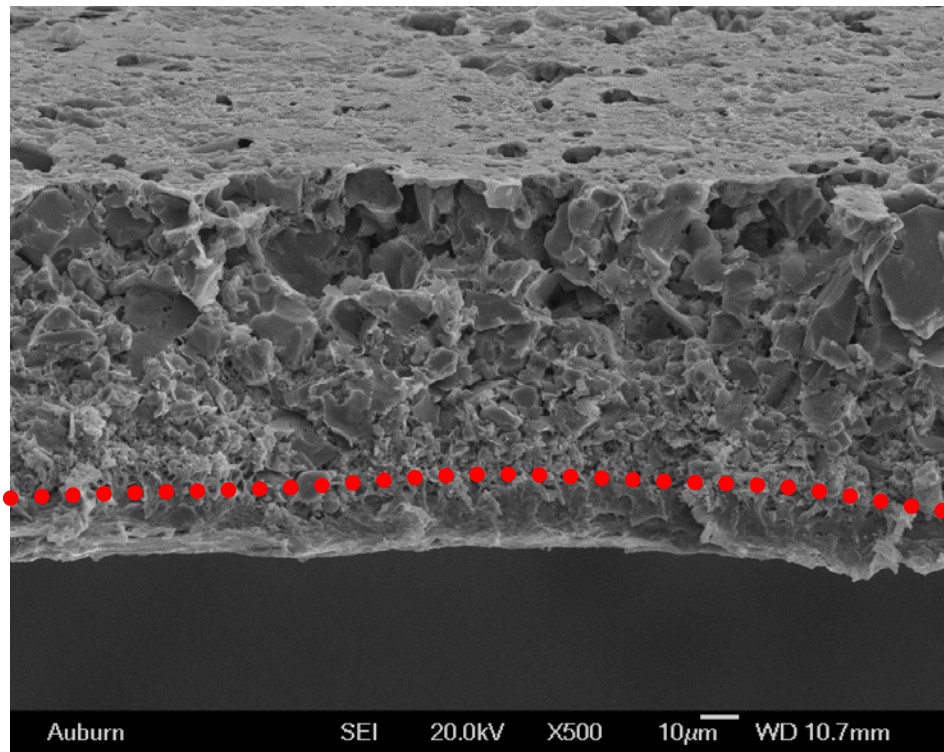


Figure 4-85 SEM fractographs of 1 layer annealed $\text{CaCu}_3\text{Ti}_4\text{O}_{12}/\text{VC88}$ composite (50 vol % μ -size $\text{CaCu}_3\text{Ti}_4\text{O}_{12}$).

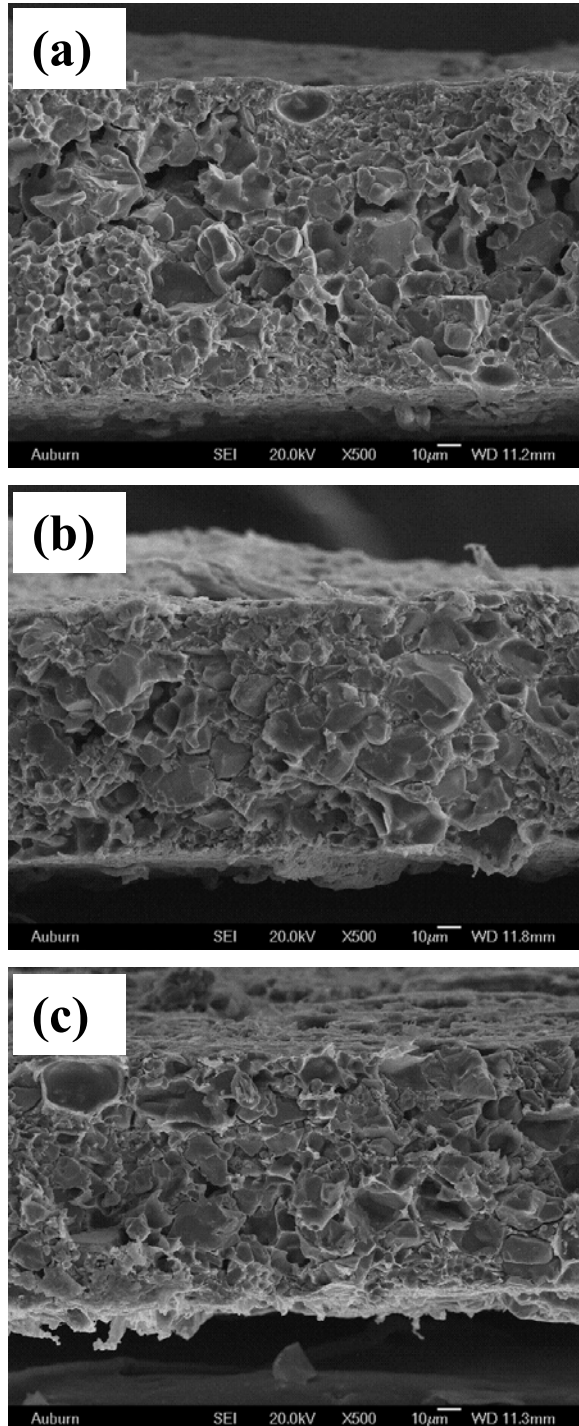


Figure 4-86 SEM fractographs of $\text{CaCu}_3\text{Ti}_4\text{O}_{12}/\text{VC88}$ composites (50 vol% μ -size $\text{CaCu}_3\text{Ti}_4\text{O}_{12}$) using 10s CC HP for (a) 2 layer, (b) 4 layer and (c) 6 layers, respectively.

4.3.5.3 Temperature Dependent of Dielectric Response

The temperature dependent studies on the $\text{CaCu}_3\text{Ti}_4\text{O}_{12}/\text{VC88}$ composites have been performed and their corresponding results are shown in Figure 4-87 to 4-92. Among them, Figure 4-87 lists the temperature dependence of pure VC88. The volume concentration of $\text{CaCu}_3\text{Ti}_4\text{O}_{12}$ varies from 10 to 50 vol% and multiple layers samples, such as two, four and six layer, were hot pressed for 10s.

In Figure 4-87, the temperature dependent of pure VC88 indicated that it posed less temperature influence and exhibited no relaxation-like peak. Moreover, according to the further experimental results in Figure 4-88 to 4-92, regardless of $\text{CaCu}_3\text{Ti}_4\text{O}_{12}$ concentration and multiple layers, it was found that they all share similar temperature dependent tendencies: the variation of dielectric constant shows less dependence with temperatures, except at low frequency such as 100 Hz. For example as temperatures increased from 25 to 125 °C at 1 kHz, dielectric constant varied from 127 to 111 for 50 vol% two layer sample, 147 to 143 for 50 vol% four layer sample, and 126 to 143 for 50 vol% six layer sample, which were summarized in Table 4-22. On the contrary, in comparison with the temperature dependent results in nano-size/micro-size $\text{CaCu}_3\text{Ti}_4\text{O}_{12}/\text{P}(\text{VDF-TrFE})$ composites, it was noticeable that they all experienced a maximum dielectric peak and then leveled off. This phenomenon is in sharp contrast with the results in $\text{CaCu}_3\text{Ti}_4\text{O}_{12}/\text{VC88}$ composites. Since it was well known that $\text{CaCu}_3\text{Ti}_4\text{O}_{12}$ shows marked contrast to known ferroelectrics and exhibits none of relaxation process, the experimental results on the polymer matrix between $\text{P}(\text{VDF-TrFE})$ and VC88 have strongly proved that the relaxation process in $\text{CaCu}_3\text{Ti}_4\text{O}_{12}/\text{P}(\text{VDF-TrFE})$ composites originated from the polymer matrix $\text{P}(\text{VDF-TrFE})$, which is widely known as ferroelectric polymers. Due to their relative high dielectric constant and less temperature dependency, it make this composite very suitable for future smart material application.

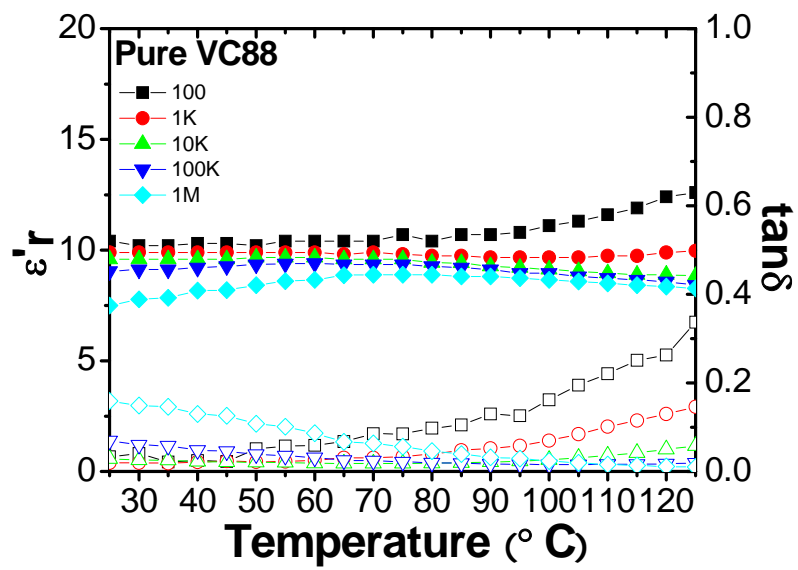


Figure 4-87 Temperature dependence of pure VC88.

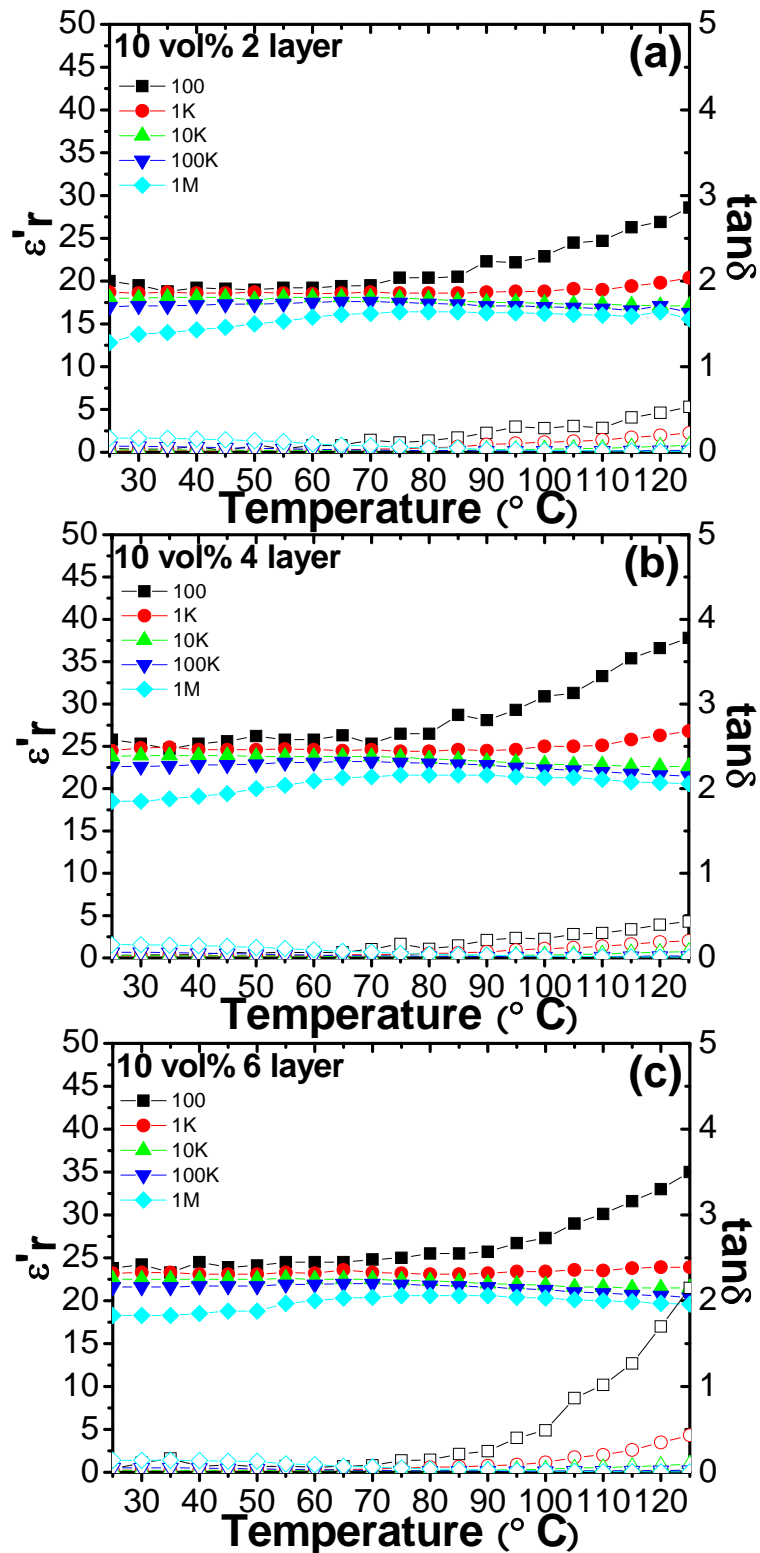


Figure 4-88 Temperature dependence of $\text{CaCu}_3\text{Ti}_4\text{O}_{12}/\text{VC88}$ composite (10 vol% μ -size $\text{CaCu}_3\text{Ti}_4\text{O}_{12}$) with: (a) 2 layer, (b) 4 layer, and (c) 6 layer 10s CC HP.

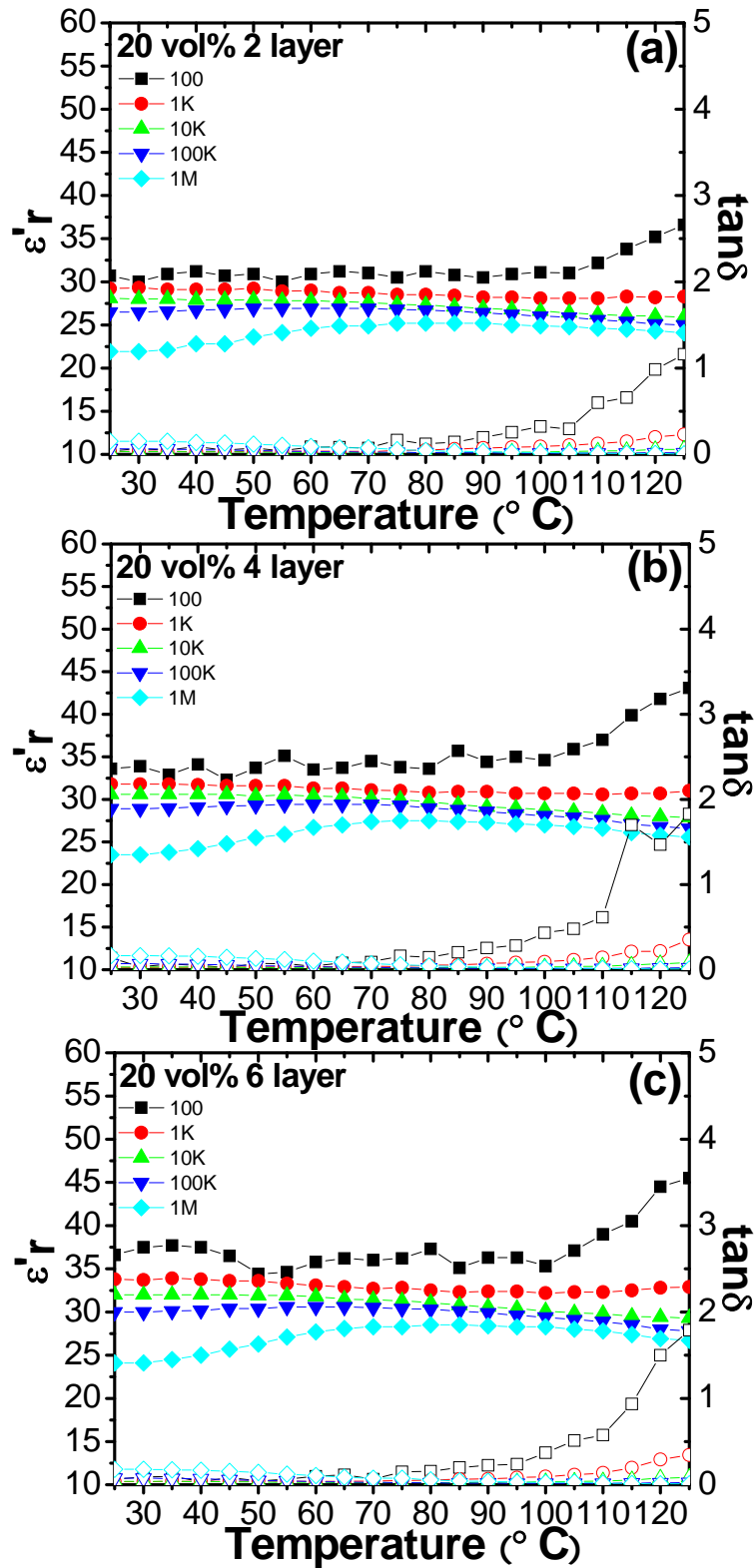


Figure 4-89 Temperature dependence of $\text{CaCu}_3\text{Ti}_4\text{O}_{12}/\text{VC88}$ composite (20 vol% μ -size $\text{CaCu}_3\text{Ti}_4\text{O}_{12}$) with: (a) 2 layer, (b) 4 layer, and (c) 6 layer 10s CC HP.

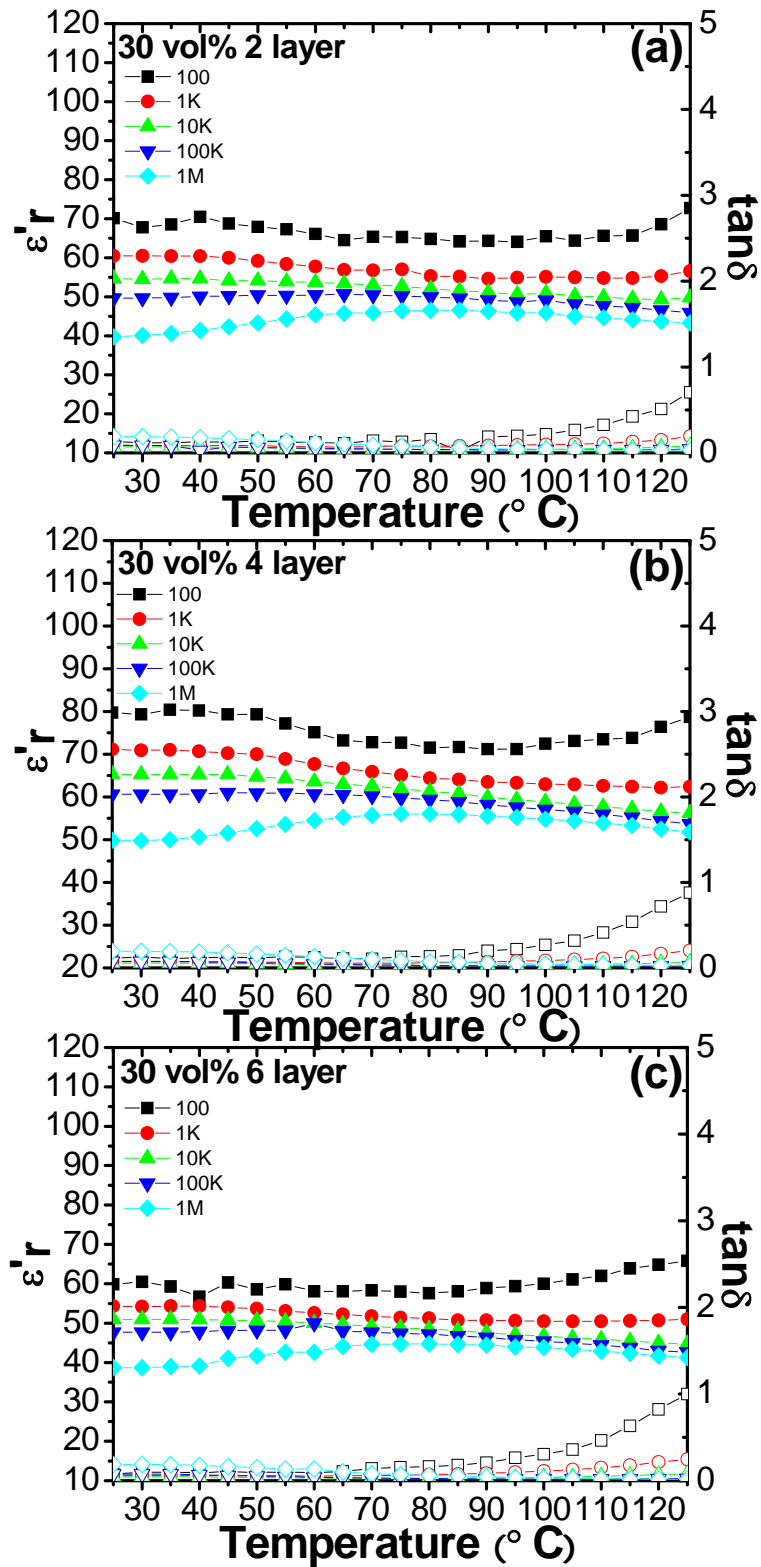


Figure 4-90 Temperature dependence of $\text{CaCu}_3\text{Ti}_4\text{O}_{12}$ /VC88 composite (30 vol% μ -size $\text{CaCu}_3\text{Ti}_4\text{O}_{12}$) with: (a) 2 layer, (b) 4 layer, and (c) 6 layer 10s CC HP.

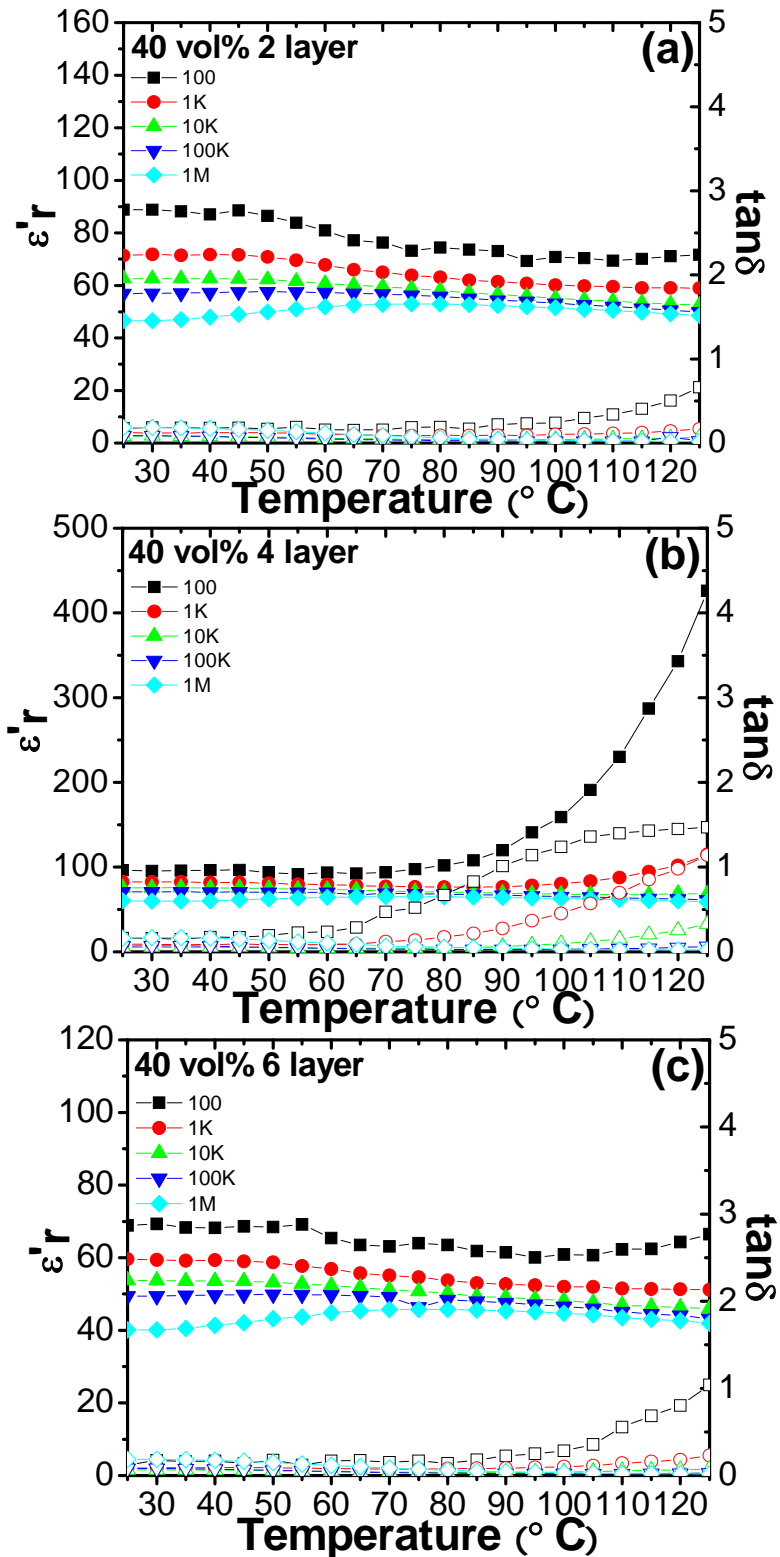


Figure 4-91 Temperature dependence of $\text{CaCu}_3\text{Ti}_4\text{O}_{12}$ /VC88 composite (40 vol% μ -size $\text{CaCu}_3\text{Ti}_4\text{O}_{12}$) with: (a) 2 layer, (b) 4 layer, and (c) 6 layer 10s CC HP.

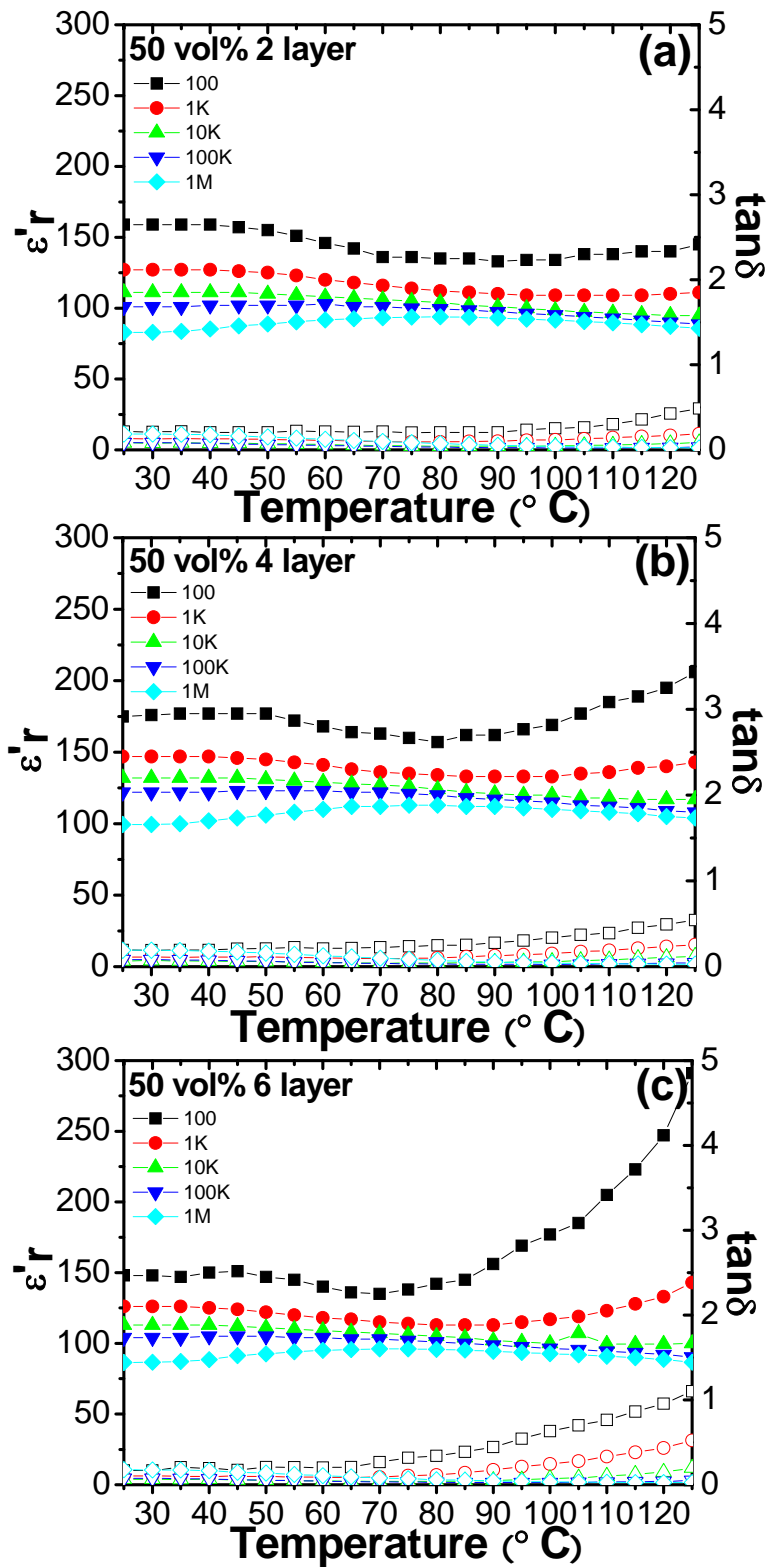


Figure 4-92 Temperature dependence of $\text{CaCu}_3\text{Ti}_4\text{O}_{12}/\text{VC88}$ composite (50 vol% μ -size $\text{CaCu}_3\text{Ti}_4\text{O}_{12}$) with: (a) 2 layer, (b) 4 layer, and (c) 6 layer 10s CC HP.

Table 4-22 Summary of dielectric constant for multiple layers $\text{CaCu}_3\text{Ti}_4\text{O}_{12}/\text{VC88}$ composite (μ -size $\text{CaCu}_3\text{Ti}_4\text{O}_{12}$) with CC HP for 10s at different temperature (1 kHz).

		Temperature ($^{\circ}\text{C}$)				
		25	50	75	100	125
10vol%	2 layer	19	19	19	19	20
	4 layer	25	25	24	25	27
	6 layer	23	23	23	23	24
20vol%	2 layer	29	29	29	28	28
	4 layer	32	32	31	31	31
	6 layer	32	34	34	32	33
30vol%	2 layer	61	60	57	55	57
	4 layer	71	70	65	63	63
	6 layer	54	54	52	51	51
40vol%	2 layer	71	71	64	60	59
	4 layer	83	81	77	80	115
	6 layer	60	59	55	52	51
50vol%	2 layer	127	125	114	109	111
	4 layer	147	145	135	133	143
	6 layer	126	122	114	117	143

4.4 Summary

0-3 composites based on micro-size $\text{CaCu}_3\text{Ti}_4\text{O}_{12}$ were prepared and their dielectric, electric properties and the microstructures of the composites were studied.

For the $\text{CaCu}_3\text{Ti}_4\text{O}_{12}/\text{P}(\text{VDF-TrFE})$ composite, the composite was prepared using solution casting method and then was thermally and mechanically treated. The morphology of the ceramics was studied using SEM. Their dielectric responses were studied over a frequency range from 100 to 1 MHz. For the $\text{CaCu}_3\text{Ti}_4\text{O}_{12}/\text{P}(\text{VDF-TrFE})$ composite, the as-cast film was treated using annealing and HP in order to modify the distribution of the $\text{CaCu}_3\text{Ti}_4\text{O}_{12}$ particles in polymer matrix and the morphology of semi-crystal polymer matrix. The annealing process resulted in a higher dielectric constant due to the increase of crystallinity with polymer matrix. For the HP treatment, it was found that the configuration of the initial stack has a strong influence on the properties of the composites. In general, the HP process is prone to result in a high dielectric response in the composite at room temperature. For example, composite with a dielectric constant of 510 and loss of 0.25 at 1 kHz was obtained at room temperature and when it reached 95 °C, a dielectric constant of 1,240 was obtained. The dielectric response of the composite was studied at different temperatures. Based on the results, it was found that the observed loss at low frequency in the composite is due to a relaxation process, and may be related to the interfacial layer between the $\text{CaCu}_3\text{Ti}_4\text{O}_{12}$ particle and polymer matrix. The dielectric response was analyzed using Cole-Cole plot. It was found that the relaxation time of the major relaxation process obtained in the composite changes with processing condition, such as annealing, HP and concentration. It indicates that the interfacial layers between ceramic particles and polymer matrix play an important role on the dielectric response of the composite. As for the HP samples, it was interestingly observed that as HP time changes, there is a critical HP time at which the composite exhibits a much higher dielectric constant. The experimental results were analyzed using different prediction models. It was found that Logarithmic mixing law, Modified logarithmic mixing law, Yamada model and Bruggeman model can fit the experimental results, and especially, the BM model can result in best match to experimental results. All the fitting results demonstrated that the effective dielectric constant of $\text{CaCu}_3\text{Ti}_4\text{O}_{12}$ actually is much smaller than the dielectric constant for $\text{CaCu}_3\text{Ti}_4\text{O}_{12}$ ceramic.

For $\text{CaCu}_3\text{Ti}_4\text{O}_{12}/\text{P}(\text{VDF-CTFE})$ 88/12 mol% (VC88) composite, similar research was carried out. Composites with a dielectric constant of 151 and loss of 0.14 at 1 kHz were obtained. Most importantly, it was found that the dielectric responses in the composites using $\text{P}(\text{VDF-CTFE})$ 88/12 mol% (VC88) as matrix are almost independent of temperature, which is good for dielectric applications.

References

- (1) Arbatti, M. Development of High-Dielectric-Constant Polymer-Ceramic Composites Based on Calcium Copper Titanate. Auburn University, Alabama, 2004.
- (2) Shan, X. B.; Yang, X.; Zhang, K. W.; Cheng, Z.-Y. *Mater. Res. Soc. Symp. Proc.* **2007**, 949, 0949-C05-07.
- (3) Arbatti, M.; Shan, X. B.; Cheng, Z.-Y. *Adv. Mater* **2007**, 19, 1369-1372.
- (4) Zhang, Q. M.; Xu, H.; Fang, F.; Cheng, Z.-Y.; Xia, F. *J. Appl. Phys* **2001**, 89, (5), 2613-2616.
- (5) Kimura, K.; Ohigashi, H. *J. Appl. Phys* **1983**, 43, (9), 834-836.
- (6) Choi, J.; Borca, C. N.; Dowben, P. A.; Bune, A.; Poulsen, M.; Pebley, S.; Adenwalla, S.; Ducharme, S.; Robertson, L.; Fridkin, V. M.; Palto, S. P.; Petukhova, N. N.; Yudin, S. G. *Phys. Rev. B* **2000**, 61, (8), 5760-5770.
- (7) Subramanian, M. A.; Li, D.; Duan, N.; B. A. Reisner; Sleight, A. W. *J. Solid State Chem* **2000**, 151, 323-325.
- (8) Homes, C. C.; Vogt, T.; Shapiro, S. M.; Wakimoto, S.; Ramirez, A. P. *Science* **2001**, 293, (27), 673-676.
- (9) Nalwa, H. S., *Ferroelectric Polymers: chemistry, physics, and applications*. Marcel Dekker, Inc.: New York. Basel. Hong Kong, 1995.

CHAPTER 5

STUDY OF DIELECTRIC BEHAVIOR ON THE $\text{CaCu}_3\text{Ti}_4\text{O}_{12}$ -BASED COMPOSITES

5.1 Introduction

There has been a great deal of research work directed towards exploring the dielectric properties in $\text{CaCu}_3\text{Ti}_4\text{O}_{12}/\text{P}(\text{VDF-TrFE})$ composites as discussed in Chapter 4. The study on $\text{CaCu}_3\text{Ti}_4\text{O}_{12}/\text{P}(\text{VDF-TrFE})$ composites revealed that process conditions such as annealing, hot pressing pattern, number of hot pressing layers and hot pressing time as well as their morphology, posed a strong impact on the dielectric properties such as its dielectric constant and break-down electric field¹⁻³. According to the experimental results, it was found that with better tuning of those processing parameters, it would give increased dielectric response.

In this chapter, based on a previous fundamental study on $\text{CaCu}_3\text{Ti}_4\text{O}_{12}/\text{P}(\text{VDF-TrFE})$ composites in Chapter 4, a more systematic study on $\text{CaCu}_3\text{Ti}_4\text{O}_{12}$ -based composites will be introduced. In order to optimize the dielectric response in $\text{CaCu}_3\text{Ti}_4\text{O}_{12}/\text{P}(\text{VDF-TrFE})$ composites, effects such as the ceramic particle size, and silane coupling are going to be studied in detail. The size effect will be studied between two different particle size categories: micro-size and nano-size. Similarly, the effect of polymer matrix will be observed within two different polymer matrices systems: $\text{P}(\text{VDF-TrFE})$ and $\text{P}(\text{VDF-CTFE})$. According to the initial purpose of improving the uniformity between the ceramic particle and polymer matrix, the silane coupling agent was incorporated and corresponding dielectric studies were carried out. Finally, it was observed that the optimum value of $\text{CaCu}_3\text{Ti}_4\text{O}_{12}$ volume concentration or silane concentration was decisive on its dielectric performance^{3,4}.

5.2 Experimental

$\text{CaCu}_3\text{Ti}_4\text{O}_{12}$ was prepared using a conventional powder processing method and the ceramic pellets were then milled to two different particles size categories: $D_{50} \approx 10.5 \mu\text{m}$ and 500 nm, respectively. The $\text{CaCu}_3\text{Ti}_4\text{O}_{12}$ - P(VDF-TrFE) 0-3 composite was prepared by solution casting method and hot pressing technique. The composite samples were pressed at a force of 7.5 tons and temperature of 200 °C. The loaded CCTO concentration varied within 0, 10, 20, 30, 40, and 50 vol%, respectively, and P(VDF-CTFE) 88/12 mol% (VC88) copolymer was selected as alternative polymer matrix in comparison to its counterpart P(VDF-TrFE) 55/45 mol%, which was already discussed in Chapter 4. The silane coupling agent used in this work was Trichloro- 1 H, 1H, 2H, 2H-Perfluorooctylsilane. The detailed experimental procedures were already described in Chapter 2.

Dielectric properties: Gold was coated on the surface of the pellets as electrodes using a Pelco SC-6 sputter coater. Agilent 4294A impedance analyzer was employed to characterize the dielectric property of the samples. The measured frequency range was from 100 Hz to 1 MHz.

Microstructure analysis: The grain size and uniformity of the ceramic were determined by scanning electron microscope with EDS (SEM JSM-7000F, JEOL).

5.3 Results and Discussion

5.3.1 Size Effect on Dielectric Behavior

In Chapter 4, the dielectric response of $\text{CaCu}_3\text{Ti}_4\text{O}_{12}$ /P(VDF-TrFE) composite based on micro-size $\text{CaCu}_3\text{Ti}_4\text{O}_{12}$ ceramic powder was discussed. It has been demonstrated in some research work that as a particle shrinks to nano-size range, its properties will be increasingly dominated by its interfacial interactions with its environment^{5, 6}. The expected Maxwell-Wagner interfacial polarization associated with such composite materials is significantly changed as the particle size is reduced. Therefore, the study of the dielectric behavior on nano-size $\text{CaCu}_3\text{Ti}_4\text{O}_{12}$ ceramic powder was designed and carried out, and then the size effect on dielectric behavior was observed.

5.3.1.1 Dielectric Behavior

In Chapter 4, the annealing effect on the $\text{CaCu}_3\text{Ti}_4\text{O}_{12}/\text{P}(\text{VDF-TrFE})$ composite was studied in detail and it was found that it had profound influence on the dielectric properties of the composite sample. Thus, regardless of un-annealed sample, this work only focused on annealed sample. $\text{CaCu}_3\text{Ti}_4\text{O}_{12}/\text{P}(\text{VDF-TrFE})$ composites were prepared with different volume concentrations (0, 10, 20, 30, 40 and 50 vol% $\text{CaCu}_3\text{Ti}_4\text{O}_{12}$), and then were followed by annealing at 125 °C for 8 hours.

Figure 5-1 illustrates the dielectric response of one layer annealed $\text{CaCu}_3\text{Ti}_4\text{O}_{12}/\text{P}(\text{VDF-TrFE})$ composite. After comparing with pure $\text{P}(\text{VDF-TrFE})$, the dielectric constant of the as-annealed composite improved from 15.5 to 37.1 as the $\text{CaCu}_3\text{Ti}_4\text{O}_{12}$ volume concentration increased from 10 to 50 vol%. All the experimental results indicated that it exhibited a linear relationship with $\text{CaCu}_3\text{Ti}_4\text{O}_{12}$ volume concentration. The comparison between nano-size and micro-size $\text{CaCu}_3\text{Ti}_4\text{O}_{12}/\text{P}(\text{VDF-TrFE})$ composite is listed in Table 5-1. This trend is very similar with the results based on the micro-size $\text{CaCu}_3\text{Ti}_4\text{O}_{12}$ powder, when the $\text{CaCu}_3\text{Ti}_4\text{O}_{12}$ volume concentration is below 30 vol% for both nano-size and micro-size ceramic particles, as shown in Figure 5-2. However, as for micro-size $\text{CaCu}_3\text{Ti}_4\text{O}_{12}$ powder, it reached a dielectric peak at 40vol% and then leveled off, as seen in Chapter 4. More specifically: when switching from nano-size to micro-size $\text{CaCu}_3\text{Ti}_4\text{O}_{12}$ powder, 14 to 25 for 10 vol% $\text{CaCu}_3\text{Ti}_4\text{O}_{12}$ composite, 23 to 34 for 20 vol% $\text{CaCu}_3\text{Ti}_4\text{O}_{12}$ composite, 29 to 43 for 30 vol% $\text{CaCu}_3\text{Ti}_4\text{O}_{12}$ composite, 33 to 105 for 40 vol% $\text{CaCu}_3\text{Ti}_4\text{O}_{12}$ composite, 35 to 67 for 50 vol% $\text{CaCu}_3\text{Ti}_4\text{O}_{12}$ composite. A reasonable explanation may come from considering their corresponding microstructure in Figure 5-3. The cross-section of nano-size composite presented two apparent interfacial layers, however, in micro-size composite, due to its relative large particle size, it can accommodate more polymer matrix in between, and thus separation of polymer layer and ceramic layer becomes less obvious. The microstructure difference may account for their difference in dielectric properties.

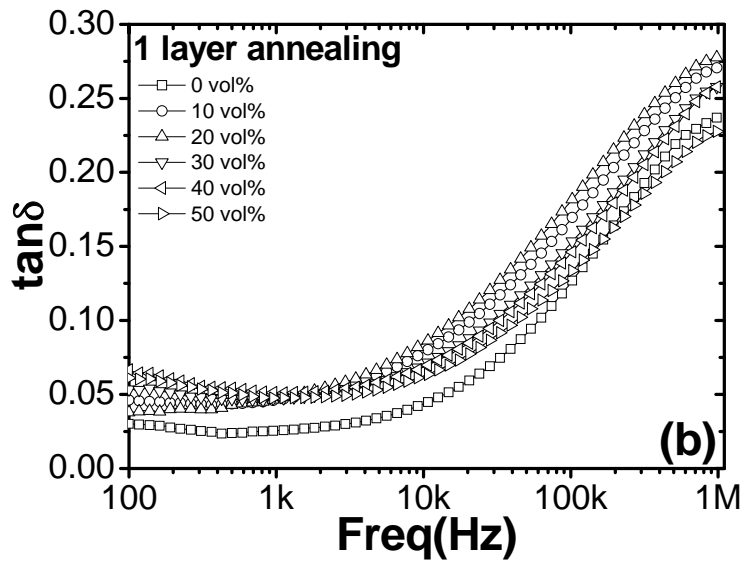
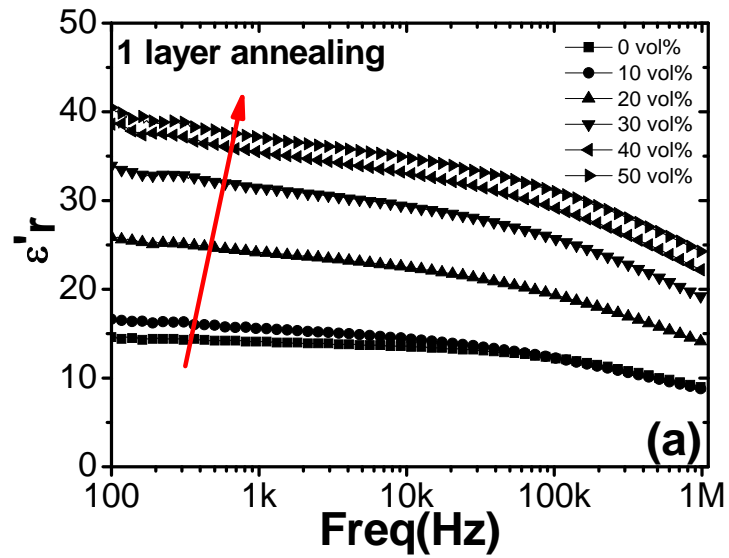


Figure 5-1 Dielectric response vs. frequency of 1 layer $\text{CaCu}_3\text{Ti}_4\text{O}_{12}$ /P(VDF-TrFE) composite (10, 20, 30, 40, and 50 vol% nano-size $\text{CaCu}_3\text{Ti}_4\text{O}_{12}$) with annealing in comparison with P(VDF-TrFE): (a) Dielectric constant vs. frequency; (b) Dielectric loss vs. frequency.

Table 5-1 Summary of dielectric data for 1 layer $\text{CaCu}_3\text{Ti}_4\text{O}_{12}$ /P(VDF-TrFE) composite (nano-size / μ -size $\text{CaCu}_3\text{Ti}_4\text{O}_{12}$) annealed at 125 °C (1 kHz).

	$\text{CaCu}_3\text{Ti}_4\text{O}_{12}$ Concentration (vol%)				
	10 vol%	20 vol%	30 vol%	40 vol%	50 vol%
Nano-1 layer ^[1]	14/0.05	23/0.05	29/0.05	33/0.05	35/0.05
Micro-1 layer ^[2]	25/0.25	34/0.08	43/0.09	105/0.2	67/0.1

^[1]: Nano-size $\text{CaCu}_3\text{Ti}_4\text{O}_{12}$.

^[2]: μ -size $\text{CaCu}_3\text{Ti}_4\text{O}_{12}$.

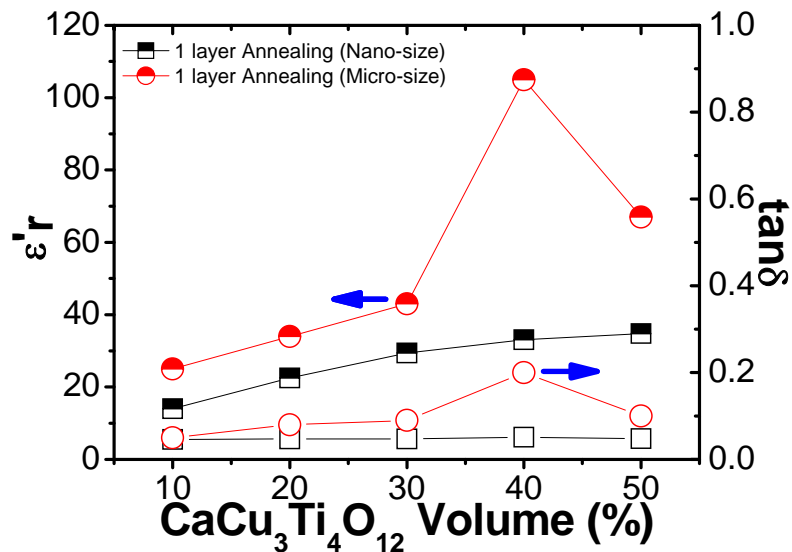


Figure 5-2 Dependence of dielectric response on $\text{CaCu}_3\text{Ti}_4\text{O}_{12}$ concentration for 1 layer $\text{CaCu}_3\text{Ti}_4\text{O}_{12}$ / P(VDF-TrFE) composite (nano-size / μ -size $\text{CaCu}_3\text{Ti}_4\text{O}_{12}$) at room temperature with annealing at 125 °C for 8 hrs.

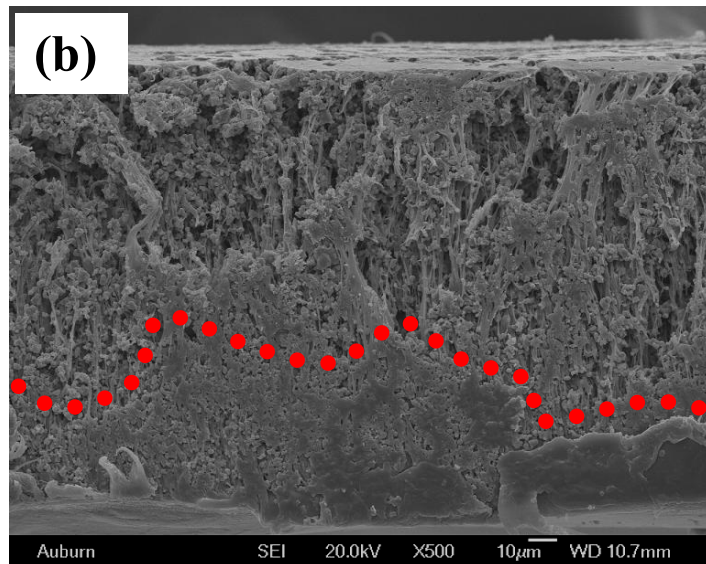
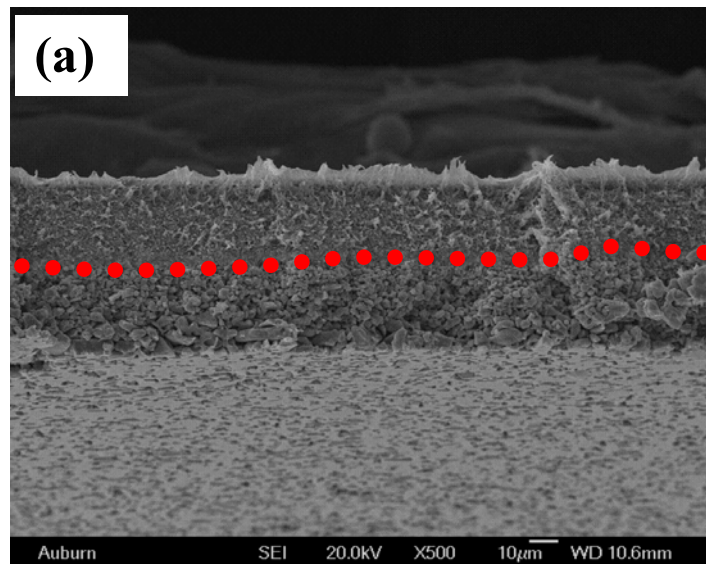


Figure 5-3 SEM fractographs of annealed $\text{CaCu}_3\text{Ti}_4\text{O}_{12}/\text{P}(\text{VDF-TrFE})$ composites with 50 vol%: (a) nano-size; (b) μ -size $\text{CaCu}_3\text{Ti}_4\text{O}_{12}$ ceramic powder.

5.3.1.2 Hot Pressing Effect

As known in Chapter 4, with hot pressing processing, a homogeneous structure can be achieved and its corresponding dielectric response could be enhanced. As for the nano-size composite, 10 to 50 vol% $\text{CaCu}_3\text{Ti}_4\text{O}_{12}$ composites were prepared and then they were hot pressed using CC HP for 10s in this work. Their corresponding experimental results are shown in Figure 5-4 to 5-8 and the summary of their dielectric constant at 1 kHz is listed in Table 5-2.

In Figure 5-4 to 5-8 and Table 5-2, the variation of dielectric constant was observed to change with $\text{CaCu}_3\text{Ti}_4\text{O}_{12}$ concentration. When the $\text{CaCu}_3\text{Ti}_4\text{O}_{12}$ concentration is small such as 10 vol%, the difference in dielectric constant between multiple layers CC HP is relatively small, which arises from the fact that there is large portion of polymer matrix, and the dispersion of ceramic into polymer matrix is not so significant as the one with higher $\text{CaCu}_3\text{Ti}_4\text{O}_{12}$ concentration. With a higher volume concentration such as 20 and 30 vol%, it was clear that both experienced a maximum value of 28 and 48, respectively, at four layers. With volume concentration such as 40 and 50 vol%, they exhibit an increasing trend up to 50 and 53, respectively, as the HP layer increases from two to six layer. Based on Figure 5-9, it was interesting to find that the dielectric peak first appeared at four layer for 20 and 30 vol% $\text{CaCu}_3\text{Ti}_4\text{O}_{12}$ composite, while it switched to six layer for 40 and 50 vol% $\text{CaCu}_3\text{Ti}_4\text{O}_{12}$ composite. At the same time, all the experimental results with different ceramic concentrations tended to give small dielectric constant loss around 0.05, which is very close to the results in 10 and 20 vol% micro-size $\text{CaCu}_3\text{Ti}_4\text{O}_{12}$ composites as shown in Chapter 4. However, comparing with the maximum dielectric constant achieved in micro-size composite, the maximum dielectric constant in nano-size composite is around 53, which was smaller than corresponding value of 182 in micro-size composite, as shown in Table 5-2. In order to study the CC hot pressing, their microstructures were studied using SEM. Figure 5-10 shows the SEM images of 50 vol% CC hot pressed $\text{CaCu}_3\text{Ti}_4\text{O}_{12}/\text{P}(\text{VDF-TrFE})$ composites. Based on SEM images, a very clear ceramic-rich layer can be observed in the internal core area, which is marked in red. This clear interfacial layer should be responsible for the poor response in nano-size $\text{CaCu}_3\text{Ti}_4\text{O}_{12}$ composite.

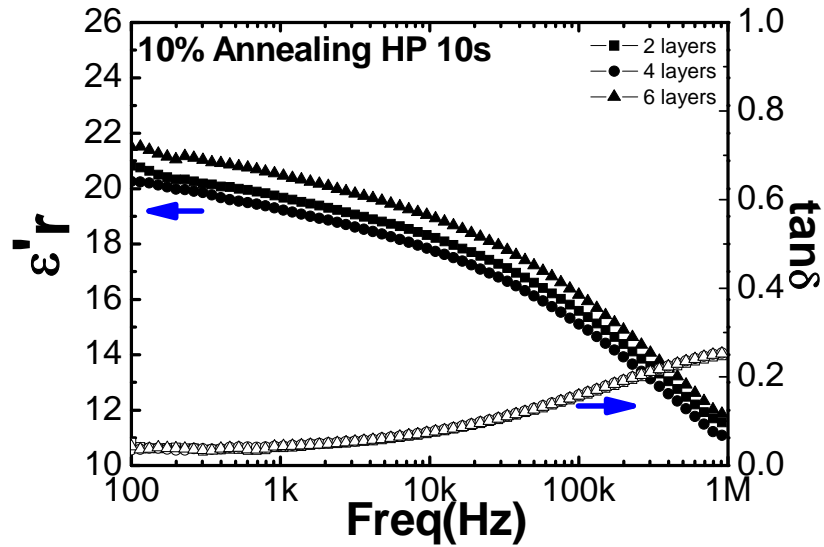


Figure 5-4 Dielectric response vs. frequency of multiple layers $\text{CaCu}_3\text{Ti}_4\text{O}_{12}/\text{P}(\text{VDF}-\text{TrFE})$ composite (10 vol% nano-size $\text{CaCu}_3\text{Ti}_4\text{O}_{12}$) with CC HP for 10s and annealing at 125°C .

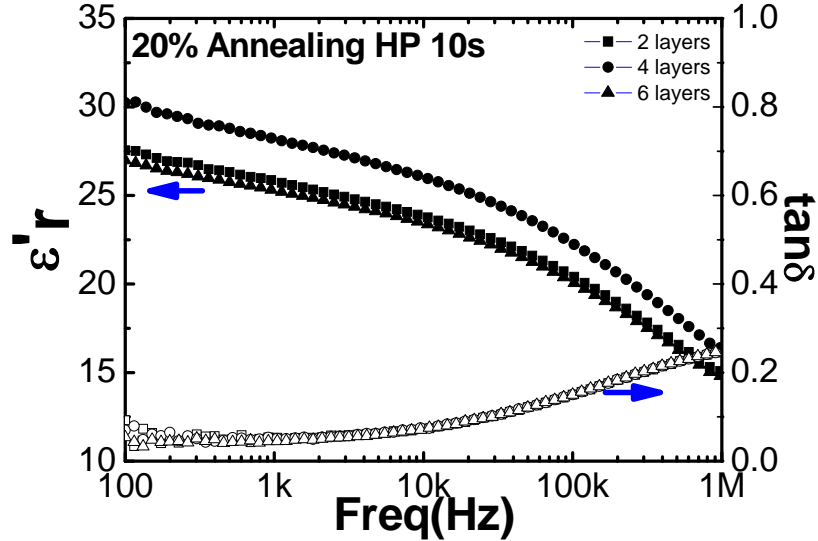


Figure 5-5 Dielectric response vs. frequency of multiple layers $\text{CaCu}_3\text{Ti}_4\text{O}_{12}/\text{P}(\text{VDF}-\text{TrFE})$ composite (20 vol% nano-size $\text{CaCu}_3\text{Ti}_4\text{O}_{12}$) with CC HP for 10s and annealing at 125°C .

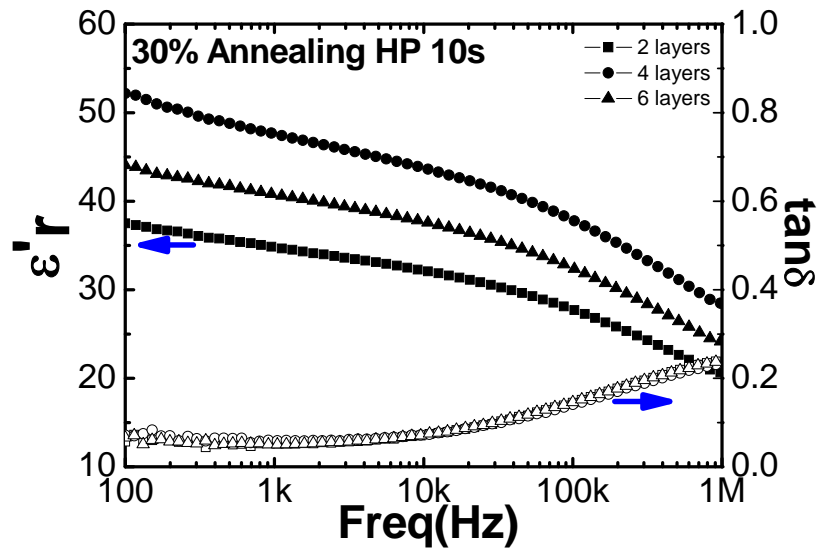


Figure 5-6 Dielectric response vs. frequency of multiple layers $\text{CaCu}_3\text{Ti}_4\text{O}_{12}/\text{P}(\text{VDF}-\text{TrFE})$ composite (30 vol% nano-size $\text{CaCu}_3\text{Ti}_4\text{O}_{12}$) with CC HP for 10s and annealing at 125 °C.

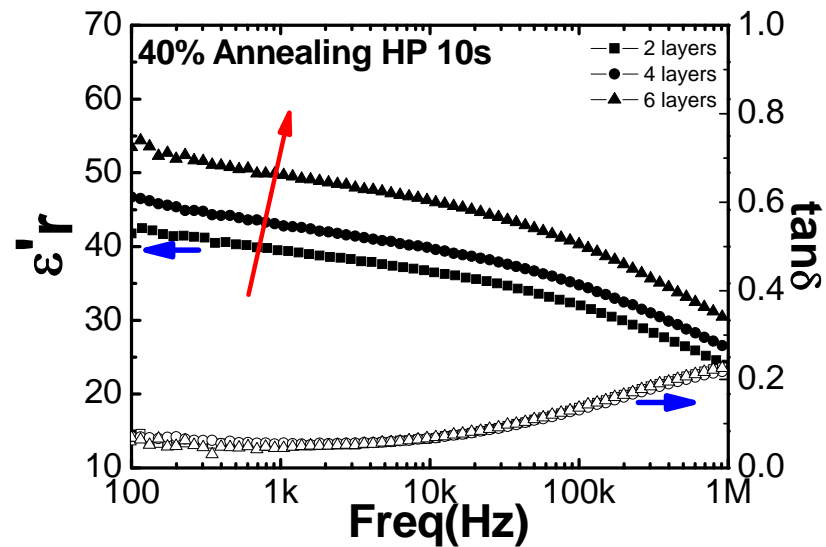


Figure 5-7 Dielectric response vs. frequency of multiple layers $\text{CaCu}_3\text{Ti}_4\text{O}_{12}/\text{P}(\text{VDF}-\text{TrFE})$ composite (40 vol% nano-size $\text{CaCu}_3\text{Ti}_4\text{O}_{12}$) with CC HP for 10s and annealing at 125 °C.

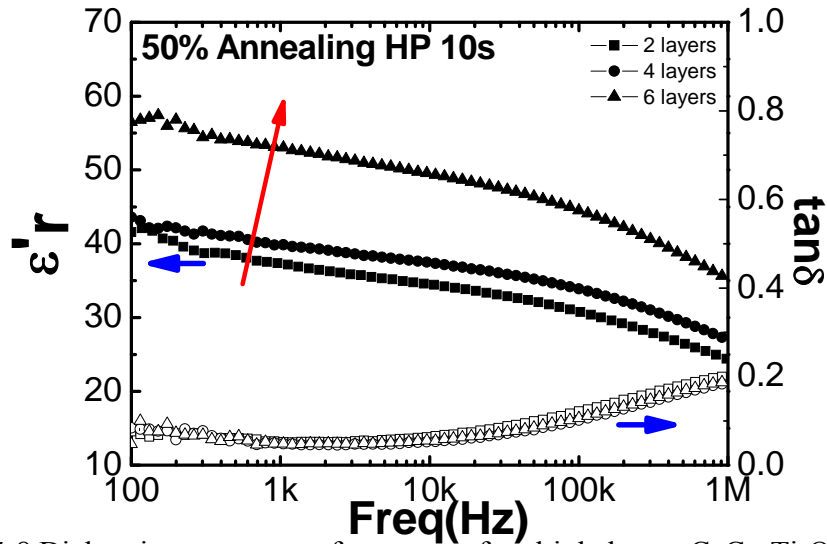


Figure 5-8 Dielectric response vs. frequency of multiple layers $\text{CaCu}_3\text{Ti}_4\text{O}_{12}/\text{P}(\text{VDF-TrFE})$ composite (20 vol% nano-size $\text{CaCu}_3\text{Ti}_4\text{O}_{12}$) with CC HP for 10s and annealing at 125°C .

Table 5-2 Summary of dielectric data for multiple layer $\text{CaCu}_3\text{Ti}_4\text{O}_{12}/\text{P}(\text{VDF-TrFE})$ composite (nano-size/ μ -size $\text{CaCu}_3\text{Ti}_4\text{O}_{12}$) with CC hot pressing for 10s (1 kHz).

	$\text{CaCu}_3\text{Ti}_4\text{O}_{12}$ Concentration (vol%)				
	10 vol%	20 vol%	30 vol%	40 vol%	50 vol%
2 layer ^[1]	20/0.04	26/0.05	35/0.05	40/0.05	37/0.05
4 layer ^[1]	19/0.04	28/0.05	48/0.06	43/0.05	40/0.05
6 layer ^[1]	21/0.04	25/0.05	41/0.05	50/0.05	53/0.05
2 layer ^[2]	28/0.05	45/0.06	50/0.1	333/0.19	165/0.25
4 layer ^[2]	27/0.05	37/0.07	54/0.10	64/0.22	94/0.15
6 layer ^[2]	27/0.05	43/0.08	82/0.15	106/0.11	182/0.20

^[1]: Nano-size $\text{CaCu}_3\text{Ti}_4\text{O}_{12}$.

^[2]: μ -size $\text{CaCu}_3\text{Ti}_4\text{O}_{12}$.

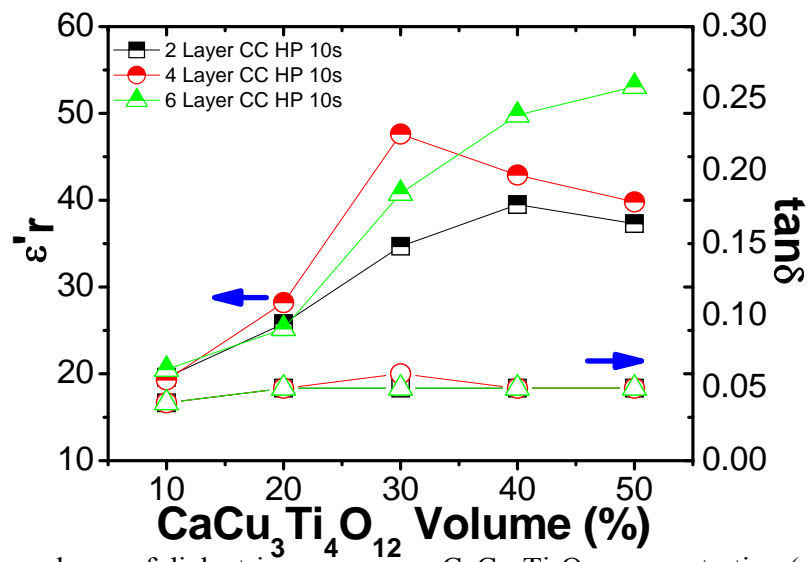


Figure 5-9 Dependence of dielectric response on $\text{CaCu}_3\text{Ti}_4\text{O}_{12}$ concentration (nano-size $\text{CaCu}_3\text{Ti}_4\text{O}_{12}$) using 10s CC HP for 2, 4, and 6 layers respectively at room temperature.

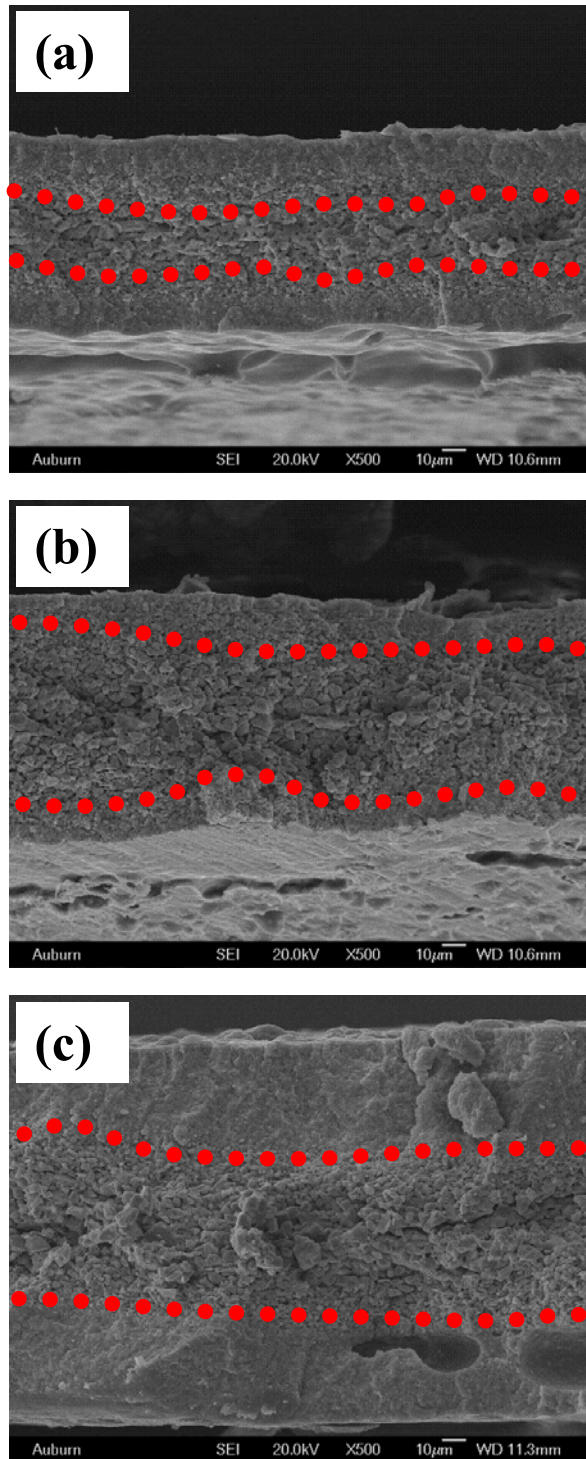


Figure 5-10 SEM fractographs of $\text{CaCu}_3\text{Ti}_4\text{O}_{12}/\text{P}(\text{VDF}-\text{TrFE})$ composites (50vol% nano-size $\text{CaCu}_3\text{Ti}_4\text{O}_{12}$) using 10s CC HP for (a) 2 layer, (b) 4 layer and (c) 6 layers, respectively.

5.3.1.3 Hot Pressing Time on Dielectric Properties

The effect of hot pressing time on the dielectric properties in nano-size $\text{CaCu}_3\text{Ti}_4\text{O}_{12}$ composite has been studied. In this work, 10 to 50 vol% $\text{CaCu}_3\text{Ti}_4\text{O}_{12}$ composites were prepared and then they were hot pressed using CC HP for 30s. Correspondingly, their experimental results are shown in Figure 5-11 to 5-15. Table 5-3 summarizes the dielectric constant at 1 kHz for two, four and six layer CC HP composite samples.

After comparing the dielectric results with 10s CC HP, the dielectric constant shared the same trend as that at low concentrations, such as 10 and 20vol% $\text{CaCu}_3\text{Ti}_4\text{O}_{12}$. The dielectric results were very similar within two, four and six layer, while for 30 to 50 vol%, four layer CC HP dominated significantly, which results in a high dielectric constant, as shown in Figure 5-16. Both the experimental results exhibited low dielectric constants, which is associated with their corresponding microstructure and was already demonstrated using SEM images in 10s CC HP. The dielectric results are relatively smaller than the one in micro-size $\text{CaCu}_3\text{Ti}_4\text{O}_{12}/\text{P}(\text{VDF}-\text{TrFE})$ composites, especially at 40 and 50 vol% in Table 5-3.

Based on results in Figure 5-16, Figure 5-17 to 5-19 presented a comparison between the model prediction and experimental data for the effective dielectric constant of $\text{CaCu}_3\text{Ti}_4\text{O}_{12}/\text{P}(\text{VDF}-\text{TrFE})$ composite after CC HP processing. Together shown were the predictions based on logarithmic mixing (LM) law, modified logarithmic mixing (MLM) law, Maxwell-Wagner (MW) model, Yamada (YA) model, series model and Bruggeman (BM) model. The determination procedures of the $\epsilon'_{r-\text{polymerc}}$ and $\epsilon'_{r-\text{ceramic}}$ have been well described in Chapter 4. The values of $\epsilon'_{r-\text{polymerc}}$ were predetermined as 20 and 14 for annealing and non-annealing samples respectively. These calculated values of $\epsilon'_{r-\text{ceramic}}$ have been listed in Table 5-4. Unlike the model prediction for micro-size multiple layers composite, most models including LM, MLM, MW, YA and BM, gave desired fitting results. Moreover, among these models, LM, MLM, YA and BM models showed best match to experimental data. The series model can only have good fitted results in low volume concentrations from 0 to 10 vol%. Especially, comparing with the CC HP fitted results in Chapter 4 and Table 5-4, it was found that their dielectric constant

tended to decrease dramatically as the $\text{CaCu}_3\text{Ti}_4\text{O}_{12}$ size changed from micro-size to nano-size. The dramatic change indicated that the size of $\text{CaCu}_3\text{Ti}_4\text{O}_{12}$ particle may play an important role in its corresponding dielectric response.

Moreover, much more detailed experiments about hot pressing time on the composite were carried out on 50 vol% nano-size $\text{CaCu}_3\text{Ti}_4\text{O}_{12}$ composite. Different hot pressing times, such as 10, 20, 30 and 40s were selected in the experiments. As shown in Figure 5-20 and Table 5-5, with increasing vol% of $\text{CaCu}_3\text{Ti}_4\text{O}_{12}$, the dielectric constant increased from 35 to 51 and then decreased to 43 for two layer CC HP. Meanwhile, it was found that for both four and six layer CC HP, the dielectric constant reached a maximum value and then degraded, as shown in Figure 5-21. The results indicated that by incorporating with the hot pressing process, the so-called interfacial layer is a dynamic process, and excessive hot time would undermine the established uniformed structure. In the experiments, the optimum time to achieve the best dielectric constant was found at 30s CC HP.

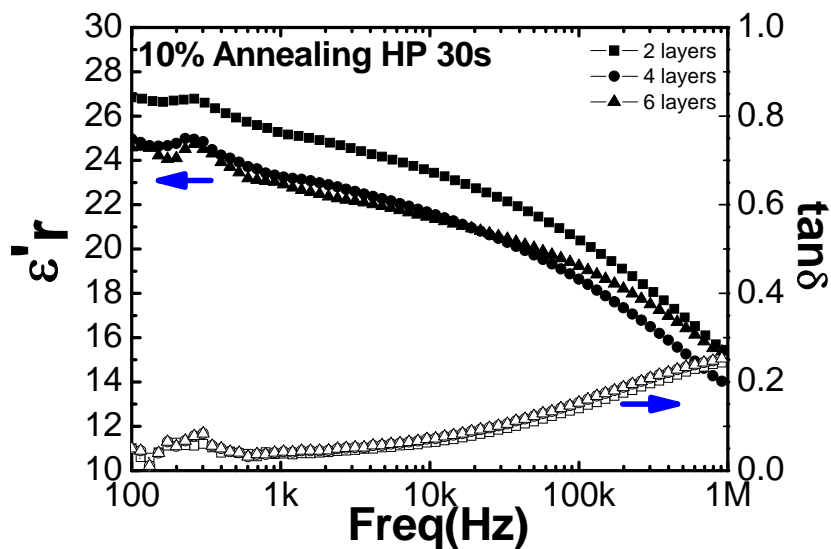


Figure 5-11 Dielectric response vs. frequency of multiple layers $\text{CaCu}_3\text{Ti}_4\text{O}_{12}/\text{P}(\text{VDF-TrFE})$ composite (10 vol% nano-size $\text{CaCu}_3\text{Ti}_4\text{O}_{12}$) with CC HP for 30s and annealing at 125°C .

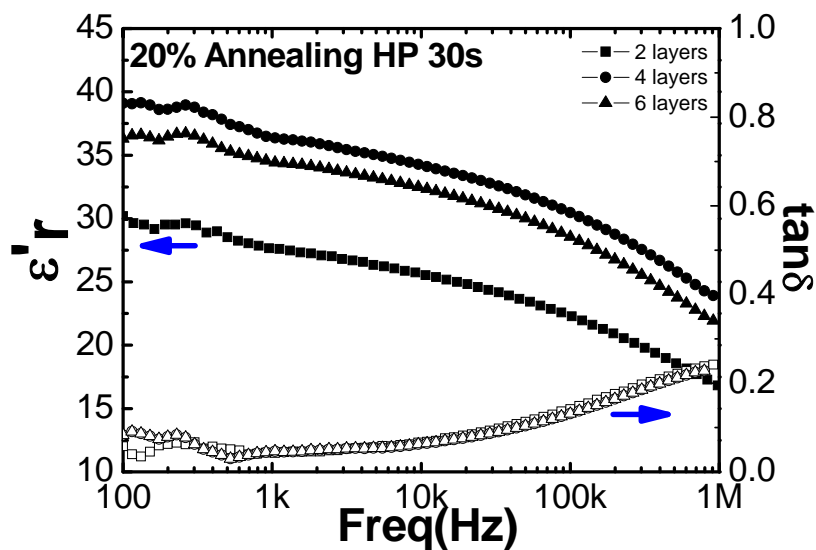


Figure 5-12 Dielectric response vs. frequency of multiple layers $\text{CaCu}_3\text{Ti}_4\text{O}_{12}/\text{P}(\text{VDF-TrFE})$ composite (20 vol% nano-size $\text{CaCu}_3\text{Ti}_4\text{O}_{12}$) with CC HP for 30s and annealing at 125°C .

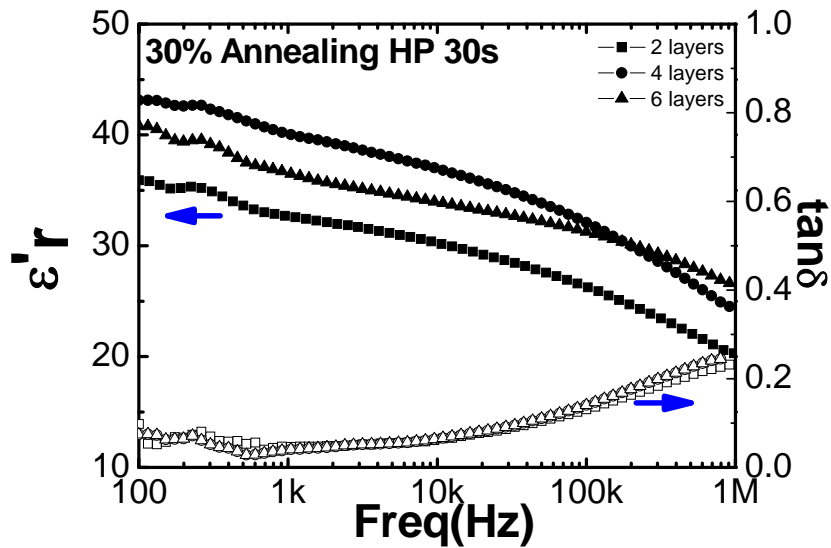


Figure 5-13 Dielectric response vs. frequency of multiple layers $\text{CaCu}_3\text{Ti}_4\text{O}_{12}/\text{P}(\text{VDF}-\text{TrFE})$ composite (30 vol% nano-size $\text{CaCu}_3\text{Ti}_4\text{O}_{12}$) with CC HP for 30s and annealing at 125°C .

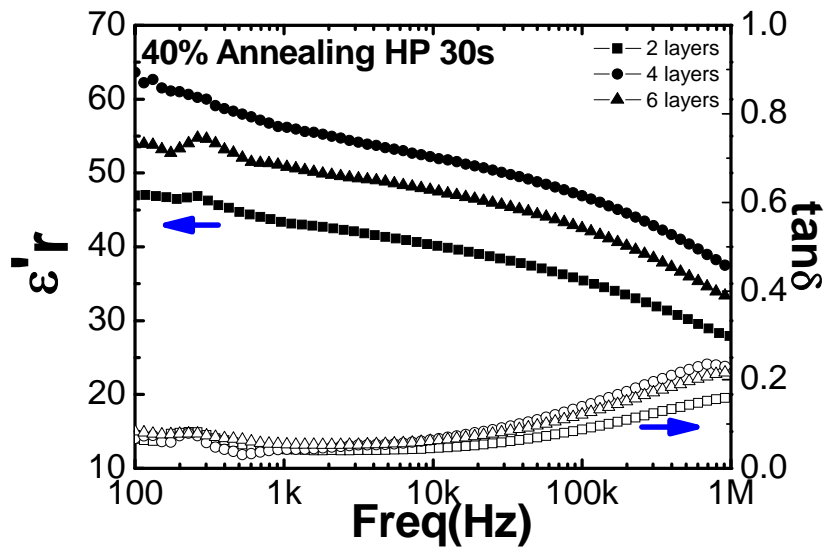


Figure 5-14 Dielectric response vs. frequency of multiple layers $\text{CaCu}_3\text{Ti}_4\text{O}_{12}/\text{P}(\text{VDF}-\text{TrFE})$ composite (40 vol% nano-size $\text{CaCu}_3\text{Ti}_4\text{O}_{12}$) with CC HP for 30s and annealing at 125°C .

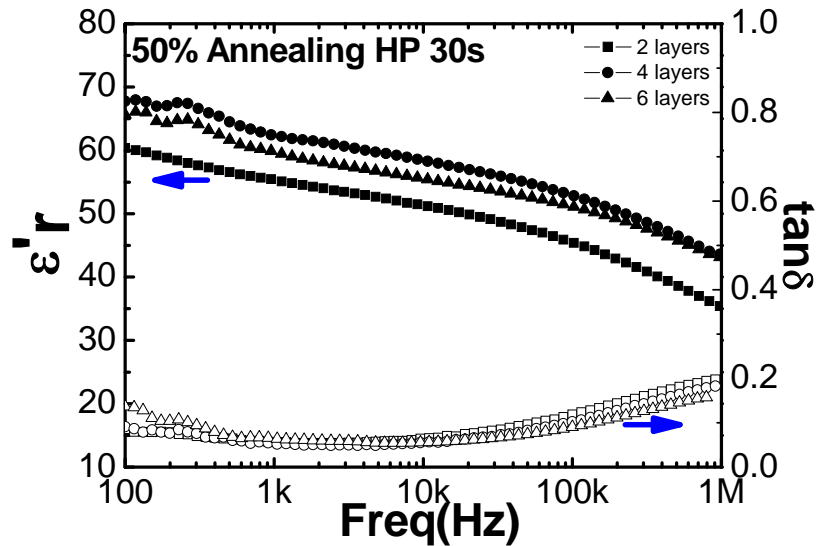


Figure 5-15 Dielectric response vs. frequency of multiple layers $\text{CaCu}_3\text{Ti}_4\text{O}_{12}/\text{P}(\text{VDF}-\text{TrFE})$ composite (50 vol% nano-size $\text{CaCu}_3\text{Ti}_4\text{O}_{12}$) with CC HP for 30s and annealing at $125\text{ }^\circ\text{C}$.

Table 5-3 Summary of dielectric data for multiple layers $\text{CaCu}_3\text{Ti}_4\text{O}_{12}/\text{P}(\text{VDF}-\text{TrFE})$ composite (nano-size/ μ -size $\text{CaCu}_3\text{Ti}_4\text{O}_{12}$) with CC hot pressing for 30s (1 kHz).

	$\text{CaCu}_3\text{Ti}_4\text{O}_{12}$ Concentration (vol%)				
	10 vol%	20 vol%	30 vol%	40 vol%	50 vol%
2 layer ^[1]	25/0.04	28/0.04	33/0.05	43/0.04	55/0.05
4 layer ^[1]	23/0.04	34/0.05	40/0.04	56/0.04	62/0.05
6 layer ^[1]	23/0.04	35/0.05	37/0.04	51/0.04	60/0.06
2 layer ^[2]	24/0.05	28/0.06	54/0.10	368/0.43	150/0.33
4 layer ^[2]	26/0.05	39/0.08	61/0.11	101/0.17	246/0.30
6 layer ^[2]	27/0.05	44/0.08	46/0.08	85/0.15	510/0.25

^[1]: Nano-size $\text{CaCu}_3\text{Ti}_4\text{O}_{12}$.

^[2]: μ -size $\text{CaCu}_3\text{Ti}_4\text{O}_{12}$.

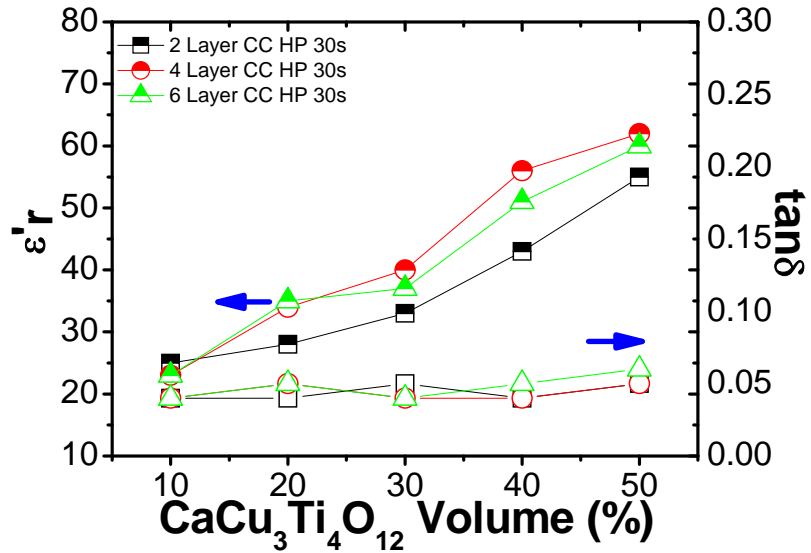


Figure 5-16 Dependence of dielectric response on $\text{CaCu}_3\text{Ti}_4\text{O}_{12}$ concentration (nano-size $\text{CaCu}_3\text{Ti}_4\text{O}_{12}$) using 30s CC HP for 2, 4, and 6 layers respectively at room temperature.

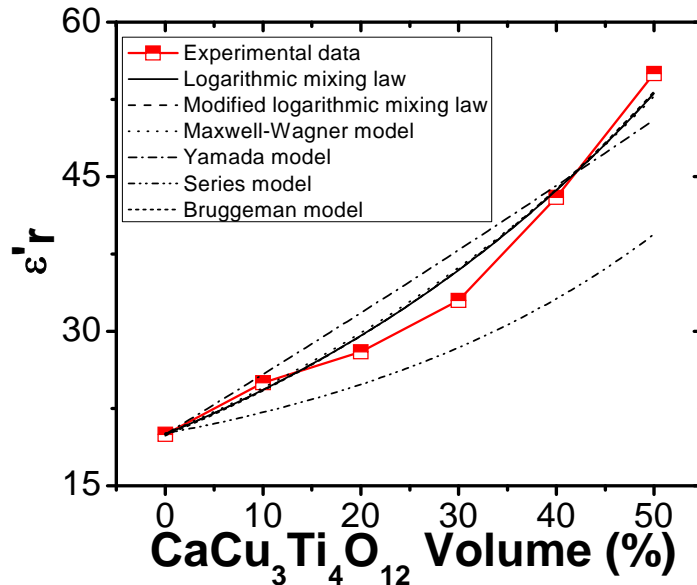


Figure 5-17 Comparison of the present model predictions with experimental data for 2 layer CC HP 30s annealed $\text{CaCu}_3\text{Ti}_4\text{O}_{12}$ /P(VDF-TrFE) sample.

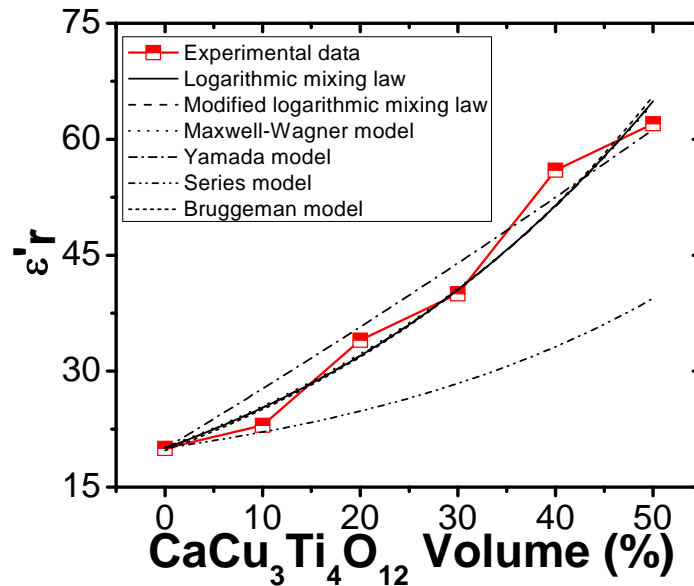


Figure 5-18 Comparison of the present model predictions with experimental data for 4 layer CC HP 30s annealed $\text{CaCu}_3\text{Ti}_4\text{O}_{12}/\text{P}(\text{VDF}-\text{TrFE})$ sample.

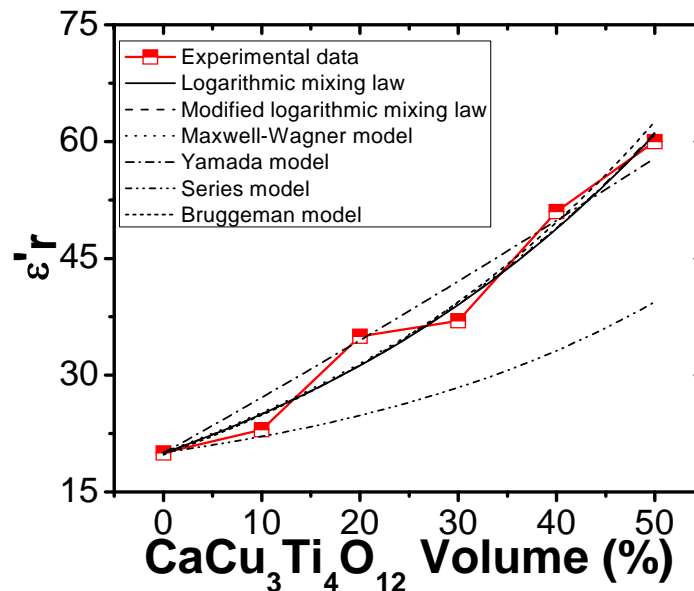


Figure 5-19 Comparison of the present model predictions with experimental data for 6 layer CC HP 30s annealed $\text{CaCu}_3\text{Ti}_4\text{O}_{12}/\text{P}(\text{VDF}-\text{TrFE})$ sample.

Table 5-4 Summary of fitted dielectric data for $\text{CaCu}_3\text{Ti}_4\text{O}_{12}$ multiple layer $\text{CaCu}_3\text{Ti}_4\text{O}_{12}/\text{P}(\text{VDF-TrFE})$ composite (nano-size $\text{CaCu}_3\text{Ti}_4\text{O}_{12}$) with CC hot pressing for 30s (1 kHz).

	2 layer	4 layer	6 layer
Logarithmic mixing law	141	211	186
Modified logarithmic mixing law	994	2,225	1,748
Maxwell-Wagner model	165	373	278
Yamada model	85	110	102
Series model	∞	∞	∞
Bruggeman model	110	150	140

Modified logarithmic mixing law: $k=0.5$.

Yamada model: $N=25$.

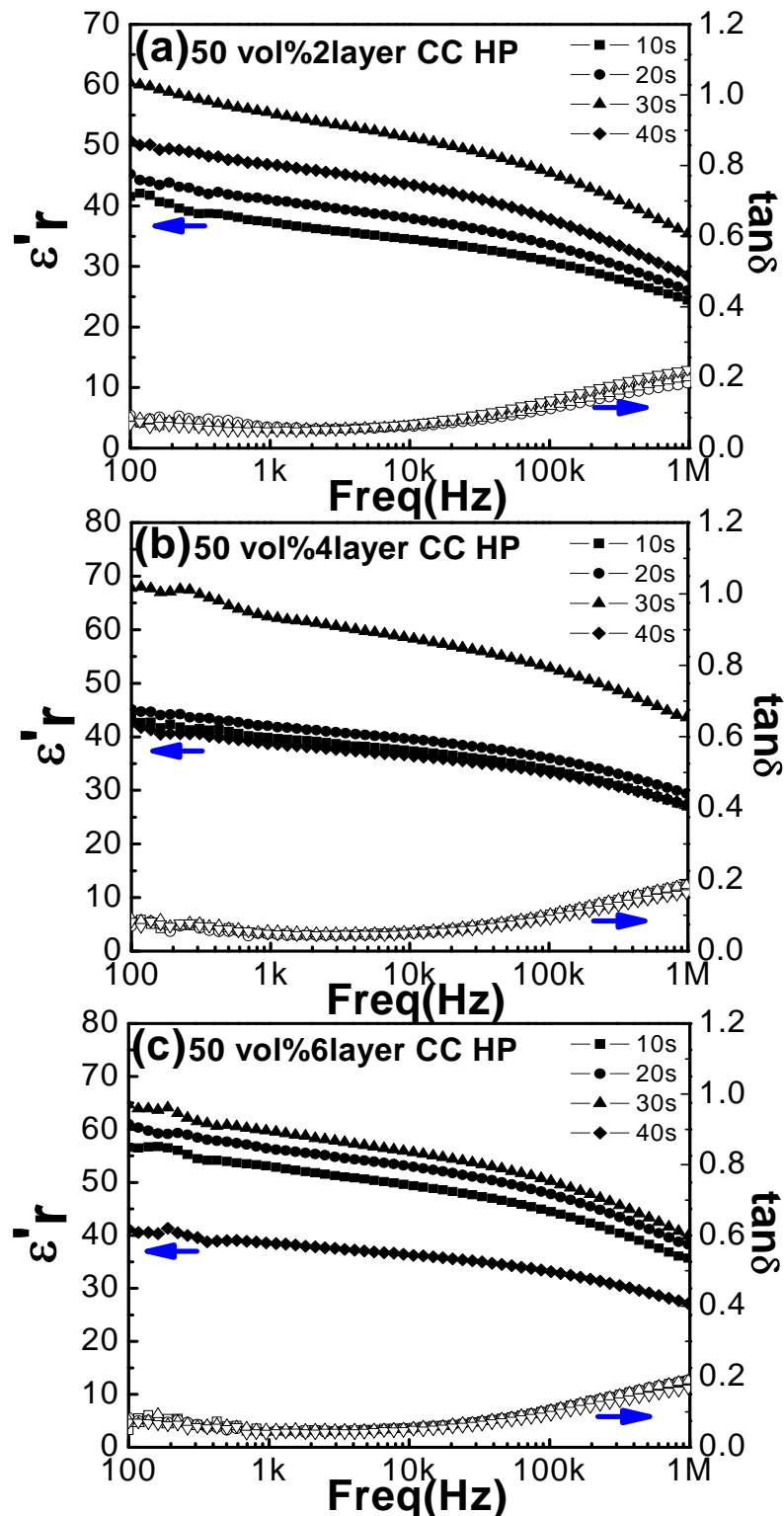


Figure 5-20 Dielectric response vs. frequency of multiple layers $\text{CaCu}_3\text{Ti}_4\text{O}_{12}$ /P(VDF-TrFE) composite (50 vol% nano-size $\text{CaCu}_3\text{Ti}_4\text{O}_{12}$): (a) 2 layer CC HP, (b) 4 layer CC HP, (c) 6 layer CC HP for 10, 20, 30 and 40s.

Table 5-5 Summary of dielectric data for multiple layers $\text{CaCu}_3\text{Ti}_4\text{O}_{12}/\text{P}(\text{VDF-TrFE})$ composite (50vol% nano-size $\text{CaCu}_3\text{Ti}_4\text{O}_{12}$) with CC hot pressing for 10, 20, 30 and 40s (1 kHz).

	CC HP Time (seconds)			
	10s	20s	30s	40s
2 layer HP	35/0.07	38/0.06	51/0.06	43/0.07
4 layer HP	40/0.05	42/0.04	62/0.05	39/0.05
6 layer HP	53/0.05	56/0.05	60/0.05	39/0.04

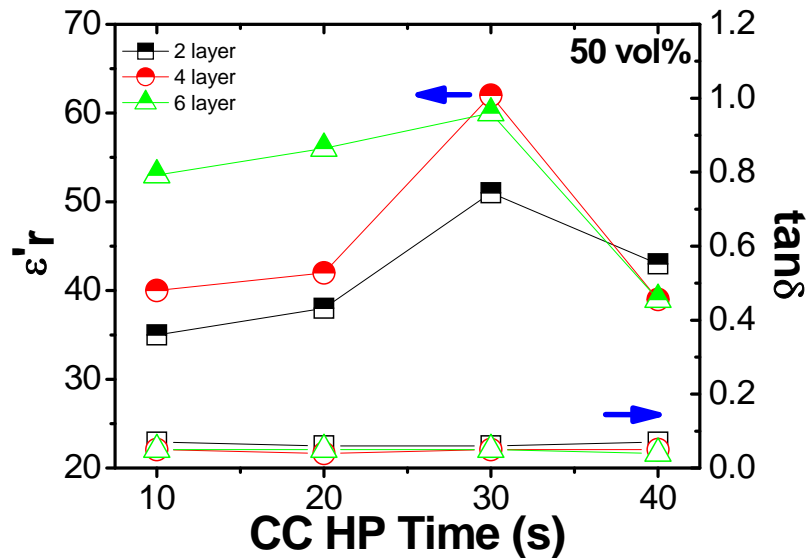


Figure 5-21 Dependence of dielectric response on $\text{CaCu}_3\text{Ti}_4\text{O}_{12}$ concentration (50 vol% nano-size $\text{CaCu}_3\text{Ti}_4\text{O}_{12}$) of 2, 4 and 6 layers CC HP for 10, 20, 30 and 40s at room temperature, respectively.

5.3.1.4 Temperature Dependent of Dielectric Response

Earlier in this chapter, we reported that the effect of hot pressing on the dielectric properties and how their corresponding microstructure is associated with the morphology changes. In order to understand how temperature would influence the dielectric behavior, temperature dependent measurements were carried out. Figure 5-22 to 5-24 illustrate the temperature dependence of the dielectric constant and loss factor for $\text{CaCu}_3\text{Ti}_4\text{O}_{12}/\text{P}(\text{VDF-TrFE})$ composites with 50 vol% $\text{CaCu}_3\text{Ti}_4\text{O}_{12}$ powder.

Based on the results shown in Figure 5-22 to 5-24, it was found that the temperature dependence of the dielectric constant was influenced by hot pressing time, varying between 10 and 30s, and multiple layers, changing from two to six layers. Clearly, it was observed that they experienced a dielectric peak, which resembles a relaxation phenomenon. In Chapter 4, for the micro-size composite, it was well known that this relaxation phenomenon is clearly associated with its polymer matrix P(VDF-TrFE). As for the peak value, more specifically as hot pressing time increased from 10 to 30s, the maximum dielectric constant at 1 kHz was changing from 96 to 146 for two layer, 88 to 117 for four layer, and 148 to 143 for six layer. The curie-temperature corresponding to this maximum value ranged between 95 and 100 °C. However, in contrast with the results of micro-size composite, those maximum values at its curie temperature were very small. With regards to micro-size composites as shown in Chapter 4, the peak value was 514 for 10s six layer CC HP, and 1,240 for 30s six layer CC HP. The possible explanation for the differences may lie in their microstructure. As we already discussed previously, the cross-section of the composite sample presented a very obvious separation between ceramic particle and polymer matrix, which was even more significant than the one observed in micro-size sample. In return, this microstructure could deteriorate the dielectric response, as well as the temperature dependence properties.

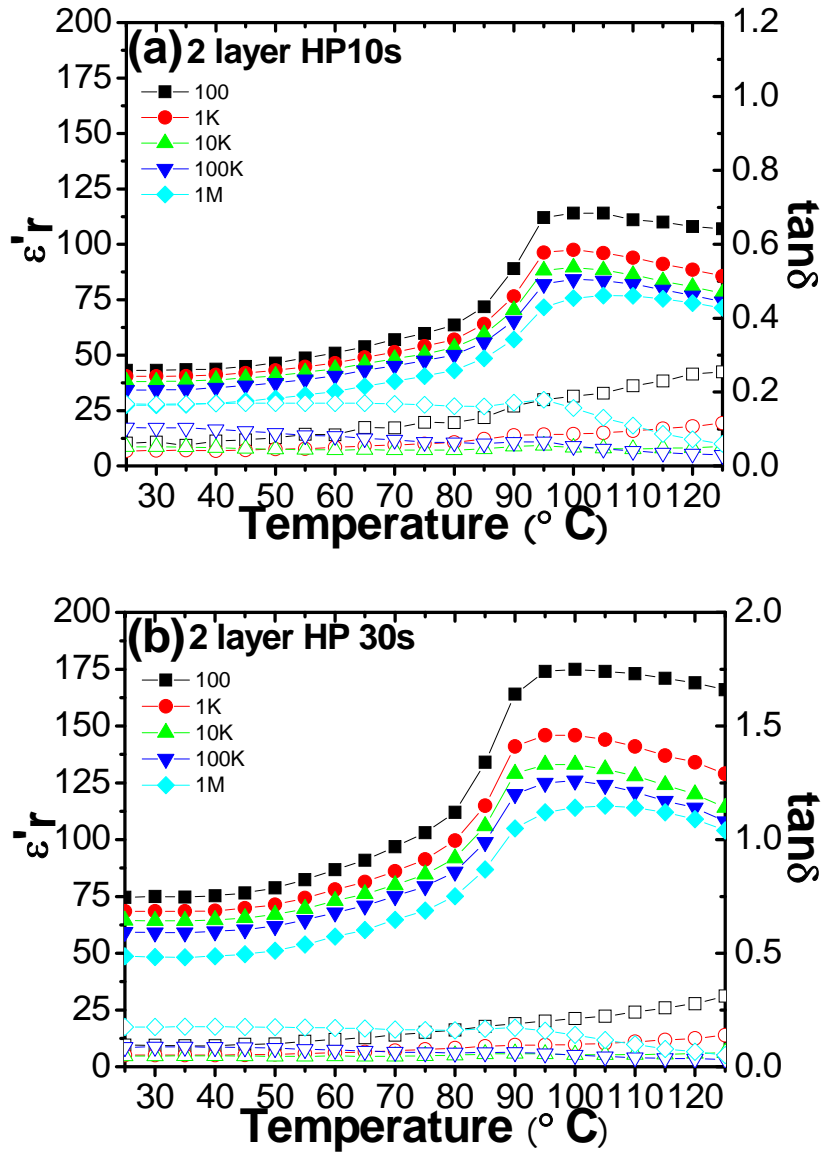


Figure 5-22 Temperature dependence of the 2 layers $\text{CaCu}_3\text{Ti}_4\text{O}_{12}/\text{P}(\text{VDF}-\text{TrFE})$ composite (50 vol% nano-size $\text{CaCu}_3\text{Ti}_4\text{O}_{12}$) for: (a) 10s, and (b) 30s CC HP.

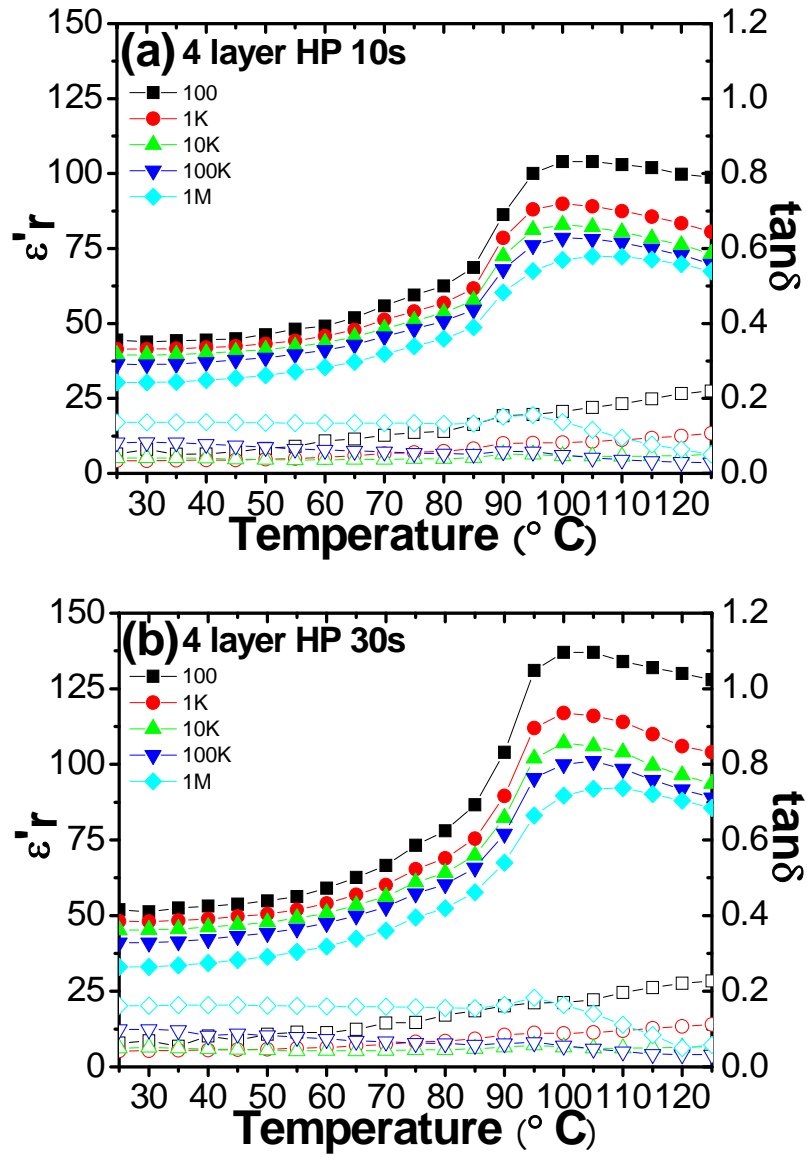


Figure 5-23 Temperature dependence of the 4 layers $\text{CaCu}_3\text{Ti}_4\text{O}_{12}/\text{P}(\text{VDF}-\text{TrFE})$ composite (50 vol% nano-size $\text{CaCu}_3\text{Ti}_4\text{O}_{12}$) for: (a) 10s, and (b) 30s CC HP.

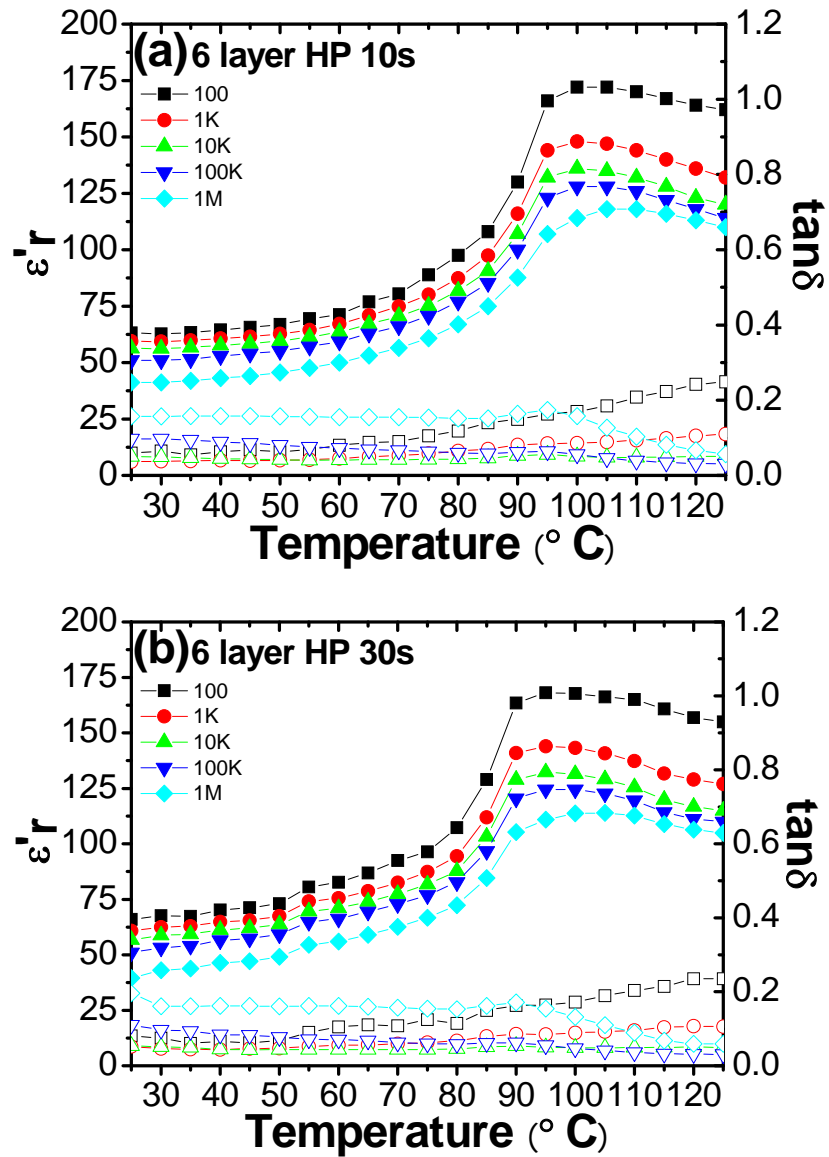


Figure 5-24 Temperature dependence of the 6 layers $\text{CaCu}_3\text{Ti}_4\text{O}_{12}/\text{P}(\text{VDF}-\text{TrFE})$ composite (50 vol% nano-size $\text{CaCu}_3\text{Ti}_4\text{O}_{12}$) for: (a) 10s, and (b) 30s CC HP.

5.3.1.5 P-E Hysteresis Loop

Since the properties of P-E loops for micro-size $\text{CaCu}_3\text{Ti}_4\text{O}_{12}/\text{P}(\text{VDF-TrFE})$ composite have been addressed in Chapter 4, in order to better understand the size effect on the P-E properties, P-E studies on nano-size $\text{CaCu}_3\text{Ti}_4\text{O}_{12}/\text{P}(\text{VDF-TrFE})$ composite were carried out in this Chapter. Figure 5-25 to 5-29 list the P-E loops of one layer $\text{CaCu}_3\text{Ti}_4\text{O}_{12}/\text{P}(\text{VDF-TrFE})$ composite with 10 to 50 vol% $\text{CaCu}_3\text{Ti}_4\text{O}_{12}$ powder. Corresponding P-E loops of multiple layers, such as two, four, six layers after CC HP 10s, are shown in Figure 5-30 to 5-32.

In Figure 5-25 to 5-29, it presented a similar trend that was also presented in micro-size $\text{CaCu}_3\text{Ti}_4\text{O}_{12}/\text{P}(\text{VDF-TrFE})$ composite: as increasing ceramic concentration from 10 to 50 vol%, the break-down field decreased from 133 MV/m to 48 MV/m, while 47 MV/m to 1.1 MV/m in micro-size $\text{CaCu}_3\text{Ti}_4\text{O}_{12}/\text{P}(\text{VDF-TrFE})$ composite. Correspondingly, the remnant polarization (P_r) decreased from 0.046 to 0.044 C/m². As for multiple layers, the break-down field changed from 14 MV/m to 8 MV/m. After comparing with micro-size $\text{CaCu}_3\text{Ti}_4\text{O}_{12}/\text{P}(\text{VDF-TrFE})$ composites, it was found that those P-E results were enormously improved. Different from the micro-size ceramic particle, the nano-size ceramic particle can improve the affinity between ceramic and polymer matrix, and then it enables the elimination of porosity due to the introduction of ceramic particle, which is essential for the break-down field improvement.

Moreover, in order to understand whether it is a simple dielectric or a ferroelectric, studies about the effects of temperature to the P-E properties were carried out. Based on their temperature dependent results, the temperature was set at its curie temperature at 95 °C and their results are shown in Figure 5-33 to 5-37. Table 5-6 shows the summary of P-E results for one layer 10 to 50 vol% $\text{CaCu}_3\text{Ti}_4\text{O}_{12}/\text{P}(\text{VDF-TrFE})$ composite at 95 °C. The break-down field decreased from 100 MV/m to 45 MV/m, as the ceramic concentration increased from 10 to 50 vol%. In contrast to P-E loops at room temperature, the polarization hysteresis loop gradually disappeared with increasing temperature for each ceramic concentration. That is, the remnant polarization (P_r) and coercive field (E_c) slowly decreased with increasing temperature, a feature reminiscent of relaxor ferroelectrics.

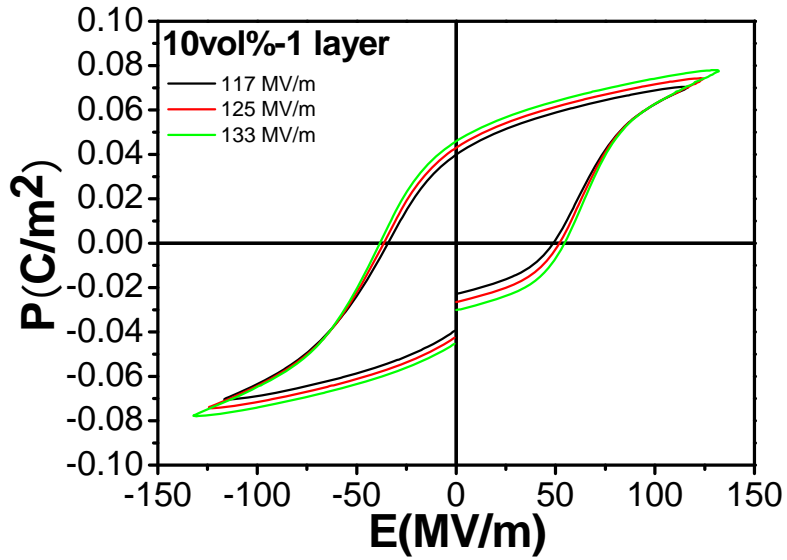


Figure 5-25 Polarization electric hysteresis loop for one layer $\text{CaCu}_3\text{Ti}_4\text{O}_{12}/\text{P}(\text{VDF}-\text{TrFE})$ composites with 10 vol% $\text{CaCu}_3\text{Ti}_4\text{O}_{12}$ powder.

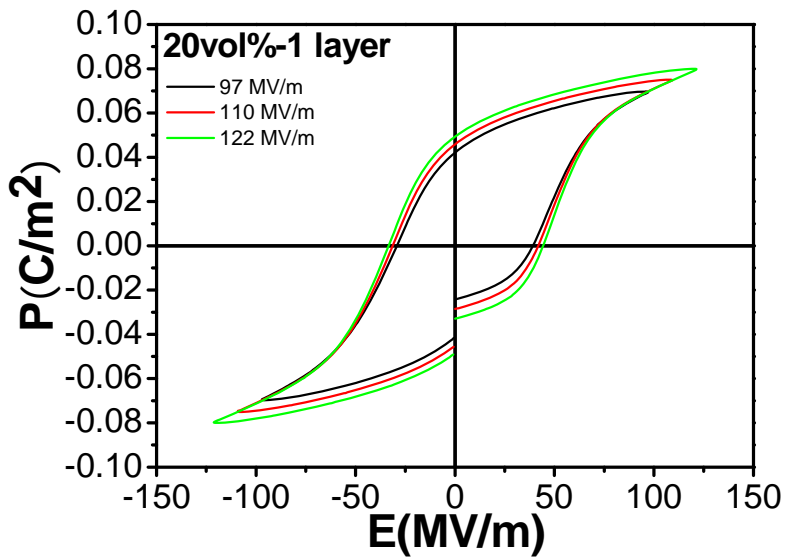


Figure 5-26 Polarization electric hysteresis loop for one layer $\text{CaCu}_3\text{Ti}_4\text{O}_{12}/\text{P}(\text{VDF}-\text{TrFE})$ composites with 20 vol% $\text{CaCu}_3\text{Ti}_4\text{O}_{12}$ powder.

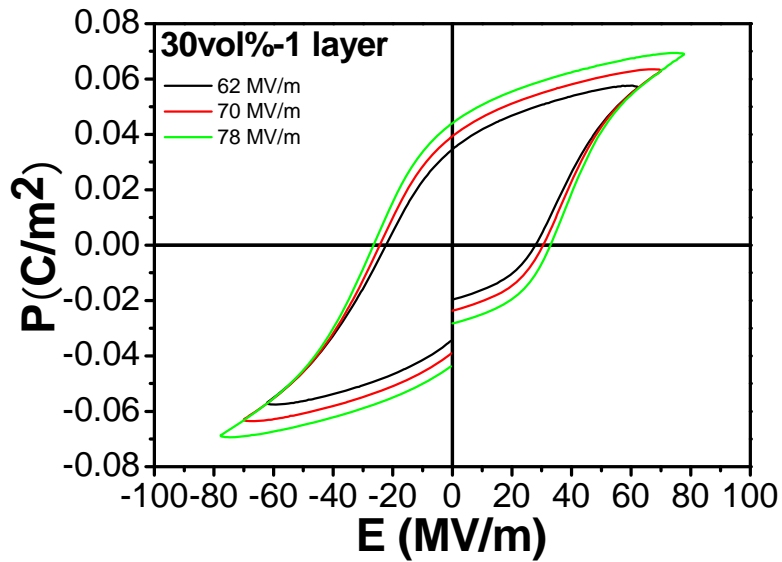


Figure 5-27 Polarization electric hysteresis loop for one layer $\text{CaCu}_3\text{Ti}_4\text{O}_{12}/\text{P}(\text{VDF}-\text{TrFE})$ composites with 30 vol% $\text{CaCu}_3\text{Ti}_4\text{O}_{12}$ powder.

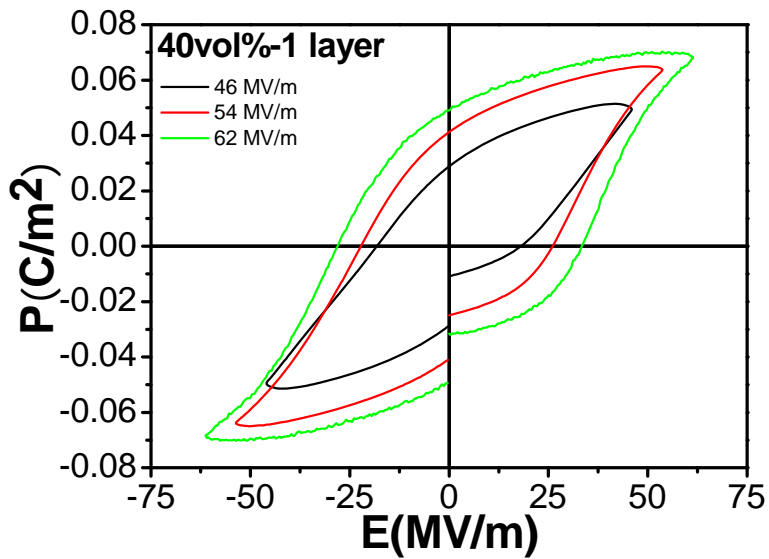


Figure 5-28 Polarization electric hysteresis loop for one layer $\text{CaCu}_3\text{Ti}_4\text{O}_{12}/\text{P}(\text{VDF}-\text{TrFE})$ composites with 40 vol% $\text{CaCu}_3\text{Ti}_4\text{O}_{12}$ powder.

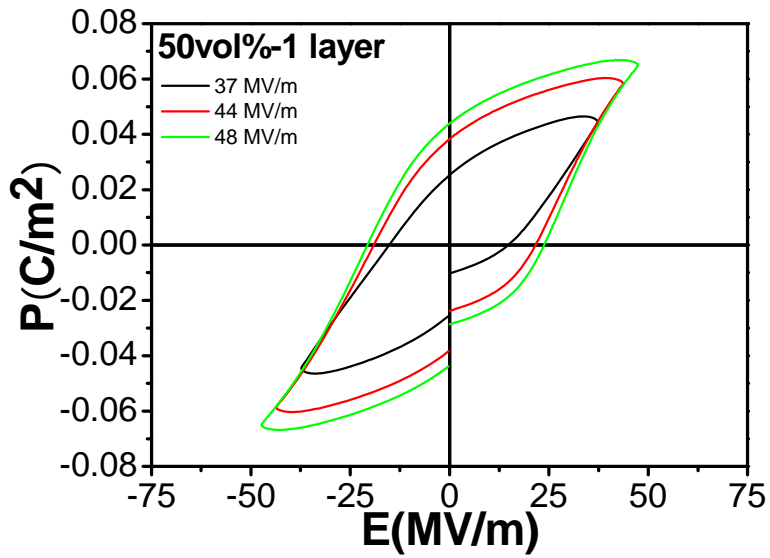


Figure 5-29 Polarization electric hysteresis loop for one layer $\text{CaCu}_3\text{Ti}_4\text{O}_{12}/\text{P}(\text{VDF-TrFE})$ composites with 50 vol% $\text{CaCu}_3\text{Ti}_4\text{O}_{12}$ powder.

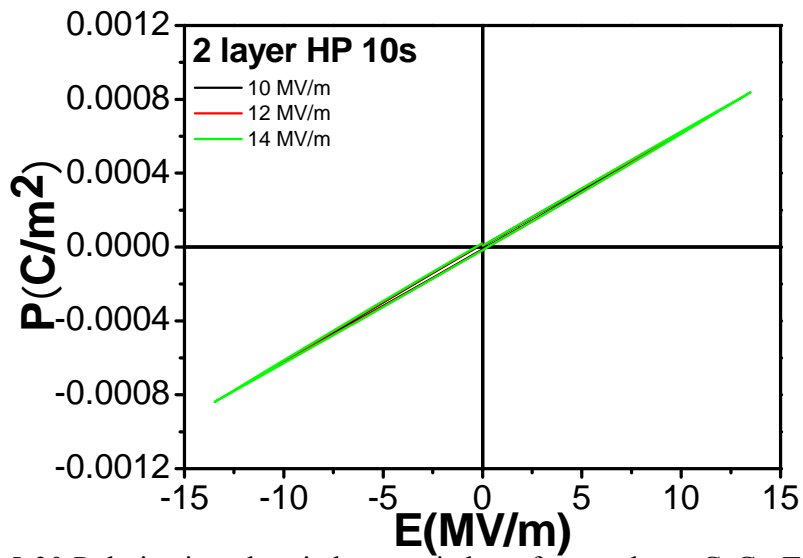


Figure 5-30 Polarization electric hysteresis loop for two layer $\text{CaCu}_3\text{Ti}_4\text{O}_{12}/\text{P}(\text{VDF-TrFE})$ composites with 50 vol% $\text{CaCu}_3\text{Ti}_4\text{O}_{12}$ powder.

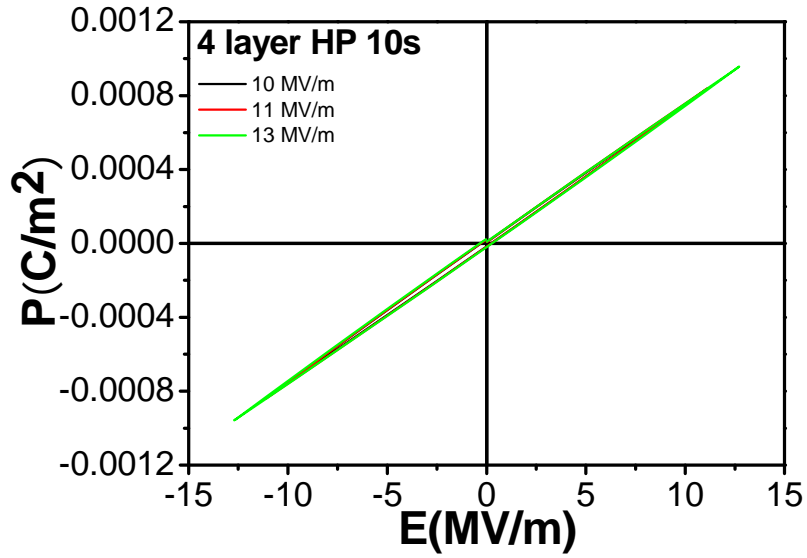


Figure 5-31 Polarization electric hysteresis loop for two layer $\text{CaCu}_3\text{Ti}_4\text{O}_{12}/\text{P}(\text{VDF-TrFE})$ composites with 50 vol% $\text{CaCu}_3\text{Ti}_4\text{O}_{12}$ powder.

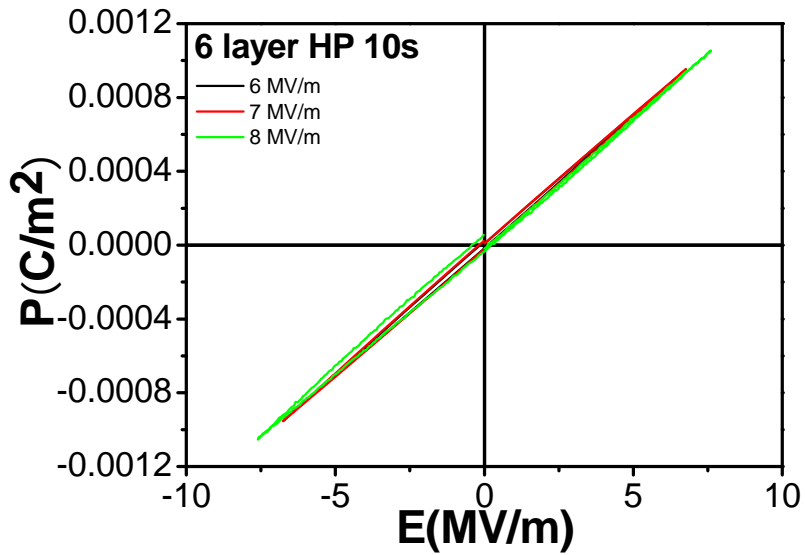


Figure 5-32 Polarization electric hysteresis loop for two layer $\text{CaCu}_3\text{Ti}_4\text{O}_{12}/\text{P}(\text{VDF-TrFE})$ composites with 50 vol% $\text{CaCu}_3\text{Ti}_4\text{O}_{12}$ powder.

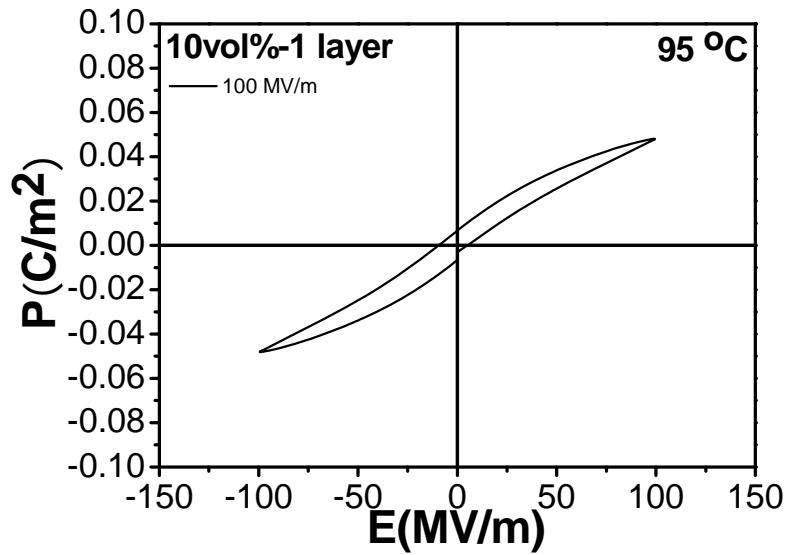


Figure 5-33 Polarization electric hysteresis loop for one layer $\text{CaCu}_3\text{Ti}_4\text{O}_{12}/\text{P}(\text{VDF-TrFE})$ composites with 10 vol% $\text{CaCu}_3\text{Ti}_4\text{O}_{12}$ powder at 95 °C.

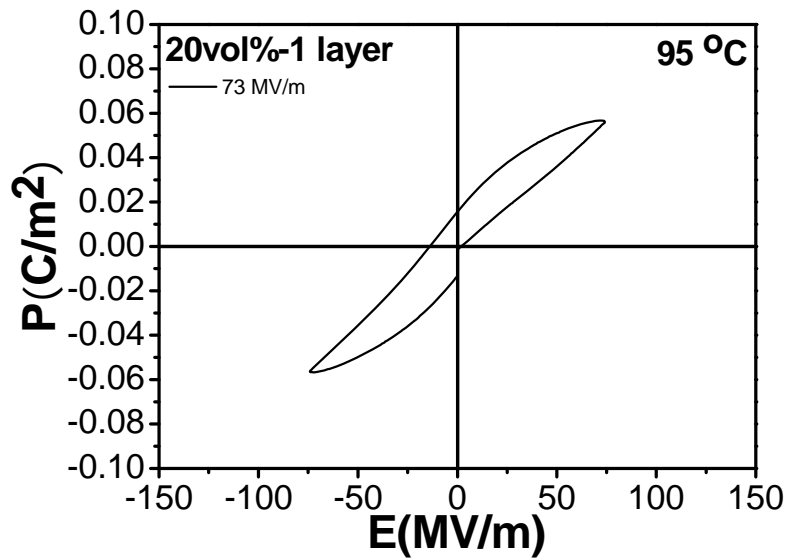


Figure 5-34 Polarization electric hysteresis loop for one layer $\text{CaCu}_3\text{Ti}_4\text{O}_{12}/\text{P}(\text{VDF-TrFE})$ composites with 20 vol% $\text{CaCu}_3\text{Ti}_4\text{O}_{12}$ powder at 95 °C.

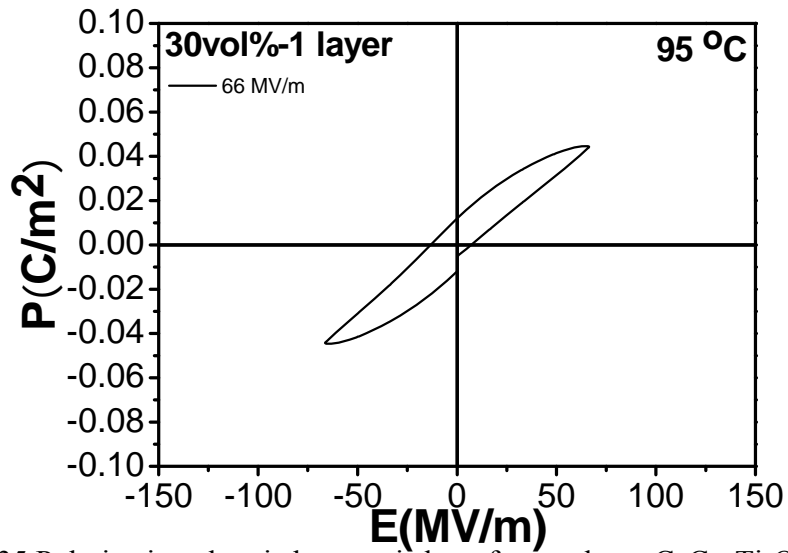


Figure 5-35 Polarization electric hysteresis loop for one layer $\text{CaCu}_3\text{Ti}_4\text{O}_{12}/\text{P}(\text{VDF}-\text{TrFE})$ composites with 30 vol% $\text{CaCu}_3\text{Ti}_4\text{O}_{12}$ powder at 95 °C.

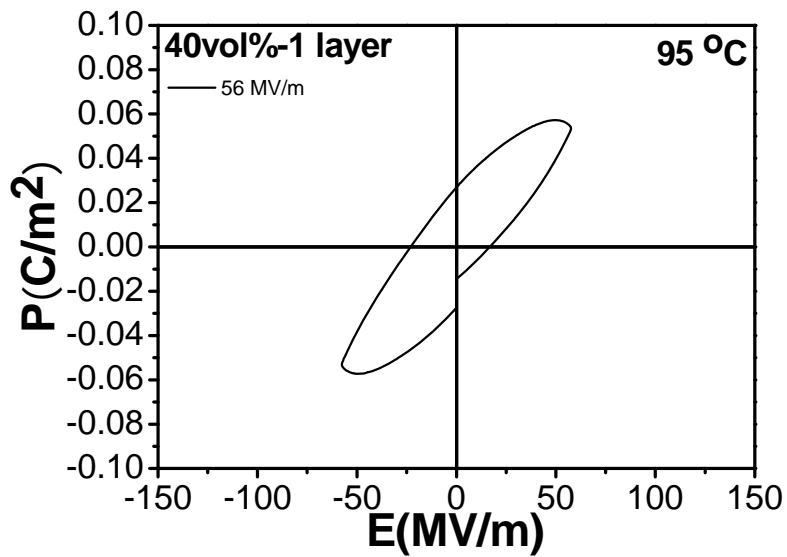


Figure 5-36 Polarization electric hysteresis loop for one layer $\text{CaCu}_3\text{Ti}_4\text{O}_{12}/\text{P}(\text{VDF}-\text{TrFE})$ composites with 40 vol% $\text{CaCu}_3\text{Ti}_4\text{O}_{12}$ powder at 95 °C.

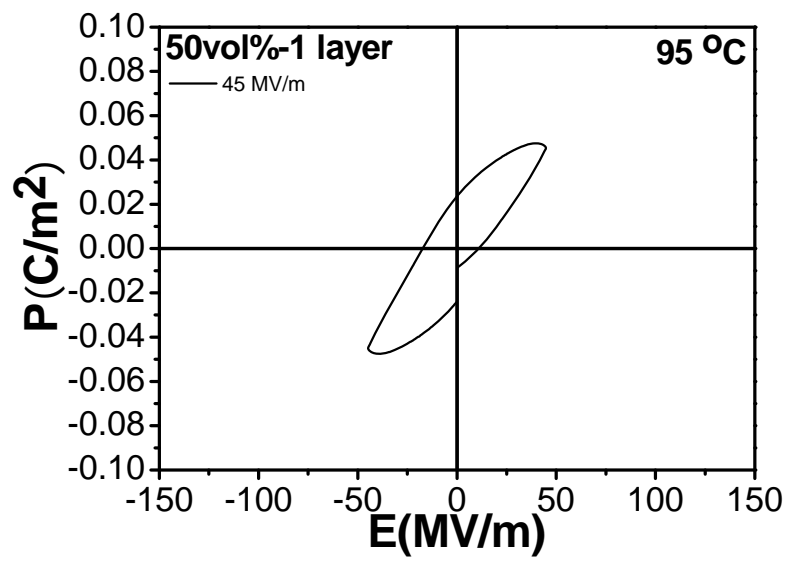


Figure 5-37 Polarization electric hysteresis loop for one layer $\text{CaCu}_3\text{Ti}_4\text{O}_{12}/\text{P}(\text{VDF}-\text{TrFE})$ composites with 50 vol% $\text{CaCu}_3\text{Ti}_4\text{O}_{12}$ powder at 95 °C.

Table 5-6 Summary of P-E results for one layer 10 to 50 vol% CaCu₃Ti₄O₁₂/P(VDF-TrFE) composite at 95 °C.

Composites	Sample	Thickness (μm)	V _{Max} (V)	E _B (MV/m)	P _{Max} ($\mu\text{C}/\text{cm}^2$)
10%	A	66	6200	93.9	4.44
	B	67	6500	97.0	4.65
	C	66	6300	95.5	4.61
	D	65	6000	92.3	4.53
	E	65	6500	100.0	4.81
	Average	65.8	6300	95.7	4.61
20%	A	46	3100	67.4	3.98
	B	46	3400	73.9	4.36
	C	48	3200	66.7	3.07
	D	47	3500	74.5	5.62
	E	48	3000	62.5	4.54
	Average	47.0	3240	69.0	4.31
30%	A	63	4000	63.5	5.58
	B	62	3700	59.7	4.39
	C	63	4000	63.5	5.09
	D	60	4000	66.7	4.44
	E	64	3900	60.9	4.47
	Average	62.4	3920	62.9	4.79
40%	A	66	3200	48.5	5.76
	B	69	4000	57.9	5.35
	C	63	3200	50.7	6.80
	D	64	3800	59.3	5.91
	E	63	3000	47.6	5.13
	Average	65	3440	52.8	5.79
50%	A	100	4500	45.0	4.55
	B	100	4100	41.0	4.84
	C	94	4000	42.5	4.95
	D	102	4000	39.2	4.09
	E	95	3500	36.8	4.75
	Average	98.2	4020	40.9	4.64

5.3.1.6 Polymer Matrix Effect on Dielectric Behavior

The size effect on dielectric properties of $\text{CaCu}_3\text{Ti}_4\text{O}_{12}/\text{VC88}$ composite was performed. $\text{CaCu}_3\text{Ti}_4\text{O}_{12}/\text{VC88}$ composite with 50 vol% nano-size $\text{CaCu}_3\text{Ti}_4\text{O}_{12}$ has been prepared and then those as-casted composite samples were annealed at 125 °C/8 hours. Figure 5-38 lists their corresponding dielectric response.

In contrast with the micro-size $\text{CaCu}_3\text{Ti}_4\text{O}_{12}/\text{VC88}$ composite, the value of dielectric constant in nano-size composite tended to be smaller and with annealing, it increased from 28.7 to 29.2, which is shown in Figure 5-38. With two, four and six layer CC HP, the effect of multiple layers dominated, as the dielectric constant increased from 54 to 79 at 1 kHz, while the dielectric loss remained at 0.03. It was also observed that this value is about half of that in micro-size composite, as can be found in Table 5-7. Figure 5-39 to 5-40 list SEM images of one layer and multiple layers $\text{CaCu}_3\text{Ti}_4\text{O}_{12}/\text{VC88}$ composite. A very clear interface between ceramic and polymer layers can also be observed in one layer composite. Under CC HP, their microstructure has been optimized, however due to its nano-size particles, there still remained clear interfaces as there were two, four and six layers CC HP. Similarly, as in P(VDF-TrFE) polymer matrix, it answered why the dielectric property was poorer than that in micro-size composite. Figure 5-41 to 5-44 illustrate temperature dependence of dielectric properties. The entire $\text{CaCu}_3\text{Ti}_4\text{O}_{12}/\text{VC88}$ composite sample with nano-size $\text{CaCu}_3\text{Ti}_4\text{O}_{12}$ exhibited a relatively flat curve as temperature increased. The temperature dependence properties are very similar with the results of micro-size $\text{CaCu}_3\text{Ti}_4\text{O}_{12}/\text{VC88}$ composite.

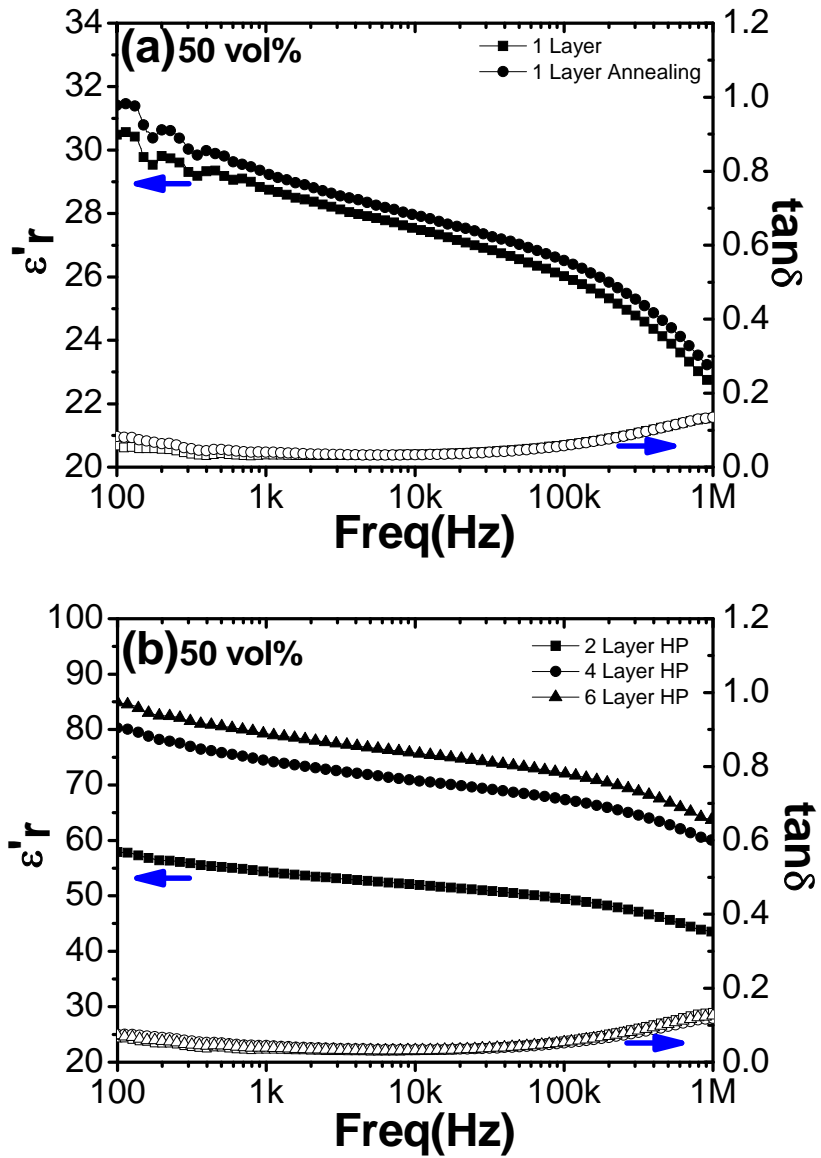


Figure 5-38 Dielectric response vs. frequency of $\text{CaCu}_3\text{Ti}_4\text{O}_{12}/\text{P}(\text{VDF-TrFE})$ composite (10 vol% nano-size $\text{CaCu}_3\text{Ti}_4\text{O}_{12}$): (a) as-casted 1 layer vs. as annealed 1 layer, (b) 2, 4, and 6 layers CC HP for 10s.

Table 5-7 Summary of dielectric data for multiple layers $\text{CaCu}_3\text{Ti}_4\text{O}_{12}/\text{VC88}$ composite (nano-size / μ -size $\text{CaCu}_3\text{Ti}_4\text{O}_{12}$) annealed at 125 °C (1 kHz).

	CC HP layers		
	2 layer	4 layer	6 layer
Nano-sample ^[1]	54/0.04	74/0.04	79/0.04
Micro-sample ^[2]	130/0.17	151/0.14	126/0.14

^[1]: Nano-size $\text{CaCu}_3\text{Ti}_4\text{O}_{12}$ ceramic powder.
^[2]: Micro-size $\text{CaCu}_3\text{Ti}_4\text{O}_{12}$ ceramic powder.

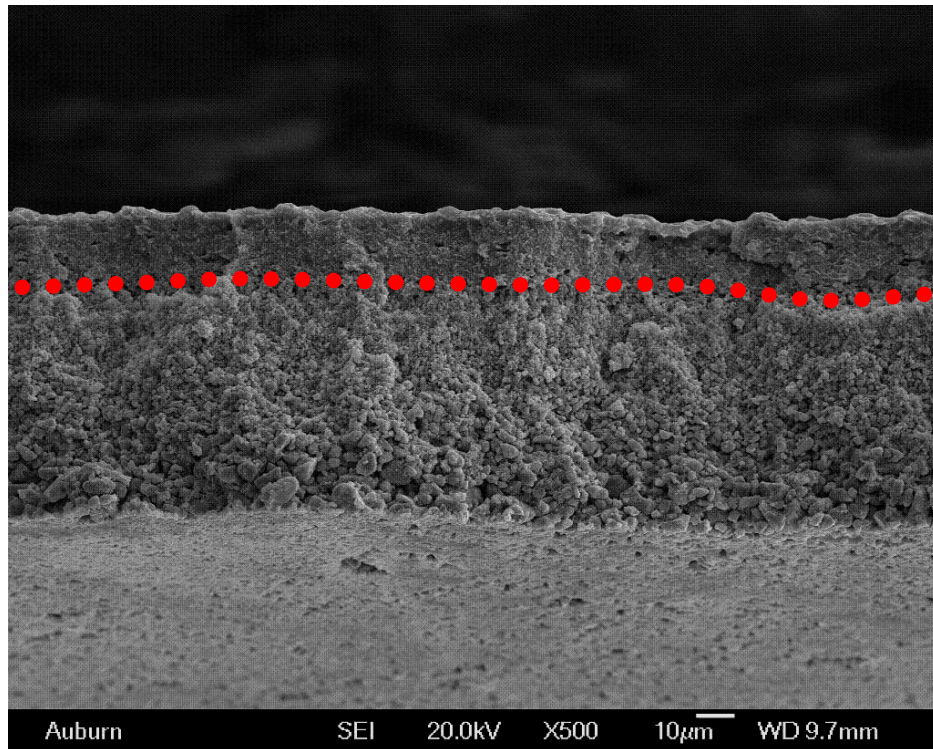


Figure 5-39 SEM fractographs of 1 layer annealed $\text{CaCu}_3\text{Ti}_4\text{O}_{12}/\text{VC88}$ composite (50 vol% nano-size $\text{CaCu}_3\text{Ti}_4\text{O}_{12}$).

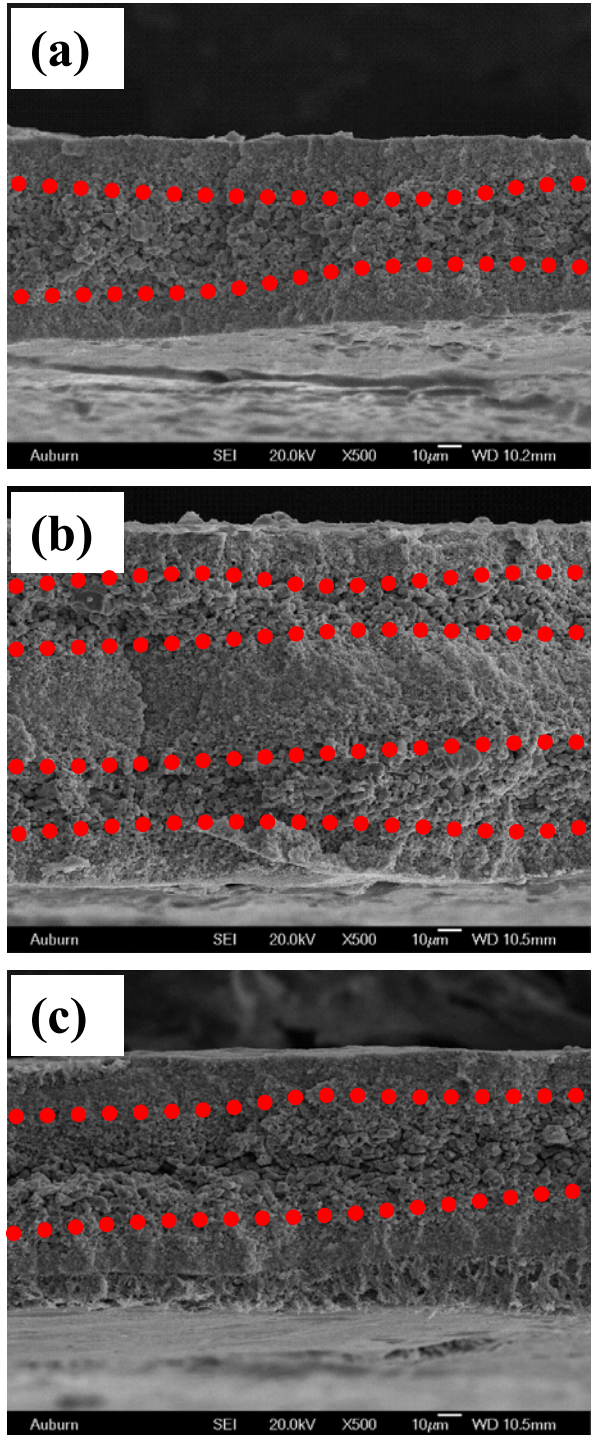


Figure 5-40 SEM fractographs of $\text{CaCu}_3\text{Ti}_4\text{O}_{12}/\text{VC88}$ composites (50 vol% nano-size $\text{CaCu}_3\text{Ti}_4\text{O}_{12}$) using 10s CC HP for (a) 2 layer, (b) 4 layer and (c) 6 layers, respectively.

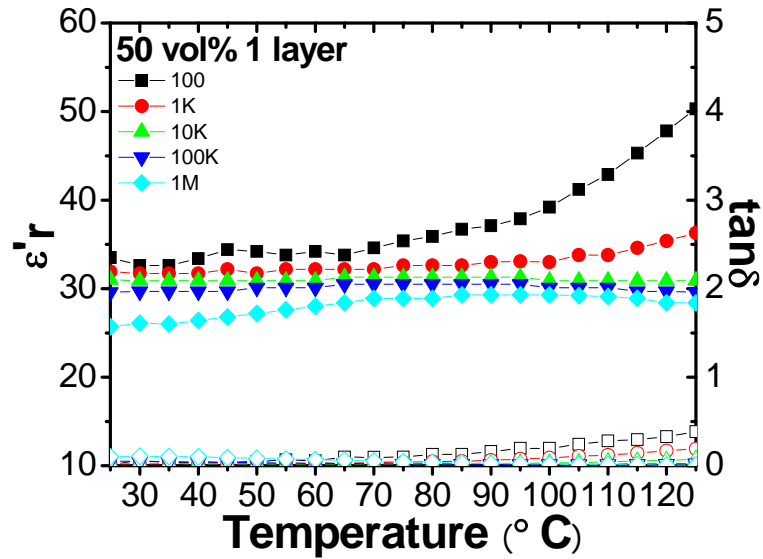


Figure 5-41 Temperature dependence of 1 layer $\text{CaCu}_3\text{Ti}_4\text{O}_{12}/\text{VC88}$ composite (50 vol% nano-size $\text{CaCu}_3\text{Ti}_4\text{O}_{12}$).

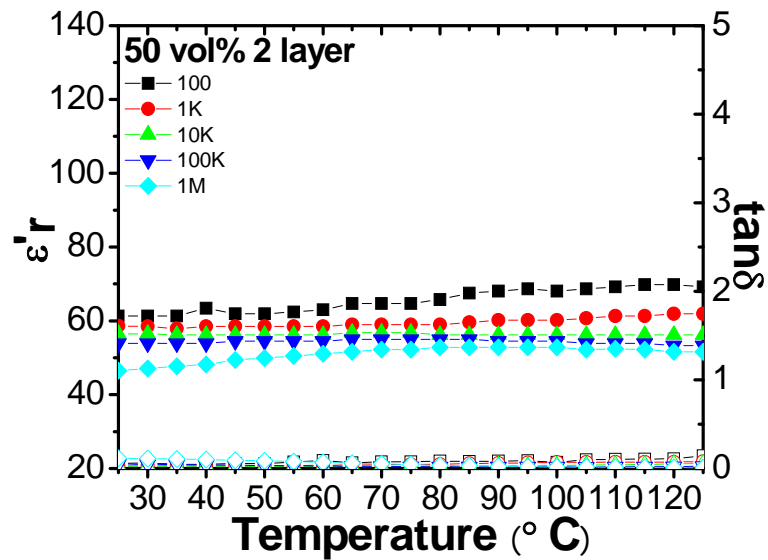


Figure 5-42 Temperature dependence of 2 layer $\text{CaCu}_3\text{Ti}_4\text{O}_{12}/\text{VC88}$ composite for 10s CC HP (50 vol% nano-size $\text{CaCu}_3\text{Ti}_4\text{O}_{12}$).

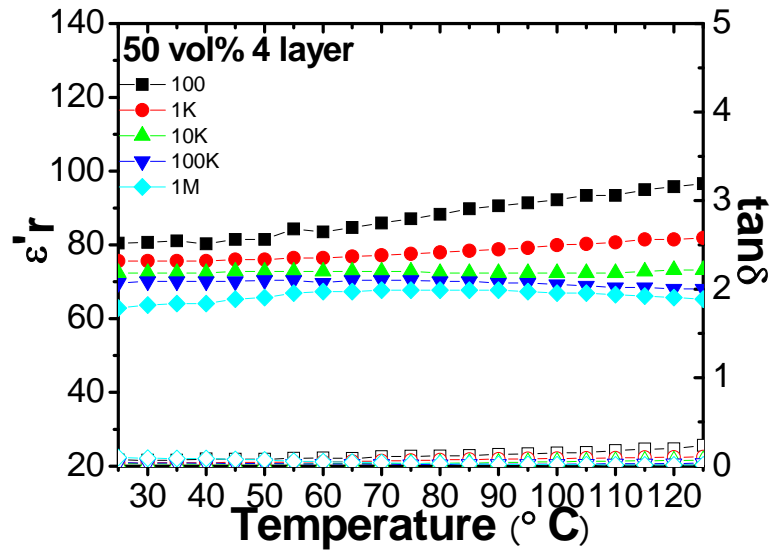


Figure 5-43 Temperature dependence of 4 layer $\text{CaCu}_3\text{Ti}_4\text{O}_{12}/\text{VC88}$ composite for 10s CC HP (50 vol% nano-size $\text{CaCu}_3\text{Ti}_4\text{O}_{12}$).

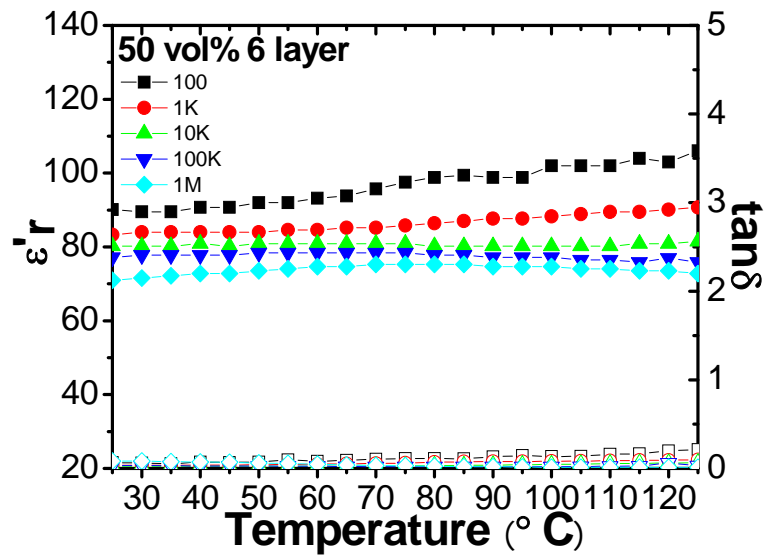


Figure 5-44 Temperature dependence of 6 layer $\text{CaCu}_3\text{Ti}_4\text{O}_{12}/\text{VC88}$ composite for 10s CC HP (50 vol% nano-size $\text{CaCu}_3\text{Ti}_4\text{O}_{12}$).

5.3.2 Silane Coupling Effect on Dielectric Behavior

In previous experiments, it was found that the microstructure played an important role on the dielectric constant. In order to optimize the microstructure, different processing, such as annealing and hot pressing, have been adopted. Especially with CC hot pressing, the apparent interfaces between polymer layer and ceramic layer were minimized, and corresponding dielectric responses were enhanced. Besides hot pressing method, another optimizing method with silane coupling agent is introduced in this work. It is known that coupling is maximized when silanes react with ceramic particles and present the maximum number of sites with reactivity specific and accessible to the polymer matrix. The interphase would then promote a dielectric response in $\text{CaCu}_3\text{Ti}_4\text{O}_{12}$ -based composite.

5.3.2.1 Theoretical Calculation for Silane Coupling Agent

In order to achieve the expected coupling effect, a theoretical calculation about the minimum amount of silane was carried out. The physical properties of silane and ceramic are shown in Table 5-8. The molecule structure of the silane coupling agent is shown in Figure 5-42.

Table 5-8 Physical properties of silane coupling agent ($\text{C}_8\text{H}_4\text{Cl}_3\text{F}_{13}\text{Si}$) and ceramic ($\text{CaCu}_3\text{Ti}_4\text{O}_{12}$).

	$M_{\text{mol}}(\text{g/mol})$	$\rho(\text{g/cm}^3)$
Silane coupling agent ($\text{C}_8\text{H}_4\text{Cl}_3\text{F}_{13}\text{Si}$):	481.55	1.638
Ceramic ($\text{CaCu}_3\text{Ti}_4\text{O}_{12}$)	614	5.267

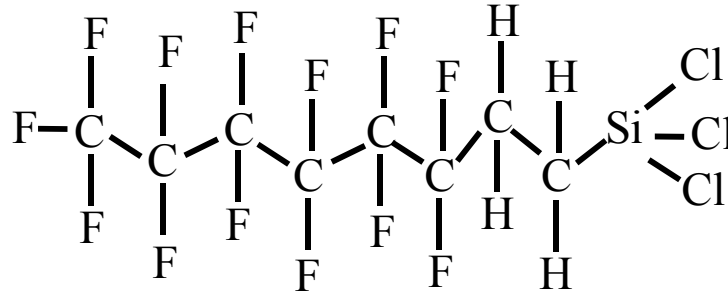


Figure 5-45 The molecule structure of the silane coupling agent ($C_8H_4Cl_3F_{13}Si$).

Silane coupling agent ($C_8H_4Cl_3F_{13}Si$):

As the silane coupling agent ($C_8H_4Cl_3F_{13}Si$) is concerned, based on the data in Table 5-1, then one molecule weight of $C_8H_4Cl_3F_{13}Si$ is given as following:

$$m_s = \frac{481.55 \times 10^{-3}}{6.023 \times 10^{23}} = 7.9952 \times 10^{-25} \text{ (kg)} \quad (5-1)$$

The single molecule volume ($C_8H_4Cl_3F_{13}Si$) is:

$$V_s = \frac{7.9952 \times 10^{-25}}{1.638 \times 10^3} = 4.8811 \times 10^{-28} \text{ (m}^3\text{)} \quad (5-2)$$

Assuming the molecule structure ($C_8H_4Cl_3F_{13}Si$) resembles cylinder structure with a radius of r and length of $10r$, then the radius can be given as below:

$$V_s = \pi r^2 10r = 10\pi r^3 \Rightarrow r = \sqrt[3]{\frac{V_s}{10\pi}} = 2.4957 \times 10^{-10} \text{ (m)} \quad (5-3)$$

The surface area of top or bottom ($C_8H_4Cl_3F_{13}Si$), which will attach the $CaCu_3Ti_4O_{12}$ particle, is given as:

$$A_s = \pi r^2 = 1.9558 \times 10^{-19} \text{ (m}^2\text{)} \quad (5-4)$$

Ceramic ($CaCu_3Ti_4O_{12}$):

Assuming the $CaCu_3Ti_4O_{12}$ weight is about 1 g and its average particle size is about 10 μm , then one particle weight is about:

$$m_c = \frac{4}{3} \pi \left(\frac{D}{2}\right)^3 \rho = \frac{4}{3} \pi \left(\frac{1 \times 10^{-6}}{2}\right)^3 5.267 \times 10^3 = 2.75 \times 10^{-12} \text{ (kg)} \quad (5-5)$$

The total number of ceramic particle is:

$$n_c = \frac{1 \times 10^{-3}}{2.75 \times 10^{-15}} = 0.3636 \times 10^9 \quad (5-6)$$

The surface area of one ceramic particle is:

$$s_c = 4\pi\left(\frac{D}{2}\right)^2 = 3.14 \times 10^{-10} (m^2) \quad (5-7)$$

The total surface area will be:

$$S_c = s_c n_c = 0.114 (m^2) \quad (5-8)$$

If the average ceramic particle size is about 500 nm, then with the same calculation procedure, the total surface area is about:

$$S_c = s_c n_c = 2.278 (m^2) \quad (5-9)$$

Theoretical Calculation

In order to cover all the $\text{CaCu}_3\text{Ti}_4\text{O}_{12}$ μ -size particle, the total number of silane molecule is given as:

$$N = \frac{1.1417}{1.9558 \times 10^{-19}} = 0.5837 \times 10^{18} \quad (5-10)$$

The corresponding total weight of silane molecule is:

$$M = \frac{0.5837 \times 10^{19}}{6.023 \times 10^{23}} \times 481.55 = 0.0004695 (g) \quad (5-11)$$

Therefore in comparison with 1 g 10 μm $\text{CaCu}_3\text{Ti}_4\text{O}_{12}$ ceramic, the minimum silane concentration is about 0.05 wt%.

With the same calculation, in comparison with 1 g 500 nm $\text{CaCu}_3\text{Ti}_4\text{O}_{12}$, the minimum silane concentration is about 0.93 wt% \approx 1 wt%.

5.3.3.1 Dielectric Behavior

The dielectric properties with silane have been studied under a series of conditions, such as annealing and various silane concentrations. The annealing effect study was performed on the $\text{CaCu}_3\text{Ti}_4\text{O}_{12}$ -based composite (micro-size $\text{CaCu}_3\text{Ti}_4\text{O}_{12}$). The annealing temperature was fixed at 125 °C for 8 hours and $\text{CaCu}_3\text{Ti}_4\text{O}_{12}$ volume concentration varied from 10 to 50 vol%. In order to study the effect of silane concentration, silane concentrations, such as 1, 5 and 10 wt%, were selected in the experiment. Figure 5-46 to 5-50 list the dielectric results of one layer as-casted composite sample. Table 5-9 summarizes the dielectric results at 1 kHz.

Their frequency dependent results were observed in Figure 46 to 5-50. When the $\text{CaCu}_3\text{Ti}_4\text{O}_{12}$ volume concentration increased from 10 to 50 and silane concentration varied from 1 to 5 wt%, it presented a general trend that annealed sample always exhibited higher dielectric results, which is consistent with previous results without silane. For example, for 50 vol% $\text{CaCu}_3\text{Ti}_4\text{O}_{12}$, the dielectric constant changed from 47 to 73 with 1 wt% silane, 145 to 154 with 5 wt% silane and 15 to 23 with 19 wt%, as shown in Table 5-9. This phenomenon is closely associated with crystallinity improvement in the composite with annealing, which has been discussed in Chapter 4. The effect of silane was observed in different $\text{CaCu}_3\text{Ti}_4\text{O}_{12}$ volume concentrations, 10 to 50 vol%. Corresponding to each individual silane concentration, a dielectric peak appeared at 40 vol% and its dielectric value differed in each silane concentration. As the $\text{CaCu}_3\text{Ti}_4\text{O}_{12}$ volume concentration was small, such as 10 and 20, the dielectric constant was indeed improved, but not that much. The maximum value of 81 appeared at 20 vol% with 1 wt % silane. As the $\text{CaCu}_3\text{Ti}_4\text{O}_{12}$ volume concentration was higher, such as 40 vol%, a maximum value of 836 was achieved, however its dielectric loss is very high. After considering its dielectric loss, an optimized value was found within 30 and 50 vol%. For both the concentration after annealing, as the silane concentration varying from 1 to 10 wt%, they exhibited maximum peaks of 118 and 154 with 5 wt% silane for 30 and 50 vol% $\text{CaCu}_3\text{Ti}_4\text{O}_{12}/\text{P}(\text{VDF}-\text{TrFE})$ composite. Those experiment results indicated that the silane concentration is also decisive for the improvement of dielectric response. More studies on the silane concentration will be performed.

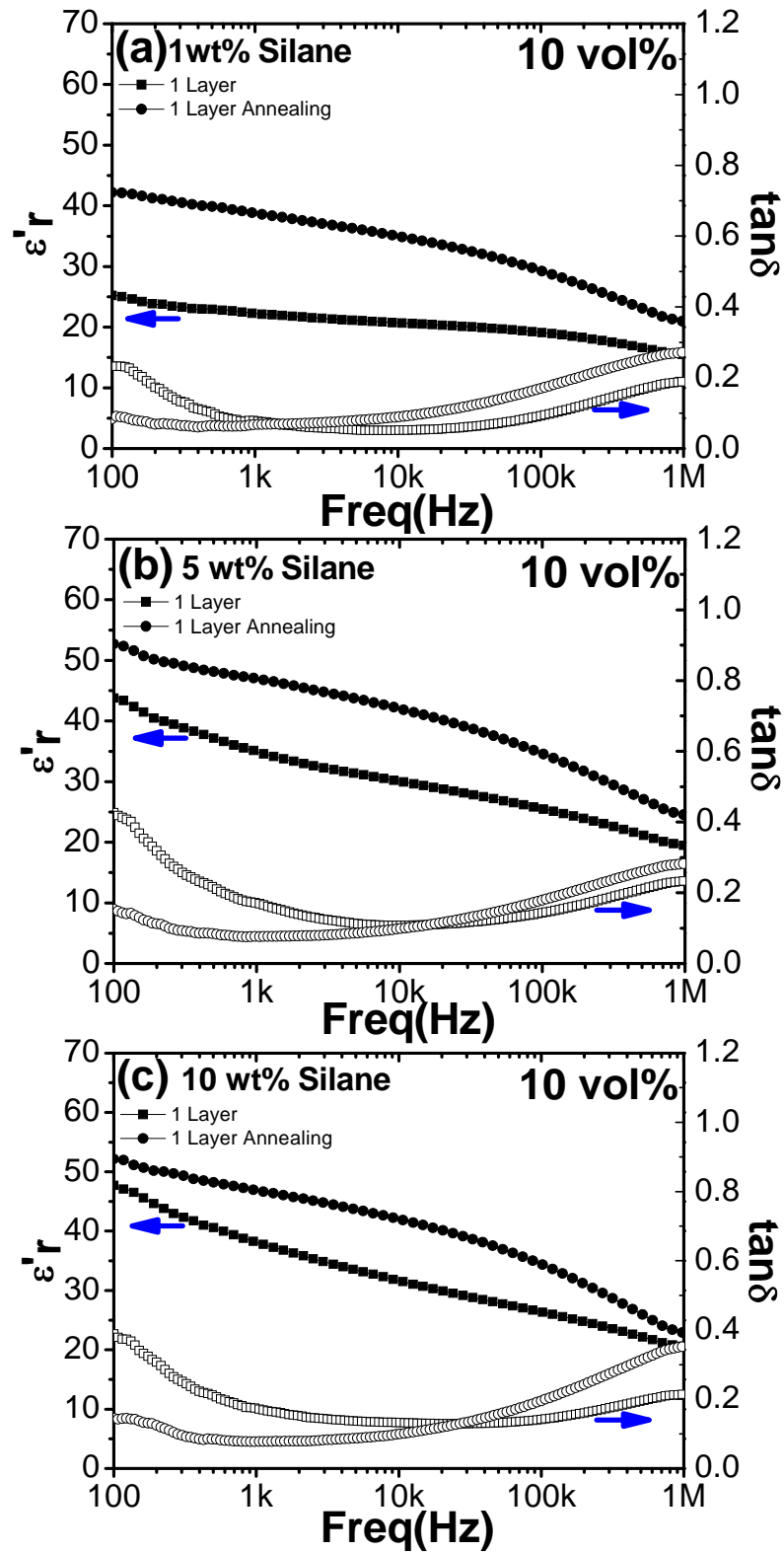


Figure 5-46 Dielectric response vs. frequency of 1 layer $\text{CaCu}_3\text{Ti}_4\text{O}_{12}/\text{P}(\text{VDF}-\text{TrFE})$ composite (10 vol% μ -size $\text{CaCu}_3\text{Ti}_4\text{O}_{12}$) with (a) 1, (b) 5, and (c) 10 wt% silane.

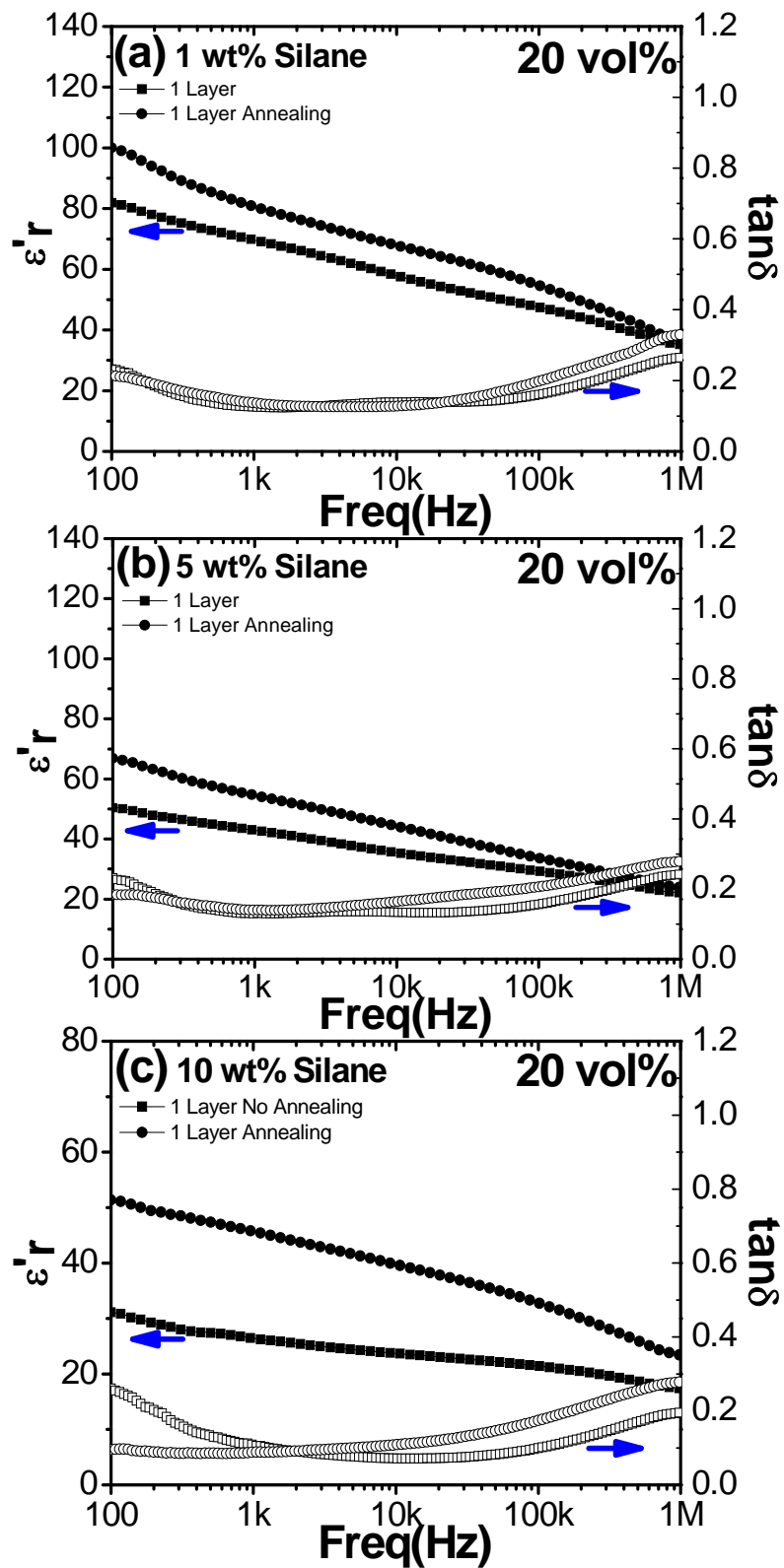


Figure 5-47 Dielectric response vs. frequency of 1 layer $\text{CaCu}_3\text{Ti}_4\text{O}_{12}/\text{P}(\text{VDF}-\text{TrFE})$ composite (20 vol% μ -size $\text{CaCu}_3\text{Ti}_4\text{O}_{12}$) with (a) 1, (b) 5, and (c) 10 wt% silane.

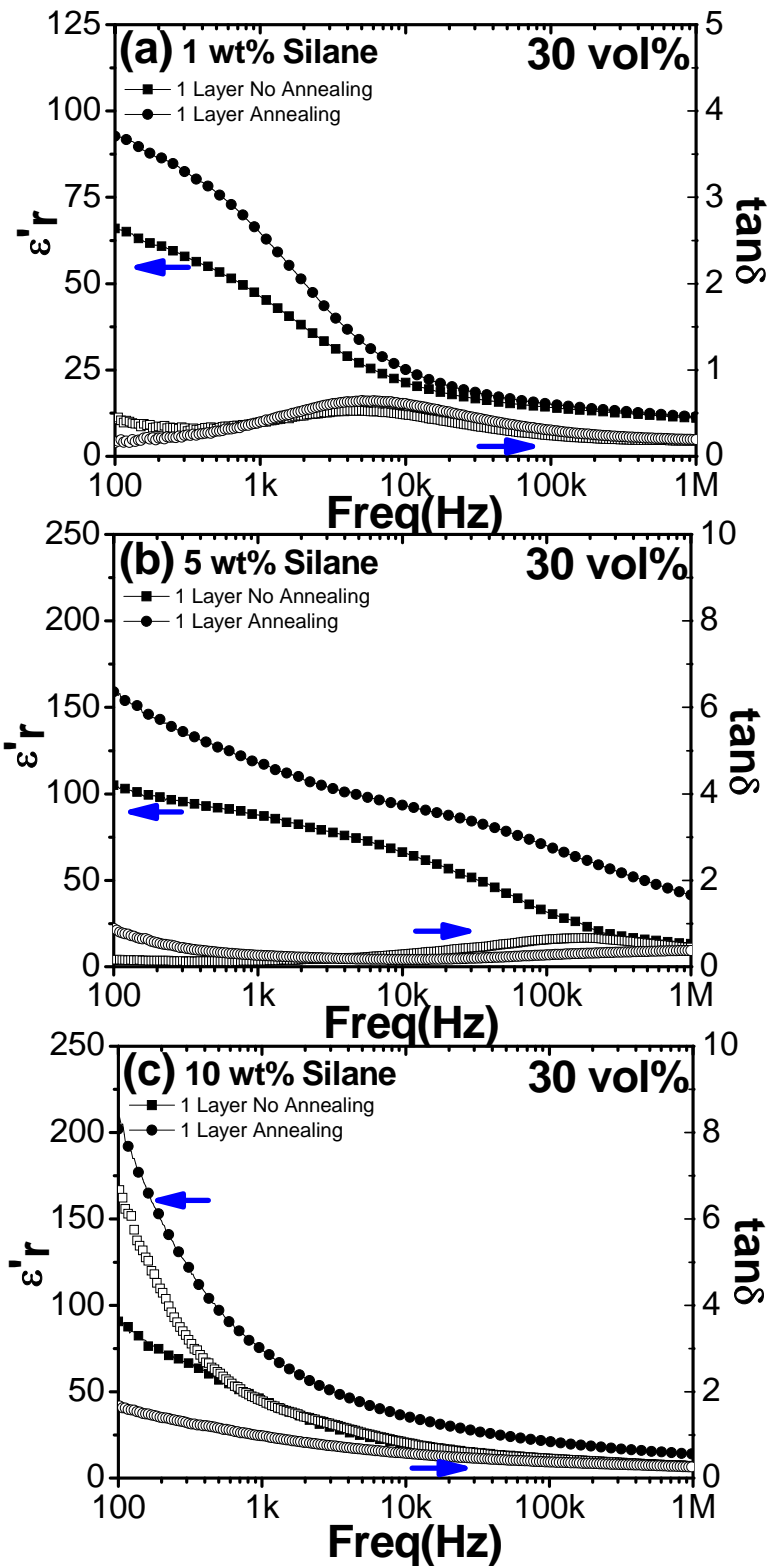


Figure 5-48 Dielectric response vs. frequency of 1 layer $\text{CaCu}_3\text{Ti}_4\text{O}_{12}/\text{P}(\text{VDF-TrFE})$ composite (30 vol% μ -size $\text{CaCu}_3\text{Ti}_4\text{O}_{12}$) with (a) 1, (b) 5, and (c) 10 wt% silane.

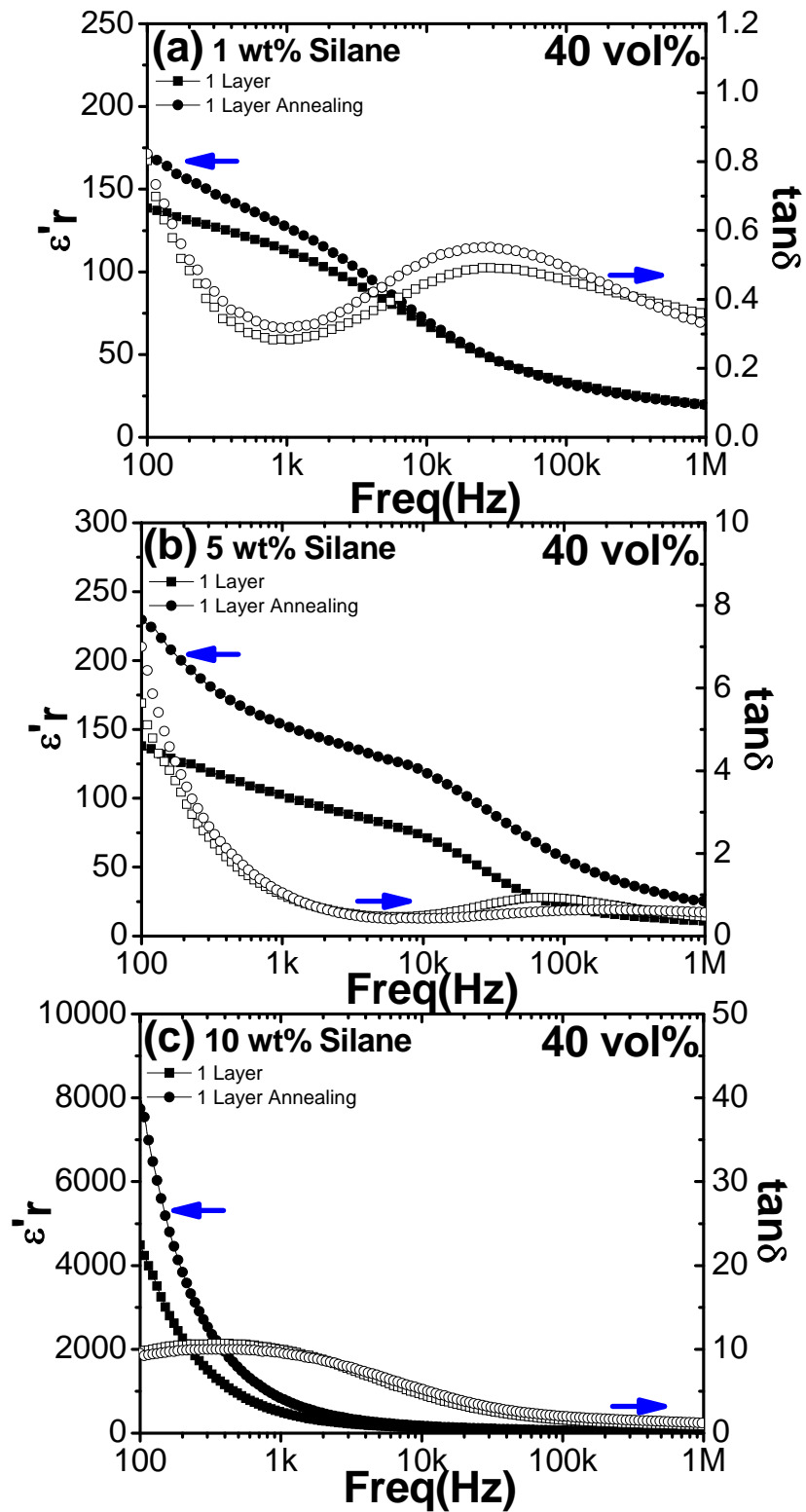


Figure 5-49 Dielectric response vs. frequency of 1 layer $\text{CaCu}_3\text{Ti}_4\text{O}_{12}/\text{P}(\text{VDF}-\text{TrFE})$ composite (40 vol% μ -size $\text{CaCu}_3\text{Ti}_4\text{O}_{12}$) with (a) 1, (b) 5, and (c) 10 wt% silane.

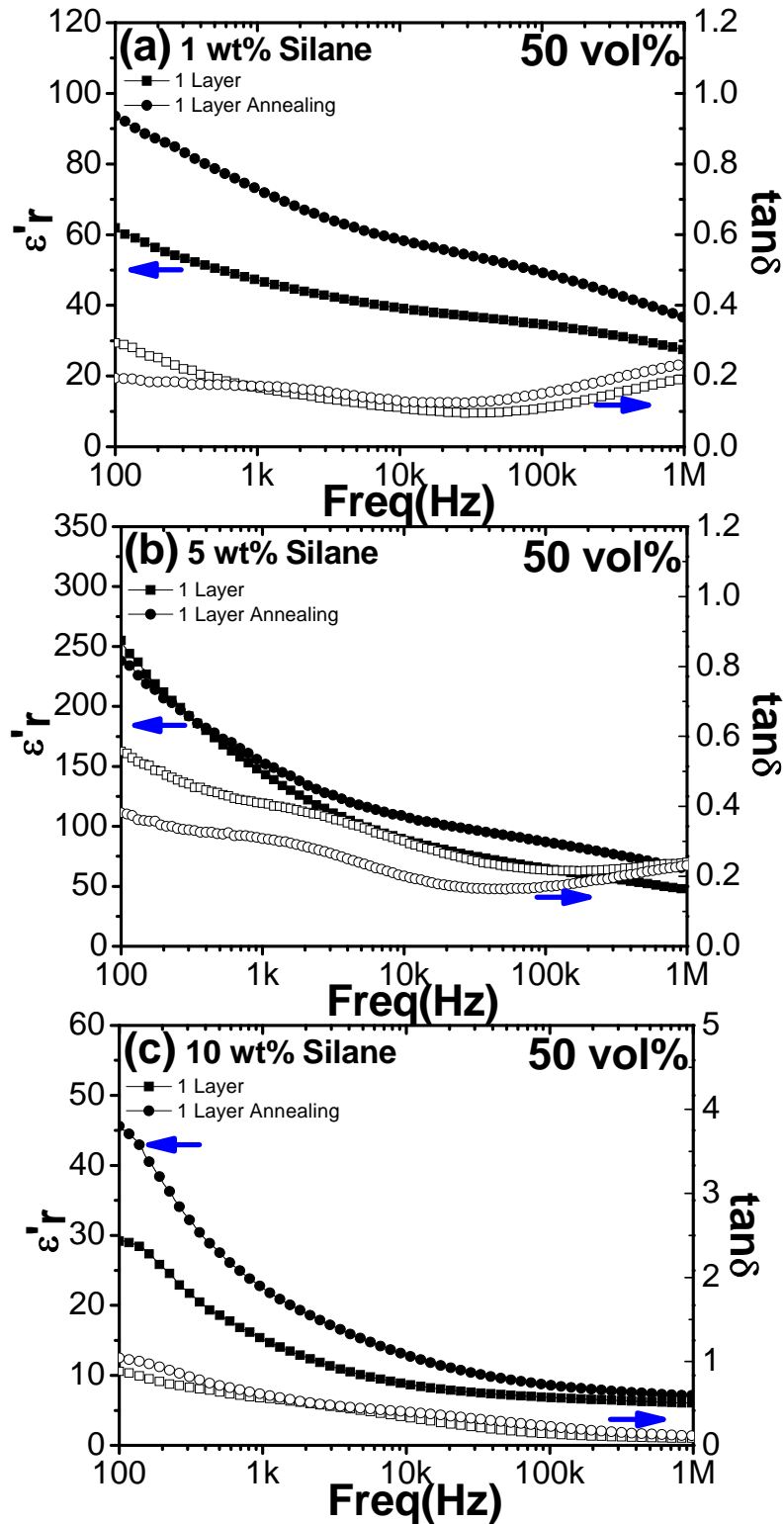


Figure 5-50 Dielectric response vs. frequency of 1 layer $\text{CaCu}_3\text{Ti}_4\text{O}_{12}/\text{P}(\text{VDF-TrFE})$ composite (50 vol% μ -size $\text{CaCu}_3\text{Ti}_4\text{O}_{12}$) with (a) 1, (b) 5, and (c) 10 wt% silane.

Table 5-9 Summary of dielectric data for 1 layer $\text{CaCu}_3\text{Ti}_4\text{O}_{12}$ /P(VDF-TrFE) composite (μ -size $\text{CaCu}_3\text{Ti}_4\text{O}_{12}$) with 0, 1, 5 and 10 wt% silane with annealed at 125 °C (1 kHz).

		CaCu ₃ Ti ₄ O ₁₂ Concentration (vol%)				
		10 vol%	20 vol%	30 vol%	40 vol%	50 vol%
1 layer ^[1]	0 wt%	18/0.04	23/0.04	32/0.06	65/0.1	69/0.1
1 layer ^[2]	0 wt%	25/0.05	34/0.08	43/0.09	105/0.2	67/0.1
	1 wt%	22/0.08	70/0.13	46/0.40	113/0.28	47/0.17
1 layer ^[1]	5 wt%	35/0.17	43/0.13	88/0.14	102/1.00	145/0.41
	10 wt%	38/0.17	26/0.11	45/1.78	505/9.99	15/0.57
	1 wt%	39/0.07	81/0.14	65/0.40	127/0.31	73/0.17
1 layer ^[2]	5 wt%	47/0.08	55/0.14	118/0.27	154/1.05	154/0.31
	10 wt%	47/0.08	46/0.09	73/0.98	836/9.55	23/0.61

^[1]: Casting at 70 °C/8 hrs.

^[2]: Casting at 70 °C/8 hr and annealing at 125 °C/8 hrs.

5.3.3.3 Silane Concentration Effect on Dielectric Behavior

As stated earlier, different silane concentrations, such as 1, 5 and 10 wt%, were used in the experiments. It was found in the experiment that the silane concentration played an important role in the dielectric properties of the $\text{CaCu}_3\text{Ti}_4\text{O}_{12}/\text{P}(\text{VDF-TrFE})$ composite. However, what about the dielectric response with low silane concentration such as below 1 wt%? Thus in the following experiments, the dielectric properties with 0.3, 0.5 and 0.75 wt% silane were observed, and the composite with 50 vol% $\text{CaCu}_3\text{Ti}_4\text{O}_{12}$ was chosen. Figure 5-51 illustrates the dielectric results for one layer 50 vol% composites with 0.3, 0.5 and 0.75 wt% silane. The corresponding dielectric results with 0.3, 0.5, 0.75, 1, 5 and 10 wt% silane at 1 kHz are summarized in Table 5-10.

Based on the results, the first impression was that the dielectric properties after annealing were better than non-annealed samples, which was consistent with previous results in $\text{CaCu}_3\text{Ti}_4\text{O}_{12}/\text{P}(\text{VDF-TrFE})$ composite. In previous experiment results, as the silane varied from 1 to 10 wt%, a one layer flexible composite sample at 5 wt% silane with better dielectric response was fabricated, whose maximum dielectric constant can be as high as 154 and loss is around 0.31. However, as silane concentration went below 1 wt%, an even better dielectric response was achieved at 0.5 wt% silane, whose dielectric constant is about 170 and loss about 0.20, as seen in Figure 5-52. The possible explanation responsible for this phenomenon is the percolation, which generated at low concentration, such as with 0.5 wt% silane, and can lead to better microstructure as seen in Figure 5-53, which corresponded to a better dielectric response. Also, with too much silane inside, it would form thick layer between ceramic and polymer matrix, which leads to high conductivity and high loss, and then results in a porous structure as shown in 5-53 (f).

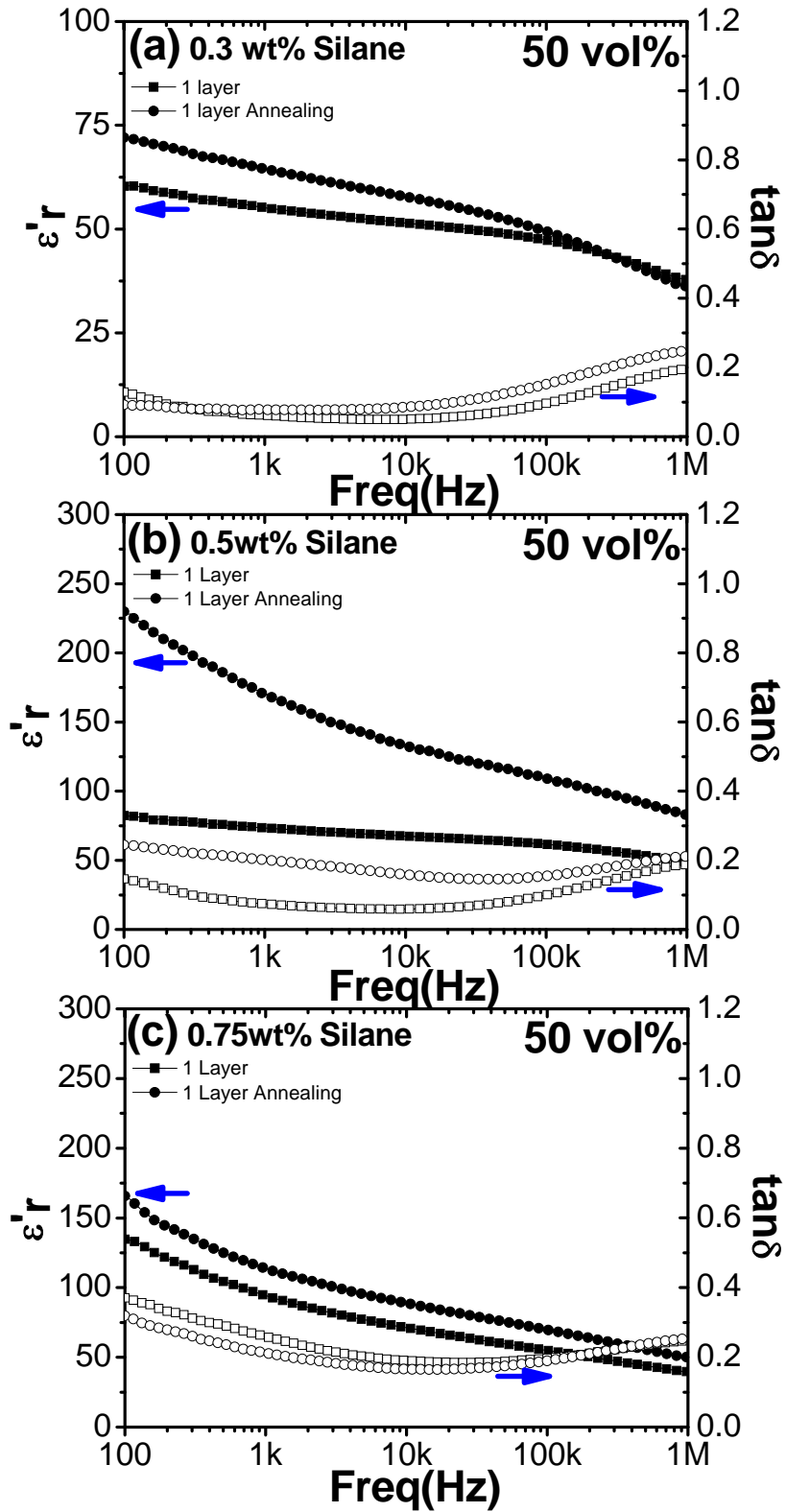


Figure 5-51 Dielectric response vs. frequency of 1 layer $\text{CaCu}_3\text{Ti}_4\text{O}_{12}/\text{P}(\text{VDF}-\text{TrFE})$ composite (50 vol% μ -size $\text{CaCu}_3\text{Ti}_4\text{O}_{12}$) with (a) 0.3, (b) 0.5 and (c) 0.75 wt% silane.

Table 5-10 Summary of dielectric data for 1 layer $\text{CaCu}_3\text{Ti}_4\text{O}_{12}/\text{P}(\text{VDF-TrFE})$ composite (μ -size $\text{CaCu}_3\text{Ti}_4\text{O}_{12}$) with 0.3, 0.5, 0.75, 1, 5 and 10 wt% silane with annealed at 125°C (1 kHz).

	Silane Concentration (wt%)					
	0.3 wt%	0.5 wt%	0.75 wt%	1 wt%	5 wt%	10 wt%
1 layer ^[1]	55/0.06	74/0.07	94/0.26	47/0.17	145/0.41	15/0.57
1 layer ^[2]	64/0.07	170/0.20	114/0.21	73/0.17	154/0.31	23/0.61

^[1]: Casting at $70^\circ\text{C}/8$ hrs.

^[2]: Casting at $70^\circ\text{C}/8$ hr and annealing at $125^\circ\text{C}/8$ hrs.

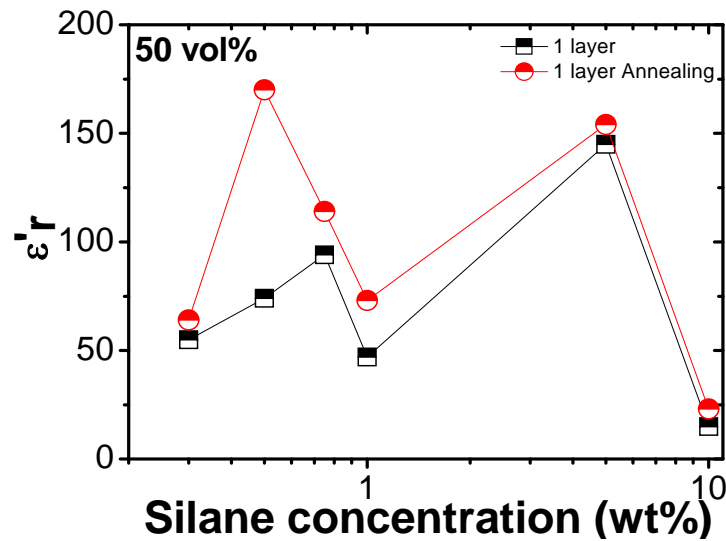


Figure 5-52 Dependence of dielectric response vs. silane coupling concentration in $\text{CaCu}_3\text{Ti}_4\text{O}_{12}/\text{P}(\text{VDF-TrFE})$ composite (μ -size $\text{CaCu}_3\text{Ti}_4\text{O}_{12}$): (a) 1 layer vs. 1 annealed layer, (b) multiple layers using 10s CC HP at room temperature.

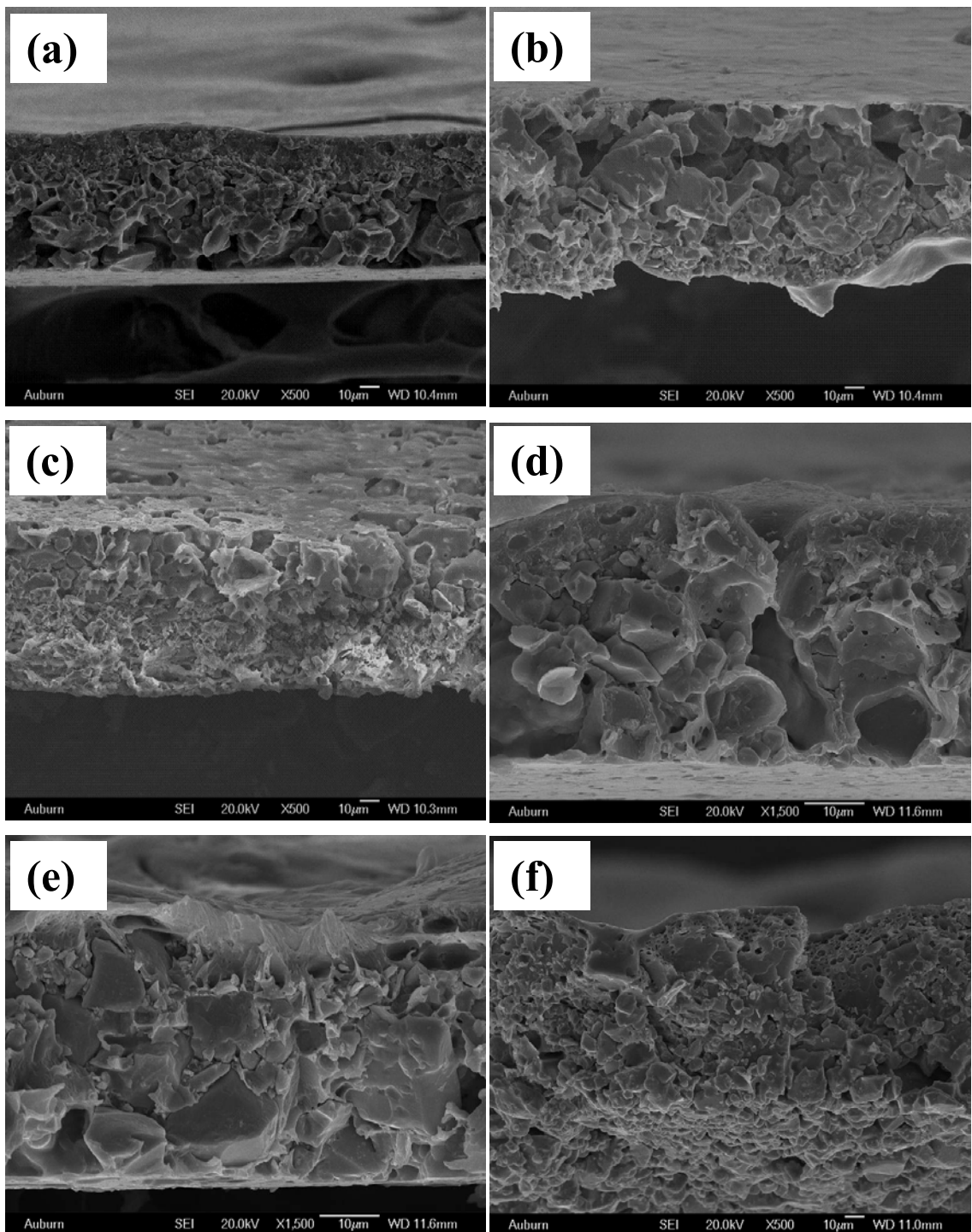


Figure 5-53 SEM fractographs of 1 layer $\text{CaCu}_3\text{Ti}_4\text{O}_{12}/\text{P}(\text{VDF-TrFE})$ composites (50vol% μ -size $\text{CaCu}_3\text{Ti}_4\text{O}_{12}$) with: (a) 0.3 wt%, (b) 0.5 wt%, (c) 0.75 wt%, (d) 1 wt%, (e) 5 wt% and (f) 10 wt% silane, respectively.

5.3.3.4 Temperature Dependent of Dielectric Response

Besides of the dielectric response, the temperature dependence properties of one layer $\text{CaCu}_3\text{Ti}_4\text{O}_{12}/\text{P}(\text{VDF-TrFE})$ composite with 0.5, 0.75 and 1 wt% silane were studied. Their experimental results are shown in Figure 5-54 to 5-56. $\text{CaCu}_3\text{Ti}_4\text{O}_{12}/\text{P}(\text{VDF-TrFE})$ composite with 50 vol% $\text{CaCu}_3\text{Ti}_4\text{O}_{12}$ powder was chosen in the work.

No matter the silane volume concentration, their temperature dependent properties with silane exhibited the similar tendency as previous results in $\text{CaCu}_3\text{Ti}_4\text{O}_{12}/\text{P}(\text{VDF-TrFE})$ composite: those curves resemble a relaxation process, which is believed to be associated with ferroelectrics: P(VDF-TrFE) polymer matrix. As for the one layer composite with 0.5 wt%, 0.75 wt% and 1 wt% silane, all the temperature dependent curves reached their dielectric peaks and then leveled off, as shown in Figure 5-54 to 5-56. It is noted that with higher silane concentration, the results at 100 Hz exhibited tailing up at high temperature and this phenomenon may be associated with increasing conductivity. Moreover, it is found that the curie-temperature exhibited an increasing trend from 95 to 105 °C as the silane concentration increased from 0.5 to 1 wt%.

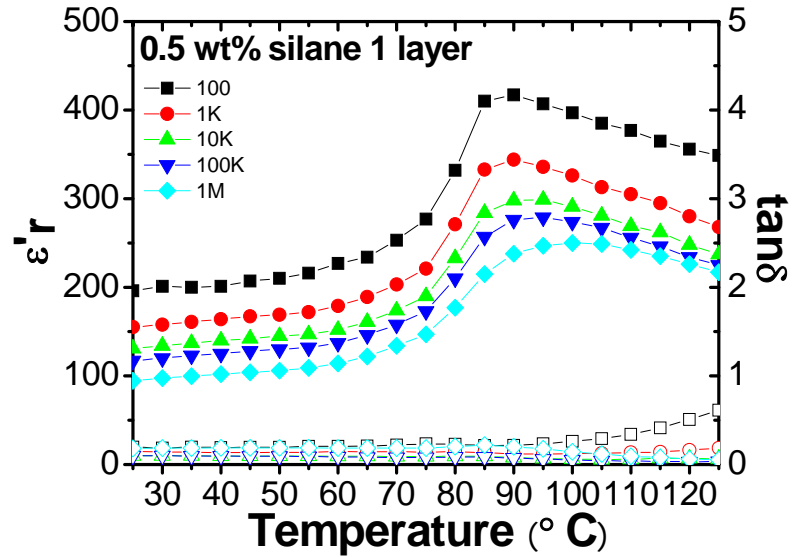


Figure 5-54 Temperature dependence of one layer $\text{CaCu}_3\text{Ti}_4\text{O}_{12}/\text{P}(\text{VDF-TrFE})$ composite (50 vol% μ -size $\text{CaCu}_3\text{Ti}_4\text{O}_{12}$) with 0.75 wt% silane.

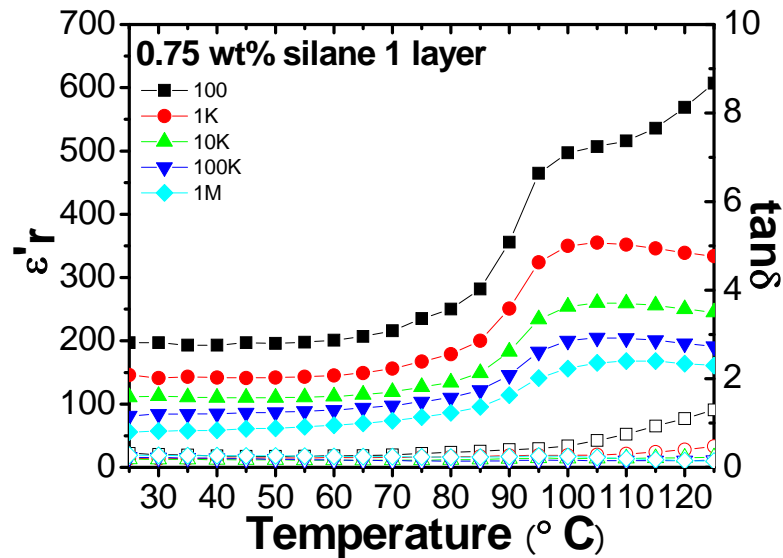


Figure 5-55 Temperature dependence of one layer $\text{CaCu}_3\text{Ti}_4\text{O}_{12}/\text{P}(\text{VDF-TrFE})$ composite (50 vol% μ -size $\text{CaCu}_3\text{Ti}_4\text{O}_{12}$) with 0.75 wt% silane.

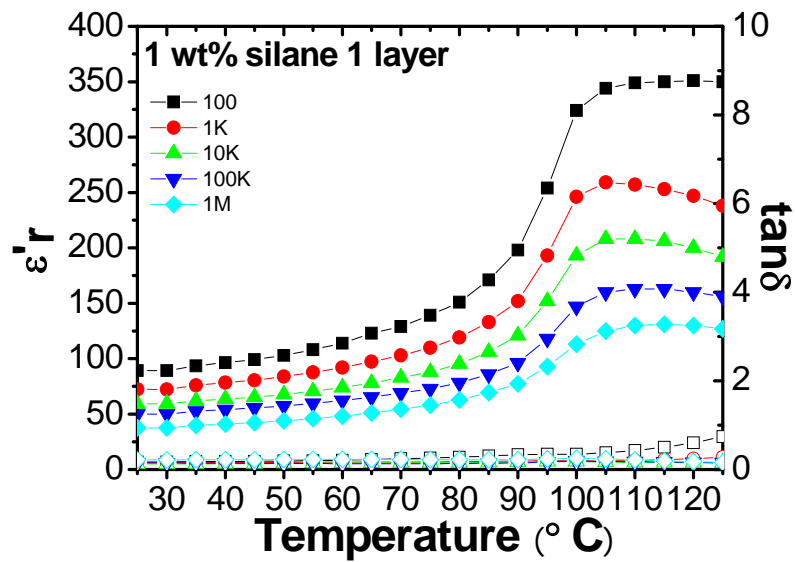


Figure 5-56 Temperature dependence of one layer $\text{CaCu}_3\text{Ti}_4\text{O}_{12}/\text{P}(\text{VDF-TrFE})$ composite (50 vol% μ -size $\text{CaCu}_3\text{Ti}_4\text{O}_{12}$) with 1 wt% silane.

5.3.3.5 Size Effect on Dielectric Behavior

The dielectric behaviors based on 50 vol% nano-size $\text{CaCu}_3\text{Ti}_4\text{O}_{12}$ ceramic particle with different silane concentrations are shown in Figure 5-54. Table 5-11 summarizes their corresponding dielectric constant at 1 kHz. As described previously in the nano-size $\text{CaCu}_3\text{Ti}_4\text{O}_{12}$ ceramic particle, the theoretical minimum silane concentration is about 1 wt%. In this work, the silane concentration varied among 1, 5 and 10 wt%. As shown in the Figure 5-57, with nano-size ceramic particle, it was found that the dielectric responses improved with 1, 5 and 10 wt% silane. In Table 5-11, the dielectric constant in a one layer annealed sample varied from 73 to 67 at 1 wt% silane, 154 to 159 at 5 wt% and 23 to 84 at 10 wt%, while the dielectric loss was stabilized below 0.31.

Figure 5-58 lists SEM images of one layer $\text{CaCu}_3\text{Ti}_4\text{O}_{12}/\text{P}(\text{VDF-TrFE})$ composites. It should be noted that the interface's problem, which used to persist in nano-size composites disappeared, and the microstructure becomes even more uniform than the previous hot pressed sample. However, with higher silane concentration, the microstructure tends to give porous structure, which is similar to the results in micro-size composites, and indicates the necessity to optimize the silane concentration. Those SEM images have corroborated with the dielectric results. The temperature dependent results in Figure 5-59 showed the same behavior as the one in the micro-size composite. Based on the dielectric results and microstructure analysis, the bridge-linked action between $\text{CaCu}_3\text{Ti}_4\text{O}_{12}$ ceramic particle and polymer matrix can be better fulfilled with nano-size $\text{CaCu}_3\text{Ti}_4\text{O}_{12}$ ceramic particle, which own higher surface-volume ratio and relative mass. In short, a more flexible composite based on coupling effect with good dielectric performance has been fabricated.

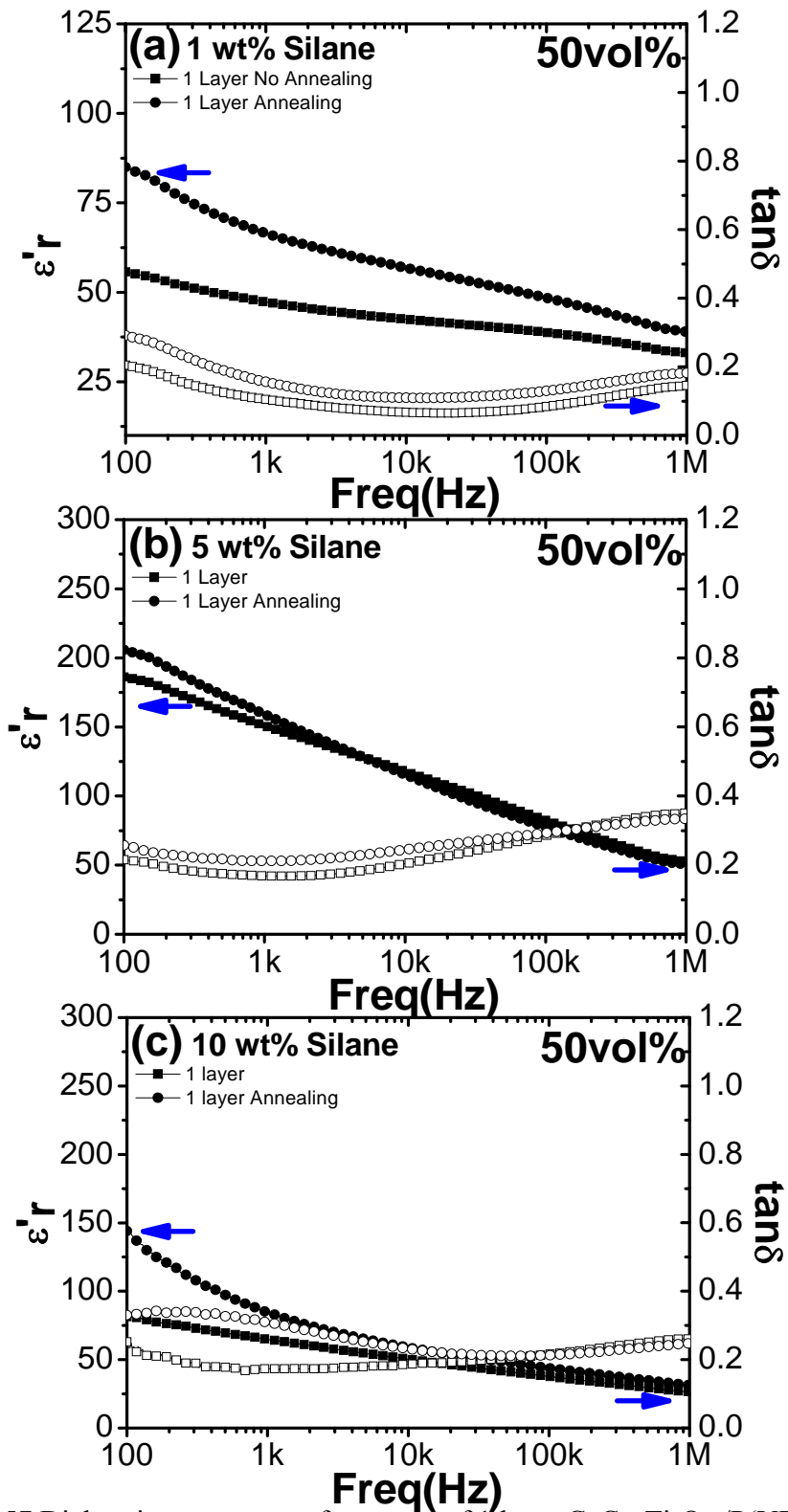


Figure 5-57 Dielectric response vs. frequency of 1 layer $\text{CaCu}_3\text{Ti}_4\text{O}_{12}/\text{P}(\text{VDF}-\text{TrFE})$ composite (50 vol% nano-size $\text{CaCu}_3\text{Ti}_4\text{O}_{12}$) with (a) 1, (b) 5 and (c) 10 wt% silane.

Table 5-11 Summary of dielectric data for 1 layer $\text{CaCu}_3\text{Ti}_4\text{O}_{12}/\text{P}(\text{VDF-TrFE})$ composite (nano-size and μ -size $\text{CaCu}_3\text{Ti}_4\text{O}_{12}$) with 1, 5 and 10 wt% silane with annealed at 125 °C (1 kHz).

		Silane concentration (wt%)		
		1 wt%	5 wt%	10 wt%
Nano-size	^[1]	47/0.1	151/0.2	65/0.2
	^[2]	67/0.2	159/0.2	84/0.3
μ -size	^[1]	47/0.2	145/0.4	15/0.6
	^[2]	73/0.2	154/0.3	23/0.6

^[1]: Casting at 70 °C/8 hrs.

^[2]: Casting at 70 °C/8 hr and annealing at 125 °C/8 hrs.

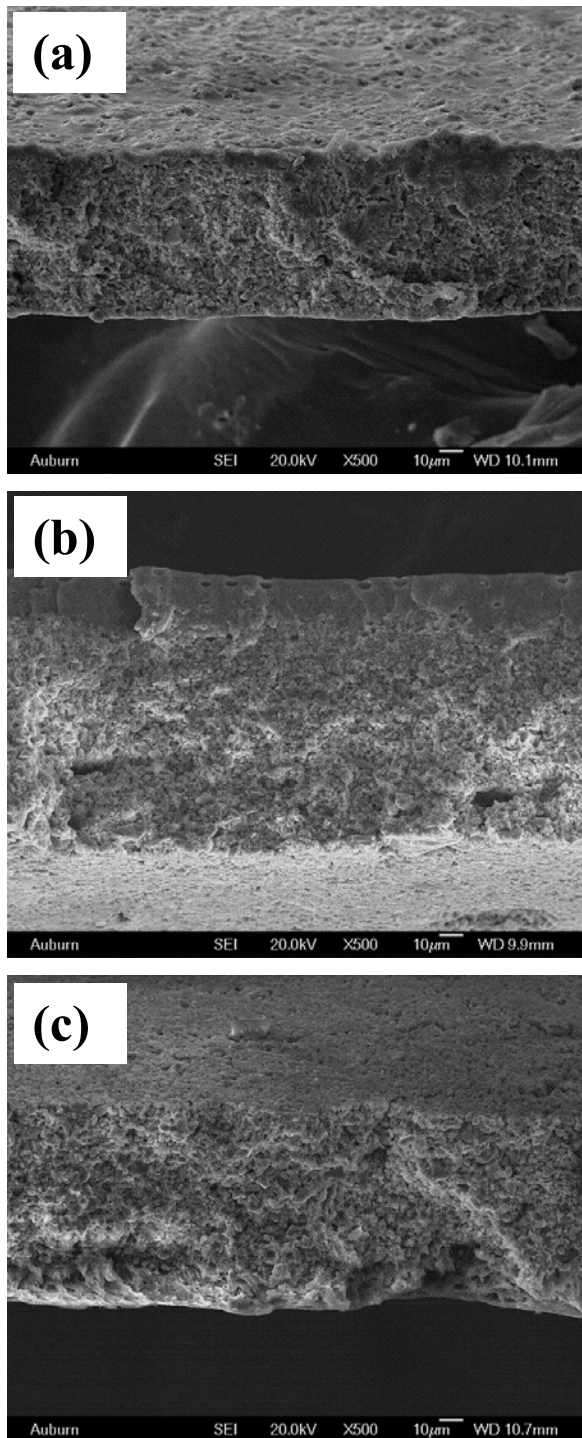


Figure 5-58 SEM fractographs of one layer $\text{CaCu}_3\text{Ti}_4\text{O}_{12}/\text{P}(\text{VDF-TrFE})$ composites (50vol% nano-size $\text{CaCu}_3\text{Ti}_4\text{O}_{12}$) with: (a) 1, (b) 5 and (c) 10 wt% silane, respectively.

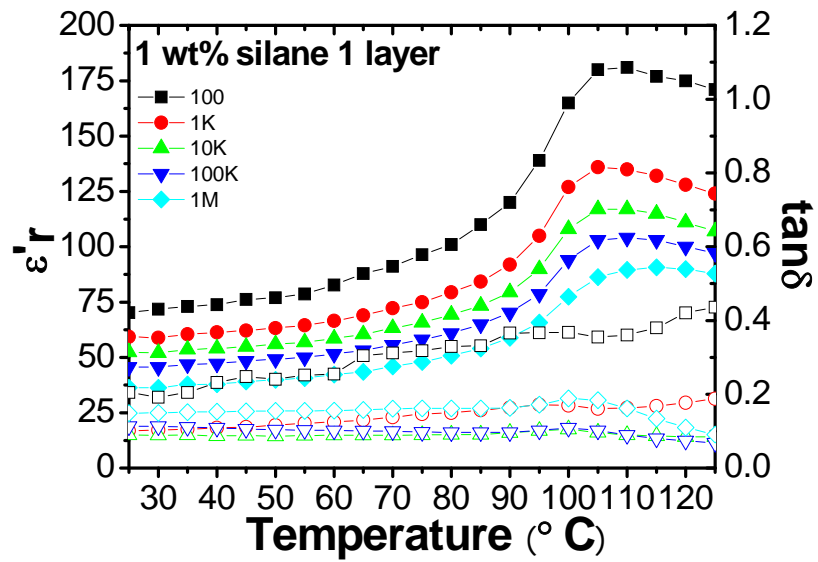


Figure 5-59 Temperature dependence of one layer $\text{CaCu}_3\text{Ti}_4\text{O}_{12}/\text{P}(\text{VDF-TrFE})$ composite (50 vol% μ -size $\text{CaCu}_3\text{Ti}_4\text{O}_{12}$) with 1 wt% silane.

5.4 Summary

Composites based on nano-size $\text{CaCu}_3\text{Ti}_4\text{O}_{12}$ ceramic particles were studied. The morphology of the ceramics was studied using SEM. Their dielectric responses were studied over a frequency range from 100 to 1 MHz. It was found that the dielectric constant in a nano-size composite is smaller than that in a micro-size composite. Based on the fitting results using different models, it was found that the effective dielectric constant of the nano-size $\text{CaCu}_3\text{Ti}_4\text{O}_{12}$ particles is much smaller than that of micro-size $\text{CaCu}_3\text{Ti}_4\text{O}_{12}$ particles. This may be caused by the interfacial layers. That is, the dielectric constant from the fitting is actually the effective dielectric constant of $\text{CaCu}_3\text{Ti}_4\text{O}_{12}$ particles and the interfacial layers. However, $\text{CaCu}_3\text{Ti}_4\text{O}_{12}/\text{P}(\text{VDF-CTFE})$ 88/12 mol% (VC88) composites exhibit a smaller difference in dielectric constant between nano-size and micro-size particles than that in $\text{P}(\text{VDF-TrFE})$ 55/45 mol% copolymer. Moreover, in order to improve the wettability between ceramic and polymer, silane has been used as a coupling agent and the silane coupling effect on the $\text{CaCu}_3\text{Ti}_4\text{O}_{12}$ -based composites was studied. Flexible composites with a dielectric constant of 159 and loss of 0.2 were obtained.

References

- (1) Arbatti, M.; Shan, X. B.; Cheng, Z.-Y. *Adv. Mater* **2007**, 19, 1369-1372.
- (2) Arbatti, M. Development of High-Dielectric-Constant Polymer-Ceramic Composites Based on Calcium Copper Titanate. Auburn University, Alabama, 2004.
- (3) Shan, X. B.; Yang, X.; Zhang, K. W.; Cheng, Z.-Y. *Mater. Res. Soc. Symp. Proc.* **2007**, 949, 0949-C05-07.
- (4) Shan, X. B.; Zhang, L.; Wu, P. X.; Xu, C. R.; Cheng, Z.-Y. *Mater. Res. Soc. Symp. Proc.*, **2009**, In Processing.
- (5) Lewis, T. J. *J. Phys. D: Appl. Phys.* **2005**, 38, 202-212.
- (6) Nelson, J. K.; Hu, Y. *J. Phys. D: Appl. Phys.* **2005**, 38, 213-222.

CHAPTER 6

CONCLUSION AND FUTURE WORKS

6.1 Summary of Results and Conclusions

(1) $\text{CaCu}_3\text{Ti}_4\text{O}_{12}$ ceramics were prepared using a conventional solid-state reaction under different conditions, such as molding pressure, milling media and time, and calcination temperature and time. Ceramic samples with a dielectric constant of 160,000 and loss of 0.15 at 1 kHz were obtained after calcination at 900 °C and sintering at 1075 °C for 72 hours.

(2) Regarding the polarization mechanism in $\text{CaCu}_3\text{Ti}_4\text{O}_{12}$ ceramic, three different processes were founded. Although the dielectric response at low frequency increases with decreasing thickness, the dielectric behavior for the high frequency relaxation process is weakly dependent on thickness.

(3) Composites based on micro-size $\text{CaCu}_3\text{Ti}_4\text{O}_{12}$ ceramic and P(VDF-TrFE) 55/45 mol% copolymer were prepared and studied. The influence of processing parameters such as annealing and HP on the properties of the composites has been studied. Flexible composite with dielectric constant of 510 and loss of 0.25 at 1 kHz was obtained at room temperature.

(4) The dielectric response of the composites was analyzed. It was found that the relaxation time of the major relaxation process obtained in the composite changes with concentration, as well as on process conditions. This indicates the existence of the interfacial layer in the composite. It was also found that the observed loss at low frequency in the composite is due to a relaxation process, instead of conductivity.

(5) The dielectric response of $\text{CaCu}_3\text{Ti}_4\text{O}_{12}/\text{P}(\text{VDF-TrFE})$ composites based on nano-size ceramic particles was studied. Compared with micro-size composites, both the dielectric constant and loss in nano-size composites are found to be smaller than that in micro-size composites.

(6) The dielectric properties of $\text{CaCu}_3\text{Ti}_4\text{O}_{12}/\text{P}(\text{VDF-CTFE})$ 88/12 mol% (VC88) composites were studied. These composites exhibited a high dielectric constant and small loss almost independent of the temperature, which is good for some applications. It was also found that the difference of dielectric constant between nano-size and micro-size particles is much smaller than that in $\text{P}(\text{VDF-TrFE})$ 55/45 mol% copolymer.

6.2 Future Works

(1) High dielectric constant has been demonstrated within $\text{CaCu}_3\text{Ti}_4\text{O}_{12}/\text{P}(\text{VDF-TrFE})$ 55/45 mol% composites. It would be interesting to prepare the $\text{CaCu}_3\text{Ti}_4\text{O}_{12}$ -based composite using a different polymer matrix in order to develop different composites for various applications.

(2) It should be noted that the high dielectric constant was observed in the composite using HP. Certainly, HP is not desirable for industrial processes. Therefore, a new process to produce high dielectric constant should be exploited, such as solution casting using silane agent and extrusion process.

(3) Three processes were founded in the $\text{CaCu}_3\text{Ti}_4\text{O}_{12}$ ceramics. Continuous study on the three processes and corresponding microstructure of the ceramics would deepen the understanding of the polarization mechanism of the ceramics.